SYNTHESIS, CHARACTERISATION AND FLUORESCENCE PROPERTIES OF SUBSTITUTED IMIDAZOLES AND BRIDGED BIS-PHENOL LIGANDS AND MAGNETIC BEHAVIOUR OF THEIR METAL COMPLEXES

BY

Raymond Akong **AKONG**

BSc. Industrial Chemistry (Ibadan); MSc. Inorganic Chemistry (Ibadan)

MATRIC NUMBER: 111717

A Thesis in the Department of Chemistry

Submitted to the Faculty of Science

In partial fulfilment of the requirement for the Degree of

DOCTOR OF PHILOSOPHY

of the

UNIVERSITY OF IBADAN

Ibadan, Nigeria

JULY, 2023

CERTIFICATION

I certify that this work was carried out by Raymond Akong AKONG (Matric No.: 111717) under my supervision in the inorganic laboratory of the Department of Chemistry, Faculty of Science, University of Ibadan, Ibadan, Nigeria; as well as the Institut Für Anorganische und Analytische Chemie (IAAC), Friedrich-Schiller Universität Jena, Germany.

Professor J. A. O. Woods
B.Sc, M.Sc, Ph.D (Ibadan)
Professor of Inorganic Chemistry
Department of Chemistry
University of Ibadan, Ibadan, Nigeria

DEDICATION

This work is dedicated to Almighty God, especially for another chance at life, and to the memory of my parents Mr. and Mrs. J. A. AKONG.

ACKNOWLEDGEMENTS

My sincere gratitude goes to my supervisor and mentor Professor J. A. O. Woods. I am greatly indebted to you and thank you for your intense support (academically, financially, morally and spiritually) in the course of my academic journey (since my undergraduate research efforts), and more especially during this work.

I thank Professor P. C. Onianwa, the Head of Department, Department of Chemistry, University of Ibadan, Ibadan, {as well as past Heads of Department – Professor T. I. Odiaka and Professor A. A. Adesomoju}, for the opportunity to carry out this work in the department. I am grateful to all members of staff (academic and non-teaching) of the department for their encouragement. I thank especially members of the inorganic unit: Professor T. I. Odiaka, Dr. Helen O. Omoregie, Dr. Tunmise T. Eugene-Osoikhia, Dr. Temitope E. Olalekan and Mr. D. T. Ibukun. Although gone to rest with the Lord, the marks of Dr. A. J. Odola, Professor Aderoju A. Osowole and Mrs. Precious Farotade {Nee Ojattah} remains indelible in the sands of time.

I deeply appreciate Dr. Abiodun O. Eseola (Redeemer's University and IAAC) for his patience, suggestions and encouragement in the course of my graduate work.

I express great thanks to Professor Dr. Winfried Plass of the Institut Für Anorganische und Analytische Chemie (IAAC), Friedrich-Schiller Universität Jena, Germany, for the opportunity to carry out bench work in his laboratory. I am grateful to all members of the Plass group: Axel, Seun, Aroua, Jens, Benjamin, Andreas, Kristine, Juliane, and Florian. I am particularly grateful for the support received during the COVID-19 period. I am also grateful to Dr. Helmar Görls (for all crystallographic measurements), Frau Werrmann (for powder diffraction measurements), and all members of the NMR and MS laboratory at IAAC.

I want to say a big thank you to my wife, Emilia and my "girls", Veronica and Valerie – your support and prayers are deeply appreciated (I love you all). I also thank my siblings Vero (Big Sis), Tonia, Comfort, Greg, Paulina, Anna and Ashi for their prayers. It would have been wonderful for "mummy" and "papa" to be physically around too, but God knows best. I express deep gratitude to my in-laws, the Okeke's – thank you all for your prayers.

I thank Pastor Ayodele, Mr. Ikpea, Mr. Oloyede Hammed, Dr. Ajayeoba Temitope as well as past and present members of the Woods group (including Dayo, Sakiru, Susan, Tega, Lawal, Tijesu, Saint, Matthew, Gift and Taiwo) – you all added spices to this journey. I also want to appreciate Pastor and Pastor Mrs. Bamgbose and all staff members (past and present) at the Educational Advancement Centre (EAC), Bodija, Ibadan – it has been great being part of the EAC family. I also say a big thank you to Professor S. I. B. Cadmus for his encouragement. I deeply appreciate the Amunde family, Mr. Aponmade, I. O (former Bursar University of Ibadan) as well as members of the legion of Mary, especially members of Queen of Apostles praesidium (at Seat of Wisdom Catholic Church, University of Ibadan) who played great roles in helping me settle in Ibadan and live out my faith in God Almighty.

May God Almighty bless and keep us all. AMEN!!!

ABSTRACT

Increasing release of harmful metal(II)/metal(III) into the environment has led to a search for ligands with high sensitive and selective abilities to detect these ions. Studies on metal(II) are known but there is need for ligands that can sense its presence at low concentration. Also, studies on metal(III) are limited due to its poor coordination with ligands. Information on the use of multi-donor imidazole derivatives as well as pentadentate S-/O-bridged bis-phenol imines, with metal-chelating ability, as sensors are scarce. Therefore, the aim of this study was to synthesise and characterise structurally diverse imidazoles, imidazole-imines, bridged bis-imine ligands, their metal complexes, and investigate the magnetic and sensing properties of these materials.

Nitro- and bis-imidazoles were prepared by one-pot reaction of appropriate aldehyde, 1,2-dicarbonyls, aniline (nitrogen-phenyl variants) and ammonium-acetate dissolved in acetic-acid and refluxed at 120^{o}C for 5 hrs. Nitrogen-methyl variants were prepared by methylation of the nitrogen-hydrogen imidazoles, using methyl-iodide and potassium carbonate. Imidazole-amines were prepared by catalytic hydrogenation of the nitro-imidazoles for 2 hrs. Tridentate-imidazole-imines were prepared by condensation of salicylaldehyde/ pyridine-2-carboxaldehyde with appropriate imidazole-amines, while the pentadentate S-/O-bridged-imines were prepared by condensation of salicylaldehyde/its derivatives with bis(2-aminophenyl)sulphide/bis(2-aminophenyl)ether. Metal complexes were prepared by reacting the imines with cobalt acetate and copper acetate, separately. The compounds were characterised by elemental analysis, Mass, NMR and IR spectroscopies, X-ray crystallography and magnetic measurements. Sensing properties of the ligands were determined using fluorescence measurements to detect metal(II) and metal(III).

Nine nitro-imidazoles (N1 – N9), seven bis-imidazoles (BI_1 – BI_7), nine imidazole-amines (A1 – A9), nine nitrogen-nitrogen-oxygen imines (I_1 – I_9), eight pentadentate-imines (H_2S_{1-7} – H_2O_1) and forty-three metal complexes were obtained. Elemental and mass analysis of some representatives: BI_1 [C,(81.99%), H(5.13%), N(10.66%); *m/z* = 515.22], I_9 [C(83.10%), H(4.78%), N(8.61%); *m/z* = 489], H_2O_1 [C(76.13%), H(4.88%), N(6.80%);

m/z = 408], Co_2S5_2 [C(39.31%), H(1.71%), N(3.48%), S(4.03%); *m/z* = 1616.5] agreed with proposed molecular formula $C_{36}H_{27.5}N_4O_{0.75}$, $C_{34}H_{23}N_3O$, $C_{26}H_{20}N_2O_3$, and $C_{52}H_{28}Br_8Co_2N_4O_4S_2$, respectively. In pentadentate-imines, phenanthrene and naphthalene substitutions resulted in downfield-shift of $OH_{phenolic}$, while *p*-methyl/bromo substitution resulted in upfield-shift. Ligands exhibited $C{=}N_{imine}$ bands around 1591-1617 cm^{-1} and OH_{phenol} bands around 3371-3383 cm^{-1}. In the complexes, these bands shifted to 1577-1605 cm^{-1} and disappeared, respectively, suggesting coordination through N_{imine} and O_{phenol} atoms. Distorted tetrahedral/square-planar, trigonal-bipyramidal and octahedral geometries were observed in the complexes. The magnetic susceptibility (cm^3Kmol^{-1}) for the dinuclear Co(II) [4.09-5.20], dinuclear Cu(II) [0.82-0.86] and trinuclear Cu(II) [1.18-1.21] complexes were larger than expected [3.75, 0.75 and 1.125, respectively], indicating orbital contribution. Extension of π-conjugation at positions 4 and 5 of the imidazole resulted in higher quantum-yields (4-10 folds), while substitution at the nitrogen-hydrogen position resulted in lower quantum-yields (4-10 folds). Among the imidazole-imines, I_9 exhibited the best selectivity for Zn^{2+} with Limit of Detection (LOD) 4.45 nM. Donor-acceptor capabilities (O-H···N), in the pentadentate-imines, enabled excited state intramolecular proton transfer behaviour and H_2O_1 exhibited best selectivity for Al^{3+} with LOD 5.48 nM.

Structures of substituted imidazoles and bridged bis-phenol imines with their cobalt(II) and copper(II) complexes were established. Structural variation aided different magnetic properties and excellent detection for aluminium(III) and zinc(II).

Keywords: N-/S-/O-donor ligands, Excited State Intramolecular Proton Transfer, Al^{3+} sensing, Zn^{2+} sensing, oxo-bridged complexes.

Word count: 498

TABLE OF CONTENTS

CHAPTER FOUR: Results and Discussion

CHAPTER FIVE: Summary, Conclusion and Recommendations

List of Tables

List of Figures

List of Schemes

List of Abbreviations

ac	– Alternating current
AcOH	– Acetic acid
BDP	– Boron dipyrromethene
bpy	– 2,2′- bipyridine
CHEF	– Chelation Enhanced Fluorescence
CW-ESR	– Continuous Wave Electron Spin Resonance
dc	– Direct current
DCM	– Dichloromethane
EDTA	– Ethylene Diamine Tetraacetic Acid.
ESICT	– Excited State Intramolecular Charge Transfer
ESIPT	– Excited State Intramolecular Proton Transfer
ESR	– Electron Spin Resonance
EtOH	– Ethanol
HDvV	– Heisenberg-Dirac-van Vleck
HOMO	– Highest Occupied Molecular Orbital
ICT	– Intramolecular Charge Transfer
LUMO	– Lowest Unoccupied Molecular Orbital
MeCN	– Acetonitrile
MeOH	– Methanol
MIC	– Maximum Inhibitory Concentration
MLCT	– Metal to Ligand Charge Transfer
MOFs	– Metal-Organic Frameworks
OLEDs	– Organic Light Emitting Diodes
PET	– Photoinduced Electron Transfer
Phen	– 1,10-phenanthroline
QTM	– Quantum Tunnelling of Magnetisation
SIM	– Single Ion Magnet
SMM	– Single Molecule Magnet
SOC	– Spin-Orbit Coupling
SOMO	– Singly Occupied Molecular Orbital
SQUID	– Superconducting Quantum Interference Device
ZFS	– Zero Field Splitting

CHAPTER ONE

INTRODUCTION

1.1 Background to the study

Organic and inorganic materials continue to show great potentials in various fields and have been used for flame retardation (He *et al*., 2020), light emitting diodes {LED} (Zhong *et al*., 2020; Li *et al*., 2020; Worku *et al*., 2020), replacing glass in display and electronic devices (Chang, 2020), in biomedicine {including health monitoring, implantation, drug delivery, tissue repairs}, motion detection, human-machine interfaces (Duan *et al*., 2020; Park *et al*., 2020; Lee *et al*., 2021), gas adsorption (Liu *et al*., 2014), light-emitting electrochemical cells (Fresta *et al*., 2018; Keller *et al*., 2014; Keller *et al*., 2016), elastic infrared {IR} transmitting materials (Kuwabara *et al*., 2020), thermally activated delayed fluorescence {TADF} emitters (Linfoot *et al*., 2014), visualisation and quantification of mechanical stress (Yamamoto *et al*., 2021) and oxygen evolution reaction (Anamika *et al*., 2020). While inorganic materials have the extra advantage of magnetic, optical, thermal and mechanical properties (Park *et al*., 2020; Fresta *et al*., 2018); organic materials are believed to be cheaper, more available, flexible to molecular modification and more amenable to wider applications (Smith *et al*., 2017; Guo *et al*., 2017; Kuwabara *et al*., 2020; Garnier *et al*., 1993).

Materials with unique electronic and photophysical properties are of great importance in chemistry and materials science, where an understanding of the relationship between functionalisation {structural modification} and properties is key (Gowda *et al*., 2011; Hrdlovic *et al*., 2010; Fresta *et al*., 2018; Kuwabara *et al*., 2020). Ligand choice has a profound role in the properties of materials as it {ligand choice} affects important properties such as Highest Occupied Molecular Orbital-Lowest Unoccupied Molecular Orbital {HOMO-LUMO} band gap/energy (Benavent *et al*., 2020; Rajakannu *et al*., 2020), rigidity {which affects emission potential and efficiency}, stability, ability to extend π-conjugation, (Yamazaki *et al*., 2020; Kumar *et al*., 2014; Kim *et al*., 2021), light harvesting (Smith *et al*., 2017; Guo *et al*., 2017), catalytic activity in chemical transformations (de

Azambuja *et al*., 2021; Tortajada *et al*., 2021; Khattak *et al*., 2019), redox potential (Timmer *et al*., 2021; Sajoto *et al*., 2005), molecular aggregation (Chan *et al*., 2021), charge transfer {CT} excited state and spin-orbit coupling {SOC} properties of systems (Shi *et al*., 2021). The nature of the ligand {multidentate, bidentate or monodentate} has been observed to affect reaction kinetics and selectivity, increase the strength of metal-ligand binding, show fewer problems {isomerism, reaction of redistribution} and offer greater thermal stabilities. Bridging ligands are known to aid diverse topologies, properties and applications (Burrows *et al*., 2021; Wurzenberger *et al*., 2020; Janiak, 2003), while the use of σ-donating aquo ligand {in place of electron donating chlorido ligand} has been observed to result in a blue-shift, higher oxidation potential and higher catalytic activity (Cuéllar *et al*., 2021). Increase {and decrease} in the π-system of a series of cyclometalating {C^N} ligands produced red-shifted emissions {although a blue-shift was expected with the reduction in the π-system} (Sajoto *et al*., 2005), while variation {arising from substituent effect} produced field-induced slow magnetic relaxation behaviour {^{t}Bu giving the best effect} and distortion from ideal square-planar geometry to a seesaw geometry resulted in higher axial magnetic anisotropy (Zhai *et al*., 2021).

Organic ligands possessing hetero-atoms are commonly known for their ease of preparation, commercial availability and ease of bond formation with metal ions. Schiff bases play an important role in inorganic chemistry, especially because of their ability to coordinate and form stable complexes with most transition metal ions – and these Schiff base complexes are increasingly utilised in the field of bioinorganic chemistry (Al-Sha'alan, 2007; Ashiq *et al*., 2013). Multidentate Schiff base ligands offer variety of coordination property as well as bridging modes allowing for multinuclear complexes (Kushvaha *et al*., 2019). The use of nitrogen-rich azole ligands has been reported to give great stability in the preparation of the very sensitive silver fulminate, aid the electrocatalytic reduction of CO_2, provide better directing ability in C-H functionalisation, as well as a rigid skeleton {with conjugated π-electrons} (Wurzenberger *et al*., 2020; Cuéllar *et al*., 2021; Mo *et al*., 2021; Li *et al*., 2021). The σ-donating ability of imidazoles {which destabilises the LUMO} has been found useful in tuning of emission energy (Pal *et al*., 2018).

There is increasing interest in the preparation of modified ligands with investigations focused on potential applications of the ligands as well as their metal complexes.

1.2 Justification of Research

An understanding of structure and property is crucial in the preparation of materials for the future. Molecular derivatisation brings about tuning of electrostatic environment, offering a systematic approach to understanding the correlation between structure and property. The functionalisation of molecules imparts substrate binding, thus the design and construction of chemosensors for selective and sensitive detection and monitoring of analytes, including heavy metal ions like Cd^{2+}, Cu^{2+}, Hg^{2+}, Zn^{2+}, M^{3+} {including Al^{3+}} is a current area of interest. Ligand design and modification is also crucial in coordination chemistry, enabling structural tuning to optimise optical and magnetic properties of transition metal complexes. Systematic tuning of molecules {through elongation of conjugation, use of heteroatoms, peripheral substitution using electron withdrawing groups [EWG's] or electron donating groups [EDG's]} is important in the investigation of molecular properties, as it gives opportunity to optimise and improve the use of materials {for different applications} with implications in supramolecular chemistry and magnetochemistry. More so, the presence of heteroatoms {N, O, S} within a fluorophore makes it suitable for recognition of metal ions (Lin *et al*., 2012; Alreja and Kaur 2015).

Reports in the use of structurally diverse ligand architectures derived from 2-(((2-(1*H*-imidazol-2-yl)phenyl)imino)methyl)phenol, *N*-(2-(1*H*-imidazol-2-yl)phenyl)-1-(pyridin-2-yl)methanimine as well as pentadentate S-/O-bridged bis-phenol imines are scarce; the potential photophysical properties and electronic variation in such materials could aid host-guest- and magnetochemistry applications.

1.3 Statement of Problem

Detrimental effects of high levels of M^{II}/M^{III} cations released into the environment create a great need for ligands/receptors which are sensitivity to these ions and possess potential for selective detection/monitoring. More so, M^{III} cations tend to exhibit poor coordination {making fluorescence turn-on challenging} and comparatively few receptors are known for M^{III} {in comparison to M^{II}}. Schiff bases possessing multiple donor sites and ability for chelation may be effective in tackling the problem of poor coordination. There

is currently a growing need for receptors with ability to sense analytes at low concentrations. The rich electronic properties, potential for structural modulation and incorporation of varieties of functionalities, make imidazoles {and by extension imidazole imines} useful candidates in molecular ion recognition. More so, a study on the effect of electron donating and electron withdrawing groups on the coordination property of oxo-bridged complexes could provide more insight into their magnetic behaviour.

1.4 Aim and Objectives of Research

The aim of this research effort was to prepare and characterise structurally diverse ligand frameworks based on imidazoles, imidazole amines/imines and bridged {S/O/N=N} bis-phenol imines and explore the sensing potential of the prepared materials. In addition, the research aimed to prepare metal (Cr, Co, Ni, Cu) complexes of the ligands and investigate their magnetic behaviour. To achieve these aim, the set objectives are as follows:

(i). Synthesise and characterise bis-imidazoles from 1,2-, 1,3- 1,4-dibenzaldehyde

(ii). Synthesise and characterise imidazoles/imidazole imines from 1,2-dicarbonyls {for the imidazoles} and salicylaldehyde {for the imidazole imines}

(iii). Synthesise and characterise bridged pentadentate bis-imine ligands

(iv). Synthesise and characterise metal complexes of these ligands

(v). Investigate the ability of the prepared ligands to detect M^{II}/M^{III} cations

(vi). Investigate the magnetic potentials of prepared complexes

CHAPTER TWO

LITERATURE REVIEW

2.1 Schiff Base

Nitrogen containing compounds offer extraordinary structural variability and can be obtained from cheap natural sources. They are generally easy to synthesise/manipulate and possess fair stability {for example against oxidation that is a common problem in phosphines} (Monge *et al*., 2013). Excellent redox properties, observed in nitrogen containing compounds, play a useful role in their applications (Kumar *et al*., 2020).

Schiff bases are condensation products of primary amines and carbonyl compounds {alkanals and alkanones} and were first reported in 19th century by Schiff Hugo Josef. The common structural feature of these class of compounds is the azomethine group with the general formula RHC=NR` {R, R` = alkyl, aryl, cycloalkyl, or heterocyclic groups, which may be substituted at various positions}. Since the azomethine {or imine} group replaces a carbonyl group (C=O), Schiff bases are considered analogues of ketones or aldehydes (Brodowska and Łodyga-Chruścińska 2014; Rahman *et al*., 2015; Ubani *et al*., 2015). They are known to exist in variety of structures, depending on the carbonyl and amine and these structural possibilities accounts for a great interest in them and their complexes (Anacoda *et al*., 2013; Liu and Hamon 2019). Schiff bases {like substituted benzene, biphenyls, stilbenes, azobenzenes, ferrocenyl} are known to constitute conjugated π-systems which may contain asymmetrically positioned electron-donor and electron-acceptor substituents – the π-system often imposes geometrical restriction and affects electronic structure. As a result of the charge transfer between the functional groups, a high degree of polarity exists within the molecules leading to variety of electronic and structural properties which are useful in electrooptic devices and data storage. The charge transfer property can be enhanced by increasing the donor-acceptor strength and increasing the length of conjugation (Yimer, 2015). The presence of a lone pair of electrons in a sp^2 hybridized nitrogen atom of the azomethine group, as well as the synthetic availability of Schiff bases, is of considerable chemical and biological importance (Patai 1970; Babahan *et al*., 2013;

Dilmaghani *et al*., 2015; Khan *et al*., 2015), hence their use in a large number of bioactive compounds as well as in industry (Nakamoto, 1963; Al-Rawi *et al*., 2013; Alhadi *et al*., 2012). The constructive physical and chemical properties as well as the large number of reactions that Schiff bases undergo also makes them important in organic synthesis, catalysis, anti-oxidative activity and anti-corrosion activity (Ashokan *et al*., 2014; Akbolat *et al*., 2012; Anacoda *et al*., 2013). The azomethine linkage {-N=CH-}, in Schiff bases, enables variable bonding potentiality during complex formation – the ligands are capable of coordinating with one or more metal ions giving rise to mono- and polynuclear complexes {especially when functional groups like –OH or –SH are in close proximity to the azomethine group} (Shrestha and Maharjan 2012; Narang *et al*., 2000; Rahman *et al*., 2015; Chitra and Parameswari 2010; Ashokan *et al*., 2014; Monfared *et al*., 2007; Leirer *et al*., 1999).

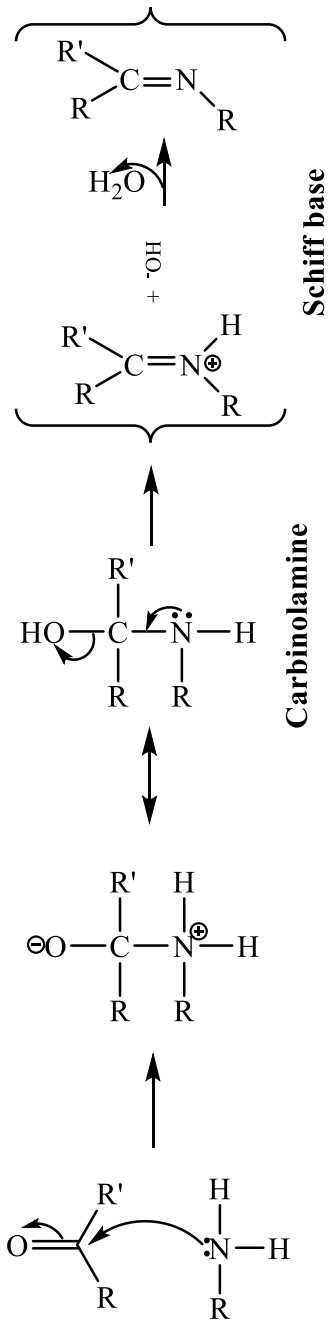

Scheme 2.1: General mechanism for Schiff base formation

2.1 Imidazoles

Heterocyclic compounds are widely distributed in nature and are essential for life (Pradhan *et al*., 2015). These cyclic organic compounds have one or more of their carbon atoms replaced by such atoms as N, O, or S. They may be simple aromatic rings or non-aromatic rings. Heterocycles containing S and/or N atoms are useful functional materials – the presence of the heteroatom helps to stabilise ions or ion radical species, increases π-conjugation {decreasing columbic repulsion}, produce intermolecular interactions which may lead to novel molecular assemblies. Ring-fused heterocycles possessing more than one nitrogen atom play an important role in biochemical processes and coordination chemistry. These ligands can act as neutral or anionic species or bridging systems, allowing various modes of coordination with metals. The growing interest in heterocyclic azo chemistry is focused on designing new materials, theoretical calculations and applications in various industrial fields (Ashish *et al*., 2011; Mahdi *et al*., 2014).

Azoles {imidazoles and triazoles} are widely studied and the imidazole ring is present in many medicinally active organic compounds and natural products such as histidine, etomidate {the *R* form}, cimetidine, omeprazole, ketoconazole {two stereochemical forms are known}, flumazenil, biotin, Lepidiline B, trifenagrel and many alkaloids {**Fig. 2.1(a)**} (Pal *et al*., 2011; Bandyopadhyay *et al*., 2011; Samanta *et al*., 2013; Wu *et al*., 2012; Kaur and Alreja 2015).

Imidazole is a planar, five membered heteroaromatic molecule with pyrrole type and pyridine type annular nitrogen atoms. The imidazole ring is biologically relevant, mimicking histidine, potentially enabling it to bind with biomolecules; the ring is an important binding site {commonly attributed to the pyridine like nitrogen within the ring}, and plays an important role in the active centre of a large number of metalloproteins {including serum albumin, peptides, pseudo-peptides, polyamines}. In comparison to pyridine, its six electrons are delocalised on five atoms, resulting in higher electron density and stronger coordination ability (Mazlan *et al*., 2014; Brooks *et al*., 1960; Török *et al*., 1998; Romero *et al*., 2014; Pradhan *et al*., 2015; Kaur and Alreja 2015; Chen, 2016). Imidazoles are weak π-acceptor ligands. They can serve as a base and as a weak acid {can acts as proton donor/acceptor and charge transfer agent}; they are susceptible to

electrophilic and nucleophilic attack {to form functional derivatives}; thermally stable and resist redox as well as acid-base conditions. They possess diverse weak interactions which allow binding with enzymes and receptors {including anions and cations} through hydrogen bonds, coordination, ion–dipole, cation–π, π–π stacking, hydrophobic effects and van der Waals forces. They possess extensive intramolecular hydrogen bonding and exist in two equivalent tautomeric forms as one of its hydrogen atoms can be located on either of the two nitrogen atoms {**Fig. 2.1**(**b{i}**)}; the imidazolium analogues {**Fig. 2.1**(**b{ii}**)} offer electrostatic interaction, aggregation, and self-assembly. The π-excessive and strong σ-donor character of imidazoles make them useful in coordination chemistry (Leirer *et al*., 1999; Romero *et al*., 2014; Ashish *et al*., 2011; Anderson *et al*., 2010; Zhang *et al*., 2014; Alabdali *et al*., 2014; Chen, 2016).

Imidazole and its derivatives have potential for manifold functionalisation, as its ring imparts useful applications in optical and chemical sensors, fuel cell membrane, luminescent materials, ion-conducting electrolytes and photovoltaic materials for solar cell application, as well as supramolecular chemistry, agrochemicals and catalysis. They are known for their therapeutic properties as antimicrobial agents, anticryptococcal agents, cytotoxic agents and are also known to display interesting spectral, magnetic and structural properties (Joseyphus and Nair 2009; Zhang *et al*., 2014; Kaur and Alreja 2015).

The activity of some 2,4,5-trisubstituted imidazoles **2.1**(**c**) against some bacterial strains showed compound **2.1**(**c{ii}**) had the best activity {compared to the standard, Ciprofloxacin}, except for *P. aeruginosa* {where compounds **2.1**(**c{iii}**) and **2.1**(**c{v}**) showed comparable activity with the standard}. Compound **2.1**(**c{iv}**) showed least activity, generally, in comparison to the other synthesised compounds (Sarala *et al*., 2016).

In a series of imidazole-based calcitonin gene-related peptide {CGRP} receptor antagonists {**Fig 2.2**(**a**)}, the most potent compounds {in the series} had IC_{50} values of 0.19 nM and 0.39 nM. Attempts to improve the potency by substitution at the C4 and C5 position of the imidazole ring {**Fig 2.2**(**b**[**i**])} did not give an increase in potency, although microsomal stability was observed to increase. The introduction of pyridine ring at the N1 position {**Fig 2.2**(**b**[**ii**])} showed similar activity as compounds in **2.2**(**a**) and poor microsomal stability was observed (Tora *et al*., 2013).

Azomethine linkage of azoles {possessing aroyl-azolyl-ethane moiety} to pyridine-2-carboxamidrazones has been observed to show interesting activity against bacterial and fungal species. In the reported use of N^1-(1-aryl-2-(1*H*-imidazol-1-yl) and 1*H*-1,2,4-triazol-1-yl)-ethylidene)-pyridine-2-carboxamidrazone derivatives as biological agents, the aryl-imidazolyl derivatives {**Fig. 2.2(c{i})**} showed slight inhibition against *S. aureus* {MIC in the range 16 – 32 mg/L}, while no inhibition was observed for the triazolyl compounds {**Fig. 2.2(c{ii})**} [MIC > 128 mg/L]. Some of the reported compounds had MIC_{90} in the range 0.125 – 2 mg/L after 24 h and 0.5 – 4 mg/L after 48 h incubation time against twenty-one {21} *C. albicans* clinical strains {which is remarkable, compared to the standard used - amphotericin B and miconazole} (Banfi *et al*., 2006).

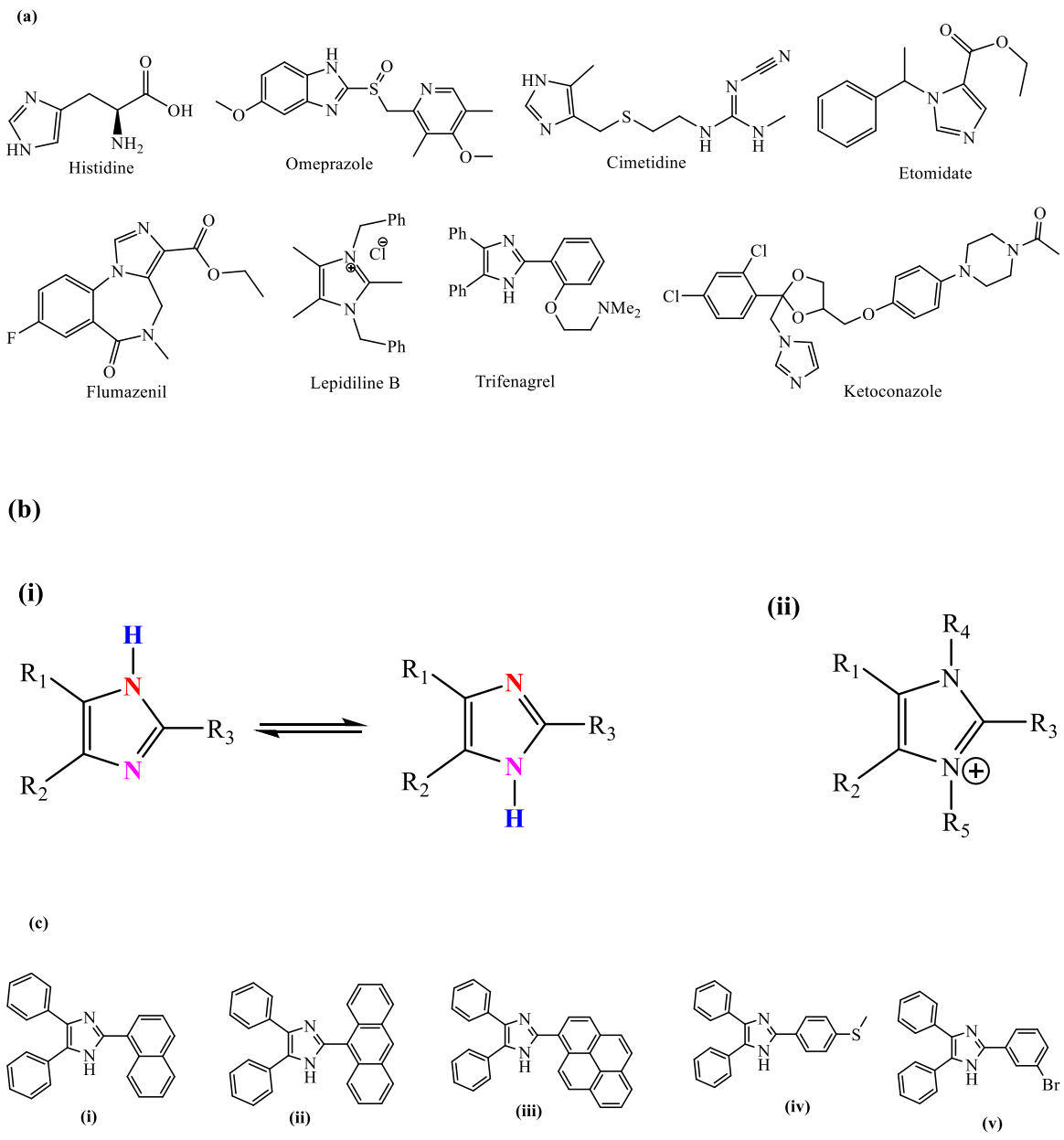

Figure 2.1: (a) Structures of some bioactive imidazoles (b) (i). Tautomeric forms of imidazole (ii). Structure of imidazolium and (c) Some biologically active 2,4,5-trisubstituted imidazoles (Sarala *et al*., 2016)

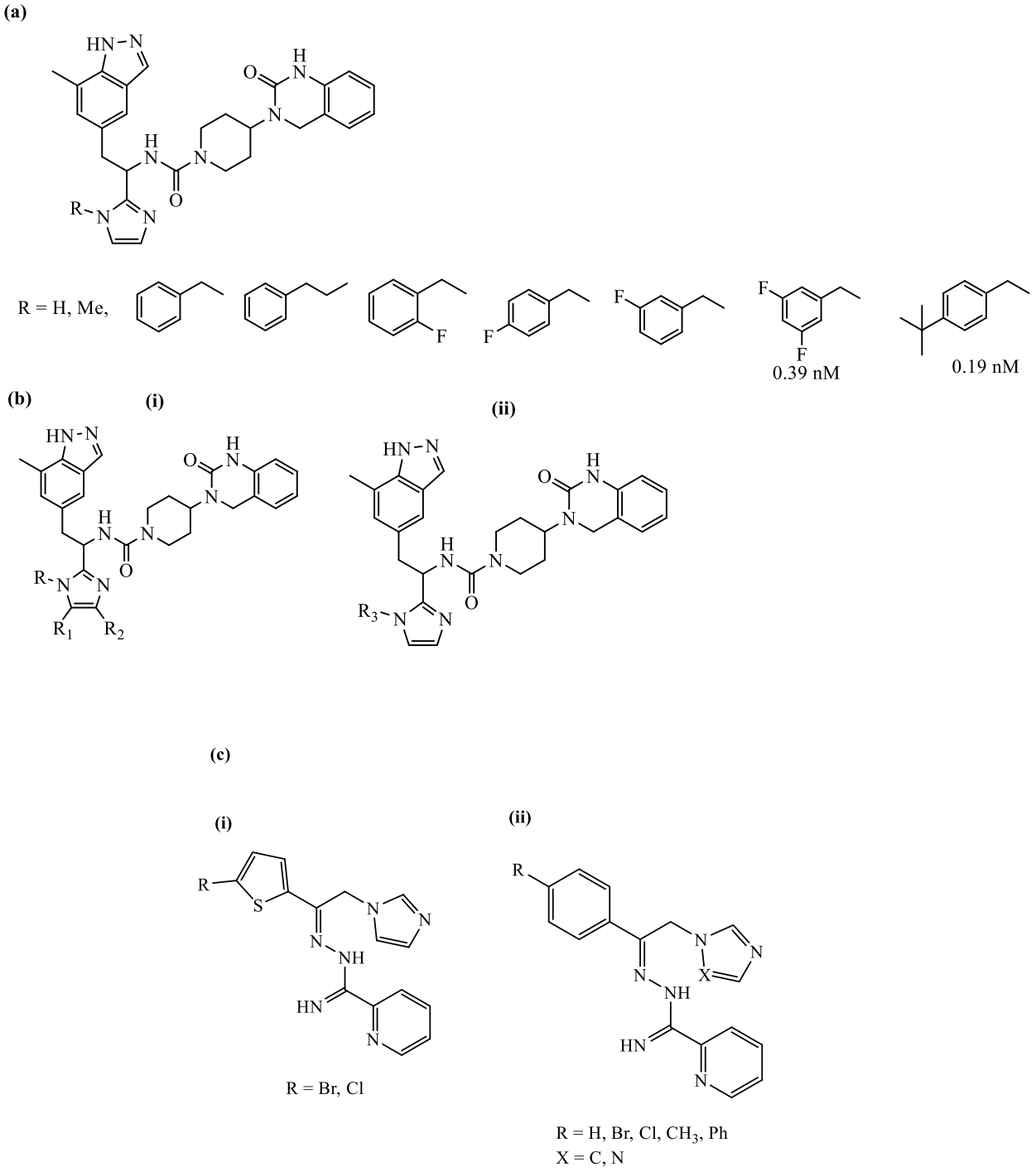

Figure 2.2: (a) - (b) Human CGRP receptor antagonist and (c) Imines used as biological agents. (Tora *et al*., 2013; Banfi *et al*., 2006)

The introduction of metal ions has been observed to show improved properties. The Co^{II}, Ni^{II} and Cu^{II} complexes, of the condensation product of imidazole–2-carboxaldehyde and glycylglycine, showed activity of the order Cu > Co > Ni > L (Joseyphus and Nair 2009). A comparative study of growth inhibition zones values of 2-(((2-(1*H*-benzo[*d*]imidazol-2-yl)phenyl)imino)methyl)-6-ethoxyphenol and its complexes against *E. Coli*, *S. aureus, B. subtilis* and *P. Fluorescence* indicated that the metal complexes exhibited slightly higher anti-bacterial activity than the free ligands (Sunitha *et al*., 2012).

In the area of organic transformation, a series of chiral imidazole-imines and imidazole-amides have been employed in asymmetric catalysis of Henry reaction {**Scheme 2.2**(**a**)}. The enantiomeric excess {*ee*} observed were generally very low {≤ 15}, although the amines {**Scheme 2.2**(**a{i}**) and (**a{ii}**)} were found to be more efficient than the less nucleophilic amides {**Scheme 2.2**(**a{iii}**) and (**a{iv}**)}, the attained *ee* increased throughout along with an increased bulk of the R group (Sívek *et al*., 2008). In another report, chiral NHC ligands were deployed in the asymmetric allylic alkylation between (*E*)-1,3-diphenylprop-3-en-1-yl acetate and dimethylmalonate {**Scheme 2.2**(**b**)} with *ee* in the range 0 – 92%. $[Pd(\eta^3\text{-}C_3H_5)Cl]_2$ was employed as the palladium source in the catalytic reaction, while the complex {**Scheme 2.2**(**b{i}**)} was prepared by reaction of appropriate ligand {**Scheme 2.2**(**b{ii}**)} with $[PdCl_2(MeCN)_2]$. Increase in the steric bulk of the NHC substituent increased the *ee*, while increase in reaction time did not affect the *ee* {although it increased the conversion rate} (Bonnet *et al*., 2003).

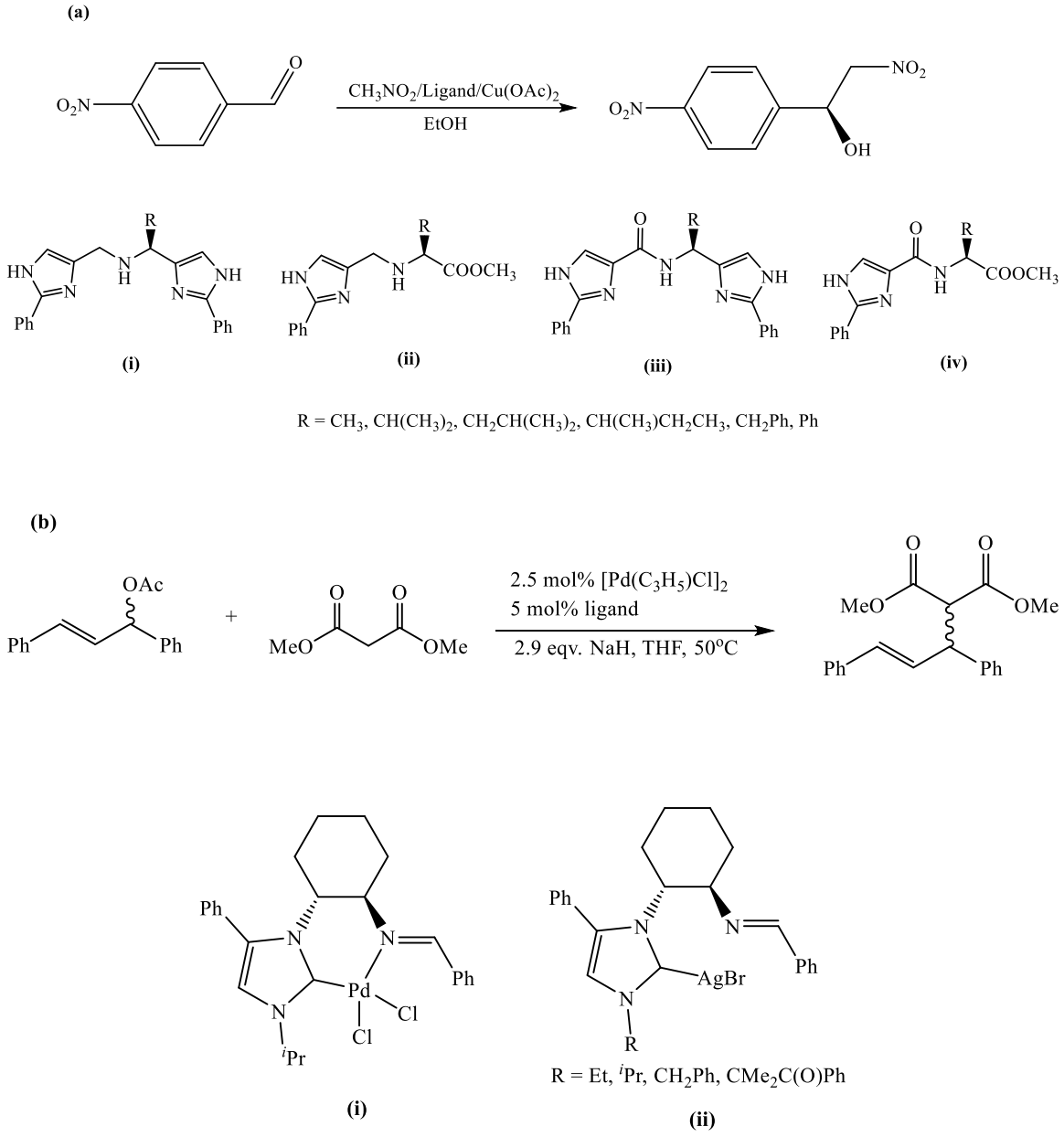

Scheme 2.2: (a) Henry reaction catalysed by chiral imidazole-imines and imidazole-amides (b). Chiral imidazole catalysed asymmetric allylic alkylation between (*E*)-1.3-diphenylprop-3-en-1-yl acetate and dimethylmalonate

The excellent fluorogenic and chromogenic properties of imidazoles allows them to be useful in the sensing of analytes. The spirolactam form of rhodamine dyes is non-fluorescent and colourless, while the amide form is known to be fluorescent and coloured. Exploring this knowledge and incorporating imidazole into the rhodamine skeleton, a turn-on fluoride ion sensor RDF-1 {**Scheme 2.3**(**a**)} has been reported. The UV-vis absorption study {in 3:7 MeCN/H_2O} of RDF-1 carried out with several anions {F^-, Cl^-, Br^-, I^-, CN^-, AcO^-, $H_2PO_4^-$, SCN^-, $P_2O_7^{4-}$, NO_3^-, NO_2^-} in 20 mM N-2-hydroxyethylpiperazine-N'-2-ethanesulfonic acid (HEPES) buffer {pH 7.4} solution did not show any observable absorption except for F^- at 528 nm when the colour changes from colourless to pink {indicating a change from the lactam form to the amide form of rhodamine}. Excitation at 500 nm did not show any fluorescence emission for all the other anions except F^- at 557 nm. Density Functional Theory {DFT} calculations indicated deprotonation of the imidazole N-H and formation of N-F bond. The RDF-1 was utilised for fluorescence imaging of fluoride in HeLa cells under physiological conditions (Gandhi and Duraisamy 2013). An imidazole-based imine ligand {**Scheme 2.3**(**b**)} has been found to exhibit a colour change from yellow to orange in the presence of Fe^{2+}/Fe^{3+} {although Cu^{2+} interferes with the process} and a "turn-on" effect in the presence of Al^{3+} and pyrophosphate. The ligand had detection limits of 0.32 µM {Fe^{2+}}, 0.27µM {Fe^{3+}} and 20.5 µM {Al^{3+}}. The association constant in the presence of Fe^{3+} {2.8 x 10^4 M^{-1}} was found to be twice that of Fe^{2+} {1.4 x 10^4 M^{-1}} (Jo *et al*., 2017).

The solid-state photoluminescent study, at room temperature, of a Zn(II) mixed ligand complex of 1,3,5-tris(1*H*-imidazol-4-yl)benzene {H_3L} and 1,4-benzenedicarboxylic acid {H_2pbdc}, [$Zn_2(H_2L)(pbdc)(\mu_2\text{-}OH)].2H_2O$, showed intense fluorescent emission at 410 nm {λ_{ex} = 348 nm}, while the ligands showed weak emissions at 408 nm {λ_{ex} = 360 nm} for H_3L and 390 nm {λ_{ex} = 355 nm} for H_2pbdc, suggesting intraligand fluorescence originated from the coordination interactions between the metal atom and the ligand, with enhanced conformational rigidity and decreased nonradiative energy loss (Chen *et al*., 2012).

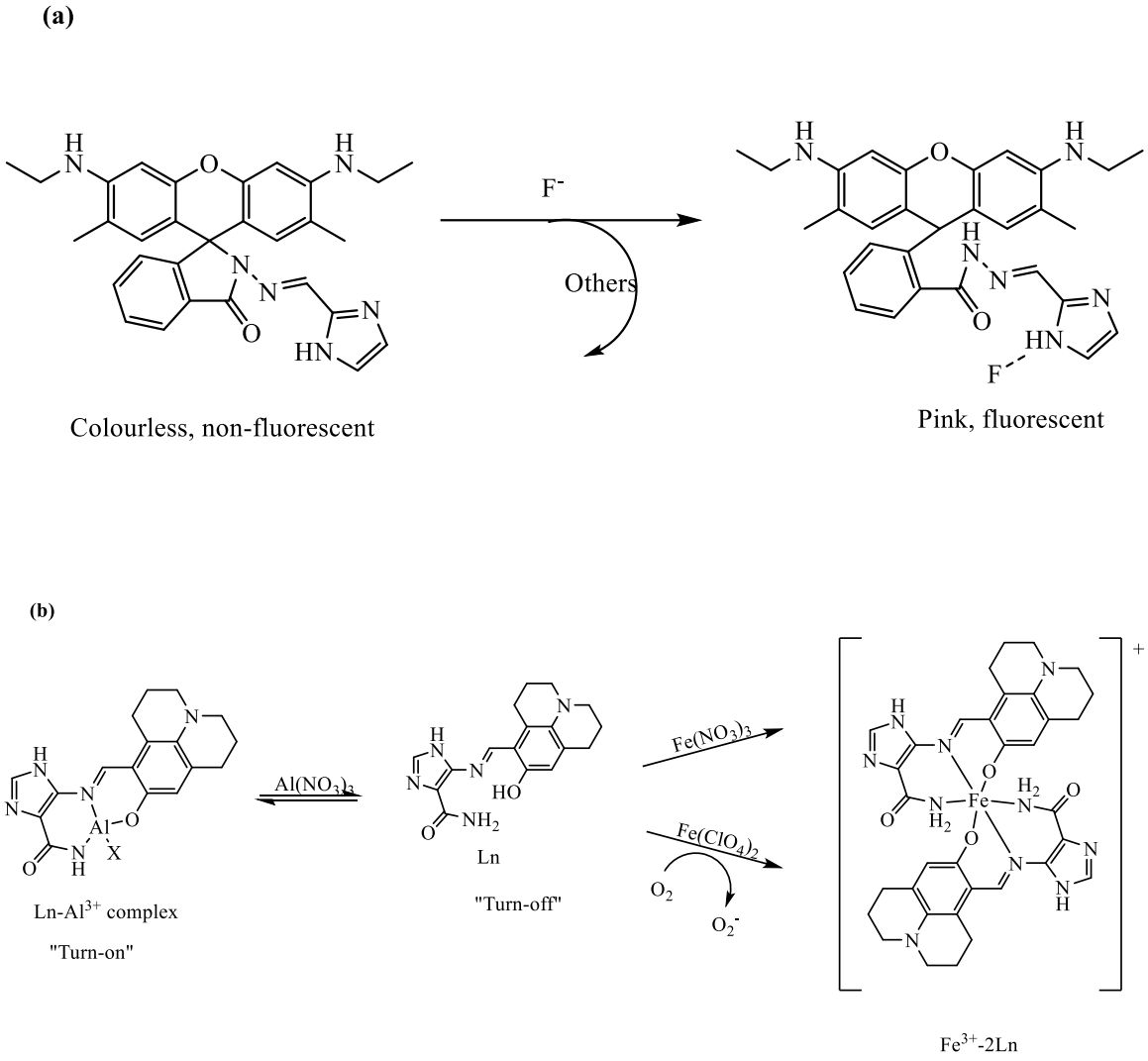

Scheme 2.3: (a) Structure of RDF-1 used for selective fluoride ion detection (b) Sensing property of the imidazole imine ligand

By incorporating the binding ability of imidazole ring, fluorogenic behaviour of quinoxaline ring and redox potential of ferrocene, two tricyclic bis(heteroaryl) imidazole bearing ferrocenyl-quinoxaline compounds {**Fig. 2.3**(**a**)} have been prepared. The compounds absorbed in the 280 nm {X = O}, 285 nm {X = N} and 325 nm regions {in both compounds}. These bands moved to lower wavenumbers {≈ 272 nm and 324 nm with a shoulder at ≈ 385 nm} in the presence of metal ions. Fluorescence studies {in MeCN} showed the compound with X = O discriminated between Cd^{2+} and Zn^{2+} (Alfonso *et al*., 2015). Two 2-pyridin-2-yl-benzimidazole compounds (6-Br-ppmbi and 6-Br-Me2-ppmbi; {**Fig. 2.3**(**b**)}) have also been prepared, where 6-Br-ppmbi exhibited strong emission at 390 nm (λ_{ex} = 320 nm) and its fluorescence emission was observed to decrease drastically upon interaction with Fe^{2+}. The compound {6-Br-ppmbi} showed low affinity for Fe^{2+} (with dissociation constant, K_d of 1.06 x 10^2) and good selectivity for Fe^{2+} over other divalent ions (Ca^{2+}, $Co^{2+,}$ Cu^{2+}, Hg^{2+}, K^+, Mg^{2+}, Na^+, Ni^{2+} and Zn^{2+}) studied (Lee *et al*., 2012).

Three {3} purine-based imine ligands {**Fig. 2.3**(**c{i}**) – (**c{iii}**)} have been studied for their Zn^{2+} selectivity. All three compounds exhibited selectivity for Zn^{2+} over other cations studied {Ca^{2+}, Mg^{2+}, Cu^{2+}, Fe^{3+}, Ni^{2+}, Co^{2+}, Hg^{2+}, K^+, Ag^+, Na^+, Mn^{2+}, Cd^{2+}} with a red shift in fluorescence emission and turn-on effect in the presence of Zn^{2+}. The fluorescence of **Fig. 2.3**(**c{i}**) is quenched in the presence of Cu^{2+}, Co^{2+} and Fe^{3+} - ascribed to the affinity of Cu^{2+} and Co^{2+} towards imidazole ring and quenching effect of Fe^{3+}. A photo-induced electron transfer {PET} mechanism is proposed for all three compounds (Pratibha *et al*., 2017). A family of imine-linked ligands, incorporating salicylaldehyde and an aliphatic alkene group {**Fig. 2.3**(**c{iv}**) – (**c{vi}**)}, in which the chelate ring of the –OH group and the sp^2 nitrogen donor aided good selectivity for Zn^{2+} {in comparison to the compounds without –OH group or sp^2 nitrogen atom} have been reported. Compound **2.3**(**c{iv}**) exhibited dual channel emission with a weak emission at 355 nm and a moderate emission at 440 nm due to existence of the receptor in keto and enol tautomeric forms as a result of Excited State Intramolecular Proton Transfer {ESIPT} involving the –OH group and the sp^2 nitrogen of the imine linkage. The similarity in the absorption spectra of the free ligand as well as in the presence of Zn^{2+} suggested changes in fluorescence {upon binding} was due to excited state phenomenon. NMR studies in DMSO-d_6:D_2O {95:5, v/v}, on addition of Zn^{2+}, showed a shift in signal {up to $\Delta\delta$ = 0.22} corresponding to –CH=N as

well as shifts in the aromatic signals {up to $\Delta\delta = 0.1$} providing insight into the importance of the sp^2 nitrogen. The signal of the –OH group could not be studied. The fluorescence enhancement upon bonding with Zn^{2+} was proposed to be due to a combination of ESIPT and PET mechanisms (Saluja *et al*., 2014). A water soluble {H_2O/HEPES, pH 7.20} β-cyclodextrin based imine ligand {**Fig. 2.3(c{vii}**)} with potential for ESIPT has also been studied for selective detection of Zn^{2+}. The compound exhibited weak fluorescence and in the presence of Zn^{2+} ion an increase in fluorescence {with a blue shift in emission wavelength} was observed with a change in colour from green to light blue, however, weak fluorescence increase was also observed for Al^{3+} and Cd^{2+} ions. More so, EDTA could not quench the fluorescence of the **vii-Zn** complex suggesting irreversibility of the bonding. The blue shift in emission wavelength was ascribed to chelate induced fluorescence enhancement {CHEF} and PET process (Liu *et al*., 2015).

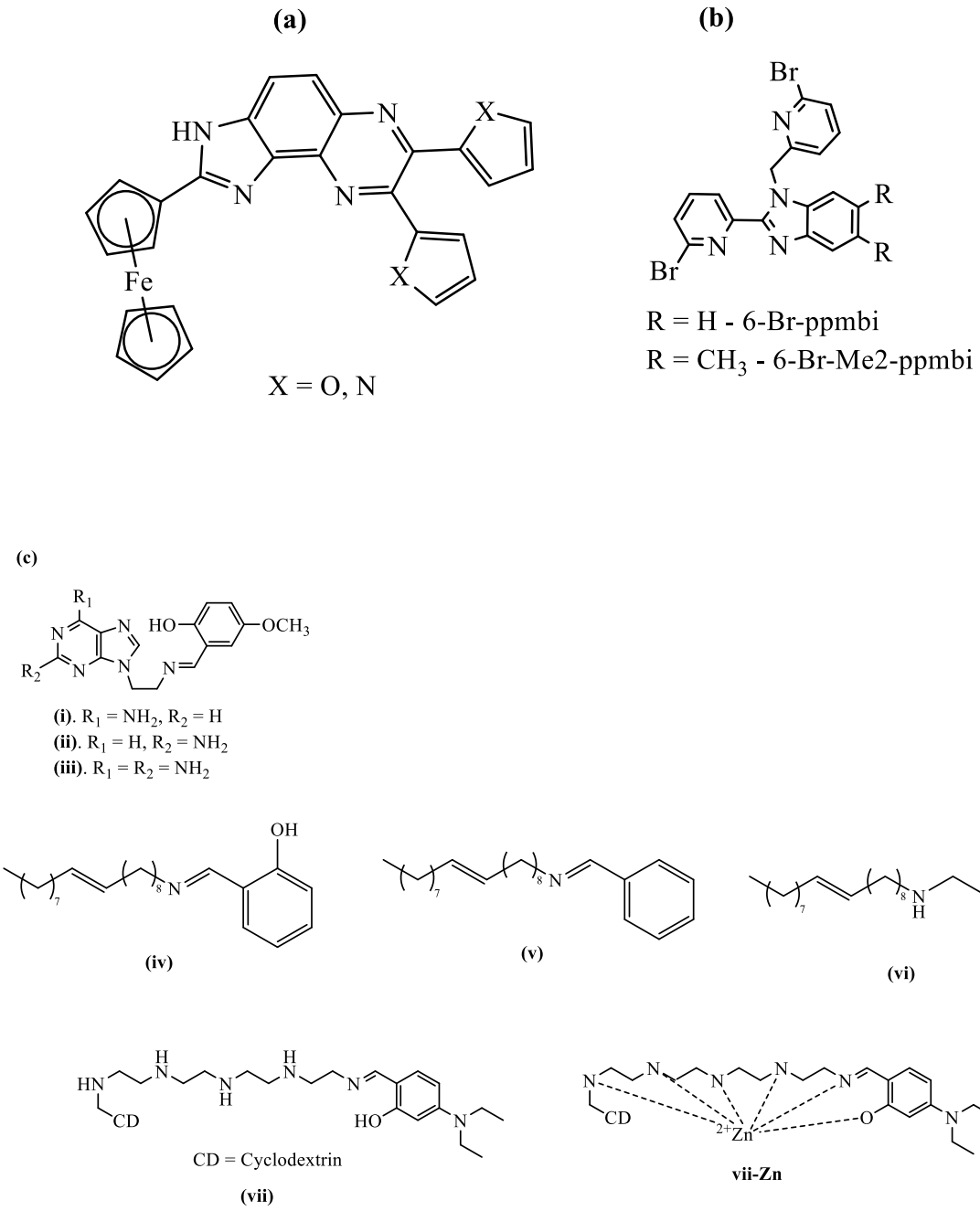

Figure 2.3: (a). Structure of tricyclic bis(heteroaryl)substituted ferrocenyl-imidazo-quinoxalines (b). Structure of 6-Br-ppmbi and 6-Br-Me2-ppmbi and (c) Structures of purine-based imine ligands, salicylaldehyde imine/amine ligands and β-cyclodextrin based imine ligand.

An N,O- phenanthrene based imidazole ligand {**Fig. 2.4**(**a**)} has been reported for the selective detection of Cu^{2+} ion. The electronic absorption spectrum of the ligand, in H_2O/MeCN (8:2 v/v), showed three bands at 259, 351 and 366 nm. Upon interaction with Cu^{2+} a new band (attributed to charge-transfer transition) at 396 nm was observed. The ligand showed strong emission at 435 nm, which was almost completely quenched in the presence of Cu^{2+} ion – an observation that was ascribed to reverse PET from the phenanthrene moiety to the phenolic oxygen and the imidazole nitrogen atoms due to decrease in electron density upon complexation. In the presence of Zn^{2+} and Cd^{2+}, however, the strong ligand fluorescence intensity was retained {ligand could not distinguish these ions} (Anbu *et al*., 2012). Modified versions of **2.4**(**a**) involving N,O- imidazole based ligand (without the phenanthrene in the structure, {**Fig. 2.4**(**b**)}) as well as N,S- imidazole based ligands {**Fig. 2.4**(**c**) **and** (**d**)} have also been deployed for the selective detection of Cu^{2+} ion. Unlike in the case of **Fig. 2.4**(**a**), a turn-off was observed in the modified variants. The observed fluorescence quenching was attributed to the paramagnetic nature of the Cu^{2+} which allowed it to participate in energy (or electron) transfer processes via a non-radiative deactivation channel, suggestive of a PET mechanism. The selectivity for Cu^{2+} ion was lost when the Br atoms in **2.4**(**c**) and (**d**) were replaced with $–CH_3$ group (Kaur and Alreja 2015; Giri and Patra 2015).

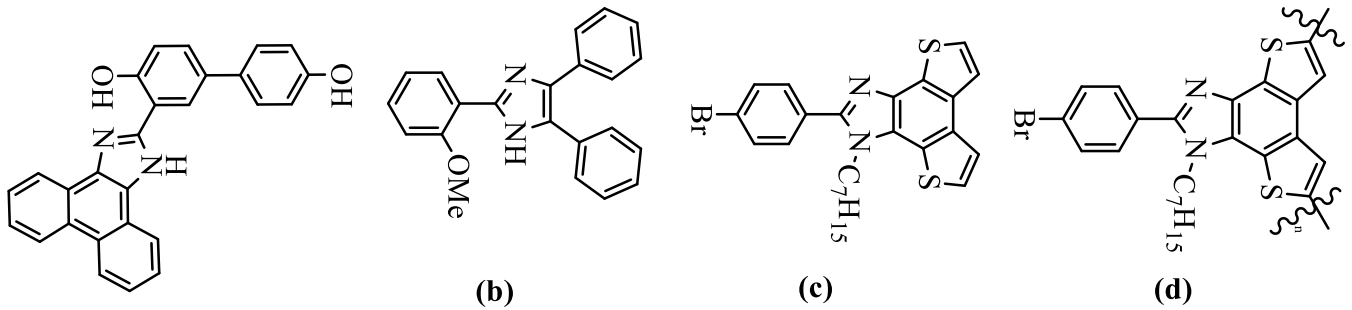

Figure 2.4: Structure of the phenanthrene and phenyl-based imidazole N,O/S ligands.

2.3 Fluorescent/Luminescent Materials

The generation and processing of signals play an important role in the design and development of sensors, optical or electronic devices. Electroluminescence devices {including light emitting diodes (LEDs), organic light emitting diodes (OLEDs), light-emitting electrochemical cells (LECs), dye-sensitised solar cells (DSSCs), sensors} find great application in different areas.

The need for fast and reliable detection of chemical species has led to increase in the design and development of sensors. Sensors play a vital role in many aspects of human life, industrial processes, food/pharmaceutical inspection, biomedicine, environmental monitoring etc. In households they are used for detection of carbon monoxide (CO), smoke; in industry they are used for process (temperature, pressure flow) monitoring. Sensors are used chiefly to measure analytes (qualitatively or quantitatively).

High levels of such substances as fluoride, phosphate, nitrate, cyanide, nitroaromatics; organic substances like 2-Methyl-2,4-pentanediol (MPD), alcohols, aldehydes, ketones are known to pose great challenges to man and the environment. Various methods such as atomic absorption spectroscopy (AAS), inductively coupled plasma mass spectroscopy (ICP-MS), anodic stripping voltammetry, flame photometry, solid-phase micro extraction (SPME), selective electrode detection, gas chromatography-mass spectrometry (GC-MS) and gas chromatography with flame ionisation detection (GC-FID), and Liquid chromatography/mass spectrometry (LC/MS) with electro spray ionisation have been employed in the detection of substances since they are able to detect {these substances} at low concentration, but these techniques tend to be time consuming, expensive, and require highly trained personnel (Zhu *et al*., 2014; Thanayupong *et al*., 2017). Similarly, in spite of the fact that positron emission tomography and magnetic resonance imaging (MRI) have been used for the detection of tumours, optical fluorescence imaging has been found to offer a better advantage of dramatic amplification in signal upon detection of some biological features (Urano, 2008).

With the great interest in analyte (cations, anions, gases) recognition and monitoring, recent efforts have been directed at inexpensive methods which are portable and show good sensitivity or selectivity. The design and development of sensors is an area

of material science that continues to gain prominence. Fluorescence spectroscopy has emerged a useful tool for detection as fluorescent sensors are often inexpensive, convenient, selective, sensitive and offer possibility for naked eye detection {useful for onsite analysis} – this high sensitivity, ease of handling and real time monitoring with fast response time of fluorescent sensors makes photoluminescence a more attractive method for sensing than other techniques (Mariappan *et al*., 2014; Thanayupong *et al*., 2017; Anbu *et al*., 2012). Fluorescent chemosensors are capable of sensing chemically, environmentally and biologically significant analytes. The high sensitivity of fluorescent sensors is commonly based on changes in intensity, energy transfer, shift in wavelength {excitation and emission}, optical changes and lifetime (Giri and Patra 2015). Generally, in order to maximise spatial resolution, fluorescence enhancement sensors {turn-on sensors} are preferred to fluorescence quenching sensors {turn-off sensors} (Alreja and Kaur 2015; Mariappan *et al*., 2014).

Fluorescent sensors have been reported for fast detection of measles virus, SARS-CoV-2 (Mayall *et al*., 2020; Hussein *et al*., 2021), gaseous molecules {including 3-hydroxy-2-butanone, hydrogen, nitrogen-dioxide, methanol} (Chen *et al*., 2020; Alenezy *et al*., 2020; Lee *et al*., 2021; Kumar *et al*., 2020), evaluation of wound infections (Thet *et al*., 2020), sweat analysis (Xu *et al*., 2020, Choi *et al*., 2020; Hussain and Park 2020), monitoring and quantification of antibiotics, superoxide {O_2^-}, peroxynitrite {$ONOO^-$} (Wu *et al*., 2020; Cabrellon *et al*., 2020; Li *et al*., 2013; Li *et al*., 2021), disease monitoring (Kim *et al*., 2020; He *et al*., 2020; Si *et al*., 2020), detection of the neurotransmitter Epinephrine (Wang *et al*., 2021), tracking lysosomal changes (Chao *et al*., 2021), determination of food quality (Liu *et al*., 2020; Zhang *et al*., 2020), monitoring of physiological pH {for proper body and cellular functions} (Ryan *et al*., 2020; Benitez-Martin *et al*., 2020), monitoring the effect of oxidative stress on heart failure (Yao *et al*., 2021), monitoring miRNA in urine for early warning of prostate cancer (Kim *et al*., 2021), evaluating abuse of psychoactive drugs (Garrido *et al*., 2020), assessment of drug induced liver injury (Chen *et al*., 2021), detection of barium daughter ions (Thapa *et al*., 2021) and polymer aging (Zhang *et al*., 2020).

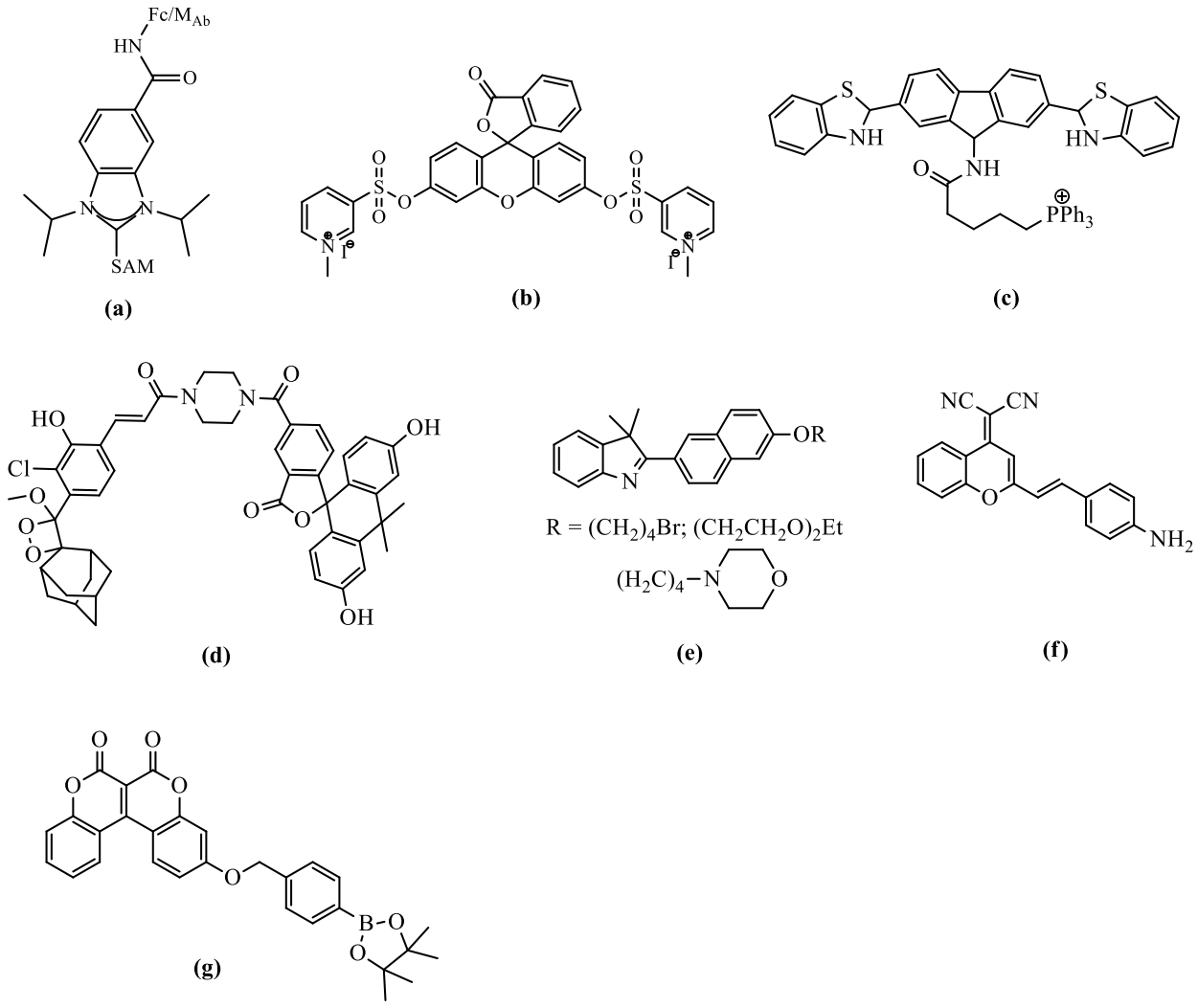

Figure 2.5: (a) NHC-based electrochemical biosensor {SAM = self-assembled-monolayer} for measles detection (b) Coumarin based sensor for O_2^- quantification (c) Benzothiazoline-triphenylphosphonium based sensor for O_2^- quantification (d) Ratio-pHCL1 for food detection (e) Indole based sensor for pH monitoring (f) Cyano-pyran for lysosomal tracking (g) Bis-coumarin for heart failure detection

Different materials have been explored in various analyte recognition/detection. These include nanomaterials (Radhakrishnan *et al*., 2020; Wu *et al*., 2020, Luo *et al*., 2020); metal complexes including metal-organic frameworks {MOF's} (Saha *et al*., 2013; Chen *et al*., 2017; Louie *et al*., 2009; Zhang *et al*., 2015; Leo *et al*., 2020; Zheng *et al*., 2020; Wang *et al*., 2021; Qin *et al*., 2021; Li *et al*., 2021); polymers (Bronson *et al*., 2005; Prabhakaran *et al*., 2007; Wang *et al*., 2020; Singh *et al*., 2015); small molecules (Eseola *et al*., 2018; Dessingou *et al*., 2005; Meng *et al*., 2017; Long *et al*., 2017).

Organic materials with favourable light and thermal stability, electron accepting properties, photoelectric properties, strong luminescence efficiency, ability to bind substrate(s) and high fluorescence quantum yield are highly sort after, especially in the field of molecular recognition. Simple organic compounds are of great interest especially due to their relative ease of preparation. Those possessing functional groups or heterocyclic rings are known to provide binding sites for selective and effective analyte recognition, thus acting as sensors. Highly substituted (tri- and tetra-) imidazoles with donor–acceptor π conjugation offer many optoelectronic applications such as Non-Linear Optics (NLO), Dye Sensitized Solar Cells (DSSC), OLEDs, and molecular switches. The amphoteric nature the imidazole ring can also impart selective and effective anion and/or cation and even neutral organic molecules receptor system (Molina *et al*., 2012; Sarala *et al*., 2016; Sinha *et al*., 2019). Fused angular and linear heterocyclic compounds also show interesting photophysical properties. The presence of π–π*, σ–π* and n–π* electronic state, in conjugated systems, help in fluorescence behaviour. The strong σ–π* and π–π* electron donor groups (-OCH_3, -CH-CH=CH-CH-) have been reported to give rise to longer emission wavelengths, while the +I effect of -CH_3 group resulted in lower emission wavelength. The presence of the –OCH_3 group increases the electron density and lowers the electron hole gap leading to higher overlap of the HOMO-LUMO orbitals. Aromatic ligands are also known to provide sterical rigidity as well as chemical stability, and π electron rich aromatic ligands impacts luminescent properties (Kumar *et al*., 2017; Zhang *et al*., 2015). Small molecules (especially conjugated ones) are known to be emissive in nature and find great use as sensors (Shigemoto *et al*., 2020).

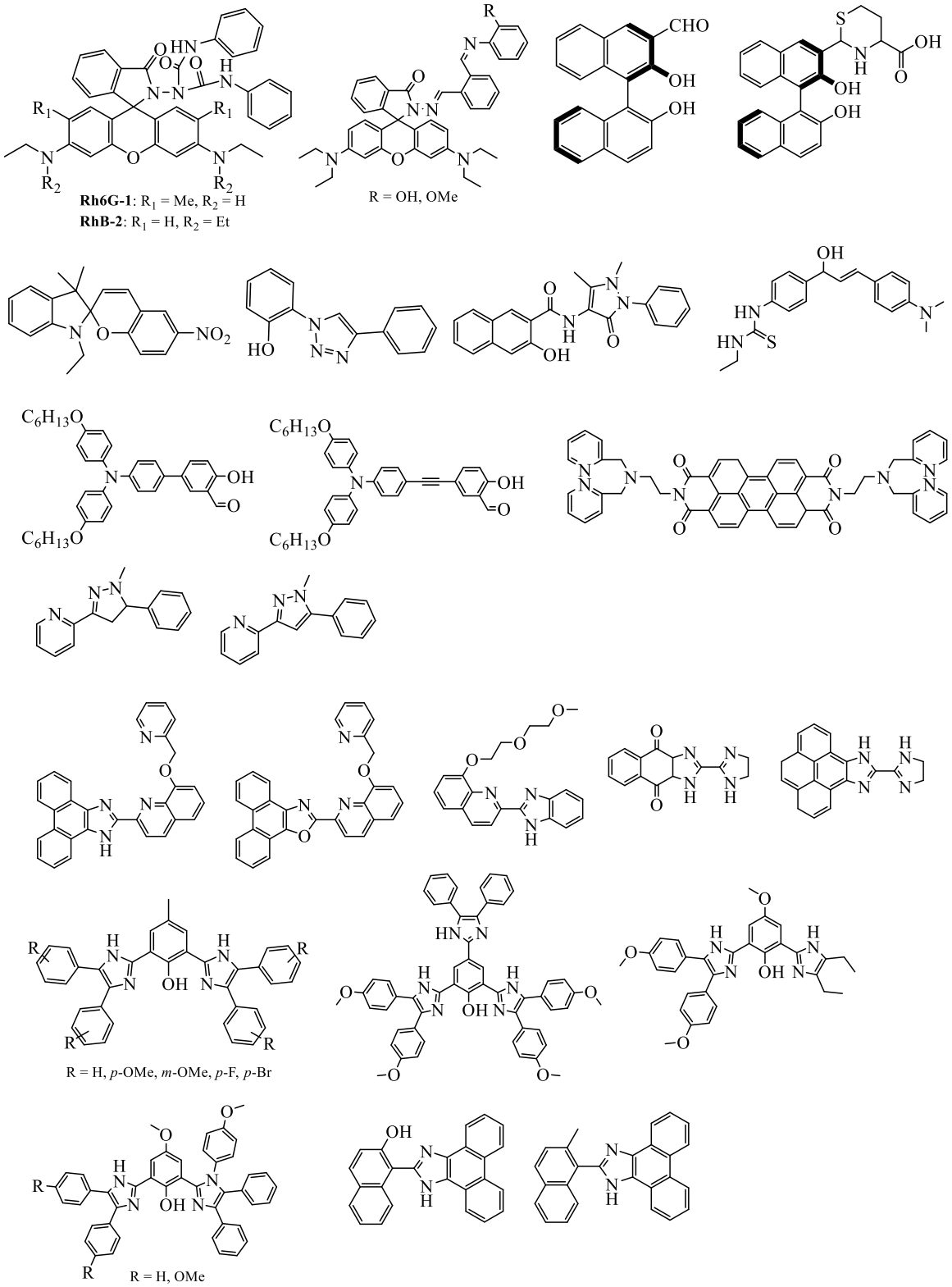

Figure 2.6: Examples of coumarin-, azole-, binaphthol based small molecules used as sensors.

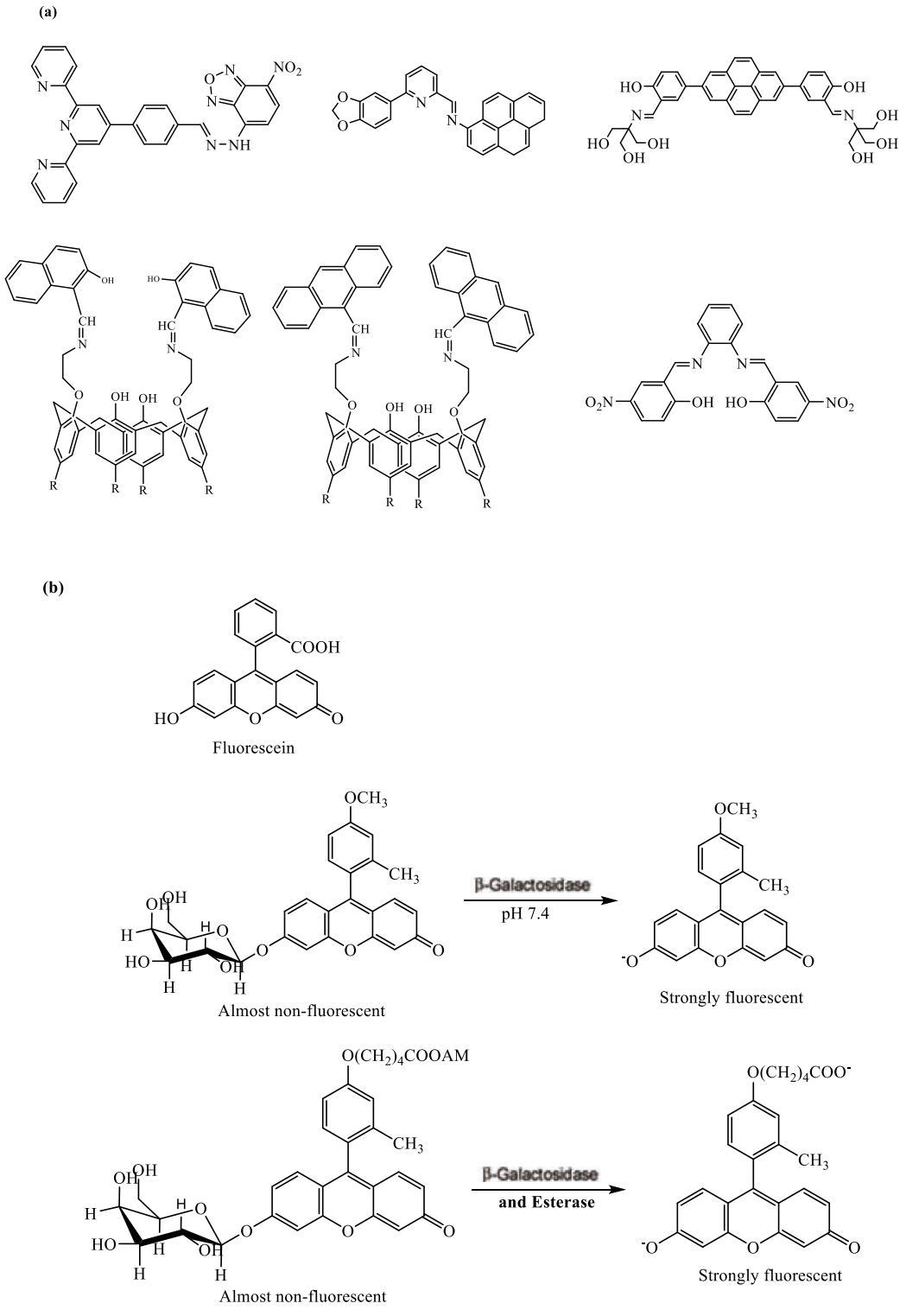

Scheme 2.4: (a) Examples of imine based small molecules used as sensors (b) Structure of fluorescein and its derivatives used for tumour sensing.

The use of fluorescein (an electron donor-fluorophore acceptor system) derivatives in tumour imaging (**Scheme 2.4**{**b**}) has been reported (Urano, 2008). The derivatives were obtained by replacement of the -COOH group of fluorescein with $–CH_3$ or $–OCH_3$ (for TG-*β*Gal) or an esterase-sensitive moiety for (AM-TG-*β*Gal) – the esterase-sensitive moiety is observed to enable easy leaching of product from the cancer cell. The fluorescence quantum efficiency of TG-*β*Gal increased 420-fold (from 0.002 to 0.84) with formation of a green colour, while the efficiency of AM-TG-*β*Gal increased ~97 fold (from 0.009 to 0.87) with same colour formation.

A CN^- ion turn-on sensor based on dicyanovinyl phenylacetylene (**Scheme 2.5**), with phenyleneethynylene as a fluorogenic rod attached to dicyanovinyl group, has been reported. The triphenylamine core of the compound acts as an electron donor, while the dicyanovinyl function acts as an electron acceptor (via its π-conjugation). The electronic absorption of the compound, measured in MeCN/HEPES buffer pH 10 (9:1 v/v), showed two bands at 368 nm and 450 nm. Upon excitation at 368 nm, the compound showed maximum emission at 460 nm with a quantum efficiency of 0.8% - the low efficiency was attributed to intramolecular charge transfer (ICT) process. Upon addition of CN^- ion (10 μM), the quantum efficiency increased to 200% due to disruption of ICT and the yellow colour of the receptor changed to colourless then green at the λ_{em}(max). Anions such as AcO^-, Br^-, Cl^-, F^-, HCO_3^-, $H_2PO_4^-$, IO_3^-, NO_2^-, NO_3^-, OH^-, SCN^- and SO_4^{2-} did not show significant changes to the fluorescence emission signal (Thanayupong *et al*., 2017). Using an anthraquinone macrocyclic crown-ether like compound (**Scheme 2.6**{**a**}), intense fluorescence enhancement in the presence of Cu^{2+} has been observed. The Cu^{2+} ion caused immediate formation of an intense yellow emission (at excitation of 360 nm), which was found to be dependent on the amount of water present in the solvent (Mariappen *et al*., 2014). A "turn-off" effect (attributed to the paramagnetic nature of the Cu^{2+} centre) was, however, observed for a naphthalene-based imine (**Scheme 2.6**{**b**}) with a monoboronic acid group as the binding site (Li *et al*., 2014).

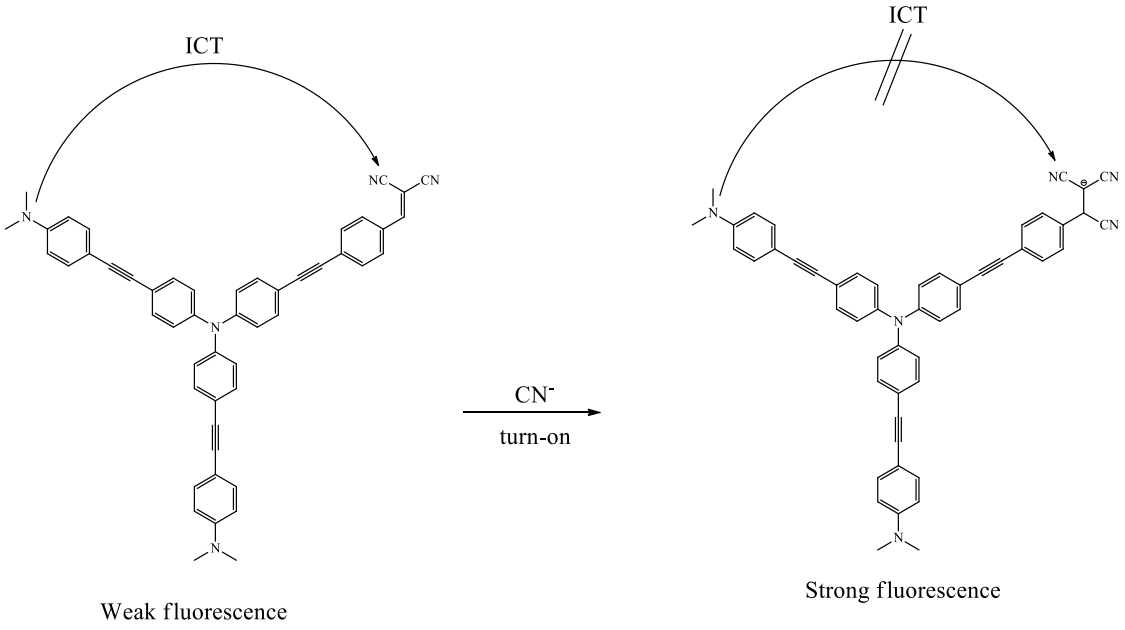

Scheme 2.5: Turn-on mechanism of the CN^- ion sensor

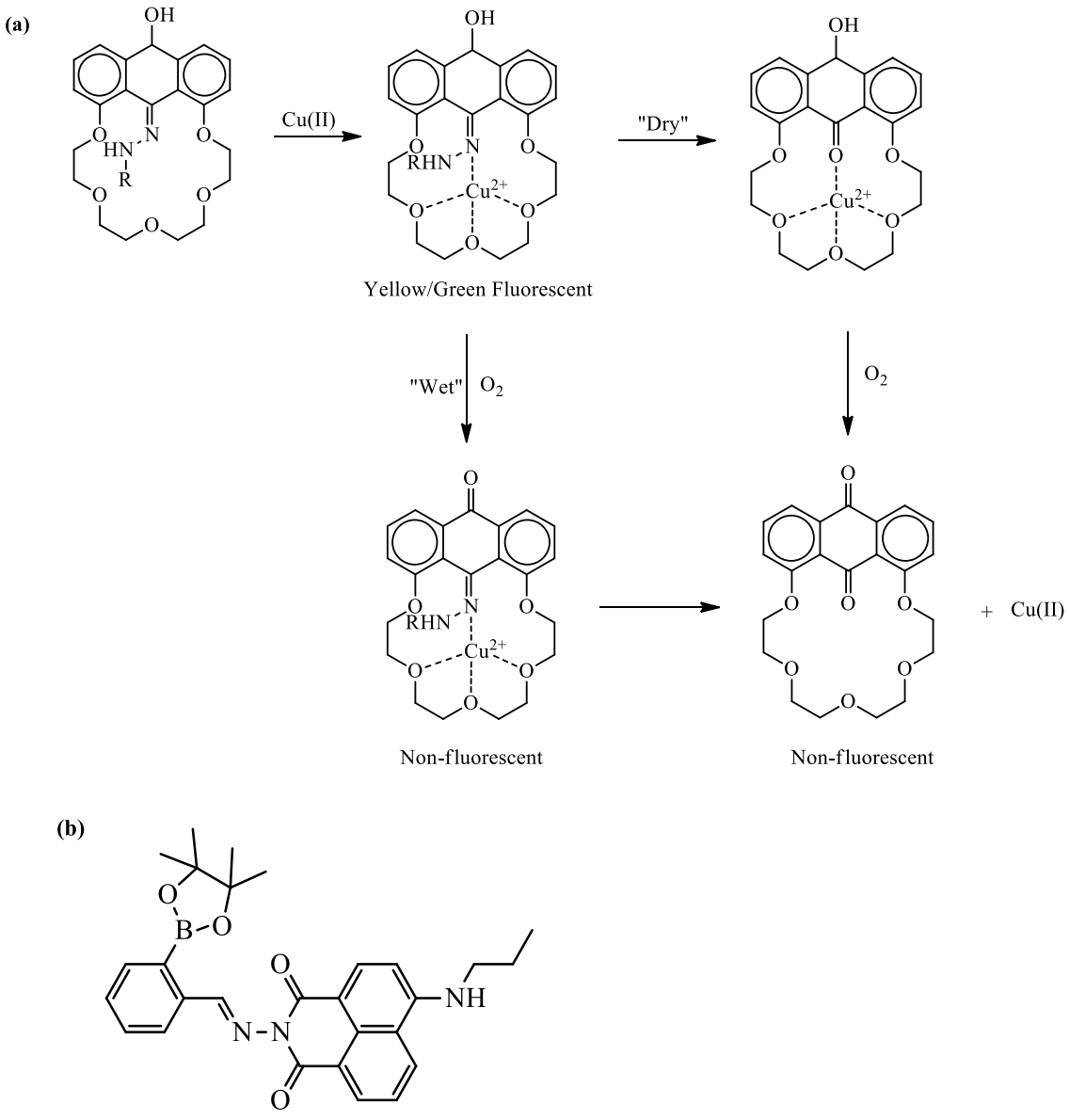

Scheme 2.6: (a) Anthraquinone crown-ether ligand and (b) Naphthalene-based imine with boronic acid binding site for Cu^{2+} sensing.

A 1,10-phenanthroline based fluorescent sensor has been designed and used for the selective recognition of Cu^{2+}, Zn^{2+} and I^- ions. The oxygen (of the amide) and the nitrogen (of the phenanthroline and pyridine) are believed to aid the detection of the Cu^{2+} and Zn^{2+} ions, by chelation (**Scheme 2.7**{**a**}), while the N-H (of the amide) aids in the detection of I^- ion (**Scheme 2.7**{**b**}). The absorption spectra of the fluorophore (in DCM) showed little changes upon addition of 100 equivalent of different cations (Na^+, K^+, Mg^{2+}, Al^{3+}, Ni^{2+}, Cu^{2+}, Fe^{2+}, Fe^{3+}, Zn^{2+}, Cd^{2+}, Co^{2+} and Mn^{2+}), while two emission peaks (at 351 and 368 nm) were observed upon excitation at 265 nm. Complete fluorescence quenching was observed upon addition of 100 equivalent of Cu^{2+} ion. The addition of same amount of Zn^{2+} resulted in quenching (through oxidative PET), accompanied by a red shift – in contrast to other metal ions tested under the identical conditions. The binding constants, K_a, calculated were 2.6 x 10^9 M^{-1} and 7.9 x 10^8 M^{-1} for Cu^{2+} and Zn^{2+} ions, respectively, while the limit of detection (*LOD*) was estimated to be 0.48 and 0.78 μM, respectively. Fluorescence studies with I^- ion showed almost complete turn-off (with no obvious change observed for F^-, AcO^-, Cl^- Br^-, I-, SO_4^{2-}, CN^-, $H_2PO_4^-$ and HSO_4^- ions), with K_a of 1.05 x 10^3 M^{-1} and estimated *LOD* of 30 μM. The Job's plot suggested the formation of 1:2 and 1:1 stoichiometry between chemosensor and Cu^{2+}/Zn^{2+} and I^- ions, respectively (Alreja and Kaur 2015).

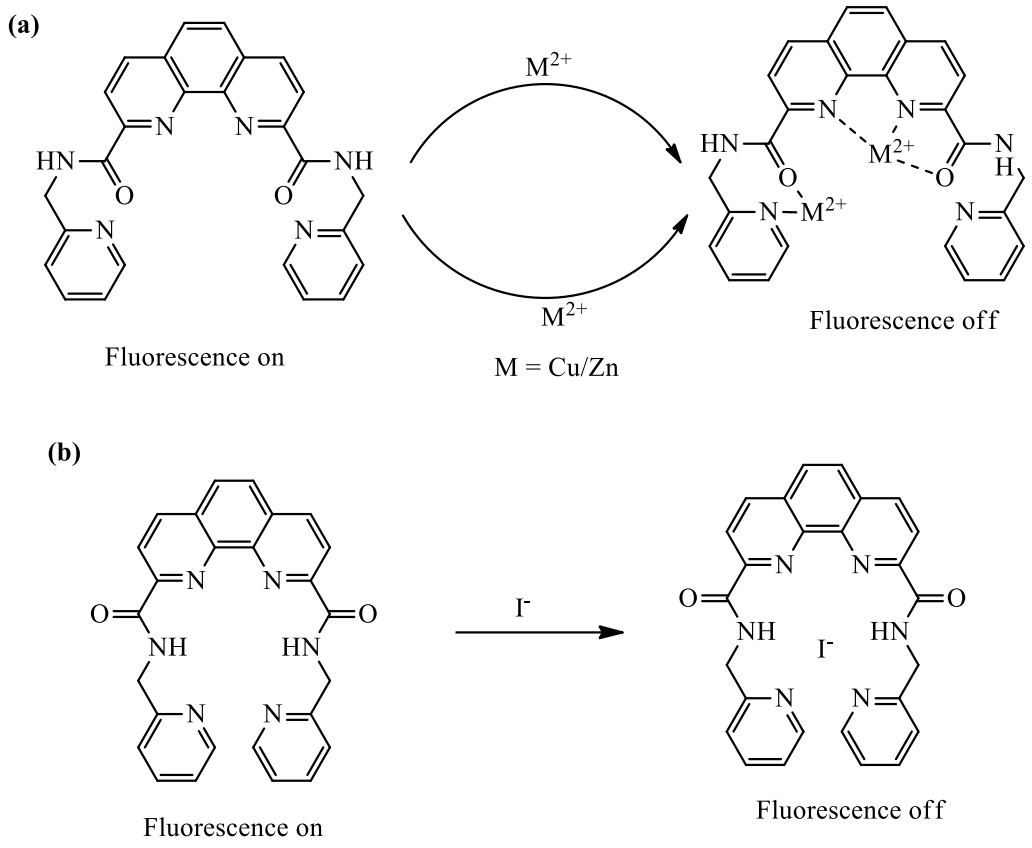

Scheme 2.7: Proposed mechanism for a phenanthroline based turn-off sensor.

2.4 Cation Sensing

The design and preparation of chemosensors for selective and efficient detection of species with biological and chemical importance is an active research area. Cations play key roles in many transformations in the human body {biological metabolism} as well as in the environment. They are non-biodegradable and are extensively used in consumer products and industry (Yannone *et al*., 2012; Kenney and Rosenzweig 2012; Turner, 2017; Malinowski *et al*., 2020; Gulcin and Alwasel 2022).

Cations are known to be important in cellular metabolism {Zn^{2+}}, electron transfer {Fe^{3+}, Cu^{2+}}, oxyhaemoglobin generation {Fe^{3+}}; signal transduction, transformation of melanin, generation of energy {Cu^{2+}}; enzyme catalysis and activation {Fe^{3+}, Cu^{2+}, Cr^{3+}}; metabolism of fats, carbohydrates, proteins and nucleic acids {Cr^{3+}}. Abnormal {high or low} levels of these ions however result in unpleasant and detrimental effect on the environment and human health including diabetes, heart disorder, liver damage, kidney damage, anaemia, dementia, osteoporosis, hemochromatosis, Huntington's disease, Alzheimer's disease, Parkinson's disease, renal failure, gastrointestinal upset, metallic taste in the mouth, blood in the urine and lethargy, plant death and soil pollution (Zhou *et al*., 2008; Sahoo and Crisponi 2019; Kilic and Bozkurt 2018; Das *et al*., 2019; Goswami *et al*., 2013; Saluja *et al*., 2014; Liu *et al*., 2015; Singh *et al*., 2007; Shahid *et al*., 2017; Liao *et al*., 2017; Kim *et al*., 2013; Roy and Rajak 2017; Mustafa and Komatsu 2016; Valle *et al*., 2009; Poschenrieder *et al*., 2019; Sangireddy *et al*., 2017).

Although aluminium is not known to have any essential function in living systems, it is useful in other human endeavours such as medicine, cosmetics and food technology. Al(III) can enter the human body through food and drinking water and excessive exposure is known to cause Parkinson's disease, dementia, Alzheimer's disease, damage to the central nervous system and osteoporosis. According to the World Health Organisation {WHO}, the average human intake of aluminium is about 3 – 10 mg day^{-1}, the tolerable weekly intake is 7 mg kg^{-1} body weight and recommended detection limit, in drinking water, is 7.41 μM (Bhattacharjee *et al*., 2014; Rondeau *et al*., 2009; Inan-Eroglu and Ayaz 2018; Jang *et al*., 2018). Development of fluorescence sensors for Al^{3+} is seriously hindered because of the strong hydration, poor coordination, and lack of spectral characteristics of Al^{3+} ions (Fan *et al*., 2014).

Zn(II) is the second most abundant transition metal ion *in vivo* and has the ability to act as a regulatory ion in metalloenzymes regulation, in many channel receptors and in cell metabolism. It is essential for proper cellular metabolism and important for fertility in males and females. It is present in RNA polymerase enzymes and important to major biological processes like gene transcription, immune function, brain function {where it serves as a neurotransmitter/modulator}; and hundreds of proteins {including zinc fingers and catalytic enzymes} depend on Zn^{2+} for their function, hence alteration in concentration of Zn^{2+} can result in protein malfunction which may lead to interruption in the absorption of iron {Fe}, magnesium {Mg} and copper {Cu} as well as affect the immune system, central nervous system, reproductive system and human growth/development (Pratibha *et al*., 2017; Saluja *et al*., 2014). The d^{10} electronic configuration of Zn^{2+} makes it magnetically inactive, thus detection {of Zn^{2+}} by fluorescence spectroscopy is attractive. More so, interference from ions such as Cu^{2+}, Hg^{2+} and Cd^{2+} occurs commonly with receptors {used for Zn^{2+} binding} (Anbu *et al*., 2012; Liu *et al*., 2015). Zn^{2+} {with an ionic radius of 0.74Å} is a harder centre than Cd^{2+} {ionic radius of 0.97Å} – the larger size of Cd^{2+} has been observed to aid better coordination in receptors (Costero *et al*., 2004).

The diversity and function of these ions in daily activities has led to an increase in the development of materials for monitoring and detection of these ions. Early efforts in Zn^{2+} detection/monitoring focused largely on materials derived from di-2-picolylamine {DPA} skeleton {**Fig. 2.7**(**a**)}. This N-based donor majorly displays PET mechanism and tend to have high sensitivity and selectivity for Zn^{2+}, but many of the reported compounds are competed for by other ions, especially Cd^{2+}, and require lengthy synthesis (Nolan *et al*., 2004; Komatsu *et al*., 2005; Lu *et al*., 2007; Liu *et al*., 2013; Louie *et al*., 2009). Materials based on such scaffolds as acridine, quinoline, pyrazine/pyrazole, fluorene octopamine, rhodamine, pyrimidine, 1,10-phenanthroline, oxazole and thioether {**Fig. 2.7**(**b**)} have also been reported although competition from Cd^{2+} is still observed and some still require lengthy synthesis. In addition to PET, other mechanisms including CHEF, ESIPT have also been observed in these systems (Ciupa *et al*., 2012; Zhang *et al*., 2013; Song *et al*., 2013; Visscher *et al*., 2016; Roy *et al*., 2016; Kang and Kim 2018; Fan *et al*., 2014; Mati *et al*., 2014; Song *et al*., 2014; Tang *et al*., 2017; Xu *et al*., 2014; Naskar *et al*., 2017; Patra *et al*., 2016; Ravikumar and Ghosh 2011). A large number of trivalent cation {M^{3+}} receptors

{**Fig. 2.8**} have been reported to date {although relatively fewer than for M^{2+}}, many of which simultaneously detect Al^{3+}, Cr^{3+} and Fe^{3+} (Wang *et al*., 2013; Goswami *et al*., 2013; Wang *et al*., 2014; Samanta *et al*., 2014; Singh *et al*., 2015; Samanta *et al*., 2016; Janakipriya *et al*., 2017; Dey *et al*., 2017; Alam *et al*., 2017; Zhan *et al*., 2019b; Kilic and Bozkurt 2018; Xu *et al*., 2014; Venkateswarulu *et al*., 2014; Presti *et al*., 2016; Meng *et al*., 2017; Jang *et al*., 2018; Wang *et al*., 2016; Jang *et al*., 2018; Liu *et al*., 2015; Lisowski and Hutchison 2009; Wang *et al*., 2019), but there is an increase in the search for receptors with ability to detect these ions singly and although receptors for Al^{3+} are known {**Fig. 2.9**}, competition from some trivalent cations as well as divalent cations {e.g Co^{2+}, Cu^{2+}, Hg^{2+}, Zn^{2+}} has been observed (Gupta *et al*., 2014; Manjunath *et al*., 2015; Simon *et al*., 2016; Qin *et al*., 2016; Kang *et al*., 2017; Gupta *et al*., 2018; Yue *et al*., 2018; Tian *et al*., 2018; Wang *et al*., 2018; Peng *et al*., 2020; Berrones-Reyes *et al*., 2019; Huang *et al*., 2019; Zeng *et al*., 2019b; Zeng *et al*., 2019a; Wang *et al*., 2019; Bai *et al*., 2019; Fan *et al*., 2019; Das *et al*., 2019; Zhan *et al*., 2019a; Li *et al*., 2019; Kumar *et al*., 2020; Durai *et al*., 2020; Erdemir and Malkondu 2021; Aydin *et al*., 2021; Liu *et al*., 2021; Chemate and Sekar 2015; Wang *et al*., 2019; Kundu *et al*., 2019; Wang *et al*., 2019; Liu *et al*., 2020).

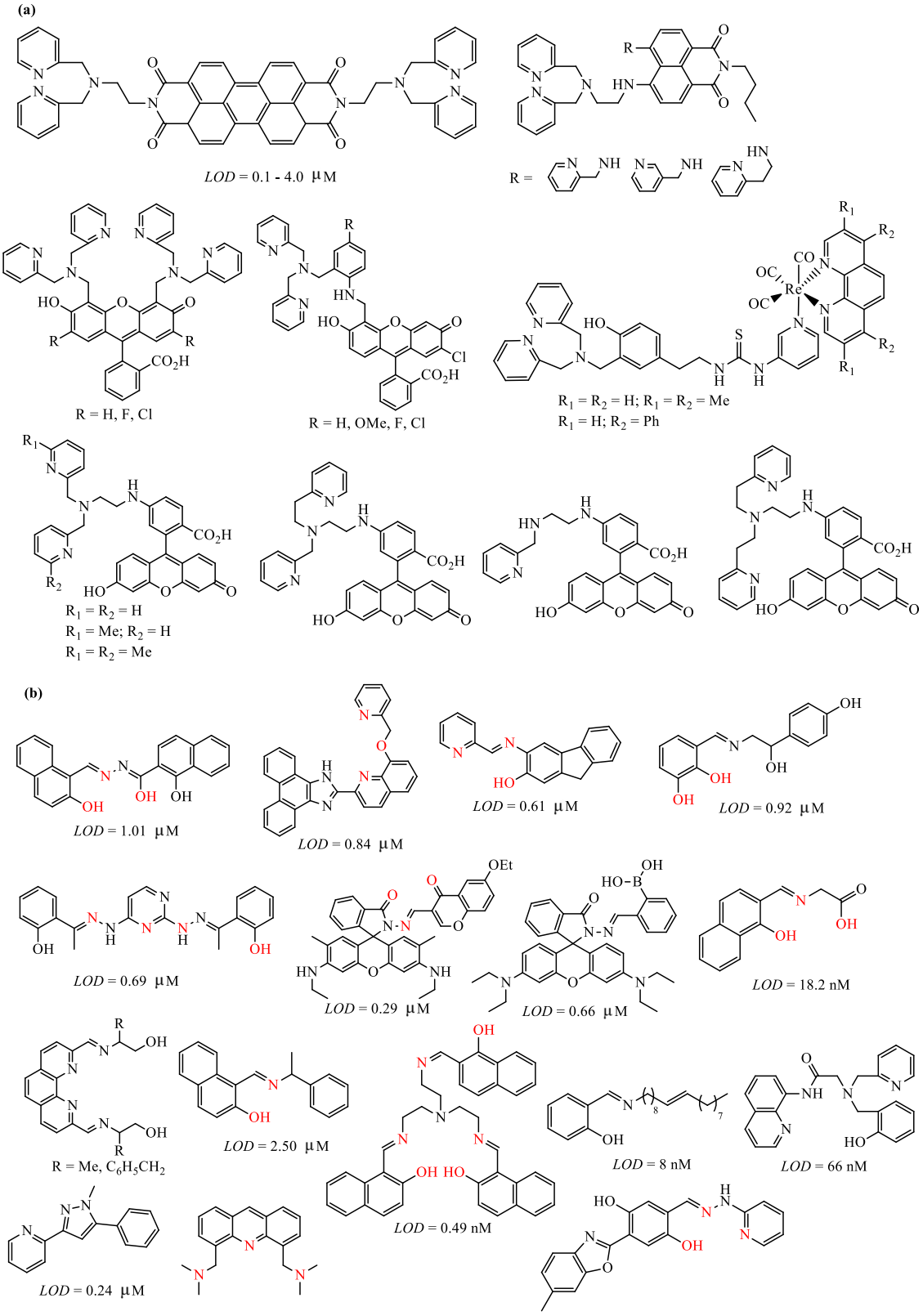

Figure 2.7: Structures of some (a) DPA based sensors (b) other scaffolds for Zn^{2+} sensing.

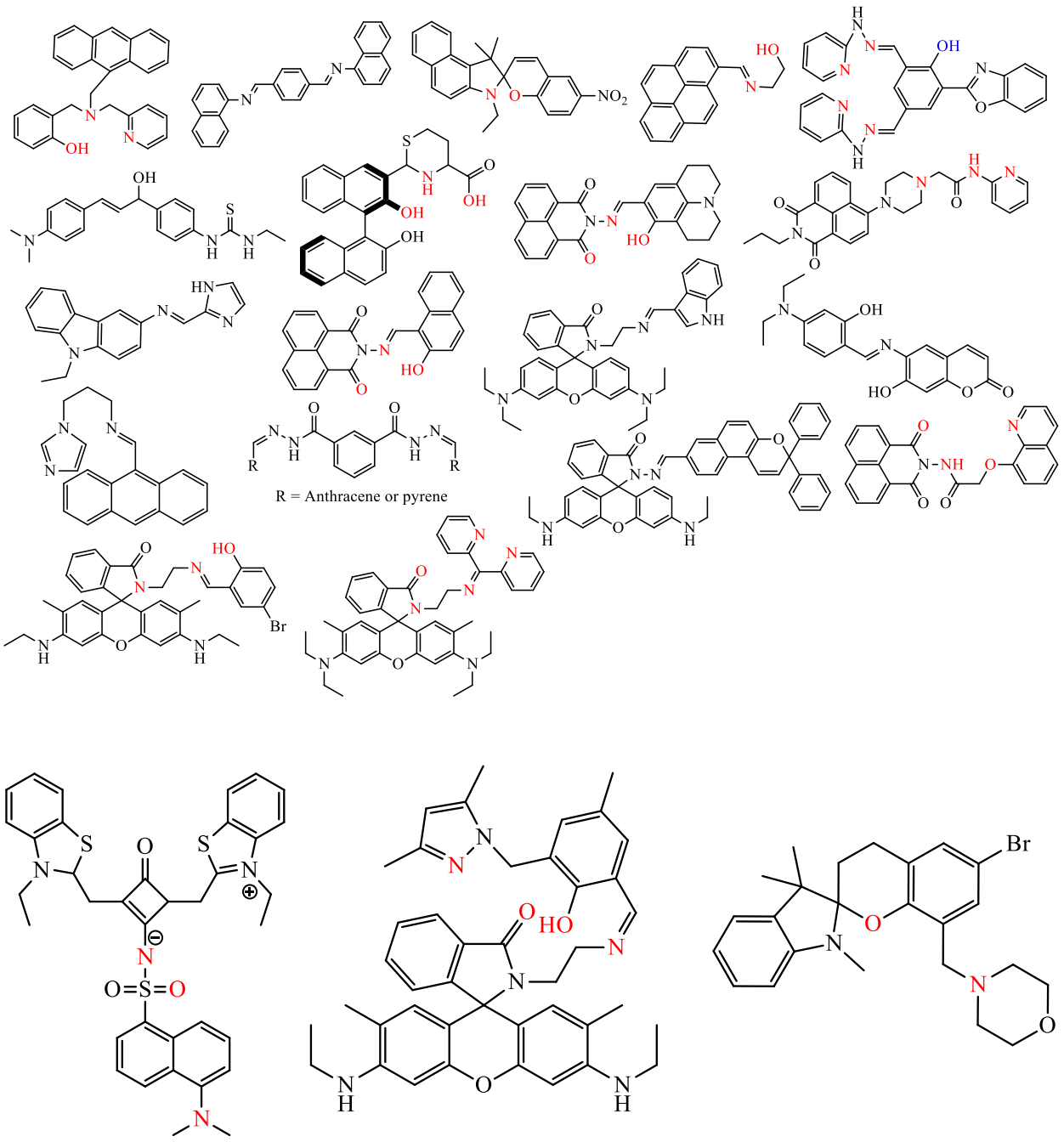

Figure 2.8: Structures of some receptors for M^{3+}

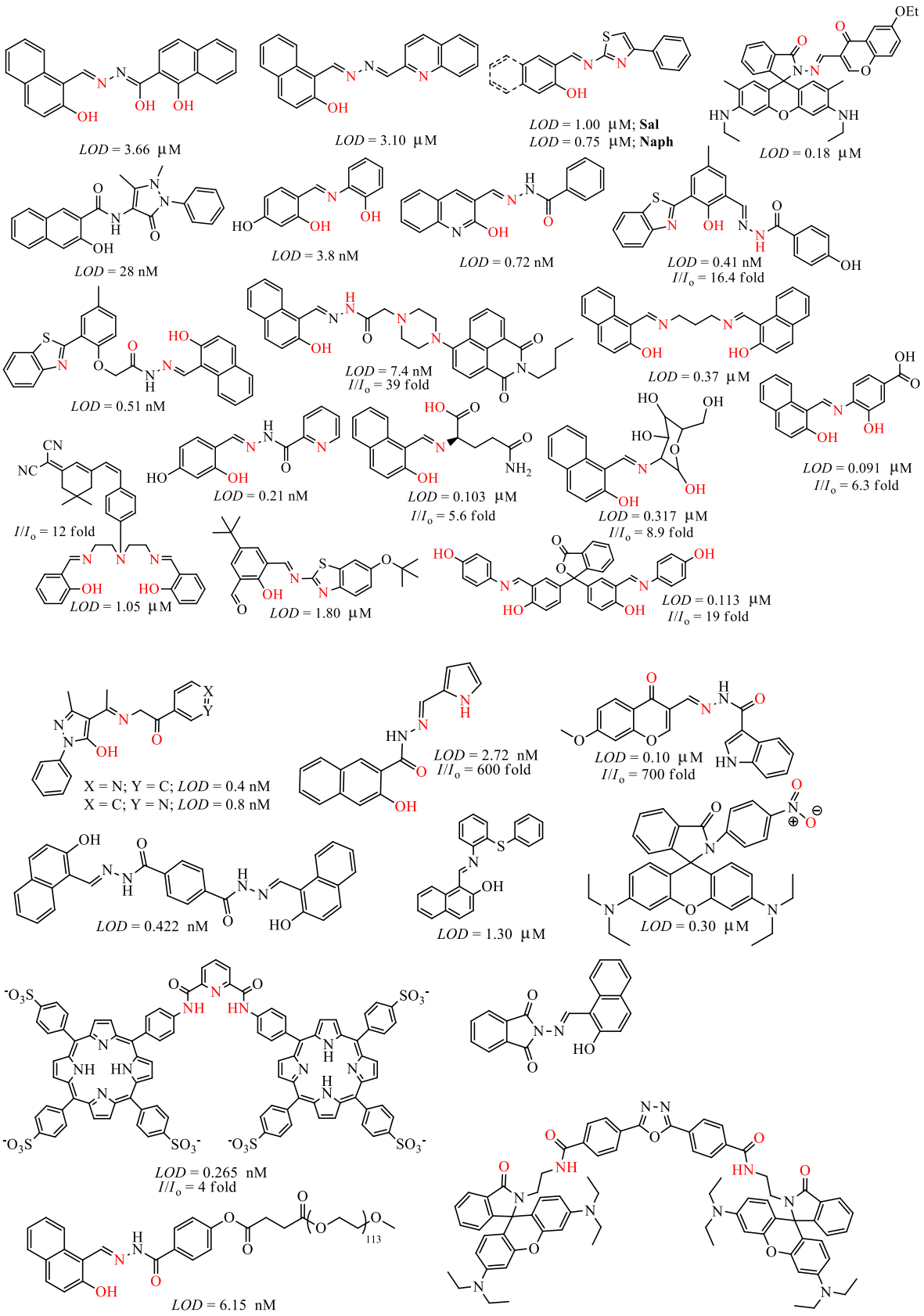

Figure 2.9: Structures of some receptors for Al^{3+}

2.5 Molecular Variation and Effect on Spectroscopic and Sensing Properties

The systematic optimisation of sensors is an active area of research. The properties of materials are greatly influenced by their structures, spatial arrangement of the molecules, the steric and electronic properties of attached functional groups, as well as the nature of the metal ions {in the case of inorganic materials}. Fluorescence properties are commonly modified through electronic effects as well as conformational changes. Desirable properties, such as selectivity for analyte(s) and intensity of the fluorescence activation, can be achieved by the introduction of functional groups which modify receptors/ligands electronic structure. Interplay of intermolecular interactions {π-π stacking, ion-π, hydrogen bonding}, electronic structures, ground and excited states of fluorescent materials have been found to impart greatly their behaviour; it can also act as a guide in the design of fluorescent materials. Molecular alterations targeting the donor {where the HOMO is localised} and/or the acceptor {where the LUMO is localised} sites affect the optical and electronic properties of materials. Electron-donating or-withdrawing groups {especially those possessing varying degrees of sterical demands} have different effects on the energies of the HOMO and LUMO, thus enabling modulation of energy gap, producing subtle or large changes in such properties as charge transport, quantum yield and redox potential. (Bartholomew *et al*., 2000; Solomatina *et al*., 2020; Santos *et al*., 2020; Longo *et al*., 2016; Varghese *et al*., 2013; Renak *et al*., 1999; Yamashita and Abe 2014; McLay *et al*., 2021; Shi *et al*., 2021; Timmer *et al*., 2021; Kim *et al*., 2019; Sajoto *et al*., 2005; Sukpattanacharoen *et al*., 2020; Kowalcyzk *et al*., 2010; Costero *et al*., 2004).

Alkyl substitution has been shown to affect solubility and melting point (suggesting good thermal durability). It has also been observed to allow control of the mesoscopic organisation of molecular layers resulting in elegant self-assembly properties (Garnier *et al*., 1993; Ebata *et al*., 2007; Hirase *et al*., 2014). Low-lying HOMO levels as well as large HOMO-LUMO energy gaps have been reported to give great stability in heteroarenes, even with linearly arranged fused rings {which commonly results in reduced stability} present in the molecule (Yamamoto and Takimiya 2007). The use of bulky electron donors (methyl, dimethylphenyl, methylphenyl and phenyl) have been shown to be useful in tuning emission colour, without greatly affecting the quantum yield (Kim *et al*., 2019). Delocalisation of π-

electrons {or π-conjugation} has been observed to give improved charge transport properties, smaller HOMO-LUMO energy gap, larger Stokes shift and longer emission wavelength (Garnier *et al*., 1993; Yamaguchi *et al*., 2008; Yao *et al*., 2021). Structural modification, resulting in asymmetrical HOMO, has also been observed to result in increased HOMO energy level, smaller emission energy and large Stokes shift (Ren *et al*., 2018).

The methylation of 3-aminoquinoline (3AQ) to give N-methylquinoli-3-amine (NMeAQ) has been reported to show changes in photophysical properties. The red shifted absorption and emission maxima observed for NMeAQ (in different solvents), is greater than those observed for 3AQ. The Stokes shift observed in the polar aprotic solvent (MeCN) is greater for NMeAQ (4,162 cm^{-1}) than for 3AQ (3,456 cm^{-1}), but in the case of the non-polar n-hexane 3AQ gave a higher value (2,735 cm^{-1}) than NMeAQ (2,475 cm^{-1}) – a similar trend {in the polar aprotic and non-polar solvents} was observed for the fluorescence quantum yield (φ_f). These observations were attributed to a decrease in the hydrogen bonding ability of NMeAQ (Agarwal, 2011). In a series of NHC^C ligands, the introduction of methyl group caused a reduction in the fluorescence quantum yield, while phenyl group resulted in an increase (although the Stokes shift, however, increased in both cases). The use of methyl substituents (on the phenyl group), however, resulted in lower quantum yields and Stokes shift (the dimethyl substitution producing the greatest effect) – the orthogonal orientation attributed to this observation (Kim *et al*., 2021). Similarly, replacing an -OH group (**Fig. 2.10**{**a**}) with methyl (**Fig. 2.10**{**b**}) has been observed to give a decrease in Stokes shift (Sinha *et al*., 2019). In a study on the effect of end-group methylation (which is usually compact and minimally disturbs the molecular electronic structure) as a tool for tuning crystal packing, intermolecular interactions, charge transport and luminescence, a family of furan/phenylene co-oligomers with the same conjugated core 1,4-bis(5-phenylfuran-2-yl)benzene and methyl substituents at *p*- and *m*-positions of the terminal phenyls (**Fig. 2.10**{**c**}) have been synthesised and utilised. The solution absorption and emission spectra of the compounds were observed to be identical, with λ_{abs} 376 nm (BPFB), 379 nm (2Me- and 4Me-BPFB), and λ_{em} 410 nm, 434 nm (BPFB); 413 nm, 438 nm (2Me- and 4Me-BPFB). The slight bathochromic shift for the methyl-substituted compounds was assumed to result from weak electron-donor effect of the methyl groups. The methyl

substituted compounds exhibited lower photoluminescence (PL) quantum yields 76% (2Me-BPFB) and 80% (4Me-BPFB), in comparison to BPFB {90%}. Solid state spectra studies of the compounds showed more pronounced red shift in λ_{em}, 498 nm (BPFB), 502 nm (2Me-BPFB); 495 nm and 521 nm (4Me-BPFB) - partially due to higher polarisability of the molecular environment in crystals, while the quantum yields are higher for the methyl substituted compounds, 76% (2Me-BPFB) and 80% (4Me-BPFB), in comparison to BPFB {45%} (Kazantsev *et al*., 2017).

The nature of substituents has been observed to affect substrate affinity with the order Ph ≈ H > Me > ^{i}Pr > Me_2. In comparison to **Fig. 2.10 d**{**i**} – {**vi**}, the possibility of favourable pre-organisation in **Fig. 2.10 d**{**vii**} – {**ix**} provided better affinity and selectivity [**Fig. 2.10 d**{**viii**} and **d**{**ix**} showed better affinity than **d**{**vii**}] – it is believed that cation – π interaction contributed to complex stabilisation (Kim and Ahn 2000). The introduction of methyl groups onto a guest molecule improved the anion binding efficiency, hence sensing behaviour, of 1,3-bis(5,6-dimethyl-1*H*-benzo[*d*]imidazol-2-yl)benzene (**Fig. 2.10**{**e**}). The ligand exhibited fluorescence quenching upon interaction with several anions (F^-, Cl^-, Br^-, I^-, CH_3COO^-, NO_2^-, BF_4^- and HSO_4^-), with the F^- showing the largest turn-off and binding constant (K_a) of 502.79 M^{-1} {other anions have K_a values in the range 18 to 242 M^{-1}} (Chetia and Iyer 2014). Structural modifications involving pyridine nitrogen position as well as change in carbon chain length in **Fig. 2.10**(**f**{**i**}) resulted in better selectivity for Cd^{2+} over Zn^{2+} (Lu, C., *et al* 2007). The inhibition of C-C rotation, upon generation of unsymmetrical analogues to **Fig. 2.11**(**a**{**i**}) {increasing coplanarity} as well as conversion of electron donor {**Fig. 2.11**(**a**{**ii**})} to electron acceptor {**Fig. 2.11**(**a**{**iii**})} has resulted in improved F^- sensing {turn-off} ability – (**a**{**iii**}) > (**a**{**ii**}) > (**a**{**i**}) (Zhang and Liu 2017). The reduction of the imine functionality in **Fig. 2.11**(**b**{**i**}) to amine **Fig. 2.11**(**b**{**ii**}) caused a loss in Hg^{2+} sensing, while the oxidation of a pyrazoline **Fig. 2.11**(**c**{**i**}) to a pyrazole **Fig. 2.11**(**c**{**ii**}), as well as substitution of O atom {**Fig. 2.11**(**d**{**i**})} with NH group {**Fig. 2.11**(**d**{**ii**})}, have resulted in reversal in Cd^{2+} and Zn^{2+} sensing {in both cases, {**i**} showed higher intensity in the presence of Cd^{2+} while {**ii**} showed higher intensity with Zn^{2+}} (Udhayakumari and Velmathi 2013; Ciupa *et al*., 2012; Zhang *et al*., 2013).

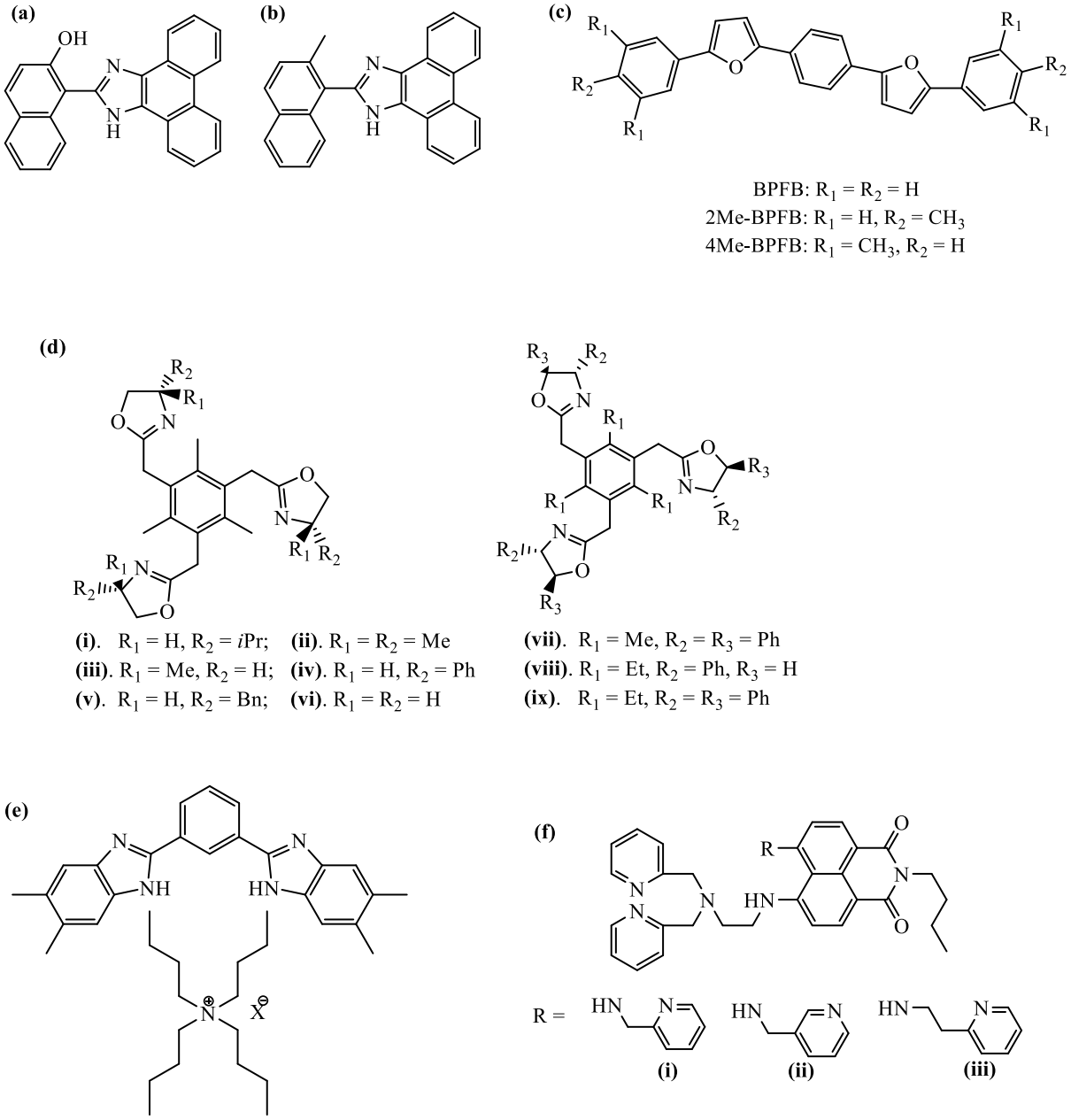

Figure 2.10: (a) – (c) Structure of some synthesised and studied furan/phenylene co-oligomer (d). Tris(oxazolines) with 2,4,6-alkylbenzene framework for *n*-$BuNH_3^+$ sensing (e). Interaction between 1,3-bis(5,6-dimethyl-1*H*-benzo[d]imidazol-2-yl)benzene and anions (f). Effect of pyridine nitrogen position and carbon chain length on Cd^{2+} and Zn^{2+} sensing

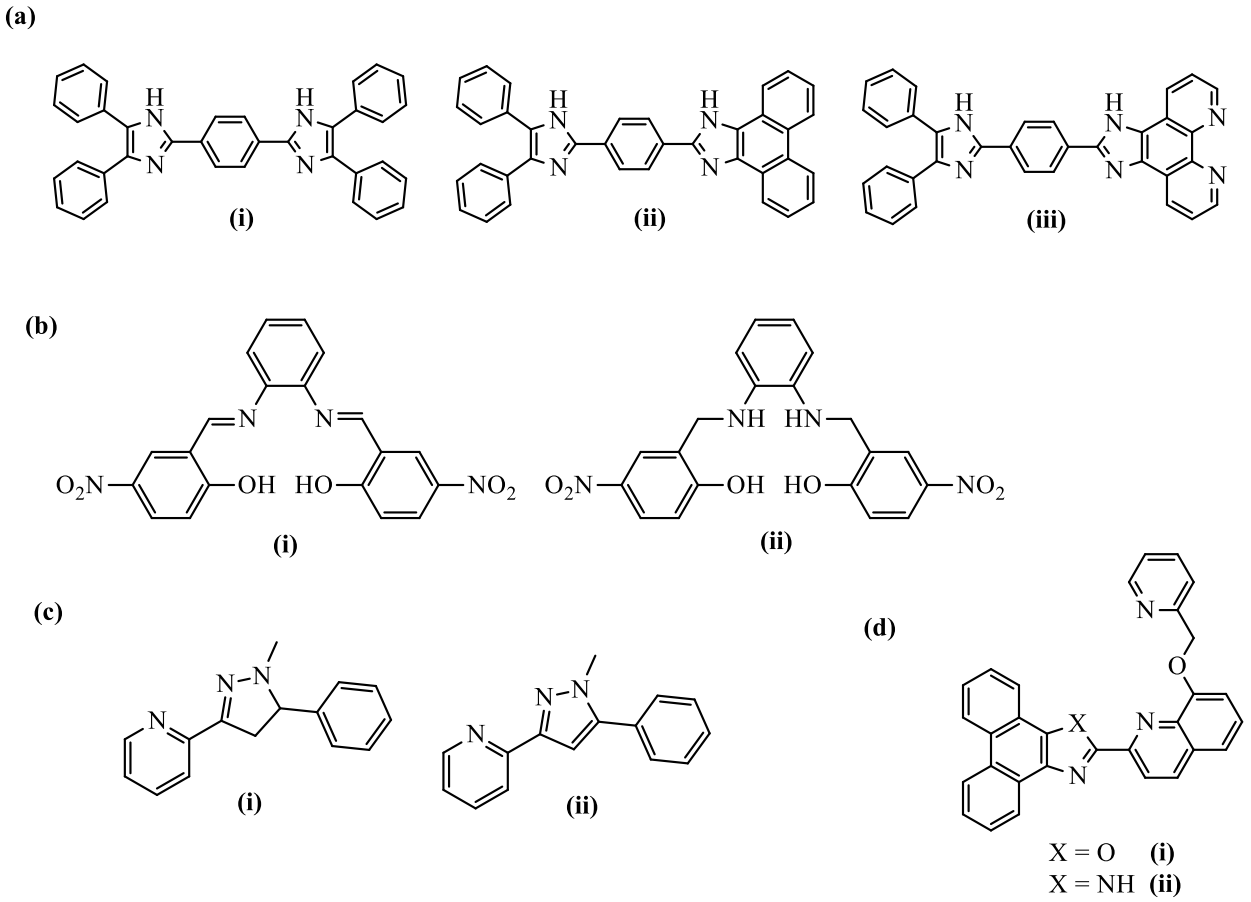

Figure 2.11: (a). Bisimidazoles for F^- sensing (b). Imine/amine for Hg^{2+} sensing (c). Pyrazoline and pyrazole receptors for Cd^{2+} and Zn^{2+} sensing (d). Phenanthro[9,10-*d*]imidazole frameworks for Cd^{2+} and Zn^{2+} sensing

Studying the effect of amino groups at position C2 and C6 of a purine based imine ligand, an increase in the association constant was observed when the amino groups were at position C2 and C6 (K_a = 5.9 x 10^5 M^{-1}) in comparison to when the amino group was at position C2 alone (1.33 x 10^5 M^{-1}) – this was attributed to increase in electron density on the purine N3 nitrogen. A higher K_a value (1.4 x 10^6 M^{-1}) was observed when the amino group was at the C6 position alone. The position of the amino group, however, did not affect the emission wavelength of the compounds (all emit at 488 nm at λ_{ex} = 345 nm), but slightly affected their fluorescence quantum yield {φ_f} (Pratibha *et al*., 2017). Computational studies on the optical properties of four triarylamine-based (TAA) donor molecules showed slight changes in absorption and emission maxima upon substituting one of the phenyl rings in **Fig. 2.12**(**a**) with methyl, α-napthyl, and β-napthyl. A blue shift was observed for the methyl (515 nm) and the α-napthyl (544 nm) substituents, while the β-napthyl molecule exhibited a red shift (559 nm), when compared to the phenyl substituent (552 nm). A similar trend was observed for the emission maxima. The least Stokes shift was observed for the methyl substituted compound (899 cm^{-1}) while the α-napthyl substituted compound showed the highest Stokes shift (1,288 cm^{-1}). The substitution of the phenyl with a methyl increased the face to face π-π packing and allowed a good π-orbital overlap (Alberga *et al*., 2017). On the assumption that the conversion of the amine group in boron dipyrromethene {BDP} chromophore to an imine could result in increased fluorescence of BDP, two different classes of fluorescent dyes {derivatives of BDP and xanthenes, **Fig. 2.12**(**b**)} have been used as turn-off/on sensors for selective detection and monitoring of aldehydes. It was observed that imine formation did not greatly affect the absorption and emission energy of the chromophores. Emission maxima recorded in MeOH were 503 nm to 507 nm {for the BDP derivatives} and 576 nm to 578 nm {for the rosamine derivatives}. These observations were attributed to the presence of methyl groups at the C-1 and C-7 positions of BDP – which resulted in twisted and conjugately uncoupled π-systems of the amino benzene and BDP moieties. However, a 135-fold increase in fluorescence quantum yield was observed for the BDP systems, with a turn-on {ascribed to PET}; while a 10-fold increase was observed for the rosamine systems (Dilek and Bane 2016).

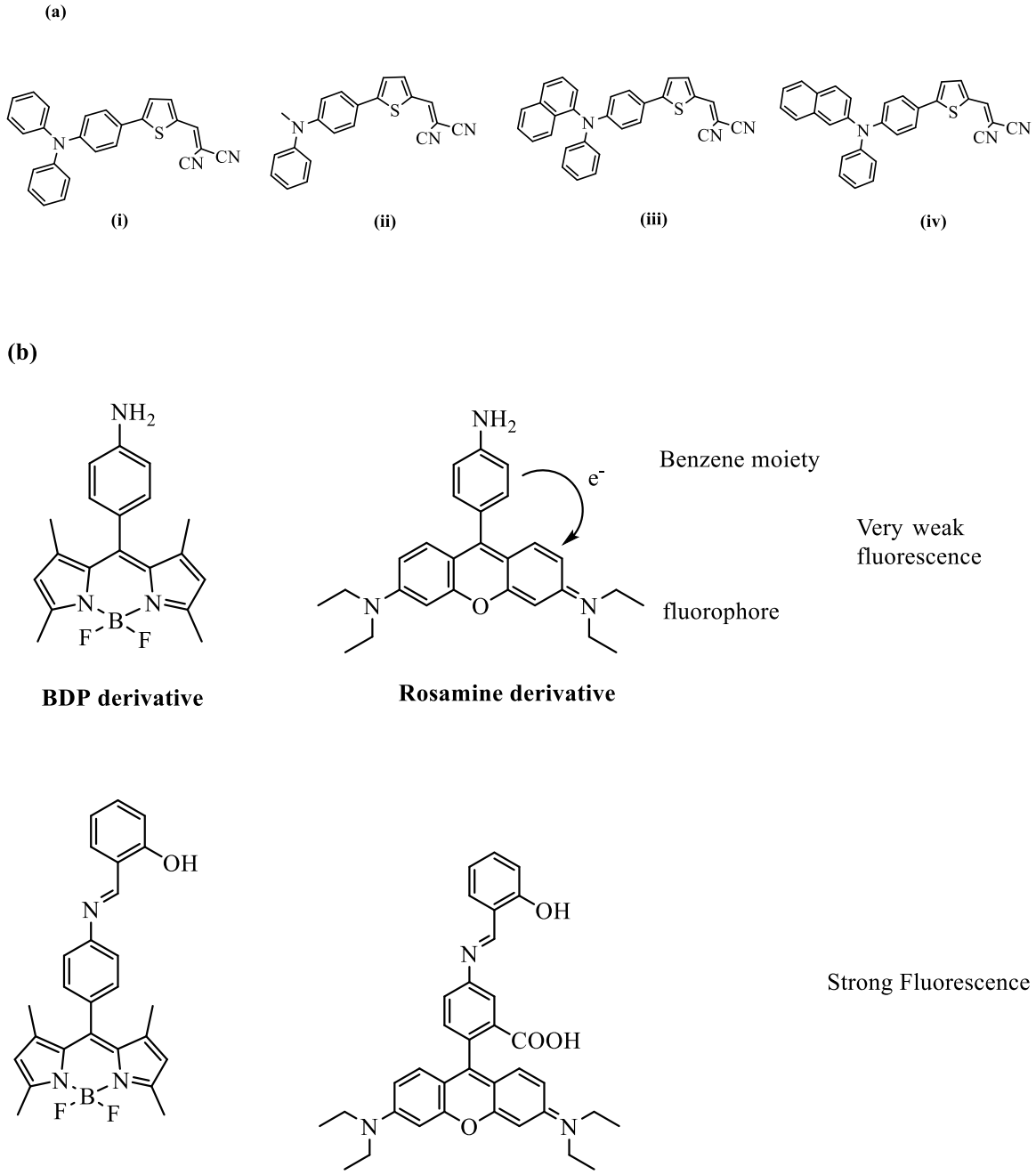

Figure 2.12: (a) Triarylamines-based (TAA) donor molecules studied (b). Structure of amine derivatives of BDP and rosamine and their respective imine derivatives.

2.6 Single Molecule/Ion Magnets (SMMs/SIMs)

There is currently a great search for materials which show potential in the storage and processing of digital information. A major requirement for the storage of information is the ability of such materials to block magnetisation at elevated temperature. Single molecule magnets {SMMs} or Single ion magnets {SIMs} possess qualities which enable them to store information with much higher densities than conventional bulk magnets and allow processing of the information at unprecedented speeds (Fondo *et al*., 2017). Magnetic bistability in SIMs/SMMs arises from the degenerate (M_S = ±S) spin components of the ground-state, with the stability of these ground-states depending on their energy difference to the M_S = 0 or ±½ components for integer or half-integer spins, respectively (Novitchi *et al*., 2017).

One of the determining factors of SMMs or SIMs being used as the smallest component of data storage is the size of the barrier to reversal of the magnetisation, U_{eff}. A high value of U_{eff} suggests a highly efficient SIM/SMM. The U_{eff} has a direct relationship with the anisotropy and spin of molecular magnets (**Eq. 2.1** and **2.2**).

$$U_{eff} = S^2 |D| \qquad \text{for integer spin} \qquad \text{Equation } \mathbf{2.1}$$

$$U_{eff} = \left(S^2 - \frac{1}{4}\right)|D| \qquad \text{for half-integer spin} \qquad \text{Equation } \mathbf{2.2}$$

where S = spin of the metal ion; D = axial zero-field splitting (ZFS) parameter. The inclusion of a non-zero, rhombic zero-field splitting (E term) removes the degeneracy of the ±M_S levels in zero field for an integer spin system, unlike for a half-integer spin system.

The consideration that molecular magnets require high uniaxial anisotropy and well-defined large spin ground states led to the preparation of complexes with high total spin, with manganese clusters {exhibiting ferro- and antiferromagnetic exchange} dominating (Barra *et al*., 1999; Hendrickson *et al*., 2001; Brockman *et al*., 2002; Brechin *et al*., 2003; Chakov *et al*., 2006; Sun *et al*., 2009; Langley *et al*., 2010; Kushch *et al*., 2012; Nguyen *et al*., 2016; Craig and Murrie 2015). A mixed-valent dodecanuclear manganese(III,IV) complex $[Mn_{12}O_{12}(OAc)_{16}(H_2O)_4].2AcOH.4H_2O$ ($Mn_{12}ac$) is among the first reported. This material was observed to have preferential direction for the resultant magnetisation arising

from the precession of the spin in a magnetic field, caused by the anisotropy associated with the metal ions in the complex. At low temperature, by flipping the orientation of the field, this preferential direction can be reversed; that is, switched from lying along the (+) *z*-axis to lying along the (-) *z*-axis (Sessoli *et al*., 1993; Chakov *et al*., 2006; Craig and Murrie 2015; Vallejo *et al*., 2013).

The observation that D has an inverse relationship to S^2 (**Eq. 2.1** and **2.2**) gave indications that U_{eff} has little or no effect on the ground-state total spin and although a large number of polynuclear materials {with high S values} have been reported (Brockman *et al*., 2002; Chakov *et al*., 2005; Langley *et al*., 2010; Hewitt *et al*., 2010; Wei *et al*., 2011; Kushch *et al*., 2012; Cornia *et al*., 2014; Nguyen *et al*., 2016), this strategy often results in materials with low magnetic relaxation barrier {and difficulty in increasing the barrier} due to the absence of Ising-type magnetic anisotropy (Fondo *et al*., 2017; Huang *et al*., 2014). Due to the above challenge other strategies have been adopted to aid understanding and possibly improve the properties of materials with slow magnetic relaxation. These include use of **(i)** *f*-block ions **(ii)** mixed 3*d*-4*f* ions **(iii)** other 3*d* ions {in addition to Mn}. While the 3*d*-4*f* clusters consist only of di-, tri- and polynuclear materials; the use of *f*-block and 3*d* ions also includes mononuclear materials.

A growing realisation that anisotropy is the crucial factor in the design of magnetic materials raised keen interests in materials with single metal centres, SIMs (Fondo *et al*., 2017; Huang *et al*., 2014). Single-ion anisotropy is known to originate from strong spin orbit coupling {SOC} and crystal field effect as the magnetic anisotropy {in SIMs} is observed to depend in the interaction between the metal centre and the ligand field, causing a preferential orientation of the magnetic moment, hence coordination geometry has a strong influence on the SIM properties (Liu *et al*., 2013).

2.6.1 Magnetic behaviour of *f*-block ions

The observation that *f* orbitals are essentially degenerate, with large SOC, has led to a search for suitable *f*-block ions in the preparation of SIMs/SMMs. Late *f*-block metals {especially lanthanides} known for their high magnetic moments, large magnetic anisotropies {arising from unquenched orbital angular momentum} and strong SOC are very suitable candidates (Xiang *et al*., 2017; Demir *et al*., 2017). Dysprosium(III) {Dy^{III}}

ions dominate, in this area, chiefly because of tendency to exhibit large magnetic anisotropy, its Kramer's ion {possessing an odd number of unpaired electrons with a doubly degenerate ground state} property as well as the large energy gap between its ground state and its first excitation level. The Kramer's ion property ensures the degeneracy of $\pm M_J$ ligand-field states {which arise from the effect of the ligand-field symmetry on the ground *J* state} is guaranteed in the absence of a direct-current (*dc*) magnetic field. More so, quantum tunnelling of magnetisation (QTM) is formally forbidden for complexes with odd electron count, although axial magnetic anisotropy, hyperfine or dipole-dipole coupling may still result in a non-zero tunnelling contribution (Novikov *et al*., 2015; Demir *et al*., 2017; Chen *et al*., 2020).

A NCN pincer type ligand Dy^{III} complex {DyNCN, **Fig. 2.13**(**a**)} has been prepared and the observed $\chi_M T$ value of 13.8 cm^3Kmol^{-1} {at room temperature} agreed with expected value for g = $^4/_3$ of the $^6H_{15/2}$ ground state of a single Dy^{III} ion. The $\chi_M T$ value decreased gradually on lowering of temperature – as a result of depopulation of the sub-states. The compound exhibited field induced slow magnetic relaxation with effective relaxation barrier {U_{eff}} of 233 cm^{-1} and relaxation time (τ_o) of 6 x 10^{-10} s – the relaxation occurred through Orbach process {via the second excited state} at high temperatures, and through QTM at low temperatures. On diluting the compound with Lu^{III} {$Dy_{0.05}Lu_{0.95}NCN$} the τ_o at low temperatures was two orders of magnitude slower than DyNCN – suggesting choking of the ground state quantum tunnelling pathway, but the magnetic dilution did not affect the τ_o at higher temperature (Guo *et al*., 2014). In the case of two Dy^{III} complexes (prepared from hydrazone imines Hhmb and H_2hmt {where Hhmb = N′-(2-hydroxy-3-methoxybenzylidene)benzohydrazide; H_2hmt = N′^{1},N′^{4}-bis(2-hydroxy-3-methoxybenzylidene) terephthalohydrazide} [**Fig. 2.13**(**b**) and (**c**)]), The Dy^{III} ions in the prepared complexes $[Dy(hmb)(NO_3)_2(DMF)_2]$ and $[Dy_2(hmt)(NO_3)_4(DMF)_4]$.DMF were in a distorted pentagonal interpenetrating tetrahedral geometry. The $\chi_M T$ (at 300 K) values of the mono- {13.55 cm^3Kmol^{-1}} and dinuclear {28.62 cm^3Kmol^{-1}} complexes were close to expected values for one {14.17 cm^3Kmol^{-1}} and two {28.34 cm^3Kmol^{-1}} uncoupled Dy^{III} ions {$S = ^5/_2$, L = 5, $^6H_{15/2}$, $g = ^4/_3$}. The $\chi_M T$ values decreased at lower temperature reaching 12.19 cm^3Kmol^{-1} (at 2 K) and 26.63 cm^3Kmol^{-1} {at 1.8 K}, respectively – suggesting weak

antiferromagnetic coupling between the metal centres. However, due to the large physical separation between Dy^{III} ions, the decrease was possibly due to thermal depopulation of the Stark sub-levels and/or presence of large anisotropy. The respective complexes had U_{eff} values of 34 K {$\tau_o = 3.2 \times 10^{-6}$ s} and 42 K {$\tau_o = 1.6 \times 10^{-6}$ s}, with the slight difference in energy barrier attributed to minor changes around the coordination environment of the metal ion (Lin *et al*., 2012). In another study of the effect of crystal field a pair of homochiral *β*-diketonate ligands (+)-3-trifluoroacetyl)camphor (*d*-Htfc) and (−)-3-trifluoroacetyl)camphor (*l*-Htfc) were used in the preparation of two enantiomeric pairs of Dy^{III} mixed complexes $[Dy(d\text{-tfc})_3(bpy)]_2$ / $[Dy(l\text{-tfc})_3(bpy)]_2$ {**bpy** = 2,2′-bipyridine} and $[Dy(d\text{-tfc})_3(phen)]\cdot 2H_2O$ / $[Dy(l\text{-tfc})_3(phen)]$ {**phen** = 1,10-phenanthroline}. The homochiral Dy^{III} *β*-diketonate stereoisomers with the **bpy** ligand showed field-induced single-ion magnet behaviours with a two-step relaxation process. No stereoisomerisation was observed for the homochiral Dy^{III} *β*-diketonate with the **phen** coligand, and it exhibited a single relaxation process of the magnetisation only. The anisotropy barriers of $[Dy(d\text{-tfc})_3(bpy)]_2$ {36.5 and 46.1 K} were slightly smaller than those of $[Dy(l\text{-tfc})_3(bpy)]_2$ {37.0 and 49.3 K}, while $[Dy(d\text{-tfc})_3(phen)].2H_2O$ had a larger energy barrier {30.5 K} than $[Dy(l\text{-tfc})_3(phen)]$ {25.1 K}. The thermally activated two-step relaxation process of the **bpy** complexes was attributed to Orbach process (Liu *et al*., 2013). A similar two-step relaxation process had been reported for the distorted square antiprism Yb^{III} complex $\{[Yb(L)(H_2O)_3(DMF)].(HL).(H_2O)\}n$ (where H_2L = 4,5-bis(carboxylic)-4',5'-methyldithiotetrathiafulvene), with the U_{eff} 28 K {$\tau_o = 3.3 \times 10^{-7}$ s} and 3.2 K {$\tau_o = 2.0 \times 10^{-4}$ s}. The decrease in $\chi_M T$ from 2.40 cm^3Kmol^{-1} {at room temperature} to 0.99 cm^3Kmol^{-1} {at 2 K} was attributed to thermal population of the crystal field levels within the ground state multiplet $^2F_{7/2}$ (Castro *et al*., 2016).

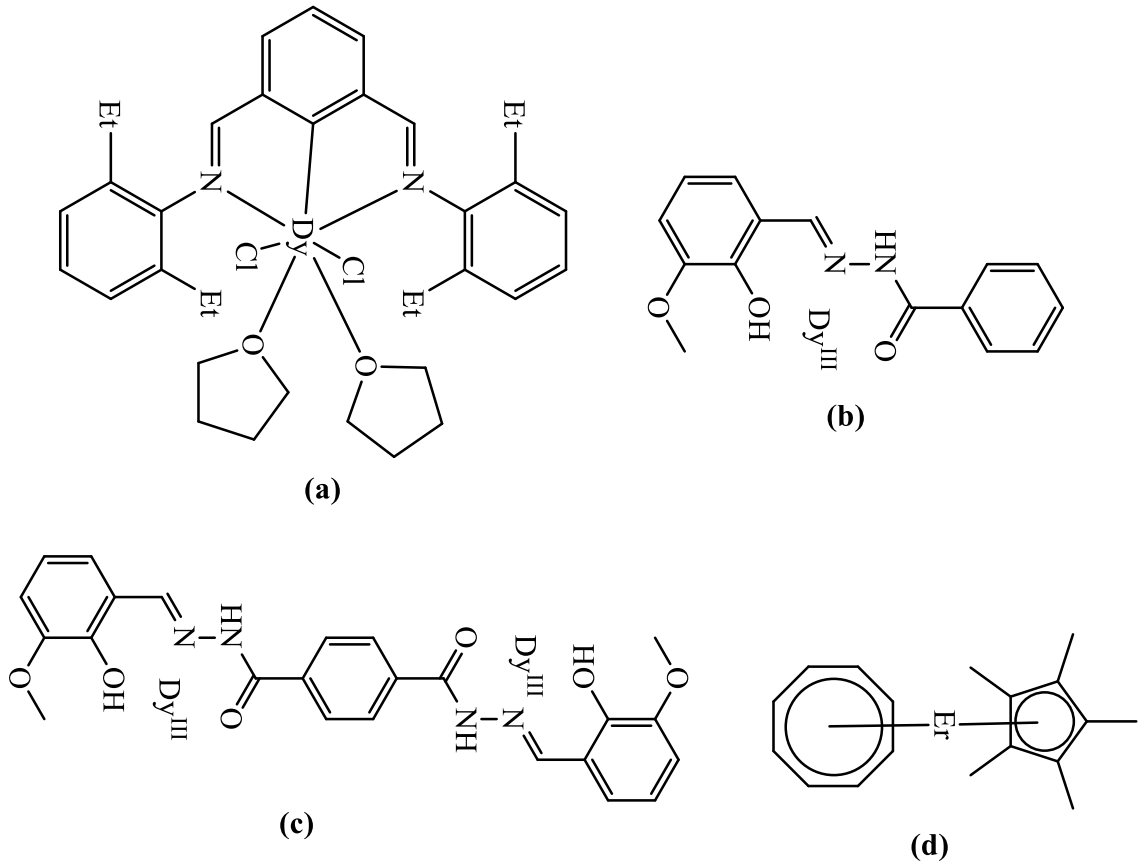

Figure 2.13: Structures of (a) DyNCN (b) complex with Hhmb (c) complex with H_2hmt and (d) [(Cp*)Er(COT)]

In the organometallic Er^{III} based compound [(Cp*)Er(COT), **Fig. 2.13(d)**] {where Cp* = $C_5Me_5^-$ and COT = $C_8H_8^{2-}$}, the ring-shaped aromatic ligands generated higher local symmetry which accounted for observed magnetic properties. The out-of-phase *ac* susceptibility ($\chi^{//}$) of the compound {at 2 to 25 K} showed a clear frequency-dependence on temperature. The $\chi^{//}$ increased on cooling {at < 10 K} suggesting QTM, due to the mixing of the Kramer's ground states. Two relaxation processes {which are thermally activated} were observed for the compound with energy barriers 323 K {τ_o = 8.17 x 10^{-11} s} and 197 K {τ_o = 3.13 x 10^{-9} s}. These relaxation processes were assumed to be from stable conformers in the crystal of the compound (Jiang *et al*., 2011). In the Ln^{III} {Ln = Yb, Er, Dy, Gd, Eu} metal complexes of a **phen** based tetrazole ligand, 2-2(*H*-tetrazol-5yl)-1,10-phenanthroline, with the general formulas $[LnL_3]\cdot MeOH$, $[LnL_2(tmh)(MeOH)].mMeOH.nH_2O$ and $[LnL_2(tta)(MeOH)]\cdot MeOH$ {tmh = 2,2,6,6-tetramethylheptanoate and tta = 2-thenoyltrifluoroacetonate} (**Scheme 2.8**), the magnetic measurements on $[LnL_3]\cdot MeOH$ {Ln = Yb, Er, Dy} revealed SMM behaviour only when an external *dc* magnetic field was applied, with U_{eff} values of 11.7 K {for Yb}, 16.0 K {for Er}, and 20.2 K {for Dy}, respectively. When one of the tridentate **phen** tetrazolate ligand was replaced by one molecule of MeOH and the *β*-diketonate ligands tmh {in $[LnL_2(tmh)(MeOH)]\cdot nH_2O\cdot mMeOH$} or tta {in $[LnL_2(tta)(MeOH)]\cdot MeOH$}, a significant increase in U_{eff} was observed – for {$[LnL_2(tmh)(MeOH)]\cdot nH_2O\cdot mMeOH$} the new values were 29.7K, 30.4 K, and 95.7 K, respectively, while for {$[LnL_2(tta)(MeOH)].MeOH$} the values were 30.3 K, 25.8 K, and 76.0 K, respectively (Jiménez *et al*., 2016).

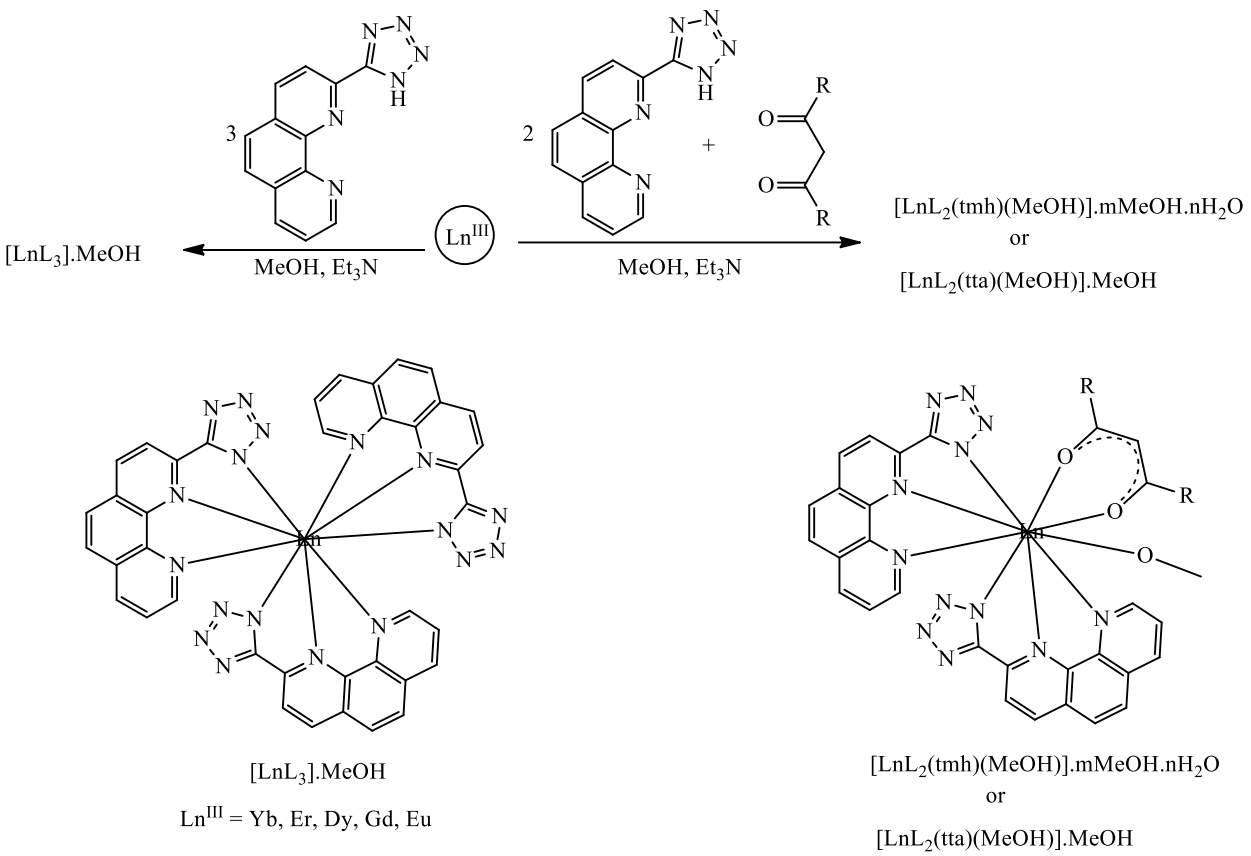

Scheme 2.8: Preparation of a series of lanthanide tetrazolate complexes.

In the Ln^{III} cyanoacetate based complexes {$[Ln_2(CNCH_2COO)_6(H_2O)_4].2H_2O$}n, (where Ln = Eu, Gd, Nd), although the Eu and Gd complexes were isostructural {with a different binding scheme in the case of Nd} the Eu complex showed field induced paramagnetism {expected for a non-magnetic ground state with mixing from higher states}, while the Gd complex did not display slow relaxation (at $H = 0$) because its low anisotropy barrier allowed fast spin reversal through classical processes. On application of an external magnetic field, however, the Gd complex induced two slow relaxation processes; caused by resonant phonon trapping (RPT) mechanism and lifting of the Kramer's degeneracy on the ground state, respectively. Heat capacity and *dc* susceptibility measurements of the Nd complex indicated that at very low temperatures the ground state Kramer's doublet had strong single ion anisotropy, with predominant anisotropy along the *z*-axis. Under an external applied field, two slow relaxation processes appeared at > 3 K – the first relaxation mechanism was of the Orbach type, with an activation energy $U/k_B = 27$ K; while the slower relaxation was caused by the direct relaxation process from the ground state to the Kramer's split levels by the applied field (Arauzo *et al*., 2014).

2.6.2 Magnetic behaviour of mixed 3*d*-4*f* clusters

This strategy involves exploration of strong magnetic interactions (in 3*d* ions) as well as large ground-state spin and magnetic anisotropies (in 4*f* ions) resulting in 3*d*-4*f* heteronuclear clusters – since the non-equivalent metal centres in these 3*d*-4*f* clusters give magnetic properties significantly different from those of homonuclear clusters as well as single-ion materials. Complexes such as Cu^{II}- Ln^{III} {Ln = Gd, Dy}, Co^{II}-Ln^{III} {Ln = La, Gd, Tb, Dy, Ho}, Ni^{II}_2-Ln^{III}_2 {Ln = Dy, Tb, Gd, Sm, Ho, Nd, Pr} and Ni^{II}-Ln^{III}-Ni^{II} {Ln = Sm, Eu, Gd, Tb} have been reported (Costes *et al*., 2000; Elmali and Elerman 2005; Basak *et al*., 2020; Georgopoulou *et al*., 2020; Shen *et al*., 2022). Coupling in Ni^{II}-Ln^{III} {Ln = Gd, Tb, Dy, Ho} tends to be ferromagnetic (Andruh, 2011).

In the heterodinuclear Zn^{II}-Ln^{III} complexes $[ZnTb(HL)(NO_3)(OAc)(H_2O)](NO_3)$(**ZnTb**),{$[ZnDy(HL)(NO_3)(OAc)(MeOH)](NO_3)$}·1¼MeOH·¼$H_2O$ (**ZnDy**), and {$[ZnEr(HL)(NO_3)(OAc)(MeOH)](NO_3)$}·MeOH·¾$H_2O$ (**ZnEr**); heterotrinuclear Zn^{II}-Ln^{III}-Zn^{II} complexes $[Zn_2Dy(L)(NO_3)_2(OAc)_2(H_2O)]$ (**Zn_2Dy**) and {$[Zn_2Er(L)(NO_3)_2(OAc)_2(H_2O)]$}·1½$H_2O$ (**Zn_2Er**); as well as the

metalloligand [Zn_2(L)(OAc)] (**Zn_2Dy**), the observed decreases in $X_M T$ value (more rapidly at < 50K) were attributed to the depopulation of the $\pm M_j$ sub-levels of the Ln^{III} ion as well as contribution from weak intermolecular interactions. The magnetisation values (4.0 – 5.4 M*s*/Nμ_B) obtained were lower than expected for Tb^{III}, Dy^{III} and Er^{III} ions which was probably due to the crystal-field effect resulting in significant magnetic anisotropy. The alternating current (*ac*) magnetic susceptibility measurements of the heterodinuclear complexes showed no observable in-phase (χ') or χ'' maxima, but under a *dc* field **ZnDy** showed frequency and temperature dependence of the χ' and χ'' susceptibility with maxima for χ' and χ'' below 15 K {indicating field induced SMM}, with a U_{eff} of 41.05K {28.53 cm^{-1}}, while the **ZnTb** and **ZnEr** showed no observable maxima for χ' and χ'', hence no slow relaxation of the magnetisation and therefore SMM behaviour. The dilution of **ZnDy** with Y^{III} gave {[$ZnDy_{0.1}Y_{0.9}$(HL)(NO_3)(OAc)(MeOH)](NO_3)}·3H_2O (**ZnDyY**), which was isostructural to **ZnDy** but does not show SMM behaviour, thus, SMM behaviour of **ZnDy** was of molecular origin and QTM was a result of hyperfine interactions. **Zn_2Dy** and **Zn_2Er** behaved as SMMs with U_{eff} of 47.69 K and 20.81 K and τ_o of 4.60 x 10^{-7} s^{-1} and 7.48 x 10^{-7} s^{-1}, respectively. The higher U_{eff} value of **Zn_2Dy** (when compared to **ZnDy**) suggested increase in Zn^{II} ion increased the effective anisotropy barrier of the system (Fondo *et al*., 2017). In a study of some octanuclear complexes [$Co^{III}_4Dy^{III}_4$(μ-OH)$_4$(μ_3-OMe)$_4$($O_2CC(CH_3)_3$)$_4$(tea)$_4$(H_2O)$_4$].4H_2O, (**CoDy1**) [$Co^{III}_4Dy^{III}_4$(μ-F)$_4$(μ_3-OH)$_4$(*o*-tol)$_8$(mdea)$_4$].3H_2O.EtOH.MeOH, (**CoDy2**) [$Cr^{III}_4Dy^{III}_4$(μ-F_4)(μ_3-OMe)$_{1.25}$(μ_3-OH)$_{2.75}$(O_2CPh)$_8$(mdea)$_4$], (**CrDy1**) [$Cr^{III}_4Dy^{III}_4$(μ_3-OH)$_4$(μ-N_3)$_4$(mdea)$_4$(piv)$_4$] (**CrDy2**) { tea^{3-} = triply deprotonated triethanolamine, $mdea^{2-}$ = doubly deprotonated N-methyldiethanolamine and *o*-tol(H) = *ortho*-toluic acid}, it was observed that (**CoDy1**) did not display slow magnetic relaxation above 2 K, while the other compounds showed SMM behaviour with U_{eff} of 39.0 cm^{-1}, 55.0 cm^{-1} and 10.4 cm^{-1}, respectively. The observation suggested that the substitution of OH^- (in **CoDy1**) with F^- (in **CoDy2**) led to quenching of QTM resulting in improved SMM behaviour and the substitution of Co^{III} {in (**CoDy2**)} with Cr^{III} {in (**CrDy1**)} led to further quenching of QTM at low temperatures. The $\chi_M T$ (at 300 K) values for (**CoDy1**) and (**CoDy2**) {56.68 and 56.27 cm^3Kmol^{-1}, respectively} were in good agreement with the expected value of 56.68 cm^3Kmol^{-1} for four Dy^{III} ions – the Co^{III} ions were in a low spin d^6 configuration so showed no contribution to the magnetic

susceptibility, except for small second-order Zeeman contribution. The $\chi_M T$ values, in both compounds {(**CoDy1**) and (**CoDy2**)}, decreased gradually then rapidly (below 50 K) suggesting weak antiferromagnetic exchange between the Dy^{III} ions and/or large single ion anisotropy (Vignesh *et al*., 2017). In the case of the heptanuclear $[Cr^{III}Dy^{III}_6(\mu_3\text{-}OH)_8(o\text{-}tol)_{12}(NO_3)(MeOH)_5].3MeOH$ complex, the observed $\chi_M T$ value {at 300 K} of 87.16 cm^3Kmol^{-1} agreed with the expected value {86.9 cm^3Kmol^{-1}} for one Cr^{III} and six Dy^{III} ions that are non-interacting. Similar to the octanuclear compounds {**CoDy1**, **CoDy2**, **CrDy1** and **CrDy2**}, the $\chi_M T$ value decreased gradually then rapidly {at < 50 K} to 14.37 cm^3 K mol^{-1} {at 2 K} – the gradual decrease was attributed to depopulation of the excited M_j Stark states of the Dy^{III} ions, while the rapid decreases indicated dominant antiferromagnetic exchange interaction. The $\chi_M T$ value at 2 K is higher than that expected for single paramagnetic Cr^{III} ion suggesting there were several close highly excited states including that of Dy^{III} ion {which possessed significant magnetic moment} (Vignesh *et al*., 2017). In the isomorphous heterometallic tetranuclear complexes $[Dy_2Co_2L_{10}(bpy)_2]$ (**DyCo**), $[La_2Ni_2L_{10}(bpy)_2]$ (**LaNi**), $[Gd_2Ni_2L_{10}(bpy)_2]$ (**GdNi**), $[Tb_2Ni_2L_{10}(bpy)_2]$ (**TbNi**), $[Dy_2Ni_2L_{10}(bpy)_2]$ (**DyNi**), and $[Ho_2Ni_2L_{10}(bpy)_2]$ (**HoNi**) {L^- = 3,5-dichlorobenzoate anion [a bridging ligand] and **bpy** is a terminal bidentate ligand}; the $\chi_M T$ of (**DyCo**) decreased gradually {from 33.78 cm^3 K mol^{-1} [at 300 K]} then increased sharply {to 36.40 cm^3 K mol^{-1} [at 2 K]} – indicating presence of some weak intramolecular ferromagnetic exchange between the two Co^{II} ions mediated by the two Dy^{III} ions. The compound (**DyCo**) had a magnetisation of 16.93 Nβ which was lower than expected (26 Nβ) due to large magnetic anisotropy. A similar observation {for $\chi_M T$} was made for (**DyNi**). The U_{eff} of (**DyCo**) was found to be 118 K {82 cm^{-1}} at zero Oe and 114 K {79.4 cm^{-1}} at 1000 Oe; while that of (**DyNi**) was 105 K {73 cm^{-1}} at zero Oe – the calculated energies of 66.1 cm^{-1} and 61.0 cm^{-1} for the first excited spin-orbit state of Dy^{III} in the respective complexes agreed with the effective energy barriers. All the other compounds generally showed a decrease in $\chi_M T$ with no increase (Zhao *et al*., 2014).

Although great strides have been made in *f*-block materials with SIM/SMM properties, the magnetic hysteresis in most of the materials are observed at very low

temperatures {and not at room temperature conditions}, limiting their use in devices (Novikov *et al*., 2015; Yang *et al*., 2022).

2.6.3 Magnetic behaviour of 3*d* ions

First row transition metal (3*d*) ions are known to have smaller magnetic moments and lower SOC constants than *f*-block ions. More so, the ligand field in 3*d* ions usually results in the quenching of the orbital angular momentum, but low oxidation states, high local coordination symmetries, and low coordination numbers usually lead to weak ligand-field and enhanced magnetic anisotropy as a result of nearly unquenched orbital angular momentum. A common feature of 3*d* transition metal ions used as SIMs is low coordination number (ranging from 2 to 6) of the metal centres, which affords a relatively weak ligand field, reducing the orbital splitting energy and increasing the magnetic anisotropy (Huang *et al*., 2014; Xiang *et al*., 2017; Zadrozny *et al*., 2013; Wu *et al*., 2017). Higher coordination number (for example eight) in late transition metals has also been observed to result in weak ligand field and strongly distorted coordination environment (Xiang *et al*., 2017).

The high-spin Fe^{II} {d^6} complex {K[(tpa^{Mes})Fe]}(Where H_3tpa^{Mes} = Tris((5-mesityl-1*H*-pyrrol-2-yl)methyl)amine), in a *dc* field, has been reported to have a *D* value of -39.6 cm^{-1} and rhombic ZFS {*E*} contribution of -0.4 cm^{-1}. The theoretical U_{eff} value (158 cm^{-1}) was higher than the observed value (42 cm^{-1}) possibly due to tunnelling effect. The bulkiness of the ligand promoted unusual geometry around the metal centre, with the Fe^{II} ion lying in a trigonal pyramidal geometry {in an N_4 coordination sphere}. The observed rhombic contribution arose from the small structural distortion around the Fe^{II} ion, which lowered the three-fold symmetry. The $\chi_M T$ value of 3.66 cm^3Kmol^{-1} (typical for $S = 2$ with $g = 2.21$) decreased below 70 K as a result of ZFS of the M_s levels – only the $|M_s| = 2$ levels are populated at low temperatures (Freedman *et al*., 2010). In the eight-coordinate complex ({[$Fe^{II}(L_1)_2$]($ClO_4)_2$}, **Fig. 2.14**), where the Fe^{II} coordinates with four N atoms and four O atoms, in a highly distorted dodecahedron, the observed room temperature magnetic moment (5.72 μ_B) was significantly higher than the spin-only value (4.90 μ_B) for high-spin Fe^{II} ion and indicated large contribution from unquenched orbital angular anisotropy. The $\chi_M T$ value of 3.58 cm^3Kmol^{-1} (at 300 K) was also significantly higher than the expected spin-only value (3.0 cm^3Kmol^{-1}) for $S = 2$, g = 2; and suggested strong SOC. The $\chi_M T$

decreased rapidly to 2.59 cm^3Kmol^{-1} (at 2 K) indicating strong magnetic anisotropy. The compound had a U_{eff} of 27 K with τ_o of 2.7 x 10^{-8} s (and D = -11.7 cm^{-1}, E = 0.08 cm^{-1}). The spin relaxation was suggested to be as a result of QTM {at low temperatures} and through Orbach mechanism {at high temperature} (Xiang *et al*., 2017). In the almost perfectly linear {bond angle of C-Fe-C = 179.2(2)°} d^7 Fe^I compound [K(Crypt-222)][(Fe(C($SiMe_3$)$_3$)$_2$], SOC caused splitting of the ^{4}E ground state into four doublets M_j $\pm^7/_2$, $\pm^5/_2$, $\pm^3/_2$ and ±½ with energy spacing ≈ 24 cm^{-1}. The $\chi_M T$ at 300 K of 3.39 cm^3Kmol^{-1} (which was close to the values observed for the Fe^{II} in **Fig. 2.14**), increased upon cooling then it gradually decreased (at 125 K) before rapidly dropping (below 5.5 K) to 0.18 cm^3Kmol^{-1} (at 2 K); the temperature profile above 5.5 K suggested presence of first order angular momentum which enabled the compound to record a U_{eff} of 226 cm^{-1} (325 K) with τ_o of 1.3 x 10^{-9} s under a zero *dc* field (one of the highest to be observed). The spin relaxation was believed to occur through Orbach mechanism with QTM observed below 20 K possibly due to intermolecular dipolar interactions with some geometric distortions (which led to deviation from strict axial symmetry inducing mixing of the ground M_j $\pm^7/_2$ levels). The compound exhibited hysteresis at 1.8 – 6.5 K under a field of 2 T (Zadrozny *et al*., 2013). A six-coordinate, Mn^{III} complex Ph_4P[Mn(opbaCl_2)(py)$_2$] {H_4opbaCl_2 = *N*,*N*'-3,4-dichloro-*o*-phenylenebis(oxamic acid), py = pyridine} has also been reported to possess field-induced slow magnetic relaxation behaviour. The manganese atom showed tetragonally elongated octahedral coordination geometry typical for d^4 Mn^{III} ion experiencing Jahn–Teller distortion. The N_2O_2 ligand formed three five-membered chelate rings that imposed a distortion around the metal centre giving rise to an axially elongated Mn^{III} ion. The compound was observed to have a D value of -3.421(2) cm^{-1} and E of -0.152(2) cm^{-1}. The calculated axial magnetic anisotropy (D_{SOC} = -2.97 cm^{-1}) was observed to be mainly as a result of second order SOC, with small spin-spin contribution (D_{SS} = -0.50 cm^{-1}). Maxima $\chi^{//}$ were seen on the application of a *dc* field of 1000 Oe, and the Arrhenius plot gave U_{eff} = 12.6 cm^{-1}. The $\chi_M T$ value of 2.99 cm^3Kmol^{-1} (at 300 K; for S = 2 with g = 2.0) decreased abruptly at 40 K to reach a value of 2.22 cm^3Kmol^{-1} (at 2.0 K) and revealed occurrence of significant ZFS – it was assumed that superparamagnetic blocking is avoided because of the fast zero-field QTM (Vallejo *et al*., 2013).

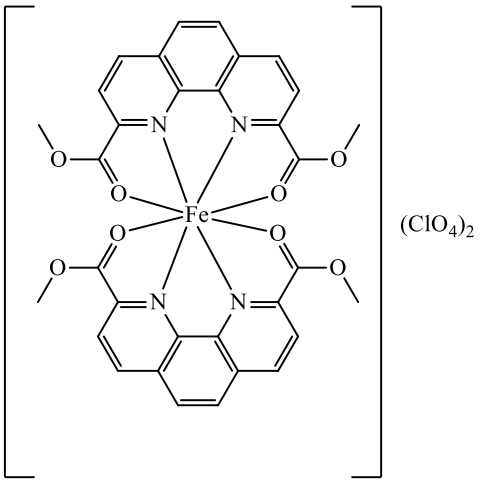

Figure 2.14: Structure of an eight coordinate Fe^{II} complex exhibiting slow magnetisation

Magnetisation studies of the seven coordinate imine complexes $[Co^{II}(H_2dapb)(H_2O)(NO_3)](NO_3)$, $[Co^{II}L_{N5}(H_2O)_2]Cl_2 \cdot 4H_2O$ (where H_2dapb = 2,6-diacetylpyridine bis(benzoylhydrazine); L_{N5} = 2,13-dimethyl-3,6,9,12-tetraaza-1(2,6)-pyridinacyclotridecaphane-2,12-diene) showed $\chi_M T$ values (at 300 K) of 2.63 and 2.61 cm^3Kmol^{-1}, respectively. The values were larger than the spin-only value (1.875 cm^3Kmol^{-1}) expected for high-spin Co^{II} ions and fell in the range (2.1 to 3.4 cm^3Kmol^{-1}) for highly anisotropic Co^{II} ions with considerable contribution from the orbital angular momentum. The $\chi_M T$ values decreased upon cooling (at 1.8 K) to 1.56 and 1.53 cm^3Kmol^{-1}, respectively, suggesting intrinsic magnetic anisotropy of the Co^{II} ions. The complexes have U_{eff} values of 56.3 cm^{-1} (81.2 K) and 20.7 cm^{-1} (29.8 K), with τ_o of 6.0 x 10^{-10} s and 1.2 x 10^{-6} s respectively. The field induced slow magnetic relaxation is suggested to be as a result of Orbach process for the former, while for the latter it is as a result dominant optical acoustic Raman process (Huang *et al*., 2014). In a pseudo-clathrochelate Co^{II} complex {in which a slight distortion resulted in the pseudo-octahedral geometry which weakens the ligand field and gave rise to a high-spin d^7 system}, the temperature profile {with $\chi_M T$ of 2.87 cm^3Kmol^{-1} (at 300 K)} followed same trend as the pentagonal bipyramidal complexes {$[Co^{II}(H_2dapb)(H_2O)(NO_3)](NO_3)$ and $[Co^{II}L_{N5}(H_2O)_2]Cl_2 \cdot 4H_2O$}, and the decreased $\chi_M T$ {upon cooling} attributed to magnetic anisotropy. The observed U_{eff} {152 cm^{-1}} was however higher than those reported for the seven coordinate complexes, and attributed to Orbach relaxation process (Novikov *et al*., 2015).

In the distorted pseudo-tetrahedral Co^{II} complexes, $[Co(L^{Br})_2]$ and $[Co(L^{Ph})_2]$.DCM, prepared from bidentate N,O type imine ligands {where HL^{Br} = 1-[*N*-(4-Bromophenyl)carboximidoyl]naphthalen-2-ol and HL^{Ph} = 1-[N-(2-Phenylphenyl)carboximidoyl]naphthalen-2-ol} (**Scheme 2.9**{**a**}); the compounds gave $\chi_M T$ value of ≈ 2.38 cm^3Kmol^{-1} (at 300 K, with g = 2.25) suggesting presence of SOC. The $\chi_M T$ value decreased gradually upon cooling, then rapidly (at < 50 K) reaching 0.99 cm^3Kmol^{-1} {$[Co(L^{Br})_2]$} and 1.77 cm^3Kmol^{-1} {$[Co(L^{Ph})_2]$} – this was attributed to magnetic anisotropy of the Co^{II} ions and/or antiferromagnetic intermolecular exchange interactions. Magnetisation plot (at 2 K and 5 T) indicated saturation was not reached for both

compounds with magnetisation ≈ 2.0, suggesting strong ZFS effects in both complexes. The *D* values for the compounds were calculated to be 36.7 cm^{-1} and -39.8 cm^{-1}, respectively. The larger *D* value of the second compound was attributed to its larger distortion from tetrahedral geometry, which encouraged mixing of the ground state with the excited states. The compounds, at 400 Oe, had U_{eff} of 36 cm^{-1} (τ_o = 5.6 x 10^{-10} s) and 43 cm^{-1} (τ_o = 8.4 x 10^{-10} s), respectively (Ziegenbalg *et al*., 2016). The *D* values of the complexes (derived from the ligands in **Scheme 2.9**{**a**}) were similar to the *D* values of previously reported Co^{II} complexes derived from the imidazole based N_2O_2 ligands {**Scheme 2.9**(**b**)} (Buchholz *et al*., 2012), but the N,O based complexes gave slightly higher U_{eff} values (at 400 Oe). The compounds (from ligands in **Scheme 2.9**{**a**}) showed no slow magnetic relaxation in the absence of an applied *dc* field, which was attributed to QTM within individual Kramer's' doublets {KDs} (Ziegenbalg *et al*., 2016).

The mixed imidazole complex $[Co^{II}(dapb)(Im)_2](H_2O)$ (where H_2dapb = 2,6-diacetylpyridine bis(benzoylhydrazine); Im = imidazole) showed $\chi_M T$ values (at 300 K) of 2.48 cm^3Kmol^{-1}, which was larger than the spin-only value (1.875 cm^3Kmol^{-1}) expected for high-spin Co^{II} ions and fell in the range (2.1 to 3.4 cm^3Kmol^{-1}) for highly anisotropic Co^{II} ions with considerable contribution from the orbital angular momentum. The $\chi_M T$ values decreased upon cooling to 1.37 cm^3Kmol^{-1} (at 1.8 K) suggesting intrinsic magnetic anisotropy of the Co^{II} ion. The complex had U_{eff} value of 62.3 cm^{-1} (89.6 K) with τ_o 8.7 x 10^{-11} s. The field induced slow magnetic relaxation was suggested to be as a result of Orbach and Raman processes (Huang *et al*., 2014). Two six-coordinate complexes, $[Co(Im)_6](BPh_4)_2$ and $[Co(Im)_6](NO_3)_2$, showed similar trend as observed in $[Co^{II}(dapb)(Im)_2](H_2O)$. The cation, $[Co(Im)_6]^{2+}$, in these complexes exhibited quasi-octahedral geometry with ideal C_i and D_{3d} symmetries, respectively. The observed $\chi_M T$ (at 300 K) of 3.05 cm^3Kmol^{-1} {$[Co(Im)_6](BPh_4)_2$} and 3.25 cm^3Kmol^{-1} {$[Co(Im)_6](NO_3)_2$} were in the expected range - suggesting strong orbital contribution. These values decreased to 1.67 cm^3Kmol^{-1} and 1.89 cm^3Kmol^{-1} (at 2 K) for the respective complexes. Magnetic relaxation appeared faster in $[Co(Im)_6](NO_3)_2$ than $[Co(Im)_6](BPh_4)_2$, with χ'' signals observed at 20.7 Hz {$[Co(Im)_6](BPh_4)_2$} and 137.9 Hz {$[Co(Im)_6](NO_3)_2$}, under a field of 1000 Oe. The compounds showed U_{eff} values of 21.6 K {τ_o = 1.5 x 10^{-6} s} and 6.3 K {τ_o = 4.5 x 10^{-5} s}, respectively (Chen *et al*., 2018).

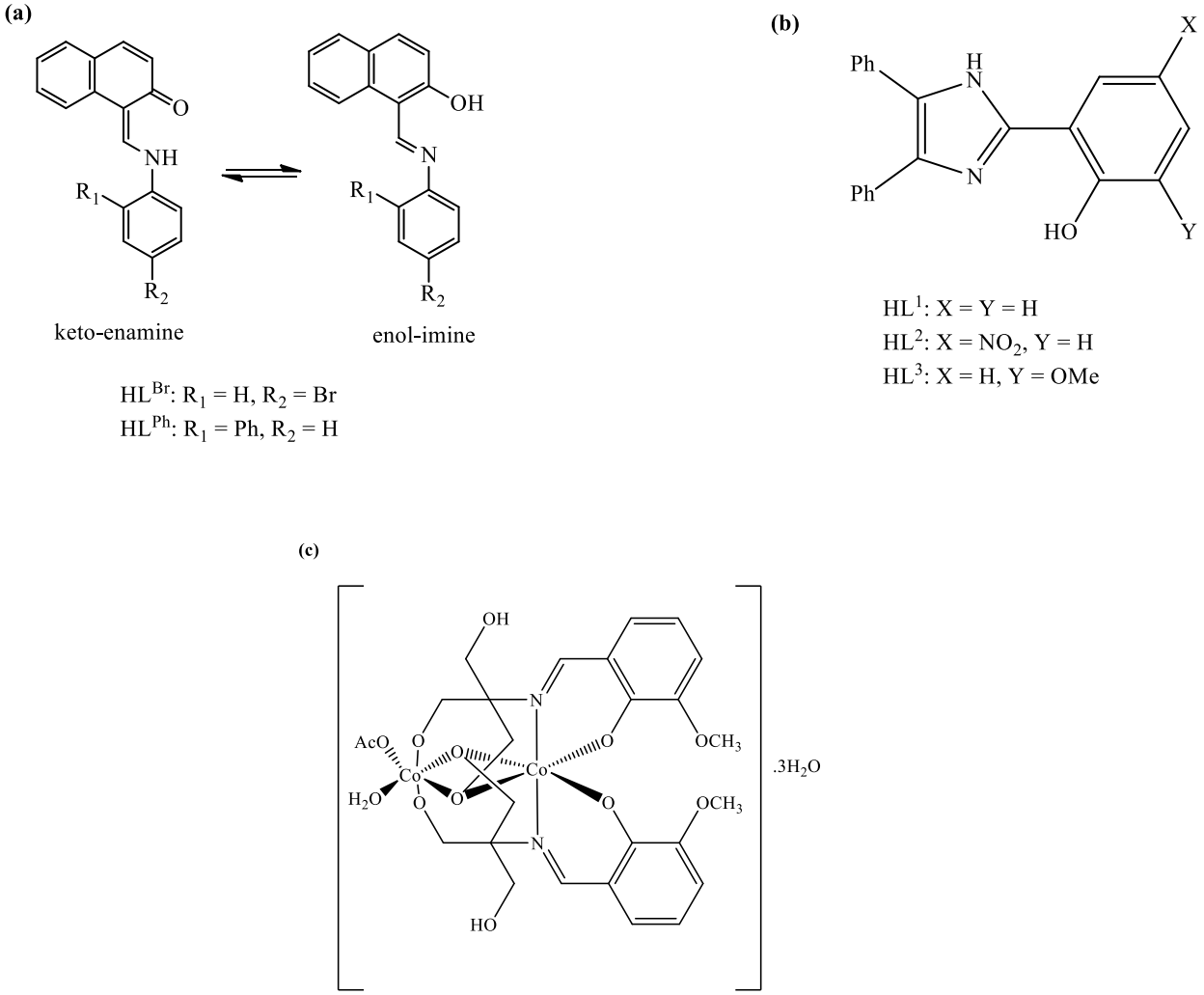

Scheme 2.9: (a). Tautomeric Equilibrium of the ligands HL^{Br} and HL^{Ph} (b). Imidazole based N,O ligands (c) Structure of $[Co^{II}Co^{III}(LH_2)_2(OAc)(H_2O)](H_2O)_3$

The coordination complex, $[Co^{II}(bpm)_2(H_2O)_2][Co^{II}(bpm)_2(N_3)_2](ClO_4)_2$ {where bpm = bis(pyrazol-1-yl)methane}, under a field of 1000 Oe gave $\chi_M T$ value of 6.68 cm^3Kmol^{-1} (at 300 K) which was expected for two single non-interacting d^7 Co^{II} ion with considerable contribution from orbital angular momentum. The $\chi_M T$ decreased slightly {upon cooling} due to ZFS of the Co^{II} ion. It was observed that the Co^{II} ion in $[Co(bpm)_2(N_3)_2]$ species was uniaxially anisotropic with a negative D value (-282.4 cm^{-1}), while the Co^{II} ion in $[Co(bpm)_2(H_2O)_2]^{2-}$ species was easy-plane anisotropic with a D = 46.3 cm^{-1} and E = -27.8 cm^{-1}. The slow magnetic relaxation, resulted from the combined uniaxial anisotropy and easy plane anisotropy, and gave a U_{eff} of 33 K, with τ_o of 1.5 x 10^{-7} s – the fast relaxation, under a zero field, was attributed to QTM through the spin-reversal barrier (Zhu *et al*., 2014). In the dinuclear mixed valence cobalt complex $[Co^{II}Co^{III}(LH_2)_2(OAc)(H_2O)](H_2O)_3$, {$LH_4$ = 2-{[(2-hydroxy-3-methoxyphenyl)methylene]amino}-2-(hydroxymethyl)-1,3-propanediol} (**Scheme 2.9**(**c**)), an effective magnetic moment, μ_{eff} of 4.97 μ_B (at 298 K) which decreased to 3.92 μ_B (at 1.9 K) was observed. The decrease was ascribed to depopulation of the magnetic energy levels. The magnetisation per formula unit of the compound (2.57) was much lower than the spin-only value (3.95), while the compound had $\chi_M T$ values of 3.06 cm^3Kmol^{-1} (at 300 K) and 1.91 cm^3Kmol^{-1} (at 2 K) - confirming the presence of a sizable magnetic anisotropy of an easy axis type. The ground term for the Co^{II} ion in **Scheme 2.9**(**c**) was found to be the orbitally degenerate ^4E_g instead of the orbital singlet $^4A_{2g}$ common to hexacoordinated Co^{II} ions (Buvaylo *et al*., 2017).

2.7 Effect of Ligand type and bridging on magnetic property

The nature of ligand has great input on observed magnetic behaviours and in this regard a variety of ligand architecture had been explored. The introduction of substituents, close binding cavities, possibilities of different coordination modes (topology), ability to participate in hydrogen bond extension and transmit electronic effect, use of paramagnetic radicals, use of rigid framework have been observed to affect magnetic properties (Thompson *et al*., 1996; Hossain *et al*., 2002; Escuer *et al*., 2004; Pasán *et al*., 2005; Yuste *et al*., 2007; Benmansour *et al*., 2008; Wei *et al*., 2011; Gao *et al*., 2013; Castro *et al*., 2014;

Liu *et al*., 2015; Chilton *et al*., 2015; Ding *et al*., 2016; Wang *et al*., 2017; Plaul *et al*., 2018; Sun *et al*., 2019; Sherstobitova *et al*., 2019; Wang *et al*., 2019).

Schiff base ligands with possibility of structural flexibility, chelate formation, N-donating and π-accepting abilities have gained prominence (Aranha *et al*., 2007; Yue *et al*., 2008; Li *et al*., 2010; Rigamonti *et al*., 2012; Dehghani-Firouzabadi *et al*., 2016; Wang *et al*., 2016; Cho *et al*., 2016; Chang *et al*., 2017; Huang *et al*., 2017; Cisterna *et al*., 2018; Pandey *et al*., 2019; Zolotukhin *et al*., 2020; Xue *et al*., 2021; Bazhenova *et al*., 2021a; Bazhenova *et al*., 2021b). Salicylaldehyde and its derivatives are prominent, especially in cases where phenoxido-bridging is desired, and subtle molecular modifications in these systems have been found to impart magnetic properties (Tuna *et al*., 1999; Tuna *et al*., 2000; Niu *et al*., 2005; Sreenivasulu *et al*., 2005; Kannappan *et al*., 2006; Roth *et al*., 2006; Yuan *et al*., 2007; Pang *et al*., 2008; Bhargavi *et al*., 2009; Chakraborty *et al*., 2009; Thakurta *et al*., 2009; Mukherjee *et al*., 2009; Naiya *et al*., 2010; Matsuoka *et al*., 2011; Rigamonti *et al*., 2011; Nematirad *et al*., 2012; Rigamonti *et al*., 2012; Lu *et al*., 2013; Wang *et al*., 2013; Sutradhar *et al*., 2013; Wang *et al*., 2013; Gao *et al*., 2013; Ghosh *et al*., 2014; Hazra *et al*., 2014; Jana *et al*., 2014; Gildea *et al*., 2014; Realista *et al*., 2016; Pogány *et al*., 2018; Wang *et al*., 2019; Yu *et al*., 2019; Pogány *et al*., 2019; Muddassir *et al*., 2020; Basak *et al*., 2020; Chen *et al*., 2020; Wang *et al*., 2020; Georgopoulou *et al*., 2020; Wang *et al*., 2022; Shen *et al*., 2022; Yang *et al*., 2022).

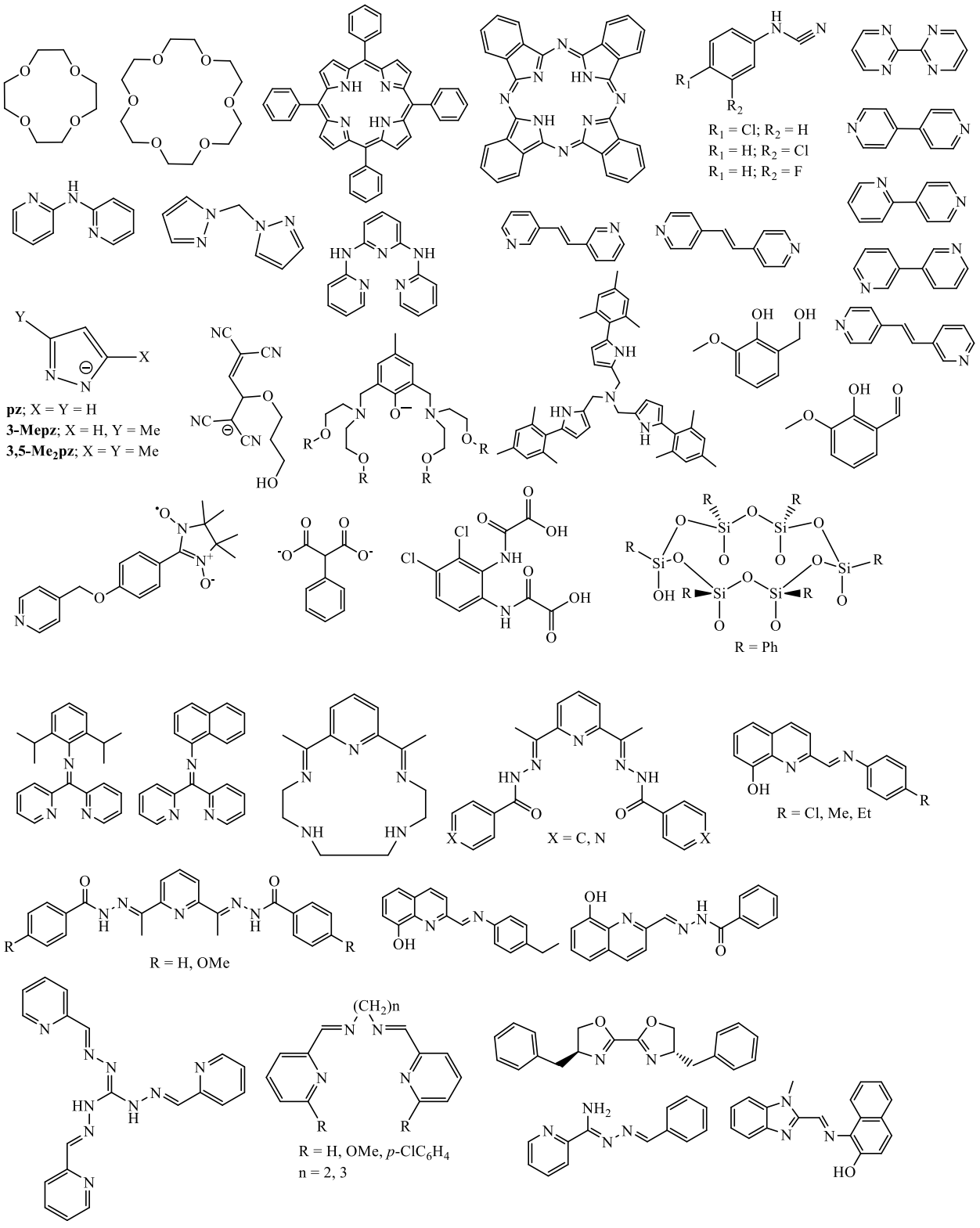

Figure 2.15: Structures of some ligands used in preparation of SIMs/SMMs

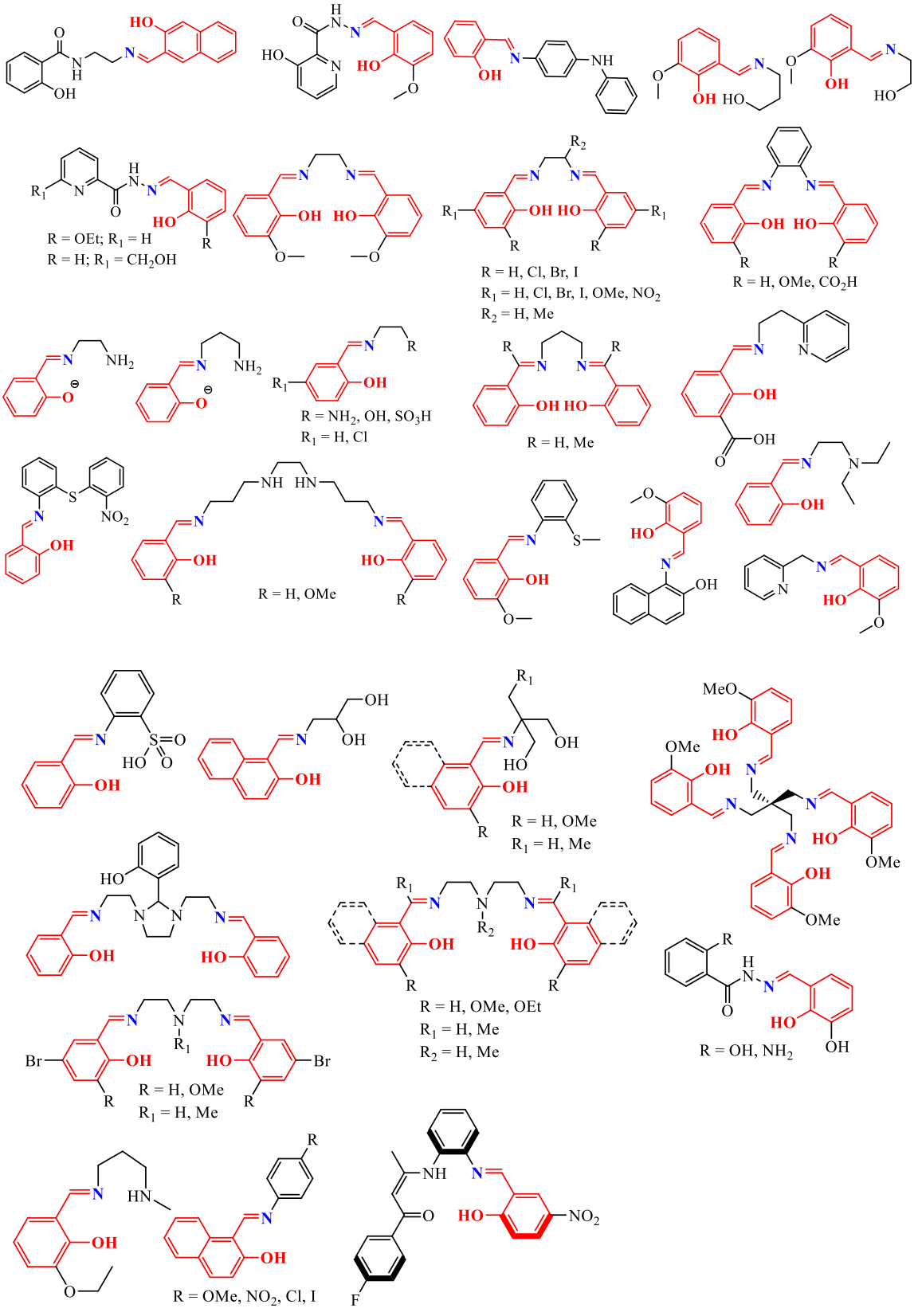

Figure 2.16: SIMs/SMMs based ligands from Salicylaldehyde and its derivatives.

In addition to backbone flexibility, certain ligands are able to generate bridges in metal complexes. The presence of μ-bridges {in complexes} have been observed to perturb magnetic exchange interactions, since these bridges have the ability to induce different stereochemical preferences on metal ions (Cornia *et al*., 1995; Costes *et al*., 2002; Kushvaha *et al*., 2019). Weak antiferromagnetic exchange interaction {J = -1.5 to -2.1 cm^{-1}}, in a series of dinuclear Co^{II} complexes, resulted in a poor pathway provided by bridging groups (Tomkowicz *et al*., 2012); a similar effect was observed in the bpe {1,2-bis(4-pyridyl)ethane} bridged mixed valent $[\{Co^{II}Co^{III}(mea)_3\}_2(bpe)_3](ClO_4)_4.1½MeOH.1½H_2O$ {J = -0.06 cm^{-1}} as well as the oxo-bridged $[Co_2(\mu\text{-}OPhR)(\mu\text{-}1,3\text{-}O_2P(OPh)_2)_2]$ {J = -1.6 cm^{-1}} and $[Co_2(\mu\text{-}OAc)\{\mu\text{-}O(N)(O{=}C)2(CH_2)_3\}(Im)_4](OTf)_2$ {J = -1 cm^{-1}} complexes (Tudor *et al*., 2008; Johansson *et al*., 2008; Brown *et al*., 2004), while carboxylate bridging in $[(L)_2Co^{II}_2(\mu\text{-}OAc)_2](BPh_4)_2$, **A**, and $[Co_2(bta)(H_2O)_6]_n.2nH_2O$, **B**, however, resulted in ferromagnetic exchange {J = +1.60(2) cm^{-1}} and {J = +5.4 cm^{-1}}, respectively. At 300 K, **A** gave μ_{eff}, in solid {and MeCN solutions at 298 K}, of 4.75 {5.05} μ_B, which was larger than expected for $S = {}^3/_2$ [$\mu_{so} = \{4S(S + 1)\}^{1/2} = 3.87\ \mu_B$], suggesting significant orbital contribution. The value was however close to the expected value when the spin momentum ($S = {}^3/_2$) and the orbital momentum (L = 3) existed independently [$\mu_{LS} = \{L(L + 1) + 4S(S + 1)\}^{1/2} = 5.20\ \mu_B$] suggesting contribution of the orbital momentum typical of the $^4T_{1g}$ ground state, under pure O_h symmetry. **B** also recorded a μ_{eff} (4.71 μ_B) greater than the spin-only value - suggesting octahedral distortion in **B** was not large enough to induce total quenching of the $^4T_{1g}$ ground state (Mishra *et al*., 2006; Fabelo *et al*., 2009). In the μ-aquo-bis(μ-carboxylato) bridged complexes $[M_2(Im)_4(OAc)_4(H_2O)]$ where M = Mn, Co, Ni, antiferromagnetic coupling was observed {Mn (J = -1.29 cm^{-1}, g = 1.89); Co (J = -1.60 cm^{-1}, g = 2.22); Ni (J = -2.47 cm^{-1}, g = 2.04)} (Schultz *et al*., 1997). The presence of a bridging hydroxide {in $Na_2[(PhSiO_2)_6Na_4Ni_4(OH)_2(O_2SiPh)_6].16^nBuOH$, **C**} and bridging chloride {in $Na[(PhSiO_2)_6Ni_6(O_2SiPh)_6Cl].12MeOH.H_2O$, **D**} generated different magnetic properties. The χT value of **C** increased upon cooling from 5.7 $emuKmol^{-1}$ {at 160 K} to 12.5 $emuKmol^{-1}$ {at 8 K} then decreased to 11.7 $emuKmol^{-1}$ {at 2.3 K}; while the initial increase was ascribed to moderate ferromagnetic coupling, the decrease was believed to be as a result of ZFS. In **D**, however, the χT value {8.4 $emuKmol^{-1}$ [at room temperature]} decreased upon cooling and got to zero (at O K), but the molar susceptibility increased then

decreased rapidly {at < 32 K} indicating antiferromagnetic interactions (Cornia *et al*., 1995). Magnetic studies of an acetate bridged complex $[Co_2(L1)(\mu\text{-}OAc)](ClO_4)_2{\cdot}½H_2O$ gave $\chi_M T$ of 4.23 cm^3Kmol^{-1} {at 300 K} and μ_{eff} of 4.09 μ_B. Although the μ_{eff} was within the expected range for dinuclear Co^{II} complexes, the $\chi_M T$ is higher than the expected value for two non-interacting high-spin Co^{II} ions (3.74 cm^3Kmol^{-1}, g = 2.00, S = $^3/_2$) but significantly lower than expected value (6.76 cm^3Kmol^{-1}, L = 3) when orbital angular momentum is included, suggesting only very minor orbital contributions. Upon cooling, the $\chi_M T$ decreased gradually reaching 0.025 cm^3Kmol^{-1} at 7 K, and indicated antiferromagnetic coupling between the two centres. The best fit to the data gave parameters J = -14.9 cm^{-1} and g = 2.16. The fitted g value was larger than the free ion g value (g_e = 2.00) and was due to second-order effects – while the $^4A_2'$ ground state arising from the trigonal bipyramidal coordination of a d^7 ion had no orbital angular momentum, admixture of the excited $^4E''$ state with the orbital angular momentum introduced second-order orbital momentum, resulting in a larger g value and magnetic moment (Horn Jr., *et al*., 2018). In the phenoxo bridged complexes $[LCo^{II}(MeOH)Gd(NO_3)_3]$, **E** and $[LCo^{III}(OAc)_2Gd(NO_3)_3]$, **F**, where the Co^{II} in **E** is five-coordinate and the Co^{III} in **F** is six-coordinate, the $\chi_M T$ of **E** {10.57 cm^3Kmol^{-1}} was slightly larger than 9.75 cm^3Kmol^{-1} expected for non-interacting Co (S = $^3/_2$) and Gd (S = $^7/_2$) spins. Upon cooling, the $\chi_M T$ increased gradually to 13 cm^3Kmol^{-1} {at 7 K} and then abruptly decreased to 8.69 cm^3Kmol^{-1} {at 2 K} – indicating the presence of a ferromagnetic interaction. In **F**, the $\chi_M T$ (7.89 cm^3Kmol^{-1}) was close to expected value (7.87 cm^3Kmol^{-1}) and was constant from room temperature to 2 K (Costes *et al*., 2002).

The magnetic interaction in oxo-bridged complexes tend to be imparted by the structural properties of the metal-oxygen (M_2O_2) core, coordination geometry (metal ions), the M-O-M angle, the M-O bond distances, the M⋯M separation, presence of co-ligands/secondary bridging groups and the out-of-plane shift of the phenyl group (Bhargavi *et al*., 2009; Chakraborty *et al*., 2009; Rigamonti *et al*., 2012; Arora *et al*., 2012; Lu *et al*., 2013; Hazra *et al*., 2014; Niu *et al*., 2015; Huang *et al*., 2017; Basak *et al*., 2020). In Co^{II} complexes, Co-O-Co bond angles less than 98° commonly results in ferromagnetic exchange {via orthogonal magnetic orbitals}, while larger bond angles {commonly greater than 100°} tend to result in antiferromagnetic coupling (Tomkowicz *et al*., 2012; Arora *et*

al., 2012; Horn Jr., *et al*., 2018; Kushvaha *et al*., 2019); while in Ni^{II} complexes, Ni-O-Ni angles less than or equal to 90^o tend to exhibit ferromagnetic exchange coupling while those with Ni-O-Ni angles greater than 90^o tend to exhibit antiferromagnetic exchange (Jiang *et al*., 2005; Mukherjee *et al*., 2009; Biswas *et al*., 2012; Niu *et al*., 2015), with stronger/more intense coupling observed as the angle increases (Niu *et al*., 2015) – although this effect becomes less important when such factors as steric effect or structural changes become more important (Ball, 1969). In Cu^{II} complexes, Cu-O-Cu angle of 106^o has been reported to exhibit antiferromagnetism while 98^o resulted in ferromagnetism (Bertrand and Kelley 1970; Youngme *et al*., 2008). More so, the coupling strength tend to vary with bridge type {μ-O^{2-}>μ-OH^->μ-H_2O}. Temperature has also been observed to affect exchange interactions in oxo-bridged complexes; a cubane type Cu^{II} complex, with Cu-O-Cu angles in the range 88° – 106°, has been found to exhibit ferromagnetism {until 7 K} and antiferromagnetism {at < 7 K} (Thakurta *et al*., 2009).

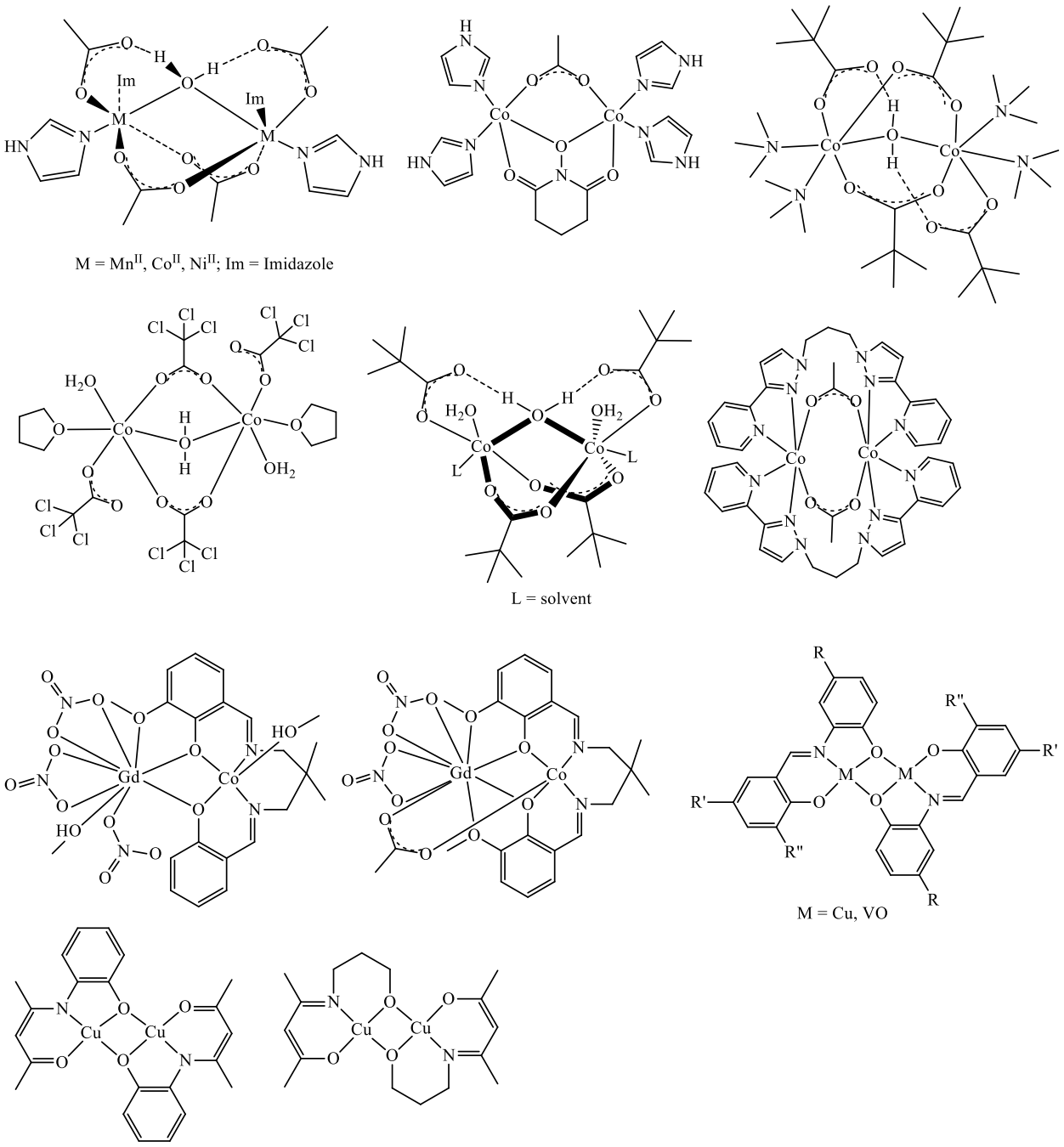

Figure 2.17: Examples of oxo-bridged complexes

2.8 Synthesis of Imidazoles

Imidazole synthesis usually consists of cyclocondensation reactions. One strategy involves the reaction of α-diketones and α-haloketones with formamide, while another uses a base-promoted reaction of tosylmethyl isocyanides and aldimines or imidoyl chlorides (Kamijo and Yamamoto 2007). Depending on the desired functionality, substitution pattern and diversity, substituted imidazoles can be prepared by: (**i**) a scaffold approach, (**ii**) a sequential condensation approach or (**iii**) a one-pot multi-component reaction {MCR's} (Gelens *et al*., 2006). The MCR strategy can increase dramatically the variety of substituents in a product and has potent applicability in the construction of a library of compounds bearing wide array of substitution while keeping a common structural scaffold (Kamijo and Yamamoto 2007). 1,2-diketones are commonly employed in the synthesis of 4,5-substituted imidazoles, with ammonium acetate used in most cases as the nitrogen source (**Scheme 2.10**{**a**}).

2,4,5-triarylimidazoles are an important group of substituted imidazoles showing biological activities, material properties and use in synthetic application (Samanta *et al*., 2013; Wu *et al*., 2012). In a preparation aimed at avoiding the use of a solvent, catalyst and solid surface, a variety of 2,4,5-triarylimidazoles were prepared by mixing 1,2-diketones, aromatic aldehydes, and ammonium acetate {NH_4OAc} in 1:1:3 ratio by direct heating at 130^oC for 3 – 6 h. The experimental procedure involved mixing benzil, aromatic aldehyde, and NH_4OAc in a round-bottom flask fitted with a $CaCl_2$-guard tube and the flask was heated in an oil bath at 130^oC (**Scheme 2.10**{**b**}). The reaction mixture was observed to melt and after some time ($\approx$ 1 – 3 h) solids were formed. On complete solid formation, the reaction was cooled to room temperature and water was added. The resulting solid mass was crushed and filtered, and the residue was washed with water and then dried. The crude product obtained was crystallised from ethanol {EtOH} in 45 – 90% yields (Samanta *et al*., 2013). In another procedure, a slight modification in the reactant ratio was used (benzil {as the 1,2-diketone}), substituted benzaldehyde and NH_4OAc {in 1:1:4}, with EtOH as reaction medium. The mixture obtained was refluxed at 140^oC for 6 h, cooled and washed three times with hot water. The solution was evaporated to dryness and the solid formed washed with methanol {MeOH} and recrystallised in hot MeOH. Final drying of the solid

under vacuum gave desired product in 67 – 87% yield (Sarala *et al*., 2016). A procedure involving the use of water {as the best solvents} in the synthesis of triarylimidazoles and tetra-substituted imidazoles has also been reported (Wu *et al*., 2012). The general protocol (**Scheme 2.10**{**c**}) involved irradiation of a mixture of benzimidazolium salt, arylaldehyde (in 1:2 molar ratio), 10% aqua NaOH and water at 350 W for 5 min in a microwave synthesizer. Acetic acid was then added until pH of 6 – 7, then NH_4OAc (10 mmol) and aldehyde (5 mmol) were added. The mixture was irradiated again for 5 min and allowed to cool to 0ºC. The solid formed was filtered and the crude product recrystallised from EtOH to yield the desired tri-substituted imidazoles (in 95% yield). Similar systems, without the imidazolium salt, have been reported in 80 – 99% yield [**Scheme 2.11**{**a**}] (Wolkenberg *et al*., 2004). A mixture of $CHCl_3$/AcOH {as the best solvent} has also been used in the four component, microwave assisted, preparation of a series of mono-, di-, tri- and tetra-substituted imidazoles (**Scheme 2.11**{**b**}). Products were obtained in <10 to 90% yields (Gelens *et al*., 2006).

(a)

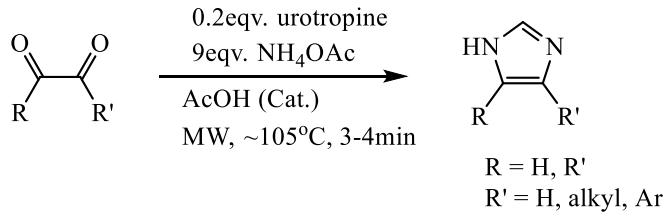

(b)

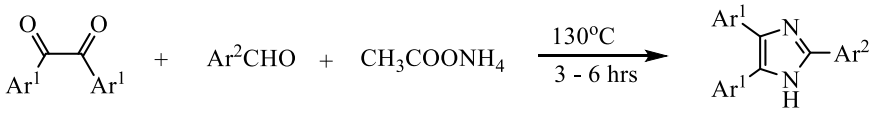

$Ar^1 = C_6H_5$, 4-CH_3-C_6H_4

$Ar^2 = C_6H_5$; 4-CH_3-C_6H_4; 4-Cl-C_6H_4; 4-Br-C_6H_4; 4CH_3O-C_6H_4; 3,4-(OCH_2O)-C_6H_3; 3-O_2N-C_6H_4; 4-$(CH_3)_2N$-C_6H_4; 3-CH_3O, 4HO-C_6H_3; 2-Thienyl; 3-Pyridyl

(c)

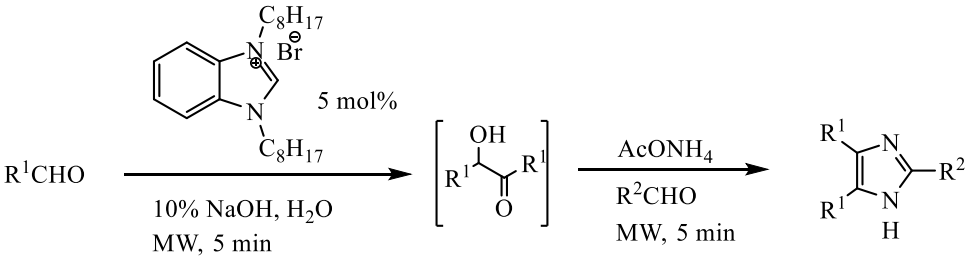

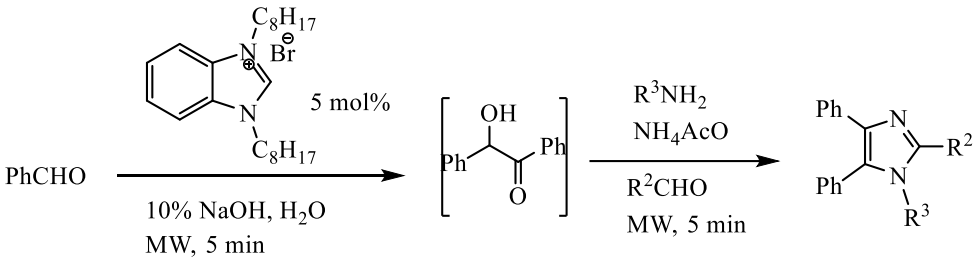

R^2 = Ph, 4-CH_3O-Ph, 4-CH_3-Ph

R^3 = Ph, 4-Cl-Ph, 3-Cl-Ph, 4-CH_3-Ph

Scheme 2.10: (a) Synthesis of a substituted imidazole (b) Solvent-free, catalyst-free synthesis of 2,4,5-triarylimidazoles (c) Microwave assisted synthesis of 2,4,5-triarylimidazoles and tetra-substituted imidazoles by Wu, L and colleagues.

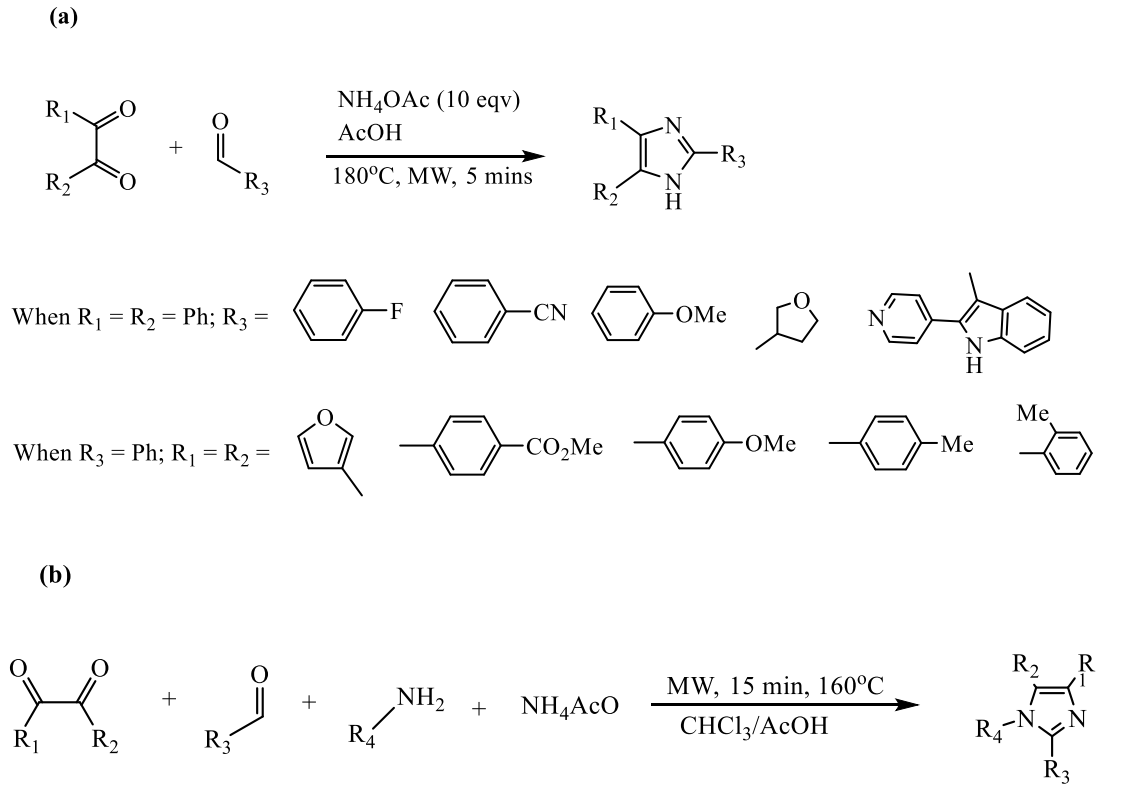

Scheme 2.11: (a) Microwave assisted organic synthesis of tri-substituted imidazoles by Wolkenberg, S. E and colleagues. (b) One-pot microwave synthesis of mono-, di-, tri-, and tetra-substituted imidazoles by Gelens, E and colleagues. (c) – (d) Synthesis of 2,4(5) substituted imidazoles

In a reported synthesis of 2,4-disubstituted imidazoles (**Scheme 2.11**{**c**}), the best yield was obtained when benzene, THF and dichloromethane {DCM} were used as solvent. The products were obtained without the use of acid catalyst and at room temperature (Bandyopadhyay *et al*., 2011). In another protocol (**Scheme 2.11**{**d**}), the use of a sonicator was required to achieve the preparation of desired products – the process involved ultrasonic irradiation of a solution of phenylglyoxal monohydrate in MeOH, followed by slow addition (syringe) of a MeOH solution of appropriate aldehyde and NH_4OAc (over 15 min). The resulting mixture was irradiated for 25 – 60 min and the MeOH evaporated under reduced pressure. The crude mass obtained was extracted with ethyl acetate and the combined organic layer washed with brine and water successively and dried over anhydrous sodium sulphate. The extract was then concentrated and the crude product purified using flash chromatography {neutral alumina, 1% triethylamine in MeOH} to afford pure compounds in 57 – 73% yield (Bandyopadhyay *et al*., 2014).

Some other cycloaddition reactions, for the preparation of imidazoles have been reported with transition metal and transition metal-based catalyst required for the transformations. A palladium catalysed multi-component reaction of imines and acid-chloride has been reported for the preparation of tetra-substituted imidazoles – the procedure was found to require bulky phosphine ligands, 4 atm of carbon monoxide (CO), an additive {LiCl was found to be the best}, and a temperature of 45^{o}C (Siamaki and Arndtsen 2006). The procedure in **Scheme 2.12** was used in the synthesis of a pyridinyl imidazole (**Scheme 2.13**) which has been shown to be a potent p38 Mitogen Activated Protein (MAP) kinase inhibitor (Lee *et al*., 1994). A palladium(0)- catalysed amino Heck reaction of amidoximes has also been used in the synthesis (**Scheme 2.14**) of 2-substituted 1-benzyl-4-methylimidazoles (Zaman *et al*., 2005).

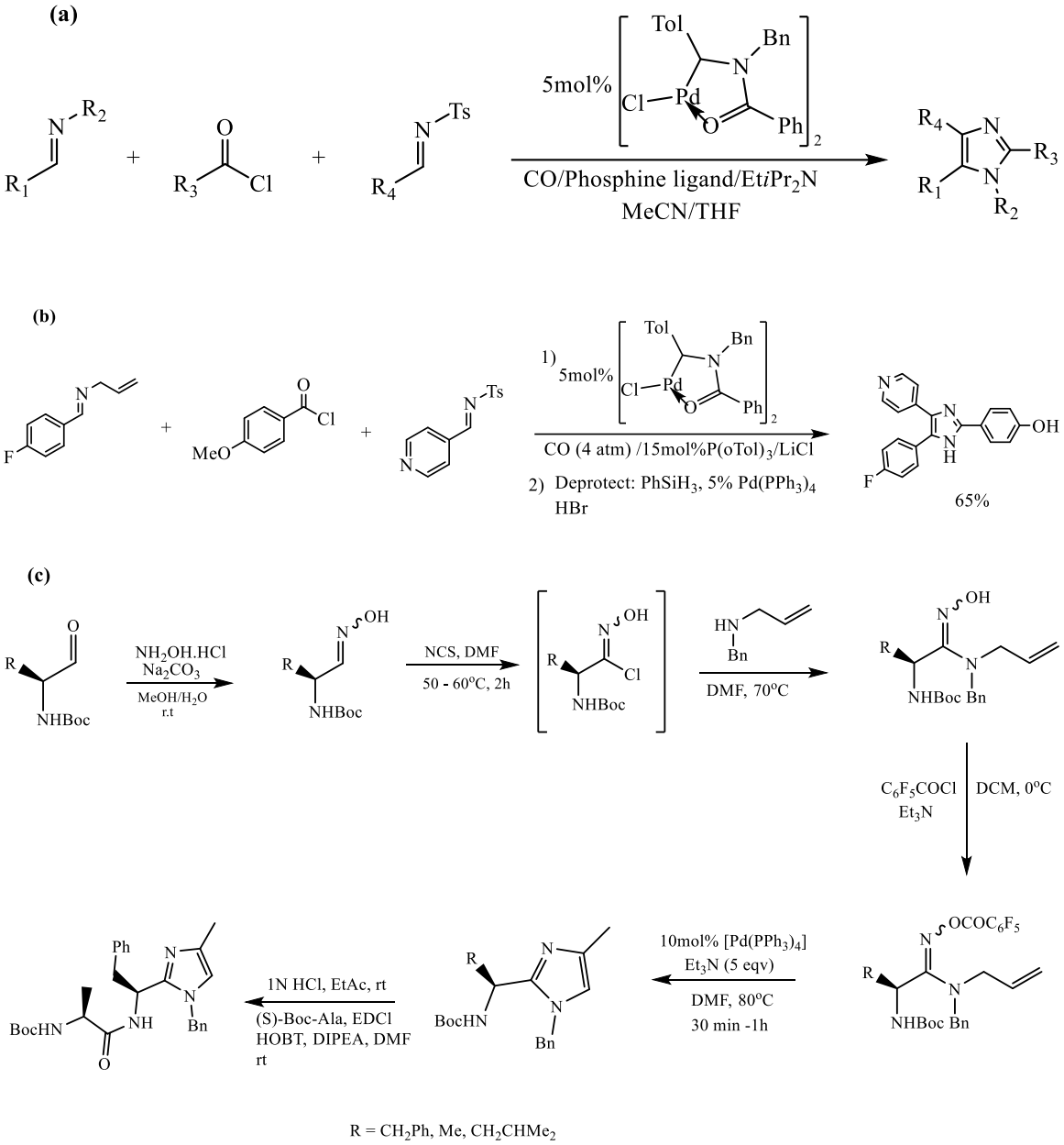

Scheme 2.12: (a) Preparation of imidazoles from imines and acid-chlorides (b) Preparation of a potent p38 MAP kinase inhibitor (c) Pd-catalysed intramolecular amino-Heck reaction of amidoximes derived from amino-acids.

A silver acetate catalysed cyclodimerisation, in a one pot sequential cascade process (**Scheme 2.13**{**a**}), has been used in the preparation of imidazoles in 88 – 90% yield (Grigg *et al*., 1999). The use of 10 mol% AgOTf/20 mol% Et_3N was observed to give incomplete reaction (even after 96 h), with other conditions kept constant (when R = Me). A similar protocol has been reported by Kamijo and Yamamoto (2007) with Cu_2O and **phen** used as catalyst (**Scheme 2.13**{**b**}). In an attempt to prepare 1,2-substituted imidazoles, with the intention of skipping the formation of amidine intermediates (**Scheme 2.13**{**c**}), a Cu(I)-induced addition of amines to nitriles has been reported – the best results were obtained when the Cu(I)-promoted formation of the amidine intermediates was carried out in the absence of solvent followed by cyclisation with trifluoroacetic acid {TFA} or hydrochloric acid {HCl} in MeOH. The cyclisation step could be done with or without the Cu salts in the reaction mixture. The "one-pot" synthesis {with the Cu salt in the mixture} appeared convenient {the Cu salt is removed after cyclisation} (Frustos *et al*., 2005). In the thiazolium catalysed preparation of di-, tri- and tetra-substituted imidazoles (**Scheme 2.13**{**d**}), the procedure for the tetra-substituted variants provided a way of setting the regiochemistry of the substituents in a single step and allowed the use of functional groups which are sensitive to acidic and basic environments (Frantz *et al*., 2004).

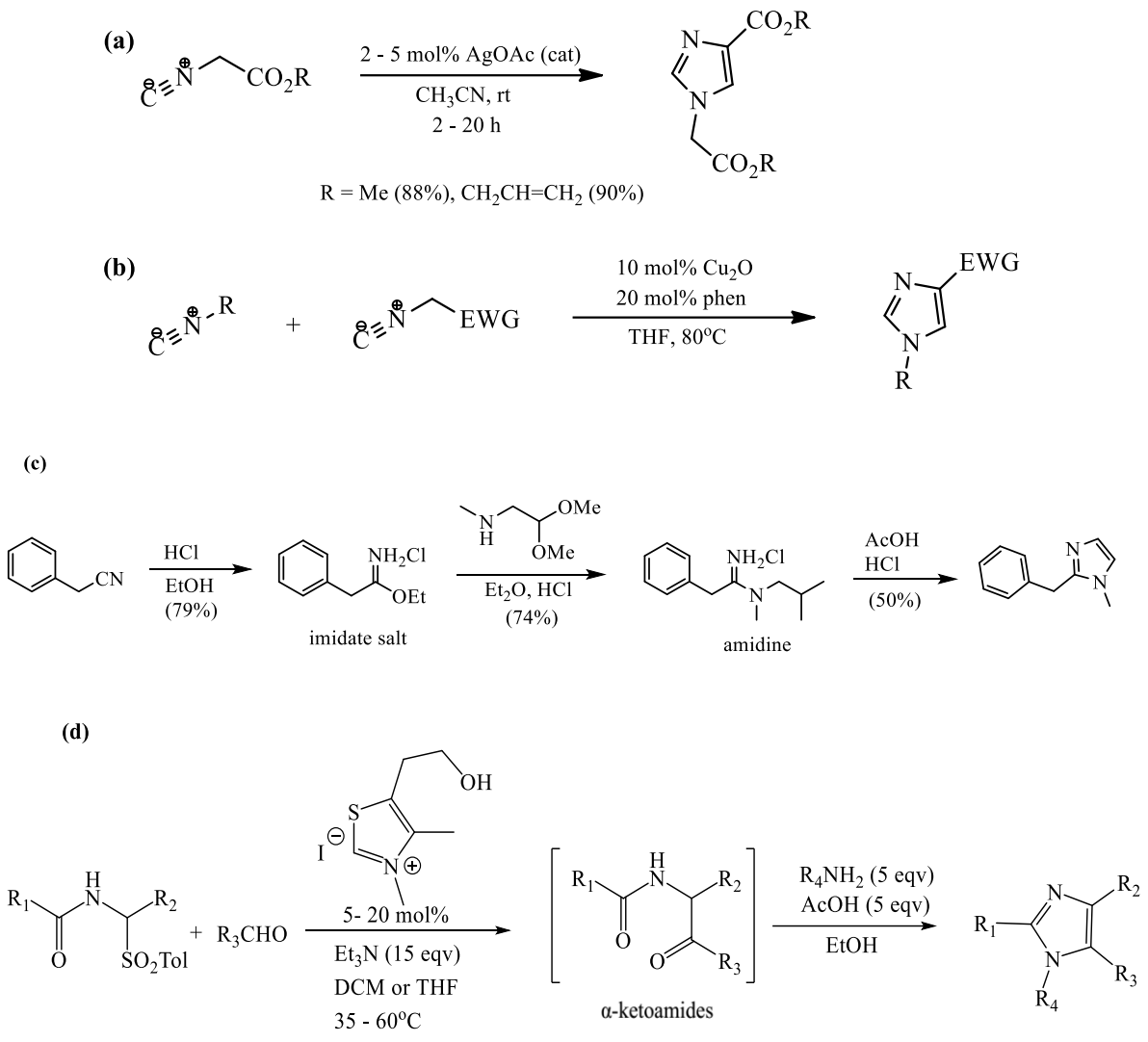

Scheme 2.13: (a) Ag-catalysed homodimerisation of isocyanides (b) Cu-catalysed cross-cycloaddition of isocyanides. (c) Preparation of 1,2-substituted imidazoles involving formation of amidine intermediate. (d) Thiazolium catalysed preparation of substituted imidazoles

2.9 Synthesis of Imidazole-Imines

The reported preparation of a series of imidazole imines of 1-(3-aminopropyl)imidazole (Apim, **Fig. 2.18**{**a**}) {using salicylaldehyde and a selection of imidazole aldehydes}, required refluxing of equimolar amounts of the amine and carbonyl compounds for 3 h in dry MeOH, followed by stirring overnight at room temperature. The oily material obtained, after solvent reduction, yielded solids after leaving to stand for 2 h to 2 months {in 73 – 95% yield} (McGinley *et al*., 2013). In the synthesis of a series of Schiff bases (**Fig. 2.18**{**b**}) derived from the condensation of imidazole-2-carboxaldehyde with 4-aminoantipyrine, L-phenylalanine, glycylglycine and 2-amino-3-carboxyethyl-4,5-dimethyl thiophene, respectively, it was observed that a base (KOH) is required for the imine formation in all cases except for the imine formed from 4-aminoantipyrine – the products were obtained in 76 – 78% yield. The imine obtained from L-phenylalanine acted as a tridentate monoanionic ligand, while the imines obtained from glycylglycine and 2-amino-3-carboxyethyl-4,5-dimethyl thiophene had bidentate behaviour (Joseyphus *et al*., 2014; Joseyphus *et al*., 2015; Joseyphus and Nair 2009; Joseph *et al*., 2017). In another preparation involving the condensation of imidazole–2-carboxaldehyde with 4-aminoantipyrine, 1g of anhydrous K_2CO_3 was added to an equimolar mixture of the reactants and refluxed for 42 h. The resulting solution was concentrated, allowed to cool and the solid obtained was filtered, washed with cold EtOH and dried to afford a red solid in 35% yield (Pearl *et al*., 2014).

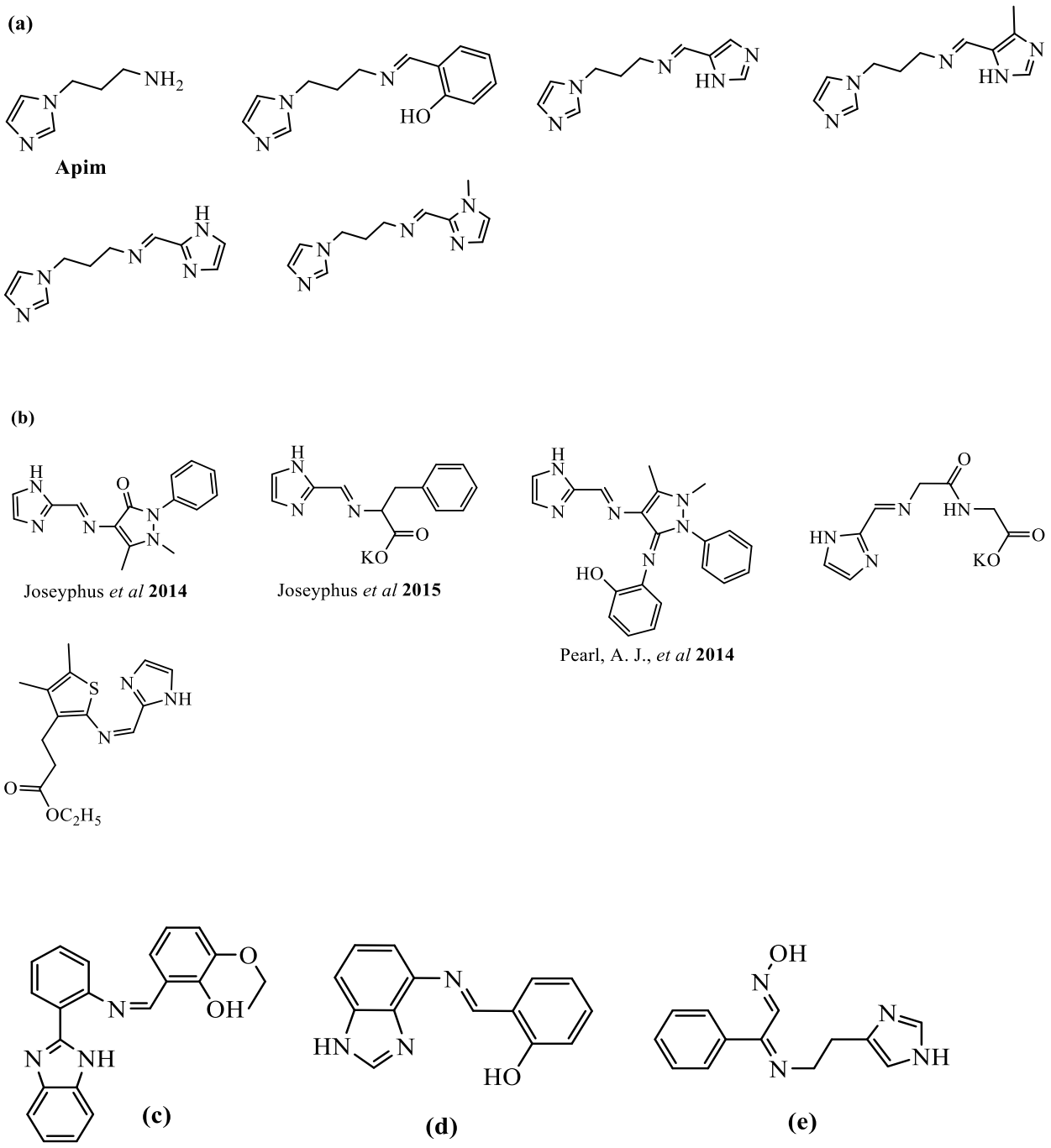

Figure 2.18: (a) Structure of Apim and its imine analogues (b) Structures of some imidazole-imines obtained from imidazole–2-carboxaldehyde (c) 2-(((2-(1*H*-benzo[*d*]imidazol-2-yl)phenyl)imino)methyl)-6-ethoxyphenol (d) 2-((1*H*-benzo[*d*]imidazol-4-ylimino)methyl)phenol and (e) inah.

In the preparation of 2-(((2-(1*H*-benzo[*d*]imidazol-2-yl)phenyl)imino)methyl)-6-ethoxyphenol {**Fig. 2.18**(**c**)} an equimolar EtOH mixture of 2-(2-aminophenyl)1-*H*-benzimidazole and 3-ethoxysalicylaldehyde (with a drop of AcOH) was heated on a steam bath for 45 – 60 min. The reaction mixture was left to stand at room temperature for 24 h, and the yellow solid product obtained dried under vacuum at room temperature (Sunitha *et al*., 2012). The imine 2-((1*H*-benzo[*d*]imidazol-4-ylimino)methyl)phenol {**Fig. 2.18**(**d**)}, obtained from 1*H*-benzo[*d*]imdazol-4-amine and 2-hydroxybenzaldehyde, was prepared in similar fashion as the imine in {**Fig. 2.18**(**c**)}. After refluxing for 3 h {at 45^{o}C}, the resulting solution was left to evaporate, by slow diffusion, in air for a week. The crystals collected were washed several times with EtOH, recrystallised from hot EtOH and dried in vacuum desiccator (Chaudhary and Mishra 2013). In the prepration of the oxime-histamine ligand (**inah**, {**Fig. 2.18**{**e**}), a suspension of histamine (4 mmol) in absolute EtOH was stirred with NaOH (8 mmol), and warmed at 323 K for 30 min. The NaCl precipitate was filtered off and the free histamine solutions added to a solution of 2-isonitrosoacetophenone in EtOH (Hung and Ferreira 2010).

In the two-step synthesis for 2-(*E*)-(1*H*-benzo[*d*]imidazole-2-yly diazenyl)-5-((*E*)-benzylideneimino)phenol (BIADPI) {**Scheme 2.14**[**a**] **–** [**b**]}, the first step involved the preparation of the imine {3-(benzylidene amino)phenol} by condensation of equimolar amounts of benzaldehyde and 3-amino phenol in the presences of 5 drops of glacial AcOH, as a catalyst {**Scheme 2.14**(**a**)}. The mixture obtained was refluxed for 5 h at 60^{o}C, cooled to room temperature and the dark yellow solid filtered and recrystallised in absolute EtOH. The second step {**Scheme 2.14**(**b**)} involved coupling of benzimidazolediazonium chloride with the imine {3-(benzylideneimino)phenol}. The precipitate obtained was filtered and washed with distilled water and EtOH and recrystallised from EtOH and dried in oven at 50^{o}C for several hours. The desired product was obtained in 79% yield (Al-Adilee, 2015). A similar coupling reaction has been used in the preparation of 2-[-2-(6-nitro benzothiazolyl)azo]imidazole (NBTAI) {**Scheme 2.14**(**c**)} and (*E*)-*N*-(1-(4-((*E*)-(4,5-diphenyl-1*H*-imidazol-2-yl)diazenyl)phenyl)ethylidene)-4-methylaniline {**Scheme 2.14**(**d**) – (**e**)} – the preparation of NBTAI involved 6-nitro benzothiazole chloride and an imidazole {in alkaline alcoholic solution} (Al-Adilee *et al*., 2013; Mahdi *et al*., 2014).

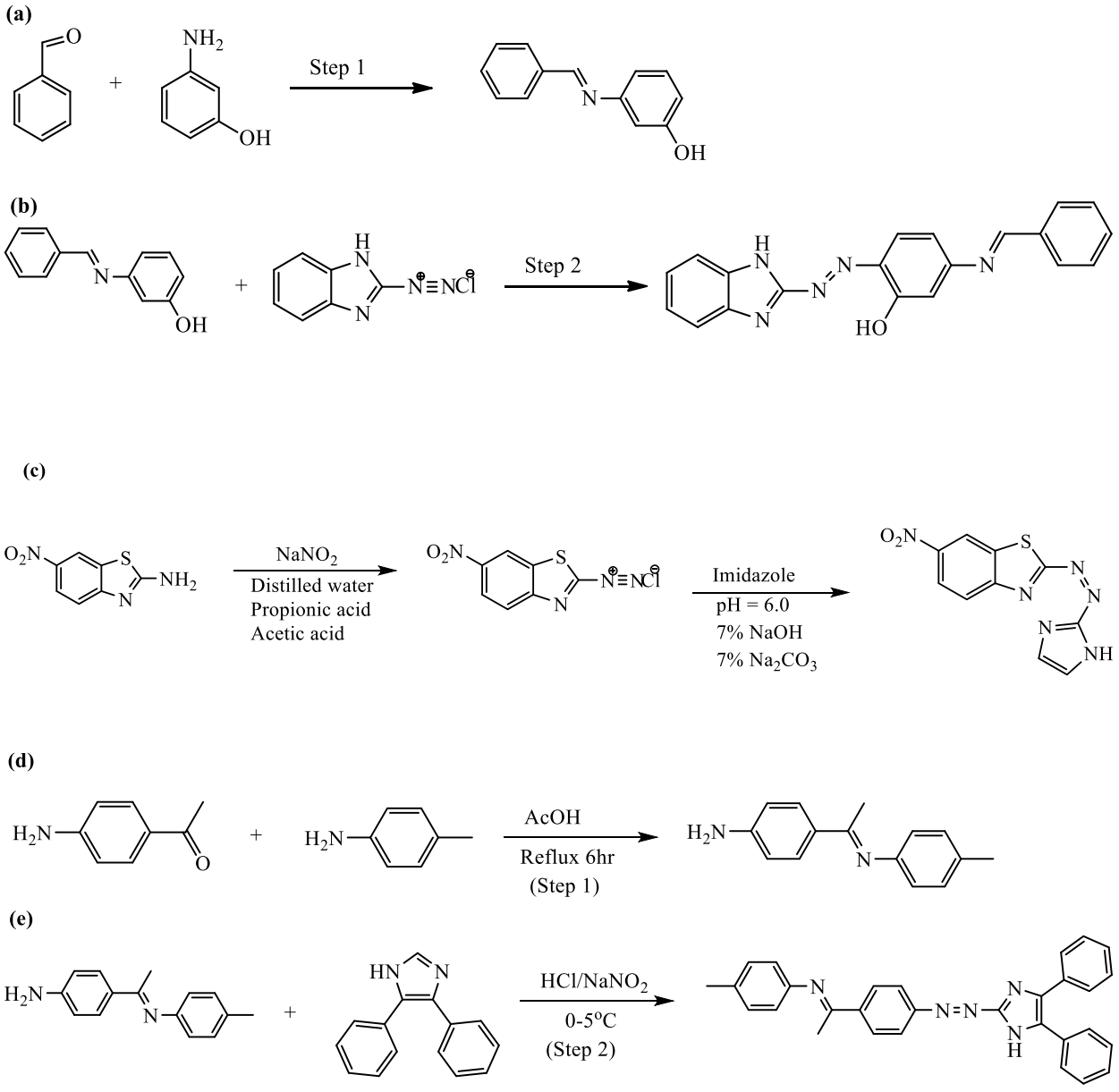

Scheme 2.14: (a) – (b) Two step synthesis of 2-(*E*)-(1*H*-benzo[*d*]imidazole-2-yly diazenyl)-5-((*E*)-benzylideneimino)phenol (BIADPI). (c) Preparation of 2-[-2-(6-nitro benzothiazolyl)azo]imidazole (NBTAI). (d) – (e) Two step synthesis of (*E*)-*N*-(1-(4-((*E*)-(4,5-diphenyl-1*H*-imidazol-2-yl)diazenyl)phenyl)ethylidene)-4-methylaniline.

2.10 Synthesis of Metal Complexes of Imidazole-Imines

In the preparation of metal complexes of a bidentate neutral imidazole ligand {**Fig. 2.19**(**a**)}, a MeOH solution of equimolar amounts of the ligand and metal chloride salts was stirred for 3 h, the solid obtained was washed with ether and EtOH and dried over anhydrous $CaCl_2$. The four coordinate complexes obtained had the formula $MLCl_2$ {M = Co, Ni, Cu, Zn} (Joseyphus *et al*., 2014). Similar protocol was used in the preparation of six coordinate metal complexes {**Fig. 2.19**(**b**)} of a ligand derived from the condensation of imidazole-2-carboxaldehyde with L-phenylalanine (Joseyphus *et al*., 2015). In a bid to study the effect of incorporating imidazoles in 1,2-diimine ligands, a series of bis-imidazole complexes {[Re(BIIM)$(CO)_3$Cl] where BIIM = $(BzImH)_2$Py, Me_4BiImH_2 and $BiBzImH_2$ (**Fig. 2.19**(**c**) – (**e**)} were prepared. Equimolar amounts of the ligands and $Re(CO)_5Cl$ were refluxed in toluene for 10 min. After cooling and filtering, the brown residue obtained was washed with toluene and Et_2O, taken up in acetone and precipitated by addition of *n*-hexane to afford microcrystalline brown materials in 19 – 33% yield (Leirer *et al*., 1999).

In the preparation of mixed ligand complexes of salicylaldehyde-4-methyl-3-thiosemicarbazone {a tridentate O,N,S Schiff base} and imidazoles, DCM solution of imidazole {or benzimidazole} was added to an EtOH {absolute} solution of appropriate metal salts {in equimolar amounts}; the mixture obtained was heated for 15 min followed by the addition of a hot EtOH solution of the O,N,S ligand. The solid obtained after volume reduction and cooling was filtered and dried. A large excess of the imidazole/benzimidazole was required for the formation of desired products (Mazlan *et al*., 2014).

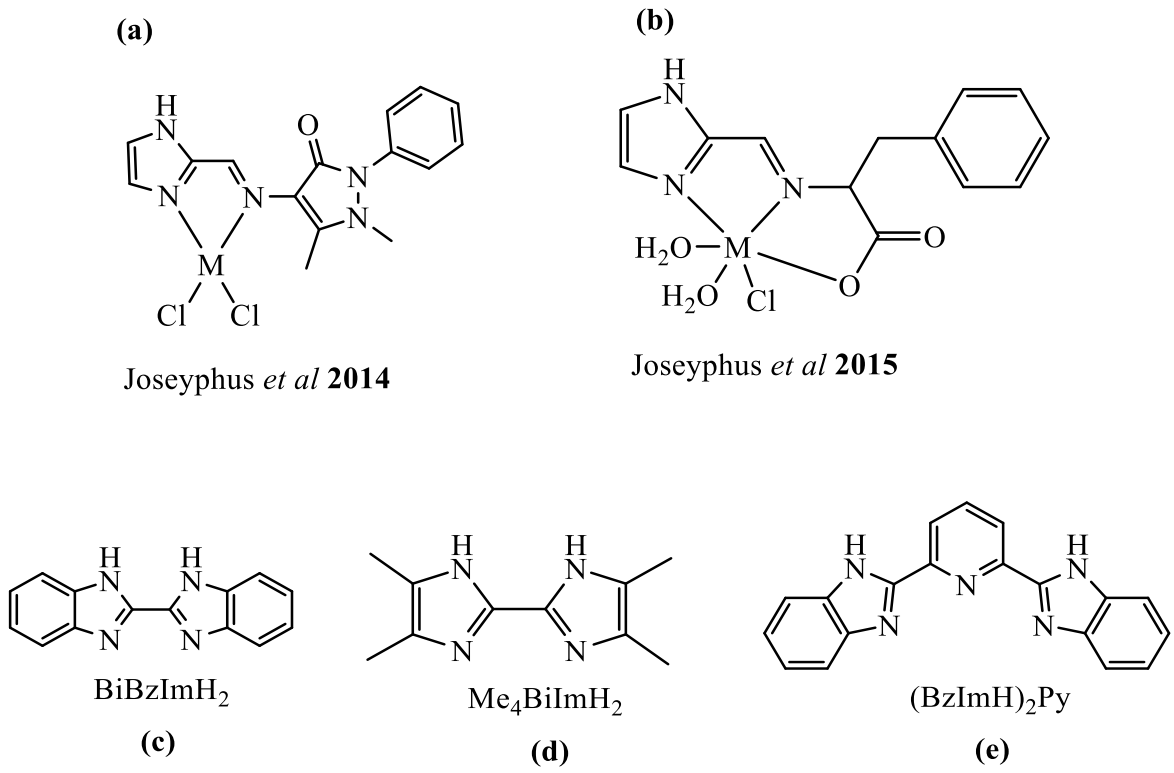

Figure 2.19: Structures of (a) – (b) some imidazole-imine complexes (c) – (e) BIIM ligands.

In the preparation of metal complexes of the azo based Schiff base ligands BIADPI {**Scheme 2.14**(**a**) – (**b**)} and NBTAI {**Scheme 2.14**(**c**)}, ethanolic solution of the ligands were mixed with appropriate metal chloride salts in 1:2 (M:L) molar ratio {except for the Zn^{II}-complex of BIADPI which was in 1:1 molar ratio}, hot NH_4OAc buffer solution was required for the NBTAI based complexes. The mixtures obtained were refluxed {in the case of BIADPI} or heated at 50 – 60 ºC {in the case of NBTAI} for 30 – 40 min, cooled and filtered. The crude materials were washed with distilled water and hot EtOH and dried to afford desired products (Al-Adilee, 2015; Al-Adilee *et al*., 2013). The metal complexes of 2-(((2-(1*H*-benzo[*d*]imidazol-2-yl)phenyl)imino)methyl)-6-ethoxyphenol (**Fig. 2.18**{**c**}) {upon reaction with metal salt, MX_2, where M= Ni^{II}, Co^{II}, Cu^{II}, Zn^{II}, Mn^{II} and VO^{IV}; X=Cl/SO_4/acetates}, as well as the Ni^{II} and Cu^{II} complexes of 2-((1*H*-benzo[*d*]imidazol-4-ylimino)methyl)phenol (**Fig. 2.18**{**d**}) were synthesised using similar protocol as the complexes of BIADPI, but refluxing was done for 4 – 5 h and the M:L ratio used was 1:1 (Sunitha *et al*., 2012; Chaudhary and Mishra 2013).

The mononuclear {$[Cu(inah)(H_2O)(NO_3)]$} and binuclear {$[Cu_2(inah)_2(ClO_4)_2](H_2O)_2$} Cu^{II} complexes of inah (**Fig. 2.18**{**e**}) have been prepared under different conditions – while the mononuclear complex was prepared under acidic condition {pH = 5; with room temperature stirring for 30 min}, the dinuclear complex was prepared under alkaline condition {pH = 10; with refluxing for 3 – 4 h} (Hung and Ferreira 2010). The chelate complexes of (*E*)-*N*-(1-(4-((*E*)-(4,5-diphenyl-1*H*-imidazol-2-yl)diazenyl)phenyl)ethylidene)-4-methylaniline were also synthesised under different pH conditions {pH = 7 for Hg^{II}; pH = 7.5 for Cu^{II}, Zn^{II} and Cd^{II}; pH = 9 for Co^{II} and Ni^{II}} (Mahdi *et al*., 2014).

The hydrothermal preparation of the coordination polymers $[Pb_2(L)_4(H_2O)].4H_2O$ and $[Ni(L)_2(H_2O)_2].2H_2O$ (where HL = 3,5-di(1*H*-imidazol-1-yl)benzoate) has been reported to require equimolar amounts of the ligand {HL}, NaOH and the respective metal nitrate salts {with water as the reaction solvent}. The mixture was sealed in an autoclave at 180ºC for 3 days and the crystals obtained were washed with water and EtOH and dried to give 38% yield {Ni^{II} complex} and 47% yield {Pb^{II} complex} (Su *et al*., 2011). A similar hydrothermal procedure has been reported for the mixed ligand complexes of 1,3,5-tris(1*H*-imidazol-4-yl)benzene (H_3L), with oxalic acid (H_2ox), 1,4-benzenedicarboxylic acid

(H_2pbdc), 1,2-phenylenediacetic acid (H_2obea), and 1,4-phenylenediacetic acid (H_2pbea). The complexes, $[Mn(H_3L)(ox)].H_2O$, $[Zn_2(H_2L)(pbdc)(\mu_2\text{-}OH)].2H_2O$, $[Co(H_3L)(obea)].3H_2O$, $[Ni(H_3L)(pbea)]$, $[Co(H_3L)(pbea)(H_2O)_2]$ and $[Co_4(H_2L)_2(pbea)_3]$, were obtained in 42 – 72% (Chen *et al*., 2012).

Two polyoxometalate-based inorganic–organic hybrid compounds (Hervé-sandwich-type polytungstoantimonates), $Na_9[\{Na(H_2O)_2\}_3\{M(C_4H_6N_2)\}_3(SbW_9O_{33})_2].28H_2O$ (M = Co, Mn) have been prepared by heating a mixture of a solution of $SbCl_3$ (in HCl) and $Na_2WO_4.2H_2O$ (in deionised water), at 80^{o}C for about 15 minutes, followed by the addition of solution of appropriate metal salt and methylimidazole (with pH adjusted to 7.45 at room temperature, by addition of 1M HCl). The solution obtained was then heated to boiling for 3 h, left to cool, filtered and the filtrate allowed to slowly evaporate at room temperature for 7 days, resulting in crystalline product (51% yield for Co and 49% yield for Mn). It was observed that methylimidazole with low concentration could not substitute coordinated water attached to the magnetic metal clusters (because of coordination competition between water and organic ligand) and that reaction time, temperature and ionic strength are key factors to obtain crystals in higher yield (Chen *et al*., 2011).

In the preparation of mononuclear complexes of Bis(1-methylimidazol-2-yl)ketone {***bik***} and bis(1-methylimidazol-2-yl)glyoxal {***big***} (**Fig. 2.20**), one equivalent of $[Os(Cym)Cl_2]_2$ was reacted with two equivalents of the respective ligand in MeCN under argon. Due to the heat sensitivity of ***big***, [(*big*)Os(Cym)Cl](PF_6) was synthesized at 60^{o}C whereas [(*bik*)Os(Cym)Cl](PF_6) was prepared under reflux conditions. The addition of $NH_4(PF_6)$ was required to precipitate the desired compounds {as PF_6 salts} (Sarper *et al*., 2010).

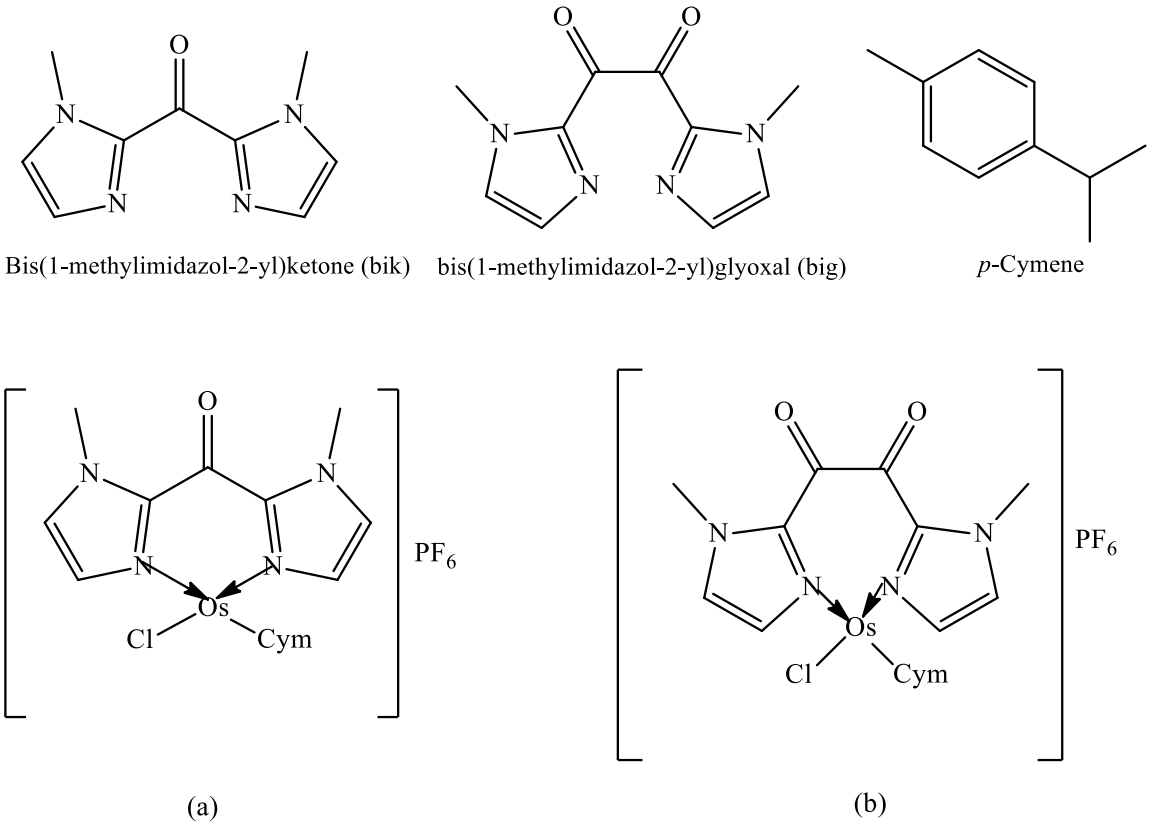

Figure 2.20: Structure of *bik* and *big* and their Osmium complexes

2.11 Characterisation of Imidazole-Imines and Their Metal Complexes

2.11.1 ^{1}H-NMR, ^{13}C-NMR and Mass spectroscopy (MS) Data

The ^{1}H-NMR spectrum of 2-(*E*)-(1*H*-benzo[*d*]imidazole-2-yly diazenyl)-5-((*E*)-benzylideneimino)phenol (BIADPI), measured in $CDCl_3$, showed peaks at δ = 6.51 – 6.54 ppm (phenol ring); δ = 6.77 ppm ($N\text{-}H_{benzimidazole}$); δ = 6.78 ppm (OH); δ = 7.27 – 7.28 ppm (phenyl ring); δ= 7.58 ppm (phenyl ring of benzimidazole); δ = 8.57 ppm (azomethine proton). The MS data of ligand (BIADPI) showed peaks at *m/z* values of 341.30 (M^+), 239, 211, 159, and 139 (the fragmentation pattern is shown in **Scheme 2.15**{**a**}) (Al-Adilee, K. J. 2015). The ^{1}H-NMR data of 2-(((2-(1*H*-benzo[*d*]imidazol-2-yl)phenyl)imino)methyl)-6-ethoxyphenol, recorded in $CDCl_3$, showed a singlet at δ = 7.3 ppm (due to the imine proton, CH=N), δ = 6.9 – 7.4 ppm {due to phenyl ring}, δ = 7.9 ppm {due to benzimidazole}, and δ = 10 ppm {due to N-H} (Sunitha *et al*., 2012). In the NMR data of some 2,4,5-triarylimidazoles {**Scheme 2.15**(**b**) **– (d**)}, the N-H peak was not observed (in $CDCl_3$) for one of the structures { **Scheme 2.15**(**b**)}, while for the other two structures it was observed at δ 12.40 ppm (in $CDCl_3$) and 12.49 ppm (in d_6-DMSO), respectively. The phenyl protons were observed in the range δ 7.19 – 7.86 ppm (with *J* values 7.2 – 8.4 Hz). The methyl group was observed at δ 2.38 ppm {**Scheme 2.15**(**b**)}, δ 3.84 ppm {**Scheme 2.15**(**c**)} and the O-H at δ 9.24 ppm {**Scheme 2.15**(**c**)}. The 2H singlet of the $–OCH_2O–$ group of **Scheme 2.15**(**d**) appeared at δ 6.08 ppm. The ^{13}C NMR (75 MHz, $CDCl_3$, δ/ppm) of **Scheme 2.15**(**b**) showed peaks at 146.2, 138.9, 132.9, 129.6, 128.6, 127.8, 127.4, 127.1, 125.2, 21.3 (Samanta *et al*., 2013). The ^{1}H NMR of compound **Scheme 2.15**(**e**) {recorded in $CDCl_3$} showed the aromatic protons at δ 6.83 – 7.91 ppm (with *J* values 8.3 – 8.5 Hz), the methyl protons resonate at δ 3.81 and 3.82, 3.81 ppm, the N-H proton was not observed; the ^{13}C NMR (also in $CDCl_3$ δ/ppm) shows peaks at 160.4 (Ar-O), 159.2 (Ar-O), 144.9 (C=N), 129.3, 127.5, 123.4, 114.2, 113.9, 55.3 (OCH_3), 55.2 (OCH_3) (Wu, L., *et al* 2012). When DMSO-d_6 was used {in place of $CDCl_3$} the aromatic N-H was observed at δ 11.8 – 12.8 ppm, the aromatic protons at δ 6.6 – 7.6 ppm and the C=N (^{13}C nmr) at δ 147 – 158 ppm (Sarala *et al*., 2016).

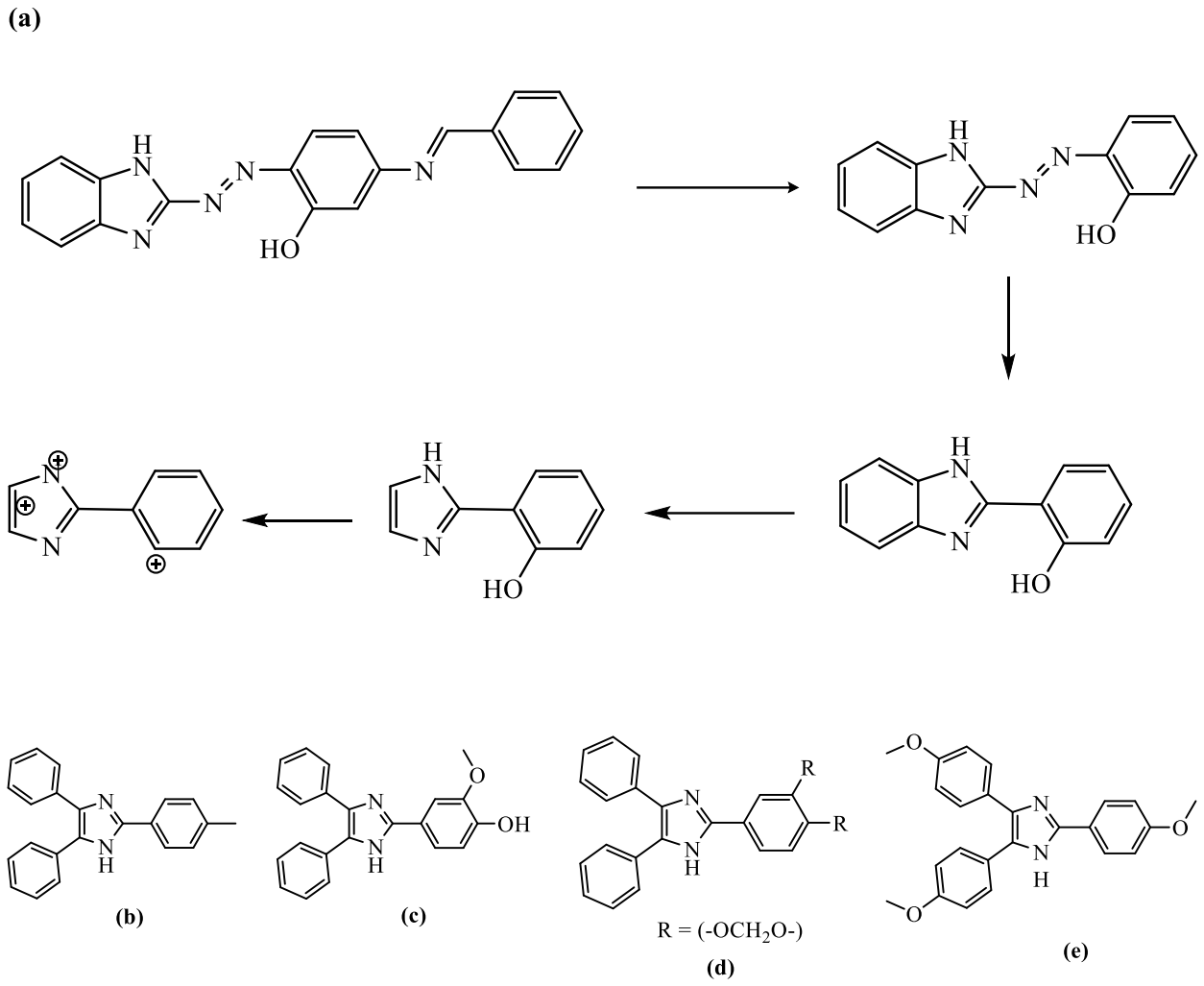

Scheme 2.15: (a) Fragmentation pattern of 2-(*E*)-(1*H*-benzo[*d*]imidazole-2-yly diazenyl)-5-((*E*)-benzylideneimino)phenol (BIADPI). (b) – (e) Structure of some 2,4,5-triarylimidazoles

All proton signals of the imidazole rings, as well as the methyl protons, of [(*bik*)Os(Cym)Cl](PF$_6$) {**Fig. 2.20(a)**} were observed to shift downfield {with respect to free ***bik***}. In contrast, the proton signals on the cymene ligand shifted upfield relative to the precursor. On complexation, one pair of imidazole–H signals of ***big*** in the aromatic region was seen at an upfield position, whereas the other pair was downfield {in comparison to the free ligand}. The methyl protons (of the imidazole nitrogen) resonated downfield with respect to free ***big***. As observed for ***bik***, complexation of ***big*** resulted in an upfield shift of the cymene proton signals when compared to the precursor (Sarper *et al*., 2010).

2.11.2 Infrared (IR) spectroscopy

The IR spectrum of 2-(*E*)-(1*H*-benzo[*d*]imidazole-2-yly diazenyl)-5-((*E*)-benzylideneimino)phenol (BIADPI) showed a band at 3323 cm^{-1} assigned to its benzimidazole N-H vibration. The band was observed to be retained in the metal complexes indicating the N-H was not involved in bonding. The phenolic (O-H) band at 3650 cm^{-1}; imine (C=N) band at 1620 cm^{-1}; and the azo (-N=N-) band at 1481 cm^{-1} were observed to shift (in varying degrees) in the metal complexes, indicating the ligand coordinates as a tridentate system. New bands were also observed in the region 447 – 424 cm^{-1}, assigned to M-O and M-N bonds in the metal complexes (Al-Adilee, 2015). In the study of the infrared absorption of 2-[-2-(6-nitro benzothiazolyl)azo]imidazole (NBTAI) and its metal complexes with Co^{II}, Ni^{II}, Cu^{II}, Zn^{II}, Cd^{II} and Hg^{II}; the ligand showed bands at 3437 cm^{-1} due to the υ(N-H) of imidazole ring; 1615 cm^{-1} and 1518 cm^{-1} due to υ(C=N) of thiazole and imidazole rings; 1459 cm^{-1} assigned to the υ(N=N) azo group; 1335 cm^{-1} and 840 cm^{-1} assigned to the υ(C-S) of the thiazole ring. In the metal complexes the bands at 3437 cm^{-1}, 1615 cm^{-1}, 1335 cm^{-1} and 840 cm^{-1} remained unchanged {suggesting N-H group, (C=N) and (C-S) of thiazole ring are not involved in coordination}; the υ(C=N) band of the imidazole ring was observed at 1517 – 1490 cm^{-1}; the υ(N=N) band shifted to 1435 – 1415 cm^{-1} with decreased or increased intensity. New absorption bands in the range of 520 – 447 cm^{-1} {assigned to υ(M-N)} were also observed. The broad bands at 3332 – 3280 cm^{-1} observed in the Co^{II}, Cu^{II}, Cd^{II} and Hg^{II} complexes suggested presence of water molecules. Thus, the IR spectra data suggested the ligand behaved as a bidentate chelating agent coordinating through the nitrogen atom of azo group nearest to thiazole ring and N3 atom

of imidazole ring to give five membered chelate ring (Al-Adilee *et al*., 2013). The IR spectrum of the ligand obtained from imidazole-2-carboxaldehyde and glycylglycine showed the azomethine (C=N) band at 1631 cm^{-1}, the imidazole nitrogen at 1612 cm^{-1} and the peptide band at 1538 cm^{-1}. These bands shifted to lower values upon complexation, showing involvement of the azomethine nitrogen, imidazole nitrogen and peptide linkage in coordination. The asymmetric carboxyl stretching $\upsilon_{asym}(COO^-)$ shifted to higher frequency, while the symmetric carboxyl stretching $\upsilon_{sym}(COO^-)$ shifted to lower frequency, indicating linkage between the metal ion and carboxylato oxygen. These asymmetric and symmetric stretching vibrations {of the carboxylato group}, in the complexes, showed separation ($\Delta\upsilon$) greater than 200 cm^{-1}, indicating monodentate binding in the complexes. The IR bands at 1364 – 1378 cm^{-1} were assigned to the presence of free NO_3^-. The broad bands observed at 3400 – 3443 cm^{-1} in the complexes were attributed to O–H stretching of lattice water molecules. The new bands observed at 520 – 567 and 434 – 463 cm^{-1} corresponded to υ(M–O) and υ(M–N) stretching, respectively. Thus, the ligand acted as a tetradentate molecule – binding through imidazole nitrogen, azomethine nitrogen, amide nitrogen and carboxylato oxygen (Joseyphus and Nair 2009). In the study of the IR spectrum of 2-(((2-(1*H*-benzo[*d*]imidazol-2-yl)phenyl)imino)methyl)-6-ethoxyphenol and its metal complexes, the free ligand showed bands at 1618 cm^{-1} (C=N stretching vibration) and 3350 cm^{-1} (N-H stretching vibration of benzimidazole moiety). In the metal complexes the C=N band shifted {indicating coordination through the imine} and the broad peaks at 3354 – 3423 cm^{-1} indicated the presence of coordinated water molecules {which was also corroborated by rocking (O-H) vibrations at 800 – 880 cm^{-1}}. The M-N bands were observed at 450 – 480 cm^{-1} and the V=O band {of the Vanadyl complex} at 985 cm^{-1} (Sunitha *et al*., 2012). The IR spectral analyses of [(*bik*)Os(Cym)Cl](PF_6) and [(*big*)Os(Cym)Cl](PF_6) {**Fig. 2.20**} revealed sharp carbonyl (C=O) absorption bands at 1648 cm^{-1} and 1673 cm^{-1}, respectively. These values indicated a shift to higher wavenumbers when compared with the observed values for the free ligands {1637 cm^{-1} for ***bik*** and 1662 cm^{-1} for ***big***}. DFT calculation of the HOMO of ***big*** indicated anti-bonding character over the carbonyl system. Electron density shifted from the HOMO orbital to the metal centre upon complexation increasing the carbonyl bond order (Sarper *et al*., 2010). The IR spectrum of 2-((1*H*-benzo[*d*]imidazol-4-ylimino)methyl)phenol showed a broad

band around 3350 cm^{-1}, medium intensity bands at 1625 cm^{-1} and in the region 3600 – 3640 cm^{-1} which were attributed to N-H stretching vibration of benzimidazole moiety, the imine and the phenolic OH groups, respectively. The metal complexes showed shift of the imine band to 1607 – 1590 cm^{-1} (indicating involvement of the imine nitrogen in coordination). New bands at 446 – 409 cm^{-1} assignable to νM-N vibration and νM-O vibration were also observed (Chaudhary and Mishra 2013).

2.11.3 Electronic spectra and Magnetic measurement Data

The UV–vis spectrum of the imine ligand obtained from imidazole–2-carboxaldehyde and glycylglycine showed a band at 320 nm assigned to $\pi - \pi^*$ transition of the azomethine chromophore. On complexation, this band shifted to lower wavelength, suggesting coordination of azomethine nitrogen with the metal. The Co^{II} and Ni^{II} complex showed a band at 545 nm and 581 nm, respectively, due to $^4A_2(F) \rightarrow {}^4T_1(F)$ {Co^{II}-complex} and $^3T_1(F) \rightarrow {}^3T_1(P)$ {Ni^{II}-complex} transitions, suggestive of tetrahedral geometry. The Cu^{II} complex showed absorption at 640 nm indicating square-planar geometry. The plot of magnetisation (*M*) versus applied field (*H*) for the Co^{II} and Ni^{II} complexes showed hysteresis loop at room temperature and gave a saturation magnetisation of 0.20 emu g^{-1}. Also, they showed coercivities of 316 and 287 Oe, respectively. The low saturation magnetisation and the presence of coercivities for the samples indicated the complexes were weakly ferromagnetic. The Cu^{II} complex did not show a hysteresis loop at room temperature, indicating that the Cu^{II} complex was paramagnetic (Joseyphus and Nair 2009). The electronic spectral (in DMSO) and observed magnetic moment of the Co^{II}, Ni^{II}, Cu^{II}, Zn^{II}, Mn^{II} and VO^{IV} complexes of 2-(((2-(1*H*-benzo[*d*]imidazol-2-yl)phenyl)imino)methyl)-6-ethoxyphenol showed the following: the Co^{II} complex had three bands at 11001, 27548 and 29498 cm^{-1} which were attributed to $^4T_{1g}(F) \rightarrow {}^4T_{2g}(F)$ (ν_1), $^4T_{1g}(F) \rightarrow {}^4A_{2g}(F)$ (ν_2) and $^4T_{1g}(F) \rightarrow {}^4T_{1g}(P)$ (ν_3) transitions, respectively, and a magnetic moment 4.28 B.M which suggested octahedral geometry; the Ni^{II} complex also showed three bands at 22371, 30303 and 32894 cm^{-1} which were assigned to $^3A_{2g} \rightarrow {}^3T_{2g}(F)$ (ν_1), $^3A_{2g} \rightarrow {}^3T_{1g}(F)$ (ν_2) and $^3T_{2g} \rightarrow {}^3T_{1g}(P)$ (ν_3) transitions, respectively, and a moment of 3.10 B.M which also suggested an octahedral field; the Cu^{II} complex had a broad band at 14556 cm^{-1} mainly due to $^2E_g \rightarrow {}^2T_{2g}$ transition which suggested an octahedral geometry. The

observed magnetic moment value was 1.67 B.M; the Mn^{II} complex showed bands at 34482, 33333 and 31645 cm^{-1}, which were assigned to $^6A_{2g}\rightarrow{}^4A_{2g}(P)$, $^6A_{1g}\rightarrow{}^4T_{1g}(P)$, $^6A_{1g}\rightarrow{}^4E_g(D)$ transitions, respectively, and a magnetic moment value of 5.47 B.M which corroborated an octahedral nature; the VO^{IV} complex showed three transitions at 28409, 32894 and 34129 cm^{-1} assigned to $^2E_g\rightarrow{}^2B_{2g}$, $^2B_{1g}\rightarrow{}^2B_{2g}$ and $^2A_{1g}\rightarrow{}^2B_{2g}$, respectively, characteristic of an octahedral geometry; the Zn^{II} complex showed no *d-d* bands {as expected for a d^{10} system} and was found to be diamagnetic in nature and on the basis of analytical, conductance and spectral data, it was assigned an octahedral geometry (Sunitha *et al*., 2012). The result of the electronic and magnetic measurements for the metal complexes of the ligand obtained from the condensation of imidazole-2-carboxaldehyde with 2-amino-3-carboxyethyl-4,5-dimethyl thiophene showed the Co^{II} complex had an absorption peak at 605 nm, assigned to $^4A_2(F)\rightarrow{}^4T_1(P)$, and a magnetic moment of 4.66 B.M corresponding to tetrahedral geometry. Similarly, the Ni^{II} and Cu^{II} complexes displayed one absorption peak {broad for Cu^{II}} at 482 nm and 661 nm, respectively, due to *d-d* transitions and were both assigned a square-planar geometry. The Zn^{II} complex displayed diamagnetism, and a tetrahedral geometry was predicted (Joseph *et al*., 2017). The electronic spectrum of 2-[-2-(6-nitro benzothiazolyl)azo]imidazole (NBTAI) in absolute EtOH (at 10^{-3}M) revealed three absorption bands at 387 nm (25840 cm^{-1}), 291 nm (34364 cm^{-1}) and 263 nm (38023 cm^{-1}) assigned to $n\rightarrow\pi^*$, $\pi\rightarrow\pi^*$ and $n\rightarrow\sigma^*$ transitions, respectively. The electronic spectrum of its Co^{II} complex showed three absorption bands at 974 nm (10235 cm^{-1}), 629 nm (15898 cm^{-1}) and 350 nm (26571 cm^{-1}) assigned to $^4T_{1g}(F)\rightarrow{}^4T_{2g}(F)$ (ν_1), $^4T_{1g}(F)\rightarrow{}^4A_{2g}(F)$ (ν_2) and $^4T_{1g}(F)\rightarrow{}^4T_{1g}(P)$ (ν_3) transitions, respectively as well as a magnetic moment of 5.07 B.M which corresponded to three unpaired electrons, and suggested a distorted octahedral structure (*Z*-out) and sp^3d^2 hybridisation. The Ni^{II} complex showed three absorption bands at 977 nm (10235 cm^{-1}), 636 nm (15723 cm^{-1}) and 589 nm (16978 cm^{-1}) assigned to $^3A_{2g}(F)\rightarrow{}^3T_{2g}(F)$ (ν_1), $^3A_{2g}(F)\rightarrow{}^3T_{1g}(F)$ (ν_2) and $^3A_{2g}(F)\rightarrow{}^3T_{1g}(P)$ (ν_3) transitions, respectively with a magnetic moment of 3.18 B.M which suggested two unpaired electrons in a high spin regular octahedral geometry and sp^3d^2 hybridisation. The Cu^{II} complex showed a broad band around at 623 nm (16051 cm^{-1}) due to $^2E_g\rightarrow{}^2T_{2g}$ transition and a magnetic moment of 1.64 B.M which suggested one unpaired electron in a distorted octahedral structure (*Z*-out or *Z*-in) and sp^3d^2 hybridisation. The spectra of the Zn^{II}, Cd^{II} and

Hg^{II} complexes did not show any *d-d* transitions and the respective absorption bands at 521 nm (15194 cm^{-1}), 518 nm (15305 cm^{-1}) and 537 nm (16622 cm^{-1}) are assigned to Metal-Ligand Charge Transfer {MLCT} transition. The complexes were found to be diamagnetic and an octahedral geometry was proposed for all three (Al-Adilee *et al*., 2013). Under similar solvent condition {as NBTAI}, the electronic spectral of the ligand BIADPI also displayed three bands at 249 nm (40161 cm^{-1}), 326 nm (30675 cm^{-1}) and 450 nm (22222 cm^{-1}) characteristic of $\pi \rightarrow \pi^*$ and $n \rightarrow \pi^*$ transitions. The band at 450 nm shifted to longer wavelength (with increasing intensity) in the metal chelate – which may be as a result of the donation of the lone pair of electrons of nitrogen of benzimidazole molecule and lone pair of nitrogen atom azo group (which is the nearest phenolic ring to metal ion) {**Fig. 2.21**(**b**) – (**c**)}. The cobalt complex showed three absorption bands at 901 nm, 598 nm and 482 nm assigned to $^1A_{2g} \rightarrow {}^1T_{2g}(\nu_1)$, $^1A_{2g} \rightarrow {}^1T_{1g}(F)(\nu_2)$ and $^1A_{2g} \rightarrow {}^1T_{1g}(P)(\nu_3)$ transitions, respectively. The magnetic moment of this complex showed diamagnetic low spin behaviour indicating Co^{II} was oxidised to Co^{III} upon complexation with the BIADPI - suggesting an angular octahedral geometry (with sp^3d^2 hybridisation). The Ni^{II} complex showed three bands at 910 nm (very weak and broad) attributed to $^3A_{2g}(F) \rightarrow {}^3T_{2g}(\nu_1)$ transition; 491 nm due to $^3A_{2g} \rightarrow {}^3T_{1g}(F)(\nu_2)$ transition; and 410 nm assigned to $^3A_{2g} \rightarrow {}^3T_{1g}(P)(\nu_3)$ transitions. Its magnetic moment of 3.28 B.M was attributed to the presence of two unpaired electrons (suggesting a high spin, octahedral geometry, with sp^3d^2 hybridisation). The Cu^{II} complex showed a broad band at 589 nm assigned to $^2E_g \rightarrow {}^2T_{2g}$ transition corresponding to a distorted octahedral geometry around the Cu^{II} ion. A magnetic moment of 1.78 B.M was observed. The Zn^{II}, Cd^{II} and Hg^{II} complexes of BIADPI showed similar electronic properties as their NBTAI counterparts {no *d-d* transitions} and the absorption bands at 536 nm, 528 nm and 575 nm, respectively, were assigned to MLCT transition. They were also diamagnetic, but the Zn^{II} complex had a different structures {in comparison to its NBTAI counterpart} – while the Cd^{II} and Hg^{II} complexes were octahedral {**Fig. 2.21**(**b**)}, the Zn^{II} had a tetrahedral geometry {**Fig. 2.21**(**c**)} (Al-Adilee, 2015).

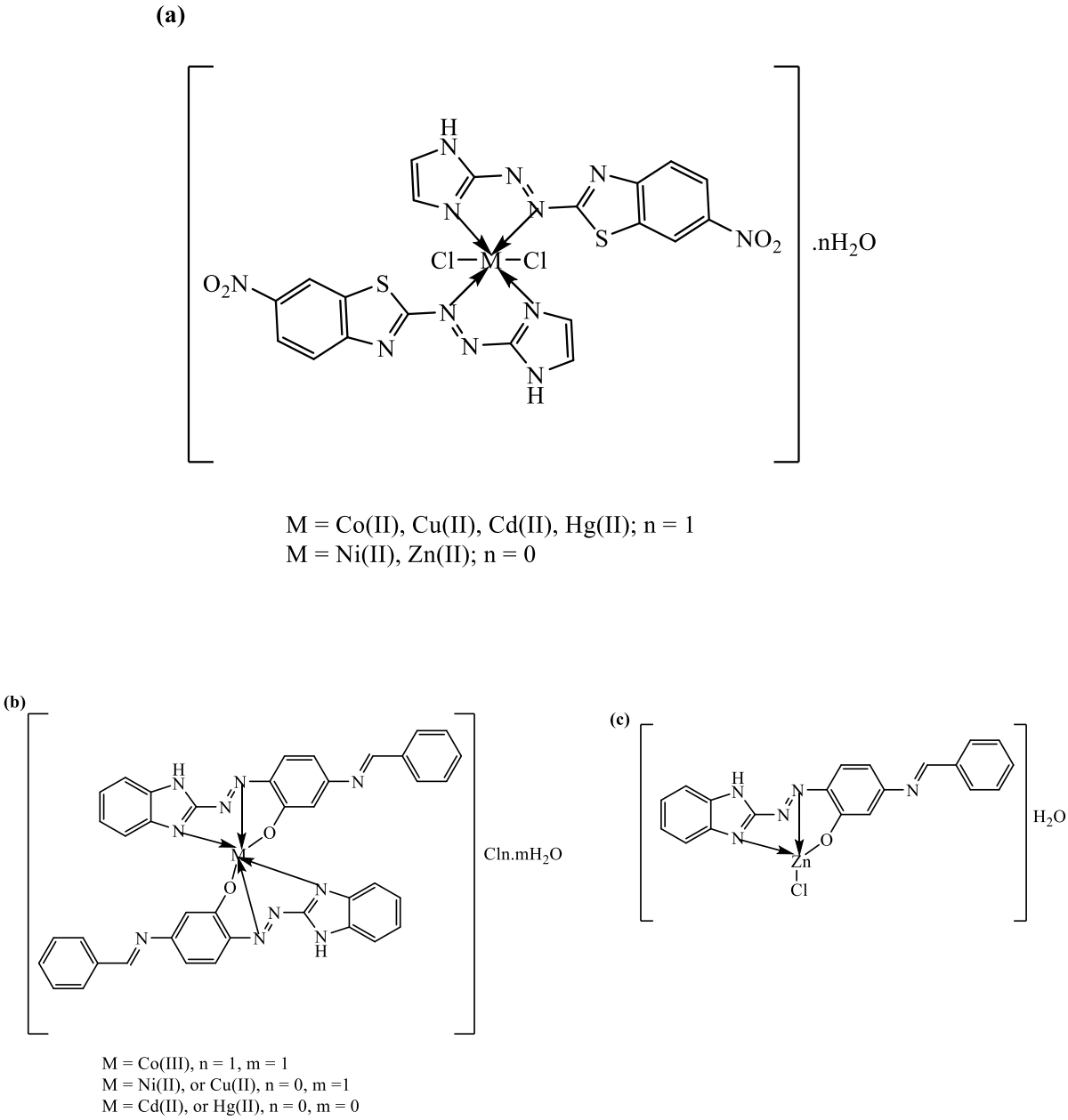

Figure 2.21: (a) Proposed structure of the metal complexes of NBTAI (b) – (c) Proposed structural formula for the metal chelate of BIADPI

2.11.4 Thermogravimetric Analysis (TGA) and Differential Temperature Analysis (DTA)

TGA of $[Pb_2(L)_4(H_2O)].4H_2O$ showed weight loss (5.67%) observed at 100 to 130^oC attributed to coordinated and uncoordinated water, while the remaining residue decomposed at 320^oC. The loss of coordinated and uncoordinated water (10.87%) observed for $[Ni(L)_2(H_2O)_2].2H_2O$ occurred at ≈ 165^oC, while the remaining residue decomposed at 265^oC. These observations showed that although the complexes had the same ligand, they had different stability (Su *et al*., 2011). Thermal stability studies of the complexes $[Mn(H_3L)(ox)].H_2O$, $[Zn_2(H_2L)(pbdc)(\mu_2\text{-}OH)].2H_2O$, $[Co(H_3L)(obea)].3H_2O$, $[Ni(H_3L)(pbea)]$, $[Co(H_3L)(pbea)(H_2O)_2]$, and $[Co_4(H_2L)_2(pbea)_3]$ showed that $[Mn(H_3L)(ox)].H_2O$ had a weight loss of 4.17% around 180°C corresponding to the release of free water molecules (calc. 4.12%), and decomposed at 360°C; $[Zn_2(H_2L)(pbdc)(\mu_2\text{-}OH)].2H_2O$ showed a weight loss of 5.81% in the temperature range of 240 – 305°C, which corresponds to the loss of the coordinated water molecules (calc. 5.78%), and further weight loss was observed at about 410°C; $[Co(H_3L)(obea)].3H_2O$ showed a weight loss of 9.01% at 110°C {liberation of the free water molecules} and decomposed at about 405°C; $[Co(H_3L)(pbea)(H_2O)_2]$ showed a total weight loss of 6.49% in the temperature range of 195 – 255°C, attributed to the loss of coordinated water molecules (calc. 6.39%), and the residue was stable up to about 470°C. No obvious weight losses were found for complexes $[Ni(H_3L)(pbea)]$ and $[Co_4(H_2L)_2(pbea)_3]$ before the decomposition of the framework occurred at about 220 and 380°C, respectively (Chen *et al*., 2012). The TG curve of $Na_9[\{Na(H_2O)_2\}_3\{Co(C_4H_6N_2)\}_3(SbW_9O_{33})_2].28H_2O$ exhibited three steps of weight loss. The first (10.46%) from 22^oC to 336^oC indicated loss of all lattice and coordinated water; the second {2.73%} from 336^oC to 377^oC, was assigned to loss of two methylimidazoles; and the last weight loss {1.43%} from 377^oC to 504^oC was attributed to loss of one methylimidazole. The TG curve of the manganese variant, $Na_9[\{Na(H_2O)_2\}_3\{Mn(C_4H_6N_2)\}_3(SbW_9O_{33})_2].28H_2O$, also showed three steps of weight loss in similar ranges, with same reasons accounting for the observed mass losses (Chen *et al*., 2011). Thermal decompositions of the metal complexes of the ligand obtained by condensation of imidazole–2-carboxaldehyde and glycylglycine showed the Cu^{II} complex

underwent decomposition in three different steps. The first weight loss of 5.10% {50 – 128^{o}C} indicated dehydration and release of loosely bound lattice water. The Differential Scanning Calorimetry {DSC} curve of the Cu^{II}-complex showed an endothermic peak at 121^{o}C {due to evaporation of lattice water}. The second weight loss of 72.34% {128 – 197^{o}C} showed partial separation of ligand and NO_3^-. The DSC curve gave a broad endothermic peak with an onset temperature at 195^{o}C, due to evaporation of Schiff base – the decomposition above 195^{o}C was likely due to NO_3^-. Final decomposition occurred above 340^{o}C {metal oxide was formed}. The DSC curve in the temperature range 340 – 400^{o}C showed an endothermic peak {metal oxide formation}. Similar TGA and DSC results were obtained for the Co^{II} and Ni^{II} complexes (Joseyphus and Nair 2009).

2.12 Theoretical Background

2.12.1 Theory of Sensors

The detection and monitoring of chemical species is of great importance in a lot of areas including environmental, medicinal/biological and security. A chemical sensor is a molecule which signals the presence of matter or energy. They are molecular receptors capable of generating analytically useful signals upon binding to specific guests, that is, they are capable of molecular recognition and signal transduction (Wong *et al*., 2017; Kanagaraj *et al*., 2014; Treto-Súarez *et al*., 2019). Chemosensors commonly consists of two essential components:

- A receptor or ion recognition unit (ionophore), which binds substrates, and
- A transducer or fluorogenic unit (fluorophore), which reports the binding event through an observable change (as an optical or electrochemical signal). It may also be called the active unit.
- Some sensors may have a third component called the linker, which can impart the geometry of the host as well as the electronic interactions between the receptor and the transducer.

The substrate/guest may cause an optical change by a change in absorbance, which allows colourimetric determination using UV/vis spectroscopy, or by emission

enhancement or quenching, which allows measurement of emission wavelength and intensity by fluorescence spectroscopy. In the case of an electrochemical change, the substrate causes a change in current or redox potential, which is measured by a voltammeter. The character of the transducer makes a sensor behave as a redox or photoactive system (Wong *et al*., 2017; Lau *et al*., 2011; Costero *et al*., 2004).

Fluorescence spectroscopy involves the use of a fluorophore as the transducer and, in comparison to other analytical techniques, offers high sensitivity, fast response time and is relatively inexpensive (Wong *et al*., 2017). Fluorescent materials are characterised by good optical properties, high stability to light and chemical agents and high quantum yield (Yamanoi *et al*., 2016). Desired colours for excitation and emission help in the choice of fluorophore. For instance, intracellular studies preclude the use of excitation wavelengths below 340 nm, while tissue experiments prefer wavelengths in the red region (de Silva *et al*., 2009).

2.12.2 Mechanisms of Detection

A variety of photophysical mechanism for signal transmission employed by sensors includes hydrogen-bonding interactions, excited-state intramolecular charge transfer {ESICT}, excited-state intramolecular proton transfer {ESIPT}, intramolecular charge transfer {ICT}, photo-induced electron transfer {PET}, excimer/exciplex formation, Förster resonance energy transfer {FRET}, proton-coupled electron transfer {PCET}, metal-ligand charge transfer {MLCT}, aggregation induced emission {AIE} and aggregation caused quenching {ACQ} among others (Thanayupong *et al*., 2017; Kowalcyzk *et al*., 2010; Alreja and Kaur 2015; Wong *et al*., 2017).

2.12.2.1 Photo-induced Electron Transfer (PET)

PET sensors are commonly electron donor-acceptor systems with a receptor-linker-fluorophore system operating as a "turn-off/on" or an intensity-based probe {**Fig. 2.22**(**a**) – (**b**)}. They commonly exhibit little or no spectral shift with increase or decrease in emission intensity. Upon excitation, the PET process occurs from the receptor HOMO to the HOMO of the excited fluorophore (which is vacated by the irradiation). This photoexcitation is localised on the acceptor (i.e fluorophore), as the HOMO of the donor (in the absence of an

analyte) lies above that of the acceptor, with possibility of electron transfer from the donor's (or receptor's) HOMO to the acceptor's HOMO. The previously excited electron is unable to return to its original ground state and a back donation occurs to the receptor leading to quenching ("turn-off") of fluorescence - the electron transfer process competes favourably with radiative decay to the ground state, substantially diminishing the fluorescence quantum yield. On binding of the receptor with a cation/analyte, the redox potential is raised, and electrons are donated from the receptor to the cation/analyte. This process lowers the energy of the receptor HOMO below that of the fluorophore HOMO {**Fig. 2.22**(**c**) – (**d**)}, preventing electron transfer and favouring fluorescence – the excited electron in the LUMO of the fluorophore returns to its original ground state with fluorescence enhancement ("turn-on"). Thus, for a "turn-off", the excited state energy of the fluorophore needs to be sufficient to provide the reduction potential of the fluorophore as well as the oxidation potential of the receptor; while in a 'turn-on', the excitation of the fluorophore results in fluorescence only because the PET process is arrested by the arrival of the analyte at the receptor site (de Silva *et al*., 2009; Kowalczyk *et al*., 2010; Wong *et al*., 2017; Kaur and Alreja 2015). PET occurs if the oxidation potential of a receptor is smaller in magnitude than that of the fluorophore. The analyte to be detected determines the choice of the receptor and the spacer must be short enough to permit reasonably fast PET rates in the 'off' state of the sensor (de Silva *et al*., 2009).

PET can be harnessed to influence fluorescence, by structural modification to include hydrophilic (for proper orientation) and hydrophobic (as electron donor) terminals in the sensor molecule (de Silva, 2012). The lone pair on a nitrogen atom could quench emission of a fluorophore via PET; with restoration of fluorescence when the nitrogen atom is involved in complexation (Geue *et al*., 2003).

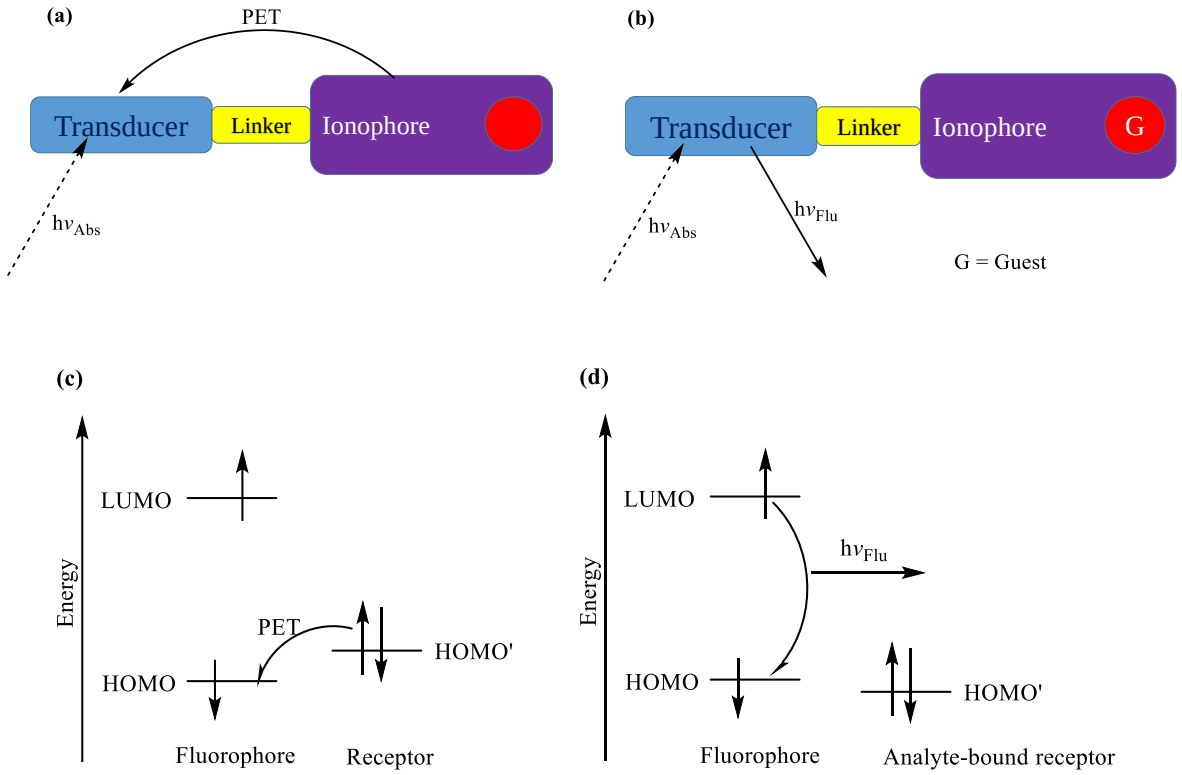

Figure 2.22: Illustration of the "on" state (a) and "off" state (b) for analyte binding involving PET mechanism and Energy diagrams depicting relative energetic dispositions of the frontier orbitals in the analyte-free (c) and the analyte-bound (d) situations.

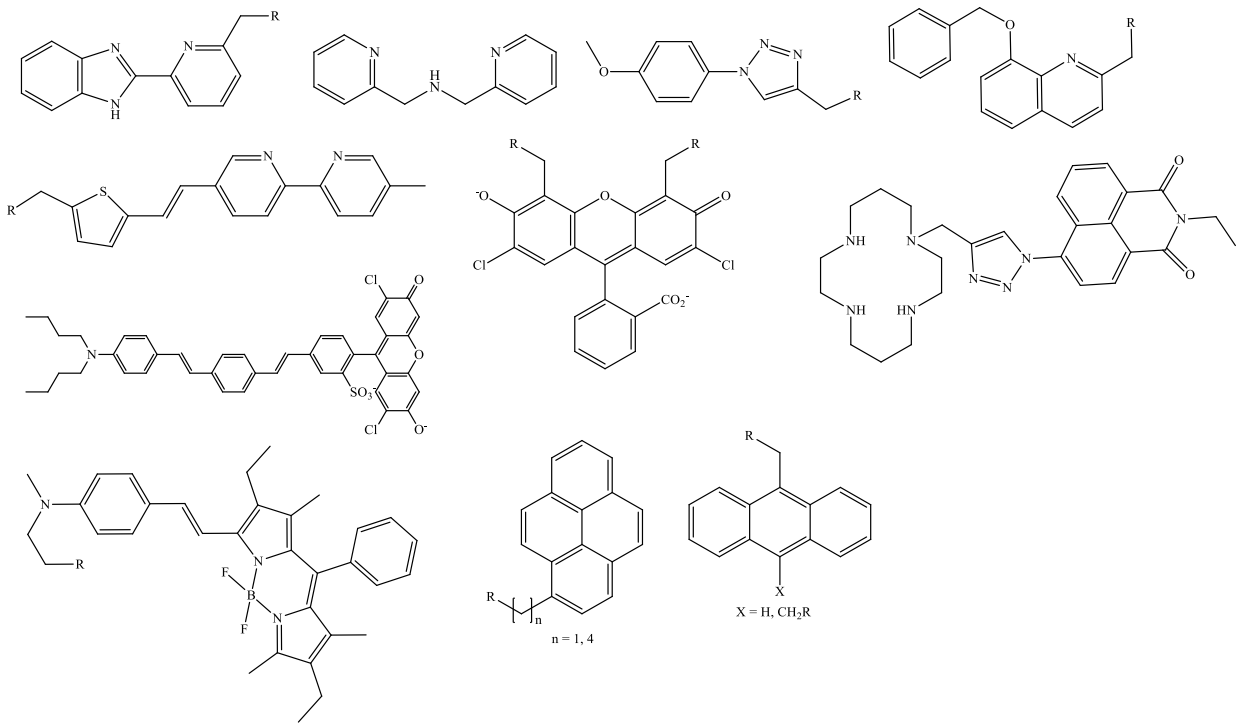

Figure 2.23: Examples of PET based sensors

2.12.2.2 Intramolecular Charge Transfer (ICT)

The presence of electron donating and electron accepting groups within a conjugated π-system of the fluorophore and receptor of a molecule is observed to lead to ICT. An increase in the electron donating ability of the electron donating group {EDG} results in a red-shift (in absorption and fluorescence response), while a decrease in the electron donating ability of the EDG results in a blue-shift. The observed charge transfer process involves redistribution of electron density from the electron donating moiety to the electron acceptor resulting in a dipole moment within the molecule. Upon analyte binding, the dipole moment increases or decreases – this increase or decrease depends on the nature of the analyte and the electrostatic relationship between the receptor and the fluorophore. An increase in dipole moment is usually accompanied by increase in molar absorptivity with a red-shift in absorption and fluorescence {since enhanced conjugation stabilises the excited state more than the ground state}; a converse observation {decrease in molar absorptivity with a blue-shift} is observed when the dipole moment decreases {reduced conjugation destabilises the excited state more than the ground state} (Wong *et al*., 2017; Lu *et al*., 2007).

ICT based molecules tend to display solvent dependent tendencies (especially with respect to fluorescence emissions), hence the charge transfer pathways depend greatly on solvent polarity {the arrangement of solvent molecules around the dipole can provide added stabilisation} (Wong *et al*., 2017; Benitez-Martin *et al*., 2020; Solomatina *et al*., 2020).

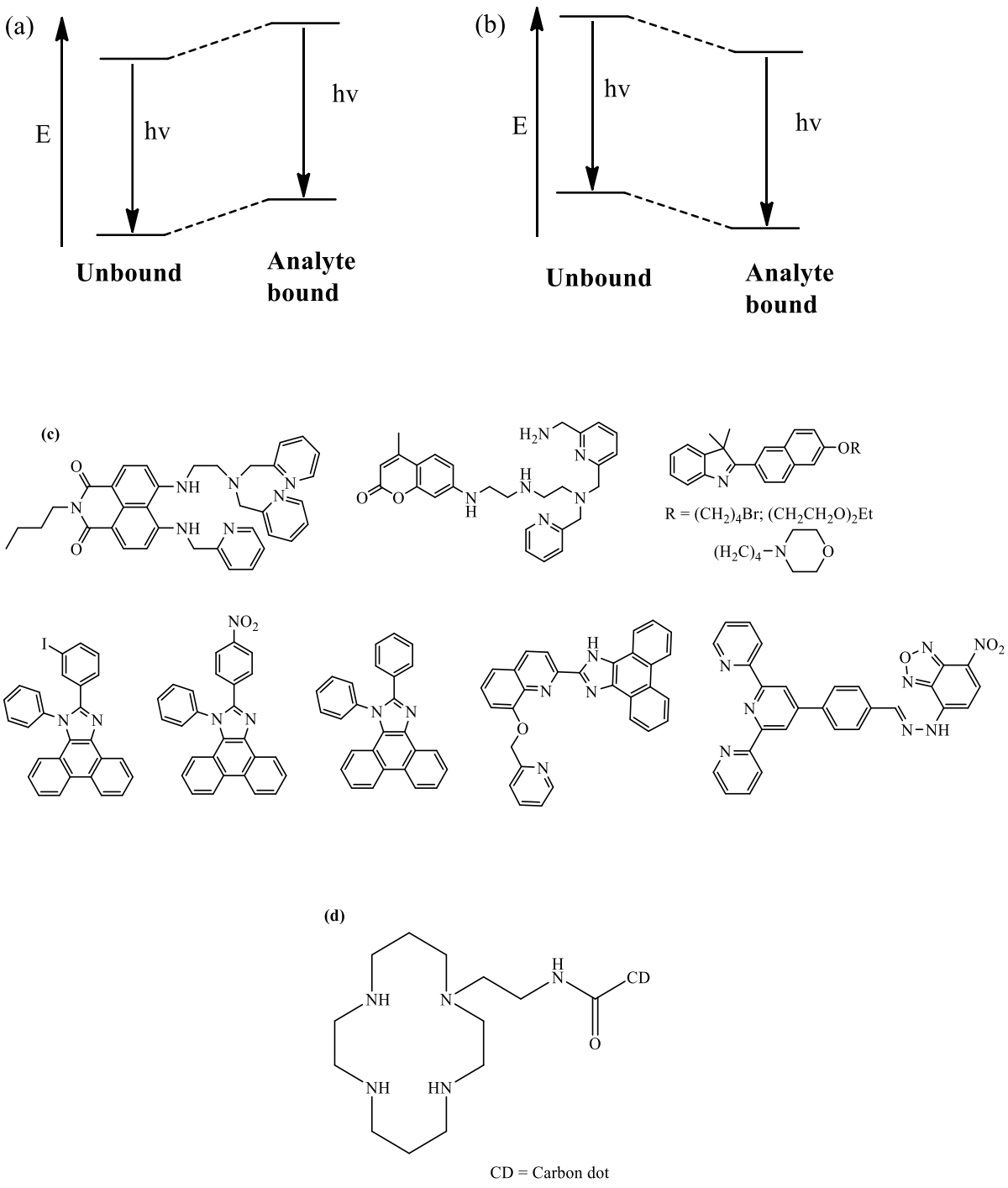

Figure 2.24: Frontier orbital energy diagrams of ICT in a state of (a) reduced dipole moment and (b) increased dipole moment. (c) Examples of ICT based and (d) FRET based sensors

2.12.2.3 Förster Resonance Energy Transfer (FRET)

This is a non-radiative transfer of energy from an excited energy donor fluorophore to an energy acceptor through long range dipole-dipole interactions. The acceptor undergoes excitation, during the FRET process, and the fluorescence emission from the original excited fluorophore is not observed. In a suitable fluorophore the wavelength of the emitted light is far red-shifted from the original excitation wavelength of the donor (Wong *et al*., 2017). The FRET process depends on:

- ✓ spectral overlap between the emission profile of the donor and the absorption profile of the acceptor
- ✓ the distance between the donor and acceptor units (ideally 10 – 100 Å)
- ✓ the orientation of the dipole moments of the donor and acceptor

When there is negligible overlap between the absorption and emission of a fluorophore unit or absence of separate interacting and proximal donor-acceptor pair in the system FRET mechanism is not proposed (Giri and Patra 2015).

2.12.2.4 Excited State Intramolecular Proton Transfer (ESIPT)

ESIPT involves very slight movement of a light hydrogen atom without energy barrier, typically on an ultra-fast (femto- to picosecond) time scale. The proton transfer (arising from the energy band gap between the local and relaxed excited states) process usually involves hydrogen bond (commonly in a five- or six-membered ring), with the donor and acceptor groups in proximity. It is very common in aromatic compounds possessing phenolic hydroxyl group and with possibility of intramolecular hydrogen bond to a nearby heteroatom (typically at < 2 Å) of the same chromophore (Yang *et al*., 2016; Zhang *et al*., 2016).

In the ground state of benzazole derivatives, two distinct intramolecular hydrogen bonded rotamers {**Fig. 2.25**(**a**) and (**b**)} have been described, with only **Fig**. **2.25**(**b**) observed to undergo ESIPT to give the phototautomer **Fig. 2.25**(**c**). The ground state energy of **Fig. 2.25**(**b**) is lower than that of **Fig. 2.25**(**a**), hence it is more stable (Wong *et al*., 2009).

In protic solvents, the intramolecular hydrogen bond is competed for by the intermolecular hydrogen bonding of the -OH group with the solvent molecules resulting in the inhibition of tautomer formation and ESIPT process {**Fig. 2.25**(**d**)}.

ESIPT based molecules are known to be sensitive to solvent polarity, type of solvent as well as hydrogen bonding. The ability of ESIPT based molecules to form intramolecular hydrogen bonds allows such molecules to exist in the keto (***K***) and enol (***E***) tautomeric forms. ESIPT is characterised by a four level photophysical process involving ground and excited states of the two tautomers, spectral sensitivity to surrounding medium and a large Stokes shifted fluorescence (blue fluorescence) in the ***E*** and ***K*** tautomeric forms. It works on the basis that the ground state of the energy acceptor is not populated. The energy transfer originates from the interaction of an excited state donor with an acceptor in its electronic ground state. Compounds exhibiting ESIPT are commonly characterised by a fast ***E*** to ***K*** intramolecular phototautomerisation and demonstrate a high energy ultra-violet (UV) ***E*** absorption coupled with tuneable ***K*** emission. In the ground state, ESIPT molecules exist in the cis-enol (***E***) form (in which intramolecular hydrogen bond is formed) and tautomerise, upon photoexcitation, to the cis-keto (***K***) form (***E****→***K****) via an extremely fast and irreversible ESIPT process – the population of the singlet excited enol (***E****) form leads to the ultrafast ESIPT process and formation of the excited cis-keto (***K****) form {which is stabilised by hydrogen bonding). The excited ***K*** form (***K****) decays radiatively to the intermediate ground state ***K*** and the ***E*** form is instantaneously recovered. The predominant absorption from ***E*** and emission from ***K**** results in an anomalously large Stokes shift, typically of about 200 nm {however, short wavelength emissions can be observed for **Fig**. **2.25**(**a**)} (Saluja *et al*., 2014; Park *et al*., 2009; Suban *et al*., 2009; Wong *et al*., 2009; Wilbraham *et al*., 2015). A Stokes shift of 4500 cm^{-1} has been observed to be too small to cause ESIPT (Suban *et al*., 2009; Zheng *et al*., 2020). The lower wavelength emission, of an ESIPT molecule, has been assigned to the ***E*** form while the higher wavelength emission was assigned to the ***K*** form (Saluja *et al*., 2014).

In the usual ESIPT process, phototautomerisation is assigned to relaxation from the excited keto tautomer, however a system has been reported with relaxation occurring from the primary excited enol state {represented with broken line arrow in **Fig**. **2.25**(**e**)}, the reported compound is observed to have low Stokes shift {27 nm} (Eseola *et al*., 2009). Dual

fluorescence (common in systems in which the enol form is stable enough) observed in certain ESIPT based molecules, has been ascribed to the long wavelength emission of **Fig**. **2.25**(**b**) and the short wavelength of **Fig**. **2.25**(**a**). One of the emission bands, of the dual fluorescence, usually arises from the enol form while the other is from the keto form. The dual fluorescence depends on the molecular structure and such external factors as solvent polarity and temperature.

ESIPT based molecules are of great interest and are useful as laser dyes, photostabilisers, fluorescent probes in biology and for electroluminescent devices (as light emitting materials).

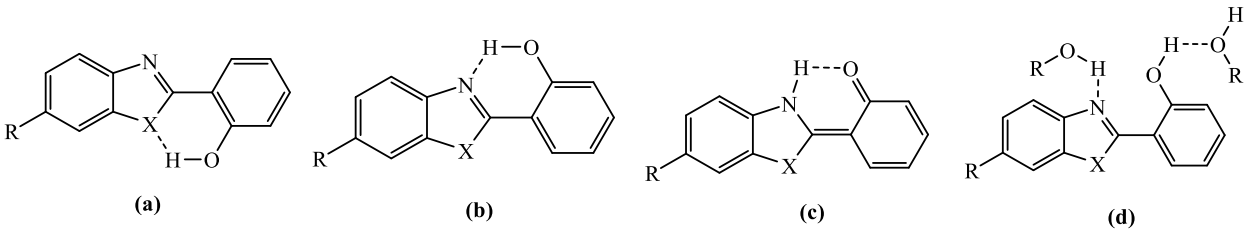

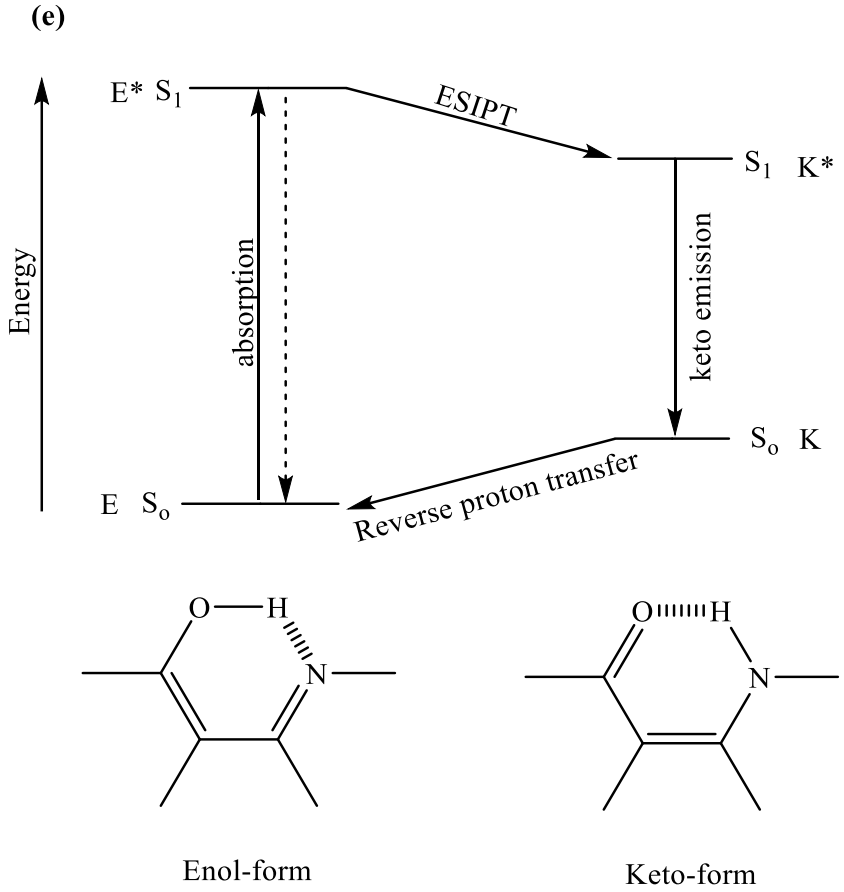

Figure 2.25: (a) – (d) Structural representation of benzazole derivatives (e) Characteristic Four-Level Photocycle Scheme of ESIPT process

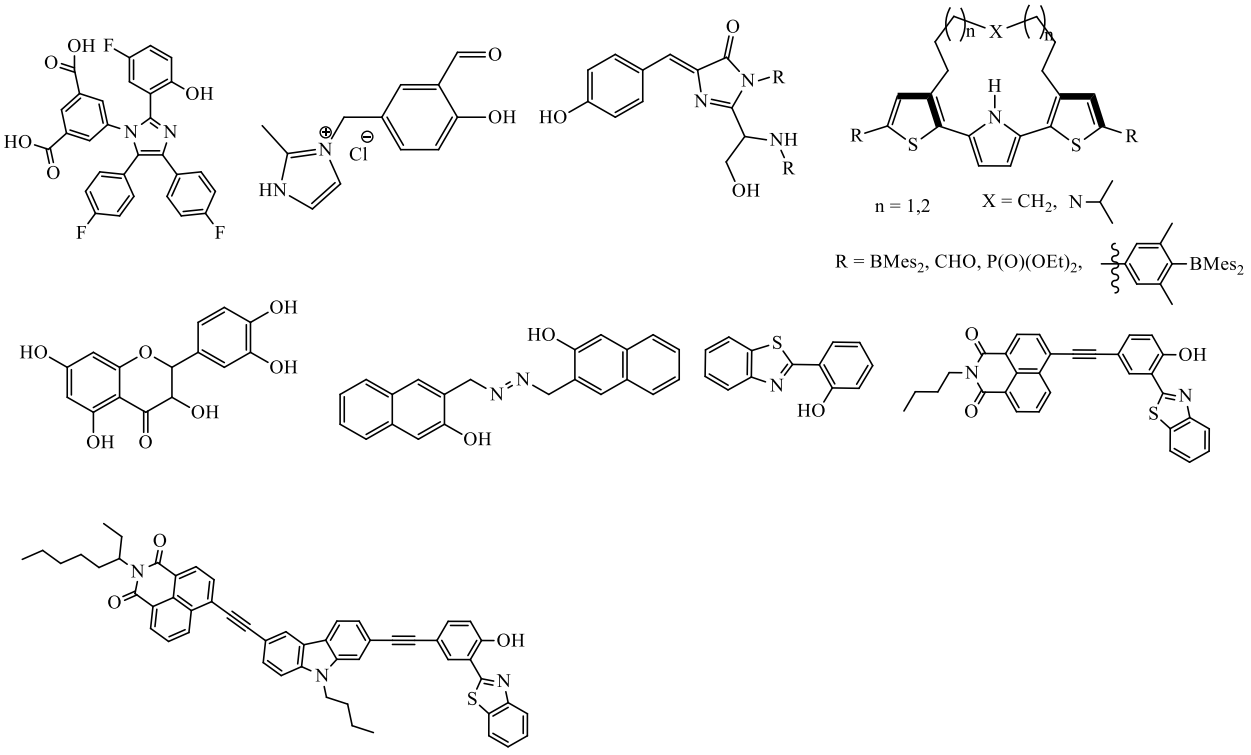

Figure 2.26: Examples of ESIPT based molecules

2.13 Determination of binding stoichiometry and binding constant

In host-guest chemistry, Job's plot (or continuous variation method) has emerged the most employed method in the determination of the binding ratio between analyte and sensor. Fluorescence or absorption titration data are fitted to appropriate binding models to obtain appropriate binding ratio {Ligand:Analyte - 1:1, 1:2, 2:1} (**Fig**. **2.27**). This method (Job's plot) has however been observed to give curves that do not fit expected outcomes (usually when more than one complex is involved), hence other techniques such as ^{1}H NMR, mass spectrophotometry have been used to help elucidate binding stoichiometry (Hibbert and Thordarson 2016; Ulatowski *et al*., 2016; Shigemoto *et al*., 2020; Song *et al*., 2013).

The binding constant of receptors can be calculated by the Benesi-Hildebrand equation for 1:1 stoichiometry (**Equation 2.3**) and 1:2 stoichiometry (**Equation 2.4**) using the equations below (Benesi and Hildebrand 1949). From **Eq. 2.3**, a linear relationship on plotting $1/F_o–F$ against function of 1/[analyte] supports 1:1 stoichiometry, while from **Eq. 2.4**, a linear graph obtained from plotting log $(F\text{-}F_o/F_\infty\text{-}F_o)$ against logC indicates 1:2 stoichiometry.

$$\frac{1}{F - F_o} = \frac{1}{K_a(F_o - F_{min})\,[\text{analyte}]} + \frac{1}{F_o - F_{min}} \qquad \text{Equation } \mathbf{2.3}$$

where F_o and F represent the fluorescence emission of sensor in the presence and absence of analyte respectively. F_{min} is the saturated emission of sensor in the presence of excess amount of analyte. [analyte] is the concentration of analyte added. K_a is the binding constant.

$$\text{Log}\ \frac{F - F_o}{F_\infty - F_o} = n\text{LogC} + \text{Log}K_a \qquad \text{Equation } \mathbf{2.4}$$

where F is the emission intensity of a chemosensor at various concentrations of metal ions. F_o and F_∞ are the limited values of F at zero and saturated concentration of metal ions, respectively. n is the number of metal ion bound by the chemosensor. C is the corresponding concentration of metal ions. K_a is the association constant of chemosensor with metal ions.

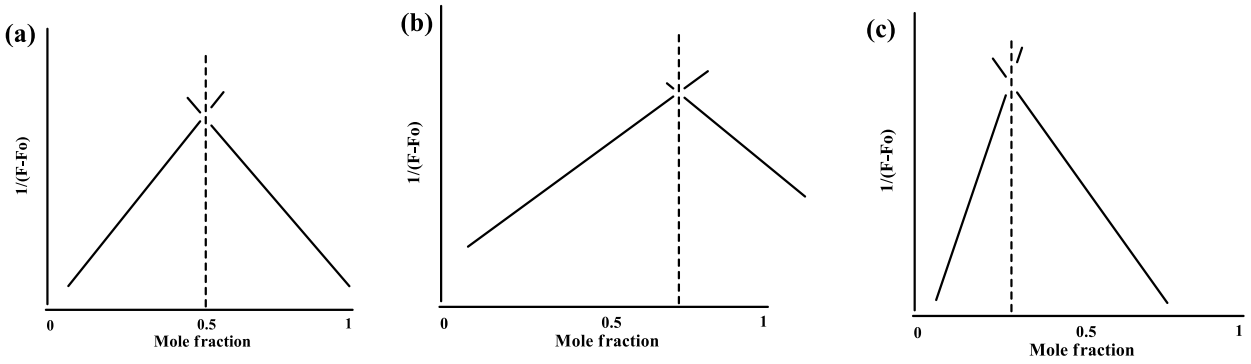

Figure 2.27: Job's plot representation for (a) 1:1 (b) 1:2 and (c) 2:1 binding ratio

The limit of detection (*LOD*) for metal ions is calculated from fluorescence titrations of metal ions, and using the expression:

$$LOD = 3\sigma/s \qquad \text{Equation } \mathbf{2.5}$$

where σ = standard deviation of response and s = slope of the calibration curve.

Linear regression graphs of titrations are used to calculate standard deviation and slope of linear response (Alreja and Kaur 2015).

2.14 Calculation of fluorescence quantum yield (Φ_f)

The fluorescence quantum yield (Φ_f) can be determined in dilute solutions with an absorbance below 0.1 at the excitation wavelength with different substances used as standard {e.g Quinine Sulfate (Φ = 0.57), Anthracene in ethanol (Φ = 0.27), Rhodamine 6G} (Dilek and Bane 2016).

The relative quantum yields are obtained by calculating the area under corrected emission spectrum of the sample and comparing these areas with the area under corrected emission spectrum of a standard solution of the reference standard. The relative quantum efficiencies of fluorescence can be obtained with the following equation:

$$\Phi_s = \Phi_r\,(A_s/A_r)[\{(1 - 10^{-Abr})/(1 - 10^{-Abs})\}](\eta_s/\eta_r)^2 \qquad \text{Equation } \mathbf{2.6}$$

where *s* and *r* represent the analyte and reference solutions respectively, Φ = quantum yield, A = area under the emission curve, Ab = absorbance at the excitation wavelength and η = refractive index of solvent used.

2.15 Slow Magnetic Relaxation

Materials which exhibit or have potential for slow magnetic property have been called SMMs or SIMs {or in some cases MSMMs} depending on the number of metal ions present in the system (Craig and Murrie 2015). SIMs/SMMs are useful for understanding the quantum phenomenon, with potential applications in quantum computing, spintronics and high-density storage device, hence the interest by scientist from diverse fields including materials science (Zhu *et al*., 2014; Zhao *et al*., 2014). At low temperatures, they have the ability to retain spin information for long periods of time and have been found to be useful in high-density information storage, although systems with shorter relaxation times may be useful in quantum computing and spin-based electronics (Demir *et al*., 2017). In a simple

term, a SMM has a large total spin (S_T) ground state and an easy-axis (z) magnetic anisotropy, which partially lifts the $2S_T + 1$-fold degeneracy of its ground state in zero magnetic field and in comparison to classical nanomagnets, SMMs offer a range of advantages including but not limited to (**i**) they consists of single, sharply defined sizes, (**ii**) they can undergo systematic changes {in the ligand and the metal ions}, (**iii**) they can dissolve in a large array of solvents (Hendrickson *et al*., 2001; Cornia *et al*., 2014).

SIMs/SMMs are molecular complexes which possess an axially bistable magnetic moment, purely of molecular origin and show slow magnetic relaxation and magnetic hysteresis, especially when a magnetising field is removed, below a certain temperature {at which digital information can be stored for 100 s} called the blocking temperature, T_B (Andruh, 2011; Zhu *et al*., 2014; Guo *et al*., 2014; Jiménez *et al*., 2016; Vingesh *et al*., 2017). The SIM/SMM behaviour is as a result of the existence of an anisotropic energy barrier U_{eff} which prevents magnetisation reversal below T_B when the polarising magnetic field is removed (Jiménez *et al*., 2016). The observed superparamagnet-like behaviour generally results from the presence of large spin ground state {S_T} and Ising-type magnetoanisotropy {D}. An anisotropic axis, in a "hard plane", is found in many SMMs and alignment of this axis with the magnetic axis of a metal ion {with maximum g_z value} results in Ising-type anisotropy. The easy axis can also act as a plane {"easy plane"} for magnetisation with $g_z < g_x \approx g_y$ (Hendrickson *et al*., 2001; Lin *et al*., 2012; Gebrezgiabher *et al*., 2020). For a SIM/SMM to function effectively as a means of data storage there must be a barrier {arising from magnetic anisotropy} to the re-orientation of the molecule's magnetisation, to prevent a loss of information. When the spin ground state of a molecule is $S > ½$, then zero-field splitting (ZFS) may arise if the symmetry is lower than cubic. The symmetry lowering may lead to the separation of excited states, which can then mix through SOC. In a situation where ZFS parameter is negative {that is, $D < 0$} an "easy-axis" magnetic anisotropy is said to occur, while for a positive ZFS parameter {that is, $D > 0$} an "easy-plane" anisotropy is said to occur { **Fig. 2.28**} (Goswami and Misra 2012).

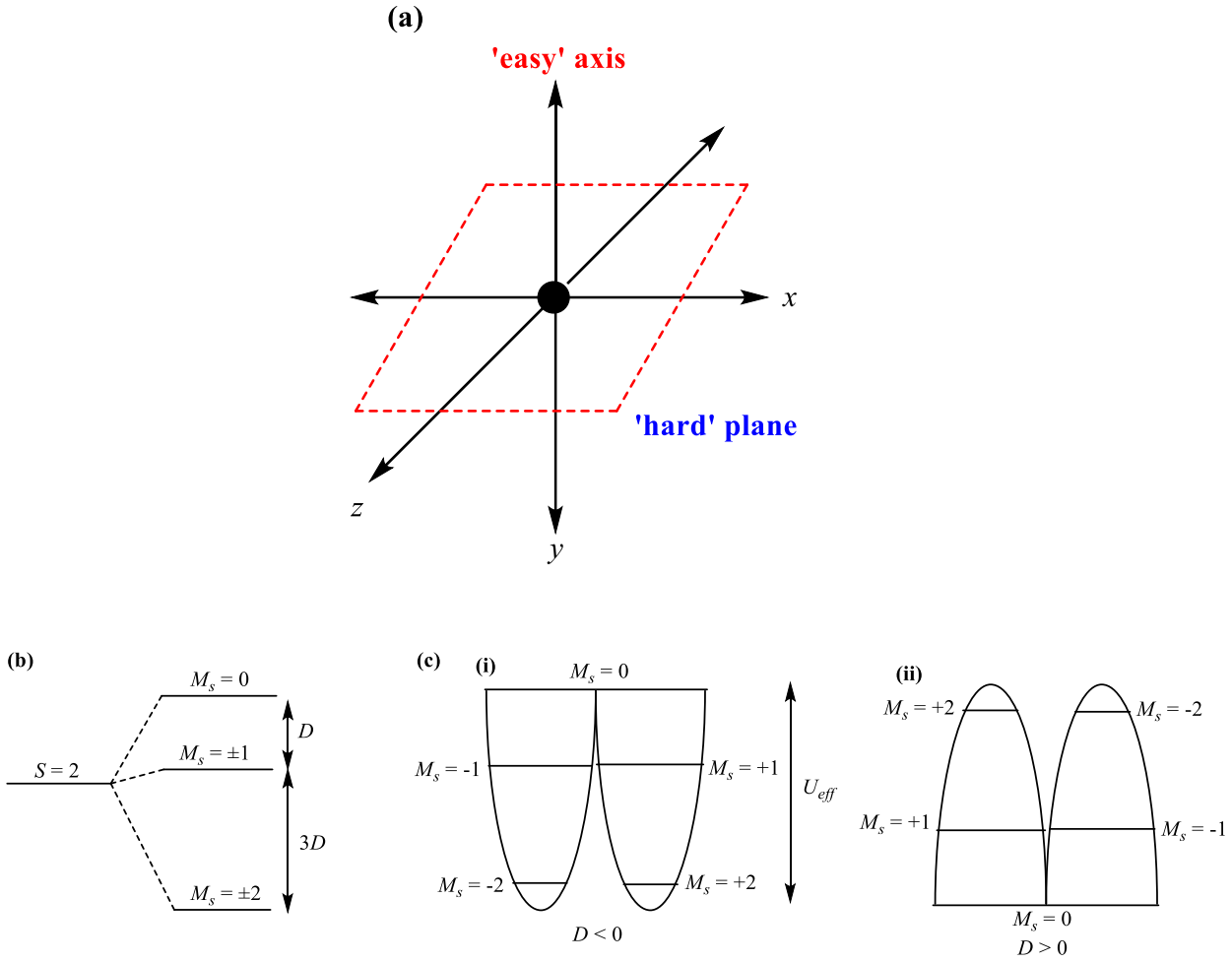

Figure 2.28: (a) Representation of the "easy" axis and "hard" plane (b) Splitting of an S = 2 state into its constituent M_S levels, induced by negative axial ZFS (c) generated double-well for (i) positive D and (ii) negative D, with the barrier to relaxation shown as U_{eff}.

2.15.1 Relaxation Processes in SIMs/SMMs

Processes that have been observed to induce loss of magnetisation include: (**i**) Orbach, (**ii**) Raman and (**iii**) direct and quantum tunnelling {**Fig. 2.29**}. While (**i**) and (**ii**) are temperature dependent {and tend to dominate at high temperatures}, (**iii**) is not {and tend to dominate at low temperatures} (Novikov *et al*., 2015; Castro *et al*., 2016). In Orbach processes, absorption of a phonon is observed to result in excitation to a real state, followed by phonon emission and relaxation; while in Raman processes, phonon absorption causes excitation of a spin to an imaginary {or virtual} state, followed by relaxation and phonon emission. Direct processes, however, involves the flipping of the spin of a molecule, followed by phonon emission. Thus, while Orbach and Raman processes are two phonon processes, direct process is a one phonon process involving relaxation of spin-lattice. Quantum tunnelling involves spin flipping by tunnelling from an M_S state on one side of a barrier to a resonant M_S state on the opposite side {e.g from the M_S = +1 level to the M_S = -1 **Fig. 2.28**[**c**]} (Frost *et al*., 2016; Gebrezgiabher *et al*., 2020).

Normally, QTM is observed in the presence of the following factors: dipole-dipole interactions {which causes mixing of Kramer's states}, hyperfine interaction and rhombic or higher-order transverse anisotropy {E}. QTM lowers the effective relaxation energy barrier, inducing a loss of remnant magnetisation and it tends to increase with decreasing S_T, thus slow relaxation of magnetisation is less frequent in mononuclear complexes {when compared with polynuclear complexes}. In *f*-block ions, spin-orbit coupling (SOC) is great enough to overcome any quenching effect from the ligand field. In *d*-block ions however, SOC is usually much weaker than the ligand field resulting in quenching of the first-order angular momentum (Jaing *et al*., 2011; Zhu *et al*., 2014; Cornia *et al*., 2014; Fondo *et al*., 2017). Thus, in 3*d* ion complexes, rational design {involving low coordination number, weak ligand field and other considerations} is helpful in achieving field induced and zero-field magnetic relaxation. Other strategies adopted in suppressing the effect of QTM include applying a static field {to remove the degeneracy of the M_s levels}, combining 3*d*-4*f* ions {to control geometry, especially since 4*f* ions tend to have high coordination numbers}, substituting the paramagnetic 3*d* ions {in 3*d*-4*f* clusters} with Zn^{II} ion {"dilution effect"} (Andruh, 2011; Zhu *et al*., 2014; Fondo *et al*., 2017).

Generally, quantum tunnelling between Kramer's states is forbidden but dipolar interaction as well as deviation from axial symmetry, could facilitate mixing of Kramer's states thus enabling quantum tunnelling. In Co^{II} ions {a Kramer's ion with half integer spin} mixing of the ground $\pm {}^{3}/_{2}$ levels causes QTM, which can be suppressed by application of a *dc* field. This dilution of the magnetic sites reduces dipole interactions, and Zeeman splitting breaks the orbital degeneracy between the Kramer's states {reducing the degree of mixing} (Jaing *et al*., 2011; Zhu *et al*., 2014; Buvaylo *et al*., 2017).

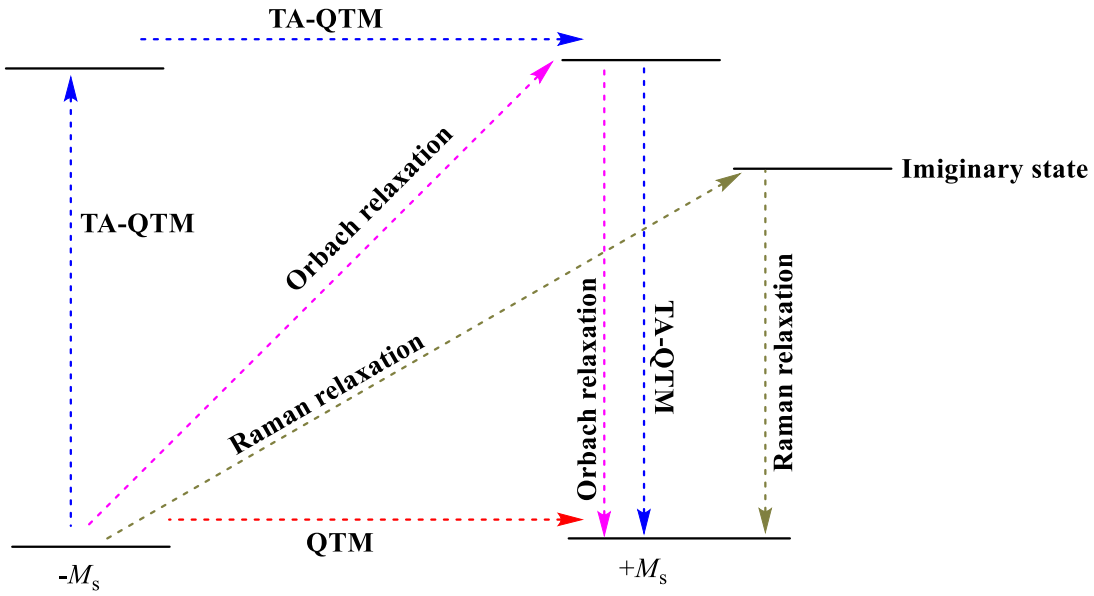

Figure 2.29: Pictorial representation of relaxation processes in SIMs/SMMs {TA-QTM = thermally assisted QTM}

2.15.2 Magnetic Exchange interactions

In situations where paramagnetic ions act independently of one another, magnetically dilute complexes are said to arise. However, under certain considerations, paramagnetic ions could influence one another {via spin-spin interactions} giving rise to exchange interactions. There are commonly two types of magnetic exchange: direct exchange and superexchange. In direct exchange, the distance between the paramagnetic ions is small – the separation is approximately the sum of their covalent radii {this allows a two-electron transfer between the paramagnetic ions}; while in superexchange intervening atoms {with diamagnetic ground states} have the ability to transfer magnetic interactions – the separation between the ions is greater than their sum of their covalent radii {the extent of the overlap between the orbitals of the metal ions and the diamagnetic atoms greatly affects the exchange} (Ball, 1969).

Since interactions of metal centres appear to be connected with the M-M distance as well as the linkage from one metal centre to the other, the sign of superexchange interactions {J_{ex}} would depend on the contribution from relevant paths. That is, the sign would be closely related to the symmetry of the orbitals of the metal centres {ions} as well as the non-magnetic ions on the path of the superexchange – a positive J_{ex} value suggests the spin vectors {in the lowest state} are parallel to one another {ferromagnetism}, while a negative value suggests the spin vectors are paired {antiferromagnetism} (Kanamori, 1959; Kobayashi *et al*., 1964).

2.15.2.1 Some Parameters Used in the Interpretation of Magnetic Exchange interactions

Deficiency in the use of the first-order isotropic {Heisenberg-Dirac-van Vleck} spin-exchange Hamiltonian expressions {$\hat{H} = -2J\hat{S}_1\hat{S}_2$}, is very common in high spin d^7 {Co^{II} ions}, due to strong anisotropy and the first-order orbital contribution of the ion {that is, first-order orbital momentum is not negligible}. To attempt quantitative approximation of magnetic data, orbitally dependent exchange interactions as well as SOC are considered, in addition to the isotropic exchange. Quantities adopted in the approximations include: axial splitting parameter {Δ}, orbital reduction factor {α}, spin-orbit coupling parameter

{λ} (Hossain *et al*., 2002; Brown *et al*., 2004; Rodriguez *et al*., 2005; Mishra *et al*., 2006; Narayanan *et al*., 2008; Arora *et al*., 2012; Goswami and Misra 2012; Daumann *et al*., 2013; Akintola *et al*., 2021).

The axial splitting parameter (Δ) is commonly used to indicate the nature of distortion around a central metal ion. In high spin d^7 {Co^{II} ions}, it is viewed as the ligand splitting of the orbital degeneracy of the $^4T_{1g}(F)$ term. Under axial distortion, the ground {$^4T_{1g}(F)$} state splits into an orbital singlet {$^4A_{1g}$} as well as a doublet {^4E_g}, with Δ as the energy between these two states {**Fig. 2.50**}; SOC splits the $^4A_{1g}$ state {into two Kramer's doublets} and the ^4E_g state {into four Kramer's doublets}. The sign of Δ is dependent on which of the two states is lower in energy; a positive value indicates an elongated axis and that the orbital singlet {$^4A_{1g}$} possess the lowest in energy, while a negative value suggest the E_g state is lower in energy.

The orbital reduction factor {α} gives an indication of the delocalisation of unpaired electrons {or spins} away from a central metal ion towards the ligand. It is a measure of the covalent nature of the bonds surrounding a central metal ion. The greater the covalence, the lower the value α. In high spin d^7 {Co^{II} ions}, the orbital reduction factor also consists of the admixture of the $^4T_{1g}(P)$ state and the ground state, $^4T_{1g}(F)$; and the stronger the admixture, the lower the value of α. The orbital reduction parameter is mathematically expressed as Ak {that is, $\alpha = Ak$}. The k parameter is concerned with the reduction of the orbital momentum arising from the delocalisation of unpaired electrons and its value is usually < 1 {and in six-coordinate high-spin d^7 Co^{II} ion it is typically in the range 0.70 – 0.95}; while the A parameter is concerned with the admixture of the $^4T_{1g}$ term of the upper ^4P into the ground ^4F states and its value is either 1 {for strong crystal fields} or $^3/_2$ {for weak crystal fields}.

The spin-orbit coupling parameter {λ} commonly has a free ion {λ_o} value of – 180 cm^{-1} and values smaller than the λ_o value suggest covalency in a material.

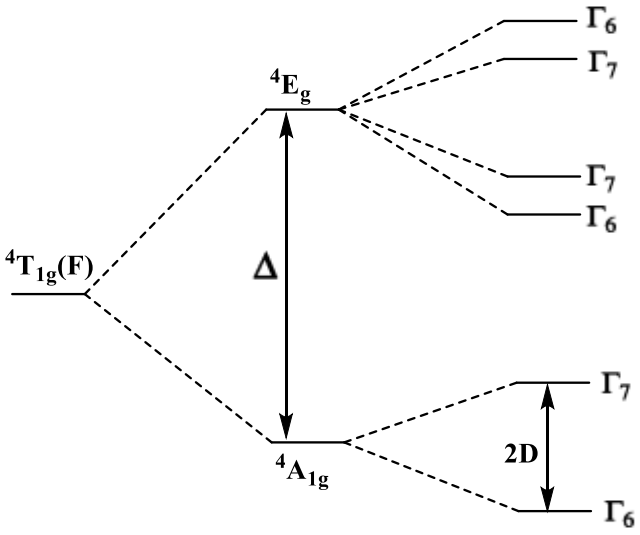

Figure 2.30: Splitting of the $^4T_{1g}(F)$ ground state under axial distortion.

2.15.2.2 Electron Spin/Paramagnetic Resonance (ESR/EPR) In Cu^{II} Complexes

Electron spin/paramagnetic resonance {ESR/EPR} is a well-established technique for elucidation of structure {solid state} and chemical bonding as well as understanding solution dynamics of paramagnetic centres like Mn^{II}, Fe^{III}, Co^{II} and Cu^{II} (Krzystek *et al*., 2006). The d^9 configuration of Cu^{II} makes it comparatively easy to use ESR in the study of coordination environment of Cu^{II} complexes (Patel and Goldberg 1972; Bowmaker *et al*., 1975; Bencini *et al*., 1978; Belford and Duan 1978; Misra and Kripal 1981; Garg *et al*., 1988; Tada and Shino 1991; Sawada *et al*., 1996; Tajima *et al*., 1997; Larin *et al*., 2004; Singh, 2008; Morgan *et al*., 2018).

The spins of a Cu^{II} ion $\{S = {}^1/_2, I = {}^3/_2\}$ are generated by weakly coupled nuclei from ligands. Since the nuclear spin, $I = {}^3/_2$, four parallel and four perpendicular {**Fig. 2.31**} hyperfine components {using $[2I + 1]$} are expected from the Cu isotopes {^{63}Cu and ^{65}Cu} (Chakradhar *et al*., 2003). ESR spectra are commonly described by *g*-tensors $\{g_{\|}, g_{\perp}\}$ and hyperfine coupling $\{A_{\|}, A_{\perp}\}$. While the parallel components $\{g_{\|}$ and $A_{\|}\}$ are commonly easy to resolve and interpret from ESR spectra, the perpendicular components $\{g_{\perp}$ and $A_{\perp}\}$ are often poorly resolved and may require indirect interpretation (Bowmaker *et al*., 1975; Misra and Kripal 1981; Sawada *et al*., 1996; Singh, 2008). The *g*-tensors give an indication of the interaction between the magnetic field and the unpaired electron and values obtained depend on the nature of the ligand and bond formed between the Cu^{II} ion and the ligand. The hyperfine coupling, however, gives insight into how the nucleus transmits experienced forces to the unpaired electron (Belford and Duan 1978; Drosou *et al*., 2022). In distorted environments, the $g_{\|}$ obtained is larger than the expected value, while the $A_{\|}$ is lower than expected (Bowmaker *et al*., 1975). ESR spectra with $g_{\perp} > g_{\|}$ suggest Cu^{II} ions in compressed tetragonal/rhombic octahedral geometry, *cis*-distorted octahedral geometry, trigonal bipyramidal geometry or linear geometry with the d_{z^2} orbital as the singly occupied molecular orbital {SOMO} (Herman, 1979; Duggan *et al*., 1980). In five-coordinate complexes, $g_{\perp} > g_{\|}$ and $|A_{\|}| \approx |A_{\perp}|$ as well as $g_3 > g_2 > g_1$ suggest a trigonal-bipyramidal geometry; while $g_{\|} > g_{\perp}$ and $|A_{\perp}| << |A_{\|}|$ suggest a square-pyramidal geometry {in both trigonal-bipyramidal and square-pyramidal geometries, the unpaired electron is commonly observed in the ground state d_{z^2} orbital with $^2A_{1g}$ term, although $d_{x^2-y^2}$ ground state has

been proposed for some square-pyramidal complexes} (Hathaway *et al*., 1970; Barbucci *et al*., 1977; Bencini *et al*., 1978; Herman, 1979; Duggan *et al*., 1980; Addison *et al*., 1981; Wei *et al*., 1994; Fleming *et al*., 1998; Humphrey *et al*., 1999; Shi *et al*., 2006; Rosu *et al*., 2011); in tetragonal Cu^{II} complexes $g_{\|} > g_{\perp}$, $A_{\|}$ is large and $A_{\perp}$ is often difficult to determine (Bencini *et al*., 1978; Bertini *et al*., 1979; Ammeter *et al*., 1979; Fleming *et al*., 1998); in square-planar and octahedral environments, $g_{\|} > g_{\perp}$ and suggests a $d_{x^2-y^2}$ ground state {which is common to tetra-, penta- and hexa-coordinate Cu^{II} complexes with tetragonal elongation} (Humphrey *et al*., 1999; Chakradhar *et al*., 2003; Gradinaru *et al*., 2007; Rosu *et al*., 2011; Łabanowska *et al*., 2012; Singh *et al*., 2014; Sinha *et al*., 2015; El-Samanody *et al*., 2017). Strongly axial ESR signals, in d^9 Cu^{II} complexes, is an indication of square-planar and square-pyramidal geometry (Drosou *et al*., 2022); in tetrahedral environments, $g_1 > g_2 > g_3 > g_e$ {and if $[\{g_2 - g_3\}/\{g_1 - g_2\}]$ is less than 1, SOMO is the $d_{x^2-y^2}$ orbital} or $g_{\|} > g_{\perp} > g_e$ which also suggest $d_{x^2-y^2}$ ground state (El-Tabl, 1998).

Some Spin Hamiltonians deployed in ESR studies of Cu^{II} complexes are given in Eqs. **2.7** – **3.2**, while some spectra line-shapes obtained are given in **Fig. 2.32** (Kivelson and Neiman 1961; Hathaway and Billing 1970; Neese, 2001; Garribba and Micera 2006; Łabanowska *et al*., 2012).

$$\mathcal{H}_s = g\beta_e S \cdot H + AS \cdot I \qquad \text{Equation } \mathbf{2.7}$$

The first term describes the spin-orbit as well as the electronic Zeeman contributions, while the second term describes the contributions from the electron and nuclear spins.

When the crystal field moves from cubic symmetry to axial and non-axial symmetry, Eq. (**2.7**) becomes Eq. (**2.8**) and Eq. (**2.9**), respectively:

$$\mathcal{H}_s = g_{\|}\beta_e H_z S_z + g_{\perp}\beta_e (H_x S_x + H_y S_y) \qquad \text{Equation } \mathbf{2.8}$$

$$\mathcal{H}_s = \beta_e (g_x H_x S_x + g_y H_y S_y + g_z H_z S_z) \qquad \text{Equation } \mathbf{2.9}$$

Where g_x, g_y and g_z are components of the g-tensor along three orthogonal axes

To accommodate D_{4h} geometry {with axial symmetry} Eq. (**2.8**) could become Eq. (**3.0**) or Eq. (**3.1**):

$$\mathcal{H}_s = \beta_e [g_{\|} H_z S_z + g_{\perp}(H_x S_x + H_y S_y)] + A_{\|} H_z I_z + A_{\perp}(H_x I_x + H_y I_y) \qquad \text{Equation } \mathbf{3.0}$$

$$\mathcal{H}_s = \beta_e[g_{\|}H_zS_z + g_{\perp}(H_xS_x + H_yS_y)] + AH_zI_z + B(H_xI_x + H_yI_y) \quad \text{Equation } \mathbf{3.1}$$

To accommodate N-donor ligands {for Cu^{II} ion in square-planar environment} Eq. (**3.2**) has been used

$$\mathcal{H}_s = \beta B[g_{\|}S_z + g_{\perp}(S_x + S_y)] + A_{\|}S_zI_z^{Cu} + A_{\perp}(S_xI_x^{Cu} + S_yI_y^{Cu}) + \sum_{Ni} SA(Ni)I^{Ni} \quad \text{Equation } \mathbf{3.2}$$

Where A(N*i*) is the hyperfine coupling tensor for the *i*th N-donor ligand

Common line-shapes observed in ESR studies of Cu^{II} ions are (**i**) Isotropic (**ii**) Axial and (**iii**) Rhombic signals.

In the case of (**i**), the Cu^{II} ion could be in an environment in which the tetragonal axes are misaligned; the symmetry is lower than octahedral, but undergoing free rotation; the symmetry is a regular octahedron, but undergoing Jahn-Teller distortion {static and/or dynamic}. The line-shape observed, in the case of (**ii**), shows dependence on the lowest *g*-tensor value: when $g > 2.04$ {**Fig. 2.32**(**b**)}, the Cu^{II} ion likely possesses axial symmetry with parallel principal axes {and tetragonal elongation} or possesses some rhombic symmetry; while for $g < 2.03$ {**Fig. 2.32**(**c**)}, the Cu^{II} ion likely possesses axial symmetry with parallel principal axes {and tetragonal compression} or possesses compressed rhombic symmetry. The line-shapes for (**iii**) appear to be consistent with situations for (**ii**) as they also show dependence on the lowest *g*-tensor value {$g > 2.04$ [**Fig. 2.32**(**d**)] and $g < 2.03$ [**Fig. 2.32**(**e**)]} and the environment of the Cu^{II} ion also appears to depend on elongation and compression {within rhombic or axial symmetry} (Hathaway and Billing 1970; Bertini *et al*., 1979; Ammeter *et al*., 1979; Rosu *et al*., 2011; Łabanowska *et al*., 2012).

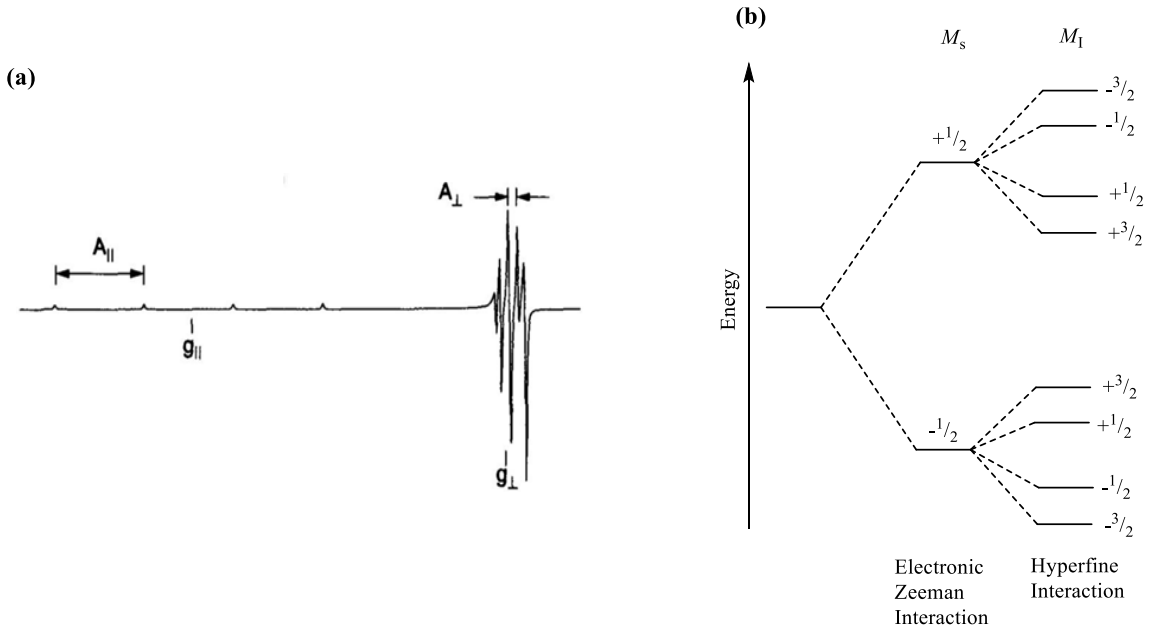

Figure 2.31: (a). X-band spectrum of Cu^{II} complexes (source: ETHzürich) (b). Energy level and possible transitions for $S = ½$, $I = {}^3/_2$

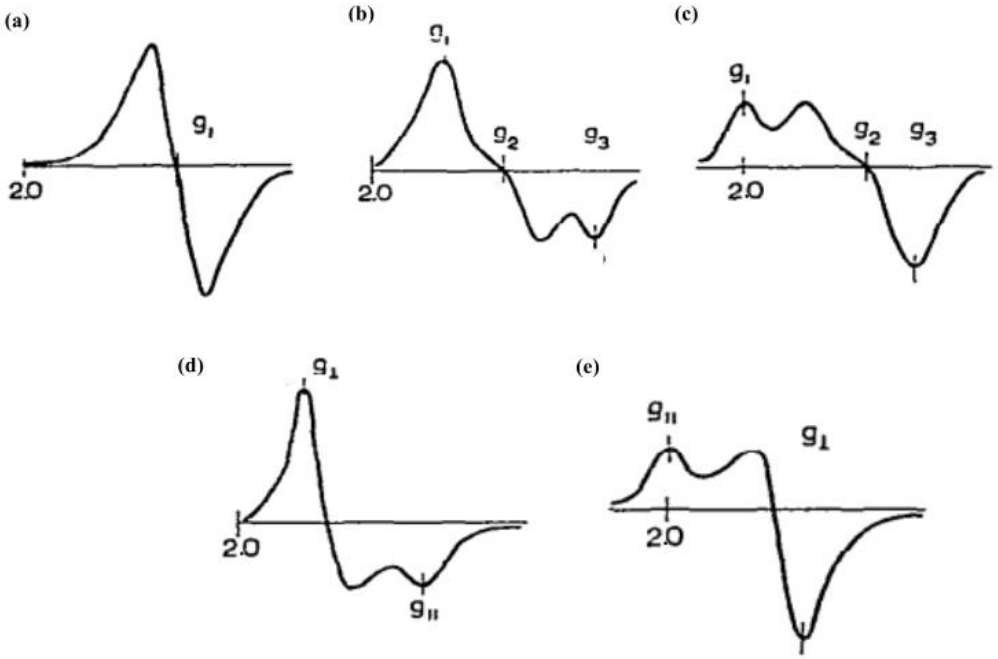

Figure 2.32: Isotropic {(a)}; Axial {(b) and (c)} and Rhombic {(d) and (e)} ESR spectra line-shapes for Cu^{II} complexes

CHAPTER THREE

MATERIALS AND METHODS

3.1 General considerations

All starting materials for synthesis were obtained commercially {from Alfa Aesar, Merck and TCI chemicals} as reagent grade and used without further purification. Thin-Layer Chromatography (TLC) was used for monitoring the reactions using precoated silica gel 60 plates. Column chromatography was performed on silica gel (60 – 120 mesh). FT-IR spectral data were measured on a VERTEX 70 IR spectrometer by Bruker Optics using the Specac Diamond ATR optional accessory in the range 4000 - 400 cm^{-1}. ^{1}H and ^{13}C NMR spectra were recorded with a Bruker AVANCE 63, 101, 250, 400 and 500 MHz spectrometer. Chemical shifts (δ) are given in parts per million (ppm) using the residue solvent peaks as a reference relative to TMS. Coupling constants (*J*) are given in hertz (Hz). Signals are abbreviated as follows: singlet, s; doublet, d; doublet-doublet, dd; triplet, t; triplet-doublet, td; multiplet, m. Mass Spectrometry (MS) analyses were conducted on a Bruker MAT SSQ 710 spectrometer. Elemental analyses were carried out on Leco CHNS-932 and El Vario III elemental analysers. Photoluminescence excitation and emission spectra were recorded on a JASCO FP-6300 spectrofluorometer at room temperature with a spectral resolution of 1 nm. UV-Visible spectra were recorded on a Varian Cary5000 UV-Vis-NIR Spectrophotometer. Simultaneous TG/DTA analyses were carried out under static air atmosphere using a Netzsch STA Luxx PC analyser up to 1000^{o}C. Magnetic susceptibility was determined on bulk vacuum dried materials in the 2 – 300 K temperature range using a Quantum Design MPMS-5 superconducting SQUID magnetometer. Data obtained were corrected for diamagnetism of the capsules used and the intrinsic diamagnetism of the constituent atoms using Pascal constants. Electron spin resonance (ESR) spectra were recorded with an X-Band ESR-ELEXSYS Spectrometer by Bruker with a 100 kHz field modulation and microwave frequencies ranging between 9.31 – 9.82 GHz. Crystallographic data were collected on a Nonius KappaCCD diffractometer, using graphite-monochromated Mo-Kα radiation. Data were corrected for Lorentz and

polarisation effects, absorption was taken into account on a semi-empirical basis using multiple-scans (Hooft, 1998; Otwinowski and Minor 1997; Sheldrick, 2002). Structures were solved by direct methods (SHELXS; Sheldrick, 2008) and refined by full-matrix least squares techniques against F_o^2 (SHELXL). All hydrogen atoms were included at calculated positions with fixed thermal parameters. All non-disordered, non-hydrogen atoms were refined anisotropically. Crystallographic data as well as structure solution and refinement details are summarised in **Chapter 4**. Diamond 4.6.8 (Brandenburg and Putz 2022), was used for structure representations.

3.2 Ultraviolet-Visible (UV-vis) and fluorescence measurements

Stock solutions (usually 100 mL) of the receptors (1 x 10^{-5} M) were prepared in appropriate solvents (MeCN; MeOH; $CHCl_3$). Solutions (50 mL) of the guest cations (1 x 10^{-2} M) were also prepared in appropriate solvents (MeCN; MeOH; $CHCl_3$) – nitrate salts of the cations studied were used in all cases, except for Ga^{3+} (where the iodide salt was used), and In^{3+}, Tl^{3+} (where the chloride salts were used). 3 mL solutions of the ligand were transferred into a 1 cm × 1 cm quartz cuvette equipped with a tiny magnetic bar and the UV-vis and fluorescence (excitation and emission) scans were obtained. The UV-vis and fluorescence scans in the presence of the guest cations were obtained by adding, separately, 6 µL (of each cation) to a 3 mL solution of the ligand, by means of a micro-syringe, and the solution stirred for ≈30 seconds (to gain homogeneity) before measurement of the UV-vis and fluorescence scans for the response absorption and emission signals. Fluorescence measurements were performed using a slit width of 5 nm x 5 nm. The results are presented in Tables **4.1** (for the Bis-imidazoles), **4.2** (for the imidazole amines), **4.3** (for the NNO and NNN imidazole imines) and **4.4** (for the imines).

3.3 Determination of the fluorescence quantum yield (Φ_f)

The fluorescence quantum yield was determined using **Eq. 2.6** with Anthracene in ethanol (Φ = 0.27) was used as the reference.

3.4 Job's plot, Association constant (K_a) and limit of detection (*LOD*)

The probable coordination between the ligands and M^{n+} ions was determined by Job's method. A fixed volume (3 mL) was used; varying the volume of the {10^{-5} M} ligands (0.0, 0.3, 0.6, 0.9, 1.2, 1.5, 1.8, 2.1, 2.4, 2.7, 3.0) and making up with appropriate volume of metal ion (of concentration 1 x 10^{-5} M). Fluorescence measurements at appropriate excitation wavelength were performed – a plot of the emission intensity against the mole fraction gave an indication of mode of binding. In the determination of K_a and *LOD*, solutions of metal ion (concentrations 0.1 – 1.0 µM) were prepared, 6 µL were added to 3 mL of the ligand solution and fluorescence measurements made at appropriate excitation wavelength. The K_a was determined using Eq. (**2.3**), while *LOD* was determined using Eq. (**2.5**).

3.5 Reagents and solvents

Isophthalaldehyde, terephthalaldehyde, 2-nitrobenzaldehyde, benzil, anisil, aniline, 9,10-phenathrenequinone, 3,4-hexanedione, ammonium acetate, acetic acid, ammonia, hydrogen, potassium carbonate (K_2CO_3), sodium hydride (NaH), iodomethane, 10%Pd/C, salicylaldehyde, pyridine-2-carboxaldehyde, bis(2-aminophenyl) sulphide, bis(2-aminophenyl) ether, 2-hydroxy-1-naphthaldehyde, 5-methylsalicylaldehyde, 5-bromosalicylaldehyde, 3,5-dibromosalicylaldehyde, 5-nitrosalicylaldehyde, *o*-vanillin, *o*-phenylenediamine, lead(IV)oxide (PbO_2), $PdCl_2(MeCN)_2$, cobalt chloride hexahydrate, celite, ethanol (EtOH), methanol (MeOH), tetrahydrofuran (THF), ethylacetate (EtOAc), hexane, dichloromethane (DCM), acetonitrile (MeCN), dimethylformamide (DMF), n-heptane and ether (Et_2O).

3.6 Preparation of Bis-imidazoles (BI_1 – BI_7)

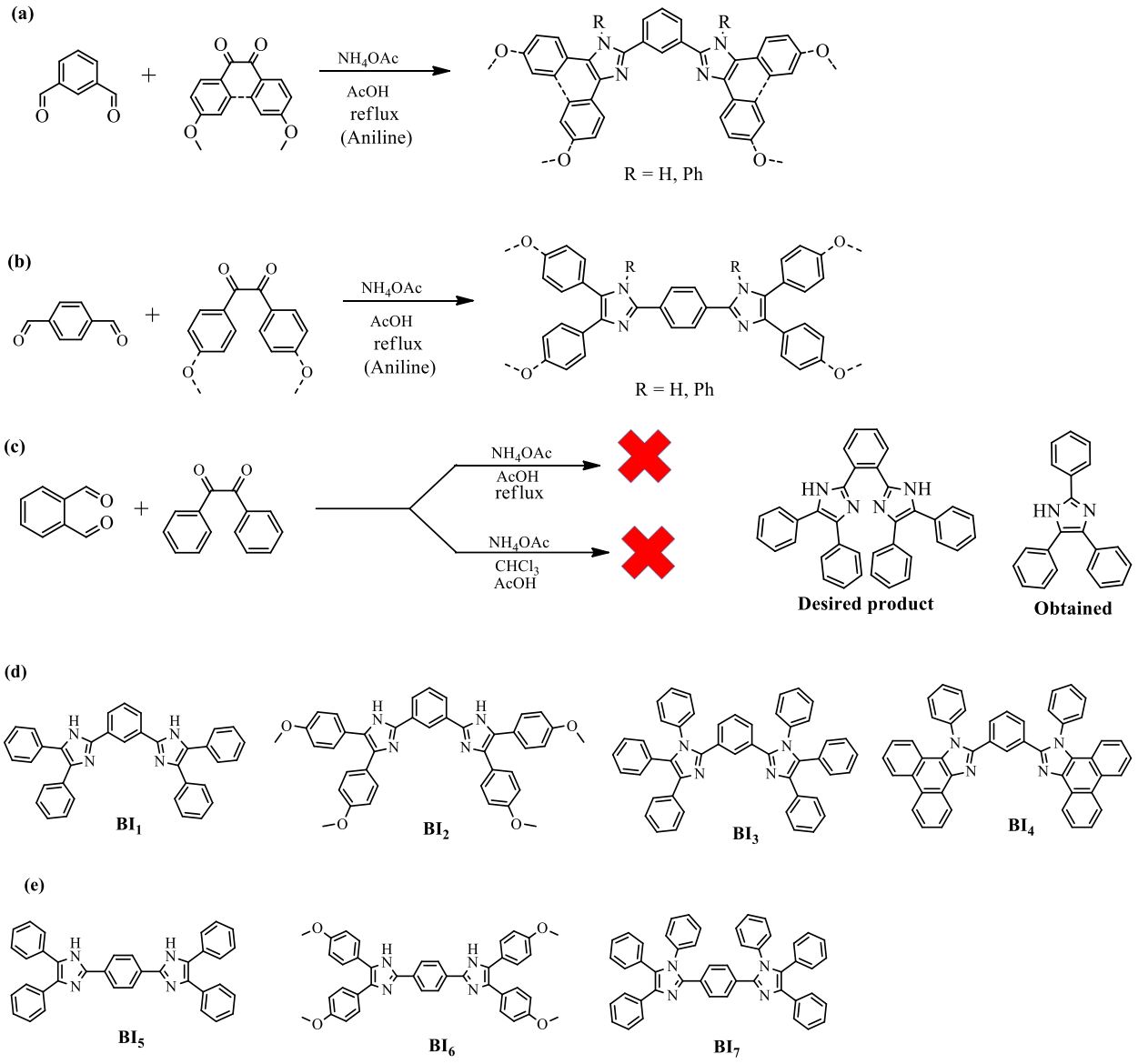

Scheme 3.1: Preparation of (a) 1,3-bis-imidazoles (b) 1,4-bis-imidazoles; (c) failed attempt at the preparation of 1,2-bis-imidazoles and List of prepared (d) 1,3-bis-imidazoles (**BI_1** – **BI_4**) (e) 1,4-bis-imidazoles (**BI_5** – **BI_7**).

The bis-imidazoles were prepared via similar procedure reported by our group (Eseola *et al*., 2018; Eseola *et al*., 2011), with slight modifications. Since a general method was adopted, a full description is given with compound **BI_1**. To obtain a pure **BI_3** washing with hot EtOAc was required, while **BI_5** required washing with hot DMF. **BI_6** and **BI_7** required purification via column chromatography (using 1:1 EtOAc/n-Heptane).

While products were obtained for the 1,3- and 1,4- series, attempts at the preparation of the 1,2-series did not yield desired products (**Scheme 3.1{c}**) - 2,4,5-triphenyl-1*H*-imidazole was obtained in the two approaches adopted (**Fig. S8**).

3.6.1: 1,3-bis(4,5-diphenyl-1*H*-imidazol-2-yl)benzene (BI_1): 0.47 g (3.50 mmol) of isophthalaldehyde, 1.48 g (7.04 mmol) of benzil and 5.40 g (70.06 mmol) of ammonium acetate were placed in a round bottom flask, followed by 15 mL of acetic acid. The mixture obtained was refluxed at 104^{o}C for 5 hours to give a clear yellow solution. On cooling a white solid was obtained. The solid was transferred into 40 mL of ice-cold water, followed by ammonia until a pH > 7. The solid was filtered, washed with water, and dried (in an oven at 70^{o}C) to afford an off-white solid. Yield = 1.73 g (96 %). Selected FTIR (ATR, cm^{-1}): 3331w, 3058b, 1652s, 1606s, 1543s, 1481s, 1444s, 1403w, 1072s, 763s, 693s, 619s, 507s. UV-Vis (MeCN, nm {ε /M^{-1} cm^{-1}}): 228 {47 633}, 309 {55 270}. ^{1}H NMR (400 MHz, DMSO-d_6) δ (ppm): 7.25 (t, *J* = 7.3 Hz, 2H, Ar-H), 7.33 (t, *J* = 7.5 Hz, 4H, Ar-H), 7.39 (t, *J* = 7.2 Hz, 2H, Ar-H), 7.46 (t, *J* = 7.4 Hz, 4H, Ar-H), 7.54 (d, *J* = 7.3 Hz, 4H, Ar-H), 7.64 – 7.57 (m, 5H, Ar-H), 8.09 (d, *J* = 7.8 Hz, 2H, Ar-H), 8.82 (s, 1H, Ar-H), 12.86 (s, 2H, -NH). ^{13}C NMR (101 MHz, DMSO-d_6) δ (ppm): 122.82, 125.42, 127.05, 127.68, 128.26, 128.68, 128.95, 129.11, 129.51, 131.35, 131.48, 135.62, 137.78, 145.81, 206.98. MS (ESI) *m/z* 515.22 (M^+, Calc. 514.62). Anal. Calc.(Found) for $C_{36}H_{27.5}N_4O_{0.75}$ C, 81.87(81.99); H, 5.25 (5.13); N, 10.61(10.66) %.

3.6.2: 1,3-bis(4,5-bis(4-methoxyphenyl)-1*H*-imidazol-2-yl)benzene (BI_2), off-white**:** 0.48 g (3.58 mmol) of isophthalaldehyde, 1.94 g (7.18 mmol) of anisil and 5.57 g (71.58 mmol) of ammonium acetate. Yield = 1.51 g (66 %). Selected FTIR (ATR, cm^{-1}): 2935w, 1613s, 1517s, 1491s, 1455w, 1294s, 1243s, 1173s, 1106s, 1029s, 970s, 829s, 767w, 697s,

591s, 531s. UV-Vis (MeCN, nm {ε /M^{-1} cm^{-1}}): 239 {44 167}, 304 {52 653}. ^{1}H NMR (400 MHz, DMSO-d_6) δ (ppm): 3.79 (d, *J* = 17.8 Hz, 12H, -OCH_3), 6.96 (dd, *J* = 47.9, 7.6 Hz, 8H, Ar-H), 7.60 – 7.40 (m, 9H, Ar-H), 8.03 (dd, *J* = 7.8, 1.5 Hz, 2H, Ar-H), 8.76 (s, 1H), 12.66 (s, 2H, -NH). ^{13}C NMR (101 MHz, DMSO-d_6) δ (ppm): 55.51, 114.12, 114.53, 122.56, 125.03, 128.78, 129.38, 130.22, 131.48, 145.16, 206.94. MS (ESI) *m/z* 635.26 (M^+, Calc. 634.72). Anal. Calc.(Found) for $C_{40}H_{35}N_4O_{4.5}$ C, 74.63(74.91); H, 5.48(5.55); N, 8.70(8.64) %.

3.6.3: 1,3-bis(1*H*-phenanthro[9,10-*d*]imidazol-2-yl)benzene (BI_3), off-white**:** 0.52 g (3.88 mmol) of isophthalaldehyde, 1.62 g (7.78 mmol) of 9,10-phenathrenequinone and 6.04 g (77.62 mmol) of ammonium acetate. Yield = 1.39 g (54 %). Selected FTIR (ATR, cm^{-1}): 3053w, 1660w, 1598w, 1495s, 1443s, 1362w, 1074w, 1027w, 764s, 694s, 531s. UV-Vis (MeCN, nm {ε /M^{-1} cm^{-1}}): 286 {47 938}. ^{1}H NMR (250 MHz, $CDCl_3$) δ (ppm): 7.03 (d, *J* = 6.8 Hz, 4H, Ar-H), 7.17 (s, 4H, Ar-H), 7.28 (dd, *J* = 9.7, 6.3 Hz, 20H, Ar-H), 7.61 (d, *J* = 7.2 Hz, 5H, Ar-H), 7.86 (s, 1H, Ar-H). ^{13}C NMR (63 MHz, $CDCl_3$) δ (ppm): 127.45, 128.11, 128.61, 128.73, 128.91, 128.98, 129.25, 129.39, 130.01, 130.81, 131.50, 131.62, 131.88, 132.07, 135.33, 137.84, 139.00, 147.26. MS (ESI) *m/z* 667.28 (M^+, Calc. 666.81). Anal. Calc.(Found) for $C_{48}H_{35.5}N_4O_{0.75}$ C, 84.74(84.74); H, 5.26(5.11); N, 8.24(8.32) %.

3.6.4: 1,3-bis(1-phenyl-1*H*-phenanthro[9,10-*d*]imidazol-2-yl)benzene (BI_4), brown**:** 0.31 g (2.31 mmol) of isophthalaldehyde, 0.96 g (4.61 mmol) of 9,10-phenathrenequinone, 0.43 mL (0.44 g, 4.71 mmol) aniline and 3.60 g (46.26 mmol) of ammonium acetate. Yield = 1.50 g (98 %). Selected FTIR (ATR, cm^{-1}): 3067w, 1650w, 1612w, 1530w, 1494s, 1451s, 1383w, 1236w, 1036w, 1004w, 756s, 725s, 701s, 616s, 532s. UV-Vis (MeCN, nm {ε /M^{-1} cm^{-1}}): 231 {55 595}sh, 258 {99 976}, 311 {30 496}, 360 {16 494}sh. ^{1}H NMR (250 MHz, $CDCl_3$) δ (ppm): 7.20 (d, *J* = 8.1 Hz, 3H, Ar-H), 7.31 (d, *J* = 8.8 Hz, 2H, Ar-H), 7.51 (d, *J* = 6.2 Hz, 8H, Ar-H), 7.68 (dd, *J* = 15.1, 6.3 Hz, 8H, Ar-H), 7.79 (t, *J* = 7.4 Hz, 2H, Ar-H), 8.00 (s, 1H, Ar-H), 8.77 (dd, *J* = 14.7, 8.3 Hz, 4H, Ar-H), 8.88 (d, *J* = 7.8 Hz, 2H, Ar-H). ^{13}C NMR (63 MHz, $CDCl_3$) δ (ppm): 121.79, 123.65, 123.93, 124.04, 125.02, 125.85, 126.55, 127.21, 128.19, 128.95, 129.07, 129.19, 130.04, 130.20, 130.50, 130.82, 131.10,

131.55, 131.78, 138.34, 139.40, 151.15. MS (ESI) *m/z* 663.25 (M^+, Calc. 662.78). Anal. Calc.(Found) for $C_{48}H_{31.5}N_4O_{0.75}$ C, 85.25(85.28); H, 4.69(4.63); N, 8.28(8.31) %.

3.6.5: 1,4-bis(4,5-diphenyl-1*H*-imidazol-2-yl)benzene (BI_5), yellow**:** 1.06 g (7.90 mmol) of terephthalaldehyde, 3.32 g (15.79 mmol) of benzil and 12.18 g (0.16 mol) of ammonium acetate. Yield = 3.59 g (88 %). Selected FTIR (ATR, cm^{-1}): 3058w, 1602w, 1486s, 1451s, 1071w, 969w, 841s, 763s, 694s, 603w, 507s. UV-Vis (MeCN, nm {ε /M^{-1} cm^{-1}}): 234 {14 298}, 355 {22 242}. ^{1}H NMR (400 MHz, DMSO-d_6) δ (ppm): 7.25 (t, *J* = 7.2 Hz, 2H, Ar-H), 7.33 (t, *J* = 7.5 Hz, 4H, Ar-H), 7.40 (t, *J* = 7.2 Hz, 2H, Ar-H), 7.47 (t, *J* = 7.4 Hz, 4H, Ar-H), 7.56 (dd, *J* = 18.1, 7.3 Hz, 8H, Ar-H), 8.20 (s, 4H, Ar-H), 12.77 (s, 2H, -NH). ^{13}C NMR (101 MHz, DMSO-d_6) δ (ppm): 125.86, 127.57, 128.69, 128.89, 129.16, 130.29, 131.46, 135.57, 137.83, 145.63, 204.38, 204.39. MS (EI) *m/z* 514 (M^+, Calc. 514.62). Anal. Calc.(Found) for $C_{36}H_{26}N_4$ C, 84.02(83.69); H, 5.09(5.11); N, 10.89(10.85) %.

3.6.6: 1,4-bis(4,5-bis(4-methoxyphenyl)-1*H*-imidazol-2-yl)benzene (BI_6), yellow**:** 1.01 g (7.53 mmol) of terephthalaldehyde, 4.08 g (15.09 mmol) of anisil and 11.64 g (0.15 mol) of ammonium acetate. Yield = 1.82 g (38 %). Selected FTIR (ATR, cm^{-1}): 1615s, 1518s, 1498s, 1443s, 1294s, 1245s, 1174s, 1106s, 1032s, 971w, 830s, 713w, 592s, 527s. UV-Vis (MeCN, nm {ε /M^{-1} cm^{-1}}): 239 {40 467}, 299 {35 163}, 366 {50 866}. ^{1}H NMR (400 MHz, DMSO-d_6) δ (ppm): 3.76 (s, 6H, -OCH_3), 3.81 (s, 6H, -OCH_3), 6.90 (d, *J* = 8.8 Hz, 4H, Ar-H), 7.03 (d, *J* = 8.7 Hz, 4H, Ar-H), 7.47 (dd, *J* = 22.0, 8.7 Hz, 8H, Ar-H), 8.15 (s, 4H, Ar-H), 12.57 (s, 2H, -NH). ^{13}C NMR (101 MHz, DMSO-d_6) δ (ppm): 55.48, 55.66, 114.11, 114.58, 123.92, 125.65, 127.87, 128.26, 128.67, 130.15, 130.24, 137.13, 144.99, 158.42, 159.25. MS (ESI) *m/z* 635.26 (M^+, Calc. 634.72). Anal. Calc.(Found) for $C_{40}H_{34}N_4O_4$ C, 75.69(75.36); H, 5.40(5.35); N, 8.83(8.93) %.

3.6.7: 1,4-bis(1,4,5-triphenyl-1*H*-imidazol-2-yl)benzene (BI_7), off-white**:** 1.02 g (7.60 mmol) of terephthalaldehyde, 3.20 g (15.22 mmol) of benzil, 1.40 mL (1.43 g, 15.33 mmol) aniline and 3.55 g (46.06 mmol) of ammonium acetate. Yield = 0.31 g (6 %). Selected FTIR (ATR, cm^{-1}): 1597w, 1496s, 1480w, 1444w, 1418w, 1372w, 1244w, 1075w, 1028w, 960s, 916s, 846s, 763s, 693s, 650s, 524w. UV-Vis (MeCN, nm {ε /M^{-1} cm^{-1}}): 240 {6 575}, 291

{6 749}, 329 {7 812}. ^{1}H NMR (400 MHz, CD_2Cl_2) δ (ppm): 7.11 (dd, *J* = 8.0, 1.5 Hz, 4H, Ar-H), 7.20 – 7.34 (m, 25H, Ar-H), 7.54 – 7.60 (m, 5H, Ar-H). MS (ESI) *m/z* 667.286 (M^+, Calc. 666.81). Anal. Calc.(Found) for $C_{48}H_{35}N_4O_{0.5}$ C, 85.31(85.13); H, 5.22(5.14); N, 8.29(8.46) %.

3.7 Preparation of NNO and NNN imidazole-based ligands

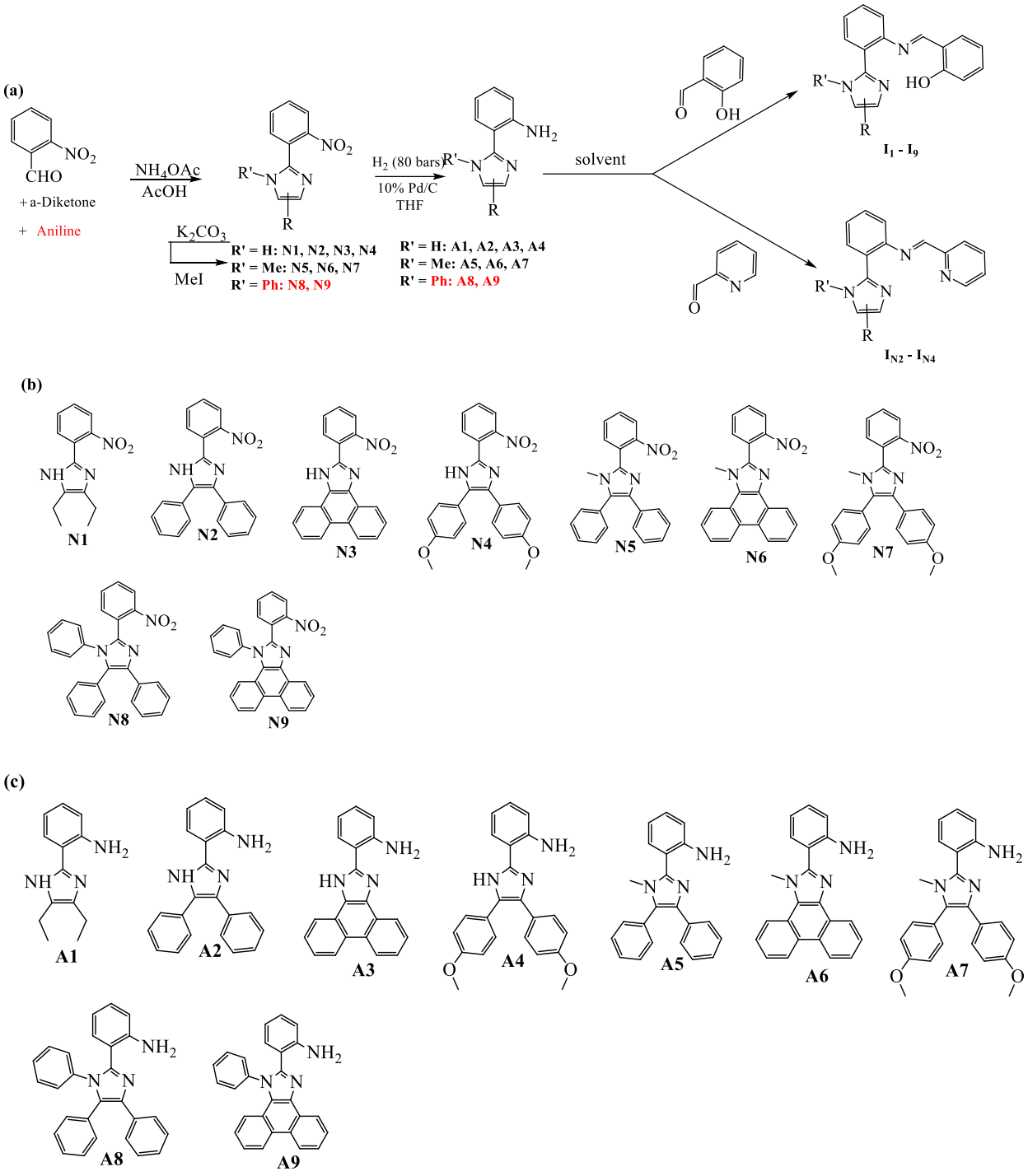

Scheme 3.2: (a) Synthetic pathway to NNO and NNN imines (b) List of prepared nitro-imidazoles (c) List of prepared imidazole amines

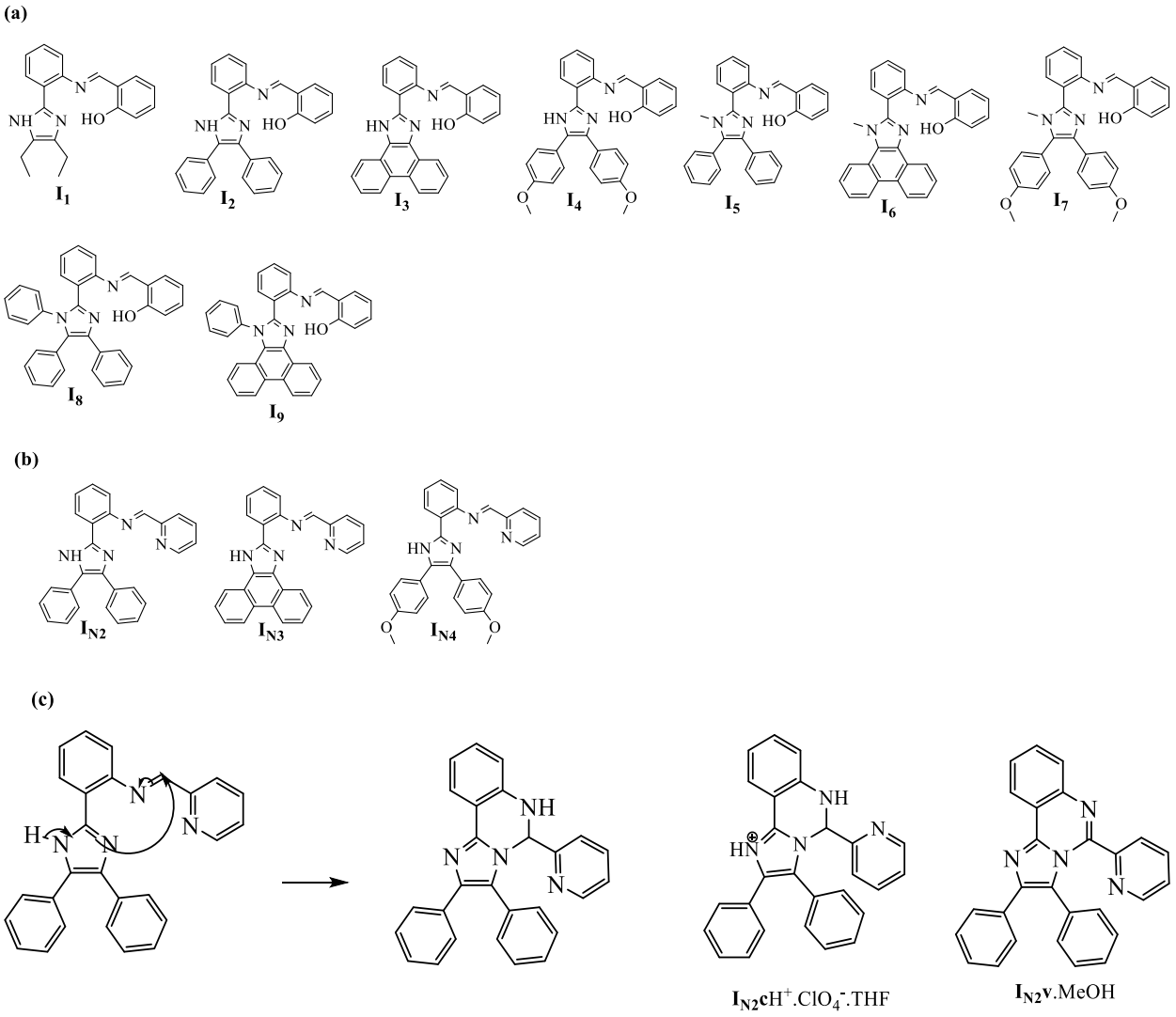

Scheme 3.3: (a) List of prepared NNO imidazole imines (b) List of prepared NNN imidazole imines (c) Proposed mechanism for ring formation in NNN imines series.

3.7.1 Preparation of nitro-imidazoles (N1 – N9)

The nitro-imidazoles (**N1**, **N2**, **N3**, **N4**, **N8**, and **N9**) were prepared using same procedure as the bis-imidazoles (**BI$_1$** – **BI$_7$**), while the methyl derivatives (**N5** – **N7**) were obtained via methylation of the **N-H** variants (**N2** – **N4**). Detailed description (for the **N-H** and **N-Ph** members) is given with **N2** (since **N1** gave a solution after work-up, requiring a different handling, its procedure is also given). A full description (for the **N-Me** variants) is given with **N5**. More so, pure products for **N1** and **N4** were obtained after column chromatography (1:1 EtOAc:hexane).

3.7.1.1: 4,5-diethyl-2-(2-nitrophenyl)-1*H*-imidazole (N1): 3.05 g (20.2 mmol) of 2-nitrobenzaldehyde was weighed and transferred into a round-bottom flask. 7.4 mL (6.96 g, 61.0 mmol) of 3,4-hexanedione and 31.11 g (0.40 moles) ammonium acetate were then added. The mixture obtained, upon adding 50 mL of acetic acid, was refluxed at ≈ 120^{o}C. After cooling, the solution obtained was transferred into ≈ 200 mL of ice-cold water and ammonia solution added until pH > 7. A solution was obtained after work-up, shaken with DCM (3 x 60 mL) and the combined volume reduced under pressure. Column chromatography (1:1 EtOAc:hexane) of the material obtained gave brown products. Yield = 3.74 g (75%). Selected IR (ATR, cm^{-1}): 3082w, 2971w, 2934w, 1594w, 1527s, 1479s, 1452w, 1353s, 1302w, 852s, 782s. ^{1}H NMR (400 MHz, DMSO-d_6) δ (ppm): 1.08 (t, J = 7.5 Hz, 3H, -CH$_3$), 1.18 (t, J = 7.6 Hz, 3H, -CH$_3$), 2.40 (q, J = 7.5 Hz, 2H, -CH$_2$), 2.56 (q, J = 7.5 Hz, 2H, -CH$_2$), 7.44 – 7.56 (m, 1H, Ar-H), 7.69 (td, J = 7.6, 1.2 Hz, 1H, Ar-H), 7.79 (d, J = 8.0 Hz, 2H, Ar-H), 12.12 (s, 1H, -NH). ^{13}C NMR (101 MHz, DMSO-d_6) δ (ppm): 15.23, 15.30, 17.57, 20.07, 124.24, 124.41, 128.80, 129.24, 129.46, 132.19, 138.41, 139.68, 148.39. MS (EI) *m/z* 245 (base peak, M$^+$, Calc. 245.28), 230 (-CH$_3$), 173, 134, 129, 104, 79, 56, 29.

3.7.1.2: 2-(2-nitrophenyl)-4,5-diphenyl-1*H*-imidazole (N2): 6.94 g (46.0 mmol) of 2-nitrobenzaldehyde, 9.67 g (46.0 mmol) of benzil and 53.15 g (0.68 moles) of ammonium acetate were weighed and transferred into a round-bottom flask. The mixture obtained, upon adding 80 mL of acetic acid, was refluxed at ≈ 120^{o}C. The solution obtained, after cooling,

was transferred into ≈ 200 mL of ice-cold water and ammonia solution added until pH > 7. The mixture obtained, after work-up, was filtered and dried in an oven at 70°C to afford a yellow product. Yield = 15.07 g (96%). Selected IR (ATR, cm^{-1}): 3000w, 1586w, 1525s, 1503w, 1482w, 1451w, 1353s, 1304w, 723s, 693s. ^{1}H NMR (400 MHz, DMSO-d_6) δ (ppm): 7.27 (dd, *J* = 23.2, 6.7 Hz, 3H, Ar-H), 7.39 – 7.54 (m, 7H, Ar-H), 7.64 (t, *J* = 7.7 Hz, 1H, Ar-H), 7.79 (t, *J* = 7.6 Hz, 1H, Ar-H), 7.93 (d, *J* = 8.0 Hz, 1H, Ar-H), 8.00 (d, *J* = 7.8 Hz, 1H, Ar-H), 12.97 (s, 1H, -NH). ^{13}C NMR (101 MHz, DMSO-d_6) δ (ppm): 123.88, 124.49, 127.21, 127.46, 128.50, 128.74, 129.23, 130.00, 130.23, 131.10, 132.59, 135.17, 137.99, 141.50, 148.80. MS (EI) *m/z* 341 (base peak, M^+, Calc. 341.36), 264, 165, 134, 104, 89, 79.

3.7.1.3: 2-(2-nitrophenyl)-1*H*-phenanthro[9,10-*d*]imidazole (N3), light brown**:** 2-nitrobenzaldehyde (4.09 g, 27.1 mmol), phenanthrene-9,10-dione (5.64 g, 27.1 mmol) and ammonium acetate (41.72 g, 0.54 moles). Yield = 5.40 g (59%). Selected IR (ATR, cm^{-1}): 3073b, 1617w, 1532s, 1453w, 1364s, 1281w, 1236w, 752s, 734s, 722s. ^{1}H NMR (400 MHz, DMSO-d_6) δ (ppm): 7.60 – 7.81 (m, 5H, Ar-H), 7.93 (t, *J* = 7.4 Hz, 1H, Ar-H), 8.11 (ddd, *J* = 18.2, 7.9, 0.9 Hz, 2H, Ar-H), 8.44 (d, *J* = 6.7 Hz, 2H, Ar-H), 8.88 (dd, *J* = 18.3, 8.2 Hz, 2H, Ar-H), 13.77 (s, 1H, -NH). ^{13}C NMR (101 MHz, DMSO-d_6) δ (ppm): 122.30, 122.38, 122.73, 124.25, 124.67, 124.74, 124.81, 125.87, 126.22, 127.26, 127.76, 128.01, 128.17, 128.38, 130.98, 131.40, 133.09, 137.52, 145.23, 149.33. MS (ESI) *m/z* 339.2 (M^+, Calc. 339.35), 338.2 (M - H, base peak).

3.7.1.4: 4,5-bis(4-methoxyphenyl)-2-(2-nitrophenyl)-1*H*-imidazole (N4), orange**:** 2-nitrobenzaldehyde (6.38 g, 42.2 mmol), anisil (11.41 g, 42.2 mmol) and ammonium acetate (48.81 g, 0.63 moles). Yield = 11.48 g (68%). Selected IR (ATR, cm^{-1}): 3063w, 2840w, 1614s, 1574w, 1518s, 1492s, 1465w, 1358s, 1244s, 1181s, 1108w, 832s, 722s. ^{1}H NMR (400 MHz, DMSO-d_6) δ (ppm): 3.75 (s, 3H, -OCH_3), 3.81 (s, 3H, -OCH_3), 6.88 (d, *J* = 8.5 Hz, 2H, Ar-H), 7.03 (d, *J* = 8.4 Hz, 2H, Ar-H), 7.41 (dd, *J* = 11.2, 8.7 Hz, 4H, Ar-H), 7.61 (td, *J* = 8.0, 1.2 Hz, 1H, Ar-H), 7.77 (td, *J* = 7.7, 1.1 Hz, 1H, Ar-H), 7.90 (dd, *J* = 8.0, 0.9 Hz, 1H, Ar-H), 7.97 (dd, *J* = 7.8, 1.0 Hz, 1H, Ar-H), 12.78 (s, 1H, -NH). ^{13}C NMR (101 MHz, DMSO-d_6) δ (ppm): 55.49, 55.66, 114.16, 114.65, 123.49, 123.93, 124.41, 127.82,

128.19, 128.54, 129.70, 129.99, 130.03, 132.46, 137.36, 140.71, 148.71, 158.54, 159.39. MS (EI) *m/z* 401 (base peak, M^+, Calc. 401.41), 386, 267, 252, 222, 201, 134, 119, 79, 28.

3.7.1.5: 1-methyl-2-(2-nitrophenyl)-4,5-diphenyl-1*H*-imidazole (N5): 7.50 g (54.3 mmol) of K_2CO_3 was added to a yellow mixture of 6.18 g (18.1 mmol) **N2**, in 90 mL acetonitrile and the brown mixture obtained was heated to reflux for ≈ 30 minutes. Upon addition of 1.70 mL (3.88 g, 27.3 mmol) of iodomethane, the yellow mixture obtained was heated overnight. The mixture was cooled, filtered through silica and washed with EtOAc. The solvent volume was reduced under pressure and the solid obtained dried in an oven at 60ºC to afford a yellow product. Yield = 5.02 g (78%). Selected IR (ATR, cm^{-1}): 3061w, 1600w, 1575w, 1522s, 1462w, 1392s, 1341s, 1066w, 1001w, 788s, 745s, 691s. ^{1}H NMR (400MHz, DMSO-d_6) δ (ppm): 3.33 (s, 3H, -CH_3), 7.14 (ddd, *J* = 7.3, 3.6, 1.2 Hz, 1H, Ar-H), 7.34 – 7.40 (m, 2H, Ar-H), 7.18 – 7.25 (m, 2H, Ar-H), 7.46 (dd, *J* = 7.9, 1.6 Hz, 2H, Ar-H), 7.50 – 7.59 (m, 3H, Ar-H), 7.77 – 7.84 (m, 1H, Ar-H), 7.87 – 7.94 (m, 2H, Ar-H), 8.14 – 8.20 (m, 1H, Ar-H). ^{13}C NMR (101 MHz, DMSO-d_6) δ (ppm): 32.58, 125.02, 125.42, 126.49, 126.79, 128.60, 129.41, 129.68, 130.47, 130.77, 131.11, 131.24, 132.74, 133.77, 134.81, 137.14, 142.83, 149.84. MS (EI) *m/z* 355 (base peak, M^+, Calc. 355.39), 307, 178, 165, 118, 104, 77.

3.7.1.6: 1-methyl-2-(2-nitrophenyl)-1*H*-phenanthro[9,10-*d*]imidazole (N6), yellow**: N3** (1.65 g, 4.9 mmol), K_2CO_3 (2.21 g, 14.6 mmol) and iodomethane (0.46 mL, 1.02 g, 7.2 mmol). Yield = 1.72 g (96%). Selected IR (ATR, cm^{-1}): 3062w, 1614w, 1575w, 1531s, 1467s, 1352s, 1158w, 1089w, 854s, 784s, 749s, 724s. ^{1}H NMR (400 MHz, DMSO-d_6) δ (ppm): 4.16 (s, 3H, -CH_3), 7.61 – 7.83 (m, 4H, Ar-H), 7.87 – 8.06 (m, 3H, Ar-H), 8.31 (d, *J* = 8.1 Hz, 1H, Ar-H), 8.48 (dd, *J* = 7.7, 1.6 Hz, 1H, Ar-H), 8.60 – 8.69 (m, 1H, Ar-H), 8.89 (d, *J* = 7.4 Hz, 1H, Ar-H), 9.00 (d, *J* = 7.8 Hz, 1H, Ar-H). ^{13}C NMR (101 MHz, DMSO-d_6) δ (ppm): 35.98, 122.23, 122.66, 123.89, 124.55, 125.37, 125.75, 126.02, 126.30, 126.49, 127.45, 127.54, 128.15, 128.27, 128.35, 129.19, 132.38, 133.92, 134.71, 137.56, 148.44, 150.11. MS (EI) *m/z* 353 (base peak, M^+, Calc. 353.37), 305, 219, 176, 165, 151, 104, 43, 28.

3.7.1.7: 4,5-bis(4-methoxyphenyl)-1-methyl-2-(2-nitrophenyl)-1*H*-imidazole (N7), golden-brown**: N4** (7.07 g, 17.6 mmol), K_2CO_3 (7.30 g, 52.8 mmol) and iodomethane (1.64 mL, 3.74 g, 26.3 mmol). Yield = 6.41 g (88%). Selected IR (ATR, cm^{-1}): 3041w, 1615w, 1578w, 1517s, 1493w, 1353s, 1248s, 1173s, 1028s, 830s, 754w. ^{1}H NMR (400 MHz, DMSO-d_6) δ (ppm): 3.30 (s, 3H, -CH_3), 3.70 (s, 3H, -OCH_3), 3.84 (s, 3H, -OCH_3), 6.76 – 6.86 (m, 2H, Ar-H), 7.11 (dd, *J* = 9.2, 2.3 Hz, 2H, Ar-H), 7.24 – 7.41 (m, 4H, Ar-H), 7.75 – 7.82 (m, 1H, Ar-H), 7.83 – 7.93 (m, 2H, Ar-H), 8.14 (dd, *J* = 8.1, 0.6 Hz, 1H, Ar-H). ^{13}C NMR (101 MHz, DMSO-d_6) δ (ppm): 32.44, 55.42, 55.65, 114.05, 115.08, 122.82, 124.95 125.58, 127.58, 127.60, 129.28, 131.03, 132.48, 132.65, 133.65, 136.97, 142.24, 149.85, 158.25, 159.92. MS (EI) *m/z* 415 (M^+, Calc. 415.44), 398, 353, 223, 208, 148 (base peak), 133, 104, 76.

3.7.1.8: 2-(2-nitrophenyl)-1,4,5-triphenyl-1*H*-imidazole (N8), golden-brown**:** 2-nitrobenzaldehyde (6.86 g, 45.4 mmol), benzil (9.55 g, 45.4 mmol), aniline (4.14 mL, 4.22 g, 45.4 mmol) and ammonium acetate (52.50 g, 0.68 moles). Yield = 17.88 g (94%). Selected IR (ATR, cm^{-1}): 3065w, 1597w, 1514s, 1495s, 1346s, 1148w, 1071w, 747s, 693s. ^{1}H NMR (400 MHz, DMSO-d_6) δ (ppm): 7.14 (dd, *J* = 6.7, 3.0 Hz, 2H, Ar-H), 7.20 (d, *J* = 7.2 Hz, 1H, Ar-H), 7.22 – 7.28 (m, 7H, Ar-H), 7.31 – 7.36 (m, 3H, Ar-H), 7.42 – 7.47 (m, 2H, Ar-H), 7.58 – 7.72 (m, 3H, Ar-H), 7.99 (dd, *J* = 8.0, 1.1 Hz, 1H, Ar-H). ^{13}C NMR (101 MHz, DMSO-d_6) δ (ppm): 124.73, 125.65, 126.81, 127.11, 128.61, 128.69, 129.02, 129.08, 129.12, 129.48, 130.44, 131.05, 131.34, 133.19, 133.49, 134.51, 135.73, 137.66, 143.07, 149.55. MS (ESI) *m/z* 418.4 (M + H, Calc. 417.47), 317.4, 215.2.

3.7.1.9: 2-(2-nitrophenyl)-1-phenyl-1*H*-phenanthro[9,10-*d*]imidazole (N9), golden-brown**:** 2-nitrobenzaldehyde (6.25 g, 41.36 mmol), phenanthrene-9,10-dione (8.62 g, 41.40 mmol), aniline (3.78 mL, 3.85 g, 41.41 mmol) and ammonium acetate (47.82 g, 0.62 moles). Yield = 14.60 g (85%). Selected IR (ATR, cm^{-1}): 3000w, 1613w, 1597w, 1526s, 1494w, 1367s, 1157w, 1038w, 752s, 708s. ^{1}H NMR (400 MHz, DMSO-d_6) δ (ppm): 7.14 (d, *J* = 7.9 Hz, 1H), 7.39 (t, *J* = 7.6 Hz, 1H, Ar-H), 7.57 – 7.63 (m, 6H, Ar-H), 7.77 (ddt, *J* = 15.4, 13.5, 6.5 Hz, 5H, Ar-H), 8.11 (d, *J* = 8.0 Hz, 1H, Ar-H), 8.53 – 8.60 (m, 1H, Ar-H), 8.91 (d, *J* = 8.2 Hz, 1H, Ar-H), 8.97 (d, *J* = 8.4 Hz, 1H, Ar-H). ^{13}C NMR (101 MHz, DMSO-d_6)

δ (ppm): 120.67, 122.44, 125.05, 127.27, 128.15, 128.99, 130.58, 131.69, 133.77, 137.23, 149.41. MS (ESI) *m/z* 416.3 (M + H, Calc. 415.45), 317.2 (base peak), 215.1.

3.7.2 Preparation of imidazole amines (A1 – A9)

A general approach was adopted in the synthesis of **A1 – A9** (a full description is given with **A1**).

3.7.2.1: 2-(4,5-diethyl-1*H*-imidazol-2-yl)aniline (A1): 3.74 g (15.3 mmol) of **N1** was weighed and transferred into a hydrogenation tube. Catalytic amount of 10%Pd/C was added followed by ≈ 50 mL of THF to obtain a mixture. The reduction was carried out using 80 bars of hydrogen at ≈ 80°C for ≈ 2 hours. The mixture obtained was filtered through a pad of celite and washed with THF. The solvent volume was reduced under pressure and the solid obtained was filtered, washed with hexane and dried (in oven at 70°C) to afford a brown product. Yield = 2.83 g (86%). Selected IR (ATR, cm^{-1}): 3460w, 3368w, 2965s, 2870w, 1616s, 1604s, 1531s, 1461s, 742s, 653w. UV-Vis (MeCN, nm {ε /M^{-1} cm^{-1}}): 231 {7 942}, 249 {10 023}, 278 {7 426}, 336 {7 381}. ^{1}H NMR (400 MHz, DMSO-d_6) δ (ppm): 1.16 (q, *J* = 7.6 Hz, 6H, -CH_3), 2.41 – 2.48 (m, 2H, -CH_2), 2.53 – 2.62 (m, 2H, -CH_2), 6.47 – 6.59 (m, 1H, Ar-H), 6.69 (dd, *J* = 8.1, 0.8 Hz, 1H, Ar-H), 6.86 (s, 2H, -NH_2), 6.93 – 7.02 (m, 1H, Ar-H), 7.58 (dd, *J* = 7.8, 1.2 Hz, 1H, Ar-H), 11.66 (s, 1H, -NH). ^{13}C NMR (101 MHz, DMSO-d_6) δ (ppm): 15.31, 15.58, 17.48, 20.07, 112.58, 115.19, 115.95, 125.73, 126.73, 128.33, 136.72, 144.50, 146.61. MS (EI) *m/z* 215 (base peak, M^+, Calc. 215.29), 200 (-CH_3), 159, 119, 65, 28.

3.7.2.2: 2-(4,5-diphenyl-1*H*-imidazol-2-yl)aniline (A2), off-white**: N2** (4.28 g, 12.5 mmol). Yield = 3.72 g (67%). Selected IR (ATR, cm^{-1}): 3463w, 3360w, 3056b, 1617s, 1601s, 1534s, 1459w, 765s, 743s, 695s. UV-Vis (MeCN, nm {ε /M^{-1} cm^{-1}}): 225 {34 584}, 294 {17 321}, 340 {17 761}. ^{1}H NMR (400 MHz, DMSO-d_6) δ (ppm): 6.60 (t, *J* = 7.5 Hz, 1H, Ar-H), 6.80 (d, J = 8.2 Hz, 1H, Ar-H), 6.98 (s, 2H, -NH_2), 7.07 (dd, *J* = 11.2, 4.1 Hz, 1H, Ar-H), 7.23 (t, *J* = 7.3 Hz, 1H, Ar-H), 7.32 (t, *J* = 7.5 Hz, 2H, Ar-H), 7.39 (t, *J* = 7.2 Hz, 1H, Ar-H), 7.45 (t, *J* = 7.4 Hz, 2H, Ar-H), 7.54 (t, *J* = 7.3 Hz, 4H, Ar-H), 7.84 (d, *J* = 7.9 Hz, 1H, Ar-H), 12.46 (s, 1H, -NH). ^{13}C NMR (101 MHz, DMSO-d_6) δ (ppm): 111.46,

115.37, 116.22, 126.79, 126.96, 127.15, 127.26, 128.76, 129.10, 129.15, 129.39, 131.46, 135.42, 135.73, 147.10, 147.23. MS (EI) *m/z* 311 (base peak, M^+, Calc. 311.38), 207, 165.

3.7.2.3: 2-(1*H*-phenanthro[9,10-*d*]imidazol-2-yl)aniline (A3), ash**: N3** (2.88 g, 8.5 mmol). Yield = 2.24 g (85%). Selected IR (ATR, cm^{-1}): 3369w, 3207w, 1614s, 1513s, 1486s, 1427s, 750s, 721s, 661w. UV-Vis (MeCN, nm {ε /M^{-1} cm^{-1}}): 231 {62 142}, 248 {54 955}, 262 {49 258}, 307 {15 145}, 356 {21 081}, 373 {20 274}. ^{1}H NMR (400 MHz, DMSO-d_6) δ (ppm): 6.74 (t, *J* = 7.3 Hz, 1H, Ar-H), 6.92 (d, *J* = 7.9 Hz, 1H, Ar-H), 7.15 – 7.22 (m, 1H, Ar-H), 7.33 (s, 2H, -NH_2), 7.59 – 7.68 (m, 2H, Ar-H), 7.75 (dd, *J* = 16.1, 8.0 Hz, 2H, Ar-H), 8.08 (d, *J* = 7.1 Hz, 1H, Ar-H), 8.61 (dd, *J* = 21.7, 7.9 Hz, 2H, Ar-H), 8.86 (dd, *J* = 12.5, 8.5 Hz, 2H, Ar-H), 13.21 (s, 1H, -NH). ^{13}C NMR (101 MHz, DMSO-d_6) δ (ppm): 111.16, 115.44, 116.63, 122.27, 122.65, 124.19, 124.52, 125.48, 125.70, 126.55, 126.98, 127.49, 127.57, 127.62, 127.84, 128.06, 130.35, 136.27, 148.15, 150.80. MS (ESI) *m/z* 310.3 (M + H, Calc. 309.36).

3.7.2.4: 2-(4,5-bis(4-methoxyphenyl)-1*H*-imidazol-2-yl)aniline (A4), ash**: N4** (12.36 g, 30.8 mmol). Yield = 10.08 g (88%). Selected IR (ATR, cm^{-1}): 3465w, 3355w, 2953w, 1615s, 1516s, 1495s, 1460w, 833s, 796w, 745s. UV-Vis (MeCN, nm {ε /M^{-1} cm^{-1}}): 236 {32 662}, 289 {19 228}, 343 {16 691}. ^{1}H NMR (400MHz, DMSO-d_6) δ (ppm): 3.75 (s, 3H, -OCH_3), 3.81 (s, 3H, -OCH_3), 6.50 – 6.63 (m, 1H, Ar-H), 6.78 (dd, *J* = 8.1, 0.8 Hz, 1H, Ar-H), 6.89 (d, *J* = 8.8 Hz, 2H, Ar-H), 6.97 (s, 2H, -NH_2), 6.99 – 7.09 (m, 3H, Ar-H), 7.44 (dd, *J* = 10.3, 8.8 Hz, 4H, Ar-H), 7.81 (dd, *J* = 7.9, 1.2 Hz, 1H, Ar-H), 12.28 (s, 1H, -NH). ^{13}C NMR (101 MHz, DMSO-d_6) δ (ppm): 55.49, 55.65, 111.71, 114.21, 114.54, 115.34, 116.16, 123.88, 126.02, 126.63, 128.14, 128.36, 129.14, 130.39, 135.05, 146.43, 147.11, 158.36, 159.26. MS (EI) *m/z* 371 (base peak, M^+, Calc. 371.43), 356 ([M – NH_2]$^+$, Calc. 355.41), 186, 167, 134, 104, 77, 28.

3.7.2.5: 2-(1-methyl-4,5-diphenyl-1*H*-imidazol-2-yl)aniline (A5), ash: **N5** (2.32 g, 6.5 mmol). Yield = 1.97 g (93%). Selected IR (ATR, cm^{-1}): 3438s, 3350w, 1614s, 1599s, 1487s, 1440w, 771s, 759s, 697s. UV-Vis (MeCN, nm {ε /M^{-1} cm^{-1}}): 283 {16 928}. ^{1}H NMR (400 MHz, DMSO-d_6) δ (ppm): 3.38 (s, 3H, -CH_3), 5.87 (s, 2H, -NH_2), 6.67 (t, *J* = 7.4 Hz, 1H,

Ar-H), 6.86 (d, *J* = 8.0 Hz, 1H, Ar-H), 7.11 – 7.19 (m, 2H, Ar-H), 7.23 (t, *J* = 7.5 Hz, 2H, Ar-H), 7.34 (dd, *J* = 7.7, 1.2 Hz, 1H, Ar-H), 7.41 – 7.46 (m, 2H, Ar-H), 7.53 (ddd, *J* = 18.3, 9.6, 4.7 Hz, 5H, Ar-H). ^{13}C NMR (101 MHz, DMSO-d_6) δ (ppm): 33.48, 113.58, 115.85, 116.01, 126.60, 128.58, 129.10, 129.52, 129.97, 130.05, 130.35, 131.17, 131.39, 135.21, 136.03, 146.26, 147.96. MS (EI) *m/z* 325 (base peak, M^+, Calc. 325.41), 309 ($[M - NH_2]^+$, Calc. 309.39), 165, 118, 103, 89, 77, 28.

3.7.2.6: 2-(1-methyl-1*H*-phenanthro[9,10-*d*]imidazol-2-yl)aniline (A6), ash**: N6** (1.65 g, 4.7 mmol). Yield = 1.29 g (85%). Selected IR (ATR, cm^{-1}): 3429b, 3319w, 1615s, 1506w, 1485w, 1459w, 745s, 720s, 694w. UV-Vis (MeCN, nm {ε /M^{-1} cm^{-1}}): 258 {56 696}, 284 {15 197}, 308 {12 562}, 358 {7 309}. ^{1}H NMR (400 MHz, DMSO-d_6) δ (ppm): 4.19 (s, 3H, -CH_3), 5.78 (s, 2H, -NH_2), 6.75 (t, *J* = 7.4 Hz, 1H, Ar-H), 6.92 (d, *J* = 8.2 Hz, 1H, Ar-H), 7.25 (t, *J* = 7.7 Hz, 1H, Ar-H), 7.39 (d, *J* = 7.6 Hz, 1H, Ar-H), 7.61 – 7.82 (m, 4H, Ar-H), 8.60 (t, *J* = 8.1 Hz, 2H, Ar-H), 8.86 (d, *J* = 8.3 Hz, 1H, Ar-H), 8.97 (d, *J* = 8.3 Hz, 1H, Ar-H). ^{13}C NMR (101 MHz, DMSO-d_6) δ (ppm): 36.21, 113.23, 116.04, 116.07, 121.83, 122.28, 123.71, 124.05, 124.85, 125.41, 125.78, 127.15, 127.20, 127.50, 127.70, 127.85, 128.51, 130.83, 131.46, 136.73, 148.40, 151.44. MS (EI) *m/z* 323 (M^+, Calc. 323.39), 307 ($[M - NH_2]^+$, Calc. 307.38), 231, 204, 190, 176, 162.

3.7.2.7: 2-(4,5-bis(4-methoxyphenyl)-1-methyl-1*H*-imidazol-2-yl)aniline (A7), off-white**: N7** (6.12 g, 14.7 mmol). Yield = 4.52 g (80%). Selected IR (ATR, cm^{-1}): 3428w, 1617s, 1517s, 1490s, 1249s, 832s, 744s, 680w. UV-Vis (MeCN, nm {ε /M^{-1} cm^{-1}}): 240 {15 274}, 284 {10 371}. ^{1}H NMR (400 MHz, DMSO-d_6) δ (ppm): 3.35 (s, 3H, -CH_3), 3.71 (s, 3H, -OCH_3), 3.84 (s, 3H, -OCH_3), 5.86 (s, 2H, -NH_2), 6.66 (dd, *J* = 11.4, 4.3 Hz, 1H, Ar-H), 6.83 (t, *J* = 8.5 Hz, 3H, Ar-H), 7.05 – 7.18 (m, 3H, Ar-H), 7.31 (dd, *J* = 7.7, 1.3 Hz, 1H, Ar-H), 7.35 – 7.42 (m, 4H, Ar-H). ^{13}C NMR (101 MHz, DMSO-d_6) δ (ppm): 33.35, 55.42, 55.63, 113.79, 114.06, 114.95, 115.82, 115.97, 123.44, 127.66, 127.96, 129.86, 130.20, 132.53, 135.75, 145.68, 147.89, 158.11, 159.74. MS (EI) *m/z* 385 (base peak, M^+, Calc. 385.45), 369 ($[M - NH_2]^+$, Calc. 369.44), 311, 193, 165, 148, 133, 113, 106, 77.

3.7.2.8: 2-(1,4,5-triphenyl-1*H*-imidazol-2-yl)aniline (A8), off-white**: N8** (6.54 g, 39.6 mmol). Yield = 10.71 g (70%). Selected IR (ATR, cm^{-1}): 3478w, 3284w, 1613s, 1596s, 1486s, 1443w, 747w, 693s. UV-Vis (MeCN, nm {ε /M^{-1} cm^{-1}}): 278 {14 050}. ^{1}H NMR (400 MHz, DMSO-d_6) δ (ppm): 6.11 (s, 2H, -NH_2), 6.20 – 6.26 (m, 1H, Ar-H), 6.63 (dd, *J* = 7.8, 1.3 Hz, 1H, Ar-H), 6.76 (d, *J* = 7.6 Hz, 1H, Ar-H), 6.91 – 6.99 (m, 1H, Ar-H), 7.14 – 7.21 (m, 3H, Ar-H), 7.22 – 7.34 (m, 10H, Ar-H), 7.46 – 7.50 (m, 2H, Ar-H). ^{13}C NMR (101 MHz, DMSO-d_6) δ (ppm): 112.90, 115.17, 115.99, 126.71, 126.89, 128.68, 128.83, 128.90, 129.07, 129.40, 129.58, 129.95, 130.50, 130.98, 131.66, 134.79, 136.20, 137.30, 145.67, 148.23. MS (EI) *m/z* 387 (base peak, M^+, Calc. 387.48), 371 ($[M - NH_2]^+$, Calc. 371.46), 310, 283, 267, 193, 180, 165, 77.

3.7.2.9: 2-(1-phenyl-1*H*-phenanthro[9,10-*d*]imidazol-2-yl)aniline (A9), off-white**: N9** (4.16 g, 10.0 mmol). Yield = 3.17 g (82%). Selected IR (ATR, cm^{-1}): 3445w, 3308w, 1612s, 1489s, 1452s, 1383s, 772s, 723s, 698s. UV-Vis (MeCN, nm {ε /M^{-1} cm^{-1}}): 257 {75 059}, 307 {25 250}. ^{1}H NMR (400 MHz, DMSO-d_6) δ (ppm): 5.93 (s, 2H, -NH_2), 6.28 – 6.39 (m, 1H, Ar-H), 6.77 (d, *J* = 7.7 Hz, 1H, Ar-H), 6.96 (dd, *J* = 7.8, 1.3 Hz, 1H, Ar-H), 6.99 – 7.05 (m, 1H, Ar-H), 7.09 (d, *J* = 7.8 Hz, 1H, Ar-H), 7.33 (t, *J* = 7.4 Hz, 1H, Ar-H), 7.51 – 7.58 (m, 1H, Ar-H), 7.60 – 7.71 (m, 6H, Ar-H), 7.78 (t, *J* = 7.2 Hz, 1H, Ar-H), 8.67 (dd, *J* = 7.9, 1.0 Hz, 1H, Ar-H), 8.88 (d, *J* = 8.3 Hz, 1H, Ar-H), 8.93 (d, *J* = 8.3 Hz, 1H, Ar-H). ^{13}C NMR (400MHz, DMSO-d_6) δ (ppm): 113.18, 115.19, 115.87, 120.75, 122.47, 122.96, 124.10, 124.92, 125.51, 126.08, 127.03, 127.06, 127.36, 127.89, 128.03, 128.81, 129.49, 130.29, 130.43, 130.75, 136.48, 138.73, 148.69, 150.40. MS (ESI) *m/z* 386.3 (M + H, Calc. 385.46), 355.4.

3.7.3 Preparation of imidazole imines (I_1 – I_9) and (I_{N2} – I_{N4})

The imidazole imines (NNO as well as NNN series) were prepared using similar procedure. Description of the procedure is made with **I_1** (for the NNO series) and **I_{N2}** (for the NNN series). **I_{N2}c.**H^+, **I_{N2}v.**MeOH and **I_{N2}v** {**Scheme 3.3**(**c**)} were obtained from a failed attempt to prepare the complexes of **I_{N2}**.

3.7.3.1: (*E*)-2-(((2-(4,5-diethyl-1*H*-imidazol-2-yl)phenyl)imino)methyl)phenol (I_1): 0.20 mL (0.2292 g, 1.9 mmol) of salicylaldehyde was added to a 20 mL hot MeOH solution of 0.4033 g (1.9 mmol) of **A1**. The set up was heated at 70^{o}C for ≈ 4hrs and the mixture obtained was filtered, washed with MeOH and dried to afford a white product**.** Yield = 0.4874 g (81%). Selected FTIR (ATR, cm^{-1}): 3383s, 2956w, 2697w, 2572w, 1616w, 1588s, 1493s, 1462s, 1434w, 1240s, 1203w, 1092s, 1049s, 748s, 709s, 637w. UV-Vis (MeCN, nm {ε /M^{-1} cm^{-1}}): 256 {3 601}, 280 {3 259}, 334 {3 608}. ^{1}H NMR (400 MHz, DMSO-d_6) δ (ppm): 0.85 (t, *J* = 7.5 Hz, 3H, -CH_3), 1.17 (t, *J* = 7.5 Hz, 3H, -CH_3), 6.14 (d, *J* = 6.7 Hz, 1H, Ar-H), 6.56 (t, *J* = 7.4 Hz, 1H, Ar-H), 6.68 (dd, *J* = 14.0, 6.3 Hz, 2H, Ar-H), 6.73 – 6.80 (m, 2H, Ar-H), 6.87 (d, *J* = 7.9 Hz, 1H, Ar-H), 6.98 (t, *J* = 7.1 Hz, 1H, Ar-H), 7.06 (t, *J* = 7.1 Hz, 1H, Ar-H), 7.64 (d, *J* = 7.0 Hz, 1H, Ar-H), 10.10 (s, 1H, -OH). ^{13}C NMR (101 MHz, DMSO-d_6) δ (ppm): 16.01, 20.44, 62.50, 114.58, 115.27, 115.92, 118.46, 119.37, 122.40, 125.90, 127.80, 129.06, 129.80, 140.32, 140.78, 153.77. MS (EI) *m/z* 319 (M^+, Calc. 319.40), 302 (-OH), 226 (loss of -PhOH), 200 (loss of -N=CHPhOH), 185 (base peak), 160, 129, 65. Anal. Calc.(Found) for $C_{20}H_{21}N_3O$: C, 75.21 (74.46); H, 6.63 (6.74); N, 13.16 (13.17) %.

3.7.3.2: (*E*)-2-(((2-(4,5-diphenyl-1*H*-imidazol-2-yl)phenyl)imino)methyl)phenol (I_2), ash**:** 1.37 mL (1.57 g, 12.9 mmol) of salicylaldehyde and 4.00 g (12.9 mmol) of **A2**. Yield = 4.82 g (90%). Selected IR (ATR, cm^{-1}): 3387s, 3045w, 1616w, 1603s, 1588w, 1538w, 1490w, 1480w, 1463w, 1343w, 1295w, 1277w, 1242s, 1013s, 750s, 735w, 691s. UV-Vis (MeCN, nm {ε /M^{-1} cm^{-1}}): 253 {15 437}, 282 {13 955}, 334 {10 637}. ^{1}H NMR (400 MHz, DMSO-d_6) δ (ppm): 6.23 (dd, *J* = 7.6, 1.3 Hz, 1H, Ar-H), 6.53 (d, *J* = 1.8 Hz, 1H, Ar-H), 6.59 (t, *J* = 7.5 Hz, 1H, Ar-H), 6.80 (ddd, *J* = 16.1, 15.2, 7.7 Hz, 4H, Ar-H), 7.01 – 7.20 (m, 5H, Ar-H), 7.24 (t, *J* = 7.4 Hz, 2H, Ar-H), 7.34 – 7.43 (m, 3H, Ar-H), 7.46 – 7.54 (m, 2H, Ar-H), 7.88 (dd, *J* = 7.6, 1.1 Hz, 1H, Ar-H), 9.92 (s, 1H, -N=CH). ^{13}C NMR (101 MHz, DMSO-d_6) δ (ppm): 63.64, 114.03, 115.76, 115.82, 118.84, 119.21, 123.21, 125.54, 126.66, 126.74, 126.90, 127.05, 128.61, 129.23, 129.39, 129.89, 130.10, 130.65, 134.87, 138.32, 141.57, 142.57. MS (EI) *m/z* 415 (M^+, Calc. 415.49), 322 (loss of -PhOH), 311, 296 (base peak, loss of -N=CHPhOH), 208, 165, 89, 28. Anal. Calc.(Found) for $C_{28}H_{21}N_3O$: C, 80.94 (80.91); H, 5.09 (5.08); N, 10.11 (10.14) %.

3.7.3.3: (*E*)-2-(((2-(1*H*-phenanthro[9,10-*d*]imidazol-2-yl)phenyl)imino)methyl)phenol (I$_3$), white**:** 0.33 mL (0.38 g, 3.1 mmol) of salicylaldehyde and 1.01 g (3.1 mmol) of **A3**. Yield = 1.00 g (75%). Selected FTIR (ATR, cm^{-1}): 3375w, 3053w, 1610s, 1591w, 1538s, 1513w, 1484w, 1473s, 1453w, 1430s, 1400s, 1362w, 1323w, 1295s, 1154s, 1103s, 1047w, 744s, 718s. UV-Vis (MeCN, nm {ε /M^{-1} cm^{-1}}): 255 {21 372}, 310 {6 307}, 358 {5 695}, 374 {6 082}. ^{1}H NMR (400 MHz, DMSO-d_6) δ (ppm): 6.20 (dd, *J* = 7.7, 1.5 Hz, 1H, Ar-H), 6.39 – 6.48 (m, 1H, Ar-H), 6.84 – 6.94 (m, 2H, Ar-H), 6.98 (dd, *J* = 8.1, 1.1 Hz, 1H, Ar-H), 7.01 – 7.08 (m, 1H, Ar-H), 7.16 – 7.26 (m, 2H, Ar-H), 7.52 – 7.60 (m, 2H, Ar-H), 7.67 (ddd, *J* = 8.4, 7.1, 1.5 Hz, 1H, Ar-H), 7.74 – 7.81 (m, 1H, Ar-H), 7.92 (d, *J* = 1.9 Hz, 1H, Ar-H), 8.05 – 8.13 (m, 2H, Ar-H), 8.70 (dd, *J* = 8.0, 1.2 Hz, 1H, Ar-H), 8.84 (d, *J* = 8.4 Hz, 1H, Ar-H), 8.90 (dd, *J* = 6.3, 3.4 Hz, 1H, Ar-H), 10.52 (s, 1H, -OH). ^{13}C NMR (101 MHz, DMSO-d_6) δ (ppm): 64.77, 113.47, 115.73, 116.25, 118.89, 119.65, 121.21, 122.63, 122.85, 124.08, 124.37, 124.48, 124.91, 125.42, 125.55, 126.19, 126.65, 127.00, 127.54, 127.84, 128.06, 128.47, 130.22, 131.30, 138.49, 141.81, 146.45, 153.86. MS (EI) *m/z* 413 (M$^+$, Calc. 413.47), 369, 320 (loss of -PhOH), 294 (base peak, loss of -N=CHPhOH), 207, 190, 45, 31. Anal Calc.(Found) for $C_{28}H_{19}N_3O$: C, 81.34 (80.31); H, 4.63 (4.79); N, 10.16 (10.01) %.

3.7.3.4: (*E*)-2-(((2-(4,5-bis(4-methoxyphenyl)-1*H*-imidazol-2-yl)phenyl)imino)methyl)phenol (I$_4$), white**:** 1.15 mL (1.32 g, 10.80 mmol) of salicylaldehyde and 4.01 g (10.80 mmol) of **A4**. Yield = 4.57 g (89%). Selected FTIR (ATR, cm^{-1}): 3371s, 3027w, 1612s, 1588w, 1489s, 1460s, 1439w, 1238s, 1176s, 1107s, 1059w, 1030s, 748s, 709w, 637w. UV-Vis (MeCN, nm {ε /M^{-1} cm^{-1}}): 283 {23 650}, 339 {16 634}. ^{1}H NMR (400 MHz, DMSO-d_6) δ (ppm): 3.72 (s, 3H, -OCH$_3$), 3.77 (s, 3H, -OCH$_3$), 6.20 (dd, *J* = 7.6, 1.2 Hz, 1H, Ar-H), 6.48 (d, *J* = 2.2 Hz, 1H, Ar-H), 6.59 (t, *J* = 7.4 Hz, 1H, Ar-H), 6.71 (d, *J* = 2.1 Hz, 1H, Ar-H), 6.73 – 6.86 (m, 5H, Ar-H), 6.92 (d, *J* = 8.8 Hz, 2H, Ar-H), 7.05 (ddd, *J* = 14.9, 10.7, 5.0 Hz, 4H, Ar-H), 7.38 – 7.49 (m, 2H, Ar-H), 7.84 (dd, *J* = 7.6, 1.0 Hz, 1H, Ar-H), 9.90 (s, 1H, -N=CH). ^{13}C NMR (101 MHz, DMSO-d_6) δ (ppm): 55.45, 55.55, 63.53, 114.06, 114.26, 114.81, 115.71, 115.82, 118.80, 119.20, 122.13, 123.05, 125.39, 125.59, 127.22, 127.66, 127.85, 129.81, 132.05, 138.16, 141.48, 142.06,

153.73, 158.35, 159.73, 206.93. MS (ESI) *m/z* 476.3 ($M + H^+$, Calc. 475.54). Anal. Calc.(Found) for $C_{30}H_{25}N_3O_3$: C, 75.77 (75.77); H, 5.30 (5.18); N, 8.84 (9.14) %.

3.7.3.5: (*E*)-2-(((2-(1-methyl-4,5-diphenyl-1*H*-imidazol-2-yl)phenyl)imino)methyl)phenol (I_5), white**:** 0.33 mL (0.38 g, 3.1 mmol) of salicylaldehyde and 1.01 g (3.1 mmol) of **A5**. Yield = 1.00 g (75%). Selected FTIR (ATR, cm^{-1}): 3059w, 1616s, 1569w, 1526w, 1503w, 1478w, 1441w, 1278s, 1228w, 1184s, 1154s, 1072w, 1030w, 763s, 696s, 634w. UV-Vis (MeCN, nm {ε /M^{-1} cm^{-1}}): 238 {16 448}, 274 {29 052}, 340 {10 875}. ^{1}H NMR (400 MHz, DMSO-d_6) δ (ppm): 3.15 (s, 3H, -CH_3), 6.98 (dd, *J* = 15.2, 7.8 Hz, 2H, Ar-H), 7.09 – 7.15 (m, 1H, Ar-H), 7.20 (t, *J* = 7.5 Hz, 2H, Ar-H), 7.40 – 7.57 (m, 9H, Ar-H), 7.63 – 7.73 (m, 4H, Ar-H), 9.09 (s, 1H, -N=CH), 12.67 (s, 1H, -OH). ^{13}C NMR (101 MHz, DMSO-d_6) δ (ppm): 32.56, 117.17, 118.77, 119.68, 119.76, 126.47, 126.51, 127.11, 127.64, 128.51, 129.22, 129.61, 130.13, 131.06, 131.25, 131.44, 132.03, 133.32, 134.10, 135.27, 136.72, 145.84, 147.33, 160.77, 164.45. MS (ESI) *m/z* 430.4 (M^+, Calc. 429.51). Anal. Calc.(Found) for $C_{29}H_{23}N_3O$: C, 81.09 (80.64); H, 5.40 (5.37); N, 9.78 (9.76) %.

3.7.3.6: (*E*)-2-(((2-(1-methyl-1*H*-phenanthro[9,10-*d*]imidazol-2-yl)phenyl)imino)methyl)phenol (I_6), brown**:** 0.35 mL (0.40 g, 3.3 mmol) of salicylaldehyde and 1.04 g (3.2 mmol) of **A6**. Yield = 1.07 g (78%). Selected FTIR (ATR, cm^{-1}): 3062w, 1613s, 1578w, 1564w, 1535w, 1448s, 1377w, 1332w, 1278s, 1181s, 1112w, 1091w, 1062w, 1038w, 750s, 725s. UV-Vis (MeCN, nm {ε /M^{-1} cm^{-1}}): 257 {70 159}, 282 {26 699}, 341 {11 242}, 356 {10 271}. ^{1}H NMR (400 MHz, DMSO-d_6) δ (ppm): 4.04 (s, 3H, -CH_3), 6.67 (d, *J* = 8.2 Hz, 1H, Ar-H), 6.88 – 6.95 (m, 1H, Ar-H), 7.23 – 7.33 (m, 1H, Ar-H), 7.53 – 7.60 (m, 1H, Ar-H), 7.69 (dddd, *J* = 14.1, 12.9, 6.9, 2.0 Hz, 8H, Ar-H), 8.52 – 8.60 (m, 2H, Ar-H), 8.88 (d, *J* = 8.2 Hz, 1H, Ar-H), 8.99 (d, *J* = 7.6 Hz, 1H, Ar-H), 9.13 (s, 1H, -N=CH), 12.37 (s, 1H, -OH). ^{13}C NMR (101 MHz, DMSO-d_6) δ (ppm): 35.56, 117.00, 118.91, 119.64, 121.67, 122.35, 123.65, 124.05, 124.89, 125.58, 125.88, 126.62, 126.88, 127.38, 127.66, 127.70, 127.75, 127.89, 128.64, 131.84, 132.47, 133.28, 134.06, 137.11, 147.82, 150.73, 160.54, 164.79. MS (EI) *m/z* 427 (M^+, Calc. 427.50), 307 (base

peak, loss of -N=CHPhOH), 260, 229, 214, 190, 153, 28. Anal. Calc.(Found) for $C_{29}H_{21}N_3O$: C, 81.48 (80.98); H, 4.95 (4.96); N, 9.83 (9.73) %.

3.7.3.7: (*E*)-2-(((2-(4,5-bis(4-methoxyphenyl)-1-methyl-1*H*-imidazol-2-yl)phenyl)imino)methyl)phenol (I_7), orange**:** 0.58 mL (0.66 g, 5.4 mmol) of salicylaldehyde and 2.08 g (5.4 mmol) of **A7**. Yield = 1.58 g (60%). Selected FTIR (ATR, cm^{-1}): 3046w, 1614s, 1564w, 1519s, 1492s, 1460s, 1389w, 1279s, 1247s, 1176s, 1110w, 1032s, 833s, 752s, 690w. UV-Vis (MeCN, nm {ε /M^{-1} cm^{-1}}): 232 {35 453}, 276 {34 582}, 338 {10 392}. ^{1}H NMR (400 MHz, DMSO-d_6) δ (ppm): 3.11 (s, 3H, -CH_3), 3.70 (s, 3H, -OCH_3), 3.83 (s, 3H, -OCH_3), 6.80 (d, *J* = 8.8 Hz, 2H, Ar-H), 6.98 (dd, *J* = 15.9, 8.0 Hz, 2H, Ar-H), 7.09 (d, *J* = 8.7 Hz, 2H, Ar-H), 7.34 – 7.52 (m, 6H, Ar-H), 7.60 – 7.74 (m, 4H, Ar-H), 9.09 (s, 1H, -N=CH), 12.69 (s, 1H, -OH). ^{13}C NMR (101 MHz, DMSO-d_6) δ (ppm): 32.46, 55.41, 55.62, 113.98, 115.04, 117.17, 118.74, 119.67, 119.75, 123.47, 127.33, 127.55, 127.62, 128.06, 128.88, 131.09, 132.01, 132.41, 133.33, 134.07, 136.53, 145.30, 147.21, 158.07, 159.81, 160.75, 164.38. MS (ESI) *m/z* 490.4 (M^+, Calc. 489.56). Anal. Calc.(Found) for $C_{31}H_{27}N_3O_3$: C, 76.05 (75.35); H, 5.96 (5.51); N, 8.58 (8.63) %.

3.7.3.8: (*E*)-2-(((2-(1,4,5-triphenyl-1*H*-imidazol-2-yl)phenyl)imino)methyl)phenol (I_8), yellow**:** 1.15 mL (1.32 g, 10.79 mmol) of salicylaldehyde and 4.16 g (10.74 mmol) of **A8**. Yield = 3.79 g (72%). Selected FTIR (ATR, cm^{-1}): 3059w, 1617s, 1599w, 1570s, 1495s, 1479w, 1393s, 1373w, 1274s, 1227w, 1187s, 1103s, 1030s, 754s, 692s. UV-Vis (MeCN, nm {ε /M^{-1} cm^{-1}}): 274 {34 018}, 339 {10 585}. ^{1}H NMR (400 MHz, DMSO-d_6) δ (ppm): 6.86 – 6.90 (m, 2H, Ar-H), 6.96 (ddd, *J* = 9.8, 8.3, 5.9 Hz, 4H, Ar-H), 7.08 (t, *J* = 7.4 Hz, 1H, Ar-H), 7.17 – 7.20 (m, 1H, Ar-H), 7.21 – 7.26 (m, 4H, Ar-H), 7.33 (ddd, *J* = 7.0, 6.3, 1.3 Hz, 4H, Ar-H), 7.37 – 7.42 (m, 2H, Ar-H), 7.51 (qd, *J* = 4.7, 2.5 Hz, 4H, Ar-H), 7.66 (dd, *J* = 7.6, 1.3 Hz, 1H, Ar-H), 8.60 (s, 1H, -N=CH), 12.61 (s, 1H, -OH). ^{13}C NMR (101 MHz, DMSO-d_6) δ (ppm): 117.12, 118.56, 119.58, 119.84, 126.72, 126.80, 126.83, 127.08, 127.31, 128.04, 128.27, 128.59, 128.68, 128.78, 128.87, 129.10, 129.40, 130.26, 131.12, 131.40, 131.66, 132.30, 133.21, 133.97, 134.96, 136.32, 137.07, 145.57, 147.52, 160.67, 163.95. MS (ESI) *m/z* 514.3 (M + Na^+, Calc. 514.57), 492.3 (M + H^+, Calc. 492.59). Anal. Calc.(Found) for $C_{34}H_{25}N_3O$: C, 83.07 (82.56); H, 5.13 (5.09); N, 8.55 (8.96) %.

3.7.3.9: (*E*)-2-(((2-(1-phenyl-1*H*-phenanthro[9,10-*d*]imidazol-2-yl)phenyl)imino)methyl)phenol (I_9), ash**:** 0.29 mL (0.33 g, 2.7 mmol) of salicylaldehyde and 1.02 g (2.7 mmol) of **A9**. Yield = 1.11 g (85%). Selected FTIR (ATR, cm^{-1}): 3062w, 1614s, 1595w, 1565s, 1530w, 1509s, 1492w, 1380s, 1348w, 1276s, 1226w, 1184w, 1152s, 1092w, 1047w, 751s, 722s. UV-Vis (MeCN, nm {ε /M^{-1} cm^{-1}}): 257 {64 265}, 282 {24 143}, 339 {9 085}, 354 {8 508}. ^{1}H NMR (400 MHz, DMSO-d_6) δ (ppm): 6.69 (d, *J* = 8.1 Hz, 1H, Ar-H), 6.90 – 6.97 (m, 1H, Ar-H), 7.11 (d, *J* = 7.6 Hz, 1H, Ar-H), 7.27 – 7.37 (m, 3H, Ar-H), 7.38 – 7.47 (m, 4H, Ar-H), 7.48 – 7.61 (m, 5H, Ar-H), 7.63 – 7.71 (m, 2H, Ar-H), 7.76 (t, *J* = 7.1 Hz, 1H, Ar-H), 8.64 (dd, *J* = 7.9, 1.2 Hz, 1H, Ar-H), 8.86 (s, 1H, -N=CH), 8.91 (d, *J* = 8.2 Hz, 1H, Ar-H), 8.96 (d, *J* = 8.4 Hz, 1H, Ar-H), 12.55 (s, 1H, -OH). ^{13}C NMR (101 MHz, DMSO-d_6) δ (ppm): 117.05, 119.68, 120.63, 124.11, 125.00, 127.10, 127.32, 127.92, 128.72, 130.11, 131.49, 133.27, 133.97, 137.75, 147.74, 150.32, 160.54, 164.25. MS (EI) *m/z* 489 (M^+, Calc. 489.57), 385, 369 (base peak, loss of -N=CHPhOH), 245, 184, 165, 28. Anal. Calc.(Found) for $C_{34}H_{23}N_3O$: C, 83.41 (83.10); H, 4.74 (4.78); N, 8.58 (8.61) %.

3.7.3.10: (*E*)-2-(4,5-diphenyl-1*H*-imidazol-2-yl)-N-(pyridin-2-ylmethylene)aniline (I_{N2}): 1.24 mL (1.39 g, 13.0 mmol) of pyridine-2-carboxaldehyde was added to a 70 mL MeOH solution of 4.03 g (12.9 mmol) of **A2**. The set up was heated at 70^{o}C for ≈ 3hrs. The solid obtained on cooling, was filtered, washed with MeOH and dried in an oven at ≈ 70^{o}C to afford an ash product. Yield = 3.78 g (73%). Selected FTIR (ATR, cm^{-1}): 3205s (N-H), 1622s (C=C, C=N), 1602w, 1584s, 1510s, 1479s, 1432s, 1411w, 1320s, 740s, 696s, 643w. UV-Vis (MeCN, nm {ε /M^{-1} cm^{-1}}): 286 {18 435}, 338 {13 950}. ^{1}H NMR (400 MHz, DMSO-d_6) δ (ppm): 6.30 - 6.31 (d, *J* = 6.31, 1H, Ar-H), 6.73 - 6.81 (m, *J* = 6.77, 3H, Ar-H), 7.08 - 7.26 (m, *J* = 7.17, 7H, Ar-H), 7.36 - 7.41 (m, *J* = 7.38, 3H, Ar-H), 7.45 (d, 1H, Ar-H), 7.50 - 7.52 (d, *J* = 7.51, 2H, Ar-H), 7.63 - 7.68 (td, *J* = 7.65, 1H, Ar-H), 7.84 – 7.86 (d, *J* = 7.85, 1H, Ar-H), 8.41 - 8.42 (d, *J* = 8.41, 1H, Ar-H). ^{13}C NMR (101 MHz, DMSO-d_6) δ (ppm): 68.90, 114.13, 115.27, 118.88, 119.95, 123.27, 123.99, 126.69, 126.87, 127.07, 128.60, 129.27, 129.42, 130.17, 130.83, 134.87, 137.66, 138.20, 141.32, 142.06, 149.77, 158.85. MS (EI) *m/z* 400 (M^+, calc. 400.47), 322 (base peak, loss of Py), 295, 165. Anal Calc.(Found) for $C_{27}H_{20}N_4$: C, 80.98 (80.56); H, 5.03 (4.97); N, 13.99 (13.95) %.

3.7.3.11: (*E*)-2-(1*H*-phenanthro[9,10-*d*]imidazol-2-yl)-N-(pyridin-2-ylmethylene)aniline (I_{N3}), off-white powder**:** 0.17 mL (0.19 g, 1.8 mmol) of pyridine-2-carboxaldehyde and 0.54 g (1.8 mmol) of **A3**. Yield = 0.51 g (73%). Selected FTIR (ATR, cm^{-1}): 3172w (N-H), 1616w (C=C, C=N), 1590w, 1523s, 1477s, 1434w, 1355w, 1325w, 742s, 718s, 614s. UV-Vis (MeCN, nm {ε /M^{-1} cm^{-1}}): 253 {50 393}, 311 {12 451}, 374 {15 756}. ^{1}H NMR (400 MHz, DMSO-d_6) δ (ppm): 6.84 – 6.88 (dd, *J* = 6.85, 1H, Ar-H), 6.91 – 6.93 (d, *J* = 6.92, 1H, Ar-H), 7.15 – 7.25 (m, *J* = 7.22, 3H, Ar-H), 7.56 – 7.59 (m, *J* = 7.58, 2H, Ar-H), 7.65 – 7.77 (tdd, *J* = 7.58, 2H, Ar-H), 7.75 – 7.78 (m, *J* = 7.76, 2H, Ar-H), 7.82 – 7.84 (d, *J* = 7.82, 1H, Ar-H), 8.04 – 8.06 (dd, *J* = 8.05, 1H, Ar-H), 8.26 – 8.28 (dd, *J* = 8.27, 1H, Ar-H), 8.41 – 8.43 (dd, *J* = 8.42, 1H, Ar-H), 8.67 – 8.70 (dd, *J* = 8.69, 1H, Ar-H), 8.83 – 8.85 (d, *J* = 8.84, 1H, Ar-H), 8.91 – 8.89 (dd, *J* = 8.90, 1H, -NH). ^{13}C NMR (101 MHz, DMSO-d_6) δ (ppm): 70.12, 114.04, 115.45, 119.08, 120.39, 121.72, 122.60, 122.84, 124.05, 124.22, 124.55, 124.84, 125.02, 125.41, 126.12, 127.06, 127.56, 127.80, 128.07, 128.44, 131.26, 138.05, 138.39, 141.74, 146.23, 149.95, 158.72. MS (EI) *m/z* 398 (M^{+}, Calc. 398.46), 382, 320 (base peak, loss of Py,), 294 (loss of N=CHPy), 190, 165, 78, 44, 28. Anal Calc.(Found) for $C_{27}H_{18}N_4$: C, 81.39 (80.69); H, 4.55 (4.66); N, 14.06 (13.62) %.

3.7.3.12: (*E*)-2-(4,5-bis(4-methoxyphenyl)-1*H*-imidazol-2-yl)-N-(pyridin-2-ylmethylene)aniline (I_{N4}), brown powder**:** 1.09 mL (1.23 g, 11.4 mmol) of pyridine-2-carboxaldehyde and 4.23 g (11.4 mmol) of **A4**. Yield = 4.08 g (77%). Selected FTIR (ATR, cm^{-1}): 3321b (N-H), 1614s (C=C, C=N), 1588w, 1540s, 1517s, 1471w, 1414w, 1344w, 1318w, 1286s, 1244s, 1079w, 1025s, 757s, 705s, 672w. UV-Vis (MeCN, nm {ε /M^{-1} cm^{-1}}): 232 {31 300}, 287 {19 309}, 342 {13 057}. ^{1}H NMR (400 MHz, DMSO-d_6) δ (ppm): 3.70 (s, 3H, -OCH_3), 3.75 (s, 3H, -OCH_3), 6.28 - 6.29 (d, *J* = 6.29, 1H, Ar-H), 6.73 - 6.84 (ddd, *J* = 6.79, 5H, Ar-H), 6.92 - 6.94 (d, *J* = 6.93, 2H, Ar-H), 7.06 - 7.11 (m, *J* = 7.09, 3H, Ar-H), 7.20 - 7.23 (dd, *J* = 7.21, 1H, Ar-H), 7.46 - 7.50 (dd, *J* = 7.47, 3H, Ar-H), 7.62 - 7.66 (td, *J* = 7.64, 1H, Ar-H), 7.86 – 7.88 (d, *J* = 7.87, 1H, Ar-H), 8.43 - 8.44 (d, *J* = 8.43, 1H, NH). ^{13}C NMR (101 MHz, DMSO-d_6) δ (ppm): 55.42, 159.81, 55.52, 68.85, 114.06, 114.39, 114.86, 115.28, 118.89, 119.93, 122.18, 123.18, 123.91, 125.81, 127.68, 127.88, 129.94, 132.24, 137.62, 138.16, 141.26, 141.62, 149.77, 158.37, 159.09. MS (EI) *m/z* 460

(M^+, Calc. 460.53), 382 (base peak, loss of Py), 341, 230, 79 (Py). Anal Calc.(Found) for $C_{29}H_{24}N_4O_2$: C, 75.63 (75.78); H, 5.25 (5.23); N, 12.17 (12.21) %.

3.7.3.13: 2,3-diphenyl-5-(pyridin-2-yl)-5,6-dihydroimidazo[1,2-*c*]quinazolin-1-ium, (**I_{N2}cH$^+$**, brown)**:** ^{1}H NMR (250 MHz, DMSO-d_6) δ (ppm): 6.75 (s, 1H, $NH_{imidazole}$), 6.94 (dd, *J* = 10.4, 7.9 Hz, 2H, Ar-H), 7.15 (d, *J* = 7.7 Hz, 1H), 7.23 – 7.59 (m, 13H, Ar-H), 7.75 (t, *J* = 7.1 Hz, 1H, Ar-H), 8.01 (d, *J* = 7.5 Hz, 2H, Ar-H), 8.42 (d, *J* = 4.5 Hz, 1H, $NH_{pyrimidine}$). ^{13}C NMR (63 MHz, DMSO-d_6) δ (ppm): 26.49 (THF), 68.39 (THF), 116.99, 121.58, 125.75, 129.05, 130.23, 130.56, 132.03, 138.93, 150.69.

3.7.3.14: 2,3-diphenyl-5-(pyridin-2-yl)imidazo[1,2-*c*]quinazoline, (**I_{N2}v.**MeOH, colourless)**:** ^{1}H NMR (400 MHz, DMSO-d_6) δ (ppm): 3.18 (d, *J* = 5.0 Hz, 3H, CH_3 of MeOH), 4.10 (dd, *J* = 10.1, 4.9 Hz, 1H, OH of MeOH), 7.06 (d, *J* = 4.2 Hz, 4H, Ar-H), 7.15 (dt, *J* = 8.6, 6.3 Hz, 2H, Ar-H), 7.27 (d, *J* = 6.7 Hz, 3H, Ar-H), 7.44 – 7.54 (m, 2H, Ar-H), 7.69 (d, *J* = 5.5 Hz, 2H, Ar-H), 7.77 – 7.87 (m, 2H, Ar-H), 7.95 – 8.06 (m, 2H, Ar-H), 8.65 (d, *J* = 6.0 Hz, 1H, Ar-H). ^{13}C NMR (101 MHz, DMSO-d_6) δ (ppm): 49.06 (CH_3 of MeOH), 151.89, 118.90, 122.86, 124.04, 124.50, 125.08, 128.04, 128.20, 128.25, 128.40, 128.44, 128.63, 129.34, 130.77, 130.88, 131.43, 134.15, 136.65, 140.31, 141.72, 143.60, 146.32, 148.53.

3.7.3.15: 2,3-diphenyl-5-(pyridin-2-yl)imidazo[1,2-*c*]quinazoline, (**I_{N2}v**, lemon-yellow)**:** ^{1}H NMR (250 MHz, DMSO-d_6) δ (ppm): 7.06 (d, *J* = 4.4 Hz, 4H, Ar-H), 7.15 (ddd, *J* = 12.3, 8.2, 4.4 Hz, 2H, Ar-H), 7.23 – 7.35 (m, 3H, Ar-H), 7.49 (dd, *J* = 6.6, 3.1 Hz, 2H, Ar-H), 7.64 – 7.74 (m, 2H, Ar-H), 7.79 – 7.89 (m, 2H, Ar-H), 8.00 (dd, *J* = 10.2, 4.4 Hz, 2H, Ar-H), 8.59 – 8.72 (m, 1H, Ar-H). ^{13}C NMR (63 MHz, DMSO-d_6) δ (ppm): 119.81, 123.77, 124.95, 125.44, 126.00, 128.95, 129.16, 129.35, 129.54, 130.25, 131.67, 131.79, 132.32, 135.05, 137.56, 141.20, 142.61, 144.50, 147.21, 149.43, 152.75.

3.8 Preparation of Sulphur (Oxygen) {ONSNO/ONONO} bridged imines (H_2S1 – H_2O1)

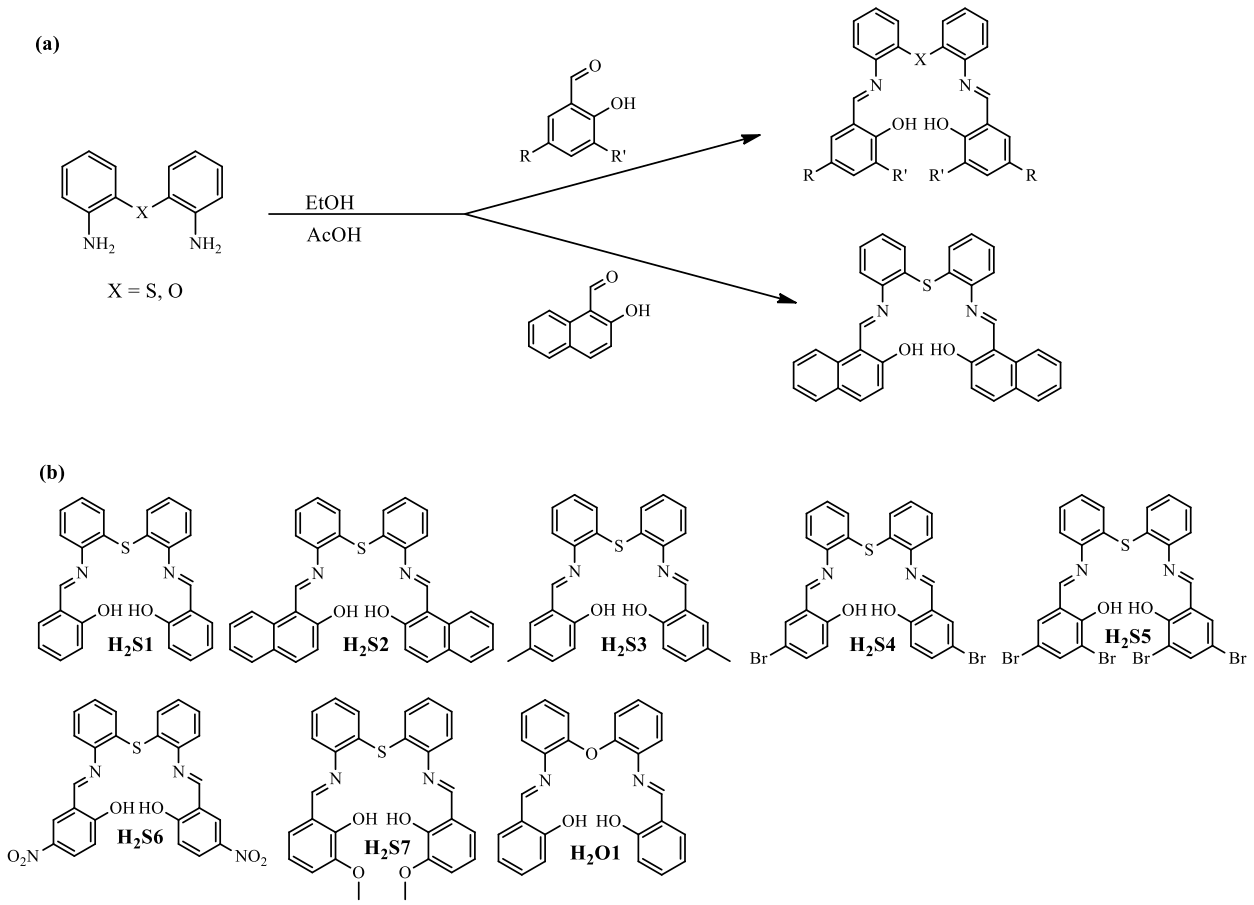

Scheme 3.4: (a) Synthetic pathway to (b) List of prepared S-/O-bridged pentadentate imines

The pentadentate (ONSNO/ONONO) imines were prepared in a similar fashion as the NNO/NNN imines, a full description is given with **H_2S1**. **H_2S1** and **H_2O1** were prepared with slight alteration to earlier reports (Guo and Yuan 2008; Pérez-Pérez, J., *et al* 2016).

3.8.1 2,2'-((1*E*,1′*E*)-((thiobis(2,1-phenylene))bis(azanylylidene))bis(methanylylidene))diphenol {H_2S1}: Drops of AcOH was added to a 50 mL EtOH solution of 2.25 g (10.4 mmol) of bis(2-aminophenyl) sulphide. Upon addition of 2.23 mL (2.56 g; 20.9 mmol) of salicylaldehyde, the yellow solution obtained was refluxed for ≈ 4 hours. The mixture obtained was filtered hot, washed with EtOH and dried under vacuum to give a yellow product. Yield = 4.28 g (96.8%). Selected IR (ATR, cm^{-1}): 3059w, 1612s, 1559s, 1497s, 1468s, 1371s, 1282s, 1228w, 1187s, 1112w, 1051w, 1035s, 644s. UV-Vis (MeOH, nm {ε /M^{-1} cm^{-1}}): 238 {17 522}, 269 {25 585}, 344 {14 813}. ^{1}H NMR (400 MHz, DMSO-d_6) δ (ppm): 6.90 – 6.92 (d, *J* = 6.91, 2H, Ar-H), 6.94 – 6.98 (td, *J* = 6.96, 2H, Ar-H), 7.16 – 7.18 (dd, *J* = 7.17, 2H, Ar-H), 7.24 – 7.28 (td, *J* = 7.26, 2H, Ar-H), 7.38 – 7.44 (m, *J* = 7.41, 4H, Ar-H), 7.52 – 7.54 (dd, *J* = 7.53, 2H, Ar-H), 7.62 – 7.64 (dd, *J* = 7.63, 2H, Ar-H), 8.94 (s, 2H, CH=N), 12.83 (s, 2H, -OH). ^{13}C NMR (101 MHz, DMSO-d_6) δ (ppm): 117.12, 119.38, 119.59, 119.66, 128.31, 129.24, 129.85, 131.65, 133.36, 134.05, 147.96, 160.72, 164.19. MS (EI) *m/z* 424 (M^+, Calc. 424.51), 391 (loss of OH groups), 318 (loss of =CHPhOH), 228 (loss of -Ph-N=CHPhOH), 197 (base peak, -PhN=CHPhOH), 180, 77 (Ph), 51**.** Anal. Calc.(Found) for $C_{26}H_{20}N_2O_2S$: C, 73.56 (73.25); H, 4.75 (4.76); N, 6.60 (6.60); S, 7.55 (7.99) %.

3.8.2 1,1'-((1*E*,1′*E*)-((thiobis(2,1-phenylene))bis(azanylylidene))bis(methanylylidene))bis(naphthalen-2-ol) {H_2S2}, yellow**:** 1.03 g (4.8 mmol) of bis(2-aminophenyl) sulphide and 1.64 g (9.5 mmol) of 2-hydroxy-1-naphthaldehyde. Yield = 2.38 g (95.2%). Selected IR (ATR, cm^{-1}): 3059s, 1620w, 1604w, 1551s, 1460s, 1418w, 1391w, 1353w, 1082s, 1056w, 1037w, 583s, 559w. UV-Vis (MeOH, nm {ε /M^{-1} cm^{-1}}): 317 {18 335}, 372 {15 155}, 464 {13 062}. ^{1}H NMR (400 MHz, DMSO-d_6) δ (ppm): 7.02 – 7.04 (d, *J* = 7.03, 2H, Ar-H), 7.20 – 7.23 (dd, *J* = 7.22, 2H, Ar-H), 7.26 – 7.30 (m, *J* = 7.28, 2H, Ar-H), 7.37 – 7.41 (t, *J* = 7.39, 2H, Ar-H), 7.46 – 7.50 (m, *J* = 7.48, 2H, Ar-H), 7.56 – 7.60 (dd, *J* = 7.58, 2H, Ar-H), 7.82 – 7.84 (d, *J*

= 7.83, 2H, Ar-H), 7.91 – 7.96 (dd, *J* = 7.94, 4H, Ar-H), 8.54 – 8.57 (d, *J* = 8.56, 2H, Ar-H), 9.73 (s, 2H, CH=N), 15.23 (s, 2H, -OH). ^{13}C NMR (101 MHz, DMSO-d_6) δ (ppm): 109.67, 119.80, 121.13, 121.26, 124.18, 127.51, 127.94, 128.33, 128.58, 129.48, 131.91, 133.31, 136.90, 146.19, 157.93, 167.26. MS (EI) *m/z* 524 (M^+, base peak, Calc. 524.63), 370 (loss of =CHnaphOH), 278 (loss of PhN=CHnaphOH), 262 (-SPhN=CHnaph), 246 (loss of -SPhN=CHnaphOH), 227, 199, 172, 144 (naphOH), 115, 45, 31. Anal. Calc.(Found) for $C_{34}H_{24}N_2O_2S$: C, 77.84 (77.33); H, 4.61 (4.58); N, 5.34 (5.26); S, 6.11 (6.36) %.

3.8.3 2,2'-((1*E*,1'*E*)-((thiobis(2,1-phenylene))bis(azanylylidene))bis(methanylylidene))bis(4-methylphenol) {H_2S3}, yellow**:** 2.04 g (9.4 mmol) of bis(2-aminophenyl) sulphide and 2.57 g (18.9 mmol) of 5-methylsalicylaldehyde. Yield = 3.87 g (90.6%). Selected IR (ATR, cm^{-1}): 3060w, 1613s, 1589w, 1567s, 1487s, 1470s, 1438s, 1381w, 1358s, 1320w, 1280s, 1059s, 1039w, 659s, 612w. UV-Vis (MeOH, nm {ε /M^{-1} cm^{-1}}): 271 {33 917}, 353 {19 214}. ^{1}H NMR (400 MHz, DMSO-d_6) δ (ppm): 2.26 (s, 6H, -CH_3), 6.79 – 6.82 (d, *J* = 6.80, 2H, Ar-H), 7.14 – 7.16 (dd, *J* = 7.15, 2H, Ar-H), 7.20 – 7.28 (m, *J* = 7.24, 4H, Ar-H), 7.40 – 7.44 (m, *J* = 7.42, 4H, Ar-H), 7.49 – 7.52 (dd, *J* = 7.50, 2H, Ar-H), 8.87 (s, 2H, CH=N), 12.52 (s, 2H, -OH). ^{13}C NMR (101 MHz, DMSO-d_6) δ (ppm): 20.36, 116.97, 119.34, 128.12, 128.21, 129.25, 129.79, 131.63, 133.04, 134.84, 148.11, 158.56, 164.03. MS (EI) *m/z* 452 (M^+, Calc. 452.57), 435 (loss of -OH), 332 (loss of =CHPh{OH}{Me}), 242 (loss of PhN=CHPh{OH}{Me}), 226 (-SPhN=CHPh{OH}), 211 (base peak, NPh-S-PhN), 196, 136, 109, 77, 32, 28. Anal. Calc.(Found) for $C_{28}H_{24}N_2O_2S$: C, 74.31 (74.24); H, 5.35 (5.30); N, 6.19 (6.14); S, 7.09 (7.31) %.

3.8.4 2,2'-((1*E*,1'*E*)-((thiobis(2,1-phenylene))bis(azanylylidene))bis(methanylylidene))bis(4-bromophenol) {H_2S4}, yellow: 2.07 g (9.6 mmol) of bis(2-aminophenyl) sulphide and 3.85 g (19.2 mmol) of 5-bromosalicylaldehyde. Yield = 4.65 g (83.5%). Selected IR (ATR, cm^{-1}): 3056w, 1613s, 1575w, 1552s, 1465s, 1435w, 1348s, 1280s, 1232w, 1172s, 1074w, 1055w, 626s. UV-Vis (MeOH, nm {ε /M^{-1} cm^{-1}}): 270 {31 132}, 352 {17 296}. ^{1}H NMR (400 MHz, DMSO-d_6)

δ (ppm): 6.87 – 6.89 (d, *J* = 6.88, 2H, Ar-H), 7.17 – 7.19 (dd, *J* = 7.18, 2H, Ar-H), 7.26 – 7.30 (m, *J* = 7.28, 2H, Ar-H), 7.41 – 7.45 (m, *J* = 7.43, 2H, Ar-H), 7.48 – 7.54 (m, *J* = 7.52, 4H, Ar-H), 7.83 (d, 2H, Ar-H), 8.90 (s, 2H, CH=N), 12.78 (s, 2H, -OH). ^{13}C NMR (101 MHz, DMSO-d_6) δ (ppm): 110.33, 119.41, 119.56, 121.53, 128.60, 129.35, 129.93, 131.80, 134.71, 136.24, 147.75, 159.72, 162.66. MS (EI) *m/z* 582 (M^+, Calc. 582.31), 565 (loss of -OH), 503 (loss of -Br), 398 (loss of =CHPh{OH}{Br}), 306 (loss of PhN=CHPh{OH}{Br}), 275 (base peak, loss of SPhN=CHPh{OH}{Br}), 258, 227 (SPhN=CHPh{OH}), 199, 139, 109, 77, 28. Anal. Calc.(Found) for $C_{26}H_{18}Br_2N_2O_2S$: C, 53.63 (53.88); H, 3.12 (3.02); N, 4.81 (4.72); S, 5.51 (5.91) %.

3.8.5 6,6'-((1*E*,1'*E*)-((thiobis(2,1-phenylene))bis(azanylylidene))bis(methanylylidene))bis(2,4-dibromophenol) {H_2S5}, orange**:** 2.03 g (9.4 mmol) of bis(2-aminophenyl) sulphide and 5.26 g (18.8 mmol) of 3,5-dibromosalicylaldehyde. Yield = 6.64 g (95.5%). Selected IR (ATR, cm^{-1}): 3081w, 1607s, 1543w, 1469w, 1440s, 1353s, 1295w, 1276s, 1228s, 1196s, 1159s, 1060w, 1038w, 687s, 659w. UV-Vis ($CHCl_3$, nm {ε /M^{-1} cm^{-1}}): 275 {27,329}, 363 {14,498}. ^{1}H NMR (400 MHz, DMSO-d_6) δ (ppm): 7.21 – 7.24 (dd, *J* = 7.22, 2H, Ar-H), 7.31 – 7.33 (td, *J* = 7.33, 2H, Ar-H), 7.21 – 7.24 (t, *J* = 7.22, 2H, Ar-H), 7.47 – 7.49 (td, *J* = 7.47, 2H, Ar-H), 7.56 – 7.58 (dd, *J* = 7.57, 2H, Ar-H), 7.86 – 7.87 (d, *J* = 7.87, 2H, Ar-H), 7.91 – 7.92 (d, *J* = 7.92, 2H, Ar-H), 8.96 (s, 2H, CH=N), 14.03 (s, 2H, -OH). ^{13}C NMR (101 MHz, DMSO-d_6) δ (ppm): 110.20, 111.71, 119.66, 121.51, 129.21, 129.59, 130.12, 132.26, 134.91, 138.12, 146.69, 156.98, 163.10, 204.39. MS (EI) *m/z* 740.10 (M^+ - not observed), 386 (loss of PhN=CHPh{OH}{Br_2}), 355 (base peak, PhN=CHPh{OH}{Br_2}), 277 (N=CHPh{OH}{Br_2}), 212 (NPh-S-PhN), 198 (NPh-S-Ph), 184 (Ph-S-Ph). Anal. Calc.(Found) for $C_{26}H_{16}Br_4N_4O_2S$: C, 42.19 (42.47); H, 2.18 (2.09); N, 3.79 (3.71); S, 4.33 (4.22) %.

3.8.6 2,2'-((*1E,1'E*)-((thiobis(2,1-phenylene))bis(azanylylidene))bis(methanylylidene))bis(4-nitrophenol) {H_2S6}, yellow: 2.26 g (10.5 mmol) of bis(2-aminophenyl) sulphide and 3.50 g (20.9 mmol) of 5-nitrosalicylaldehyde. Yield = 5.11 g (95.0%). Selected IR (ATR, cm^{-1}): 3072w, 1613s, 1576s, 1514s, 1475s, 1443w, 1339s, 1296s, 1180s, 1128w, 1099s, 1055w, 1039w, 666s, 637s. UV-Vis (MeOH, nm {ε /M^{-1} cm^{-1}}): 269 {7 724}, 305 {7 672}, 496 {1 992}. ^{1}H NMR (400 MHz, Acetone-d_6) δ (ppm): 7.10 (d, *J* = 9.3 Hz, 2H, Ar-H), 7.34 (t, *J* = 7.8 Hz, 4H, Ar-H), 7.47 (d, *J* = 8.4 Hz, 2H, Ar-H), 7.61 (d, *J* = 7.9 Hz, 2H, Ar-H), 8.24 – 8.33 (m, 2H, Ar-H), 8.60 (d, *J* = 2.8 Hz, 2H, Ar-H), 9.12 (s, 2H, CH=N). MS (EI) *m/z* 515 (M + H, Calc. 514.51), 497 (loss of OH), 273 (SPhN=CHPh{OH}{NO_2}), 242 (base peak, PhN=CHPh{OH}{NO_2}), 227 (SPhN=CHPh{OH}), 212 (NPh-S-PhN), 195, 184, 167, 165, 109, 65, 43, 28. Anal. Calc.(Found) for $C_{26}H_{18}N_4O_6S$: C, 60.69 (60.63); H, 3.53 (3.55); N, 10.89 (10.85); S, 6.23 (6.27) %.

3.8.7 6,6'-((1*E*,1'*E*)-((thiobis(2,1-phenylene))bis(azanylylidene))bis(methanylylidene))bis(2-methoxyphenol) {H_2S7}, orange**:** 0.84 g (3.9 mmol) of bis(2-aminophenyl) sulphide and 1.19 g (7.8 mmol) of *o*-vanillin. Yield = 1.79 g (95.2%). Selected IR (ATR, cm^{-1}): 3059w, 1610s, 1562s, 1456s, 1382s, 1247s, 1195s, 1078s, 1037w, 634w. ^{1}H NMR (400 MHz, DMSO-d_6) δ (ppm): 3.78 (s, 6H, -OCH_3), 6.88 – 6.92 (t, *J* = 6.90, 2H, Ar-H), 7.11 – 7.17 (ddd, *J* = 7.14, 4H, Ar-H), 7.21 – 7.29 (m, *J* = 7.25, 4H, Ar-H), 7.40 – 7.45 (td, *J* = 7.43, 2H, Ar-H), 7.54 – 7.56 (dd, *J* = 7.55, 2H, Ar-H), 8.94 (s, 2H, C=NH), 12.95 (s, 2H, -OH). ^{13}C NMR (101 MHz, DMSO-d_6) δ (ppm): 56.25, 116.30, 119.09, 119.41, 119.57, 124.67, 128.37, 129.25, 129.84, 131.63, 147.87, 148.31, 150.88, 164.47. MS (EI) *m/z* 484 (M^+, Calc. 484.57), 451 (Loss of OH groups), 350 (loss of =CHPh{OH}{OMe}), 258 (base peak, loss of PhN=CHPh{OH}{OMe}), 243, 226 (loss of SPhN=CHPh{OH}{OMe}), 211 (NPh-S-PhN), 196, 184 (Ph-S-Ph), 150 (N=CHPh{OH}{OMe}), 135, 109, 77, 32, 28. Anal. Calc.(Found) for $C_{28}H_{24}N_2O_4S$: C, 69.40 (69.59); H, 4.99 (5.05); N, 5.78 (5.75); S, 6.62 (6.97) %.

3.8.8 2,2'-((*1E,1'E*)-((oxybis(2,1-phenylene))bis(azanylylidene))bis(methanylylidene))diphenol {H_2O1}, yellow: 0.95 g (4.7 mmol) of bis(2-aminophenyl) ether and 1.05 mL (1.20 g, 9.9 mmol) salicylaldehyde. Yield = 1.94 g (92.8%). Selected IR (ATR, cm^{-1}): 3061w, 1615s, 1591w, 1571s, 1479s, 1449s, 1396w, 1365w, 1283s, 1150s, 1109s, 1047w, 1032w, 651s. UV-Vis (MeOH, nm {ε /M^{-1} cm^{-1}}): 228 {45 873}, 269 {28 067}, 341 {25 114}. ^{1}H NMR (400 MHz, DMSO-d_6) δ (ppm): 6.86 (d, *J* = 8.2 Hz, 2H, Ar-H), 6.90 – 7.00 (m, 4H, Ar-H), 7.23 – 7.33 (m, 4H, Ar-H), 7.34 – 7.41 (m, 2H, Ar-H), 7.58 (dt, *J* = 7.6, 1.6 Hz, 4H, Ar-H), 9.00 (s, 2H, C=NH), 13.14 (s, 2H, -OH). ^{13}C NMR (101 MHz, DMSO-d_6) δ (ppm): 117.10, 119.42, 119.45, 119.70, 120.63, 125.00, 128.73, 133.11, 133.82, 139.22, 150.26, 160.94, 164.27. MS (EI) *m/z* 408 (M^+, Calc. 408.45), 391 (loss of OH), 315 (loss of PhOH), 301 (loss of =CHPhOH), 288 (loss of N=CHPhOH), 271 (Ph-O-PhN=CHPh), 221 (=NPh-O-PhN=), 212 (loss of PhN=CHPhOH), 196 (Ph-O-Ph), 181, 168, 139, 120, 77, 65, 51, 39. Anal. Calc.(Found) for $C_{26}H_{20}N_2O_3$: C, 76.45 (76.13); H, 4.94 (4.88); N, 6.86 (6.80) %.

3.9 Preparation of azo bridged-imines ($H_2AI_1 – H_2AI_3$)

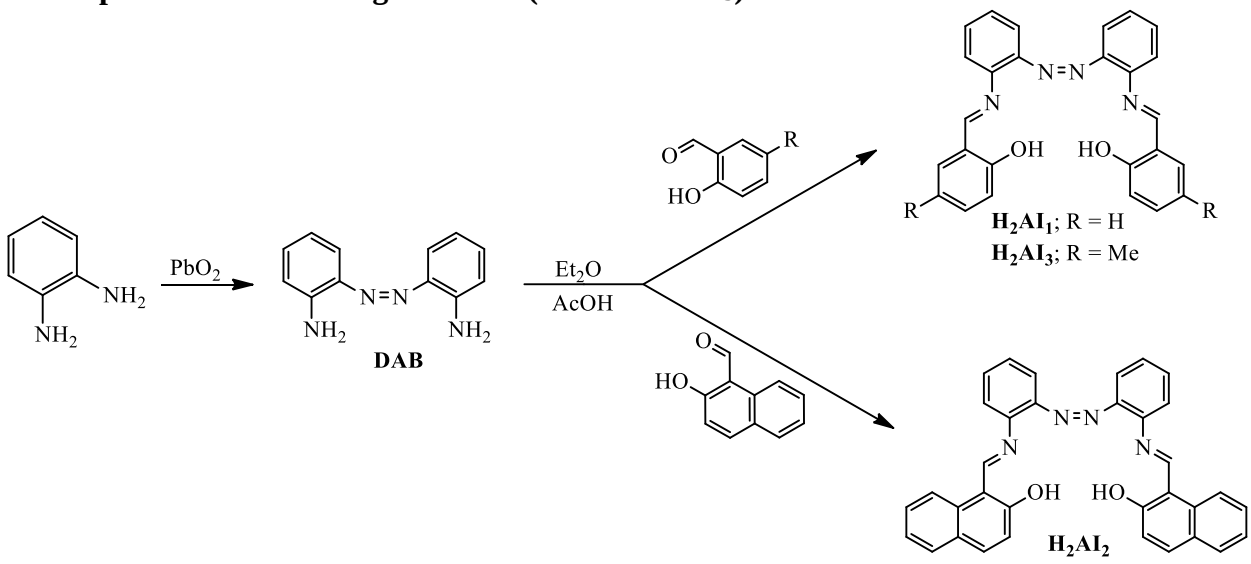

Scheme 3.5: Synthetic pathway to diazo bridged-imines **($H_2AI_1 – H_2AI_3$)**

The azo-imines were prepared in a fashion similar to their pentadentate (ONSNO/ONONO) analogues, a full description is given with **H_2AI_1**.

3.9.1 2,2'-Diaminoazobenzene (DAB): 20.14 g (84.20 mmol) of PbO_2 was added to a 200 mL EtOAc solution of 4.53 g (41.89 mmol) *o*-phenylenediamine. The dark brown mixture obtained was refluxed for ≈ 2 hours, filtered and washed with EtOAc. A reddish-brown crystalline product was obtained after purification by column chromatography using n-Heptane:EtOAc (2:1). Yield = 1.32 g (14.9 %). ^{1}H NMR (400 MHz, DMSO-d_6) δ (ppm): 6.39 (s, 4H, Ar-H), 6.57 – 6.63 (m, 2H, Ar-H), 6.84 (dd, *J* = 8.2, 1.1 Hz, 2H, Ar-H), 7.12 (ddd, *J* = 8.3, 7.1, 1.5 Hz, 2H, Ar-H), 7.66 (dd, *J* = 8.1, 1.4 Hz, 2H, Ar-H). ^{13}C NMR (101 MHz, DMSO-d_6) δ (ppm): 116.08, 117.19, 122.25, 131.70, 137.12, 145.75. MS (EI) *m/z* 212 (base peak, M^+, Calc. 212.25), 196 (loss of NH_2), 183 (loss of NH_4), 169, 120 (loss of $PhNH_2$), 106 (loss of $NPhNH_2$), 92 ($PhNH_2$), 65, 52, 39.

3.9.2 2,2'-((1*E*,1'*E*)-(((*Z*)-diazene-1,2-diylbis(2,1-phenylene))bis(azanylylidene))bis(methanylylidene))diphenol {**H_2AI_1**}: Drops of AcOH was added to a 40 mL Et_2O solution of 1.03 g (4.85 mmol) of **DAB**, followed by 1.05 mL (1.20 g, 9.85 mmol) salicylaldehyde. The slurry obtained was heated under reflux for 5 hours. The mixture was filtered hot and dried in air to afford a red product. Yield = 1.78 g (87.3 %). Selected IR (ATR, cm^{-1}): 3425w, 1611s, 1549w, 1448w, 1270s, 1110s, 1032w, 753s, 619w, 513s. UV-Vis (MeOH, nm {ε /M^{-1} cm^{-1}}): 287 {14 664}. ^{1}H NMR (400 MHz, $CDCl_3$) δ (ppm): 6.86 (t, *J* = 7.4 Hz, 2H, Ar-H), 6.95 – 7.03 (m, 2H, Ar-H), 7.27 – 7.37 (m, 8H, Ar-H), 7.43 – 7.49 (m, 2H, Ar-H), 7.75 (dd, *J* = 8.0, 1.1 Hz, 2H, Ar-H), 8.60 (s, 2H, C=NH), 13.56 (s, 2H, -OH). ^{13}C NMR (101 MHz, $CDCl_3$) δ (ppm): 117.04, 117.51, 118.97, 119.50, 120.58, 127.45, 132.23, 132.34, 133.38, 146.55, 161.71, 164.13. MS (EI) *m/z* 420 (base peak, M^+, Calc. 420.46), 316 (loss of =CHPhOH), 300 (loss of N=CHPhOH), 223 (loss of PhN=CHPhOH), 210 (loss of NPhN=CHPhOH), 196 (loss of N=NPhN=CHPhOH), 182, 167, 141, 115, 91, 77, 51.

3.9.3 1,1'-((1*E*,1'*E*)-(((*Z*)-diazene-1,2-diylbis(2,1-phenylene))bis(azanylylidene))bis(methanylylidene))bis(naphthalen-2-ol) {**H_2AI_2**}, red: 1.00 g (4.71 mmol) of **DAB** and 1.63 g (9.47 mmol) 2-hydroxy-1-naphthaldehyde. Yield = 2.10 g (85.7 %). Selected IR (ATR, cm^{-1}): 3058w, 1620s, 1584s, 1479w, 1309w, 1282s, 1210w, 1039w, 958w, 740s, 527s, 478s. UV-Vis (MeOH, nm {ε /M^{-1} cm^{-1}}): 316; 341; 499. MS (EI) *m/z* 520 (M^+, Calc. 520.58), 259 (base peak, loss of N-PhN=CH(naphOH)), 231, 220, 144, 115, 77, 65, 28. Anal. Calc.(Found) for $C_{34}H_{24}N_4O_2$: C, 78.44 (78.15); H, 4.65 (4.66); N, 10.76 (10.81) %.

3.9.4 2,2'-((1*E*,1'*E*)-(((*Z*)-diazene-1,2-diylbis(2,1-phenylene))bis(azanylylidene))bis(methanylylidene))bis(4-methylphenol) {**H_2AI_3**}, orange-red: 1.01 g (4.75 mmol) of **DAB** and 1.30 g (9.47 mmol) 5-methylsalicylaldehyde. Yield = 2.06 g (96.7 %). Selected IR (ATR, cm^{-1}): 3069w, 1602s, 1567s, 1479s, 1323s, 1234w, 1153s, 1040w, 822s, 756s, 595w, 422s. UV-Vis (MeOH, nm {ε /M^{-1} cm^{-1}}): 294 {7 948}. MS (ESI) *m/z* 502.3 ($[M + Na + MeOH]^+$, Calc. 503.55), 471.3 ($[M + Na]^+$, Calc. 471.51), 225.2 (base peak, loss of N-Ph-N=CHPh{OH}{Me}). Anal. Calc.(Found) for $C_{28}H_{24}N_4O_2$: C, 74.98 (74.31); H, 5.39 (5.47); N, 12.49 (12.65) %.

3.10 Preparation of metal complexes

3.10.1 Nitro-imidazole palladium complexes

3.10.1.1 Pd-N1: 0.0739 g (0.30 mmol) of ligand (**N1**) and 0.0783 g (0.30 mmol) of $PdCl_2(MeCN)_2$ were placed in a vial. 2 mL MeCN was added and the set-up allowed to stand at room temperature for weeks to afford orange crystals suitable for x-ray. Yield = 0.0686 g (49.0 %). Selected IR (ATR, cm^{-1}): 3074b, 1617w, 1532s, 1453s, 1364s, 877s, 822s, 780s, 614s. Anal. Calc.(Found) for $C_{15}H_{18}Cl_2N_4O_2Pd$: C, 38.86 (39.17); H, 3.91 (3.91); N, 12.08 (12.09) %.

3.10.1.2 [Pd-N3]2.5H_2O: 0.0167 g (4.92×10^{-5} mol) of ligand (**N3**) and 0.0130 g (5.01×10^{-5} mol) of $PdCl_2(MeCN)_2$ were placed in a vial. 2 mL MeCN was added and the set-up allowed to stand at room temperature for weeks to afford orange crystals suitable for x-ray. Yield (0.0222 g, 74.7 %). Selected IR (ATR, cm^{-1}): 3075w, 1616w, 1575s, 1459s, 1346s,

854s, 754s, 613w. Anal. Calc.(Found) for $C_{23}H_{21}Cl_2N_4O_{4.5}Pd$: C, 45.83 (45.85); H, 3.51 (3.16); N, 9.29 (8.99) %.

3.10.1.3 [Pd-N9]0.5H_2O: 0.2046 g (0.49 mmol) of ligand (**N9**) and 0.1282 g (0.49 mmol) of $PdCl_2(MeCN)_2$ were weighed and transferred into a vial. 4 mL MeOH was added and the mixture stirred for ≈ 5 hours at room temperature. The mixture was filtered, washed with MeOH and dried under vacuum to give a green product. Yield = 0.1996 g (63.0 %). Selected IR (ATR, cm^{-1}): 3065w, 1524s, 1416w, 1353s, 853s, 723s, 693s. Anal. for $C_{29.5}H_{22}Cl_2N_4O_{2.5}Pd$ Calc. (Found): C, 54.18 (54.34); H, 3.29 (3.19); N, 8.72 (8.21) %.

3.10.2 NNO/NNN imines cobalt complexes

The cobalt complexes were prepared using equimolar amount of the metal salt, the imidazole-imine ligand (and the co-ligand, hydroxyquinone) with appropriate solvent. The reaction was carried out at room temperature for ≈ 2 – 3 hrs to afford the respective complexes.

3.10.2.1 [Co(I_2)Cl]0.75H_2O.0.5MeOH (M1), green powder: 4 mL MeOH solution of 0.1989 g (0.84 mmol) of $CoCl_2.6H_2O$ was added dropwise to 8 mL MeOH suspension of 0.3478 g (0.84 mmol) of **I_2**. The green mixture obtained was stirred at room temperature, filtered, washed with MeOH and dried (under pressure and later at 50^oC). Yield = 0.1291 g (29 %). Selected IR (ATR, cm^{-1}): 3606w, 3412w, 3059w, 1604s, 1583s, 1528s, 1506w, 1459s, 1461s, 1392s, 1180s, 1147s, 1030w, 764s, 682s, 524w. UV-Vis (DCM, nm {ε /M^{-1} cm^{-1}}): 288 {28 373}, 399 {7 049}. MS (EI) *m/z* 508 ([M-0.75H_2O, 0.5MeOH]$^+$, Calc. 508.86), 471 (base peak, [M-(0.75H_2O, 0.5MeOH)^{37}Cl]$^+$, Calc. 473.41), 311 ([M-(0.75H_2O, 0.5MeOH)^{37}Cl CoOPhCH=]$^+$, Calc. 309.36), 165 ([CoOPhCH=]$^+$, Calc. 164.05), 149 ([CoOPh]$^+$, Calc. 151.03), 121, 105, 93, 76, 65, 28. Anal. for $C_{28.5}H_{23.5}ClCoN_3O_{2.25}$ Calc.(Found): C, 63.58 (63.44); H, 4.40 (4.02); N, 7.80 (8.02) %.
A repeat of the procedure at 50^oC gave a green product and a yield of 0.1187 g (29 %)

3.10.2.2 [Co(I_2)$_2$]Cl.MeOH (M2), brown crystals**:** In attempt to grow suitable crystals for x-ray crystallographic study of **M1**; 0.0550 g (0.18 mmol) of **A2**, 0.019 mL (0.0218 g, 0.18 mmol) of salicylaldehyde and 0.0419 g (0.018 mmol) of $CoCl_2.6H_2O$ were left in a vial, after addition of 2 mL MeOH. Crystals suitable for x-ray determination were obtained after several days. Yield = 0.0131 g (8 %). Selected IR (ATR, cm^{-1}): 3050w, 1601s, 1583w, 1522s, 1461s, 1436s, 1369s, 1317s, 1235w, 1188s, 1146s, 1026w, 868w, 750s, 695s, 562w, 470s. Anal. for $C_{57}H_{44}ClCoN_6O_3$ Calc.(Found): C, 71.66 (71.47); H, 4.64 (4.25); N, 8.80 (9.29) %.

3.10.2.3 [Co(I_2)(OAc)]0.75H_2O (M3), brown powder**:** 4 mL 50% MeOH solution of 0.2025 g (0.81 mmol) of $Co(OAc)_2.4H_2O$ was added dropwise to 8 mL MeOH suspension of 0.3373 g (0.81 mmol) of **I_2**. The brown mixture obtained was stirred at room temperature, filtered, washed with EtOH and dried (under pressure and later at 50^oC). Yield = 0.3819 g (86 %). Selected IR (ATR, cm^{-1}): 1608w, 1586s, 1570s {ν_{asym} (COO^-)}, 1527w, 1507w, 1491w, 1461s, 1436s, 1399w {ν_{sym} (COO^-)}, 1322w, 1183s, 1147s, 1078w, 801w, 754s, 697s, 524w. UV-Vis (DCM, nm {ε /M^{-1} cm^{-1}}): 288 {21 142}, 401 {5 114}. MS (EI) *m/z* 472 ([M-(0.75H_2O, OAc)]$^+$, Calc. 473.41), 335, 266, 190, 165 ([CoOPhCH=]$^+$, Calc. 164.05), 97, 69, 60, 45, 43 (base peak), 29. Anal. for $C_{30}H_{24.5}CoN_3O_{3.75}$ Calc.(Found): C, 66.00 (65.94); H, 4.52 (4.14); N, 7.70 (7.76) %.

3.10.2.4 [Co(I_2)HQ].2CH_3OH (M4), brown powder**:** 4 mL 50% MeOH solution of 0.1282 g (0.51 mmol) of $Co(OAc)_2.4H_2O$ was added dropwise to 6 mL MeOH suspension of 0.2136 g (0.51 mmol) **I_2**, followed by 2 mL MeOH solution of 0.0747 g (0.51 mmol) 8-hydroxyquinoline to give a dark brown mixture. The mixture was stirred at room temperature, filtered, washed with MeOH and dried. Yield = 0.1911 g (55%). Selected IR (ATR, cm^{-1}): 3057w, 1603w, 1577s, 1497s, 1464s, 1377s, 1319s, 1279s, 1237w, 1147s, 868s, 738s, 698s, 505s. UV-Vis (DCM, nm {ε /M^{-1} cm^{-1}}): 245 {30 924}sh, 296 {17 060}sh, 317 {14 973}sh. MS (EI) *m/z* 472 ([M-(HQ)(2CH_3OH)]$^+$, Calc. 473.41), 415 ([M-(HQ)(2CH_3OH)Co]$^+$, Calc. 414.48) 311 ([M-(HQ)(2CH_3OH)CoOPhCH=]$^+$, Calc. 309.36), 145(base peak, HQ, Calc. 144.5), 117, 89, 63, 43, 28. Anal. for $C_{39}H_{26}CoN_4O_4$ Calc.(Found): C, 68.72 (68.71); H, 5.03 (4.66); N, 8.22 (8.23) %.

3.10.2.5 [Co(I_{N2})Cl_2] (M5), brown powder**:** 4 mL MeOH solution of 0.1939g (0.82 mmol) of $CoCl_2.6H_2O$ was added dropwise to 8 mL MeOH suspension of 0.3266g (0.82 mmol) of $\mathbf{I_{N2}}$. The dark brown mixture obtained was stirred at room temperature, filtered, washed with MeOH and dried (under pressure and later at 50°C). Yield = 0.3328 g (77 %). Selected IR (ATR, cm^{-1}): 3150w, 1625w, 1599s, 1489s, 1354s, 1304s, 1263s, 1071w, 674s, 615w, 560w, 497s. MS (EI) *m/z* 495 ($[M-^{35}Cl]^+$, Calc. 494.86), 493 ($[M-^{37}Cl]^+$, Calc. 494.86), 456 ($[M-^{37}Cl_2]^+$, Calc. 456.41), 398 ($[M-^{35}Cl_2Co]^+$, Calc. 398.47), 322 (base peak, $[M-^{35}Cl_2CoPy]^+$, Calc. 322.38), 294 ($[M-^{35}Cl_2CoPyCH{=}N]^+$, Calc. 295.36), 165 ($[CoPyCH{=}N]^+$, Calc. 164.05), 103, 93, 78, 36, 28. Anal. for $C_{27}H_{20}Cl_2CoN_4$ Calc. (Found): C, 61.15 (60.95); H, 3.80 (3.86); N, 10.56 (10.37) %.

3.10.2.6 [Co(I_4)Cl]1.5MeOH (M6), green powder**:** 2 mL MeOH solution of 0.0571 g (0.24 mmol) of $CoCl_2.6H_2O$ was added dropwise to 6 mL MeOH suspension of 0.1077 g (0.23 mmol) of $\mathbf{I_4}$. The green mixture obtained was stirred at room temperature, filtered, washed with MeOH and Et_2O, and dried. Yield = 0.0804 g (62 %). Selected IR (ATR, cm^{-1}): 3619s, 3423b, 1620s, 1586w, 1550s, 1519s, 1462w, 1398s, 1285s, 1241s, 1131s, 1023s, 833s, 798s, 755s, 592s, 512s. UV-Vis (DCM, nm {ε /M^{-1} cm^{-1}}): 242 {38 931}, 286 {32 117}, 381 {8 929}sh, 397 {8 474}sh. MS (EI) *m/z* 568 ($[M-1.5CH_3OH]^+$, Calc. 568.92), 532 (base peak, $[M-(1.5CH_3OH)Cl]^+$, Calc. 533.46), 517 ($[M-(1.5CH_3OH)OCl]^+$, Calc. 517.46), 371 ($[M-(1.5CH_3OH)CoClOPhCH{=}]^+$, Calc. 369.42), 266, 205, 71, 57, 36, 28. Anal. for $C_{31.5}H_{30}ClCoN_3O_{4.5}$ Calc. (Found): C, 61.32 (61.15); H, 4.90 (4.52); N, 6.81 (7.02) %.

3.10.2.7 [Co(I_4)(OAc)] (M7), brown powder**:** 4 mL 50% MeOH solution of 0.1750 g (0.70 mmol) of $Co(OAc)_2.4H_2O$ was added dropwise to an 8 mL MeOH suspension of 0.3327 g (0.70 mmol) of $\mathbf{I_4}$. The brown mixture obtained was stirred at room temperature, filtered, washed with hot MeOH and dried. Yield = 0.3115 g (75 %). Selected IR (ATR, cm^{-1}): 1606s, 1569s {ν_{asym} (COO^-)}, 1519s, 1498s, 1461s, 1402s, {ν_{sym} (COO^-)}, 1298w, 1247s, 1181s, 1148s, 1031s, 832s, 753s, 678s, 608s, 595w, 495s. UV-Vis (DCM, nm {ε /M^{-1} cm^{-1}}): 243 {33 518}, 288 {28 851}, 388 {7 305}sh. MS (EI) *m/z* 489 ($[M-(OPhCH{=})]^+$, Calc. 487.39), 399 ($[M-(OPhCH{=})(OAc)(CH_3O)]^+$, Calc. 397.32), 385 ([M-

(OPhCH=N)(OAc)(CH_3O)]$^+$, Calc. 383.31), 370 ([M-(OPhCH=N)(OAc)(CH_3O)CH_3]$^+$, Calc. 368.27), 355 ([M-(CH_3COO)CoOPhC=N]$^+$, Calc. 355.41), 237 ([Co(OAc)(OPhCH=N)]$^+$, Calc. 237.10), 223 ([Co(OAc)(OPhCH=)]$^+$, Calc. 223.09), 209 ([Co(OAc)(OPh)]$^+$, Calc. 210.07), 118 ([Co(OAc)]$^+$, Calc. 117.98), 108 ($PhOCH_3$, Calc. 107.13), 94 (base peak), 78, 65, 51, 39, 28. Anal. for $C_{32}H_{27}CoN_3O_5$ Calc.(Found): C, 64.87 (64.92); H, 4.59 (4.57); N, 7.09 (7.11) %.

3.10.2.8 [Co(I$_7$)Cl] (M8), green powder**:** 2 mL MeOH solution of 0.0477 g (0.20 mmol) of $CoCl_2.6H_2O$ was added dropwise to 5 mL MeOH suspension of 0.0975 g (0.20 mmol) of **I$_7$**. The green mixture obtained was stirred at room temperature, filtered, washed with MeOH and Et_2O, and dried. Yield = 0.0572 g (49 %). Selected IR (ATR, cm^{-1}): 3094w, 1620s, 1601s, 1578s, 1519s, 1494s, 1289s, 1251s, 1174s, 1033s, 832s, 752s, 545s, 518s. UV-Vis (DCM, nm {ε /M^{-1} cm^{-1}}): 238 {34 652}, 282 {28 188}, 391 {6 367}. MS (EI) *m/z* 582 ([M-(0.25CH_3OH)]$^+$, Calc. 582.94), 545 (base peak, [M-(0.25CH_3OH)Cl]$^+$, Calc. 547.49), 515 ([M-(0.25CH_3OH)ClOCH_3]$^+$, Calc. 516.46), 488 ([M-(0.25CH_3OH)Cl$(OCH_3)_2$]$^+$, Calc. 485.42), 384 ([M-(ClCoOPhCH=)]$^+$, Calc. 383.44), 273, 223, 205, 148, 122, 36. Anal. for $C_{31.25}H_{27}ClCoN_3O_{3.25}$ Calc. (Found): C, 63.51 (63.40); H, 4.61 (4.51); N, 7.11 (7.10) %.

3.10.2.9 [Co(I$_8$)Cl] (M9), green**:** 4 mL MeOH solution of 0.1576 g (0.66 mmol) of $CoCl_2.6H_2O$ was added dropwise to a 10 mL MeOH suspension of 0.3259 g (0.66 mmol) of **I$_8$**. The green mixture obtained was stirred at room temperature, filtered, washed with hot MeOH and dried (under pressure and later at 50^{o}C). Yield = 0.1452 g (37 %). Selected IR (ATR, cm^{-1}): 1605s, 1577s, 1524s, 1425s, 1375w, 1284w, 1144s, 1027w, 803s, 692s, 522s, 493w. UV-Vis (DCM, nm {ε /M^{-1} cm^{-1}}): 278 {37 014}, 393 {8 050}. MS (EI) *m/z* 584 (M$^+$, Calc. 584.96), 548 (base peak, [M-Cl]$^+$, Calc. 549.51), 387 ([M-(ClCoOPhCH=)]$^+$, Calc. 385.46), 371 ([M-(ClCoOPhCH=N)]$^+$, Calc. 371.45), 274, 180, 165, 36. Anal. for $C_{34}H_{24}ClCoN_3O$ Calc. (Found): C = 69.81 (70.39), H = 4.14 (4.43), N = 7.18 (7.34) %. Green crystals suitable for x-ray were obtained by self assembly {**See Fig. 4.5**(**d**)}.

3.10.3 ONSNO/ONONO imines metal complexes

3.10.3.1 Preparation of ONSNO/ONONO imines cobalt complexes

The Co^{II} complexes {except **[Co_2S1_2]3H_2O**} were obtained after reacting appropriate ligand with $Co(OAc)_2.4H_2O$ in 1:1 ratio, in MeOH, at room temperature for ≈ 10 hours, a full description is given with **[Co_2S2_2]3.5H_2O**. Crystals suitable for crystallographic measurements were obtained for **[Co_2S2_2]3.5H_2O** and **[Co_2S5_2]** after dissolving the complexes in hot DCM (layered with Et_2O), while those for **[Co_2S4_2]1.5H_2O**, **[Co_2S7_2]6H_2O** and **[Co_2S8_2]0.5H_2O** were obtained after dissolving the complexes in hot THF (layered with Et_2O).

3.10.3.1.1 [Co_2S1_2]3H_2O: 0.1008 g (0.2 mmol) of **H_2S1** and 0.0591 g (0.2 mmol) of $Co(OAc)_2.4H_2O$ were placed in a vial. 4 mL MeCN was added and the set-up allowed to stand for days. The brown crystals (suitable for crystallographic measurement) obtained was filtered, washed with MeCN and dried in air to afford a dark brown product. Yield = 0.1322 g (54.7 %). Selected IR (ATR, cm^{-1}): 1603s, 1574s, 1523s, 1460s, 1434s, 1374s, 1299br, 1181s, 1146s, 1032s, 976s, 920s, 856s, 753s, 597s. UV-Vis (MeCN, nm {ε /M^{-1} cm^{-1}}): 231 {28,526}, 267 {22,782}. Anal. for $C_{52}H_{42}Co_2N_4O_7S_2$ Calc.(Found): C, 61.42 (61.72); H, 4.16 (3.86); N, 5.51 (5.47); S, 6.31 (6.06) %.

3.10.3.1.2 [Co_2S2_2]3.5H_2O: 0.1460 g (0.6 mmol) of $Co(OAc)_2.4H_2O$ was added to a 4 mL MeOH slurry of 0.30 g (0.6 mmol) of **H_2S2**. The mixture obtained was stirred at room temperature and the brown mixture obtained was filtered, washed with MeOH and dried in air to afford a dark brown product. Yield = 0.3275 g (46.7 %). Selected IR (ATR, cm^{-1}): 3392br, 3054w, 1614w, 1599s, 1571s, 1532s, 1506w, 1450s, 1424s, 1356s, 1091w, 1034s, 609w, 561s, 536w, 497s, 468s. UV-Vis (MeCN, nm {ε /M^{-1} cm^{-1}}): 269 {101,823}, 324 {55,262}, 421 {48,843}. MS (ESI) *m/z* 1185.1 (base peak, $[Co_2S2_2]^+ + Na^+$, Calc. 1186.09), 1162.1 ($[Co_2L2_2]^+$, Calc. 1163.10). Anal. for $C_{68}H_{51}Co_2N_4O_{7.5}S_2$ Calc.(Found): C, 66.61 (66.66); H, 4.19 (3.99); N, 4.57 (4.82); S, 5.23 (5.10) %.

3.10.3.1.3 [Co_2S3_2]$2H_2O$, dark brown: 0.1140 g (0.5 mmol) of $Co(OAc)_2.4H_2O$ and 0.2067 g (0.5 mmol) of **H_2S3**. Yield = 0.2259 g (46.9 %). Selected IR (ATR, cm^{-1}): 3065w, 1604s, 1573s, 1539w, 1520s, 1454w, 1433s, 1375s, 1297w, 1063w, 1033s, 645s, 523w, 496w, 462w, 446s. UV-Vis (MeCN, nm {ε /M^{-1} cm^{-1}}): 294 {36,305}, 420 {17,935}. Anal. for $C_{56}H_{48}Co_2N_4O_6S_2$ Calc.(Found): C, 63.75 (63.88); H, 4.59 (4.50); N, 5.31 (5.33); S, 6.08 (5.92) %.

3.10.3.1.4 [Co_2S4_2]$1.5H_2O$, dark brown: 0.16 g (0.6 mmol) of $Co(OAc)_2.4H_2O$ and 0.37 g (0.6 mmol) of **H_2S4**. Yield = 0.40 g (48.2 %). Selected IR (ATR, cm^{-1}): 3394br, 1603s, 1574s, 1509s, 1442s, 1366s, 1299s, 1158s, 1064w, 1031w, 754s, 665s, 630s, 542w. UV-Vis (MeCN, nm {ε /M^{-1} cm^{-1}}): 248 {19,920}, 412 {5,612}. MS (ESI) *m/z* 1298.4 ([Co_2S4_2]H_2O, Calc. 1296.45). Anal. for $C_{52}H_{35}Br_4Co_2N_4O_{5.5}S_2$ Calc.(Found): C, 47.84 (47.76); H, 2.70 (2.62); N, 4.29 (4.22); S, 4.91 (4.78) %.

3.10.3.1.5 [Co_2S5_2], reddish-brown: 0.11 g (0.4 mmol) of $Co(OAc)_2.4H_2O$ and 0.32 g (0.4 mmol) of **H_2S5**. Yield = 0.33 g (47.9 %). Selected IR (ATR, cm^{-1}): 3052w, 1606w, 1591w, 1511s, 1492w, 1300s, 1227s, 1186s, 1062w, 1037w, 748s, 702s, 549w, 508s, 439s. UV-Vis (MeCN, nm {ε /M^{-1} cm^{-1}}): 248 {92,587}, 417 {30,451}. MS (ESI) *m/z* 1616.5 ([Co_2S5_2]$^+$ + Na^+, Calc. 1617.02), 820.6 (base peak, [CoS5]$^+$ + Na^+, Calc. 820.01). Anal. for $C_{52}H_{28}Br_8Co_2N_4O_4S_2$ Calc.(Found): C, 39.18 (39.31); H, 1.77 (1.71); N, 3.51 (3.48); S, 4.02 (4.03) %.

3.10.3.1.6 [Co_2S6_2]$2H_2O$, light-brown: 0.15 g (0.6 mmol) of $Co(OAc)_2.4H_2O$ and 0.30 g (0.6 mmol) of **H_2S6**. Yield = 0.36 g (52.4 %). Selected IR (ATR, cm^{-1}): 3424br, 3060w, 1602s, 1576w, 1543w, 1459s, 1308s, 1177s, 1098s, 753s, 642w, 496w, 435w. UV-Vis (MeCN, nm {ε /M^{-1} cm^{-1}}): 248 {92,587}, 417 {30,451}. Anal. for $C_{52}H_{36}Co_2N_4O_{14}S_2$ Calc.(Found): C, 52.98 (52.87); H, 3.08 (2.90); N, 9.51 (9.36); S, 5.44 (5.37) %.

3.10.3.1.7 [Co_2S7_2]6H_2O, reddish-brown: 0.0724 g (0.3 mmol) of $Co(OAc)_2.4H_2O$ and 0.14 g (0.3 mmol) of **H_2S7**. Yield = 0.1266 g (36.8 %). Selected IR (ATR, cm^{-1}): 3313br, 3059w, 1612s, 1559s, 1539w, 1436s, 1392w, 1234s, 1193s, 1080s, 675w, 639w, 617w, 588w, 539s, 449s, 428w. UV-Vis (MeCN, nm {ε /M^{-1} cm^{-1}}): 245 {71,388}, 305 {49,067}, 418 {19,267}. MS (ESI) *m/z* 1106.1 ([Co_2S7_2]$^+$ + Na^+, Calc. 1105.97). Anal. for $C_{56}H_{56}Co_2N_4O_{14}S_2$ Calc.(Found): C, 56.47 (56.55); H, 4.74 (4.41); N, 4.70 (4.56); S, 5.38 (4.96) %.

3.10.3.1.8 [Co_2O1_2]0.5H_2O, light-brown: 0.08 g (0.3 mmol) of $Co(OAc)_2.4H_2O$ and 0.12 g (0.3 mmol) of **H_2S8**. Yield = 0.12 g (43.5 %). Selected IR (ATR, cm^{-1}): 3055w, 1611s, 1598s, 1457s, 1383w, 1294s, 1147w, 1031w, 753s, 544w, 493w, 447w. UV-Vis (MeCN, nm {ε /M^{-1} cm^{-1}}): 235 {72,502}, 285 {43,130}, 383 {25,680}. MS (ESI) *m/z* 953.1 ([Co_2S8_2]$^+$ + Na^+, Calc. 953.72), 529.1 (base peak, [CoS8]$^+$ + MeCN + Na^+, Calc. 529.41), 488.1 ([CoS8]$^+$ + Na^+, Calc. 488.36). Anal. for $C_{52}H_{37}Co_2N_4O_{6.5}$ Calc.(Found): C, 66.46 (66.44); H, 3.97 (3.79); N, 5.96 (5.98) %.

3.10.3.2 Preparation of ONSNO/ONONO imines nickel complexes

The nickel complexes were prepared adopting a similar approach as the Co^{II} complexes. Crystals suitable for crystallographic measurements for **Ni_2S1_2** and **Ni_2S3_2** were obtained by slow evaporation of appropriate solvent containing equivalent amounts of the ligand and $Ni(OAc)_2.4H_2O$, while those for **Ni_2S2_2.THF**, **NiS5(H_2O).2THF** were obtained by dissolving the complex in THF then layering in Et_2O.

3.10.3.2.1 [Ni_2S1_2]2.5H_2O, green: 0.1016 g (0.4 mmol) of $Ni(OAc)_2.4H_2O$ and 0.1732 g (0.4 mmol) of **H_2S1**. Yield = 0.1666 g (41 %). Selected IR (ATR, cm^{-1}): 3360w, 3054w, 1605s, 1575w, 1521s, 1438s, 1375s, 1291s, 1177s, 1032w, 751s, 607w, 494w. UV-Vis (DCM, nm {ε /M^{-1} cm^{-1}}): 248 {65 252}sh, 293 {49 804}, 421 {21 084}. Anal. Calc.(Found) for $C_{52}H_{41}N_4Ni_2O_{6.5}S_2$ C, 62.00 (62.16); H, 4.10 (3.85); N, 5.56 (5.61); S, 6.37 (6.34) %.

3.10.3.2.2 [Ni_2S2_2]4H_2O, brown: 0.0507 g (0.2 mmol) of $Ni(OAc)_2.4H_2O$ and 0.1061 g (0.2 mmol) of **H_2S2**. Yield = 0.1059 g (42 %). Selected IR (ATR, cm^{-1}): 3615s, 3050w, 1603s, 1574s, 1533s, 1450s, 1390s, 1182s, 1091w, 745s, 647w, 562w, 522s. UV-Vis (DCM, nm {ε /M^{-1} cm^{-1}}): 244 {118 584}, 274 {90 737}, 331 {51 565}, 440 {35 515}. Anal. Calc.(Found) for $C_{68}H_{52}N_4Ni_2O_8S_2$ C, 66.15 (66.11); H, 4.25 (4.00); N, 4.54 (4.58); S, 5.19 (5.08) %.

3.10.3.2.3 [Ni_2S3_2]1.5H_2O, light-brown: 0.0828 g (0.3 mmol) of $Ni(OAc)_2.4H_2O$ and 0.1503 g (0.3 mmol) of **H_2S3**. Yield = 0.1466 g (42 %). Selected IR (ATR, cm^{-1}): 3437w, 3062w, 1616s, 1597s, 1524s, 1453s, 1368s, 1138s, 1033w, 750s, 553w, 488s. UV-Vis (DCM, nm {ε /M^{-1} cm^{-1}}): 296 {37 429}, 434 {14 544}. Anal Calc.(Found) for $C_{56}H_{47}N_4Ni_2O_{5.5}S_2$ C, 64.33 (64.26); H, 4.53 (4.45); N, 5.36 (5.40); S, 6.13 (6.03) %.

3.10.3.2.4 [Ni_2S4_2]1.5H_2O, light-green: 0.0547 g (0.2 mmol) of $Ni(OAc)_2.4H_2O$ and 0.1276 g (0.2 mmol) of **H_2S4**. Yield = 0.1155 g (40.4 %). Selected IR (ATR, cm^{-1}): 3445w, 3063w, 1606s, 1575w, 1511s, 1449s, 1357s, 1286s, 1157s, 1064w, 750s, 633s, 546s, 450w. UV-Vis (DCM, nm {ε /M^{-1} cm^{-1}}): 257 {55 988}, 301 {32 564}sh, 434 {16 693}. Anal. Calc.(Found) for $C_{52}H_{35}N_4Ni_2O_{5.5}S_2$ C, 47.86 (47.90); H, 2.70 (2.55); N, 4.29 (4.36); S, 4.91 (4.93) %.

3.10.3.2.5 [NiS5(H_2O)], brown: 0.0420 g (0.2 mmol) of $Ni(OAc)_2.4H_2O$ and 0.1244 g (0.2 mmol) of **H_2S5**. Yield = 0.1010 g (74.2 %). Selected IR (ATR, cm^{-1}): 3587s, 3057br, 1604s, 1575s, 1494s, 1435s, 1369w, 1271w, 1139s, 1063w, 755s, 694s, 525w, 477w. UV-Vis (DCM, nm {ε /M^{-1} cm^{-1}}): 253 {34 412}, 300 {20 859}, 446 {10 803}. Anal. Calc.(Found) for $C_{26}H_{16}Br_4N_2NiO_3S$ C, 38.33 (38.58); H, 1.98 (1.96); N, 3.44 (3.43); S, 3.39 (3.86) %.

3.10.3.2.6 [Ni_2S6_2]2.5H_2O, green: 0.0662 g (0.3 mmol) of $Ni(OAc)_2.4H_2O$ and 0.1367 g (0.3 mmol) of **H_2S6**. Yield = 0.1431 g (45.4 %). Selected IR (ATR, cm^{-1}): 3060br, 1616s, 1539s, 1485s, 1300s, 1246w, 1129w, 1099s, 753s, 644w, 555w, 505w. UV-Vis (DCM, nm {ε /M^{-1} cm^{-1}}): 235 {4 682}, 305 {3 733}, 406 {5 209}. Anal. Calc.(Found) for $C_{52}H_{37}N_8Ni_2O_{14.5}S_2$ C, 52.60 (52.62); H, 3.14 (3.16); N, 9.44 (9.16); S, 5.40 (4.63) %.

3.10.3.3 Preparation of copper complexes

The Cu^{II} complexes of **H_2S2** and **H_2S3** were prepared via same route as the Co^{II} complexes, while those for **H_2S1** and **H_2O1** were prepared by placing the respective ligand and metal salt (in 1:1 ratio) in appropriate solvent. In the case of **H_2S2** the solvent used is observed to affect the product obtained – while chloroform gives a trinuclear complex {with acetate bridging}, THF gives a dinuclear complex {and no acetate present inside or outside the coordination sphere}.

3.10.3.3.1 [$Cu_3S1_2(OAc)_2$]2.75H_2O: 0.1170 g (0.28 mmol) of **H_2S1** and 0.0550 g (0.28 mmol) of $Cu(OAc)_2.H_2O$ were placed in a vial followed by 2 mL of DCM. The set-up was left to stand for one week at room temperature. Brown crystals (suitable for crystallographic measurement) were obtained, filtered and dried in air. Yield = 0.0496 g (14.9 %). Selected IR (ATR, cm^{-1}): 3048w, 1609s, 1569w, 1541w, 1515s, 1432s, 1376s, 1330w, 1310w, 1180s, 1145s, 1019w, 972s, 860s, 754s, 679s, 547s, 518s. UV-Vis (DCM, nm {ε /M^{-1} cm^{-1}}): 246 {9.27 x 10^4}, 274 {7.20 x 10^4}, 388 {2.57 x 10^4}. Anal. Calc.(Found) for $C_{56}H_{47.5}Cu_3N_4O_{10.75}S_2$ C, 55.90 (55.78); H, 3.98 (3.61); N, 4.66 (4.57); S, 5.33 (5.03) %.

3.10.3.3.2 [$Cu_3S2_2(OAc)_2$]5.5H_2O: 0.2188 g (0.42 mmol) **H_2S2** and 0.0834 g (0.42 mmol) of $Cu(OAc)_2.H_2O$ were placed in a vial followed by 2 mL $CHCl_3$. The set-up was left to stand for days at room temperature. Brown crystals (suitable for crystallographic measurement) were obtained, filtered and dried in air. Yield = 0.2300 g (38.0 %). Selected IR (ATR, cm^{-1}): 3367w, 1603s, 1534s, 1368s, 1184s, 1039w, 749s, 649w, 540w. MS (ESI) *m/z* 608.1 ($[CuS2]^+ + Na^+$, Calc. 609.15), 586.2 (base peak, $[CuS2]^+$, Calc. 586.16). UV-Vis (DCM, nm {ε /M^{-1} cm^{-1}}): 321 {4.69 x 10^4}, 411 {2.54 x 10^4}. Anal. Calc.(Found) for $C_{72}H_{61}Cu_3N_4O_{13.5}S_2$ C, 59.52 (59.50); H, 4.23 (4.23); N, 3.86 (4.62); S, 4.41 (5.03) %.

3.10.3.3.3 [Cu_2S2_2].2THF: 0.0990 g (0.19 mmol) of **H_2S2** and 0.0377 g (0.19 mmol) of $Cu(OAc)_2.H_2O$ were weighed and transferred into a vial. 2 mL of THF was added and the set-up left for days. Brown crystals (suitable for crystallographic measurements) were obtained, filtered, washed with THF and dried in air. Yield = 0.1069 g (43.0 %). Selected IR (ATR, cm^{-1}): 3055w, 1614w, 1602s, 1575s, 1534s, 1455s, 1433s, 1396s, 1364s, 1182s,

1061s, 829s, 741s, 562s, 504s, 464s. Anal. Calc.(Found) for $C_{76}H_{60}Cu_2N_4O_6S_2$ C, 69.33 (68.94); H, 4.59 (4.51); N, 4.26 (4.25); S, 4.87 (4.69) %.

3.10.3.3.4 $[Cu_2S3_2]3H_2O$: 5 mL 40% MeOH solution of 0.0903 g (0.45 mmol) of $Cu(OAc)_2.H_2O$ was added to a 10 mL MeOH suspension (yellow) of 0.2044 g (0.45 mmol) **H_2S3**. The green mixture, which later turned brown, obtained was stirred at room temperature, filtered, washed with MeOH and dried in air to afford a brown product. Yield = 0.1488 g (30.4 %). Selected IR (ATR, cm^{-1}): 1621s, 1589s, 1447s, 1324s, 1159s, 1039w, 753s, 614w, 525s. UV-Vis (DCM, nm {ε /M^{-1} cm^{-1}}): 274 {5.40 x 10^4}sh, 403 {1.85 x 10^4}. MS (EI) *m/z* 513 ($[CuS3]^+$, Calc. 514.10). Anal. Calc.(Found) for $C_{56}H_{50}Cu_2N_4O_7S_2$ C, 62.15 (62.40); H, 4.66 (4.35); N, 5.18 (4.91); S, 5.93 (5.71) %. Crystals suitable for x-ray measurement were obtained by placing the ligand and metal salt (in 1:1 ratio) in a vial and layering with THF.

3.10.3.3.5 $[Cu_2O1_2]1.5H_2O$: 0.0804 g (0.20 mmol) of **H_2O1** and 0.0393 g (0.20 mmol) of $Cu(OAc)_2.H_2O$ were placed in a vial followed by 2 mL of MeCN. The set-up was left to stand for one week at room temperature. Brown crystals (suitable for crystallographic measurement) were obtained, filtered and dried in air. Yield = 0.0875 g (46.0 %). Selected IR (ATR, cm^{-1}): 3356br, 1603s, 1578s, 1434s, 1324s, 1174s, 1040s, 748s, 607w, 528w. UV-Vis (DCM, nm {ε /M^{-1} cm^{-1}}): 243 {5.21 x 10^4}, 289 {4.08 x 10^4}, 409 {1.91 x 10^4}. Anal. Calc.(Found) for $C_{52}H_{39}Cu_2N_4O_{7.5}$ C, 64.59 (64.12); H, 4.07 (4.30); N, 5.79 (5.51) %.

3.10.3.4 Preparation of chromium complex

3.10.3.4.1 $[CrO1(ONO_2)]0.5H_2O.0.2MeCN$: 0.0129 g (0.03 mmol) of **H_2O1** and 0.0127 g (0.03 mmol) of $Cr(NO_3)_3.9H_2O$ were weighed into a vial, 2 mL MeCN was added and the set-up left to stand for 7 days. The green crystals (suitable for crystallographic measurements) obtained was filtered, washed with MeCN and dried in air. Yield = 0.0121 g (71.2 %). Selected IR (ATR, cm^{-1}): 1610s, 1584s, 1536s, 1486w, 1465s, 1441s, 1382s, 1349s, 1312s, 1240s, 1199w, 1156w, 1123w, 1101s, 1004s, 929s, 847s, 822s, 748s, 621s, 552s, 518s, 456s. Anal. Calc.(Found) for $C_{26.4}H_{19.6}CrN_{3.2}O_{6.5}$ C, 58.98 (58.83); H, 3.67 (3.45); N, 8.34 (8.41) %.

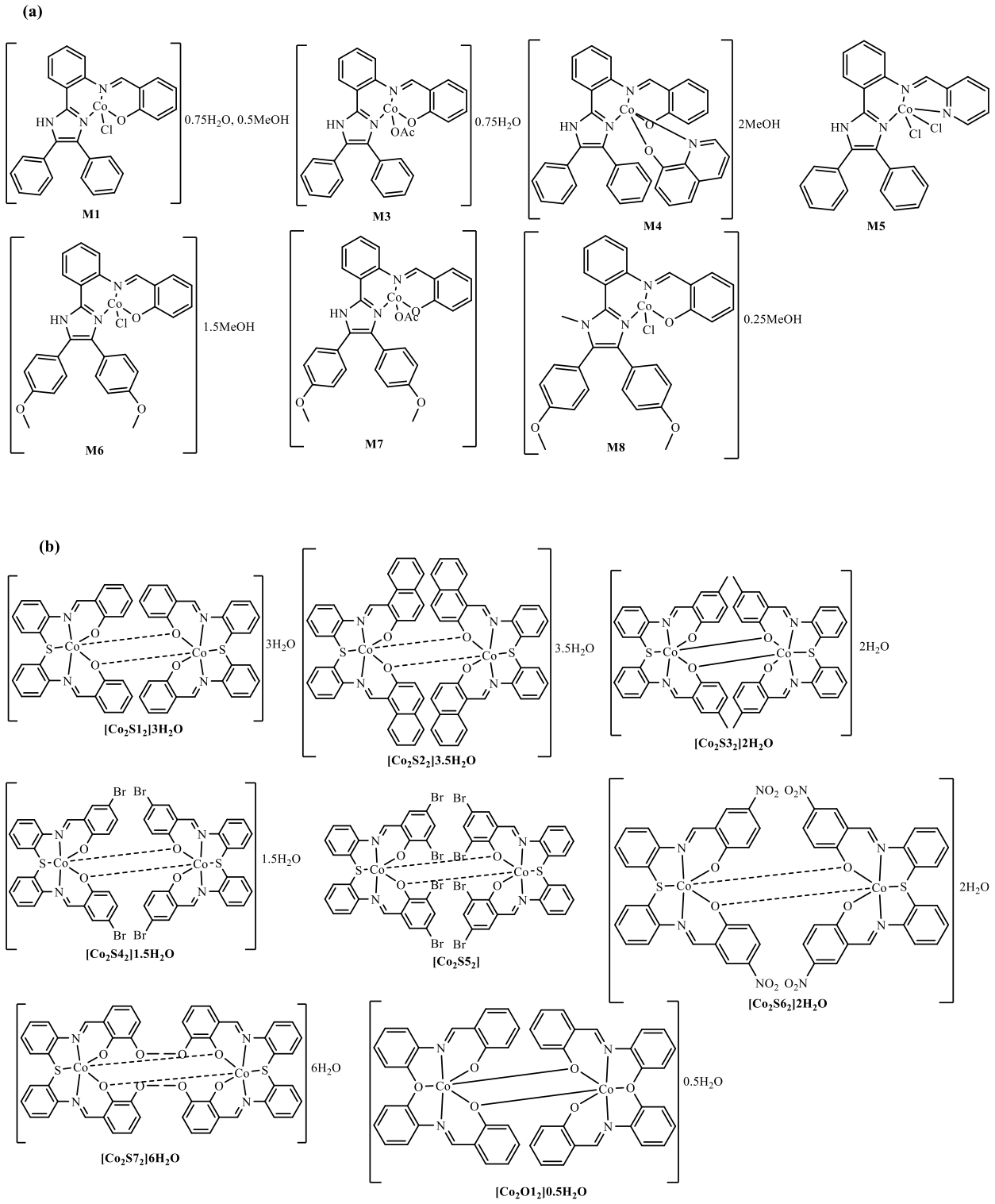

Figure 3.1: (a) Proposed structures for Co^{II} NNO/NNN imine complexes. (b) Proposed structure for the dinuclear Co^{II} pentadentate imine complexes

CHAPTER FOUR

RESULTS AND DISCUSSION

4.1 Synthesis

Difficulties were encountered in the preparation of the 1,2-bisimidazoles series, even with adoption of different strategies. Similar challenges have been reported in literature (Yamashita and Abe 2014). The 1,3- and 1,4- series were obtained in low to excellent yields.

The NNO and NNN imidazole imines were obtained in three steps: a first step involving a one pot synthesis of the nitro-imidazoles; followed by reduction {using hydrogen at 80 bars} to afford respective amines; the final step involved condensation of the appropriate amines with salicylaldehyde {for NNO imines} or pyridine-2-carboxaldehyde {for NNN imines} in 1:1 ratio. The reaction of the amines with salicylaldehyde gave isolable products, however, only the **N-H** variants {excluding **A1**} gave isolable products with pyridine-2-carboxaldehyde. In the failed cases with pyridine-2-carboxaldehyde, TLC showed new products were formed but isolation by column chromatography/precipitation {by means of different solvents} generated the starting amines {chromatography} or an oily mixture {precipitation}. The isolated compounds were obtained in excellent yields. The preparation of the pentadentate {ONSNO/ONONO} imines followed same procedure as the NNO/NNN imines and products were also obtained in excellent yields. The azo-imines were prepared in two steps: a first step involving the oxidation of *o*-phenylenediamine {using PbO_2}, followed by condensation of the diamine obtained with appropriate aldehyde derivative to give respective imines. While the azo-diamine was obtained in poor yield, the reddish coloured imines were obtained in excellent yields. Attempts to prepare other analogues {similar to those of the pentadentate imines} proved difficult {analysis of the materials obtained did not fit expected outcomes}.

4.2 ^{1}H-NMR of the compounds

Selected nuclear magnetic resonance (NMR) chemical shift values for the prepared organic molecules are presented in **Tables 4.1** – **4.2**.

The presence of the methoxy group {in the bis-imidazole series, **BI$_2$** and **BI$_6$**} resulted in a slight upfield shift in the N-H$_{imidazole}$ peak {**Table 4.1**(**a**), **Fig. S44** and **Fig. S45**}. This trend was also observed for **N4** and **A4** {in comparison to **N2** and **A2**, respectively} {**Table 4.1**(**b**), **Fig. S46** and **Fig. S47**}. The introduction of π-electron rich phenanthrene {**Phen**}, produced the most downfield shift of the N-H$_{imidazole}$ {**Fig. S46** and **Fig. S47**} – while the methoxy group gave rise to ≈ 0.20 ppm shift, the **Phen** group gave rise to ≈ 0.80 ppm. Substitution at the **N-H** position {**N-Me** and **N-Ph**} of the imidazole amines generally resulted in an upfield shift in the NH$_{2amine}$ peak {**Table 4.1**(**b**) and **Fig. S48** – **S50**} – while the NH$_{2amine}$ of the **N-H** analogues generally resonated around 7.00 ppm, it resonated around 6.00 ppm in the substituted analogues. This trend {upfield shift upon substitution} was also observed for the N=CH peak of the imidazole imines {**Table 4.1**(**b**) and **Fig. S51** – **S53**}, while a downfield shift was observed with respect to the OH peak {**Fig. S52**}.

In comparison to **H$_2$S1**, the introduction of π-electron rich naphthalene as well as replacing **S** with the more electronegative **O**, gave rise to a downfield shift in the N=CH and OH peaks {naphthalene showing the greatest shift} {**Table 4.2** and **Fig. S54** – **S55**}. The *p*-methyl and *p*-bromo substitutions only resulted in slight changes in the chemical shift values of the N=CH and OH peaks; the dibromo {*o* and *p*} and *o*-methoxy substitutions produced a downfield shift in the OH peak but no significant shift in the N=CH peak {**Table 4.2** and **Fig. S54** – **S55**}.

Table 4.1(a): Effect of structural modification on the N-H chemical shift values of the bis-imidazole **{BI_1 – BI_7}**

	N-H δ (ppm)
BI_1	12.86
BI_2	12.66
BI_3	Absent
BI_4	Absent
BI_5	12.77
BI_6	12.57
BI_7	Absent

Table 4.1(b): Effect of structural modification on the N-H, NH_2, O-H and N=CH chemical shift values of the nitro-imidazoles **{N1 – N9},** imidazole-amines **{A1 – A9}** and imidazole-imines **{1a – 1i}.**

	N-H δ (ppm)			N-H δ (ppm)	NH_2 δ (ppm)			O-H δ (ppm)	N=CH δ (ppm)
N1	12.12		**A1**	11.66	6.86		**1a**	10.10	N.O[a]
N2	12.97		**A2**	12.46	6.98		**1b**	N.O[a]	9.92
N3	13.77		**A3**	13.21	7.33		**1c**	10.52	N.O[a]
N4	12.78		**A4**	12.28	6.97		**1d**	N.O[a]	9.90
N5	Absent		**A5**	Absent	5.87		**1e**	12.67	9.09
N6	Absent		**A6**	Absent	5.78		**1f**	12.37	9.13
N7	Absent		**A7**	Absent	5.86		**1g**	12.69	9.09
N8	Absent		**A8**	Absent	6.11		**1h**	12.61	8.60
N9	Absent		**A9**	Absent	5.93		**1i**	12.55	8.86

[a]Not observed, possibly due to overlap with the π-conjugated protons.

Table 4.2: Effect of structural modification on the O-H and N=CH chemical shift values of the ONSNO/ONONO imines **{H_2S1 – H_2O1}.**

	O-H δ (ppm)	N=CH δ (ppm)
H_2S1	12.83	8.94
H_2S2	15.23	9.73
H_2S3	12.52	8.87
H_2S4	12.78	8.90
H_2S5	14.03	8.96
H_2S6	N.O[a]	9.12
H_2S7	12.95	8.94
H_2O1	13.14	9.00

[a]Not observed, possibly due to poor solubility of the nitro analogue

4.3 Mass Spectrophotometry (MS) of the compounds

Proposed fragmentation of the nitro-imidazoles {**Schemes 4.1 – 4.3**}, imidazole amines {**Schemes 4.4 – 4.6**}, tridentate NNO imines {**Scheme 4.7**}, tridentate NNN imines {**Scheme 4.8**}, pentadentate ONSNO/ONONO imines {**Schemes 4.9 – 4.11**}, pentadentate diazo imines {**Scheme 4.12**} and the Co^{II} complexes of the NNO/NNN imines {**Schemes 4.13 – 4.15**} are presented below. In almost all cases {nitro-imidazoles as well as imidazole amines} the molecular ion $\{M^+\}$ generated the base peak {a similar trend was not observed in the NNO/NNN imines and their Co^{II} complexes}. Electrospray ionisation {ESI} measurement of **N3** as well as its amine {**A3**} gave only the M^+. ESI measurement of **H_2S5** also gave its M^+, which was not observed with high energy electron impact {EI} technique. The loss of $-NH_2$ group was observed in the imidazole amines.

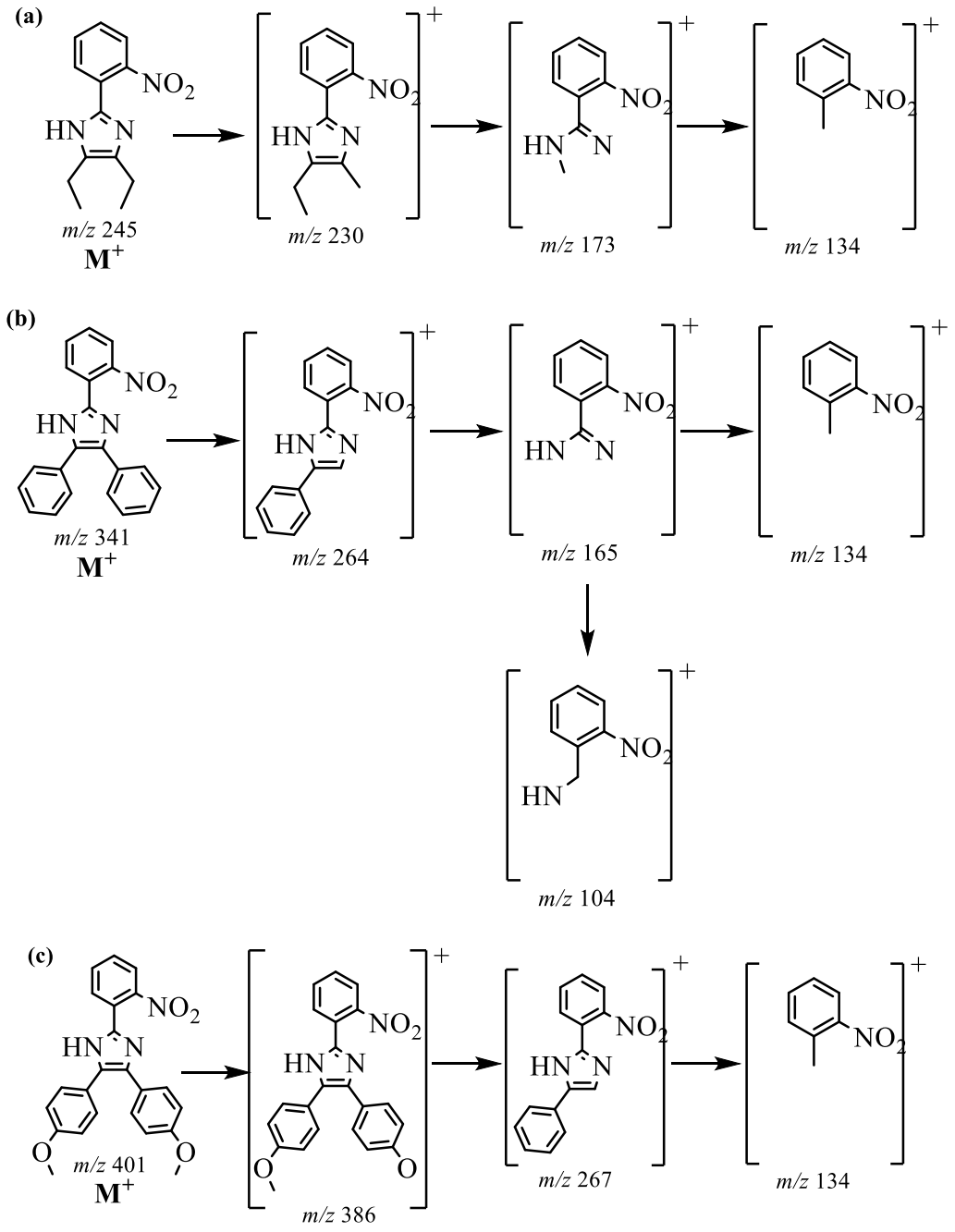

Scheme 4.1: Proposed fragmentation pattern of (a) **N1,** (b) **N2** and (c) **N4.**

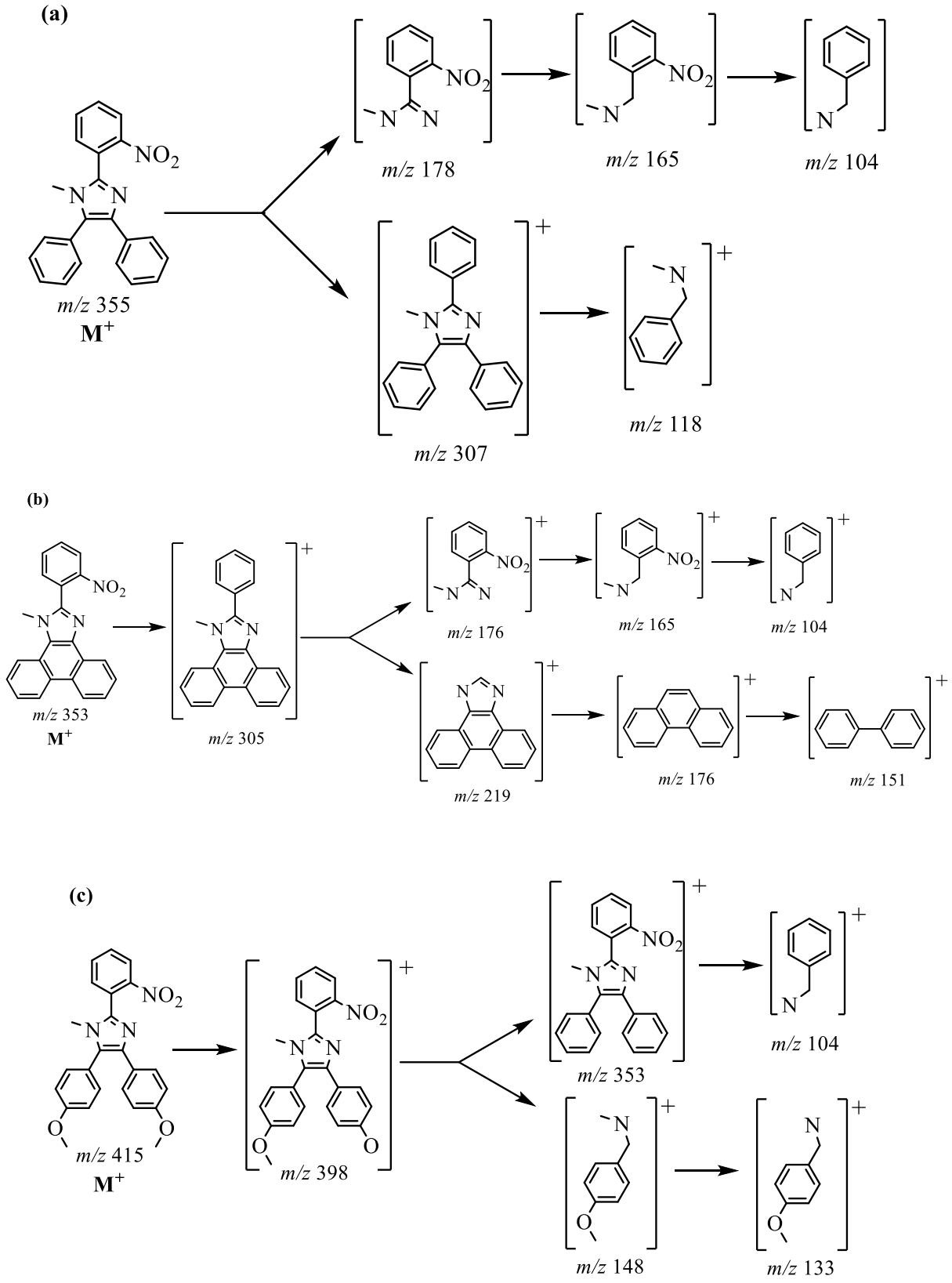

Scheme 4.2: Proposed fragmentation pattern of (a) **N5,** (b) **N6** and (c) **N7**

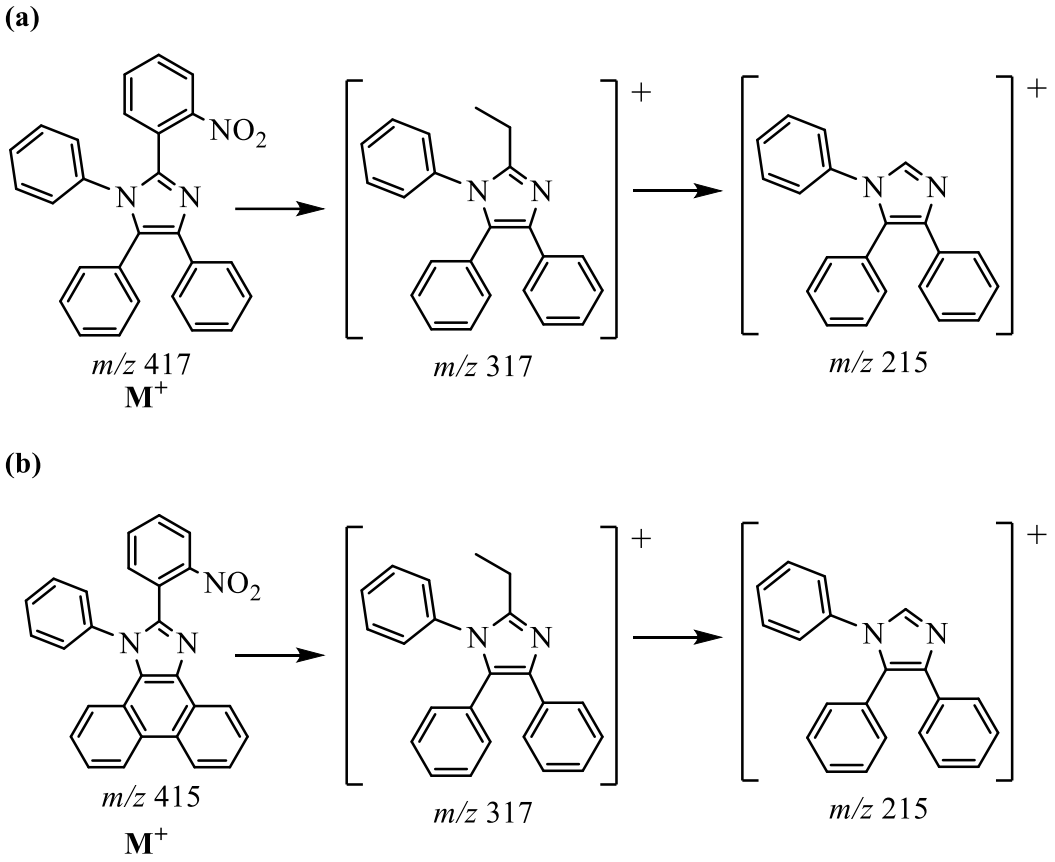

Scheme 4.3: Proposed fragmentation pattern of (a) **N8** and (b) **N9**

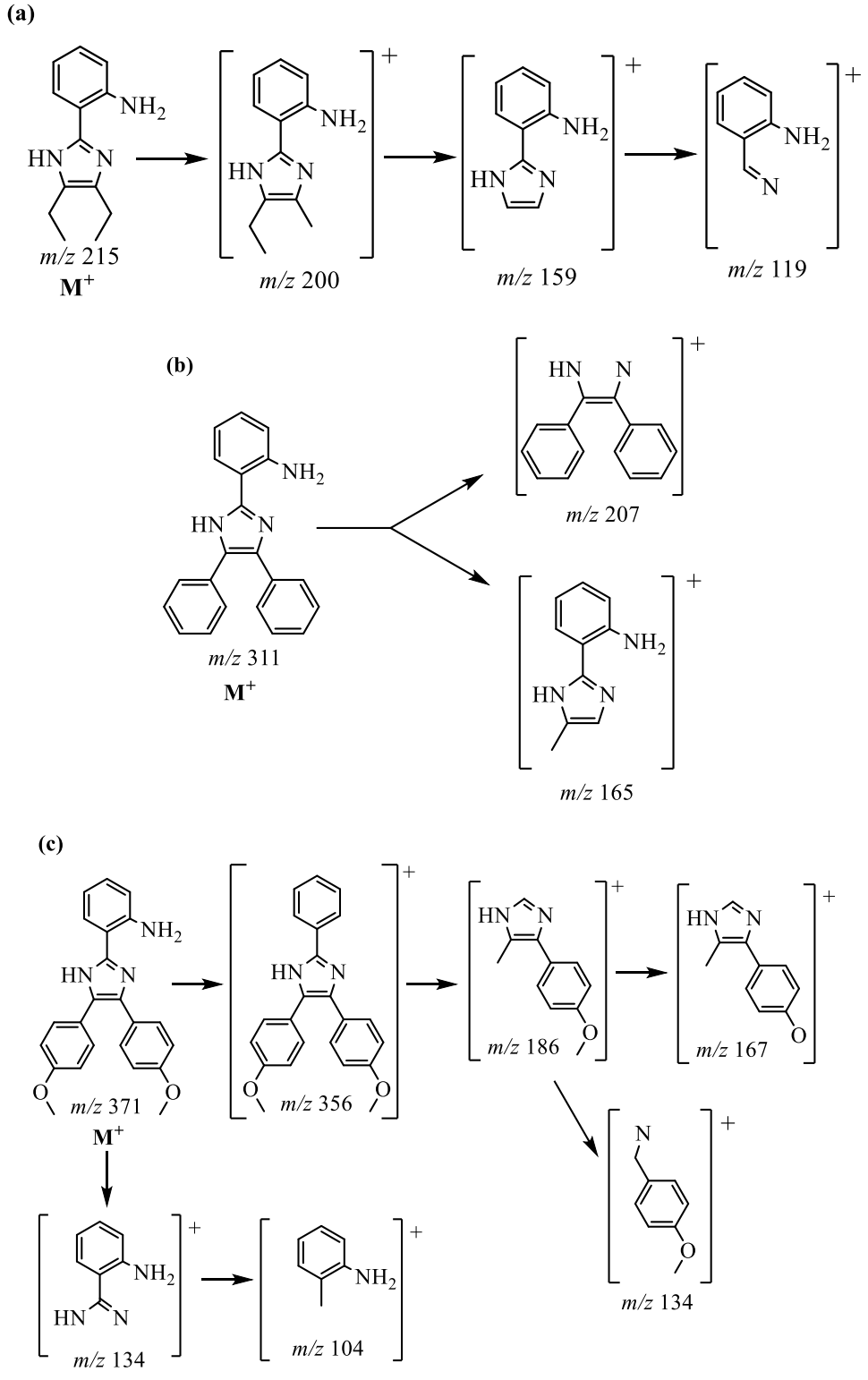

Scheme 4.4: Proposed fragmentation pattern of (a) **A1,** (b) **A2** and (c) **A4**

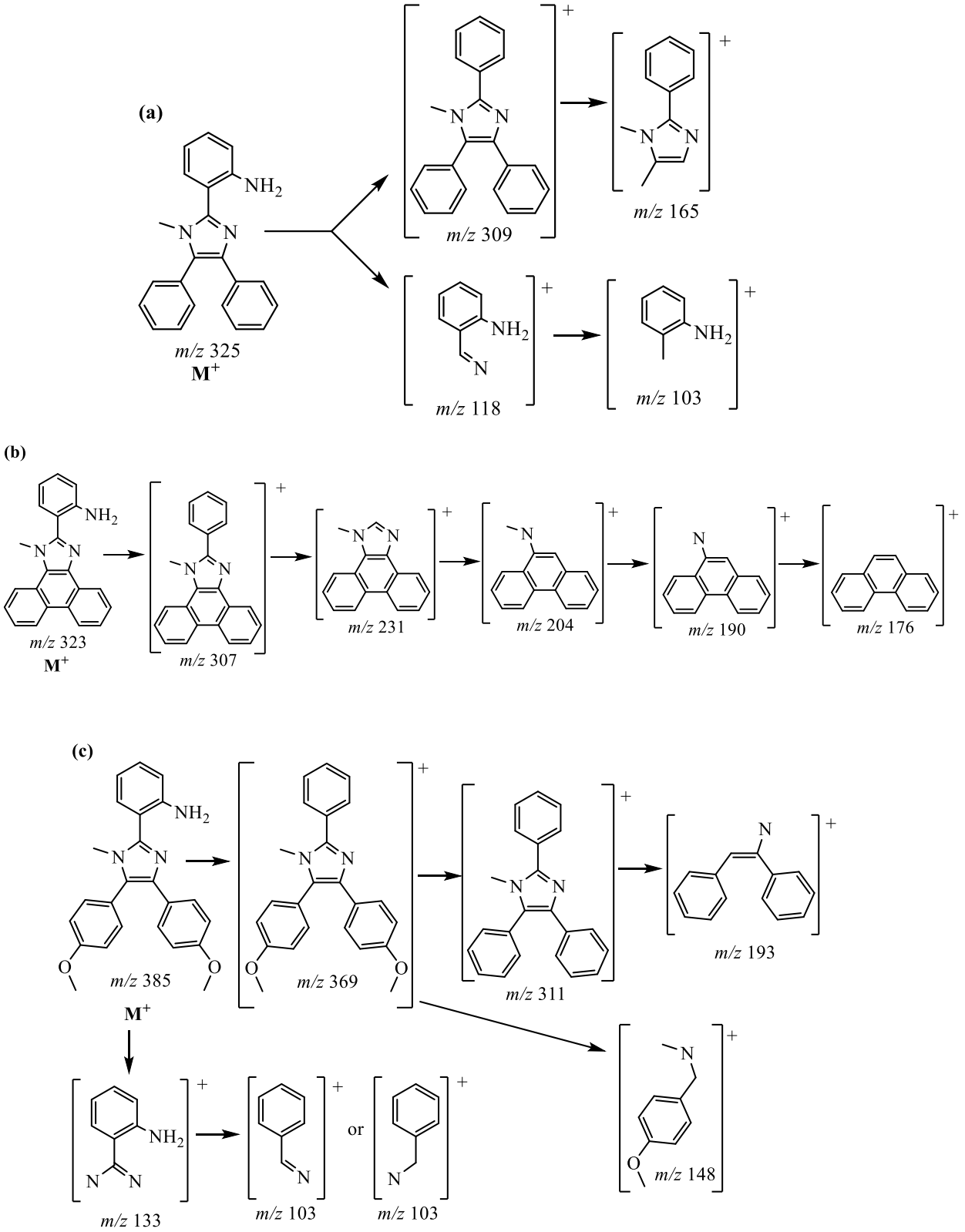

Scheme 4.5: Proposed fragmentation pattern of (a) **A5,** (b) **A6** and (c) **A7**

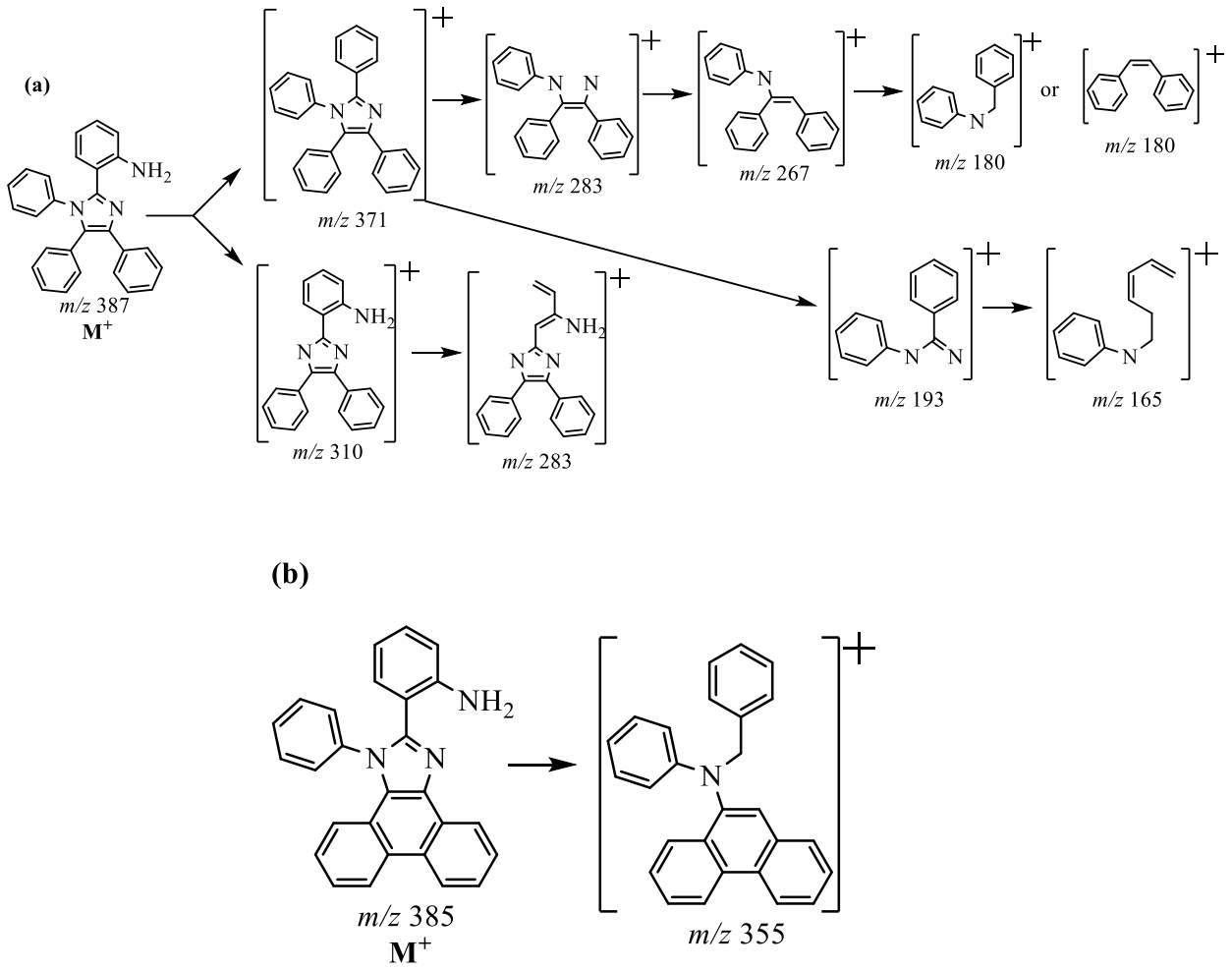

Scheme 4.6: Proposed fragmentation pattern of (a) **A8** and (b) **A9**

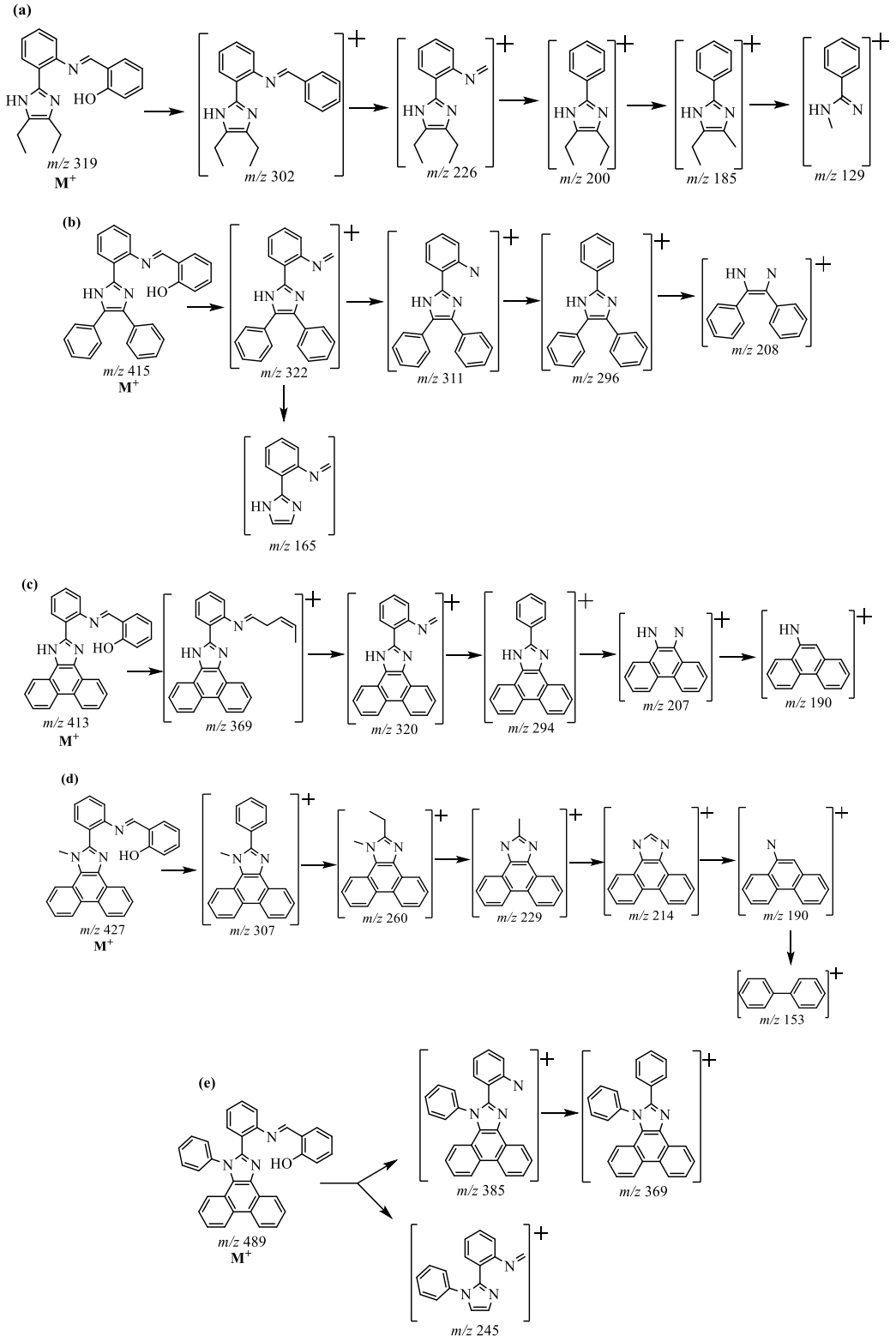

Scheme 4.7: Proposed fragmentation pattern of (a) **I_1,** (b) **I_2,** (c) **I_3,** (d) **I_6** and (e) **I_9**

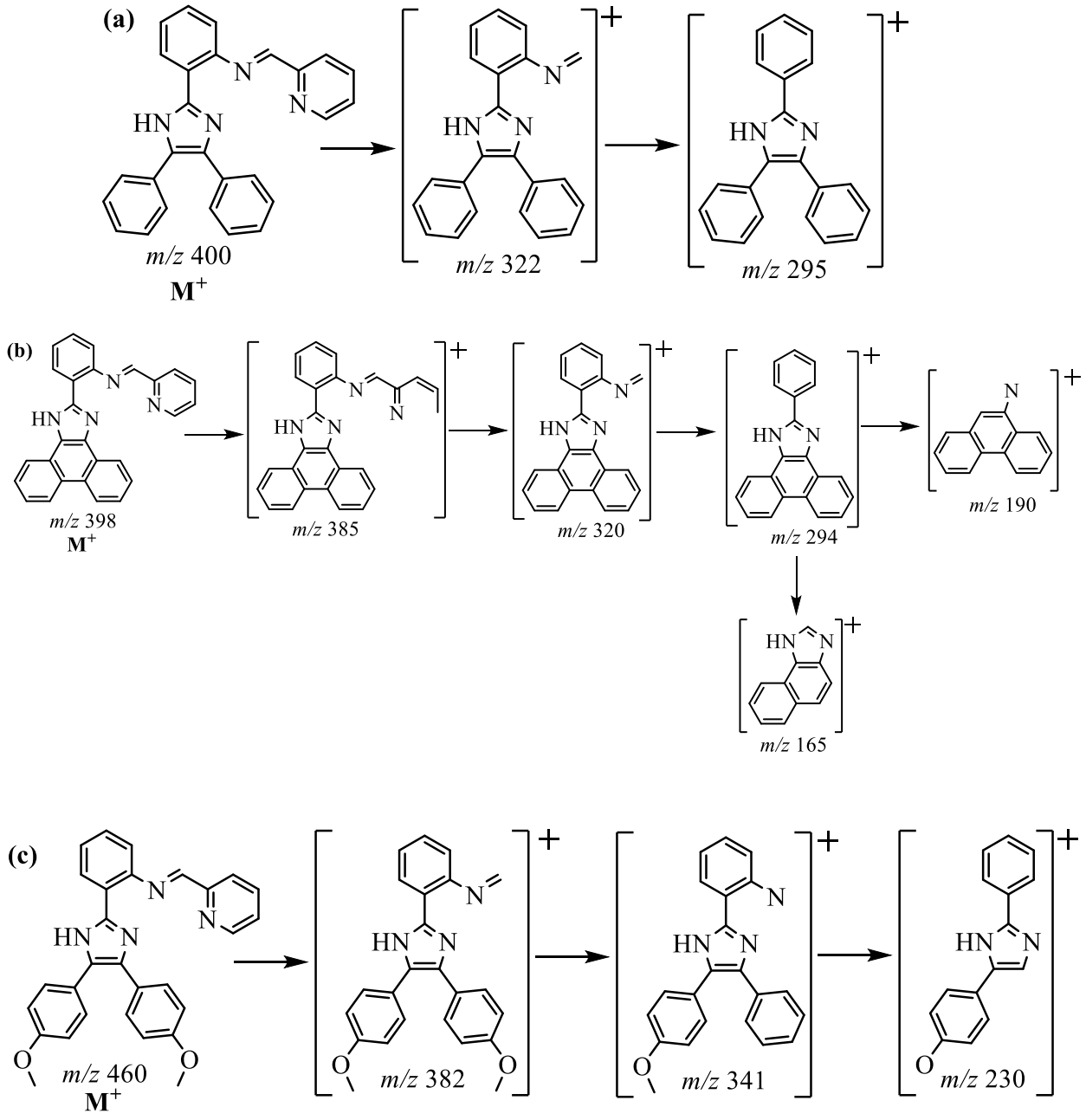

Scheme 4.8: Proposed fragmentation pattern of (a) $\mathbf{I_{N2}}$, (b) $\mathbf{I_{N3}}$ and (c) $\mathbf{I_{N4}}$

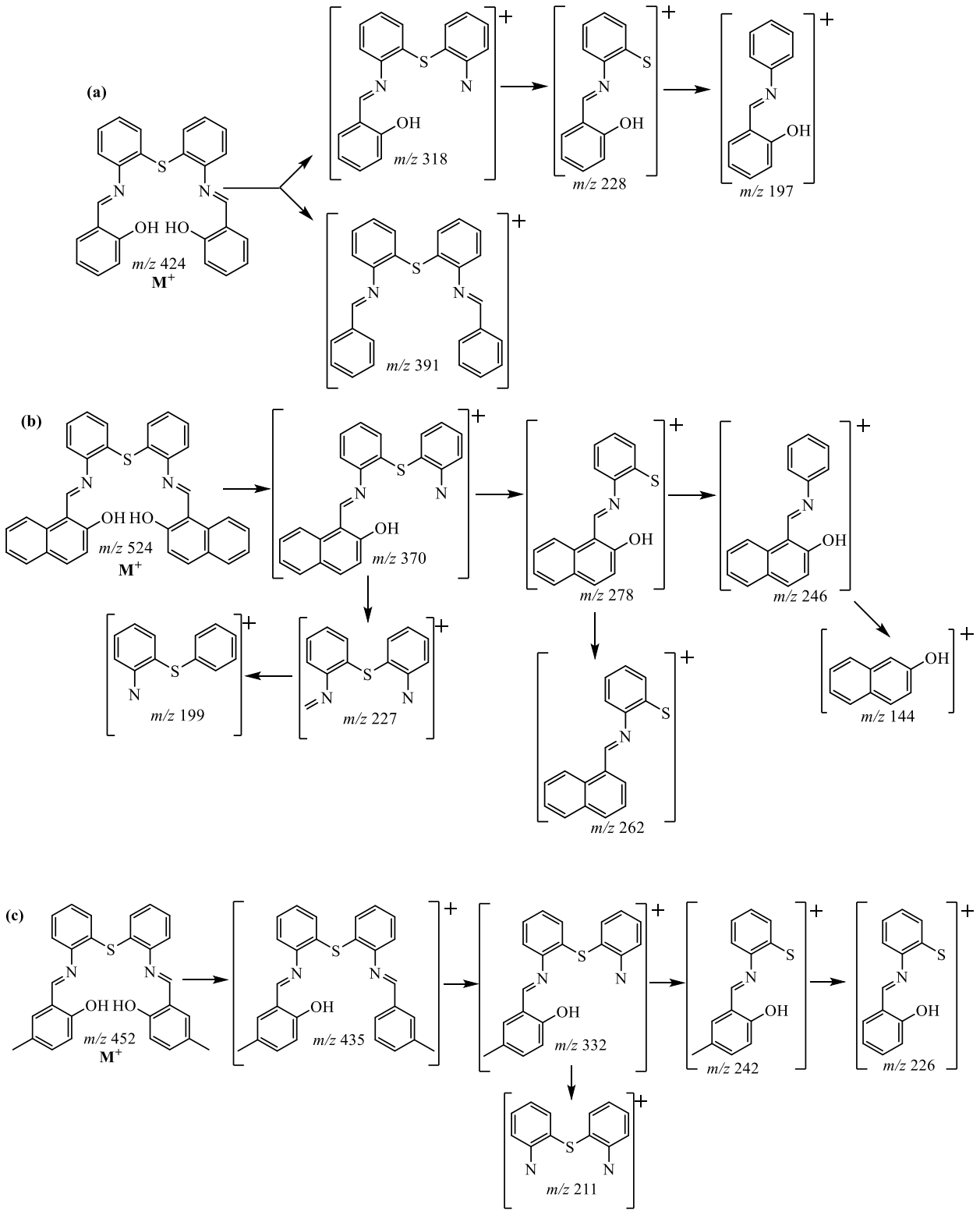

Scheme 4.9: Proposed fragmentation pattern of (a) **H_2S1,** (b) **H_2S2** and (c) **H_2S3**

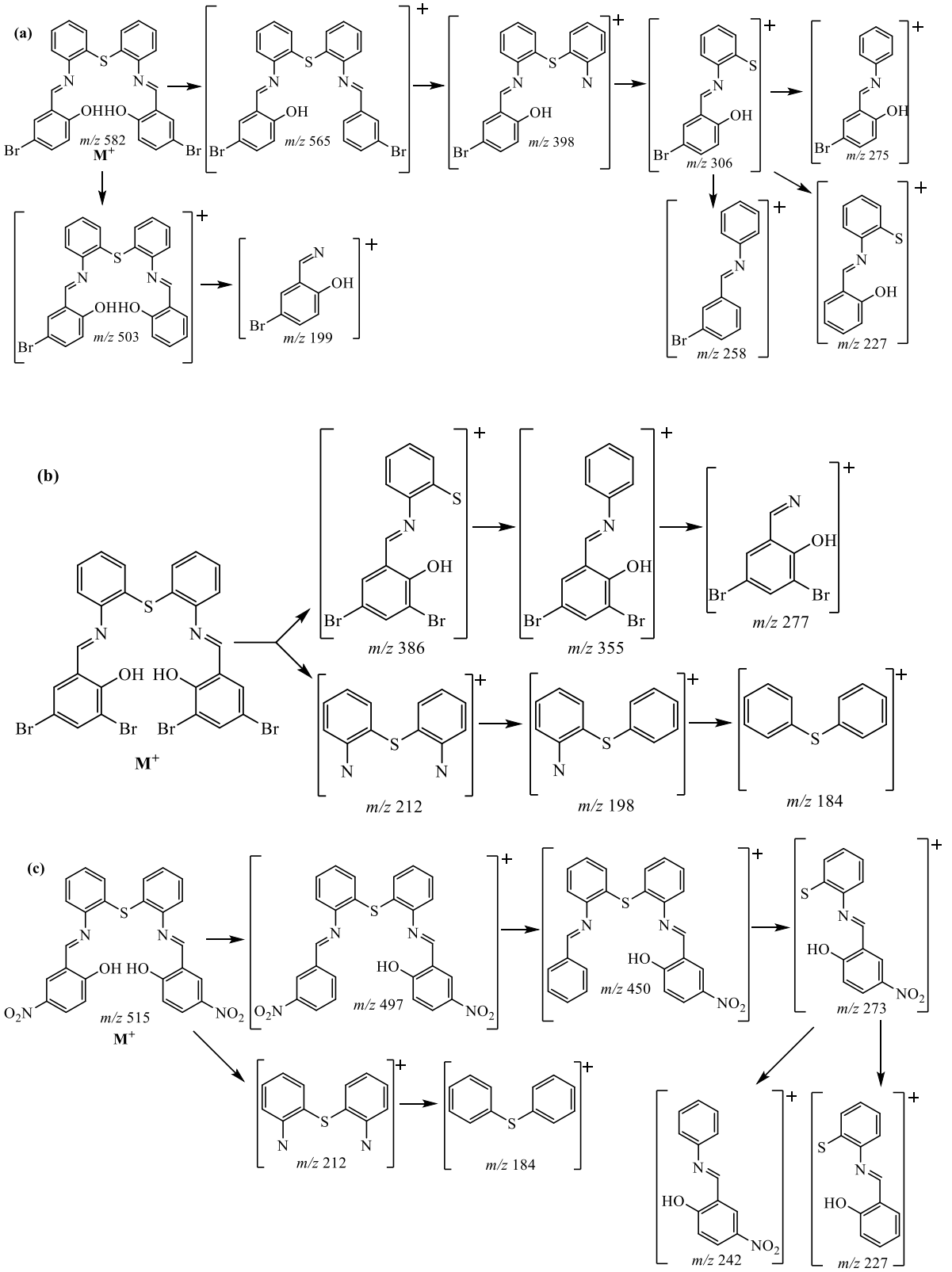

Scheme 4.10: Proposed fragmentation pattern of (a) **H_2S4,** (b) **H_2S5** and (c) **H_2S6**

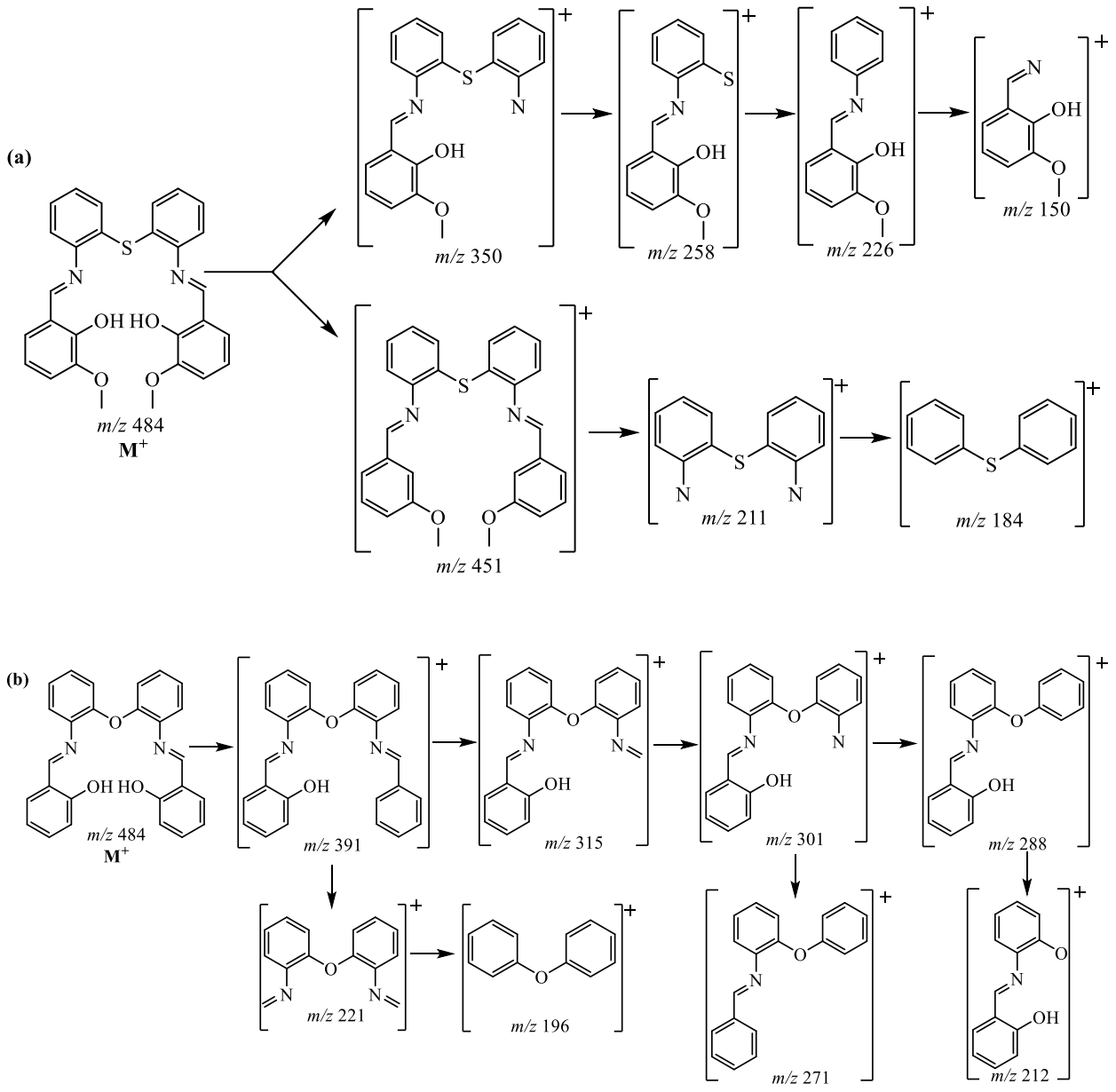

Scheme 4.11: Proposed fragmentation pattern of (a) **H_2S7** and (b) **H_2O1**

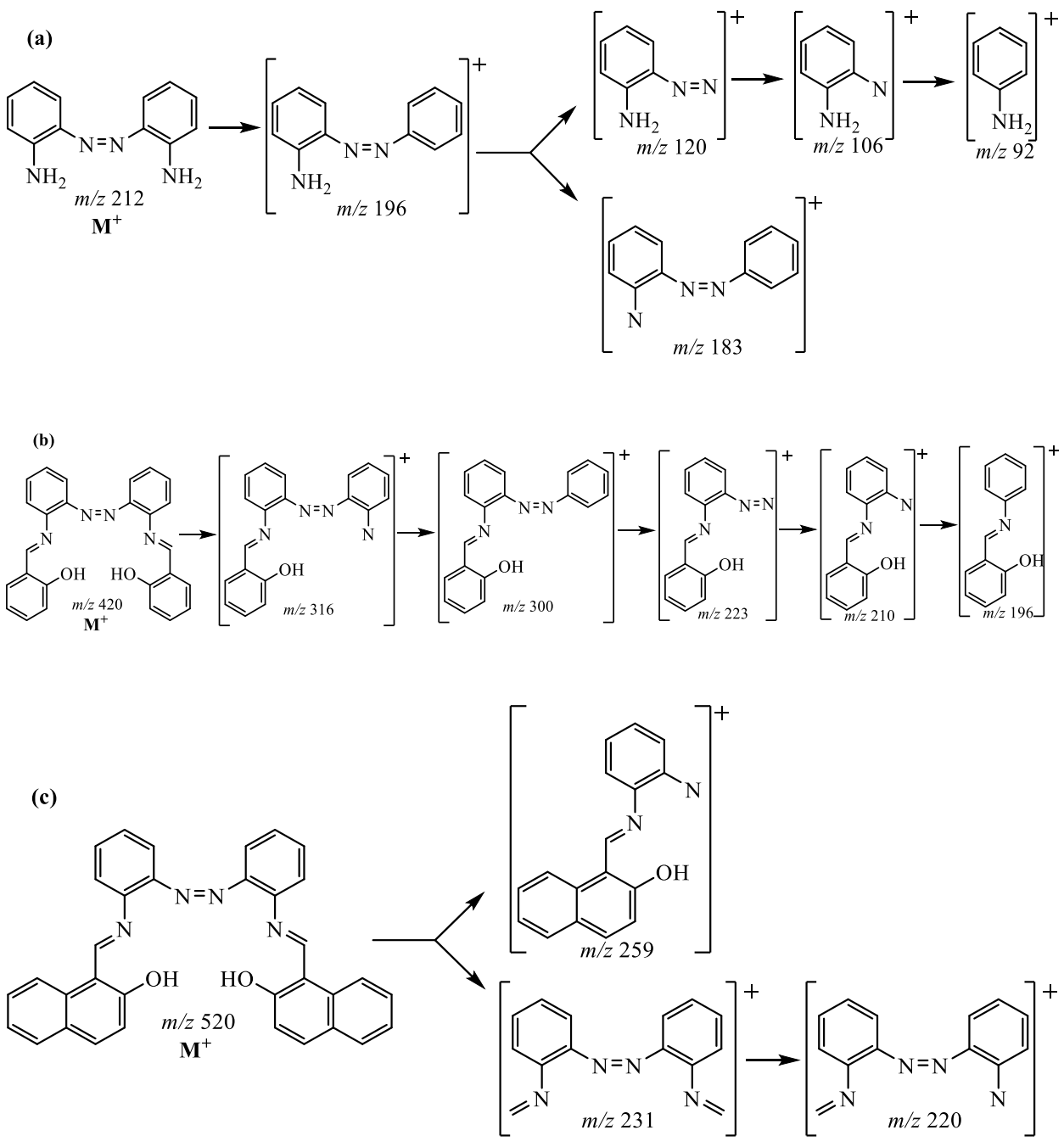

Scheme 4.12: Proposed fragmentation pattern of (a) **DAB,** (b) **H_2AI_1** and (c) **H_2AI_2**

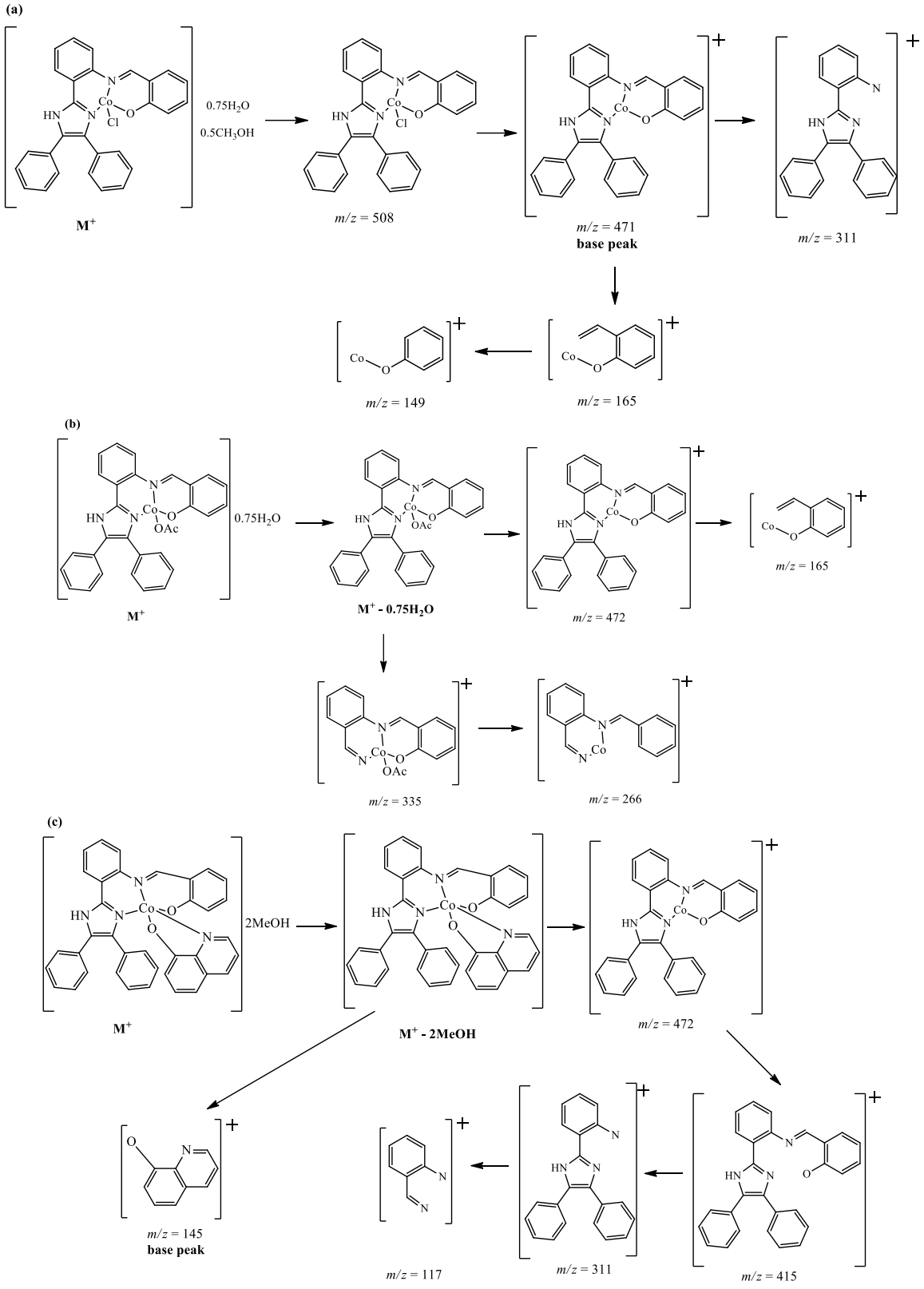

Scheme 4.13: Proposed fragmentation pattern of (a) **M1,** (b) **M3** and (c) **M4**

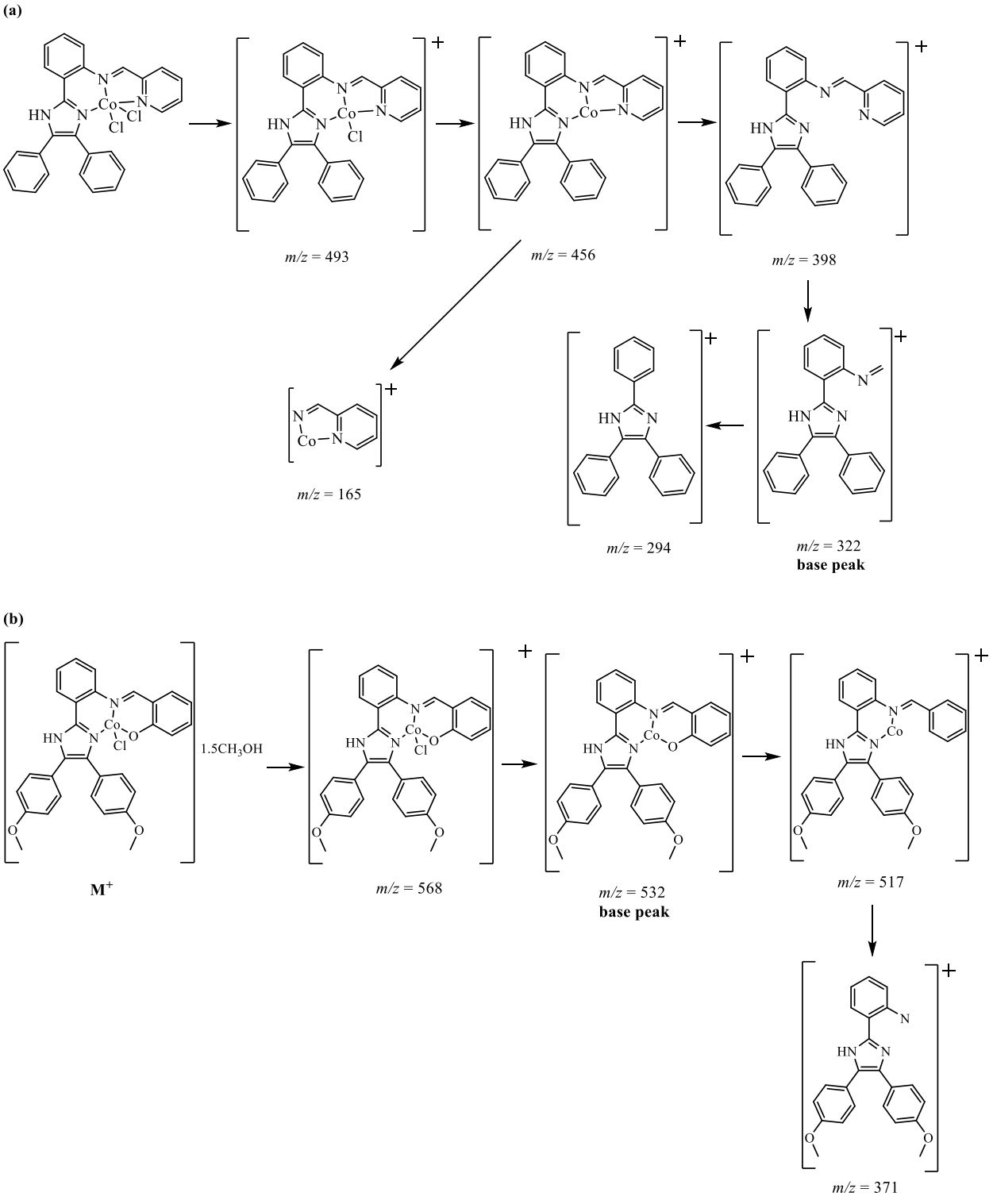

Scheme 4.14: Proposed fragmentation pattern of (a) **M5** and (b) **M6**

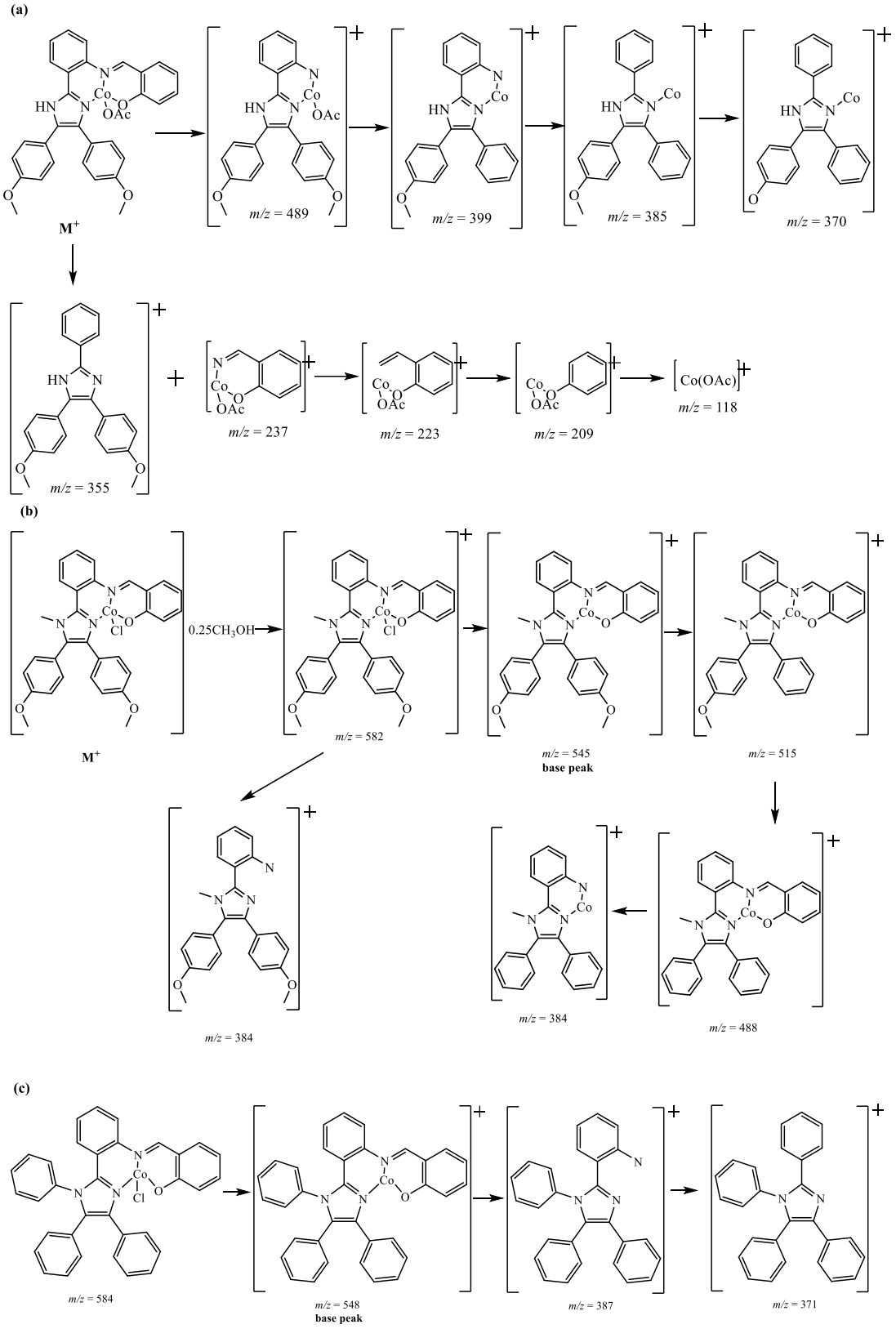

Scheme 4.15: Proposed fragmentation pattern of (a) **M7,** (b) **M8** and (c) **M9**

4.4 Thermal Stability of the compounds

4.4.1 Thermal stability of the NNO imidazole imines and the Co^{II} complexes

The thermogravimetric {TG} curves of the NNO imines are presented in **Fig. S57 – S64**, and the data in **Table 4.3**. All the compounds exhibited multistage decomposition with thermal stabilities ≥ 250°C and complete decomposition occurring at ≥ 475°C {the **Phen** based compounds showed complete decomposition at temperatures higher than those observed for the **Ph** and **MeOPh** analogues}. Generally, the observed stability trend was **Phen** ≈ **MeOPh** > **Ph**, the exception was **I_9** which showed a slight change at ≈ 210°C before a more significant change at ≈ 325°C. The loss of the PhOH group in **I_9** occurred over a long temperature range {in two phases}.

Like the NNO imines, the Co^{II} complexes displayed multistage decomposition {**Fig. S65 – S71** and **Table 4.4**}. The loss of solvents {H_2O, MeOH}, in **M1**, **M4** and **M6**, occurred at ≤ 100°C, suggesting they were not coordinated (Joseyphus and Nair 2009; Su *et al*., 2011; Chen *et al*., 2011).

4.4.2 Thermal stability of the pentadentate (ONSNO/ONONO) complexes

Like the NNO series, the dinuclear Co^{II} complexes {**Fig. S72 – S79** and **Table 4.5**}, di- and tri-nuclear Cu^{II} complexes {**Fig. S80 – S84** and **Table 4.6**} and mononuclear Cr^{III} complex {**Fig. S85** and **Table 4.6**} exhibited multistage decomposition. Loss of solvents {H_2O, THF, MeCN} was observed in the range ≤ 100°C to < 300°C.

Table 4.3: TG data of the NNO imidazole imines

Compound	Temperature (ºC)	Experimental %	Theoretical %	Loss fragment
I_2	250	43.41 {180.37 g}	44.34	HOPhN=CHPh
	400			Rest of the organic molecule
	> 525			
I_3	273	4.31 {17.81 g}	4.11	OH of phenol
	300	4.48 {18.51 g}	4.36	H_2O {OH of phenol + H of imidazole}
	400	21.31 {84.20 g}	22.47	Ph-CH= {from phenol side}
	500	18.44 {76.03 g}	18.40	Ph from imidazole side of the structure
	> 600			Rest of the organic molecule
I_4	270	5.59 {26.58 g}	6.53	MeO
	325	24.16 {107.39 g}	24.10	PhOMe
	> 450			Rest of the organic molecule
I_5	200	51.91 {222.96 g}	51.52	Portion of Imidazole ring + 2 Ph
	475			Rest of the organic molecule
	> 575			
I_6	275	42.49 {181.65 g}	43.09	HOPhN=CHPh
	500			Rest of the organic molecule
	> 575			
I_7	275	8.62 {42.20 g}	9.81	MeO + OH
	350			Rest of the organic molecule
	> 475			
I_8	275	39.28 {193.10 g}	39.92	HOPhN=CHPh
	400	7.69 {22.71 g}	8.81	C=N of Imidazole ring
	500	28.43 {76.58 g}	28.63	Ph on N of Imidazole ring
	> 575			Rest of the organic molecule
I_9	210	0.92	19.20	PhOH
	325	17.38 {93.03 g}		
	475	6.71 {27.01 g}	6.82	N=CH
	520	16.47 {63.03 g}	17.07	Portion from Ph of imidazole side
	> 600			Rest of the organic molecule

Table 4.4: TG data of the Co^{II} NNO complexes

Compound	Temperature (ºC)	Experimental %	Theoretical %	Loss fragment
M1	< 100	2.68 {14.43 g}	2.51	H_2O
	325	6.25 {32.81 g}	5.48	H_2O + MeOH
	400	11.85 {60.30 g}	10.11	Cl + O from phenol group
	> 475			Rest of the complex
M3	293	10.87 {59.35 g}	10.81	AcO
	> 600			Rest of the complex
M4	100	24.04 {163.87 g}	24.82	OPhCH + 2 MeOH
	< 375			
	> 375			Rest of the complex
M5	280	24.34 {129.08 g}	24.54	PyCH=N + portion of Ph on Imidazole ring
	< 500			
	> 550			Rest of the complex
M6	< 100	7.31 {45.10 g}	7.79	MeOH
	275			
	< 325			
	> 425			Rest of the complex
M7	250	12.25 {72.58 g}	12.84	Ph from Phenol side
	> 575			Rest of the complex
M9	325	21.92 {128.23 g}	21.80	OPh + Cl
	< 475			
	> 500			Rest of the complex

Table 4.5: TG data of the dinuclear Co^{II} {ONSNO/ONONO} complexes

Compound	Temperature (ºC)	Experimental %	Theoretical %	Loss fragment
$[Co_2S1_2]3H_2O$	< 100	4.95 {50.34 g}	5.32	H_2O
	125	13.87 {133.55 g}	13.62	OPh-CH=N-C
	150			
	175			
	250	17.62 {146.55 g}	17.70	C_5H_4-S-C_4H_3
	375	20.83 {142.59 g}	21.06	H_2C-N=CH-PhO
	525	26.76 {144.60 g}	26.68	OPh-CH=N-C_2H
	> 725			Rest of the complex
$[Co_2S2_2]3.5H_2O$	< 100	36.58 {448.53 g}	36.17	H_2O + ONaph-CH=N-Ph-S-Ph-N=CH
	350			
	425	28.29 {221.41 g}	27.89	O-Naph + Ph
	500	19.74 {111.41 g}	19.16	S-Ph
	> 650			Rest of the complex
$[Co_2S3_2]2H_2O$	< 100	26.80 {282.74 g}	27.43	H_2O + OPh(Me)-CH=N-Ph-S-C
	375			
	400	34.53 {264.38 g}	34.39	C_5H_4-N=CH-PhO + C_5H_6
	450	19.59 {98.40 g}	20.53	Ph-N=CH
	> 650			Rest of the complex
$[Co_2S4_2]1.5H_2O$	< 100	76.36 {1003.60 g}	76.88	H_2O + **S4** + OPh(Br)-CH=N-Ph-S-Ph-N
	375			
	500			
	> 675			Rest of the complex
$[Co_2S5_2]$	375	12.98 {206.91 g}	13.16	$C_4H_2Br_2$
	400	53.35 {738.45 g}	53.32	**S5**
	500			
	> 625			Rest of the complex
$[Co_2S6_2]2H_2O$	< 100	22.12 {260.77 g}	22.08	H_2O + (O_2N)Ph-CH=N-Ph
	325			
	375	47.22 {433.78 g}	47.72	OPh(NO_2)-CH=N-Ph-S + O + OPh(NO_2)-CH
	450			
	> 500			Rest of the complex
$[Co_2S7_2]2H_2O$	< 100	22.43 {267.15 g}	22.61	H_2O + OPh(OMe)-CH=N-C
	175			
	325	36.61 {337.47 g}	36.17	OPh(OMe)-CH=N-Ph-S-Ph
	< 425			
	> 425			Rest of the complex
$[Co_2O1_2]0.5H_2O$	< 100	11.16 {104.88 g}	10.76	H_2O + OPh
	375			
	425	71.80 {602.15 g}	71.74	CH=N-Ph-O-Ph-N=CH-PhO + Ph-O-Ph-N=CH-PhO
	> 500			Rest of the complex

Table 4.6: TG data of the di-/tri-nuclear Cu^{II} and mononuclear Cr^{III} {ONSNO/ONONO} complexes

Compound	Temperature (ºC)	Experimental %	Theoretical %	Loss fragment
$[Cu_3S1_2(OAc)_2]2.75H_2O$	175	4.18 {50.30 g}	4.12	H_2O
	200	33.87 {390.77 g}	33.76	OAc + OPhCH=N-Ph-S-Ph-N=C
	275			
	350	43.17 {329.94 g}	43.23	OPhCH=N-Ph-S-Ph-N=CH
	> 650			Rest of the complex
$[Cu_3S2_2(OAc)_2]5.5H_2O$	< 100	4.86 {70.62 g}	4.96	H_2O
	175			
	300	57.03 {787.58 g}	57.93	**S2** + O-Naph-CH=N-Ph-S
	> 500	25.35 {140.44 g}	25.66	O-Naph
	> 650			Rest of the complex
$[Cu_2S2_2]2THF$	100	56.48 {743.59 g}	56.43	THF + **S2** + Ph
	250			
	350			
	375	21.32 {122.30 g}	21.30	S-Ph-N
	> 675			Rest of the complex
$[Cu_2S3_2]3H_2O$	100	2.52 {27.27 g}	2.50	H_2O
	175	18.94 {199.86 g}	19.50	H_2O + MePh-CH=N-Ph
	325	55.43 {462.82 g}	55.76	**S3** + Me
	> 600			Rest of the complex
$[Cu_2O1_2]1.5H_2O$	< 100	1.87 {18.08 g}	1.86	H_2O
	100	8.27 {78.48 g}	8.02	H_2O + O-C_4H_3
	150			
	325	74.04 {646.30 g}	73.40	**O1** + C_2H-CH=N-Ph-O-Ph-N
	> 450			Rest of the complex
$[Cr^{III}O1(ONO_2)]0.5H_2O.0.2MeCN$	125	31.79 {170.92 g}	31.86	H_2O + MeCN + ONO_2 + OPh
	275			
	375	54.18 {198.48 g}	53.29	CH=N-Ph-O-Ph
	> 425			Rest of the complex

4.5 Structural properties of compounds

4.5.1 Structural property of the palladium(II) complexes of the nitro-imidazoles

The crystal structures and crystallographic analyses of **Pd-N1** and **Pd-N3** are presented in **Fig. 4.1** and **Table 4.7**(**a**) respectively. The compounds crystallise in a monoclinic $P2_1/n$ and $P2_1/c$ space groups, respectively. The asymmetric units of **Pd-N1** and **Pd-N3** contained one Pd(II) ion, two neutral N donor atoms {one from the imidazole ligand and one from acetonitrile} and two chloride ions; resulting in a four-coordinate square planar geometry. The Pd-N bond lengths were ≈ 2.0 Å while the Pd-Cl bond lengths were ≈ 2.3 Å {**Table 4.7**(**b**)}; the bond distances agreed with earlier reports (Jose *et al*., 2018; Liu *et al*., 2019).

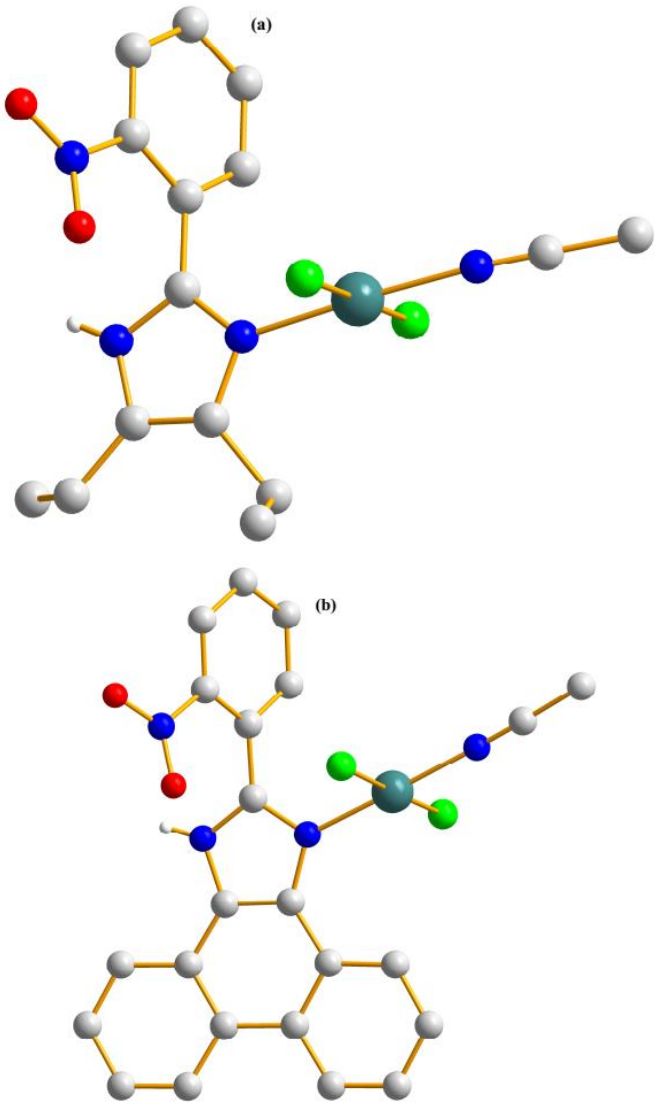

Figure 4.1: Molecular structure of (a) **Pd-N1** (b) **Pd-N3.** Solvents and some hydrogens are omitted for clarity.

Table 4.7(a): Crystallographic Data and Structure Refinement Parameters for **Pd-N1, Pd-N3.**

	Pd-N1	**Pd-N3**
Formula	$C_{15}H_{18}Cl_2N_4O_2Pd$	$C_{23}H_{16}Cl_2N_4O_2Pd$
Fw (g mol^{-1})	463.63	557.72
Cryst. syst.	Monoclinic	Monoclinic
Space group	$P2_1/n$	$P2_1/c$
a (Å)	12.3432(2)	8.1027(1)
b (Å)	11.9659(2)	19.0460(3)
c (Å)	13.1306(3)	17.2076(2)
α (deg)	90	90
β (deg)	108.350(1)	93.272(1)
γ (deg)	90	90
V ($Å^3$)	1840.74(6)	2652.69(6)
z	4	4
T(K)	133(2)	133(2)
δ_{Calc}(Mg/m^3)	1.673	1.602
F(000)	928	1288
μ(mm^{-1})	1.313	0.938
θ range for data collection (deg)	1.98 - 27.48	2.37 – 27.48
Measd reflns	14200	20779
Unique refln (R_{int})	4212 (0.0341)	6088 (0.0306)
No. of param	242	350
GOF on F^2	1.043	1.058
R1[I>2σ(I)]	0.0293	0.0288
wR2(all data)	0.0735	0.0698

Table 4.7(b): Selected bond lengths (Å) and angles (^{o})

	Pd-N1	**Pd-N3**
Pd(1)-N(1)	1.995(2)	1.9956(17)
Pd(1)-N(4)	2.004(2)	1.996(2)
Pd(1)-Cl(1)	2.3044(7)	2.2964(6)
Pd(1)-Cl(2)	2.2993(7)	2.2959(6)
N(1)-Pd(1)-N(4)	177.13(8)	178.74(8)
N(1)-Pd(1)-Cl(2)	90.31(7)	90.12(5)
N(4)-Pd(1)-Cl(2)	87.72(6)	89.66(6)
N(1)-Pd(1)-Cl(1)	89.56(7)	90.02(5)
N(4)-Pd(1)-Cl(1)	92.39(6)	90.16(6)
Cl(2)-Pd(1)-Cl(1)	179.80(2)	178.13(2)

4.5.2 Structural property of the imidazole amines, NNO imines and their metal complexes

The crystal structure and crystallographic analysis of **I_9.MeOH** is presented in **Fig. 4.2** and **Table 4.8**(**a**) respectively. **I_9.MeOH** crystallised in a triclinic Pī space group. The C=N_{imine} and hydrogen bond distances {**Table 4.8**(**b**)} agreed with reported ranges (Jiménez-Sánchez *et al*., 2014; Kanmazalp *et al*., 2019).

The crystal structures for imidazole amine complexes, **A2-CdI_2**, **A8-CdI_2**, **A8-$CoCl_2$** and **A9-$CuCl_2$.MeCN**, are presented in **Fig. 4.3**. The structures for the Zn(II) imine complexes, **1c-$ZnCl_2$.MeCN**, **1h-$ZnCl_2$** and **1i-$ZnCl_2$.2MeCN** are presented in **Fig. 4.4**; and their crystallographic data in **Table 4.9**. The crystal structures and crystallographic data for the cobalt imine complexes, **[Co(1a)$_2$]Cl**, **M2**, **M5** and **M9** are presented in **Fig. 4.5** and **Table 4.11**, respectively.

A2-CdI_2 and **A9-$CuCl_2$.MeCN** crystallised in the monoclinic $P2_1/c$ and $P2_1/n$ space groups, respectively; while **A8-CdI_2** and **A8-$CoCl_2$** crystallised in the triclinic P-1 and Pī space groups, respectively. The asymmetric unit of **A2-CdI_2** contained one Cd(II) ion connected four heteroatoms {$N_{imidazole}$ and N_{amine} atoms} and one iodide ion, resulting in two six-membered chelate rings with a five-coordinate {trigonal bipyramidal} geometry. The amine {**A2**} acted as neutral ligand resulting in a cationic complex. The asymmetric units of **A8-CdI_2**, **A8-$CoCl_2$** and **A9-$CuCl_2$.MeCN** contained one M(II) ion {M = Cd, Co and Cu, respectively}, two heteroatoms {$N_{imidazole}$ and N_{amine} atoms} and two X^- ions {X = I, Cl and Cl, respectively}, resulting in a six-membered chelate ring with four-coordinate {distorted tetrahedral [for **A8**] and square planar [for **A9**]} geometries. The amines {**A8** and **A9**} acted as neutral ligands in the neutral complexes obtained. The coordination bond length {**Table 4.12**} showed M-N followed the order Cd > Co ≈ Cu, and M-Cl followed Cu > Co.

I_3-$ZnCl_2$.MeCN and **I_8-$ZnCl_2$** crystallised in the orthorhombic Pbcn and Pbca space groups, respectively; while **I_9-$ZnCl_2$.2MeCN** crystallises in the monoclinic $P2_1/n$ space group. The asymmetric units of the complexes contained one Zn(II) ion, three heteroatoms {$N_{imidazole}$, N_{imine} and O_{phenol} atoms} and one chloride ion, resulting in a two six-membered chelate rings with a four-coordinate {distorted tetrahedral} geometry. The ligands acted as monoanionic molecules. The Zn-O, Zn-N and Zn-Cl bond lengths {**Table 4.10**} were in the

range 1.9202(13) – 1.9305(0), 1.9905(13) – 2.0362(13) and 2.2158(0) – 2.2233(5), respectively. In comparison to **I_9.MeOH**, the $C=N_{imine}$ of the complexes increased, while the $C\text{-}O_{phenol}$ decreased.

The cobalt complexes, [**Co(I_1)$_2$]Cl**, **M2**, **M5** and **M9**, crystallised in the monoclinic $P2_1/n$, triclinic $P\bar{1}$, monoclinic $P2_1/n$ and orthorhombic Pbca space groups, respectively. In the case of [**Co(I_1)$_2$]Cl** and **M2**, Co(II) was oxidised to Co(III) with a Cl^- {counter ion} outside the coordination sphere. Their asymmetric units contained one Co(III) ion and six heteroatoms {$N_{imidazole}$, N_{imine} and O_{phenol} atoms}, resulting in cationic complexes possessing four six-membered chelate rings with a six-coordinate {distorted octahedral} geometry. The asymmetric unit of **M5** contained one Co(II) ion, three heteroatoms {$N_{imidazole}$, N_{imine} and $N_{pyridine}$ atoms} and two Cl^- ions, resulting in two six-membered chelate rings with a five-coordinate {trigonal-bipyramidal} geometry. The asymmetric unit of **M9** contained one Co(II) ion, three heteroatoms {$N_{imidazole}$, N_{imine} and O_{phenol} atoms} and one Cl^- ion, resulting in two six-membered chelate rings with a four-coordinate {distorted tetrahedral} geometry. The NNO ligands {**I_1**, **I_2** and **I_8**} acted as monoanionic molecules, while **I_{N2}** acted as a neutral molecule. The Co-O, and Co-N bond lengths {**Table 4.12**} were in the range 1.868(3) – 1.899(2) and 1.9141(3) – 2.010(4), respectively. As seen in the Zn(II) complexes, the $C=N_{imine}$ of the cobalt complexes {in comparison to **I_9.MeOH**} increased, while the $C\text{-}O_{phenol}$ {NNO series} decreased.

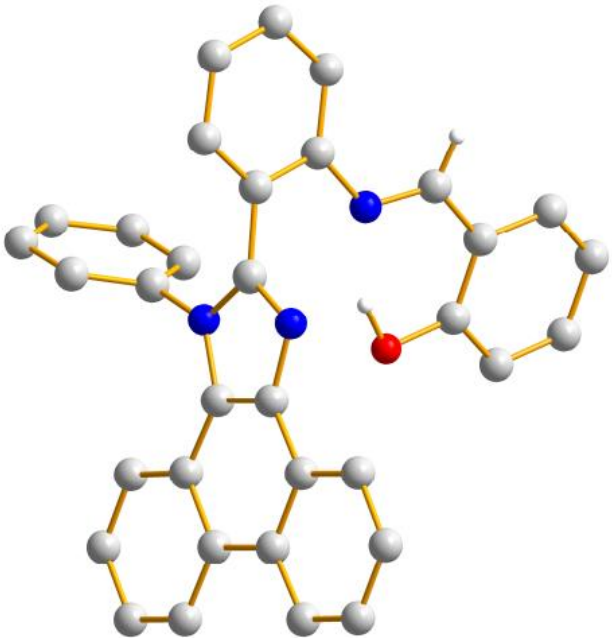

Figure 4.2: Molecular structure of **I9.MeOH.** Solvents and some hydrogens are omitted for clarity.

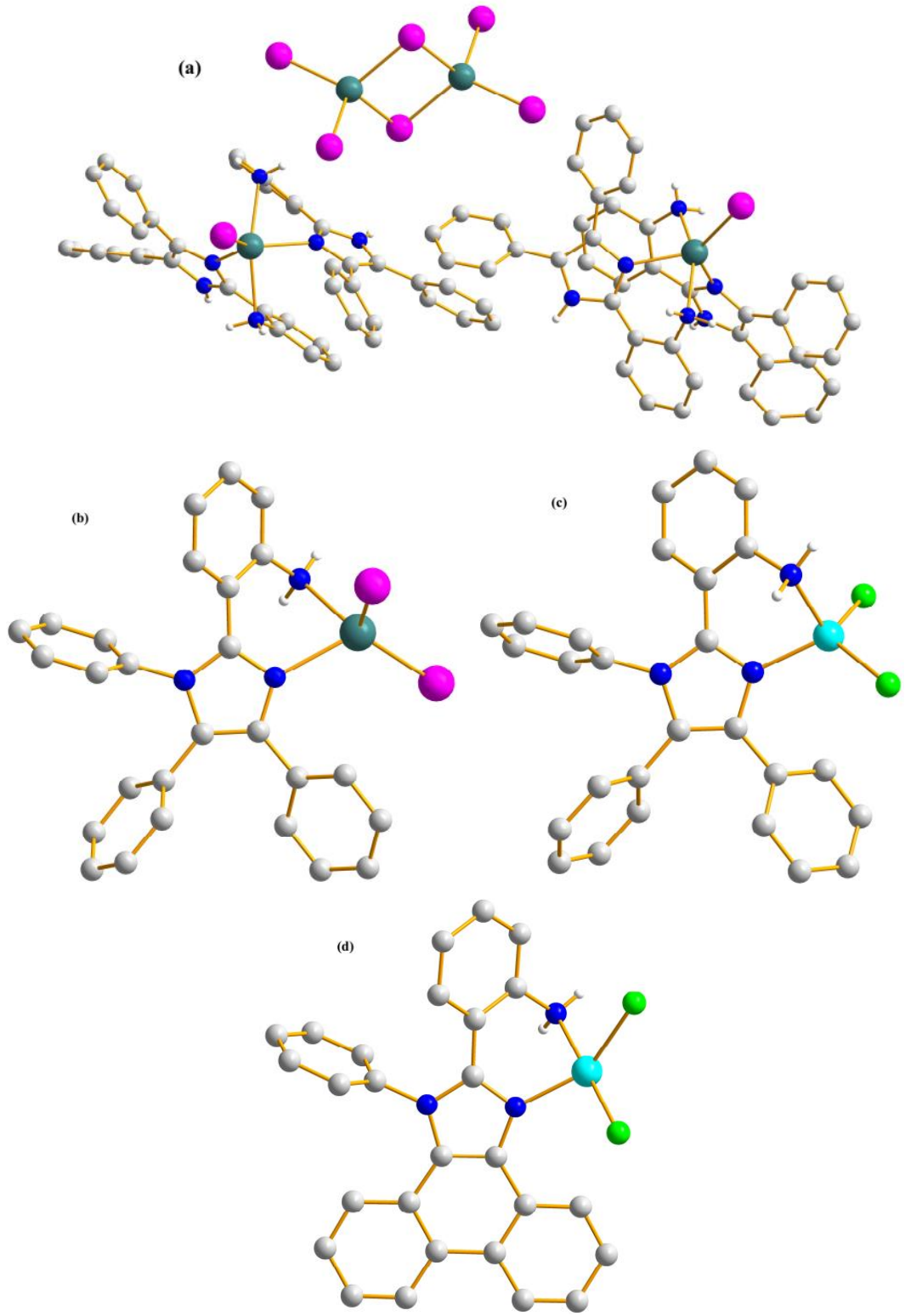

Figure 4.3: Molecular structures of (a) **A2-CdI_2** (b) **A8-CdI_2** (c) **A8-$CoCl_2$** and (d) **A9-$CuCl_2$.MeCN.** Solvents and some hydrogens are omitted for clarity.

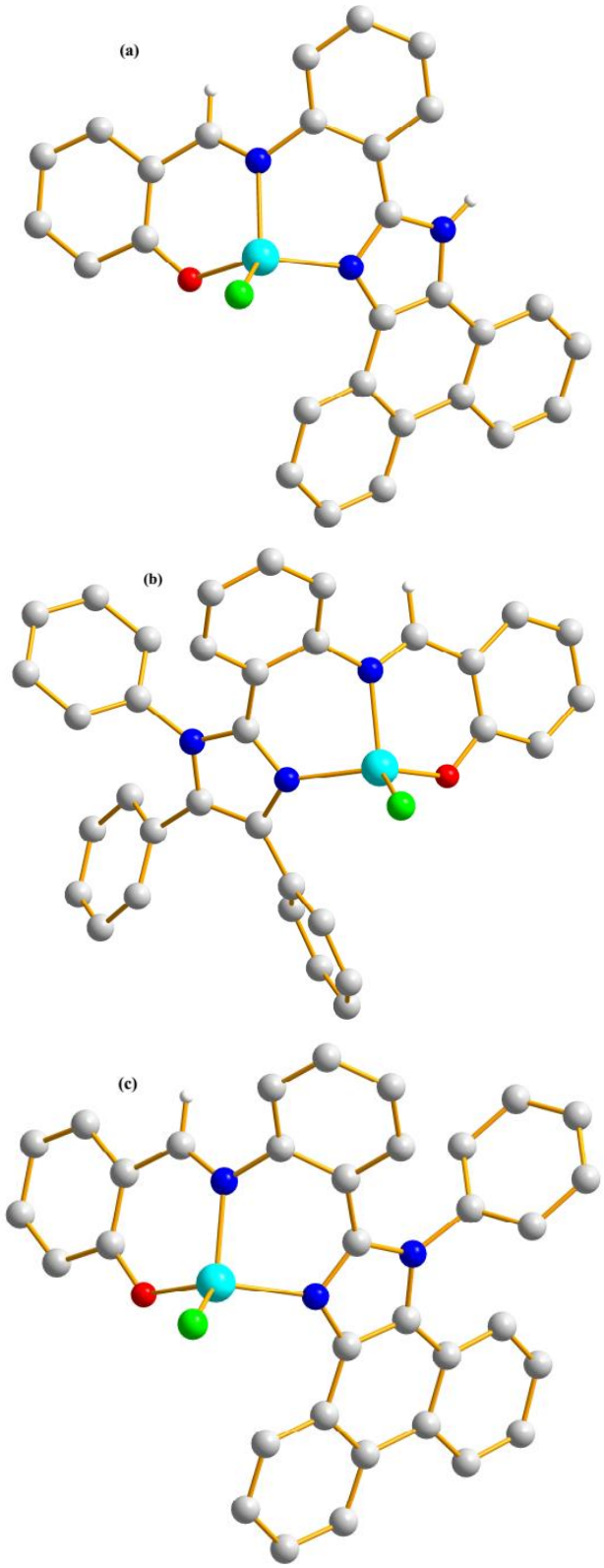

Figure 4.4: Molecular structures of (a) **1c-$ZnCl_2$.MeCN** (b) **1h-$ZnCl_2$** and (c) **1i-$ZnCl_2$.2MeCN.** Solvents and some hydrogens are omitted for clarity.

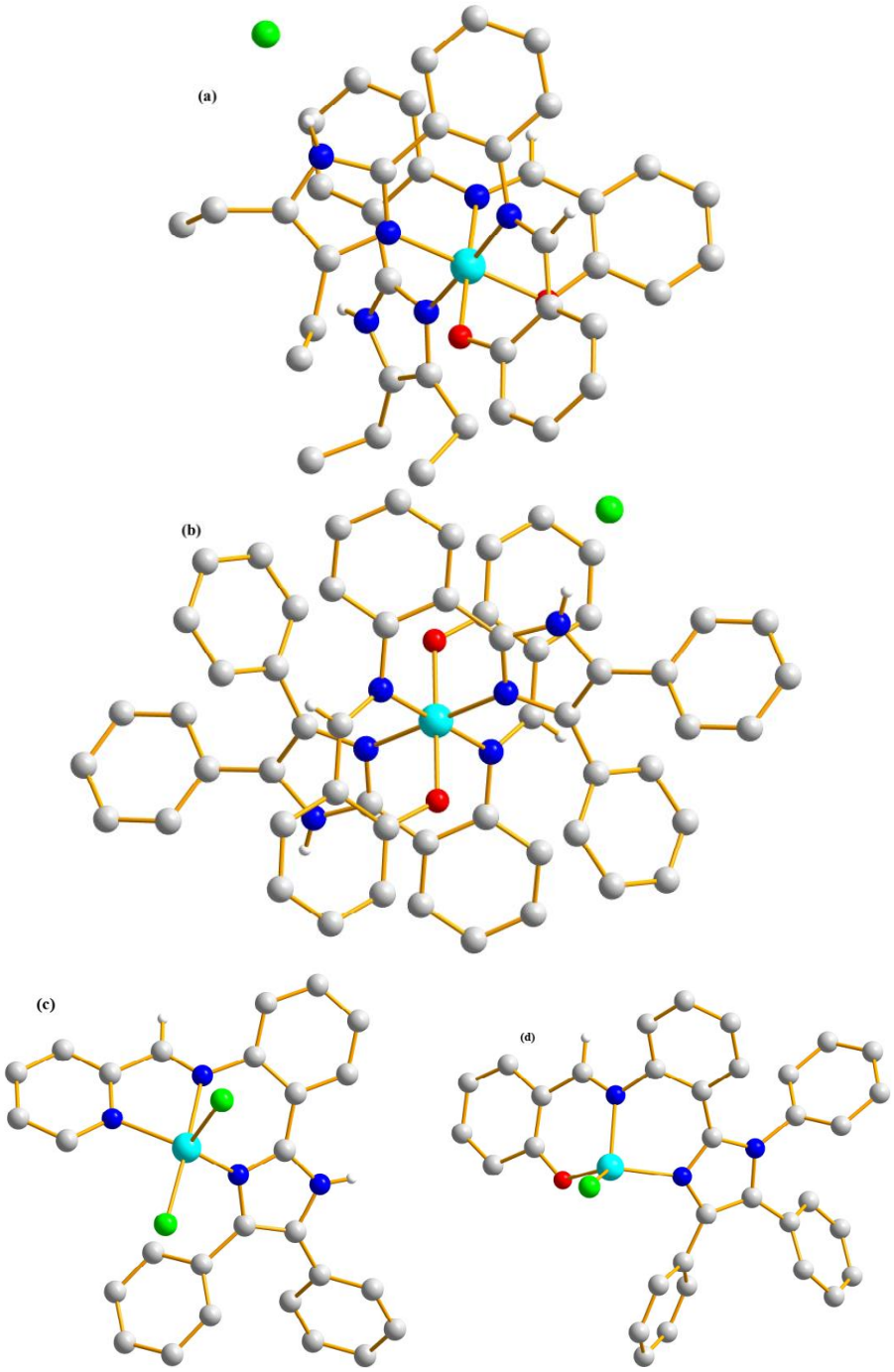

Figure 4.5: Molecular structures of (a) **[Co(I$_1$)$_2$]Cl** (b) **M2 (c) M5,** and (d) **M9.** Solvents and some hydrogens are omitted for clarity.

Table 4.8(a): Crystallographic Data and Structure Refinement Parameters for **I_9.MeOH.**

	I_9.MeOH
Formula	$C_{35}H_{27}N_3O_2$
Fw (g mol^{-1})	521.60
Cryst. syst.	Triclinic
Space group	Pī
a (Å)	10.4422(3)
b (Å)	11.4333(2)
c (Å)	13.0546(3)
α (deg)	98.735(1)
β (deg)	113.262(1)
γ (deg)	102.928(1)
V ($Å^3$)	1344.42(5)
z	2
T(K)	133(2)
δ_{Calc}(Mg/m^3)	1.288
F(000)	548
μ(mm^{-1})	0.081
θ range for data collection (deg)	2.14 – 27.48
Measd reflns	19439
Unique refln (R_{int})	6103(0.0219)
No. of param	381
GOF on F^2	1.037
R1[I>2σ(I)]	0.0429
wR2(all data)	0.1068

Table 4.8(b): Selected bond lengths (Å)

	I_9.MeOH
$C=N_{imine}$	1.2804(0)
$C-O_{phenol}$	1.3483(0)
C=N···HO	1.7052(0)
N_{imine}···O_{phenol}	2.6106(0)

Table 4.9: Crystallographic Data and Structure Refinement Parameters for **A2-CdI_2**, **A8-CdI_2**, **A8-$CoCl_2$**, **A9-$CuCl_2$.MeCN**, **I_3-$ZnCl_2$.MeCN**, **I_8-$ZnCl_2$**, and **I_9-$ZnCl_2$.2MeCN**

	A2-CdI_2	**A8-CdI_2**	**A8-$CoCl_2$**	**A9-$CuCl_2$.MeCN**
Formula	$C_{84}H_{68}Cd_4I_8N_{12}$	$C_{27}H_{21}CdI_2N_3$	$C_{27}H_{17}Cl_2CoN_3$	$C_{29}H_{22}Cl_2CuN_4$
Fw (g mol^{-1})	2710.30	753.67	513.27	560.95
Cryst. syst.	Monoclinic	Triclinic	Triclinic	Monoclinic
Space group	$P2_1/c$	P-1	Pī	$P2_1/n$
a (Å)	18.2910(3)	9.7532(2)	9.1480(3)	13.2587(5)
b (Å)	10.4421(2)	11.1838(2)	11.4605(4)	10.5155(3)
c (Å)	25.1769(4)	13.0352	12.3983(4)	17.7623(6)
α (deg)	90	97.266(1)	81.756(2)	90
β (deg)	105.062(1)	95.235(1)	89.579(2)	93.477(2)
γ (deg)	90	111.499(1)	68.429(2)	90
V ($Å^3$)	4643.50(14)	1297.64(4)	1194.86(7)	2471.89(14)
z	2	2	2	4
T(K)	133(2)	133(2)	133(2)	133(2)
δ_{Calc}(Mg/m^3)	1.938	1.929	1.427	1.507
F(000)	2544	716	522	1148
μ(mm^{-1})	3.610	3.240	0.962	1.127
θ range for data collection (deg)	1.67 – 27.48	1.93 - 27.48	2.38 - 27.48	1.98 - 27.48
Measd reflns	32331	18411	11817	14251
Unique refln (R_{int})	10596(0.0429)	5892(0.0233)	5375(0.0653)	5618(0.0444)
No. of param	563	306	302	334
GOF on F^2	1.034	1.074	1.164	1.117
R1[I>2σ(I)]	0.0667	0.0210	0.0865	0.0481
wR2(all data)	0.1691	0.0457	0.1588	0.0983

	I_3-$ZnCl_2$.MeCN	**I_8-$ZnCl_2$**	**I_9-$ZnCl_2$.2MeCN**
Formula	$C_{30}H_{21}ClN_4OZn$	$C_{34}H_{24}ClN_3OZn$	$C_{38}H_{28}ClN_5OZn$
Fw (g mol^{-1})	554.33	591.38	671.47
Cryst. syst.	Orthorhombic	Orthorhombic	Monoclinic
Space group	Pbcn	pbca	$P2_1/n$
a (Å)	28.3695(4)	10.0462(1)	12.5256(2)
b (Å)	12.1407(2)	23.1008(3)	14.2437(2)
c (Å)	14.3497(2)	23.8712(3)	18.8020(3)
α (deg)	90	90	90
β (deg)	90	90	109.140(1)
γ (deg)	90	90	90
V ($Å^3$)	4942.40(13)	5539.91(11)	3169.05(8)
z	8	8	4
T(K)	133(2)	133(2)	133(2)
δ_{Calc}(Mg/m^3)	1.490	1.418	1.407
F(000)	2272	2432	1384
μ(mm^{-1})	1.134	1.016	0.899
θ range for data collection (deg)	2.31 - 27.46	2.37 – 27.48	2.24 - 27.48
Measd reflns	38042	56659	25171
Unique refln (R_{int})	5657(0.0353)	6325(0.0322)	7274(0.0360)
No. of param	339	457	426
GOF on F^2	1.045	1.107	1.048
R1[I>2σ(I)]	0.0283	0.0349	0.0341
wR2(all data)	0.0716	0.0790	0.0800

Table 4.10: Selected bond lengths (Å) and angles (°)

	A2-CdI_2	**A8-CdI_2**
Cd(1)-N(1)	2.296(6)	2.323(2)
Cd(1)-N(4)	2.309(8)	
Cd(1)-N(3)	2.433(6)	2.321(2)
Cd(1)-N(6)	2.434(7)	
Cd(1)-I(1)	2.7218(7)	2.7115(2)
Cd(1)-I(2)		2.7029(2)

	A8-$CoCl_2$		**A9-$CuCl_2$.MeCN**
Co(1)-N(1)	2.028(4)	Cu(1)-N(1)	2.041(2)
Co(1)-N(3)	2.060(4)	Cu(1)-N(3)	2.026(3)
Co(1)-Cl(1)	2.2411(15)	Cu(1)-Cl(1)	2.2401(8)
Co(1)-Cl(2)	2.2296(15)	Cu(1)-Cl(2)	2.3541(8)

	A2-CdI_2	**A8-CdI_2**
N(1)-Cd(1)-N(4)	104.2(3)	
N(1)-Cd(1)-N(3)	73.4(2)	78.92(7)
N(4)-Cd(1)-N(3)	87.0(2)	
N(1)-Cd(1)-N(6)	92.2(2)	
N(4)-Cd(1)-N(6)	73.6(3)	
N(3)-Cd(1)-N(6)	152.4(3)	
N(1)-Cd(1)-I(1)	127.81(17)	100.59(5)
N(4)-Cd(1)-I(1)	127.95(19)	
N(3)-Cd(1)-I(1)	104.91(16)	109.93(5)
N(6)-Cd(1)-I(1)	102.51(19)	
N(3)-Cd(1)-I(2)		113.32(5)
N(1)-Cd(1)-I(2)		118.87(5)
I(2)-Cd(1)-I(1)		125.397(8)

	A8-$CoCl_2$		**A9-$CuCl_2$.MeCN**
N(1)-Co(1)-N(3)	90.34(16)	N(1)-Cu(1)-N(3)	82.45(10)
N(1)-Co(1)-Cl(2)	112.33(12)	N(1)-Cu(1)-Cl(1)	97.06(7)
N(1)-Co(1)-Cl(1)	115.74(13)	N(1)-Cu(1)-Cl(2)	148.05(7)
N(3)-Co(1)-Cl(2)	109.07(14)	N(3)-Cu(1)-Cl(1)	176.65(8)
N(3)-Co(1)-Cl(1)	108.43(13)	N(3)-Cu(1)-Cl(2)	87.02(8)
Cl(1)-Co(1)-Cl(2)	117.29(6)	Cl(1)-Cu(1)-Cl(2)	91.72(3)

	I_3-$ZnCl_2$.MeCN	**I_8-$ZnCl_2$**	**I_9-$ZnCl_2$.2MeCN**
Zn(1)-O(1)	1.9286(11)	1.9305(0)	1.9202(13)
Zn(1)-N(1)	1.9950(13)	2.0278(0)	2.0361(14)
Zn(1)-N(3)	2.0362(13)	2.0306(0)	2.0090(15)
Zn(1)-Cl(1)	2.2177(4)	2.2158(0)	2.2233(5)
$C=N_{imine}$	1.2972(0)	1.2986(0)	1.2945(0)
$C-O_{phenol}$	1.3086(0)	1.2821(0)	1.3099(0)
O(1)-Zn(1)-N(1)	117.41(5)	118.255(1)	120.29(6)
O(1)-Zn(1)-N(3)	93.76(5)	95.326(1)	94.90(6)
N(1)-Zn(1)-N(3)	92.06(5)	89.918(0)	90.80(6)
O(1)-Zn(1)-Cl(1)	109.11(4)	116.927(0)	114.67(4)
N(1)-Zn(1)-Cl(1)	118.28(4)	114.462(1)	113.01(4)
N(3)-Zn(1)-Cl(1)	123.65(4)	117.082(0)	119.90(5)

Table 4.11: Crystallographic Data and Structure Refinement Parameters for **[Co(I$_1$)$_2$]Cl, M2, M5** and **M9**

	[Co(1a)$_2$]Cl	**M2**	**M5**	**M9**
Formula	$C_{40}H_{40}ClCoN_6O_2$	$C_{58.50}H_{50}ClCoN_6O_{4.50}$	$C_{27}H_{20}Cl_2CoN_4$	$C_{34}H_{24}ClCoN_3O$
Fw (g mol^{-1})	731.16	1003.43	530.30	584.94
Cryst. syst.	Monoclinic	Triclinic	Monoclinic	Orthorhombic
Space group	$P2_1/n$	$P\bar{1}$	$P2_1/n$	pbca
a (Å)	8.4102(2)	11.6766(4)	11.917(1)	10.0067(1)
b (Å)	14.7878(4)	12.0221(3)	7.3736(6)	23.1121(4)
c (Å)	28.6164(9)	18.0503(5)	26.1852(22)	23.7408(4)
α (deg)	90	91.260(2)	90	90
β (deg)	97.383(1)	101.215(1)	96.169(1)	90
γ (deg)	90	101.085(2)	90	90
V (Å^3)	3529.47(17)	2434.45(12)	2287.60(33)	5490.67(14)
z	4	2	4	8
T(K)	133(2)	133(2)	133(2)	133(2)
δ_{Calc}(Mg/m^3)	1.376	1.369	1.540	1.415
F(000)	1528	1046	1084	2408
μ(mm^{-1})	0.607	0.564	0.756	1.008
θ range for data collection (deg)	1.55 - 27.44	1.94 – 27.48	2.76 – 28.13	1.76 – 27.48
Measd reflns	22726	22961	39762	37365
Unique refln (R_{int})	7939(0.0872)	10899(0.0448)	5550 (0.0439)	6277(0.1141)
No. of param	463	644	387	361
GOF on F^2	1.115	1.025	1.037	1.139
R1[I>2σ(I)]	0.0687	0.0711	0.0303	0.0824
wR2(all data)	0.1308	0.1900	0.0748	0.2180

Table 4.12: Selected bond lengths (Å) and angles (°)

	[Co(I$_1$)$_2$]Cl	**M2**	**M5**	**M9**
Co(1)-O(1)	1.890(2)	1.884(2)		1.868(3)
Co(1)-O(2)	1.899(2)	1.884(2)		
Co(1)-N(1)	1.943(3)	1.958(3)	2.0815(2)	2.010(4)
Co(1)-N(2)	1.956(3)	1.958(3)	2.1484(1)	2.008(4)
Co(1)-N(3)	1.914(3)	1.927(3)	2.0697(1)	
Co(1)-N(4)	1.935(3)	1.927(3)		
Co(1)-Cl(1)			2.3798(1)	2.2293(15)
Co(1)-Cl(2)			2.2749(1)	
C=N$_{imine}$	1.2977(0)	1.2935(0)	1.2772(1)	1.3029(0)
	1.2942(0)			
C – O$_{phenol}$	1.3024(0)	1.3141(0)		1.2984(0)
	1.3066(0)			
O(1)-Co(1)-O(2)	86.97(11)	179.998(1)		
O(1)-Co(1)-N(1)	89.31(11)	90.88(10)		119.64(16)
O(1)-Co(1)-N(2)	92.87(12)	89.12(10)		
O(1)-Co(1)-N(3)	91.81(12)	90.67(11)		94.72(16)
O(1)-Co(1)-N(4)	177.52(12)	89.33(11)		
O(2)-Co(1)-N(1)	175.18(12)	89.12(10)		
O(2)-Co(1)-N(2)	90.20(11)	90.88(10)		
O(2)-Co(1)-N(3)	90.32(11)	89.33(10)		
O(2)-Co(1)-N(4)	91.38(11)	90.67(11)		
N(1)-Co(1)-N(2)	93.03(12)	180.00(12)	78.784(3)	
N(1)-Co(1)-N(3)	86.75(12)	86.92(11)	122.345(4)	90.36(15)
N(1)-Co(1)-N(4)	92.44(12)	93.09(11)		
N(2)-Co(1)-N(4)	85.29(12)	86.92(11)		
N(2)-Co(1)-N(3)	175.31(13)	93.08(11)	76.352(3)	
N(3)-Co(1)-N(4)	90.04(12)	179.999(1)		
O(1)-Co(1)-Cl(1)				115.77(12)
N(1)-Co(1)-Cl(1)			118.476(3)	114.86(12)
N(1)-Co(1)-Cl(2)			101.023(3)	
N(2)-Co(1)-Cl(1)			84.415(2)	
N(2)-Co(1)-Cl(2)			176.181(3)	
N(3)-Co(1)-Cl(1)			109.775(2)	116.63(12)
N(3)-Co(1)-Cl(2)			100.713(2)	

4.5.3 Structural property of NNN imines and their metal complexes

Unlike the NNO imines, a cyclisation process was observed upon interaction of the NNN imines (**I_{N2}** and **I_{N4}**) with Zn(II) and Cd(II) salts, **Fig. 4.6**. While one of the cyclised form of **I_{N4}** was outside the coordination sphere in the Zn(II) complex (**Fig. 4.6**{**c**}), the Cd(II) complex (**Fig. 4.6**{**b**}) did not show this. A coordination complex (**Fig. 4.6**{**d**}) was obtained when **I_{N4}** interacted with CdI_2, which was not observed for the $CdCl_2$ counterpart (**Fig. 4.6**{**b**}). In addition to the metal complexes, {**[ZnCl(I_{N2})(I_{N2c})][$ZnCl_3(OH_2)$]**, **[CdCl(I_{N4})(I_{N4c})$CdCl_3$]MeCN**, **[ZnCl(I_{N4})(I_{N4c})$ZnCl_3$]I_{N4c}2MeOH**, **[CdI(I_{N4})(I_{N4c})][CdI_4]3MeOH**}, the cyclised compounds, **(I_{N2c})$H^+ClO_4^-$THF** and **I_{N2v}.MeOH**, were also obtained in the presence of $Fe(ClO_4)_3$ and $Co(OAc)_2.4H_2O$, respectively, **Fig. 4.7**. The crystallographic data for the compounds are presented in **Table 4.13**.

[ZnCl(I_{N2})(I_{N2c})][$ZnCl_3(OH_2)$] and **[CdCl(I_{N4})(I_{N4c})$CdCl_3$]MeCN** are isostructural and crystallised in the triclinic P-1 space group, respectively; while **[ZnCl(I_{N4})(I_{N4c})$ZnCl_3$]I_{N4c}2MeOH** and **[CdI(I_{N4})(I_{N4c})][CdI_4]3MeOH** crystallised in the monoclinic $P2_1/n$ and C2/c space groups, respectively. The asymmetric unit of **[ZnCl(I_{N2})(I_{N2c})][$ZnCl_3(OH_2)$]** contained one Zn(II) ion connected to four heteroatoms {two $N_{imidazole}$, N_{imine} and N_{py} atoms} and one chloride ion, resulting in one five-membered and one six-membered chelate ring with a five-coordinate {trigonal bipyramidal} geometry. The NNN imines {**I_{N2} and I_{N2c}**} acted as neutral ligands resulting in a cationic complex {**[ZnCl(I_{N2})(I_{N2c})]$^+$**}. **[CdCl(I_{N4})(I_{N4c})$CdCl_3$]MeCN** had two coordination environments; a Cd(II) ion that is structurally similar to the Zn(II) centre in **[ZnCl(I_{N2})(I_{N2c})]$^+$** and a second Cd(II) ion connected to the N_{py} atom of **$2d_c$** and three chloride ions, resulting in a four-coordinate {distorted tetrahedral} geometry – this four-coordinate centre resulted in a neutral complex. Although **[ZnCl(I_{N4})(I_{N4c})$ZnCl_3$]I_{N4c}2MeOH** crystallises distinctly, its coordination environments are structurally similar to that of **[CdCl(I_{N4})(I_{N4c})$CdCl_3$]MeCN**. Although **[CdI(I_{N4})(I_{N4c})][CdI_4]3MeOH** crystallised distinctly, its asymmetric unit is similar to **[ZnCl(I_{N2})(I_{N2c})][$ZnCl_3(OH_2)$]** and a cationic complex {**[CdI(I_{N4})(I_{N4c})]$^+$**} also arose.

The Zn-N and Cd-N bond lengths were in the range 2.049 – 2.3238 Å and 2.264 – 2.4263 Å respectively, while the N-Zn-N and N-Cd-N angles were in the range 74.44 – 168.29^{o} and 69.05 – 120.90^{o}, respectively {**Table 4.14**}.

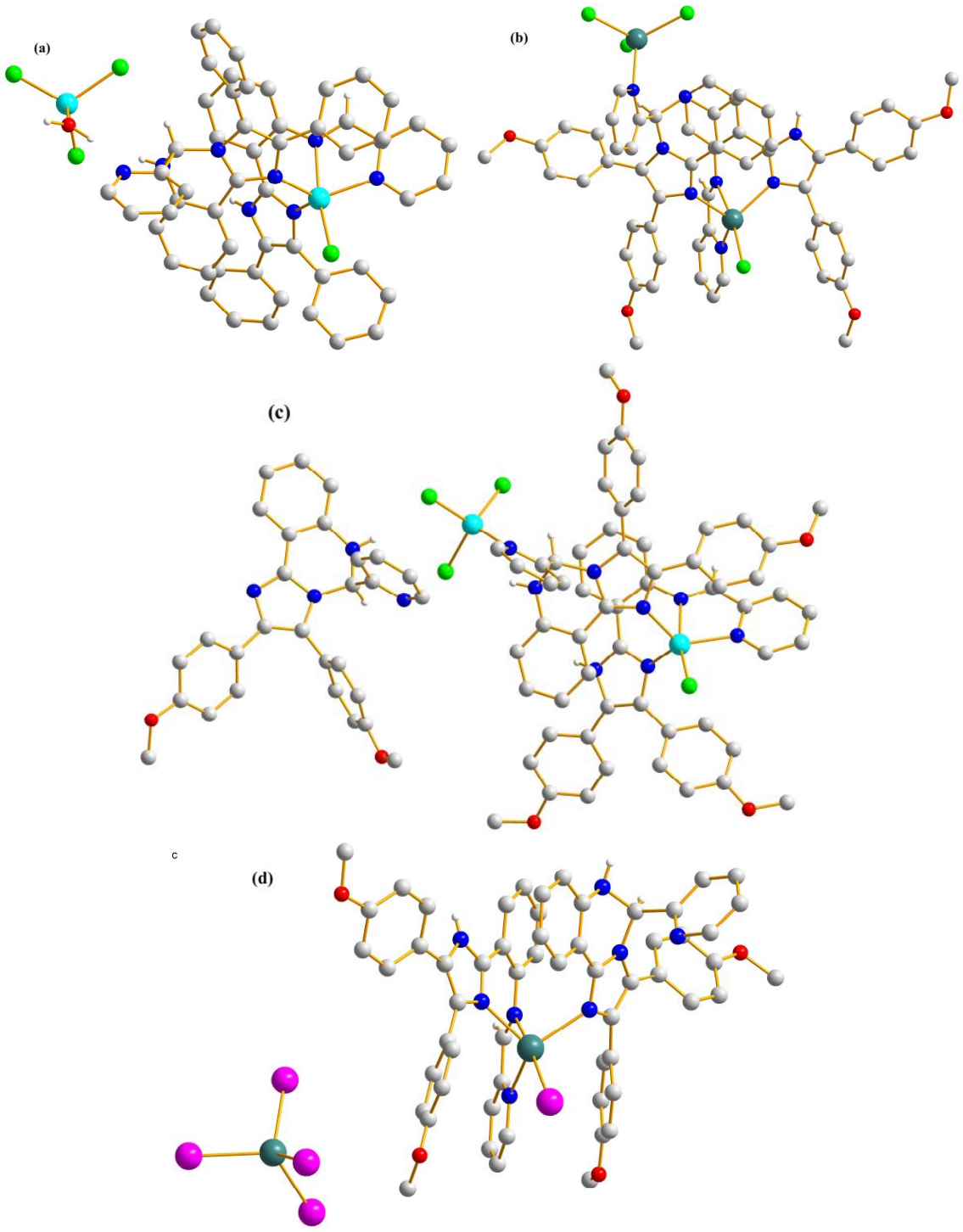

Figure 4.6: Molecular structures of (a) **[ZnCl(I_{N2})(I_{N2c})][$ZnCl_3(OH_2)$]** (b) **[CdCl(I_{N4})(I_{N4c})$CdCl_3$]MeCN** (c) **[ZnCl(I_{N4})(I_{N4c})$ZnCl_3$]I_{N4c}2MeOH** and (d) **[CdI(I_{N4})(I_{N4c})][CdI_4]3MeOH.** Solvents and some hydrogens are omitted for clarity.

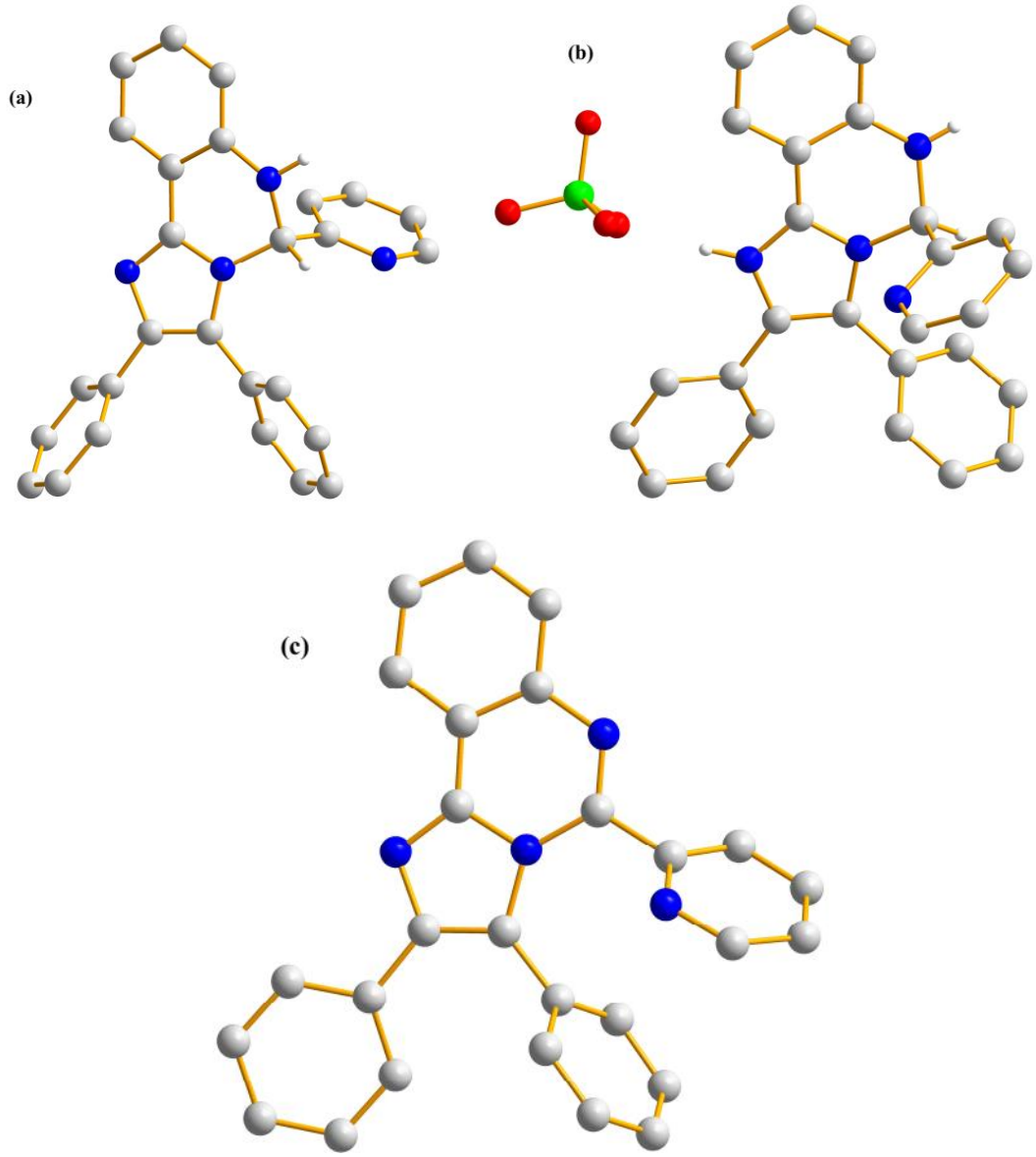

Figure 4.7: Molecular structures of (a) $\mathbf{I_{N2c}}$ (b) $\mathbf{(I_{N2c})H^{+}ClO_4^{-}THF}$ and (c) $\mathbf{I_{N2v}}$**.MeOH.** Solvents and some hydrogens are omitted for clarity.

Table 4.13: Crystallographic Data and Structure Refinement Parameters for **I_{N2c}, $I_{N2c}H^+.ClO_4^-.THF$, I_{N2v}.MeOH, [ZnCl(I_{N2})(I_{N2c})][$ZnCl_3(OH_2)$], [CdCl(I_{N4})(I_{N4c})$CdCl_3$]MeCN, [ZnCl(I_{N4})(I_{N4c})$ZnCl_3$]I_{N4c}·2MeOH,** and **[CdI(I_{N4})(I_{N4c})][CdI_4]·3MeOH.**

	I_{N2c}	$I_{N2c}H^+.ClO_4^-.THF$	I_{N2v}·MeOH	[ZnCl(I_{N2})(I_{N2c})][$ZnCl_3(OH_2)$]
Formula	$C_{27}H_{20}N_4$	$C_{31}H_{29}ClN_4O_5$	$C_{28}H_{22}N_4O$	$C_{54}H_{42}Cl_4N_8OZn_2$
Fw (g mol^{-1})	400.47	573.03	430.49	1091.49
Cryst. syst.	Monoclinic	Triclinic	Triclinic	Triclinic
Space group	$P2_1/c$	P-1	P-1	P-1
a (Å)	15.8578(6)	9.2057(3)	9.0863(4)	14.1925(2)
b (Å)	10.7742(4)	11.1064(3)	10.7718(4)	15.6136(3)
c (Å)	11.8939(3)	13.3831(5)	12.1969(4)	25.8143(4)
α (deg)	90	98.891(2)	105.347(2)	86.963(1)
β (deg)	94.867(2)	90.8570(10)	95.438(2)	86.104(1)
γ (deg)	90	93.835(2)	108.636(2)	83.546(1)
V (Å^3)	2024.81(12)	1348.40(8)	1069.63(7)	5665.02(16)
z	4	2	2	4
T(K)	133(2)	133(2)	133(2)	133(2)
δ_{Calc}(Mg/m^3)	1.314	1.411	1.337	1.280
F(000)	840	600	452	2232
μ(mm^{-1})	0.079	0.192	0.084	1.087
θ range for data collection (deg)	2.29 – 27.45	1.86 – 27.48	1.77 – 27.47	1.50 – 27.48
Measd reflns	14650	15181	11056	42807
Unique refln (R_{int})	4596 (0.0612)	6110 (0.0747)	4835 (0.0365)	25063 (0.026)
No. of param	360	378	300	1313
GOF on F^2	1.132	1.048	1.054	1.068
R1[I>2σ(I)]	0.0592	0.0669	0.0630	0.0609
wR2(all data)	0.1209	0.1890	0.1371	0.1498

	[CdCl(I_{N4})(I_{N4c})$CdCl_3$]·MeCN	[ZnCl(I_{N4})(I_{N4c})$ZnCl_3$]I_{N4c}·2MeOH	[CdI(I_{N4})(I_{N4c})][CdI_4]·3MeOH
Formula	$C_{60}H_{50}Cd_2Cl_4N_9O_4$	$C_{89}H_{80}Cl_4N_{12}O_8Zn_2$	$C_{61}H_{60}Cd_2I_5N_8O_7$
Fw (g mol^{-1})	1327.69	1718.19	1876.52
Cryst. syst.	Triclinic	Monoclinic	Monoclinic
Space group	P-1	$P2_1/n$	C2/c
a (Å)	14.0634(3)	14.4706(2)	30.7277(6)
b (Å)	15.6228(3)	22.3107(4)	13.5061(3)
c (Å)	16.5193(3)	27.4057(4)	33.4618(6)
α (deg)	84.359(1)	90	90
β (deg)	67.762(1)	103.565(1)	112.595(1)
γ (deg)	83.217(1)	90	90
V (Å^3)	3330.30(12)	8601.1(2)	12821.1(5)
z	2	4	4
T(K)	133(2)	133(2)	133(2)
δ_{Calc}(Mg/m^3)	1.324	1.327	1.623
F(000)	1338	3560	6152
μ(mm^{-1})	0.847	0.744	2.002
θ range for data collection (deg)	1.32 – 27.48	1.79 – 27.48	1.67 – 27.46
Measd reflns	43199	60605	43149
Unique refln (R_{int})	15176 (0.0365)	19570 (0.0505)	14537 (0.0479)
No. of param	722	1066	739
GOF on F^2	1.134	1.142	1.090
R1[I>2σ(I)]	0.0682	0.0594	0.0483
wR2(all data)	0.1628	0.1388	0.1032

Table 4.14: Selected bond lengths (Å) and angles (°)

	[$Zn(I_{N2})(I_{N2c})Cl]^+$	$[ZnCl(I_{N4})(I_{N4c})ZnCl_3]$		$[CdCl(I_{N4})(I_{N4c})CdCl_3]$	$[CdI(I_{N4})(I_{N4c})]^+$
Zn(1) – N(1)	2.056(3)	2.049(3)	Cd(1) – N(1)	2.264(4)	2.269(4)
Zn(1) – N(3)	2.217(3)	2.200(3)	Cd(1) – N(3)	2.409(5)	2.401(4)
Zn(1) – N(4)	2.101(3)	2.154(3)	Cd(1) – N(4)	2.338(5)	2.356(4)
Zn(1) – N(5)	2.110(3)	2.166(3)	Cd(1) – N(5)	2.313(4)	2.333(4)
Zn(1) – Cl(1)	2.3238(9)	2.2954(9)	Cd(1) – Cl(1)	2.4263(14)	
			Cd(1) – I(1)		2.7612(4)
N(1)-Zn(1)-N(3)	79.56(11)	79.65(10)	N(1)-Cd(1)-N(3)	73.86(16)	73.86(13)
N(1)-Zn(1)-N(4)	116.46(11)	116.66(10)	N(1)-Cd(1)-N(4)	113.89(17)	112.57(14)
N(1)-Zn(1)-N(5)	106.94(11)	105.44(10)	N(1)-Cd(1)-N(5)	106.03(15)	104.47(13)
N(1)-Zn(1)-Cl(1)	111.82(8)	111.60(8)	N(1)-Cd(1)-Cl(1)	116.07(12)	
N(3)-Zn(1)-N(4)	75.00(11)	74.44(10)	N(3)-Cd(1)-N(4)	68.95(19)	69.05(13)
N(3)-Zn(1)-N(5)	83.56(11)	83.75(10)	N(3)-Cd(1)-N(5)	82.05(15)	79.71(13)
N(3)-Zn(1)-Cl(1)	168.29(8)	167.98(7)	N(3)-Cd(1)-Cl(1)	166.94(13)	
N(4)-Zn(1)-N(5)	126.18(11)	127.16(10)	N(4)-Cd(1)-N(5)	119.93(16)	120.90(14)
N(4)-Zn(1)-Cl(1)	96.69(8)	96.04(8)	N(4)-Cd(1)-Cl(1)	98.50(15)	
N(5)-Zn(1)-Cl(1)	95.20(8)	96.73(7)	N(5)-Cd(1)-Cl(1)	102.14(11)	
N(8)-Zn(2)-Cl(2)		107.83(8)	N(8)-Cd(2)-Cl(2)	109.93(13)	
N(8)-Zn(2)-Cl(3)		109.96(8)	N(8)-Cd(2)-Cl(3)	97.03(12)	
N(8)-Zn(2)-Cl(4)		106.26(8)	N(8)-Cd(2)-Cl(2)	109.42(13)	
Cl(2)-Zn(2)-Cl(3)		110.89(4)	Cl(2)-Cd(2)-Cl(3)	113.80(8)	
Cl(2)-Zn(2)-Cl(4)		108.65(4)	Cl(2)-Cd(2)-Cl(4)	115.03(9)	
Cl(3)-Zn(2)-Cl(4)		113.03(4)	Cl(3)-Cd(2)-Cl(4)	110.11(9)	
			N(1)-Cd(1)-I(1)		115.79(9)
			N(3)-Cd(1)-I(1)		167.16(9)
			N(4)-Cd(1)-I(1)		98.67(10)
			N(5)-Cd(1)-I(1)		104.69(9)

4.5.4 Structural properties of the pentadentate imines and their metal complexes

The crystal structures and crystallographic analyses of **H_2S1**, **H_2S3** and **H_2S5.CHCl$_3$** are presented in **Fig. 4.8** and **Table 4.15**, respectively. The compounds crystallised in a tetragonal $I4_1/a$ space group, monoclinic $P2_1/n$ space group and triclinic P-1 space group, respectively. The differences in the crystal packing produced slight changes in the C-S, C=N_{imine} and C-O_{phenol} bond lengths {**Table 4.16**}; while the unsubstituted **H_2S1** was symmetrical, the substituted analogues **H_2S3** and **H_2S5.CHCl$_3$** were unsymmetrical {about the S-bridge}. The C=N_{imine} and hydrogen bond distances are similar to those of **I_9.MeOH**. The structural properties of **H_2S1** are in close agreement with earlier report (Guo and Yuan 2008), although the crystal of **H_2S1** was obtained from MeOH while the earlier report was from ethyl acetate/toluene {1:4}.

X-ray data of the cobalt complexes {**Co_2S1$_2$.MeCN**, **Co_2S2$_2$**, **Co_2S4$_2$.3THF**, **Co_2S5$_2$.4DCM**, **Co_2S7$_2$.THF** and **Co_2O1$_2$**} are presented in **Fig. 4.9**, **Table 4.17** and **Table 4.18**. **Co_2S1$_2$.MeCN** and **Co_2S7$_2$.THF** crystallised in the triclinic Pī and P-1 space groups, respectively. **Co_2S2$_2$**, **Co_2S4$_2$.3THF** and **Co_2O1$_2$** crystallised in the monoclinic $P2_1/c$, $P2_1/n$ and C2/c space groups, respectively. **Co_2S5$_2$.4DCM** crystallised in the orthorhombic Aba2 space group. The asymmetric units of the complexes contained two Co(II) ions connected by oxo-bridges. Each Co(II) ion is connected to six heteroatoms {O_{phenol}, N_{imine} and S/O atoms}, resulting in two six-membered and two five-membered chelate rings in a distorted octahedral {O_h} geometry, except for **Co_2O1$_2$** which assumed a trigonal prismatic {D_{3h}} geometry {**Table. 4.18** and **Fig. 4.13**}. The ligands acted as dianionic molecules.

X-ray data of the nickel complexes {**Ni_2S1$_2$**, **Ni_2S2$_2$.THF**, **Ni_2S3$_2$** and **NiS5(H_2O).2THF**} are presented in **Fig. 4.10** and **Table 4.19** respectively. Unlike the homo-dinuclear Co(II) complex obtained with **H_2S5** {**Co_2S5$_2$.4DCM**}, a mononuclear complex {**NiS5(H_2O).2THF**} was obtained with Ni(II), with oxygen {from water molecule} occupying the sixth coordination site. **Ni_2S1$_2$** and **NiS5(H_2O).2THF** crystallised in the triclinic P-1 space group, respectively; while **Ni_2S2$_2$.THF** and **Ni_2S3$_2$** are isostructural and crystallised in the monoclinic $P2_1/c$ space group. Like the homo-dinuclear Co(II) complexes, the asymmetric units of the homo-dinuclear Ni(II) complexes contained two Ni(II) ions connected by oxo-bridges. Each Ni(II) ion is connected to six heteroatoms

{O_{phenol}, N_{imine} and S}, resulting in two six-membered and two five-membered chelate rings in a distorted octahedral geometry. The ligands acted as dianionic molecules. The asymmetric unit of the mononuclear complex {**NiS5(H_2O).2THF**} also has a Ni(II) ion connected to six heteroatoms {O_{phenol}, N_{imine}, S and O_{water} atoms}, resulting in two six-membered and two five-membered chelate rings in a distorted octahedral geometry.

X-ray data for **[CrS2(NO_3)].MeCN**, [**ZnS2($Cl)_2$].THF** and **[CrO1(NO_3)]** are presented in **Fig. 4.11** and **Table 4.21** respectively. The complexes crystallised in the orthorhombic P n a 21, monoclinic $P2_1/c$ and triclinic P-1 space groups, respectively. Unlike corresponding Co(II) {**Fig. 4.9** [**a**] and [**f**]} and Ni(II) complexes {**Fig. 4.10** [**b**]}, mononuclear complexes were obtained for Cr(III) and Zn(II) cases. In **[CrS2(NO_3)].MeCN**, Cr-atom bonds with the bridging S-atom {as observed for the Co(II) {**Fig. 4.9** [**a**]} and Ni(II) analogues (**Fig. 4.10** [**b**])}, while the Cr-atom in **[CrO1(NO_3)]** does not bond with the bridging O-atom {unlike in the Co(II) analogue (**Fig. 4.9** [**f**])}. The inability of the Cr-atom to bond with the bridging O-atom could be attributed to the distance {3.1574(1) Å} between the atoms, the corresponding Co-O bond length is ≈2 Å. Similarly, the distance {4.1366(1) Å} between the Zn-atom and bridging S-atom, in [**ZnS2($Cl)_2$].THF**, could be responsible for their inability to bond.

The asymmetric unit of **[CrS2(NO_3)].MeCN** contained one Cr(III) ion, connected to six heteroatoms {O_{phenol}, N_{imine}, S and $O_{nitrate}$}, resulting in two six-membered and two five-membered chelate rings in a distorted octahedral geometry. Its Cr-O {1.895(3) Å and 1.922(4) Å}, Cr-N {2.021(3) Å and 2.044(4) Å} bond lengths as well as the O-Cr-O angle {92.63(15)^o} are comparable to previously reported complexes, although 1.895(3) Å is shorter than for most (Liu *et al*., 2014; Liu *et al*., 2015; Schuman *et al*., 2021). The asymmetric unit of [**ZnS2($Cl)_2$].THF** has one Zn(II) ion, two oxygen atoms {O_{phenol}} and two chloride ions, in a four-coordinate distorted tetrahedral geometry. The asymmetric unit of **[CrO1(NO_3)]** has one Cr(III) ion, connected to six heteroatoms {O_{phenol}, N_{imine}, and $O_{nitrate}$}, resulting in two six-membered and one seven-membered chelate rings in a distorted octahedral geometry. The Cr-O {1.8946(12) Å and 1.9027(12) Å}, Cr-N {2.0344(14) Å and 2.0824(14) Å} bond lengths as well as the O-Cr-O angle {90.84(5)^o} in **[CrO1(NO_3)]** were very similar to those of **[CrS2(NO_3)].MeCN**. In all cases, the ligands acted as dianionic molecules.

Crystal structures of **[$Cu_3S1_2(OAc)_2$].2DCM**, **[$Cu_3S2_2(OAc)_2$].6$CHCl_3$**, **[Cu_2S2_2].2THF**, **[Cu_2S3_2].THF** and **[Cu_2O1_2].2MeCN** are presented in **Fig. 4.12**. Crystallographic data and structure refinement parameters as well as selected bond lengths and angles are presented in **Table 4.23** and **Table 4.24**(**a**), respectively. The complexes crystallised in the triclinic P-1, monoclinic $P2_1/n$, triclinic P-1, triclinic P-1 and monoclinic C2/c space groups, respectively. Although the nuclearity of **[$Cu_3S1_2(OAc)_2$].2DCM** differs from that of **[Cu_2S2_2].2THF** and **[Cu_2S3_2].THF**, all three complexes are isostructural. More so, phenoxo and acetate bridging were observed in the trinuclear complexes, but not in the dinuclear complexes. Similarly, although **[Cu_2O1_2].2MeCN** is isostructural to **Co_2O1_2**, oxo-bridging was not observed in **[Cu_2O1_2].2MeCN** but observed in **Co_2O1_2** {**Fig. 4.9** [**f**]}.

In the trinuclear complexes, the asymmetric units of the terminal ends contained one Cu(II) ion, connected to six heteroatoms {O_{phenol}, N_{imine}, S and $O_{acetate}$}, resulting in one six-membered and one five-membered chelate rings {with the S-bridged ligand} as well as a four-membered chelate ring {with the acetate} in a distorted octahedron; while the asymmetric unit at the centre contained one Cu(II) ion, connected to six heteroatoms {O_{phenol}, N_{imine} and $O_{acetate}$}, resulting in two six-membered chelate rings {with the S-bridged ligand} also in a distorted octahedron. In both complexes, monoatomic bridging mode was observed. The asymmetric units in each of the dinuclear complexes are similar to one another. Each unit consists of one Cu(II) ion, two oxygen atoms {O_{phenol}} and two nitrogen atoms {N_{imine}}, resulting in two six-membered chelate rings in a four-coordinate environment. Unlike in the trinuclear complexes where all the Cu(II) centres showed similar geometry {distorted octahedron}, Continuous Shape Measurements (CSM) {**Table 4.24**(**b**)} revealed the Cu(II) centres in the dinuclear complexes exhibited different geometries. The Cu(II) ions in **[Cu_2S2_2].2THF** exhibited square-planar geometry {D_{4h} symmetry}, while the Cu(II) ions in **[Cu_2O1_2].2MeCN** exhibited seesaw geometry {C_{2v} symmetry}. In **[Cu_2S3_2].THF** however, the Cu(II) ions exhibited two different geometries {square-planar and seesaw}.

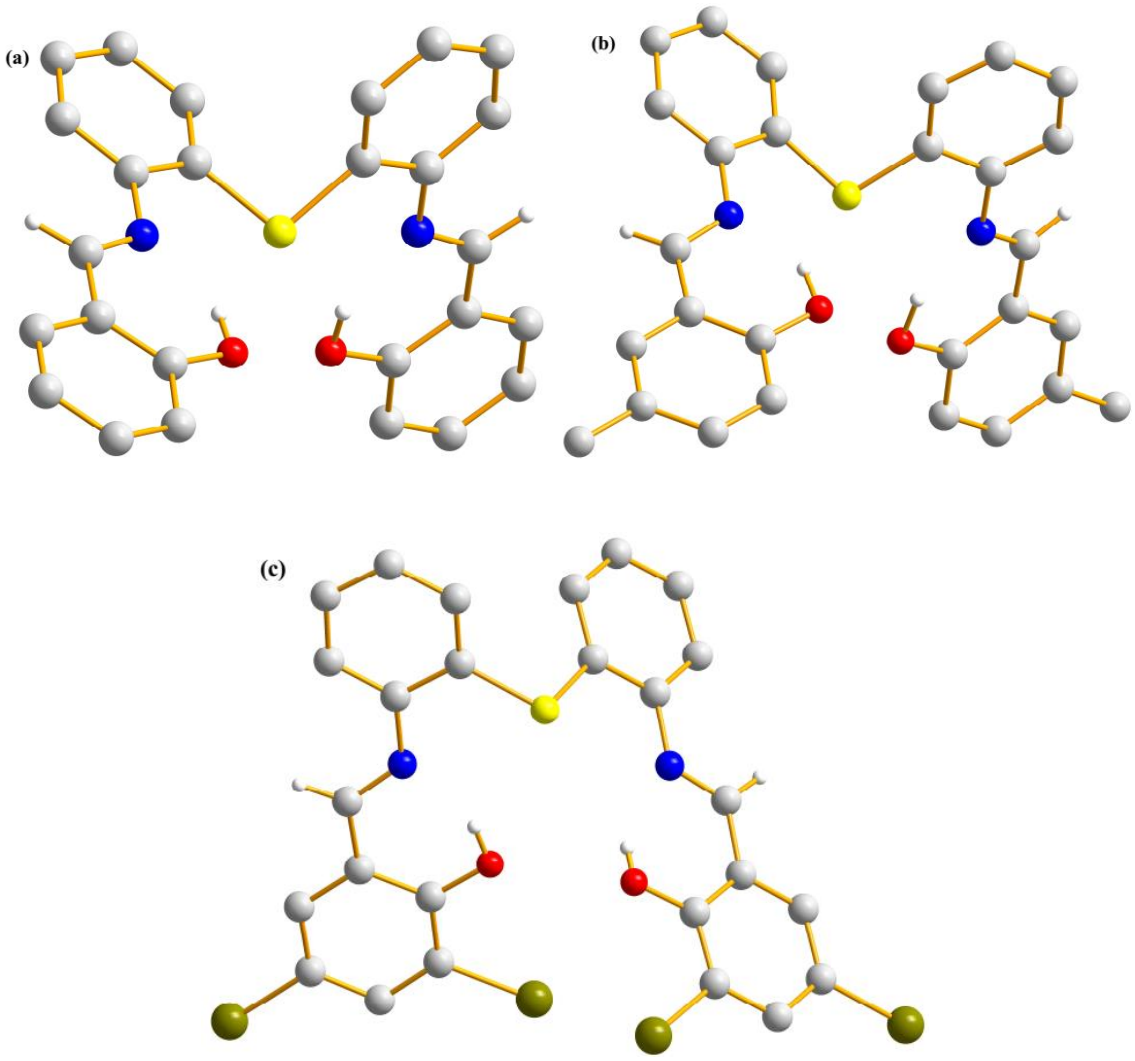

Figure 4.8: Molecular structures of (a) **H_2S1** (b) **H_2S3** and (c) **H_2S5.$CHCl_3$.** Solvents and some hydrogens are omitted for clarity.

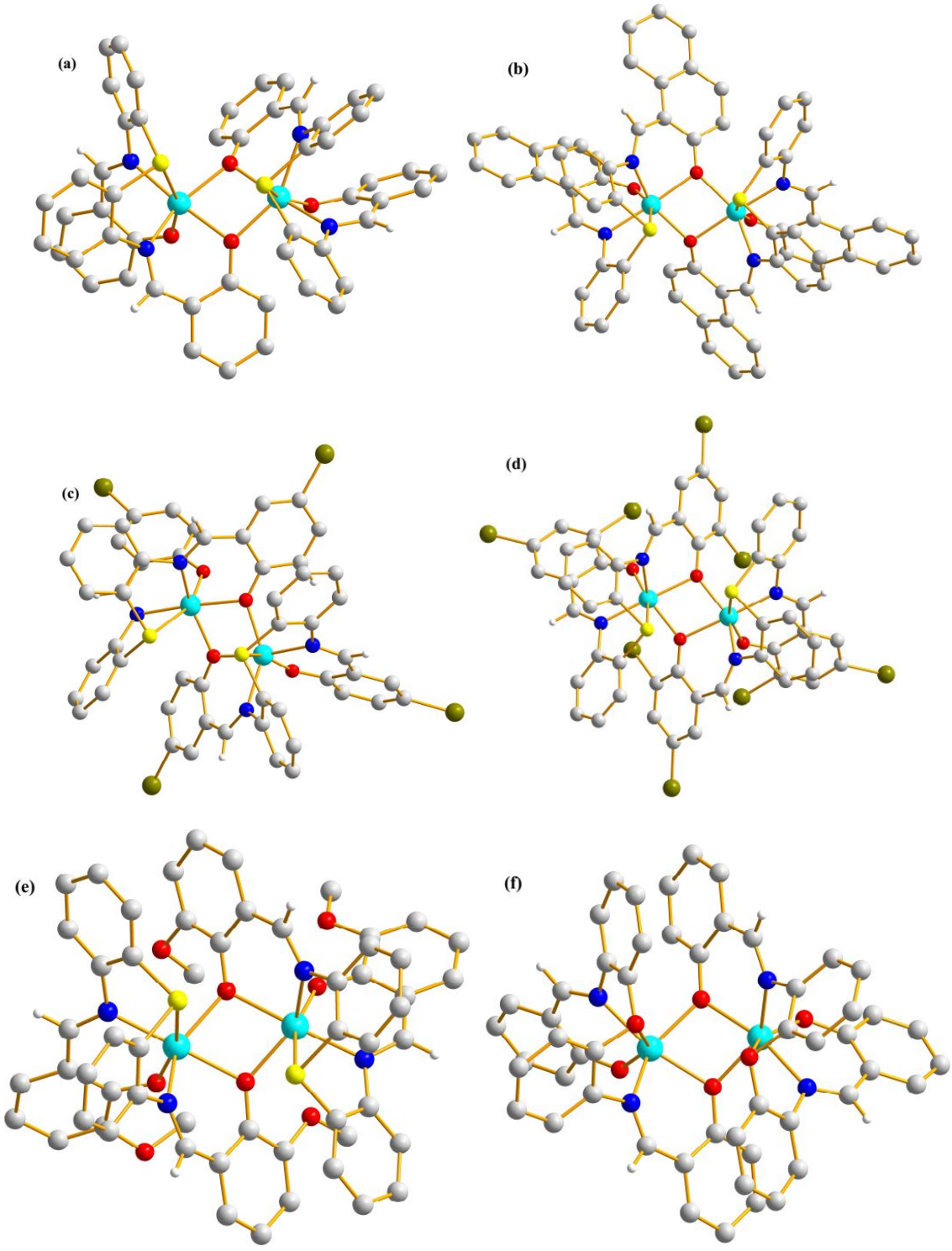

Figure 4.9: Molecular structures of (a) **Co_2S1_2.MeCN** (b) **Co_2S2_2** (c) **Co_2S4_2.3THF** (d) **Co_2S5_2.4DCM** (e) **Co_2S7_2.THF** and (f) **Co_2O1_2.** Solvents and some hydrogens are omitted for clarity.

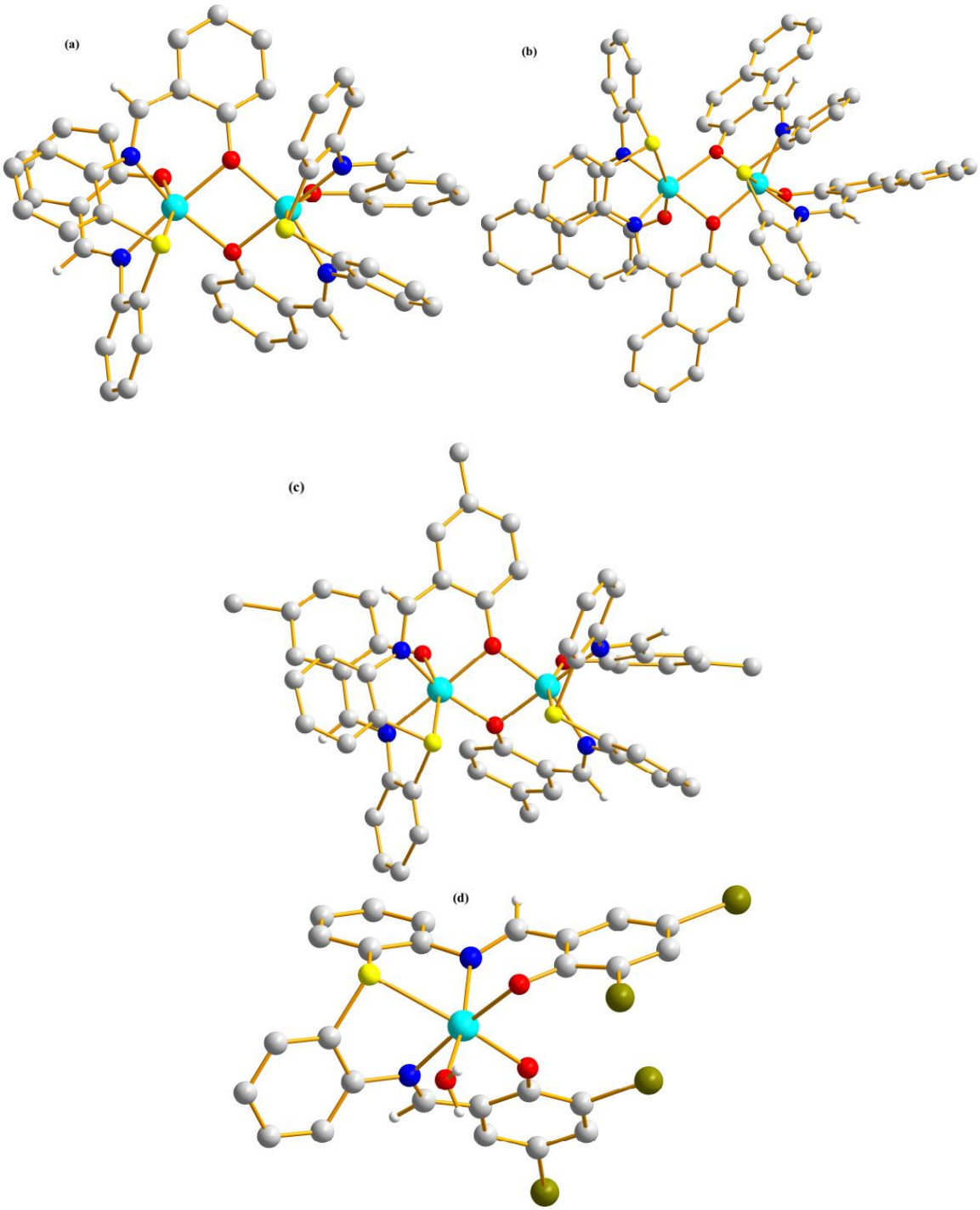

Figure 4.10: Molecular structures of (a) **Ni_2S1_2** (b) **Ni_2S2_2.THF** (c) **Ni_2S3_2** and (d) **$NiS5(H_2O)$.2THF.** Solvents and some hydrogens are omitted for clarity.

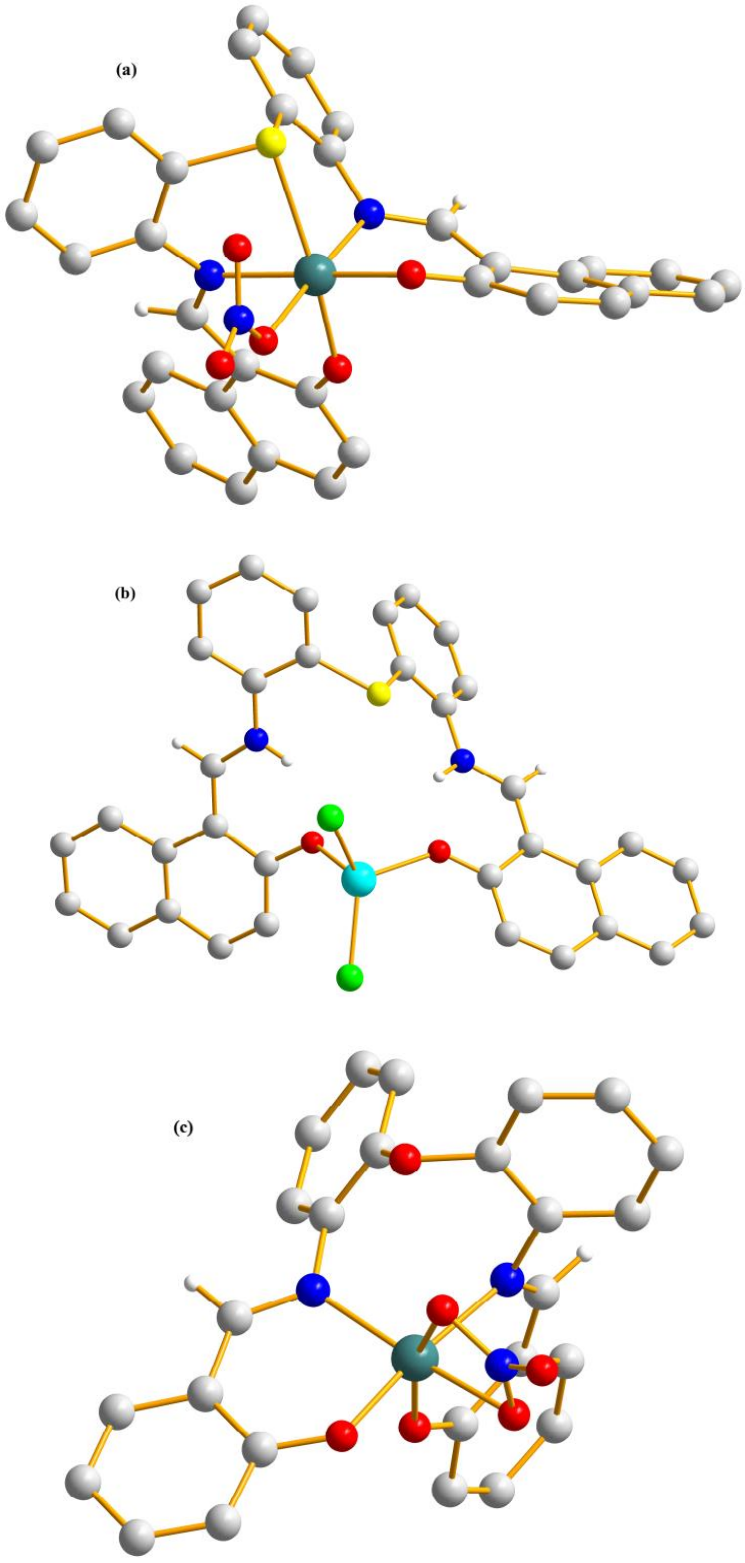

Figure 4.11: Molecular structures of (a) **[CrS2(NO$_3$)].MeCN** (b) **[ZnS2(Cl)$_2$].THF** and (c) **[CrO1(NO$_3$)].** Solvents and some hydrogens are omitted for clarity.

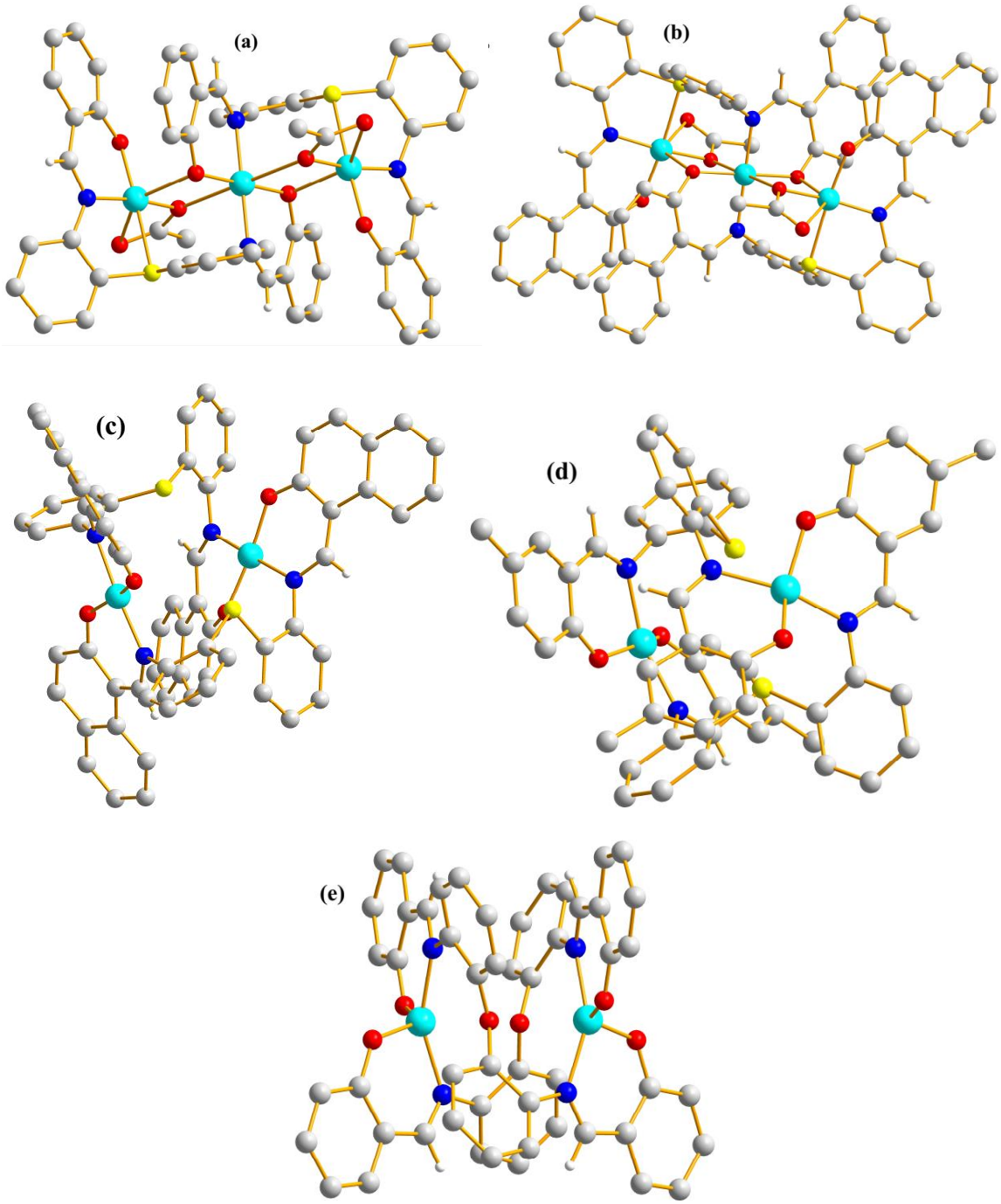

Figure 4.12: Molecular structures of (a) **[$Cu_3S1_2(OAc)_2$].2DCM** (b) **[$Cu_3S2_2(OAc)_2$].6$CHCl_3$** (c) **[Cu_2S2_2].2THF** (d) **[Cu_2S3_2].THF** and (e) **[Cu_2O1_2].2MeCN.** Solvents and some hydrogens are omitted for clarity.

Table 4.15(a): Crystallographic Data and Structure Refinement Parameters for **H_2S1, H_2S3,** and **$H_2S5.CHCl_3$.**

	H_2S1	**H_2S3**	**$H_2S5.CHCl_3$**
Formula	$C_{20}H_{20}N_2O_2S$	$C_{28}H_{24}N_2O_2S$	$C_{27}H_{17}Br_4Cl_3N_2O_2S$
Fw (g mol^{-1})	424.50	452.55	859.47
Cryst. syst.	Tetragonal	Monoclinic	Triclinic
Space group	$I4_1/a$	P 21/n	P-1
a (Å)	11.1640(3)	9.5767(3)	8.0137(2)
b (Å)	11.1640(3)	24.0341(8)	13.1092(3)
c (Å)	33.0991(6)	20.3301(5)	13.9000(3)
α (deg)	90	90	81.596(1)
β (deg)	90	101.690(2)	86.538(1)
γ (deg)	90	90	81.928(1)
V ($Å^3$)	4125.30(17)	4582.3(2)	1429.06(6)
z	8	8	2
T(K)	133(2)	133(2)	133(2)
δ_{Calc}(Mg/m^3)	1.367	1.312	1.997
F(000)	1776	1904	832
μ(mm^{-1})	0.184	0.170	6.017
θ range for data collection (deg)	1.93 - 27.47	1.33 – 27.49	2.32 – 27.48
Measd reflns	23889	30901	19199
Unique refln (R_{int})	2376 (0.0828)	10324 (0.0763)	6479 (0.0361)
No. of param	181	615	360
GOF on F^2	1.226	1.186	1.084
R1[I>2σ(I)]	0.0732	0.0780	0.0293
wR2(all data)	0.1479	0.1380	0.0675

Table 4.15(b): Selected bond lengths (Å)

	H_2S1	**H_2S3**	**$H_2S5.CHCl_3$**
C – S	1.7759(0)	1.7705(0)	1.7746(0)
		1.7759(0)	1.7817(0)
$C=N_{imine}$	1.2826(0)	1.2844(0)	1.2781(0)
		1.2862(0)	1.2871(0)
$C – O_{phenol}$	1.3517(0)	1.3486(0)	1.3407(0)
		1.3523(0)	1.3389(0)
C=N···HO	1.8324(0)	1.797(0)	2.0343(0)
		1.8111(0)	1.8163(0)
N_{imine}····O_{phenol}	2.5926(0)	2.5975(1)	2.6583(0)
		2.6241(1)	2.5746(1)

Table 4.16: Crystallographic Data and Structure Refinement Parameters for **Co_2S1_2.MeCN, Co_2S2_2, Co_2S4_2.3THF, Co_2S5_2.4DCM, Co_2S7_2.THF** and **Co_2O1_2**

	Co_2S1_2.MeCN	**Co_2S2_2**	**Co_2S4_2.3THF**	**Co_2S5_2.4DCM**
Formula	$C_{52}H_{36}N_4Co_2O_4S_2$	$C_{68}H_{44}Co_2N_4O_4S_2$	$C_{64}H_{56}Br_4Co_2N_4O_7S_2$	$C_{56}H_{36}Br_8Cl_8Co_2N_4O_4S_2$
Fw (g mol^{-1})	1044.94	1163.05	1494.74	1933.75
Cryst. syst.	Triclinic	Monoclinic	Monoclinic	Orthorhombic
Space group	Pī	$P2_1/c$	$P2_1/n$	Aba2
a (Å)	12.8956(3)	14.1235(4)	19.2280(5)	23.4931(6)
b (Å)	14.4316(4)	21.3736(6)	16.5106(5)	14.6340(4)
c (Å)	14.6966(3)	20.3838(6)	20.5956(5)	18.9118(5)
α (deg)	63.961(1)	90	90	90
β (deg)	73.027(1)	100.468(2)	111.360(1)	90
γ (deg)	87.096(1)	90	90	90
V (Å^3)	2340.86(10)	6050.8(3)	6089.3(3)	6501.8(3)
z	2	4	4	4
T(K)	133(2)	133(2)	133(2)	133(2)
δ_{Calc}(Mg/m^3)	1.482	1.277	1.630	1.975
F(000)	1076	2392	3000	3736
μ(mm^{-1})	0.855	0.668	3.295	5.868
θ range for data collection (deg)	1.66 – 27.48	2.15 – 27.49	1.75 – 27.47	1.96 – 27.48
Measd reflns	22982	62412	43605	37924
Unique refln (R_{int})	10626 (0.0284)	13841 (0.0542)	13784 (0.0651)	7410 (0.0474)
No. of param	633	767	756	381
GOF on F^2	1.084	1.107	1.133	1.121
R1[I>2σ(I)]	0.0423	0.0721	0.0545	0.0335
wR2(all data)	0.0892	0.1595	0.1006	0.0696

	Co_2S7_2.THF	**Co_2O1_2**
Formula	$C_{58}H_{48}Co_2N_4O_{8.5}S_2$	$C_{52}H_{36}Co_2N_4O_6$
Fw (g mol^{-1})	1118.98	930.71
Cryst. syst.	Triclinic	Monoclinic
Space group	P-1	C2/c
a (Å)	11.6803(2)	18.5147(3)
b (Å)	18.5194(3)	16.9738(3)
c (Å)	23.9533(4)	19.3087(3)
α (deg)	80.5510(10)	90
β (deg)	77.9450(10)	116.118(1)
γ (deg)	80.7560(10)	90
V (Å^3)	4955.32(15)	5448.43(16)
z	4	4
T(K)	133(2)	133(2)
δ_{Calc}(Mg/m^3)	1.500	1.135
F(000)	2312	1912
μ(mm^{-1})	0.818	0.654
θ range for data collection (deg)	1.52 – 27.48	1.75 – 27.48
Measd reflns	49820	35995
Unique refln (R_{int})	22490 (0.0636)	6230 (0.0368)
No. of param	1350	289
GOF on F^2	1.100	1.072
R1[I>2σ(I)]	0.0815	0.0338
wR2(all data)	0.1664	0.0798

Table 4.17: Selected bond length (Å) and bond angle (^{o})

	Co_2S1_2.MeCN	**Co_2S2_2**	**Co_2S4_2.3THF**	**Co_2S5_2.4DCM**	**Co_2S7_2.THF**	**Co_2O1_2**
Co(1) – O(2)	1.9778(16)	1.994(3)	1.966(3)	1.966(4)	2.095(3)	1.9387(11)
Co(1) – O(3)	2.0426(16)	2.043(3)	2.049(3)	2.022(4)	2.029(3)	2.0125(11)
Co(1) – N(2)	2.0876(19)	2.057(3)	2.093(3)	2.061(5)	2.139(4)	2.0849(14)
Co(1) – N(1)	2.1025(19)	2.083(3)	2.121(3)	2.109(5)	2.066(4)	2.1014(13)
Co(1) – O(1)	2.1090(16)	2.102(3)	2.099(3)	2.101(4)	1.976(3)	2.0876(11)
Co(1) – S(1)	2.6050(7)	2.6973(11)	2.7044(12)	2.7533(19)	2.7442(14)	
Co(2) – O(4)	1.9966(16)	2.000(3)	1.973(3)		1.974(3)	
Co(2) – O(1)	2.0424(16)	2.082(3)	2.017(3)		2.038(3)	
Co(2) – O(3)	2.0778(16)	2.087(3)	2.106(3)		2.124(3)	
Co(2) – N(4)	2.0778(19)	2.057(3)	2.090(3)		2.068(4)	
Co(2) – N(3)	2.1185(19)	2.099(3)	2.115(3)		2.109(4)	
Co(2) – S(2)	2.6934(7)	2.5801(11)	2.7566(12)		2.6744(14)	
Co(1) – Co(2)	3.2030(1)	3.2138(1)	3.2424(1)	3.1998(1)	3.2367(0)	3.1625(0)
S(1) – S(2)	3.4858(1)	3.5635(1)	3.6048(1)	3.5967(1)	3.7291(1)	
O(2) – O(4)						3.3872(1)
O(2)-Co(1)-O(3)	105.39(7)	106.33(12)	113.55(12)	118.96(18)	117.55(14)	114.83(5)
O(2)-Co(1)-N(2)	89.49(7)	87.31(12)	90.66(12)	91.81(19)	90.40(14)	92.25(5)
O(3)-Co(1)-N(2)	98.63(7)	105.95(11)	96.81(11)	101.99(19)	106.65(14)	100.88(5)
O(2)-Co(1)-N(1)	92.73(7)	97.13(13)	94.47(13)	93.03(19)	99.35(14)	83.23(5)
O(3)-Co(1)-N(1)	152.20(7)	149.41(12)	144.01(12)	139.14(19)	134.28(14)	140.07(5)
N(2)-Co(1)-N(1)	102.51(7)	94.29(12)	105.34(13)	101.6(2)	98.62(16)	102.95(5)
O(2)-Co(1)-O(1)	91.34(6)	91.73(11)	90.77(12)	85.28(17)	84.31(13)	98.89(5)
O(3)-Co(1)-O(1)	76.90(6)	77.55(10)	74.93(10)	75.45(19)	73.88(13)	74.47(5)
N(2)-Co(1)-O(1)	175.51(7)	176.49(12)	171.48(11)	174.5(2)	174.17(14)	166.06(5)
N(1)-Co(1)-O(1)	81.86(7)	82.48(11)	82.92(12)	83.28(19)	84.69(14)	93.29(5)
O(2)-Co(1)-S(1)	159.83(5)	159.86(9)	156.73(9)	157.74(14)	161.55(10)	
O(3)-Co(1)-S(1)	91.57(5)	87.44(9)	86.97(8)	81.87(13)	78.17(10)	
N(2)-Co(1)-S(1)	77.01(5)	74.59(9)	75.43(9)	75.11(15)	75.04(11)	
N(1)-Co(1)-S(1)	75.99(6)	75.92(10)	72.03(9)	72.64(15)	72.34(11)	
O(1)-Co(1)-S(1)	103.30(5)	105.80(8)	105.77(8)	109.11(13)	110.63(9)	
O(4)-Co(2)-O(1)	105.52(7)	105.50(11)	108.95(12)		111.86(14)	
O(4)-Co(2)-O(3)	93.54(7)	90.02(11)	89.57(11)		90.36(15)	
O(1)-Co(2)-O(3)	77.61(6)	77.02(10)	75.43(10)		73.07(12)	
O(4)-Co(2)-N(4)	87.71(7)	85.48(12)	90.72(13)		81.92(13)	
O(1)-Co(2)-N(4)	105.38(7)	106.05(11)	99.89(12)		99.19(15)	
O(3)-Co(2)-N(4)	176.34(7)	175.09(12)	175.12(12)		170.92(15)	
O(4)-Co(2)-N(3)	96.25(7)	95.69(12)	97.32(13)		84.49(14)	
O(1)-Co(2)-N(3)	150.62(7)	149.01(11)	145.56(12)		137.94(15)	
O(3)-Co(2)-N(3)	81.64(7)	80.68(11)	83.10(12)		105.76(14)	
N(4)-Co(2)-N(3)	94.81(8)	97.81(12)	101.69(13)		101.54(16)	
O(4)-Co(2)-S(2)	159.30(5)	160.95(8)	159.18(9)		164.27(10)	
O(1)-Co(2)-S(2)	89.65(5)	87.91(8)	88.49(9)		81.01(10)	
O(3)-Co(2)-S(2)	103.59(5)	106.42(9)	106.24(8)		111.34(10)	
N(4)-Co(2)-S(2)	74.51(6)	77.71(9)	74.70(10)		74.63(11)	
N(3)-Co(2)-S(2)	75.21(5)	78.00(9)	71.90(9)		77.04(12)	

Table 4.18: Continuous Shape Measurements (CSM) for **[Co_2S1_2]MeCN, [Co_2S2_2], [Co_2S4_2]3THF, [Co_2S5_2]4DCM, [Co_2S7_2]THF** and **[Co_2O1_2]**

	Label	HP-6	PPY-6	OC-6	TPR-6	JPPY-6
	Shape	Hexagon	Pentagonal Pyramid	Octahedron	Trigonal Prism	Johnson Pentagonal Pyramid
	Symmetry	D_{6h}	C_{5v}	O_h	D_{3h}	C_{5v}
[Co_2S1_2]MeCN		32.040[a] 32.429[b]	20.277[a] 19.823[b]	**3.305[a]** **3.530[b]**	8.426[a] 9.908[b]	23.809[a] 22.817[b]
[Co_2S2_2]		31.675[a] 32.136[b]	18.760[a] 18.502[b]	**3.830[a]** **3.714[b]**	9.692[a] 8.989[b]	21.612[a] 21.614[b]
[Co_2S4_2]3THF		31.987[a] 32.735[b]	18.376[a] 18.471[b]	**4.553[a]** **4.863[b]**	7.761[a] 6.406[b]	21.648[a] 21.920[b]
[Co_2S5_2]4DCM		30.945[a] 30.945[b]	16.104[a] 16.105[b]	**5.746[a]** **5.746[b]**	6.259[a] 6.259[b]	18.921[a] 18.922[b]
[Co_2S7_2]THF		32.283[a] 31.311[b]	16.667[a] 14.886[b]	**4.930[a]** **5.938[b]**	6.479[a] 6.889[b]	20.106[a] 17.932[b]
[Co_2O1_2]		30.661[a] 30.661[b]	16.521[a] 16.522[b]	7.625[a] 7.625[b]	**6.901[a]** **6.901[b]**	20.094[a] 20.093[b]

a = values obtained for same Co(II) ion
b = values obtained for same Co(II) ion

Table 4.19: Crystallographic Data and Structure Refinement Parameters for **Ni_2S1_2, Ni_2S2_2.THF, Ni_2S3_2** and **$NiS5(H_2O)$.2THF**

	Ni_2S1_2	**Ni_2S2_2.THF**	**Ni_2S3_2**	**$NiS5(H_2O)$.2THF**
Formula	$C_{52}H_{36}N_4Ni_2O_4S_2$	$C_{72}H_{52}N_4Ni_2O_5S_2$	$C_{56}H_{48}N_4Ni_2O_4S_2$	$C_{34}H_{34}Br_4N_2NiO_6S$
Fw (g mol^{-1})	962.39	1234.71	1022.52	977.04
Cryst. syst.	Triclinic	Monoclinic	Monoclinic	Triclinic
Space group	P-1	$P2_1/c$	$P2_1/c$	P-1
a (Å)	14.6104(3)	14.2178(8)	18.6212(4)	9.1800(2)
b (Å)	15.8796(3)	21.3407(10)	14.7283(4)	13.9926(4)
c (Å)	25.3392(5)	20.2718(9)	23.1267(7)	15.4975(4)
α (deg)	94.784(1)	90	90	65.759(1)
β (deg)	104.350(1)	99.950(3)	94.495(2)	76.361(1)
γ (deg)	108.122(1)	90	90	81.929(1)
V ($Å^3$)	5330.08(19)	6058.3(5)	6323.2(3)	1761.84(8)
z	4	4	8	2
T(K)	133(2)	133(2)	133(2)	133(2)
δ_{Calc}(Mg/m^3)	1.199	1.354	1.074	1.842
F(000)	1984	2560	2128	968
μ(mm^{-1})	0.828	0.746	0.701	5.193
θ range for data collection (deg)	1.37 - 27.48	1.40 – 27.48	1.64 – 27.48	2.29 – 27.48
Measd reflns	40221	42342	45576	19856
Unique refln (R_{int})	23213 (0.0640)	13449 (0.0915)	14412 (0.0869)	7960 (0.0356)
No. of param	1142	766	617	459
GOF on F^2	1.087	1.108	1.039	1.108
R1[I>2σ(I)]	0.1900	0.0991	0.1411	0.0406
wR2(all data)	0.4715	0.1873	0.3432	0.0815

Table 4.20: Selected bond length (Å) and bond angle (°)

	Ni_2S1_2	**Ni_2S2_2.THF**	**Ni_2S3_2**	**NiS5(H_2O).2THF**
Ni(1) – O(1)	2.0098(0)	2.044(4)	2.0363(1)	2.038(2)
Ni(1) – O(2)	1.9877(0)	1.998(4)	1.9987(0)	1.988(2)
Ni(1) – O(3)	2.0407(0)	2.043(4)	2.0327(0)	
Ni(1) – O_{water}				2.055(3)
Ni(1) – N(1)	2.0349(0)	2.040(5)	2.0490(1)	2.047(3)
Ni(1) – N(2)	2.0569(0)	2.030(5)	2.0556(0)	2.060(3)
Ni(1) – S(1)	2.5563(0)	2.6197(19)	2.5848(1)	2.5578(10)
Ni(2) – O(4)	2.001(0)	2.008(4)	1.9841(1)	
Ni(2) – O(1)	2.0498(0)	2.068(4)	2.0382(1)	
Ni(2) – O(3)	2.0158(0)	2.0759(4)	2.0382(1)	
Ni(2) – N(4)	2.0289(0)	2.028(5)	2.0481(1)	
Ni(2) – N(3)	2.0559(0)	2.044(5)	2.0532(0)	
Ni(2) – S(2)	2.5753(0)	2.5458(19)	2.5876(1)	
O(2)-Ni(1)-O(1)	89.759(2)	89.87(17)	92.365(1)	88.26(10)
O(2)-Ni(1)-O(3)	103.163(2)	101.93(18)	99.615(1)	
O(1)-Ni(1)-O(3)	78.203(2)	79.43(16)	79.241(1)	
O(2)-Ni(1)-O_{water}				98.58(11)
O(2)-Ni(1)-O_{water}				89.16(11)
N(1)-Ni(1)-O_{water}				165.89(12)
O_{water}-Ni(1)-N(2)				86.13(12)
O_{water}-Ni(1)-S(1)				90.84(8)
O(2)-Ni(1)-N(1)	99.695(2)	97.2(2)	86.317(1)	94.50(11)
O(2)-Ni(1)-N(2)	86.972(2)	86.63(19)	95.122(1)	88.91(11)
O(1)-Ni(1)-N(1)	86.902(2)	84.69(18)	85.384(1)	85.97(11)
O(1)-Ni(1)-N(2)	175.615(2)	176.2(2)	178.619(2)	174.09(11)
N(1)-Ni(1)-N(2)	96.213(2)	94.3(2)	95.135(1)	99.43(12)
O(2)-Ni(1)-S(1)	161.323(2)	162.41(13)	160.454(1)	163.52(8)
O(1)-Ni(1)-S(1)	106.461(2)	106.29(14)	104.743(1)	105.46(7)
O(3)-Ni(1)-S(1)	89.463(2)	88.14(13)	92.918(1)	
N(1)-Ni(1)-S(1)	78.452(1)	77.91(16)	77.242(1)	77.76(9)
N(2)-Ni(1)-S(1)	77.255(1)	77.01(15)	76.625(1)	78.21(9)
N(1)-Ni(1)-O(3)	157.385(2)	155.02(19)	159.052(1)	
N(2)-Ni(1)-O(3)	93.594(2)	102.74(17)	100.568(2)	
O(1)-Ni(2)-O(3)	77.858(2)	78.49(15)	92.909(1)	
O(3)-Ni(2)-O(4)	89.196(2)	89.57(17)	79.329(1)	
O(1)-Ni(2)-O(4)	103.580(2)	101.19(17)	99.654(1)	
O(4)-Ni(2)-N(4)	86.339(2)	85.65(19)	85.210(1)	
O(4)-Ni(2)-N(3)	93.339(2)	96.01(19)	94.870(1)	
O(3)-Ni(2)-N(4)	174.801(2)	175.2(2)	179.111(2)	
O(3)-Ni(2)-N(3)	88.748(2)	83.72(18)	87.964(1)	
O(1)-Ni(2)-N(4)	97.993(2)	102.95(18)	100.357(2)	
O(1)-Ni(2)-N(3)	156.517(2)	155.03(18)	159.230(1)	
O(1)-Ni(2)-S(2)	89.328(2)	88.37(13)	91.839(1)	
O(3)-Ni(2)-S(2)	105.457(2)	106.31(13)	103.126(1)	
O(4)-Ni(2)-S(2)	162.360(2)	162.93(12)	161.795(1)	
N(3)-Ni(2)-S(2)	78.167(1)	79.92(15)	78.179(1)	
N(4)-Ni(2)-S(2)	77.435(1)	78.39(15)	76.039(1)	
N(3)-Ni(2)-N(4)	98.548(2)	96.2(2)	94.892(1)	

Table 4.21: Crystallographic Data and Structure Refinement Parameters for **[CrS2(NO_3)].MeCN, [ZnS2(Cl_2)].THF** and **[CrO1(NO_3)].**

	[CrS2NO_3].MeCN	**[ZnS2(Cl_2)].THF**	**[CrO1(NO_3)]**
Formula	$C_{36}H_{25}CrN_4O_5S$	$C_{38}H_{32}Cl_2N_2O_3SZn$	$C_{26}H_{18}CrN_3O_6$
Fw (g mol^{-1})	677.66	732.98	520.43
Cryst. syst.	Orthorhombic	Monoclinic	Triclinic
Space group	P n a 21	$P2_1/c$	P-1
a (Å)	16.9966(3)	11.2253(4)	9.1725(2)
b (Å)	12.9751(2)	16.7570(7)	9.8604(2)
c (Å)	13.5122(2)	18.5175(7)	13.6151(3)
α (deg)	90	90	80.296(1)
β (deg)	90	105.887(2)	74.373(1)
γ (deg)	90	90	69.700(1)
V ($Å^3$)	2979.88(8)	3350.1(2)	1108.38(4)
z	4	4	2
T(K)	133(2)	133(2)	133(2)
δ_{Calc}(Mg/m^3)	1.511	1.453	1.559
F(000)	1396	1512	534
μ(mm^{-1})	0.508	0.996	0.567
θ range for data collection (deg)	2.18 – 27.48	2.24 – 27.48	2.21 – 27.48
Measd reflns	32479	32741	16775
Unique refln (R_{int})	6631 (0.0358)	7664 (0.0519)	5041 (0.0293)
No. of param	426	432	325
GOF on F^2	1.040	1.129	1.056
R1[I>2σ(I)]	0.0465	0.0525	0.0341
wR2(all data)	0.1201	0.1038	0.0848

Table 4.22: Selected bond lengths (Å) and bond angles (°)

	[CrS2NO$_3$].MeCN	**[ZnS2(Cl)$_2$].THF**	**[CrO1(NO$_3$)]**
Cr(1) – O(1)	1.895(3)		1.9027(12)
Cr(1) – O(2)	1.922(4)		1.8946(12)
Cr(1) – O$_{nitrate}$	2.039(3)		2.0737(12)
Cr(1) – O$_{nitrate}$			2.0778(12)
Zn(1) – O(1)		1.997(2)	
Zn(1) – O(2)		1.977(2)	
Cr(1) – N(1)	2.044(4)		2.0344(14)
Cr(1) – N(2)	2.021(3)		2.0824(14)
Cr(1) – S(1)	2.4777(13)		
Zn(1) – Cl(1)		2.2337(8)	
Zn(1) – Cl(2)		2.2231(8)	
O(1)-Cr(1)-O(2)	92.63(15)		90.84(5)
O(1)-Cr(1)-O$_{nitrate}$	85.78(14)		99.88(5)
O(2)-Cr(1)-O$_{nitrate}$	92.69(17)		86.66(5)
O(1)-Cr(1)-O$_{nitrate}$			86.18(5)
O(2)-Cr(1)-O$_{nitrate}$			162.33(5)
O$_{nitrate}$-Cr(1)-O$_{nitrate}$			62.58(5)
O(1)-Zn(1)-O(2)		95.53(9)	
O(1)-Cr(1)-N(1)	88.69(16)		90.79(5)
O(2)-Cr(1)-N(1)	176.44(14)		91.80(6)
N(1)-Cr(1)-O$_{nitrate}$	84.10(17)		168.08(5)
N(1)-Cr(1)-O$_{nitrate}$			105.65(5)
O(1)-Cr(1)-N(2)	91.32(13)		172.98(5)
O(2)-Cr(1)-N(2)	86.57(16)		90.50(5)
N(2)-Cr(1)-O$_{nitrate}$	176.97(15)		90.46(5)
N(2)-Cr(1)-O$_{nitrate}$			86.32(5)
N(1)-Cr(1)-N(2)	96.71(16)		96.05(6)
O(2)-Cr(1)-S(1)	99.85(11)		
O(1)-Cr(1)-S(1)	163.74(11)		
S(1)-Cr(1)-O$_{nitrate}$	103.87(11)		
N(1)-Cr(1)-S(1)	79.48(11)		
N(2)-Cr(1)-S(1)	79.16(10)		
O(1)-Zn(1)-Cl(1)		100.10(6)	
O(2)-Zn(1)-Cl(1)		107.74(7)	
O(1)-Zn(1)-Cl(2)		117.44(7)	
O(2)-Zn(1)-Cl(2)		115.29(6)	
Cl(1)-Zn(1)-Cl(2)		117.65(3)	

Table 4.23: Crystallographic Data and Structure Refinement Parameters for **$[Cu_3S1_2(OAc)_2].2DCM$, $[Cu_3S2_2(OAc)_2].6CHCl_3$, $[Cu_2S2_2].2THF$, $[Cu_2S3_2].THF$** and **$[Cu_2O1_2].2MeCN$.**

	$[Cu_3S1_2(OAc)_2].2DCM$	**$[Cu_3S2_2(OAc)_2].6CHCl_3$**	**$[Cu_2S2_2].2THF$**
Formula	$C_{58}H_{46}Cl_4Cu_3N_4O_8S_2$	$C_{72}H_{50}Cl_{18}Cu_3N_4O_8S_2$	$C_{76}H_{60}Cu_2N_4O_6S_2$
Fw (g mol^{-1})	1323.59	2070.10	520.43
Cryst. syst.	Triclinic	Monoclinic	Triclinic
Space group	P-1	$P2_1/n$	P-1
a (Å)	11.5361(4)	14.1768(2)	15.0244(4)
b (Å)	11.8096(4)	14.0130(2)	18.9129(5)
c (Å)	12.1254(4)	21.1027(3)	22.4967(6)
α (deg)	108.866(1)	90	91.757(2)
β (deg)	94.322(2)	91.101(1)	107.640(2)
γ (deg)	102.938(2)	90	90.837(2)
V (Å^3)	1530.81(9)	4191.48(10)	6087.2(3)
z	1	2	4
T(K)	133(2)	133(2)	133(2)
δ_{Calc}(Mg/m^3)	1.649	1.640	1.437
F(000)	757	2082	2728
μ(mm^{-1})	1.535	1.435	0.829
θ range for data collection (deg)	1.89 – 27.48	1.75 – 27.48	1.42 – 25.68
Measd reflns	17167	33331	64037
Unique refln (R_{int})	6834 (0.0349)	9575 (0.0360)	22950 (0.0656)
No. of param	386	512	1621
GOF on F^2	1.036	1.074	1.085
R1[I>2σ(I)]	0.0660	0.0403	0.0877
wR2(all data)	0.1747	0.0945	0.1663

	$[Cu_2S3_2].THF$	**$[Cu_2O1_2].2MeCN$**
Formula	$C_{60}H_{52}Cu_2N_4O_5S_2$	$C_{56}H_{42}Cu_2N_6O_6$
Fw (g mol^{-1})	1100.25	1022.03
Cryst. syst.	Triclinic	Monoclinic
Space group	P-1	C2/c
a (Å)	11.5317(2)	21.9554(7)
b (Å)	15.5408(4)	18.9854(5)
c (Å)	19.3960(5)	21.6590(7)
α (deg)	104.330(2)	90
β (deg)	101.075(1)	99.211(2)
γ (deg)	103.043(2)	90
V (Å^3)	3165.73(15)	8911.8(5)
z	2	8
T(K)	133(2)	133(2)
δ_{Calc}(Mg/m^3)	1.154	1.523
F(000)	1140	4208
μ(mm^{-1})	0.783	1.018
θ range for data collection (deg)	2.96 – 27.48	1.63 – 27.48
Measd reflns	31965	56897
Unique refln (R_{int})	14311 (0.0432)	10219 (0.0621)
No. of param	662	634
GOF on F^2	1.055	1.083
R1[I>2σ(I)]	0.0677	0.0499
wR2(all data)	0.1312	0.0945

Table 4.24(a): Selected bond lengths (Å) and bond angles (°)

	$[Cu_3S1_2(OAc)_2].2DCM$	**$[Cu_3S2_2(OAc)_2].6CHCl_3$**	**$[Cu_2S2_2].2THF$**	**$[Cu_2S3_2].THF$**	**$[Cu_2O1_2].2MeCN$**
Cu(1) – O(1)	1.919(3)	1.9319(17)	1.908(4)	1.895(2)	1.9162(19)
Cu(1) – O(1#)			1.896(4)	1.892(2)	1.940(2)
Cu(1) – O(2)	2.320(3)	2.3732(17)			
Cu(1) – $O_{acetate}$	1.948(3)	1.9427(17)			
Cu(1) – $O_{acetate}$	2.707(3)	2.7985(0)			
Cu(1) – N(1)	1.952(3)	1.943(2)	1.984(5)	1.974(3)	1.981(2)
Cu(1) – N(1#)			1.989(5)	1.980(3)	1.988(2)
Cu(1) – S(1)	2.4063(12)	2.4015(6)			
Cu(2) – O(2)	1.914(3)	1.9229(16)	1.882(4)	1.888(3)	1.9070(19)
Cu(2) – O(2#)			1.894(4)	1.894(2)	1.9069(19)
Cu(2) – $O_{acetate}$	2.471(3)	2.5346(0)			
Cu(2) – N(2)	2.007(4)	1.9801(19)	1.981(5)	1.974(3)	1.953(2)
Cu(2) – N(2#)			1.987(5)	1.973(3)	1.953(2)
O(1)-Cu(1)-O(2)	95.59(12)	95.64(7)			
O(1)-Cu(1)-O(1#)			174.31(18)	145.18(11)	127.51(8)
O(1)-Cu(1)-$O_{acetate}$	89.37(13)	90.92(8)			
O(2)-Cu(1)-$O_{acetate}$	86.66(11)	86.08(7)			
$O_{acetate}$-Cu(1)-$O_{acetate}$	53.998(2)	52.156(1)			
O(1)-Cu(1)-N(1)	94.00(14)	91.63(8)	89.89(18)	94.60(11)	95.34(9)
O(1)-Cu(1)-N(1#)			89.83(18)	92.92(11)	95.25(9)
O(1#)-Cu(1)-N(1)			90.38(18)	91.42(11)	97.04(9)
O(1#)-Cu(1)-N(1#)			90.18(18)	94.63(10)	95.25(9)
O(2)-Cu(1)-N(1)	101.82(13)	101.71(7)			
$O_{acetate}$-Cu(1)-N(1)	170.50(13)	171.52(8)			
O(1)-Cu(1)-S(1)	177.31(10)	175.16(6)			
O(2)-Cu(1)-S(1)	87.10(8)	88.52(4)			
$O_{acetate}$-Cu(1)-S(1)	90.85(10)	91.83(5)			
N(1)-Cu(1)-S(1)	85.37(11)	85.09(6)			
N(1)-Cu(1)-N(1#)			177.16(19)	157.17(12)	153.92(9)
O(2)-Cu(2)-O(2#)	180.0	180.00(9)	173.90(19)	156.69(13)	138.88(12)
O(2)-Cu(2)-N(2#)	89.69(14)	89.60(7)	88.14(18)	90.74(12)	95.11(9)
O(2)-Cu(2)-N(2)	90.31(14)	90.40(7)	91.31(19)	92.72(11)	96.58(9)
O(2#)-Cu(2)-N(2)			90.72(18)	91.53(11)	95.11(9)
O(2#)-Cu(2)-N(2#)			89.72(18)	92.57(12)	96.58(9)
N(2)-Cu(2)-N(2#)	180.0(2)	180.0	178.8(2)	161.20(12)	146.28(13)

Table 4.24(b): Continuous Shape Measurements (CSM) for **$[Cu_2S2_2].2THF$**, **$[Cu_2S3_2].THF$** and **$[Cu_2O1_2].2MeCN$**

			Values obtained from CSM calculations		
Label	**Shape**	**Symmetry**	**$[Cu_2S2_2].2THF$**	**$[Cu_2S3_2].THF$**	**$[Cu_2O1_2].2MeCN$**
SP-4	Square-planar	D_{4h}	**0.189**[a] **0.132**[b]	**3.389**[a] 6.294[b]	11.625[a] 11.624[b]
T-4	Tetrahedron	T_d	29.944[a] 31.567[b]	17.603[a] 12.904[b]	7.808[a] 7.808[b]
SS-4	Seesaw or Sawhorse (*cis*- divacant octahedron	C_{2v}	15.921[a] 16.728[b]	8.380[a] **5.565**[b]	**2.788**[a] **2.790**[b]
vTBPY-4	Axially vacant trigonal bipyramid	C_{3v}	31.313[a] 32.609[b]	19.671[a] 14.840[b]	9.307[a] 9.305[b]

a = values obtained for same Cu(II) ion
b = values obtained for same Cu(II) ion

4.5.5 Structural properties of the diazo imine

The crystal structure and crystallographic data of **H_2AI_1** is presented in **Fig. 4.13** and **Table 4.25** respectively. **H_2AI_1** crystallises in an orthorhombic Pbca space group. Like **H_2S3** and **$H_2S5.CHCl_3$**, **H_2AI_1** is unsymmetrical {**Table 4.25**}. The $C{=}N_{imine}$ and hydrogen bond distances are similar to those of the pentadentate imines, although the hydrogen bond distances are relatively shorter.

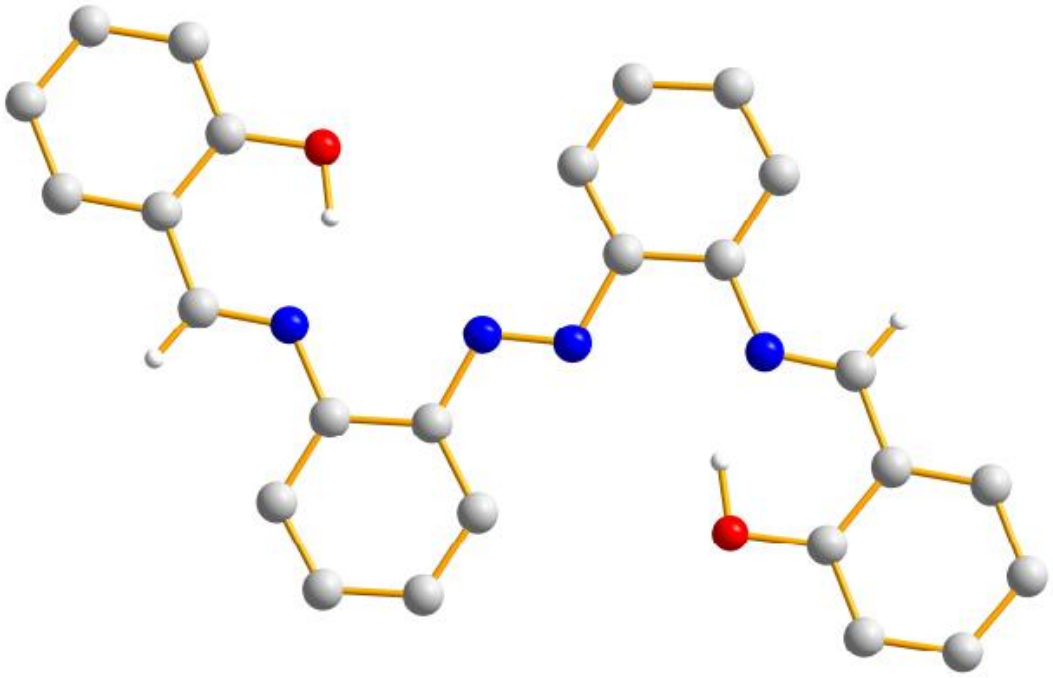

Figure 4.13: Molecular structure of **H_2AI_1.** Some hydrogens are omitted for clarity.

Table 4.25(a): Crystallographic Data and Structure Refinement Parameters for **H_2AI_1.**

	H_2AI_1
Formula	$C_{26}H_{20}N_4O_2$
Fw (g mol^{-1})	420.46
Cryst. syst.	Orthorhombic
Space group	Pbca
a (Å)	16.5862(5)
b (Å)	11.4376(2)
c (Å)	21.1899(6)
α (deg)	90
β (deg)	90
γ (deg)	90
V ($Å^3$)	4019.86(18)
z	8
T(K)	133(2)
δ_{Calc}(Mg/m^3)	1.389
F(000)	1760
μ(mm^{-1})	0.091
θ range for data collection (deg)	2.28 - 27.48
Measd reflns	27989
Unique refln (R_{int})	4603 (0.0823)
No. of param	297
GOF on F^2	1.128
R1[I>2σ(I)]	0.0626
wR2(all data)	0.1300

Table 4.25(b): Selected bond lengths (Å)

	H_2AI_1
N – N	1.2515(0)
$C=N_{imine}$	1.285()
	1.2812(0)
$C – O_{phenol}$	1.3478(0)
	1.3503(0)
C=N···HO	1.6326(0)
	1.6511(0)
N_{imine}···O_{phenol}	2.5581(1)
	2.5720(1)

4.6 Spectroscopic properties of the compounds

4.6.1 Spectroscopic properties of the bis-imidazoles (**BI$_1$** – **BI$_7$**)

The photophysical properties of the **BI$_1$** – **BI$_7$** series are summarised in **Table 4.26**(**a**). Absorption bands in the 228 – 258 nm region are assignable to $\pi \rightarrow \pi^*$ transitions, while bands in the 286 – 366 range are attributed to $n \rightarrow \pi^*$ transitions (Khan *et al*., 2019; Mamiya *et al*., 2016). In comparison to **BI$_1$** {λ_{max}[abs] 309 nm}, a blue shift {5 – 51 nm} was observed in the absorption maxima of the 1,3-series, while a red shift {20 – 57 nm} was observed for the 1,4-series. **BI$_7$** showed the weakest absorption in the series {**Fig. 4.14**[**a**]}, with extinction coefficients {ε} in the range 6 575 – 7 812 M^{-1} cm^{-1}. The 1,3-series {**BI$_1$** – **BI$_4$**} exhibited much higher ε values in comparison to the 1,4-series {**BI$_6$** giving the highest values in this family}. The observed ε values are typical for $\pi \rightarrow \pi^*$ transitions in arene based systems (Mamiya *et al*., 2016).

4.6.2 Spectroscopic properties of the imidazole amines (**A1** – **A9**)

The photophysical properties of **A1** – **A9** are presented in **Table 4.26**(**b**). Like the bis-imidazoles, the imidazole amines also exhibited $\pi \rightarrow \pi^*$ transitions {in the range 225 – 262 nm} as well as $n \rightarrow \pi^*$ transitions {in the range 278 – 373 nm}. **A1** absorbed maximally at 249 nm. In comparison to **A1**, other members of the **N-H** series showed a blue shift {13 – 24 nm} in their absorption maxima, while the **N-Me** and **N-Ph** analogues showed a red shift {6 – 34 nm}, except for **A7** {which showed a 9 nm blue shift}. The **Phen** analogues exhibited the strongest absorption {ε = 56 700 – 75 100 M^{-1} cm^{-1}}, while the ethyl analogue gave the weakest absorption {ε = 10 000 M^{-1} cm^{-1}} (**Fig. 4.15**{**a**}). **A1** exhibited dual emission (**Fig. 4.15**{**b**}), a primary band at 377 nm {possibly due to enol form} and a secondary band at 510 nm {possibly due to keto form}. The introduction of the arene group produced a red shift in the emission maxima {24 – 40 nm, in comparison to the primary emission of **A1**}, substitution of the **N-H** group {generating the **N-Me** and **N-Ph** analogues} resulted in only a slight red shift. This substitution, however, produced a great effect on the Stokes shift {Δν} (**Fig. 4.15**{**e**} and {**f**}). While the **N-H** analogues gave Δν values in the range 42 – 66 nm {3 325 – 4 781 cm^{-1}}, substitution produced Δν values in the range 115 – 149 nm {10 027 – 13 333 cm^{-1}}. The large Stokes shift {arising from enol-keto

tautomerisation} observed for the **N-Me** and **N-Ph** derivatives suggested structural relaxation in this series as well as potential ability to overcome such problems as concentration quenching, scattering, and reabsorption of emitted light (Suzuki *et al*., 2018; Wilbraham *et al*., 2015). The **N-H** analogues were more emissive {**Fig. 4.15**[**c**]} and **Phen** incorporation greatly affected the fluorescence intensities of the compounds – the **Phen** systems showed the highest intensity in each {**N-H**, **N-Me**, and **N-Ph**} series. The emissive nature of the compounds followed the order **Phen** > **MeO** > **Ph** and this enhancement of spectroscopic properties could be attributed to the structural rigidity as well as extension of π-conjugation in the **Phen** core. Substitution at the **N-H** position led to 1 to 5-fold reduction in fluorescence quantum yield {Φ_f}, while substitution on the arene ring led to 1 to 9-fold increase in Φ_f. The large Stokes shift as well as the bathochromic shift {absorption and emission} strongly suggested ESIPT mechanism for the imidazole-amines.

4.6.3 Spectroscopic properties of the imidazole imines ($\mathbf{I_1}$ – $\mathbf{I_9}$) and ($\mathbf{I_{N2}}$ – $\mathbf{I_{N4}}$)

The photophysical properties of $\mathbf{I_1}$ – $\mathbf{I_9}$ and $\mathbf{I_{N2}}$ – $\mathbf{I_{N4}}$ are presented in **Table 4.27**(**a**). The imidazole imines, like their amine precursor, exhibited $\pi \rightarrow \pi^*$ transitions {in the range 232 – 257 nm} as well as $n \rightarrow \pi^*$ transitions {in the range 274 – 374 nm}. $\mathbf{I_1}$ absorbed maximally at 334 nm and {in comparison to $\mathbf{I_1}$} all other NNO imines showed a blue shift {51 – 102 nm} in their absorption maxima. Similarly, a blue shift {33 – 54 nm}, in absorption maxima, was observed for the NNN imines, when compared with $\mathbf{I_{N2}}$ {λ_{max}[abs] = 286 nm}. The trend in extinction coefficients {ε} of the NNO series was similar to that observed for the amine precursor. The **Phen** analogues gave the strongest absorptions {ε = 21 400 – 70 200 M^{-1} cm^{-1}}, while the ethyl analogue gave the weakest absorption {ε = 3 600 M^{-1} cm^{-1}} (**Fig**. **4.16**{**a**}). In comparison to $\mathbf{I_2}$ – $\mathbf{I_4}$, $\mathbf{I_{N2}}$ – $\mathbf{I_{N4}}$ showed slightly stronger absorptions. In contrast to **A1**, $\mathbf{I_1}$ showed a single emission band {emitting maximally at 392 nm}. All other members of the NNO series, when compared with $\mathbf{I_1}$, exhibited a red shifted {11 – 30 nm} emission maxima, except for $\mathbf{I_5}$ which showed a 79 nm blue shift. Substitution of the phenol group {in the NNO imines} with pyridine {in the NNN imines} did not appear to affect emission maxima, as $\mathbf{I_2}$ – $\mathbf{I_4}$ and $\mathbf{I_{N2}}$ – $\mathbf{I_{N4}}$ emitted maximally at very similar wavelengths. In contrast to corresponding amine precursors, the **N-H** analogues {NNO series} showed very large Stokes shift 117 – 147 nm {10 091 – 12 667 cm^{-1}}, except

for **I_1** with Δv of 56 nm {4 252 cm^{-1}} (**Fig. 4.16**{**d**}). The **N-Me** and **N-Ph** analogues {**Fig. 4.16**[**e**] and [**f**]} exhibited large Δv 118 – 154 nm {10 152 – 13 898 cm^{-1}}, except for **I_5** with a value {28 nm [3 139 cm^{-1}]} even lower than for **I_1**. The NNN imines {**Fig. 4.17**[**d**]} gave slightly large Δv 76 – 146 nm {5 832 – 12 687 cm^{-1}}, although they generally showed lower values than corresponding NNO analogue. The emission intensities of the NNO imines followed a similar trend as the amine precursors, with the order **N-H** > **N-Ph** > **N-Me**. The lower intensities of the imines {when compared with the corresponding amine precursor} is attributed to C=N isomerisation. The large Stokes shift observed for the imines is attributed to ESIPT.

4.6.4 Spectroscopic properties of the pentadentate imines {H_2S1 – H_2O1} and (H_2AI_1 – H_2AI_3)

The photophysical properties of **H_2S1** – **H_2O1** {except **H_2S7**} are presented in **Table 4.27**(**b**). The measurements were done in MeOH {except for **H_2S5** which was recorded in $CHCl_3$, due to better solubility}. The compounds absorbed predominantly in the n → π* region {269 – 496 nm} (**Fig. 4.18**{**a**}). They absorbed maximally around 269 nm, suggesting little effect of the structural modification. **H_2S2**, however, absorbed maximally at 317 nm, the red shift {48 nm} arose due to extension of π-conjugation by the naphthalene moiety. In comparison to **H_2S1**, the compounds displayed a red shift in their emission maxima {the bromo and nitro groups with the highest shift}. **H_2S1**, **H_2S2**, **H_2S3** and **H_2O1** exhibited Δv < 100 nm which suggested they do not display ESIPT behaviour {seen in the NNO and NNN imines which also have the ability for proton transfer}. **H_2S2**, however, is the most emissive in this series {**Fig. 4.18**[**b**] and [**c**]}.

The photophysical properties of **H_2AI_1** – **H_2AI_3** are presented in **Table 4.27**(**c**). Although the azo-imines showed much lower absorption {ε values 7 900 – 14 700 M^{-1} cm^{-1}} than corresponding ONSNO/ONONO imines, they showed mainly n → π* absorptions {287 – 499 nm}, with maximum absorptions observed in the range 287 – 316 nm {**Fig. 4.19**[**a**]}. Methyl substitution resulted in ≈2 fold hyperchromic shift in emission band and a slight {7 nm} red shift in absorption maxima {**Fig. 4.19**[**b**]}. In comparison to the S- and O- bridged materials, the N=N bridged **H_2AI_1** showed a red shift in emission band {**Fig. 4.19**[**c**]} – this trend was also observed for the methyl substituted variants. The azo-imines

also showed much higher Δv, suggesting ESIPT mechanism, although they showed low fluorescence quantum yield.

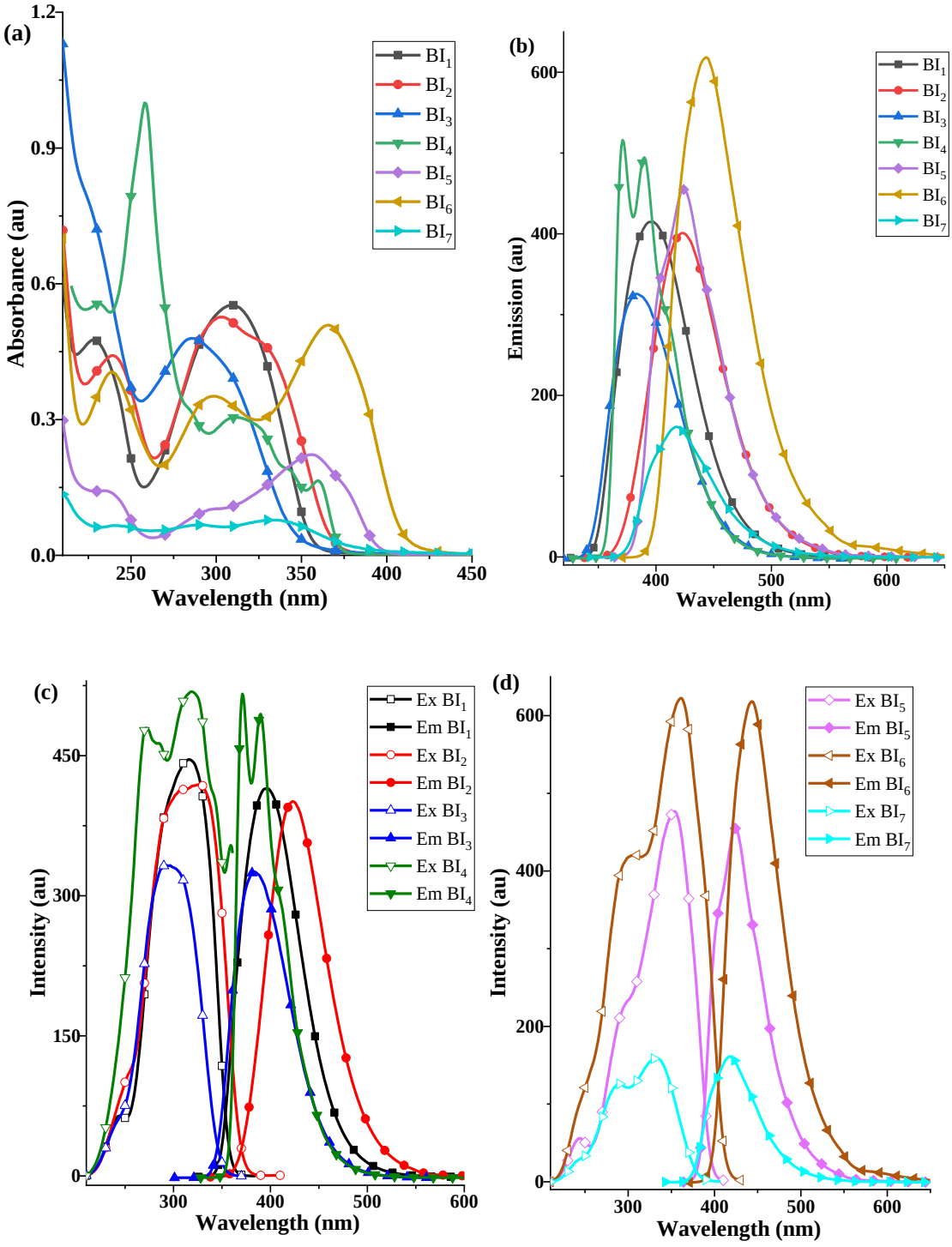

Figure 4.14: (a) Electronic (b) Emission spectra of **BI_1 – BI_7** and Excitation and Emission spectra of (c) **BI_1 – BI_4** and (d) **BI_5 – BI_7**

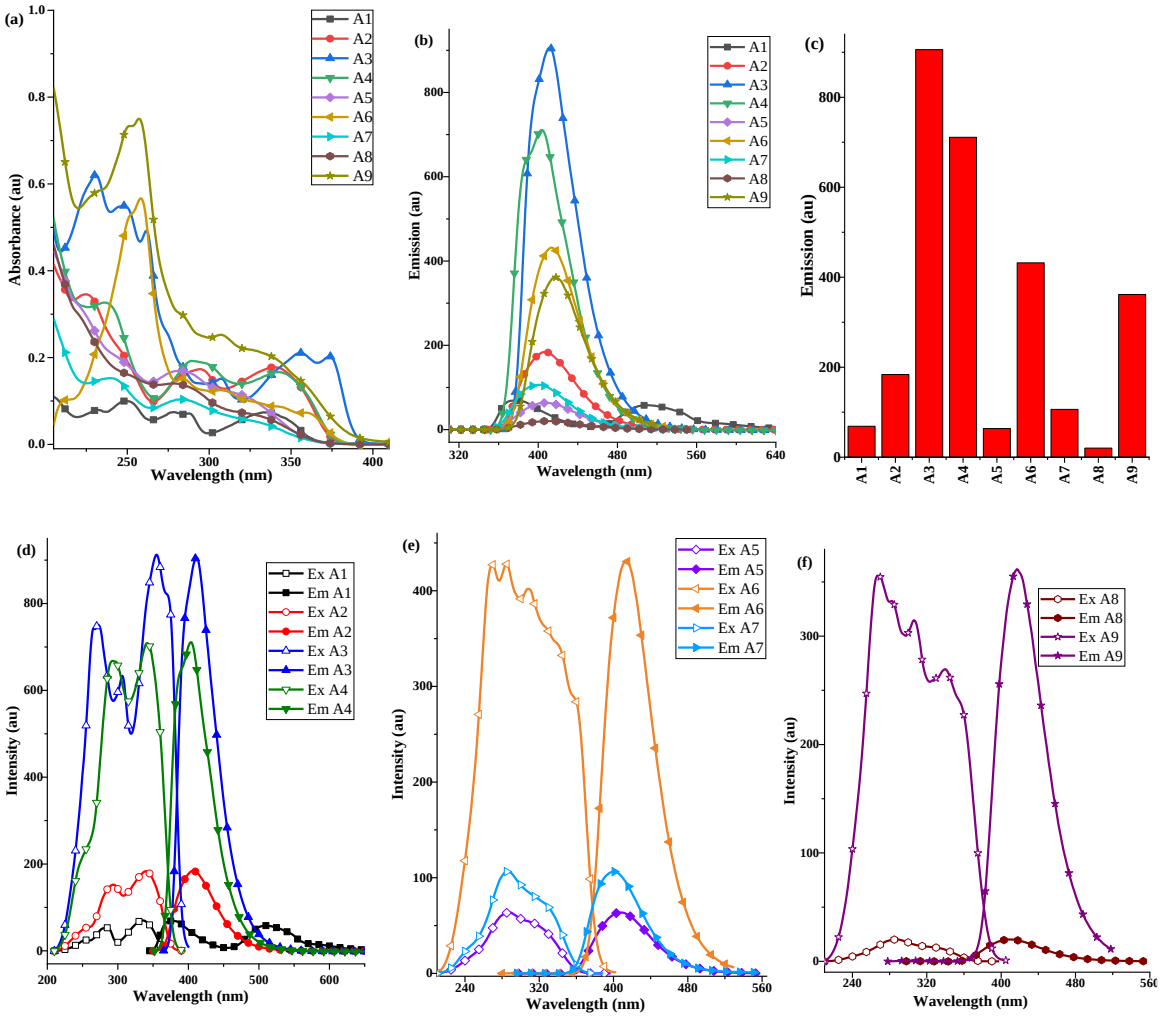

Figure 4.15: (a) Electronic spectra (b) Emission spectra (c) Emission maxima of **A1 – A9** and Excitation and Emission spectra of (d) **A1 – A4** (e) **A5 – A7** (f) **A8 – A9**

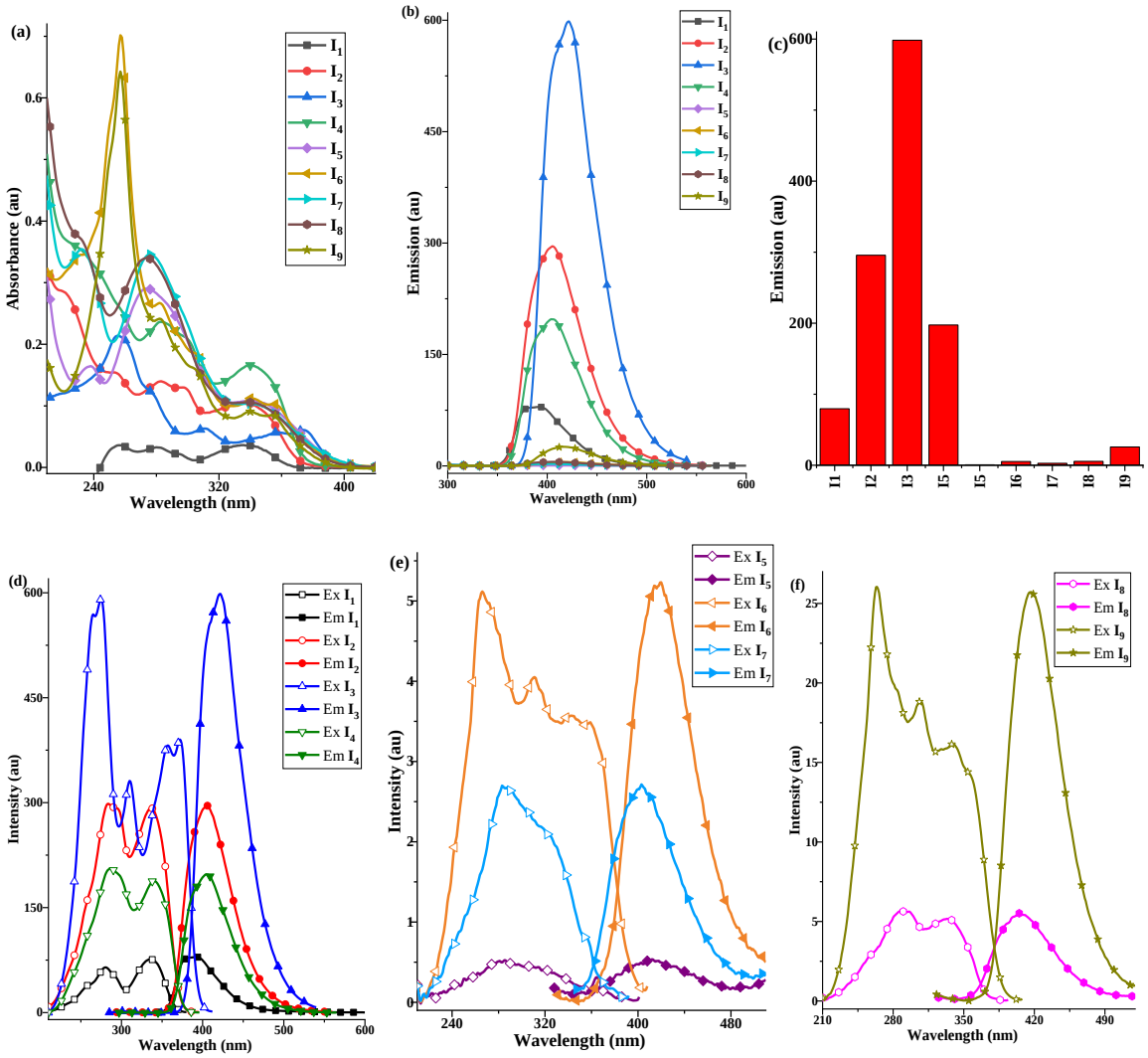

Figure 4.16: (a) Electronic spectra (b) Emission spectra (c) Emission maxima of **I_1 – I_9** and Excitation and Emission spectra of (d) **I_1 – I_4** (e) **I_5 – I_7** (f) **I_8 – I_9**

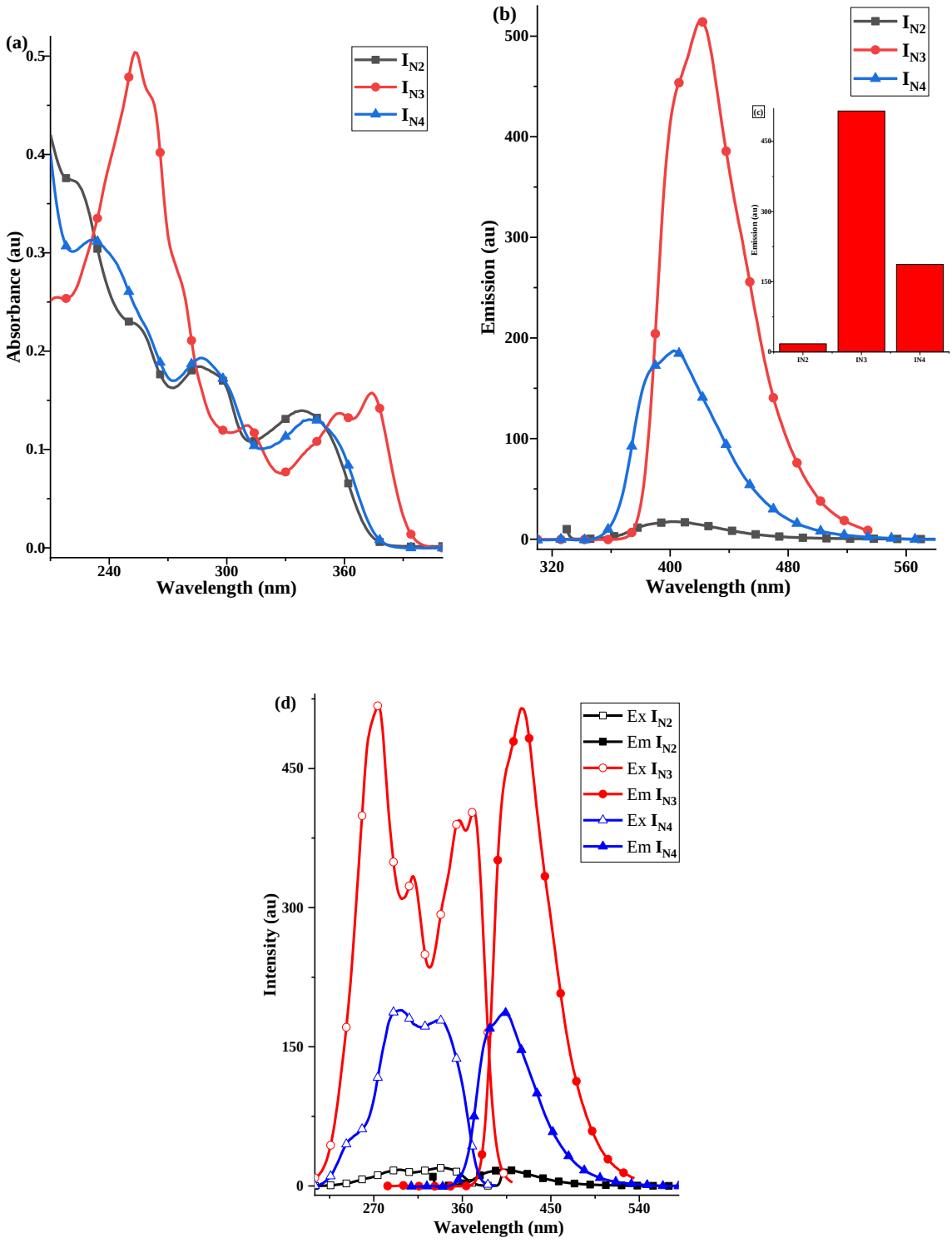

Figure 4.17: (a) Electronic (b) Emission {inset: (c) Emission maxima} of $\mathbf{I_{N2} - I_{N4}}$ and (d) Excitation and Emission spectra of $\mathbf{I_{N2} - I_{N4}}$

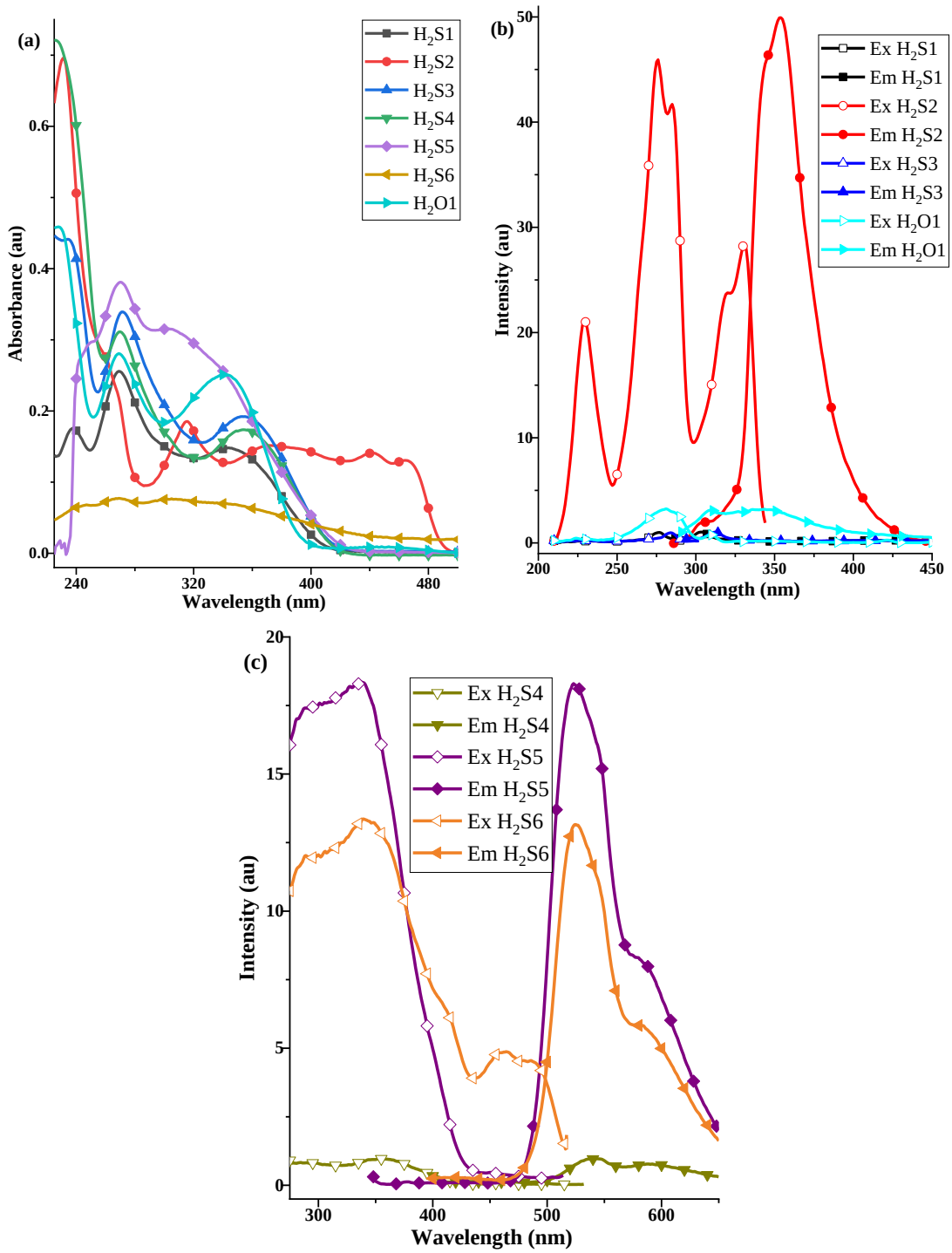

Figure 4.18: (a) Electronic spectra of **H2S1 – H2O1** and Excitation and Emission spectra of (b) **H2S1 – H2S3, H2O1** (c) **H2S4 – H2S6**

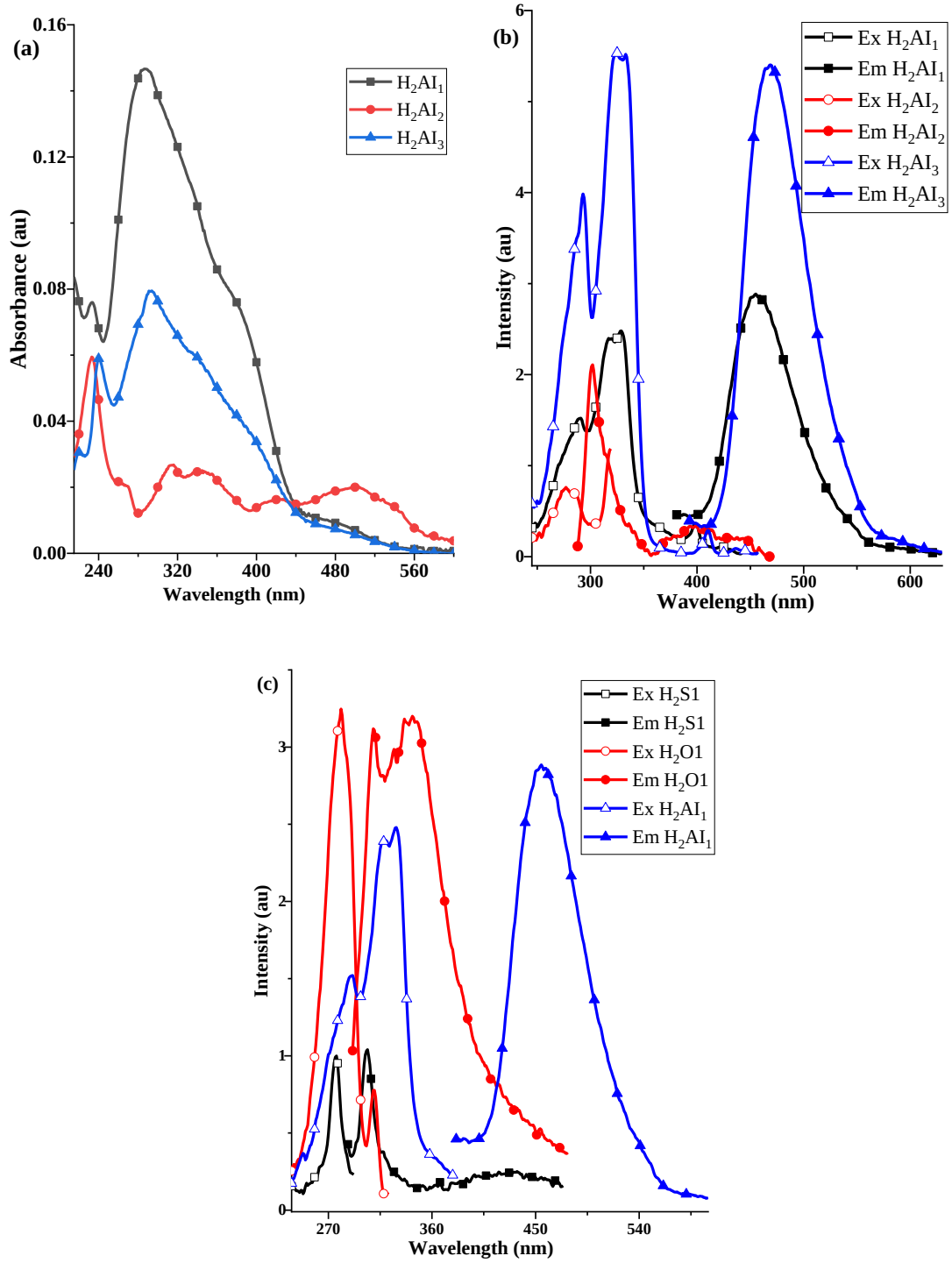

Figure 4.19: (a) Electronic (b) Excitation and Emission spectra of **H_2AI_1 – H_2AI_3** and (c) Effect of S, O and N=N substitution on emission profile.

Table 4.26(a): Photophysical properties of **BI_1 - BI_7**

	λ (Abs) /nm	**λ (Ex) /nm**	**λ_{max} (Em) /nm**	**Δv /nm**	**ε x 10^4 /M^{-1} cm^{-1}**	**Φ_f**
BI_1	228, 309[a]	316	397	81 (6,457[b])	5.53	0.28
BI_2	239, 304[a]	328	423	95 (6,847[b])	5.27	0.44
BI_3	286[a]	300	384	84 (7,292[b])	4.79	
BI_4	231, 258[a], 311, 360	322	371	49 (4,102[b])	9.99	
BI_5	234, 355[a]	354	424	70 (4,664[b])	2.22	0.67
BI_6	239, 299, 366[a]	361	443	82 (5,127[b])	5.09	0.85
BI_7	240, 291, 329[a]	333	418	85 (6,107[b])	0.78	0.56

a = **λ_{max}** *b* = Stokes shift in cm^{-1}

Table 4.26(b): Photophysical properties of **A1 – A9**

	λ (Abs) /nm	**λ (Ex) /nm**	**λ_{max} (Em) /nm**	**Δv /nm**	**ε x 10^4 /M^{-1} cm^{-1}**	**Φ_f**
A1	231, 249[a], 278, 336	335	377 (510)	42 (175)	1.00	0.222
				3,325 (10,242[b])		
A2	225[a], 294, 340	340	406	66 (4,781[b])	3.46	0.175
A3	231[a], 248, 262, 307, 356, 373	355	411	56 (3,838[b])	6.21	0.703
A4	236[a], 289, 343	342	404	62 (4,487[b])	3.27	0.618
A5	283[a]	288	408	120 (10,212[b])	1.69	0.111
A6	258[a], 284, 308, 358	270	413	143 (12,824[b])	5.67	0.549
A7	240[a], 284	286	401	115 (10,027[b])	1.53	0.136
A8	278[a]	288	409	121 (10,272[b])	1.41	0.044
A9	257[a], 307	268	417	149 (13,333[b])	7.51	0.392

a = **λ_{max}** *b* = Stokes shift in cm^{-1}

Table 4.27(a): Photophysical properties of **I_1 – I_9** and **I_{N2} – I_{N4}**

	λ (Abs) /nm	**λ (Ex) /nm**	**λ_{max} (Em) /nm**	**Δν /nm**	**ε x 10^4 /M^{-1} cm^{-1}**	**Φ_f**
I_1	256, 280, 334[a]	336	392	56 (4,252[b])	0.36	0.057
I_2	253[a], 282, 334	284	405	121 (10,520[b])	1.54	0.434
I_3	255[a], 310, 358, 374	275	422	147 (12,667[b])	2.14	0.819
I_4	283[a], 339	287	404	117 (10,091[b])	2.37	0.172
I_5	238, 274[a], 340	285	313	28 (3,139[b])	2.91	0.001
I_6	257[a], 282, 341, 356	266	420	154 (13,784[b])	7.02	0.004
I_7	232[a], 276, 338	283	403	120 (10,522[b])	3.55	0.002
I_8	274[a], 339	287	405	118 (10,152[b])	3.40	0.004
I_9	257[a], 282, 339, 354	264	417	153 (13,898[b])	6.43	0.022
I_{N2}	286[a], 338	325	401	76 (5,832[b])	1.84	0.006
I_{N3}	253[a], 311, 374	274	420	146 (12,687[b])	5.03	0.422
I_{N4}	232[a], 287, 342	298	403	105 (8,743[b])	3.13	0.104

a = **λ_{max}** *b* = Stokes shift in cm^{-1}

Table 4.27(b): Photophysical properties of **H_2S1 – H_2O1**[a]

	λ(Abs) /nm	**λ (Ex) /nm**	**λ_{max} (Em) /nm**	**Δν /nm**	**ε x 10^4 /M^{-1} cm^{-1}**	**Φ_f**
H_2S1	269[b], 344	277	303	26 (3,098[c])	2.56	0.0035
H_2S2	317[b], 372, 464	276	354	78 (7,983[c])	1.83	0.0812
H_2S3	271[b], 353	284	312	28 (3,160[c])	3.39	0.0020
H_2S4	270[b], 352	354	538	184 (9,661[c])	3.11	0.0053
H_2S5[d]	270[b], 303	338	523	185 (10,465[c])	3.81	0.0020
H_2S6	269[b], 305, 496	340	525	185 (10,364[c])	N.D[e]	N.D[e]
H_2O1	269[b], 341	281	343	62 (6,433[c])	2.81	0.0083

a = **H_2S7** is not included due to very poor solubility in solvents tested, *b* = **λ_{max}**, *c* = Stokes shift in cm^{-1}, *d* = done in $CHCl_3$, *e* = Not determined due to incomplete solubility

Table 4.27(c): Photophysical properties of **H_2AI_1 – H_2AI_3**

	λ_{max} (Abs) /nm	**λ (Ex) /nm**	**λ_{max} (Em) /nm**	**Δν /nm**	**ε x 10^4 /M^{-1} cm^{-1}**	**Φ_f**
H_2AI_1	287[a]	326	455	129 (8,697[b])	1.47	0.0019
H_2AI_2	316[a], 341, 499	275	302	27 (3,251[b])	N.D[c]	N.D[c]
H_2AI_3	294[a]	336	469	133 (8,440[b])	0.79	0.0054

a = **λ_{max}**, *b* = Stokes shift in cm^{-1}, *c* = Not determined due to incomplete solubility

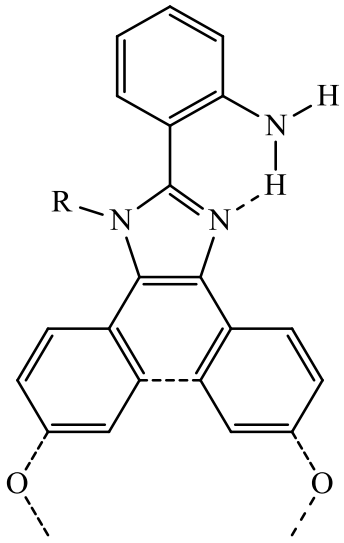

R = H, Me, Ph

Figure 4.20: Intramolecular hydrogen bonding leading to ESIPT in the imidazole amines

4.7 Magnetic properties of the metal complexes

4.7.1 Magnetic properties of the NNO/NNN imine complexes

The *dc* susceptibility measurements for the NNO/NNN imine complexes (**M1**, **M3**, **M5, M7** and **M9**) were performed on powder samples and recorded over a temperature range of 2 – 300 K. The data is presented in **Fig. 4.21** – **Fig. 4.25**. ^{1}H nmr study of **M2** {**Fig. S56**} revealed protons in the aromatic region only, suggesting the octahedral d^6 Co^{III} ions is in a low-spin state {$t_{2g}^6\ e_g^0$ configuration} – thus, **M2** is diamagnetic.

In the four-coordinate complexes (**M1**, **M3**, **M7** and **M9**) the observed room temperature effective magnetic moment {μ_{eff}} of 4.5, 4.7, 4.3 and 4.05 μ_B, respectively were higher than expected for square planar geometry {2.1 – 2.8 μ_B}, but typical for high spin d^7 systems in a tetrahedral field {4.2 – 4.8 μ_B}, suggesting $e^4t_2^3$ configuration. The values were much larger than the spin-only value {3.87 μ_B; three {3} unpaired electrons} for systems with $S = {}^3/_2$ and $g = 2.0$, suggesting significant influence of orbital contribution to the magnetic moment. Although the μ_{eff} value of **M9** was lower than for **M1**, **M3** and **M7**, it still conforms to tetrahedral d^7 Co^{II} ions possessing orbital contribution (Holm and Cotton 1959; Holm and Cotton 1960). The room temperature $\chi_M T$ values of the complexes **M1**, **M3**, **M7** and **M9** {2.6, 2.7, 2.35 and 2.05 cm^3Kmol^{-1}, respectively} were larger than expected for mononuclear Co^{II} ions {1.875 cm^3Kmol^{-1} for $S = {}^3/_2$ and $g = 2.0$}, also indicating strong contribution of orbital angular momentum. The observed μ_{eff} of the five-coordinate **M5** {4.5 μ_B} was higher than expected for d^7 high spin Co^{II} ions {three (3) unpaired electron} system {3.87 μ_B}; the higher value probably due to second-order Zeeman effect as well as SOC {arising from mixing of ground and higher terms} – the orbital contribution is believed to be more significant than the Zeeman effect; and the value also supports a trigonal bipyramidal geometry {**Fig. 4.5**[**c**]} (Dori and Gray 1968; Preti *et al*., 1977; Thompson *et al*., 1977; Carabineiro *et al*., 2008; Spillecke *et al*., 2022). Like the four-coordinate complexes, the $\chi_M T$ value (at 300 K) for **M5** {2.5 cm^3Kmol^{-1}} fits commonly observed values {2.1 – 3.4 cm^3Kmol^{-1}} and was larger than expected for mononuclear Co^{II} ions {1.875 cm^3Kmol^{-1}}, indicating strong orbital contribution to angular momentum (Massoud *et al*., 2008; Mondal *et al*., 2019; Acharya *et al*., 2020). The observed decrease in the μ_{eff} and $\chi_M T$ values of the complexes {plots **a** and **b** in **Fig. 4.21** – **Fig. 4.25**},

upon cooling, indicated depopulation of the $S = {}^{3}/_{2}$ sublevel, presence of SOC as well as possible antiferromagnetism (Buchholz *et al*., 2012; Huang *et al*., 2014; Nemec *et al*., 2015; Antal *et al*., 2016; Smolko *et al*., 2017; Acharya *et al*., 2020). Replacing Cl^- (in **M1**) with AcO^- (in **M3**) generated only a slight increase in μ_{eff} and $\chi_M T$ (at 300 K), while the introduction of MeO group (in **M7**) appeared to cause a decrease in both values (at 300 K). The complexes showed good conformity with the Curie-Weiss law, $\chi_M = C/(T - \Theta)$, {plot **c** in **Fig. 4.21** – **Fig. 4.25**}, suggesting presence of antiferromagnetism (Narayanan *et al*., 2008).

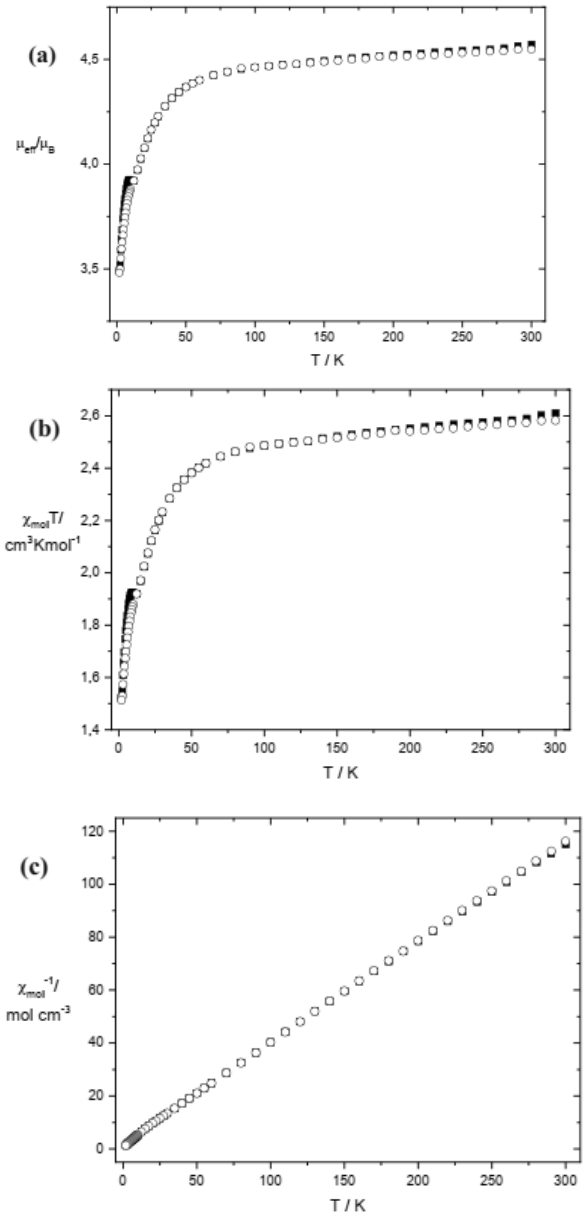

Figure 4.21: Variable Temperature plots of (a) effective magnetic moment {μ_{eff}} (b) $\chi_M T$ (c) Curie-Weiss law of **M1**

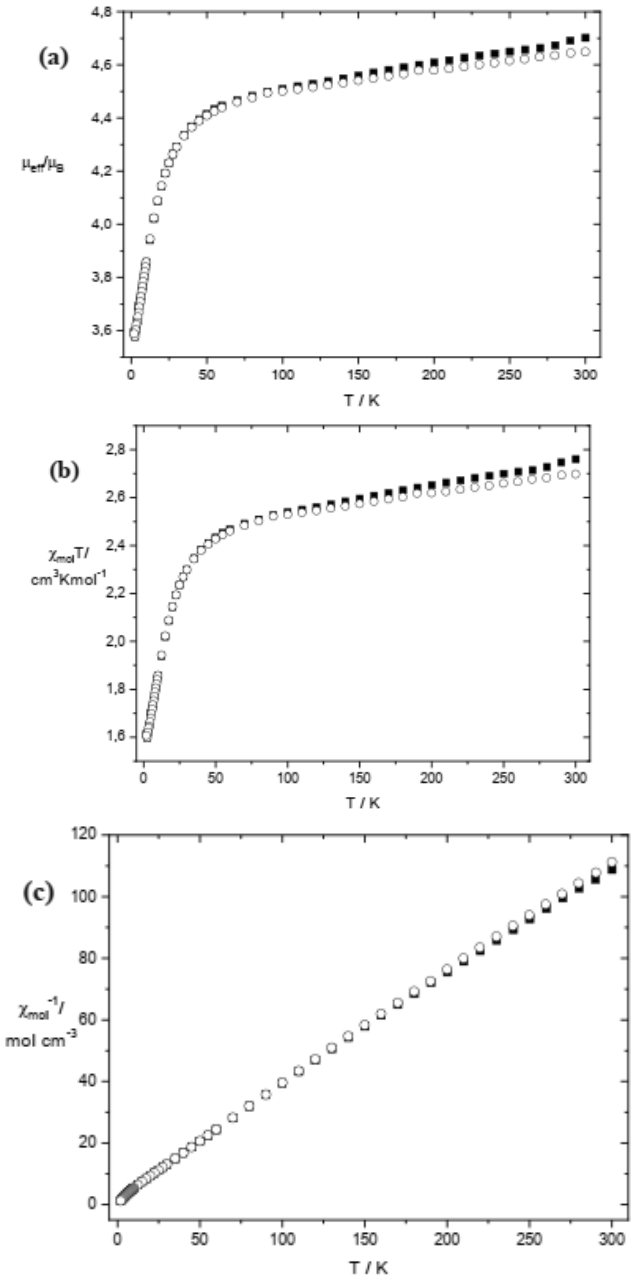

Figure 4.22: Variable Temperature plots of (a) effective magnetic moment $\{\mu_{\text{eff}}\}$ (b) $\chi_M T$ (c) Curie-Weiss law of **M3**

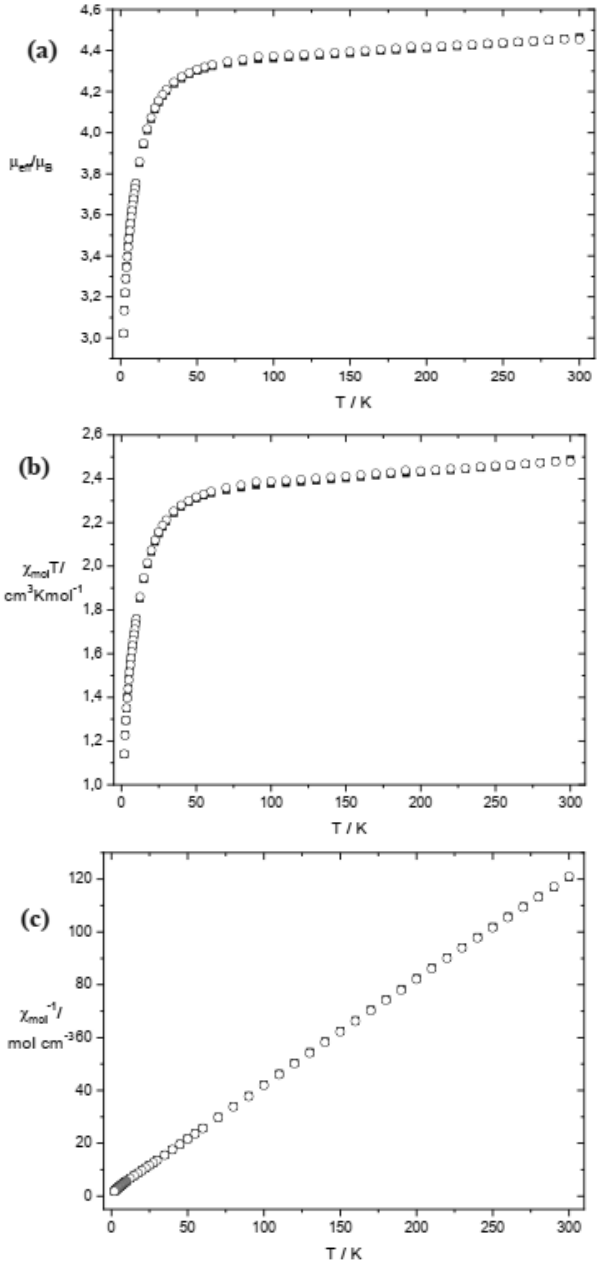

Figure 4.23: Variable Temperature plots of (a) effective magnetic moment $\{\mu_{\text{eff}}\}$ (b) $\chi_M T$ (c) Curie-Weiss law of **M5**

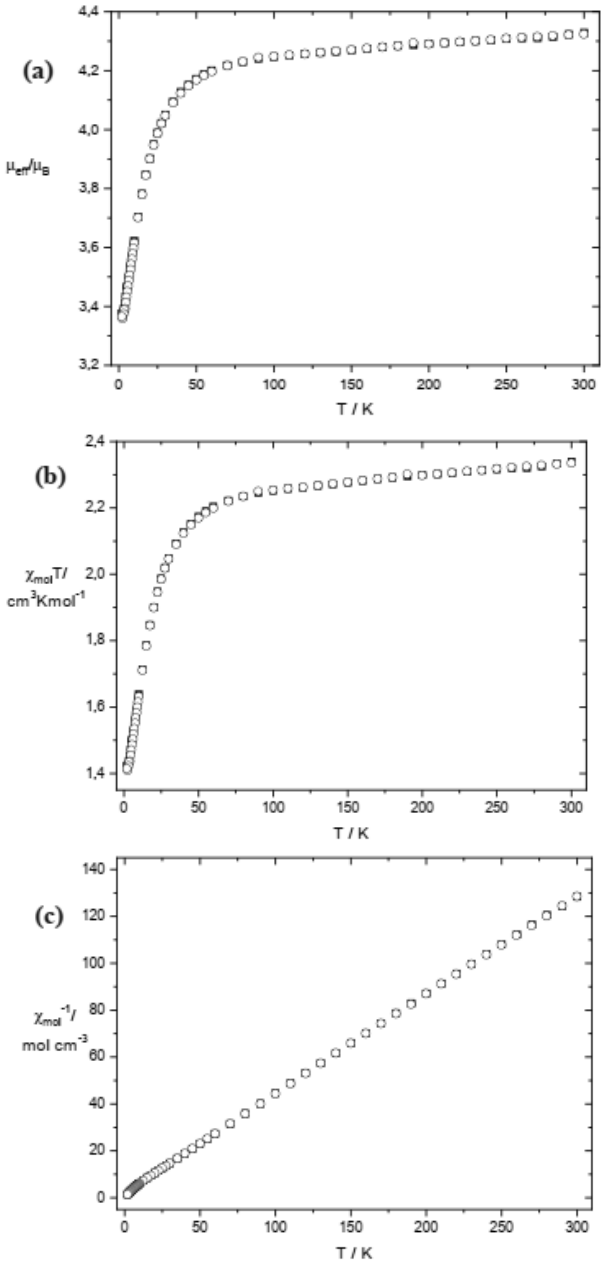

Figure 4.24: Variable Temperature plots of (a) effective magnetic moment {μ_{eff}} (b) $\chi_M T$ (c) Curie-Weiss law of **M7**

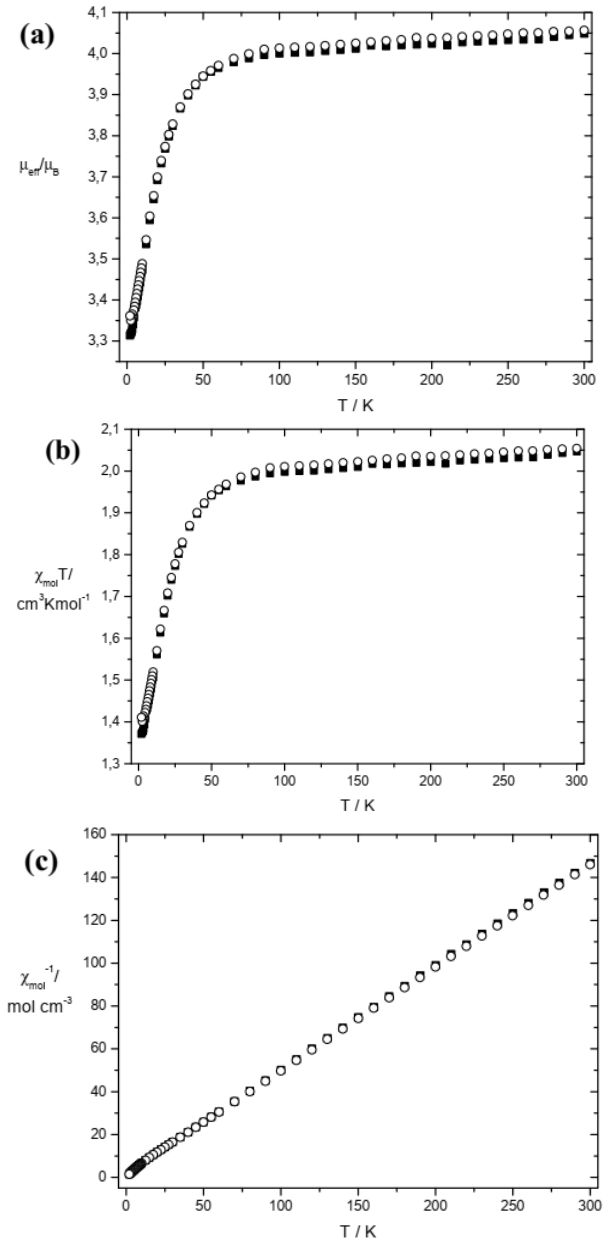

Figure 4.25: Variable Temperature plots of (a) effective magnetic moment {μ_{eff}} (b) $\chi_M T$ (c) Curie-Weiss law of **M9**

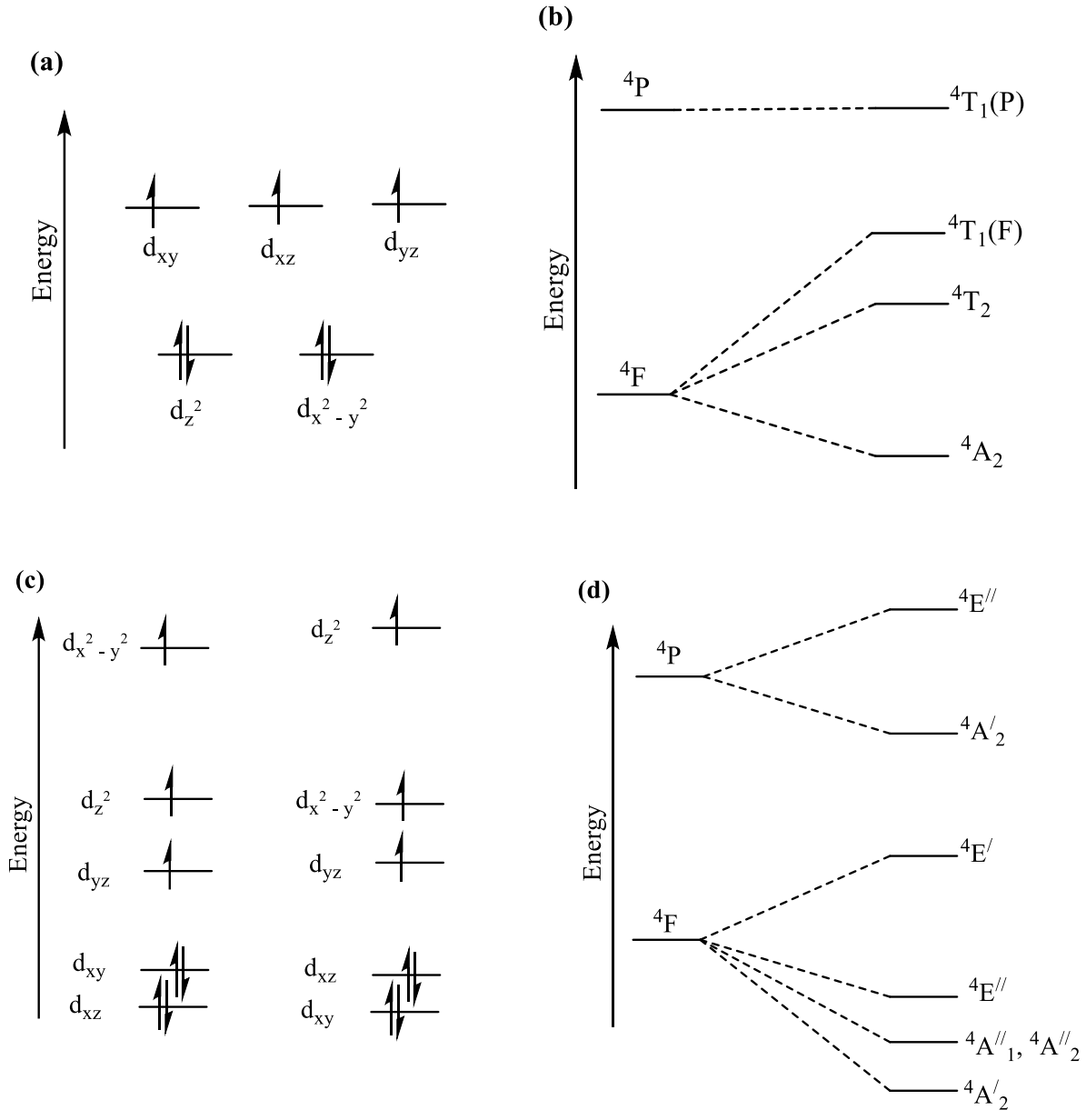

Figure 4.26: (a) Ligand field {*d*-orbital} splitting {for d^7 Co^{II} ion} and (b) simplified energy level diagram for tetrahedral ligand field. (c) Ligand field {*d*-orbital} splitting {for d^7 Co^{II} ion} and (d) simplified energy level diagram for trigonal bipyramidal {D_{3h}} ligand field.

4.7.2 Magnetic properties of the pentadentate imine complexes

The susceptibility ($\chi_M T$) for the mononuclear Cr^{III} complex, the di- and mono-nuclear Ni^{II} complexes {**[Ni_2S2_2]4H_2O** and **[NiS5(H_2O)]**} and the di- and tri-nuclear Cu^{II} complexes {**[$Cu_3S1_2(OAc)_2$]2.75H_2O**, **[$Cu_3S2_2(OAc)_2$]5.5H_2O**, **[Cu_2S2_2]2THF** and **[Cu_2O1_2]1.5H_2O**} were recorded at 2 kOe, over a temperature range of 2 – 300 K; while that of the eight dinuclear Co^{II} complexes were recorded under a 1000 G field, over a temperature range of 2 – 300 K. The effective magnetic moment, μ_{eff}, were calculated using $\mu_{eff} = 2.828(\chi_M T)^{½}$.

The room temperature $\chi_M T$ value {**Fig. 4.27(a)**} of the Cr^{III} complex {1.88 cm^3Kmol^{-1}} was close to the spin-only value for a free or weakly coupled d^3 Cr^{III} ion {1.875 cm^3Kmol^{-1} for $S = {}^3/_2$} suggesting absence of orbital contribution to the angular momentum. This value was nearly constant even up to 50 K, with a sharp decrease observed at < 20 K. The plot trend suggested zero-field splitting (ZFS) and/or weak antiferromagnetic interactions (Chérif *et al*., 2013; Liu *et al*., 2014; Su *et al*., 2016; Dridi *et al*., 2018; Bazhenova *et al*., 2021). The observed μ_{eff} of the Cr^{III} complex {3.88 μ_B at 300 K} was in close agreement with the spin-only value {3.87 μ_B, $S = {}^3/_2$} expected for three unpaired electrons in an isolated Cr^{III} ion {$t_{2g}{}^3$ configuration} and supports the octahedral geometry around the Cr^{III} ion (Chandra and Gupta 2002; Alonso *et al*., 2011; Liu *et al*., 2014; Su *et al*., 2016; Schuman *et al*., 2021). Fitting was performed applying the simple Hamiltonian in Eq. (**4.1**) and using PHI (Chilton *et al*., 2013) to arrive at the following values $g = 2.00$ {which was close to the isotropic value $g_e = 2.0023$}, $D = –1.17 \pm 0.05$ cm^{-1} {an "easy-axis" type magnetic anisotropy}, and $zJ = –0.064 \pm 0.001$ cm^{-1}. The zJ represents intermolecular coupling between Cr^{III} centres in neighbouring molecules, which occurs via π-π interactions. Since the ground and excited states in d^3 Cr^{III} ions {in a distorted O_h field} are well separated, the low ZFS value {$D = –1.17 \pm 0.05$ cm^{-1}} was expected (Pedersen and Toftlund 1974; Karunadasa *et al*., 2010). Although the D value was lower than observed for some reported Cr^{III} complexes (Pedersen and Toftlund 1974; Goswami and Misra 2012;

Semenaka *et al*., 2010; Karunadasa *et al*., 2010), the negative sign suggested **[CrO1(ONO$_2$)]0.5H$_2$O.0.2MeCN** was a good SMM candidate (Goswami and Misra 2012).

$$\hat{H} = g\mu_B B\hat{S} + D[\hat{S}_z^2 - \tfrac{1}{3}S(S+1)] \qquad \text{Equation } \mathbf{4.1}$$

The first term in Eq. (**4.1**) takes into consideration the Zeeman contribution, where g is the Landé factor {or Zeeman/giromagnetic tensor}; μ_B is the Bohr magneton; B is the applied magnetic field. The second term takes into consideration the zero-field splitting {ZFS} of the d^3 Cr^{III} quartet species {$S = {}^3/_2$}, with D as the axial second order ZFS parameter.

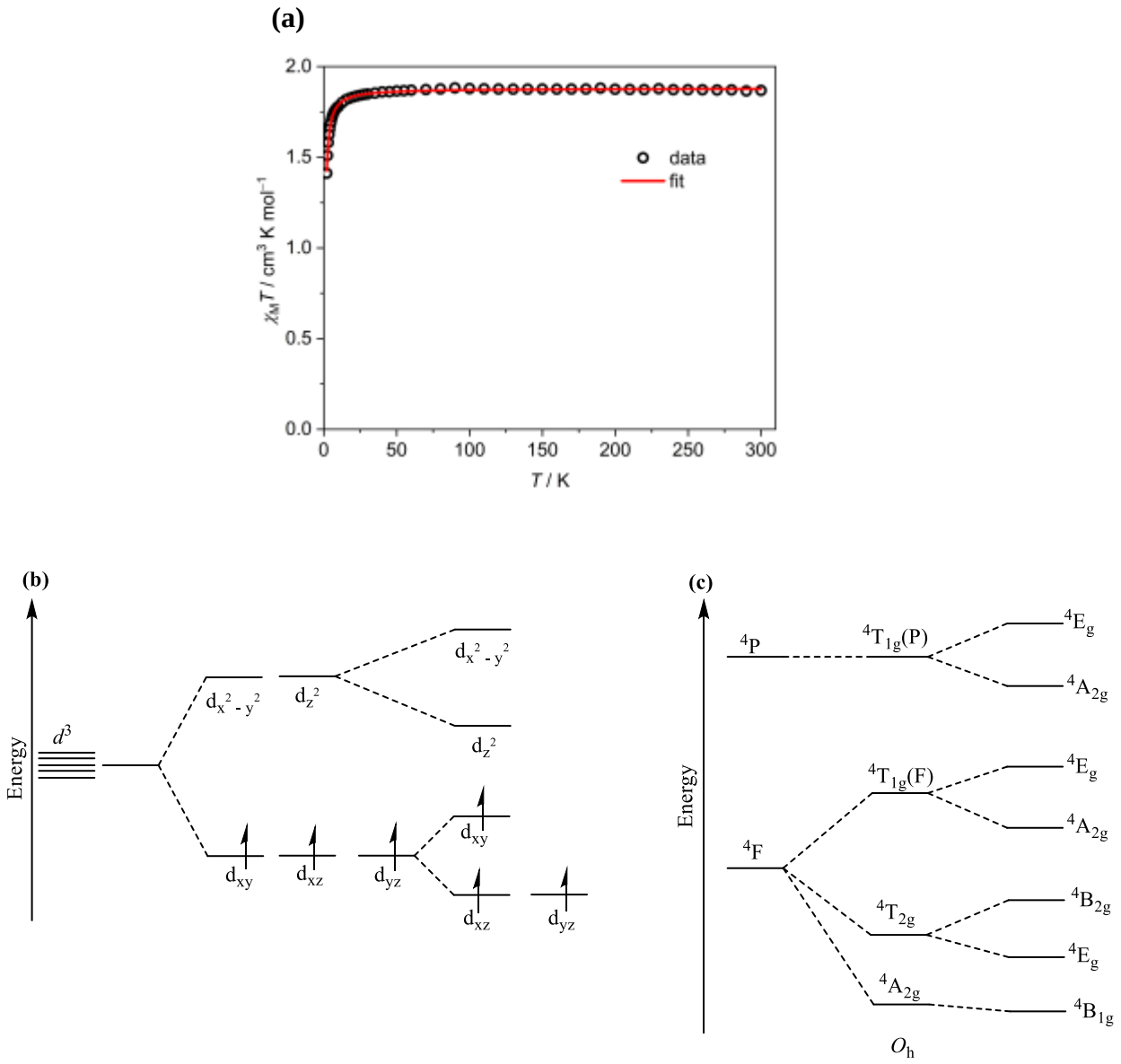

Figure 4.27: (a) Temperature-dependent $\chi_M T$ plot for **[CrO1(ONO$_2$)]0.5H$_2$O.0.2MeCN.** Red line represented best fit of data. (b) Ligand field {*d*-orbital} splitting {for d^3 Cr^{III} ion} and (c) simplified energy level diagram for Octahedral {O_h} ligand field.

The room temperature $\chi_M T$ values {**Fig. 4.28**} of the dinuclear Co^{II} complexes were in the range 4.09 – 5.20 cm^3Kmol^{-1}. These values {5.20, 4.78, 4.23, 4.33, 4.53, 4.09, 4.28 and 4.60 cm^3Kmol^{-1}, respectively} were larger than those expected for two non-interacting Co^{II} ions {3.75 cm^3Kmol^{-1} for $S = {}^3/_2$ and $g = 2.0$} suggesting orbital contribution to their angular momentum. Upon temperature lowering, the $\chi_M T$ values decreased smoothly due to depopulation of the higher energy states {Kramer's doublet} of the Co^{II} ions with $^4T_{1g}$ ground state, arising from SOC as well as the strong possibility of antiferromagnetic exchange interactions between the Co^{II} ions (Mishra *et al*., 2006). The SOC splits the ground state {$^4T_{1g}$} into 12 fold degenerate levels {consisting of a Kramer's doublet, a quartet and a sextet} (Fink *et al*., 1999; Fabelo *et al*., 2008; Frost *et al*., 2016). The μ_{eff} values of the complexes {6.45, 6.18, 5.82, 5.88, 6.02, 5.72, 5.85 and 6.07 μ_B respectively} were larger than the expected spin only {μ_{so}} value {$\mu_{so} = \{4S(S + 1)\}^{1/2} = 3.87\ \mu_B$; $S = {}^3/_2$}; they were also larger than the value expected when spin momentum and orbital momentum exist independently {$\mu_{LS} = \{L(L + 1) + 4S(S + 1)\}^{1/2} = 5.20\ \mu_B$, $L = 3$, $S = {}^3/_2$} therefore supporting the contribution of orbital angular momentum typical for the $^4T_{1g}$ term. The Co^{II} ions existed predominantly in severely distorted octahedral {O_h} environment {**Table 4.18**}, and were bridged over a μ_2-phenoxo bridge {**Fig. 4.9**}. The O_h geometry around the metal ions suggested the Lloret approach as the best way to describe the magnetic behaviour. As mentioned in section **2.5.2.1**, the Heisenberg-Dirac-van Vleck model does not sufficiently represent anisotropic high-spin d^7 Co^{II} centres {especially in O_h field}, hence, the coupling exchange {J_{ex}}, axial distortion parameter {Δ}, orbital reduction factor (α) and spin-orbit coupling parameter (λ) were selected, while fitting was carried out using PHI (Chilton *et al*., 2013). A single set of parameters was applied {to avoid overparameterisation} to both Co^{II} centres. The applied Hamiltonian is in Eq. (**4.2**) below:

$$\hat{H} = (-2J_{ex})\hat{S}_1\hat{S}_2 + \alpha\lambda L_i \cdot \hat{S}_i + \alpha 2\Delta(3L_{zi}^2 - L_i^2) + \mu_B(\alpha L_i + S_i \cdot g_o)B \qquad \text{Equation } \mathbf{4.2}$$

where $i = 1$, 2 and $g_o = 2.0023$. Also due to the correlation between the λ and α parameters, as seen in the second term of the Hamiltonian, the former is fixed as -170 cm^{-1}, close to the value for the free ion (Hossain *et al*., 2002). Experimental data in each case was obtained using the values in **Table 4.28**.

The sign of the exchange {J_{ex}} in all eight compounds was consistent with the decrease in the $\chi_M T$ data {**Fig. 4.28**}. The observed antiferromagnetic exchange followed expected trend for dinuclear Co^{II} complexes with Co-O-Co bond angles > 90^o (Brown *et al*., 2001; Hossain *et al*., 2002; Zeng *et al*., 2004; Jung *et al*., 2009; Daumann *et al*., 2013; Li *et al*., 2015; Khandar *et al*., 2015; Alam *et al*., 2016; Sushila *et al*., 2022). The exchange was expected to be mediated through the two phenoxo bridges linking the Co^{II} ions in each complex. The slight variation in magnitude of the coupling suggested that the nature of the phenoxo-bridges can and does influence the strength of the interactions between the two metal ions {Fabelo *et al*., 2009; Alam *et al*., 2016; Sushila *et al*., 2022}.

A variation is seen in the axial distortion parameter, Δ, of the complexes except for **$[Co_2S2_2]3.5H_2O$** and **$[Co_2S3_2]2H_2O$** {**Table 4.28**}. This {variation} could be attributed to the distorted octahedral environment of the Co^{II} ions in each case; which was in part due to the steric factors as well as the presence of the sulphur donor which should result in an elongation along the Co–S bond vector. The aforementioned steric factors would come into play due to the way the materials were expected to pack resulting in medium to large scale distortions around the Co^{II} ions. The similarities in the values for the distortion parameter in **$[Co_2S2_2]3.5H_2O$** and **$[Co_2S3_2]2H_2O$** should be regarded as mere coincidence as the geometrical influence of both their ligands is expected to be quite different.

As described in section **2.5.2.1**, the α parameter gives an idea of the measure of covalency as well as the extent of the admixture between the T_{1g} states of the F and P terms. The greater the covalency {or the stronger the admixture}, the lower the value of α. Except for **$[Co_2S1_2]3H_2O$**, the values of α observed for the complexes fall below the range {-1.05 to -1.425} expected for Co^{II} ions in a high spin octahedral geometry {Fabelo *et al*., 2009}. Although, the observed lower values might suggest increased covalence arising from the Co–S bond, it is much more likely that it was due to stronger admixing between the T_{1g} states of the F and P terms {Lloret *et al*., 2008}.

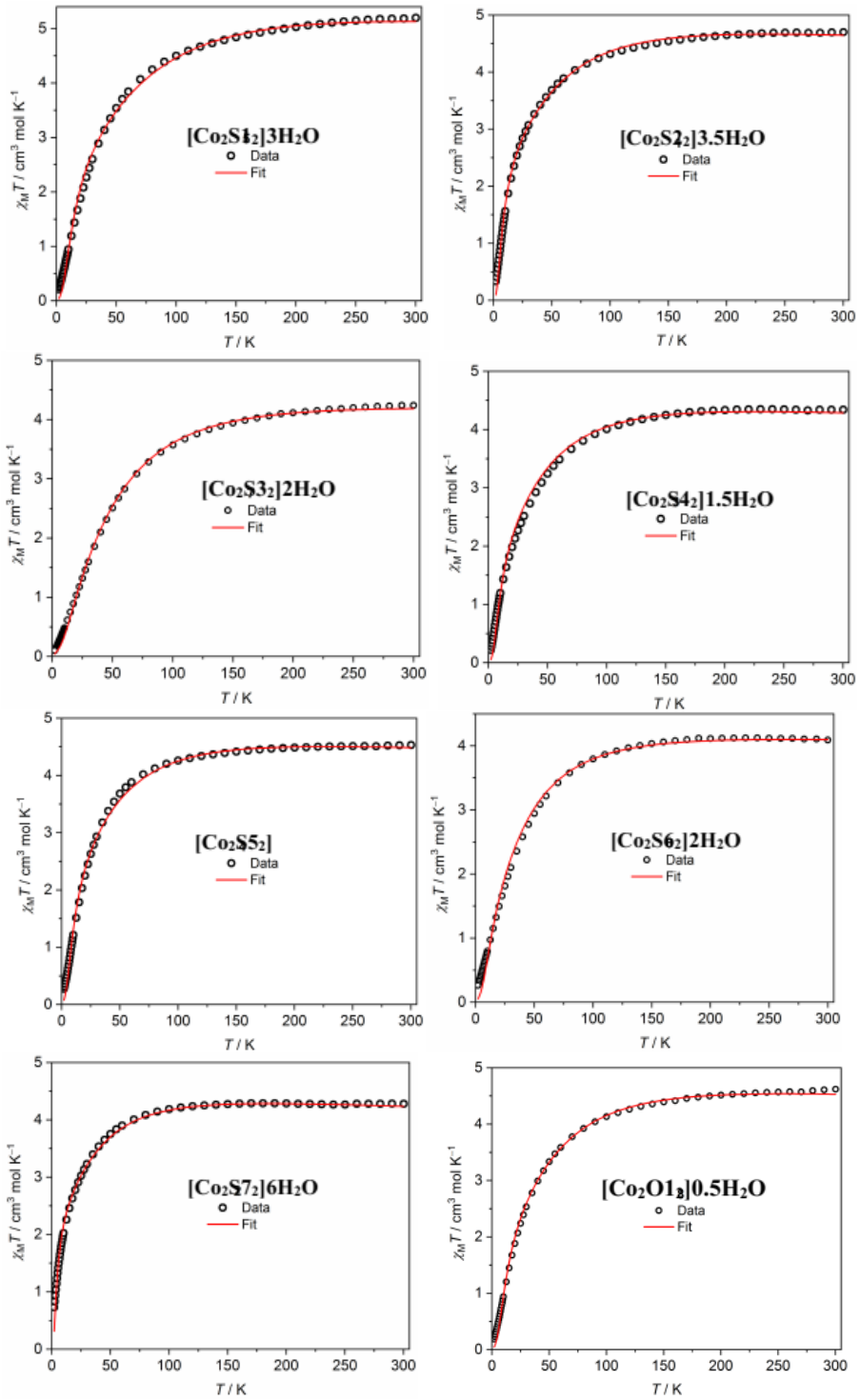

Figure 4.28: Temperature-dependent plots of $\chi_M T$ for **[Co2S12]3H2O – [Co2O12]0.5H2O** measured at *dc* field of 1000 G. Lines represent best fit of data.

Table 4.28: Summary of fitted parameters obtained for **[Co$_2$S1$_2$]3H$_2$O – [Co$_2$O1$_2$]0.5H$_2$O*.**

	J_{ex} (cm^{-1})	Δ (cm^{-1})	α
[Co$_2$S1$_2$]3H$_2$O	-5.04 ± 0.13	-214 ± 18	-1.01 ± 0.012
[Co$_2$S2$_2$]3.5H$_2$O	-2.80 ± 0.06	-283 ± 20	-0.51 ± 0.010
[Co$_2$S3$_2$]2H$_2$O	-10.5 ± 0.28	-283 ± 29	-0.60 ± 0.008
[Co$_2$S4$_2$]1.5H$_2$O	-4.41 ± 0.14	-243 ± 33	-0.57 ± 0.011
[Co$_2$S5$_2$]	-3.18 ± 0.07	-440 ± 32	-0.71 ± 0.009
[Co$_2$S6$_2$]2H$_2$O	-6.44 ± 0.24	-355 ± 48	-0.50 ± 0.014
[Co$_2$S7$_2$]6H$_2$O	-1.63 ± 0.05	-361 ± 34	-0.51 ± 0.010
[Co$_2$O1$_2$]0.5H$_2$O	-4.86 ± 0.12	-278 ± 22	-0.72 ± 0.009

*Displayed error values refer to uncertainties in calculation from PHI and not experimental error from measurements.

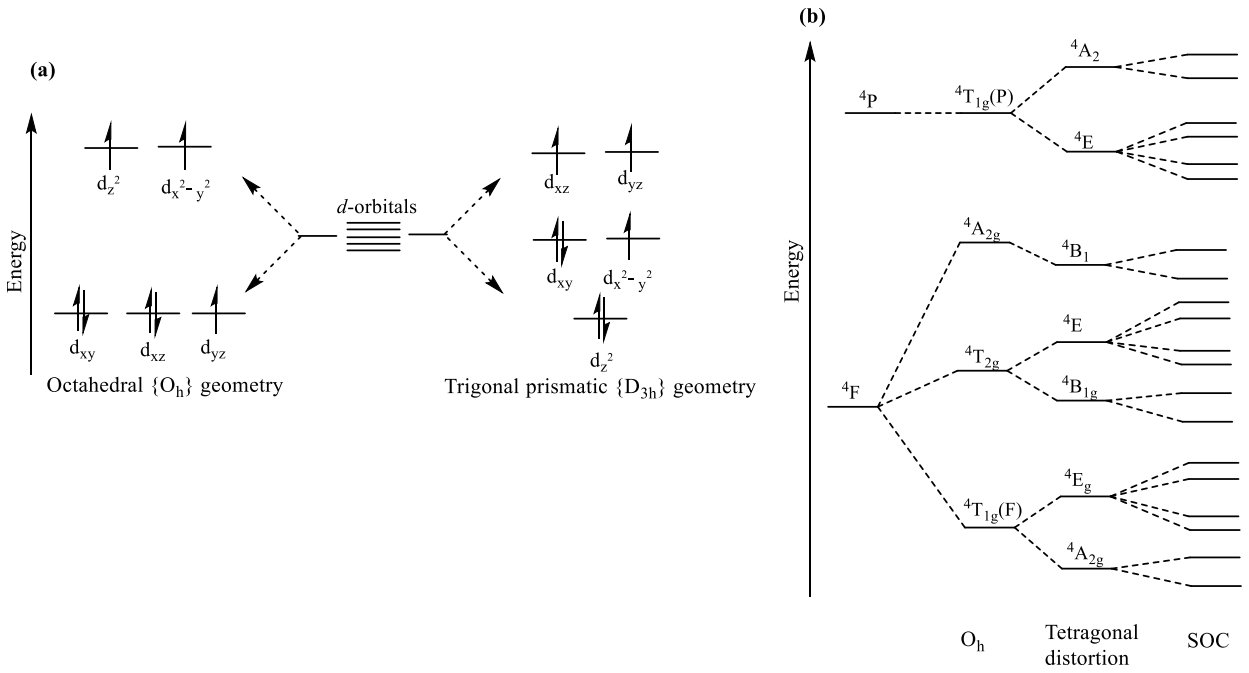

Figure 4.29: (a) Ligand field {*d*-orbital} splitting and (b) simplified energy level diagram for six coordinate, d^7 Co^{II} ion.

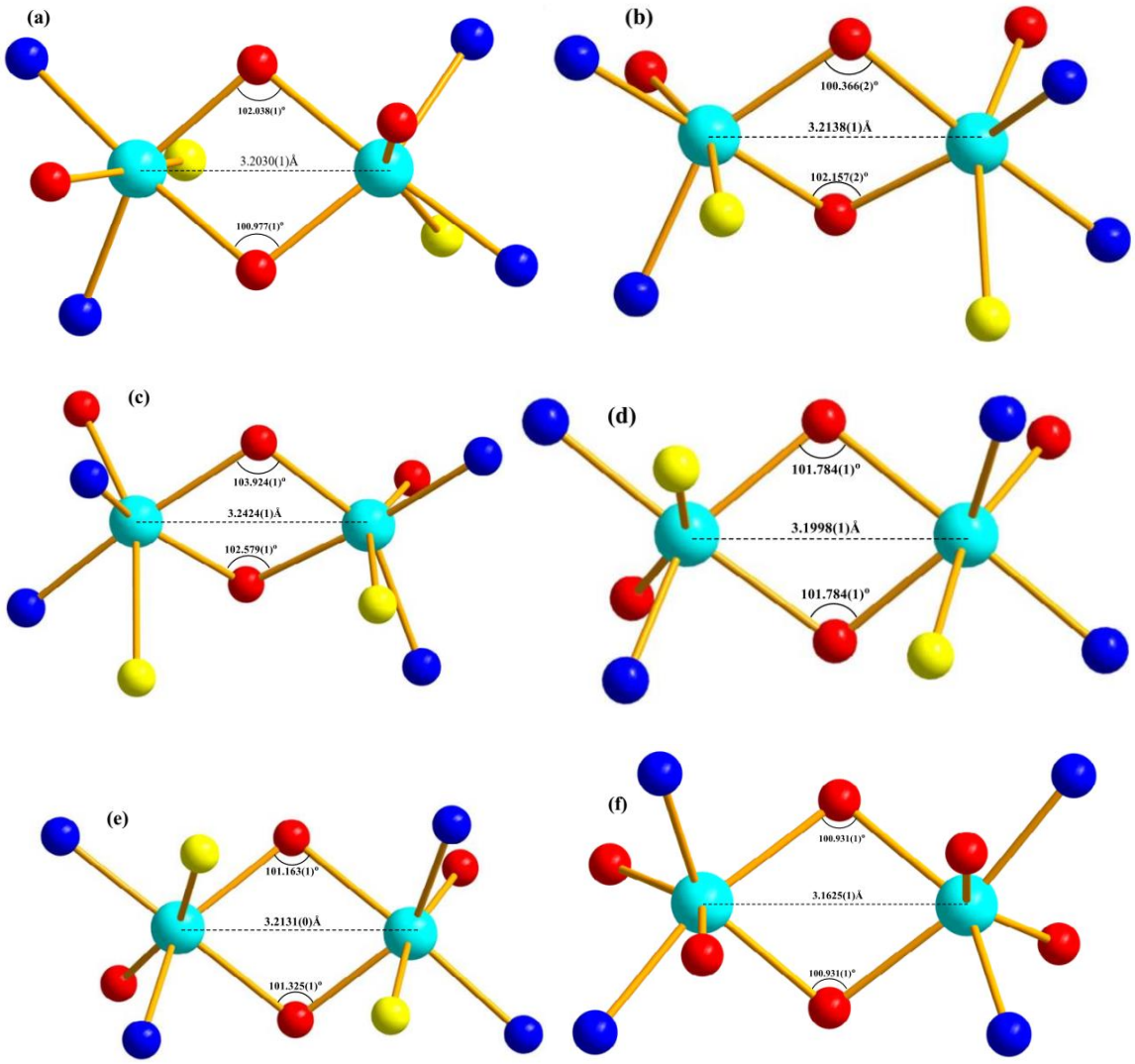

Figure 4.30: Co-Co distance and Co-$O_{(phenoxo)}$-Co bridge angles for (a) **$[Co_2S1_2]3H_2O$** (b) **$[Co_2S2_2]3.5H_2O$** (c) **$[Co_2S4_2]1.5H_2O$** (d) **$[Co_2S5_2]$** (e) **$[Co_2S7_2]6H_2O$** and (f) **$[Co_2O1_2]0.5H_2O$**

The room temperature $\chi_M T$ values {**Fig. 4.31**(**a**) and (**b**)} for the dinuclear **[Ni$_2$S2$_2$]4H$_2$O** {2.3 cm^{3}Kmol^{-1}} and the mononuclear **[NiS5(H$_2$O)]** {1.23 cm^{3}Kmol^{-1}} were slightly higher than expected for two non-interacting Ni^{II} ions and a single Ni^{II} ion {2.0 and 1.0 cm^{3}Kmol^{-1}, for S = 1} respectively. The slightly higher values might be ascribed to minimal spin-orbital contribution from the $^3T_{2g}$ state, since no orbital contribution is expected from the $^3A_{2g}$ ground term (Horn Jr., *et al*., 2018). Upon cooling {in both cases}, a slight increase in the $\chi_M T$ value was observed until a maximum around 17.5 K. The downturn in the $\chi_M T$ curve {at < 17.5 K} can be attributed to the ZFS at low temperatures. The μ_{eff} values of the complexes {4.29 μ_B, for **[Ni$_2$S2$_2$]4H$_2$O** and 3.14 μ_B for **[NiS5(H$_2$O)]**} were larger than the expected spin only {μ_{so}} values {4.00 μ_B and 2.83 μ_B respectively, for S = 1} and also supported orbital contribution from the excited $^3T_{2g}$ term. Fitting for **[Ni$_2$S2$_2$]4H$_2$O** was performed by applying the Hamiltonian in Eq. (**4.3**) and using PHI (Chilton *et al*., 2013) to arrive at the following values g = 2.16, D = –20 cm^{-1} {an "easy-axis" type magnetic anisotropy}, J_{ex} = –1.96 cm^{-1} and zJ = –0.7 cm^{-1}; while the fitting for **[NiS5(H$_2$O)]** was performed by applying the Hamiltonian in Eq. (**4.1**) and using PHI to arrive at the following values g = 2.20, D = +12.8 cm^{-1} {an "easy-plane" type magnetic anisotropy}, and zJ = +0.83 cm^{-1}.

$$\hat{H} = J_{ex}(S_1S_2) + g\mu_B B\hat{S} + D[\hat{S}_z^2 - \tfrac{1}{3}S(S+1)] \qquad \text{Equation } \mathbf{4.3}$$

Comparison of the fits obtained using PHI and the relevant Hamiltonians in Eqs. (**4.1**) and (**4.3**) showed a few differences. The similarity in their g-tensors could be as a result of the likeness in their geometric environments {**Table 4.20**}. The dinuclear analogue showed a weak antiferromagnetic exchange which was mediated over its μ_2-phenoxo bridge. In addition both complexes displayed weak $\pi - \pi$ interactions of similar magnitudes and this would account for the slight increase in the $\chi_M T$ values as the temperature decreased. Another difference between the two complexes can be seen in the type of ZFS they displayed, while **[Ni$_2$S2$_2$]4H$_2$O** displayed an "easy-axis" type of anisotropy {D = –20 cm^{-1}}, **[NiS5(H$_2$O)]** displayed an "easy-plane" type of anisotropy {D = +12.8 cm^{-1}}. The difference in the values of this last parameter in both cases may be simply attributed to the nuclearity displayed by both compounds resulting in an alteration in the lowest lying levels arising from the split of the $^3A_{2g}$ term.

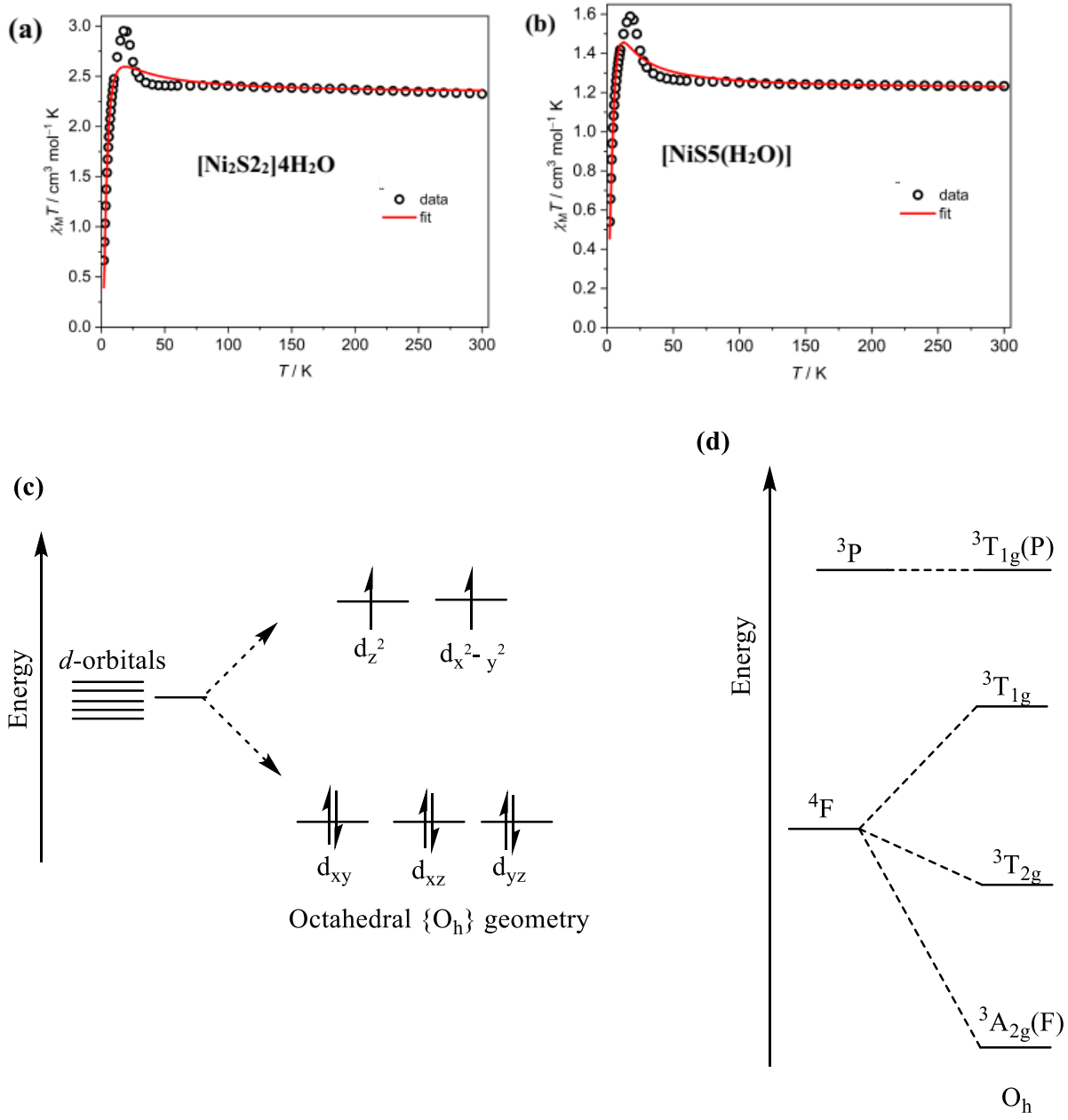

Figure 4.31: Temperature-dependent $\chi_M T$ plot for (a) **[Ni2S22]4H2O** and (b) **[NiS5(H2O)].** Red lines represent best fit of data. (c) Ligand field {*d*-orbital} splitting and (d) simplified energy level diagram for six coordinate, d^8 Ni^{II} ion.

The room temperature $\chi_M T$ values {**Fig. 4.32**} for the trinuclear **[Cu$_3$S1$_2$(OAc)$_2$]2.75H$_2$O** and **[Cu$_3$S2$_2$(OAc)$_2$]5.5H$_2$O** {1.18 and 1.21 cm^{3}Kmol^{-1}, respectively} and the dinuclear **[Cu$_2$S2$_2$]2THF** and **[Cu$_2$O1$_2$]1.5H$_2$O** {0.86 and 0.82 cm^{3}Kmol^{-1}, respectively} were only slightly larger than expected for three non-interacting Cu^{II} ions {1.125 cm^{3}Kmol^{-1}, S = ½ and g = 2.0}, and two non-interacting Cu^{II} ions {0.75 cm^3 K mol^{-1}, S = ½ and g = 2.0}. In the dinuclear complexes, these values remained constant until low temperatures when they began to decrease suggesting the onset of antiferromagnetic exchange between the Cu^{II} ions, while in the trinuclear complexes a decrease was seen at temperatures around 100 K suggesting stronger antiferromagnetic interactions in the trinuclear complexes as compared with the dinuclear complexes.

The dinuclear complexes were fitted with the simple HDvV Hamiltonian $\hat{H} = -J\hat{S}_1\hat{S}_2$, giving rise to the values g = 2.10 and J_{ex} = –0.4 cm^{-1} {for **[Cu$_2$S2$_2$]2THF**} and g = 2.13 and J_{ex} = –1.7 cm^{-1} {for **[Cu$_2$O1$_2$]1.5H$_2$O**}. In the case of the trinuclear complexes, this HDvV Hamiltonian was modified to account for a third Cu^{II} centre within a linear arrangement resulting in the new equation $\hat{H} = -J(\hat{S}_1\hat{S}_2 + \hat{S}_2\hat{S}_3)$ and the derived values were g = 2.13 and J_{ex} = –33.0 cm^{-1} {for **[Cu$_3$S1$_2$(OAc)$_2$]2.75H$_2$O**} and g = 2.12 and J_{ex} = –30.5 cm^{-1} {for **[Cu$_3$S2$_2$(OAc)$_2$]5.5H$_2$O**}.

Like in the case of the Ni^{II} complexes, the similarities in the g-tensors {of the four complexes} could be due to the similar geometric environment of the Cu^{II} centres {**Table 4.24**(**a**)}. The exchange coupling {J_{ex}} showed an organisation in two groups – the extremely weakly-coupled and the weakly coupled systems. The differences in magnitude of coupling in both groups {extremely weakly-coupled and weakly coupled} can be simply ascribed to the variation in the structures of the relevant magnetic units {that is, di- and tri-nuclear cores}. In the case of the dinuclear complexes, the Cu^{II} centres are well-separated {4.9924(1) Å for **[Cu$_3$S1$_2$(OAc)$_2$]2.75H$_2$O** and 4.7026(1) Å for **[Cu$_2$O1$_2$]1.5H$_2$O**} and the possibility of exchange was limited to the chance of weak interaction via the O and S atoms, respectively, bridging the phenyl groups in their ligands. In contrast, within the trinuclear units, the Cu^{II} atoms are much closer {3.2033(1) Å for **[Cu$_2$S2$_2$]2THF** and 3.2609(0) Å for **[Cu$_2$O1$_2$]1.5H$_2$O**} and with the shorter distance between the bridging O atoms and the Cu atoms, there was a higher possibility of exchange interactions within the Cu$_3$ units of both

{**[$Cu_3S1_2(OAc)_2$]2.75H_2O** and **[$Cu_3S2_2(OAc)_2$]5.5H_2O**} complexes. The similarities in their structures was further highlighted by the insignificant differences in the values of the exchange between their Cu^{II} centres. The oxo bridging angles of the trinuclear complexes were very close {Cu-$O_{(phenoxo)}$-Cu is 97.855(2)^o for **[$Cu_3S1_2(OAc)_2$]2.75H_2O** and 98.216(1)^o for **[$Cu_3S2_2(OAc)_2$]5.5H_2O**; while Cu-$O_{(acetate)}$-Cu was 92.147(2)^o for **[$Cu_3S1_2(OAc)_2$]2.75H_2O** and 92.533(1)^o for **[$Cu_3S2_2(OAc)_2$]5.5H_2O**}. The Cu-O-Cu bond angle is believed to play a vital role in coupling exchange, with higher angles resulting in higher J_{ex} values (Biswas *et al*., 2011).

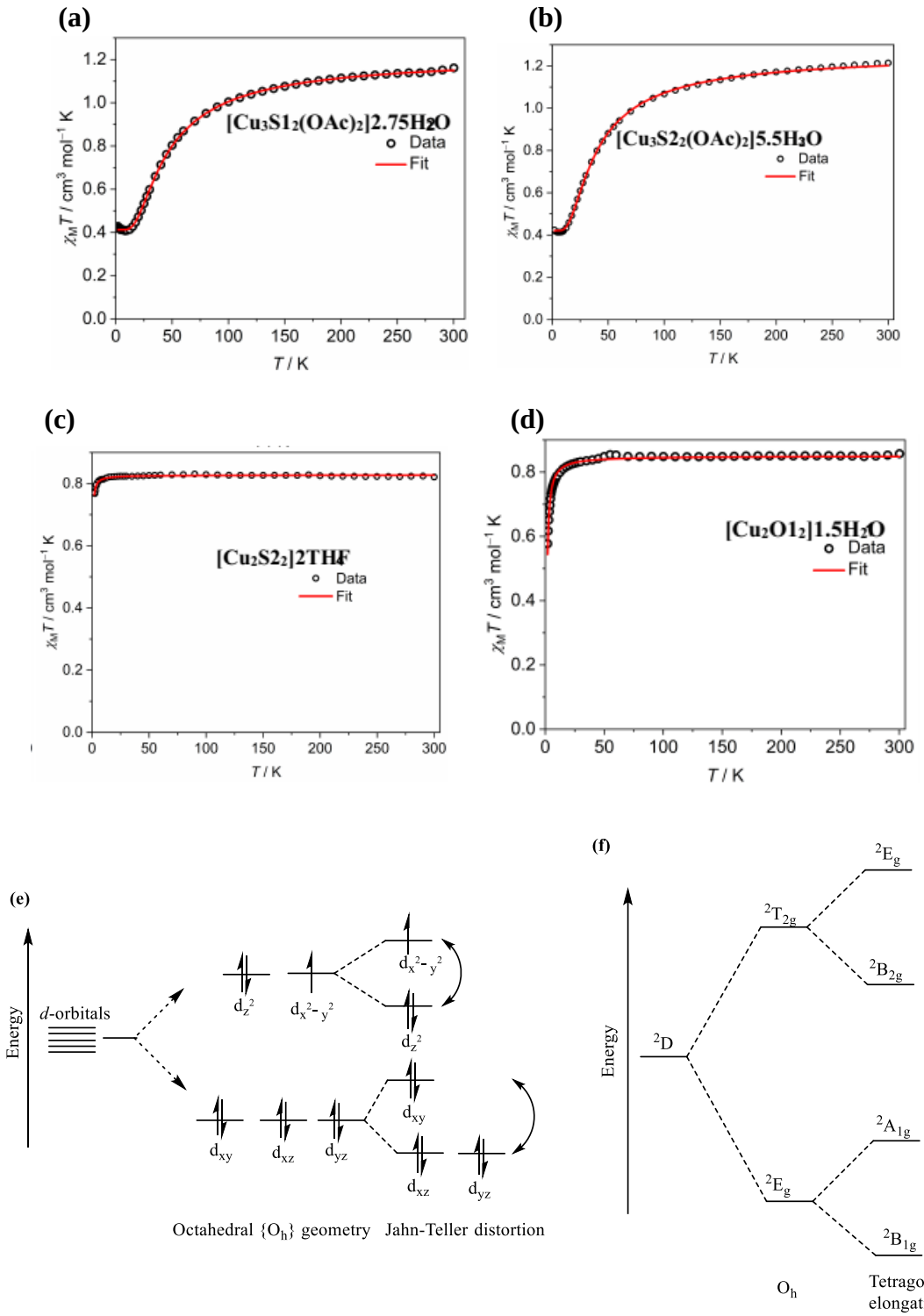

Figure 4.32: Temperature-dependent $\chi_M T$ plot for (a) **$[Cu_3S1_2(OAc)_2]2.75H_2O$,** (b) **$[Cu_3S2_2(OAc)_2]5.5H_2O$,** (c) **$[Cu_2S2_2]2THF$** and (d) **$[Cu_2O1_2]1.5H_2O$.** Red lines represent best fit of data. (e) Ligand field {*d*-orbital} splitting and (f) simplified energy level diagram for six coordinate, d^9 Cu^{II} ion.

The ESR spectra are displayed in **Fig. 4.33 – 4.36** while the derived parameters from simulating the plots are displayed in **Tables 4.29**(**a**) and (**b**). With the exception of **[Cu_2O1_2]1.5H_2O**, the ESR spectra obtained {at room and low temperatures} were similar; while the other complexes displayed axial structure in their spectra {due to the geometric environments within which the Cu^{II} centres reside}, **[Cu_2O1_2]1.5H_2O** adopted an isotropic structure {possibly due to the geometry around the Cu^{II} centres which leaned toward a more exotic see-saw geometry [**Table 4.24**(**b**)]}. The generally observed trend, in the complexes, $g_{\parallel} > g_{\perp} > g_e$ {where $g_e = 2.0023$} corroborated a distorted geometry {in the complexes} with tetragonal distortion along the *z*-axis as well as a $^2B_{1g}$ ground term {in the six-coordinate complexes} (Chakradhar *et al*., 2003).

Upon dissolution in dichloromethane {DCM} followed by freezing, the behaviours of the complexes became even more differentiated. **[$Cu_3S1_2(OAc)_2$]2.75H_2O** and **[Cu_2O1_2]1.5H_2O** showed a mixture of rhombic and axial spectra and gave rise to an intermediate appearance, while **[$Cu_3S2_2(OAc)_2$]5.5H_2O** and **[Cu_2S2_2]2THF** showed a retention of their solid state axial spectra with increased broadening in the linewidths. These differences can be explained by their structures in which **[$Cu_3S1_2(OAc)_2$]2.75H_2O** and **[Cu_2O1_2]1.5H_2O** showed the possibility of additional coordination or reorientation in a rhombic fashion around one of the Cu^{II} centres, whereas the other two complexes did not demonstrate this likelihood in their structures. Overall, the variation in the structure was clearly demonstrated and proven using both SQUID magnetometry as well as CW-ESR measurements. The solution behaviour of the complexes was even more intriguing particularly with the differentiation in behaviour based on possibility of coordination rearrangements in each of the structures.

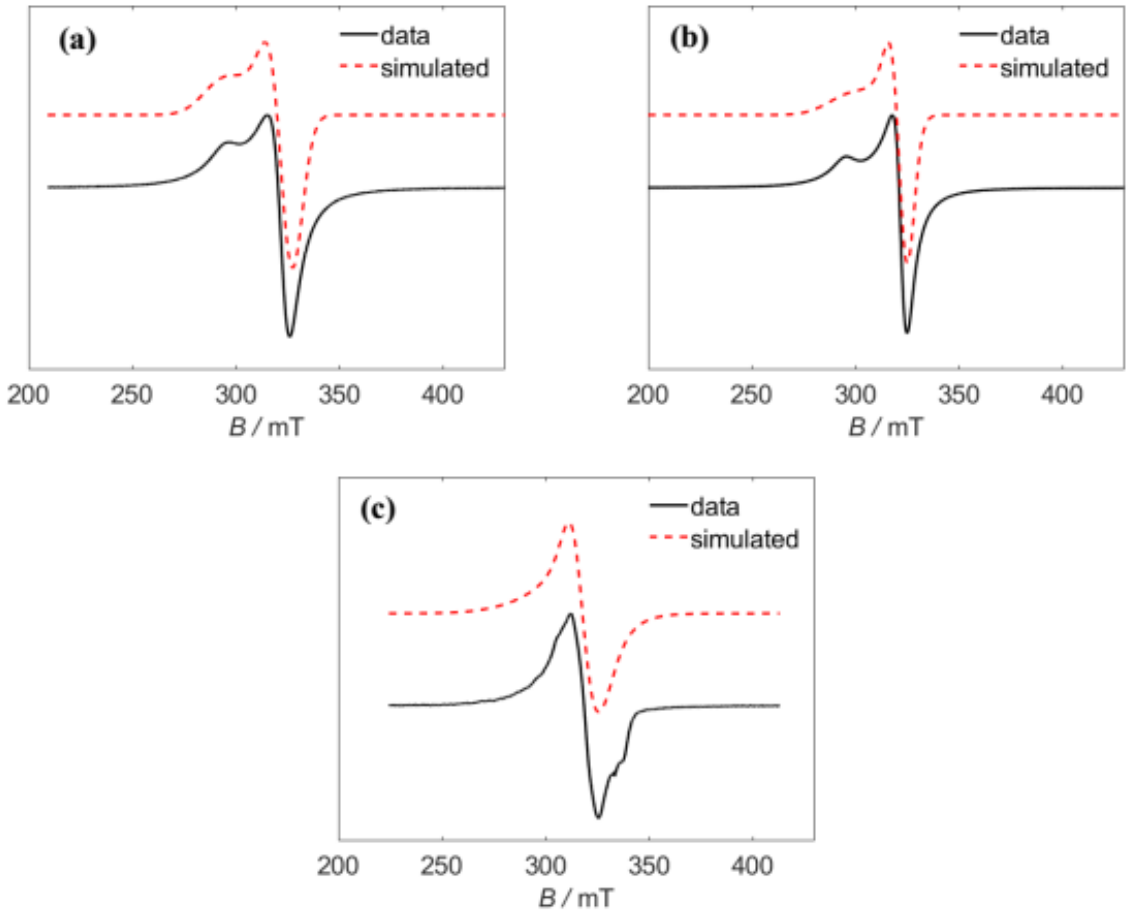

Figure 4.33: ESR spectra for **[$Cu_3S1_2(OAc)_2$]2.75H_2O** recorded in powder at (a) 295 K (b) 95 K and (c) in DCM {frozen solution} at 93 K.

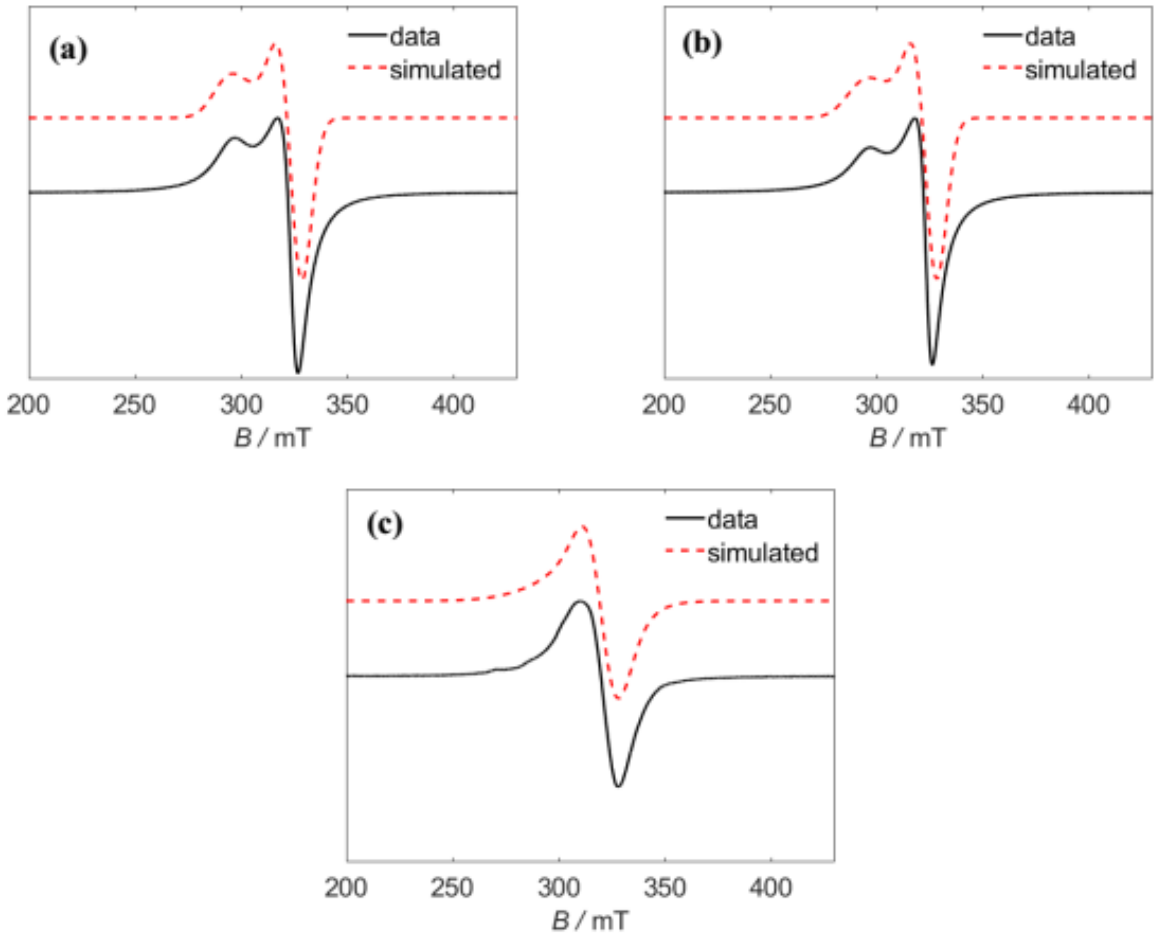

Figure 4.34: ESR spectra for **$[Cu_3S_2(OAc)_2]5.5H_2O$** recorded in powder at (a) 295 K (b) 95 K and (c) in DCM {frozen solution} at 95 K.

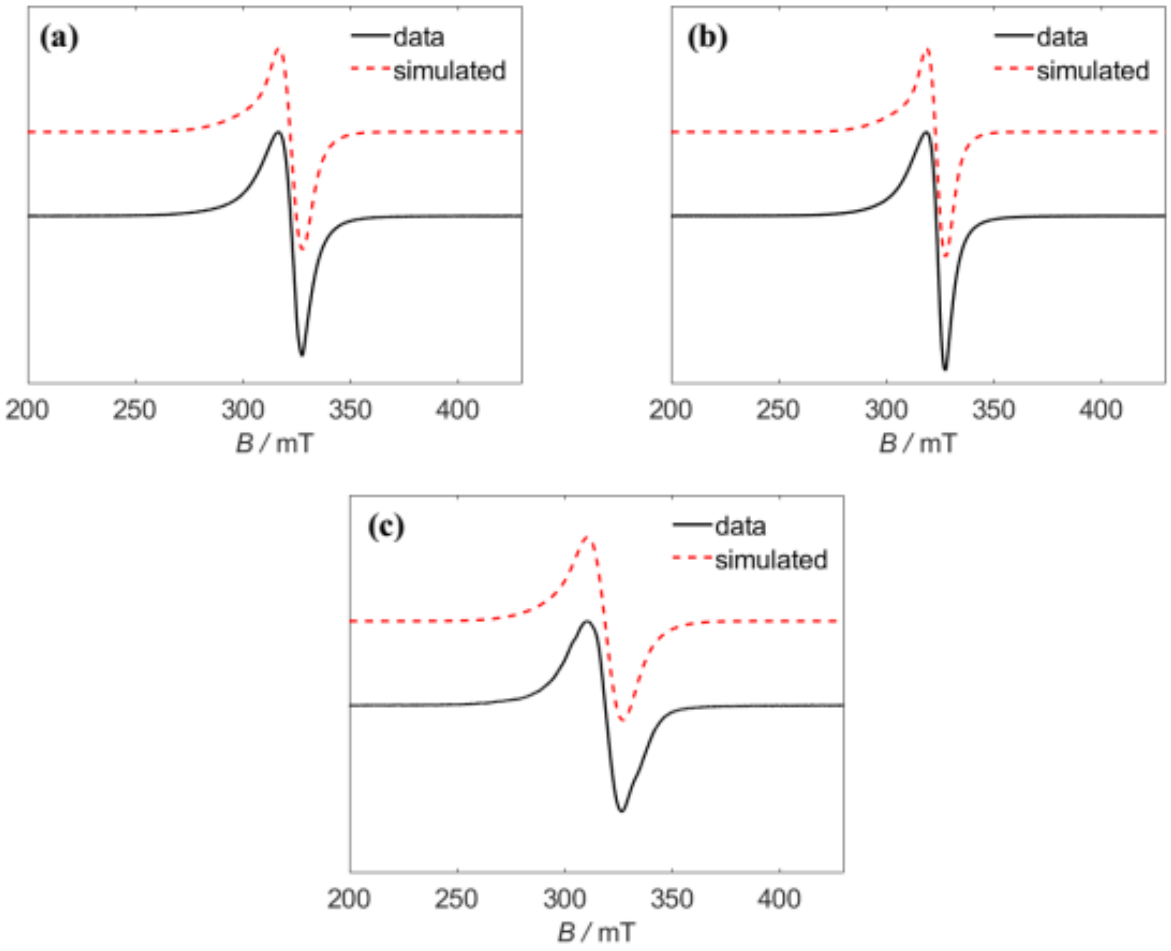

Figure 4.35: ESR spectra for **[Cu_2S_2]2THF** recorded in powder at (a) 295 K (b) 93 K and (c) in DCM {frozen solution} at 93 K.

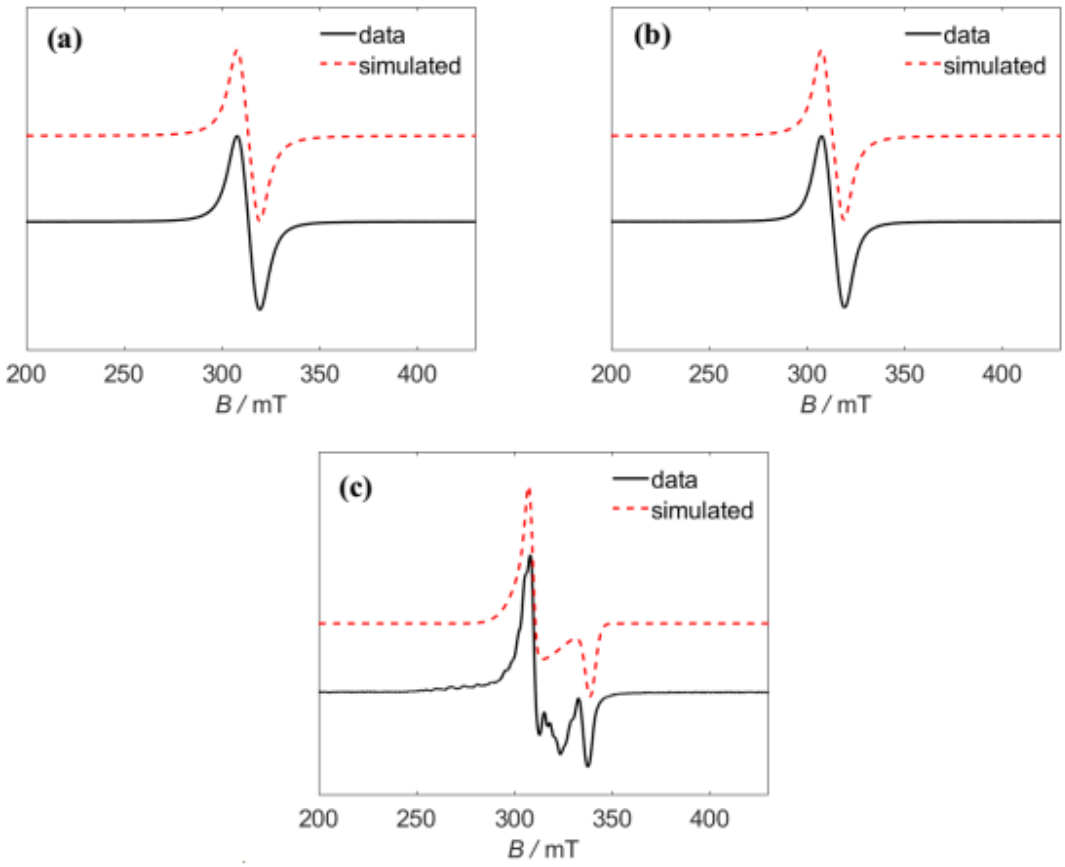

Figure 4.36: ESR spectra for **[Cu_2O1_2]1.5H_2O** recorded in powder at (a) 295 K (b) 97 K and (c) in DCM {frozen solution} at 85 K.

Table 4.29(a): ESR data for **$[Cu_3S1_2(OAc)_2]2.75H_2O$** and **$[Cu_2O1_2]1.5H_2O$**

	$[Cu_3S1_2(OAc)_2]2.75H_2O$	
	295 K	**95 K**
$g_\perp$	2.06	2.07
$g_\parallel$	2.28	2.26
$H_\perp$ Strain (MHz)	388	263
$H_\parallel$ Strain (MHz)	725	800
	93 K (Frozen)	
g_x	2.18	
g_y	2.09	
g_z	2.06	
H_x Strain (MHz)	1290	
H_y Strain (MHz)	250	
H_z Strain (MHz)	626	

	$[Cu_2O1_2]1.5H_2O$	
	295 K	**97 K**
g_{iso}	2.13	2.13
A_{iso} (MHz)	75.1	78.3
Linewidth (mT)	12.4	11.4
	85 K (Frozen)	
g_x	2.17	
g_y	2.16	
g_z	1.97	
H_x Strain (MHz)	689	
H_y Strain (MHz)	115	
H_z Strain (MHz)	159	

Table 4.29(b): ESR data for **$[Cu_3S2_2(OAc)_2]5.5H_2O$** and **$[Cu_2S2_2]2THF$**

	$[Cu_3S2_2(OAc)_2]5.5H_2O$			**$[Cu_2S2_2]2THF$**	
	295 K	**95 K**		**295 K**	**93 K**
$g_\perp$	2.05	2.05		2.06	2.06
$g_\parallel$	2.26	2.27		2.17	2.17
$H_\perp$ Strain (MHz)	363	325		293	236
$H_\parallel$ Strain (MHz)	562	586		1304	1087
	95 K (Frozen)			**93 K (Frozen)**	
$g_\perp$	2.08			2.08	
$g_\parallel$	2.19			2.15	
$H_\perp$ Strain (MHz)	471			448	
$H_\parallel$ Strain (MHz)	1604			1576	

4.8 Sensor properties of the receptors (Ligands)

4.8.1 Sensing properties of the bis-imidazoles (**BI_1** – **BI_7**)

In the 1,3-bisimidazole series, **BI_4** exhibited a clear sensitivity {turn-off} towards Cr^{3+} and Fe^{3+} ions {**Fig. 4.37**[**d**]} while other tested ions {Ag^{+}, Al^{3+}, Cd^{2+}, Co^{2+}, Cu^{2+}, Hg^{2+}, K^{+}, Li^{+}, Mg^{2+}, Na^{+}, Ni^{2+}, Pb^{2+}, and Zn^{2+}} showed very minimal effect. The dual emission of the receptor {**BI_4**} also disappeared upon contact with Cr^{3+} and Fe^{3+} ions. Although **BI_2** showed ratiometric turn-off in the presence of the +3 ions {Al, Cr, Fe}; turn-off was also observed for Cu^{2+}, Hg^{2+} and Zn^{2+} {**Fig. 4.37**[**b**]}. Substitution at the **N-H** position appeared to affect the quenching property of Cu^{2+} ion. While the **N-H** analogues {**BI_1** and **BI_2**} showed almost complete quenching, upon contact with Cu^{2+}, the **N-Ph** analogues {**BI_3** and **BI_4**} gave minimal reduction in fluorescence intensity {**BI_4** showing the least} (**Fig. 4.37**).

The 1,4-series, however, did not show selectivity, although **BI_6** and **BI_7** exhibited ratiometric behaviour in the presence of the +3 ions {Al, Cr and Fe}. While **BI_6** showed a turn-off {**Fig. 4.38**[**b**]}, **BI_7** showed a turn-on {**Fig. 4.38**[**c**]}. As observed in the 1,3-series, interaction with Cu^{2+} ions produced different effects in the **N-H** and **N-Ph** members of the 1,4-series {**Fig. 4.38**}.

4.8.2 Sensing properties of the imidazole amines (**A1** – **A9**)

The effect of metal ions {Ag^{+}, Al^{3+}, Cd^{2+}, Co^{2+}, Cr^{3+}, Cu^{2+}, Fe^{3+}, Hg^{2+}, K^{+}, Li^{+}, Mg^{2+}, Na^{+}, Ni^{2+}, Pb^{2+}, and Zn^{2+}} on the imidazole amine receptors is presented in **Fig. 4.39** {**N-H** analogues}, **Fig. 4.40** {**N-Me** analogues} and **Fig. 4.41** {**N-Ph** analogues}. Generally, the imidazole amines appeared to have preference for the +3 ions {Al, Cr, Fe}. The ethyl based **A1** showed the most sensitivity, with a disappearance of its dual emission {in the presence of the ions} (**Fig. 4.39**{**a**}); while **A2** exhibited a ratiometric turn-on for the ions, **A7** showed a ratiometric turn-off {**Fig. 4.39**[**a**] and **Fig. 4.40**[**c**]}. In addition to the +3 ions, **A4** showed prospect in the detection of Zn^{2+} {**Fig. 4.39**[**d**]}. Unlike the bis-imidazoles, interaction of Cu^{2+} ions with the **N-H** analogues did not lead to complete quenching {except for **A1**}, with a turn-on observed for **A3**. Substitution at the **N-H** position however, still resulted in reduction in fluorescence intensity, although a turn-on was observed for **A6** and almost complete quenching in **A7**.

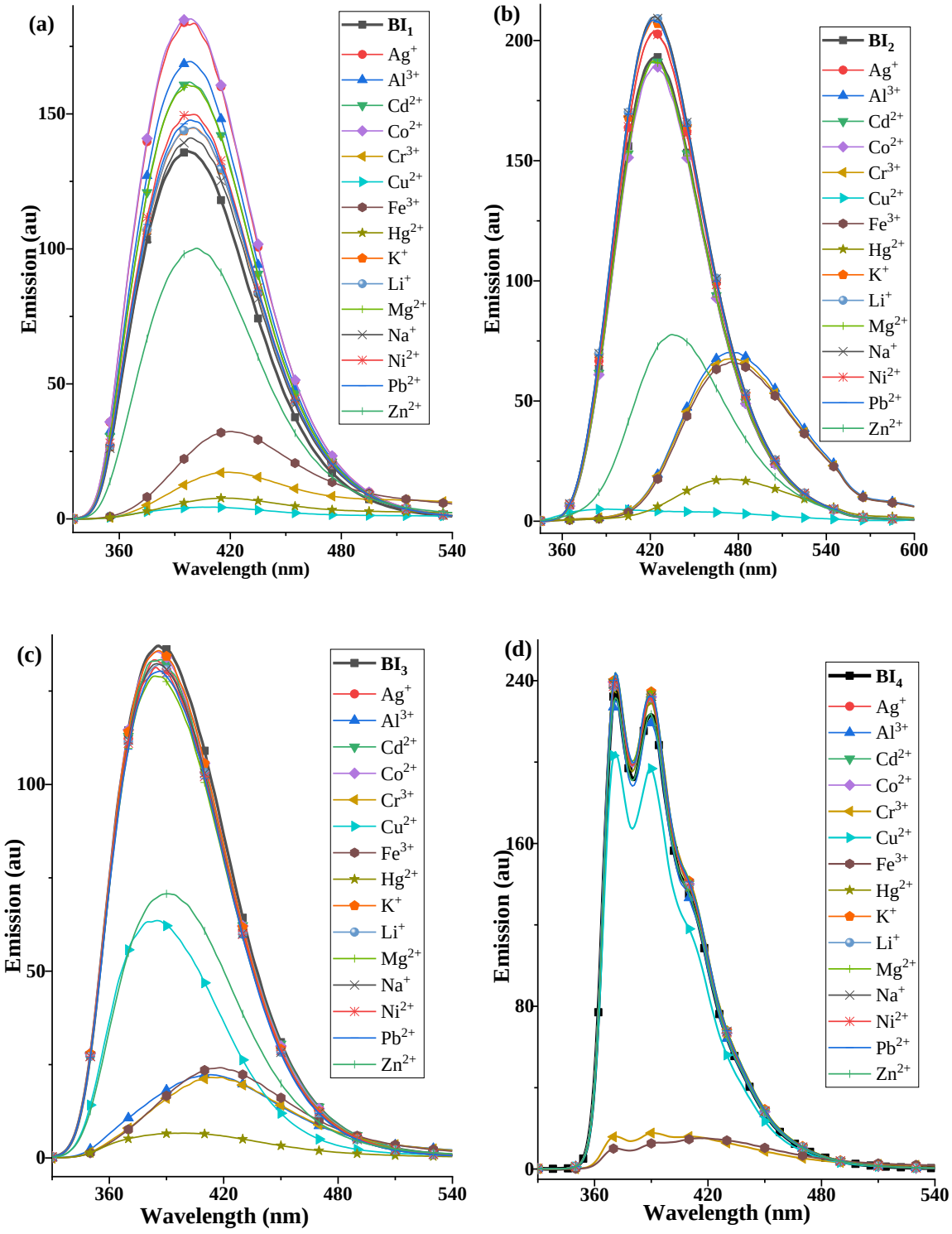

Figure 4.37: Emission spectra of (a) **BI1** (b) **BI2** (c) **BI3** and (d) **BI4** in the presence of tested cations.

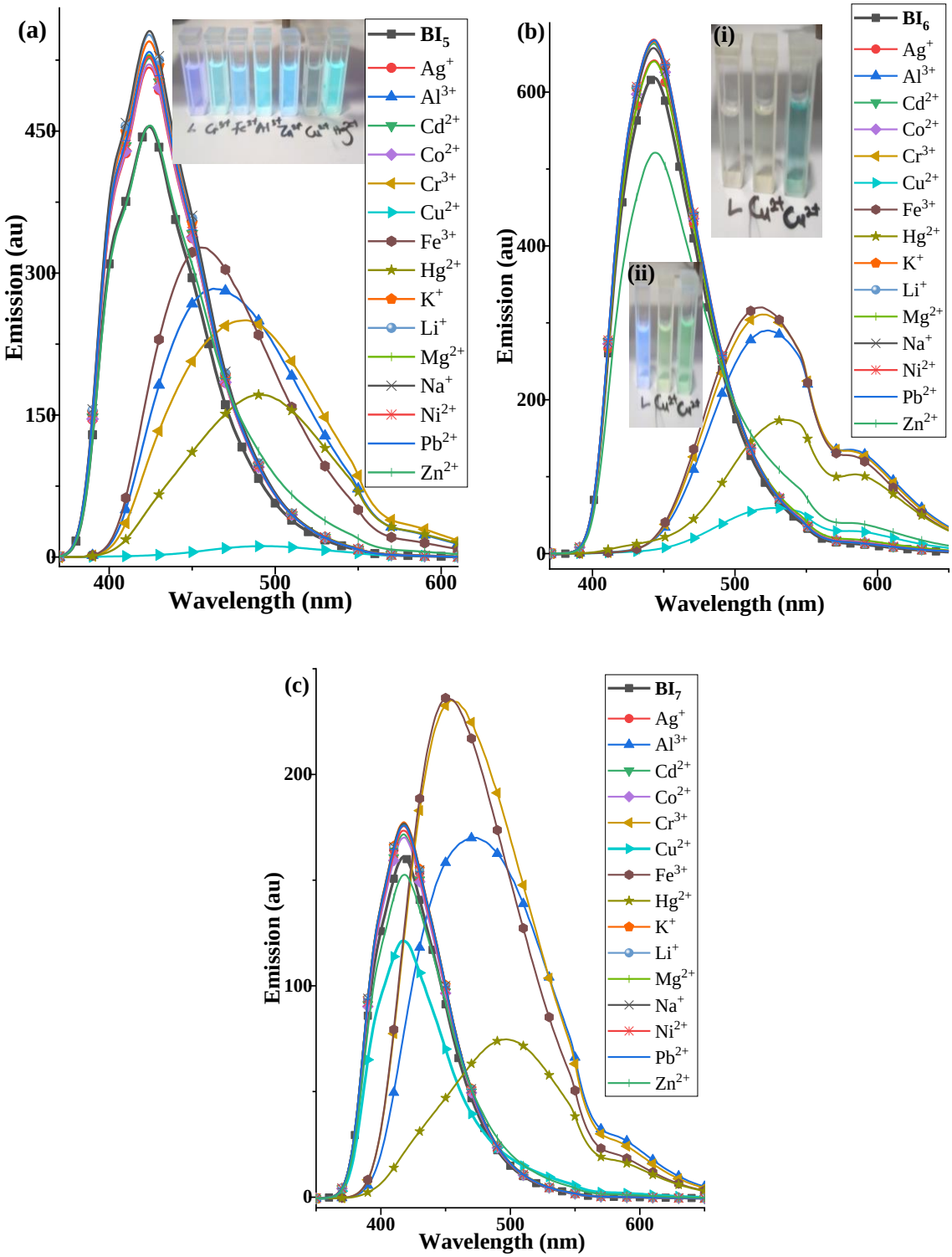

Figure 4.38: Emission spectra of (a) **BI5** (b) **BI6** {inset colour change in the presence of Cu^{2+}} and (c) **BI7** in the presence of tested cations.

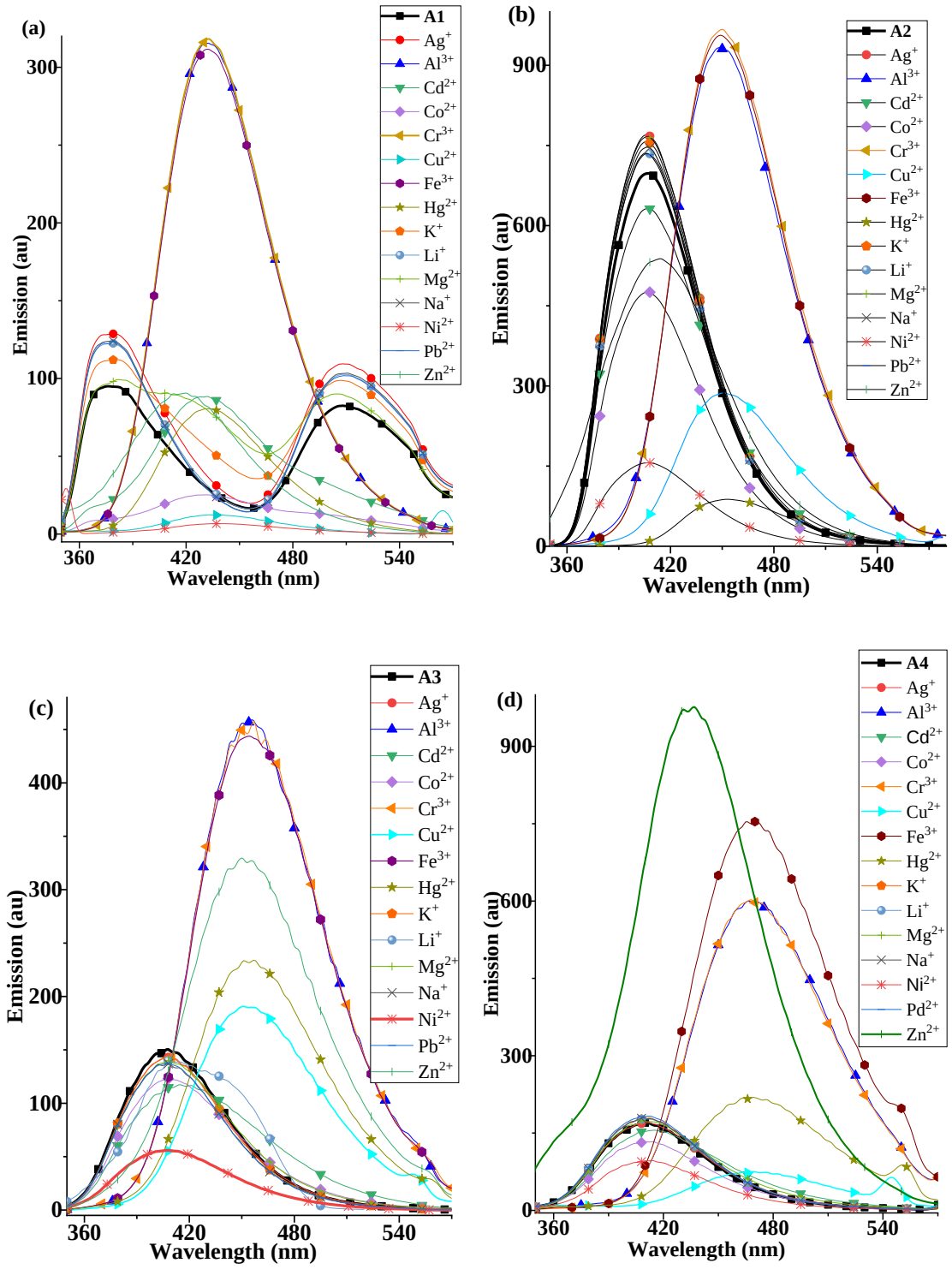

Figure 4.39: Emission spectra of (a) **A1** (b) **A2** (c) **A3** and (d) **A4** in the presence of tested cations.

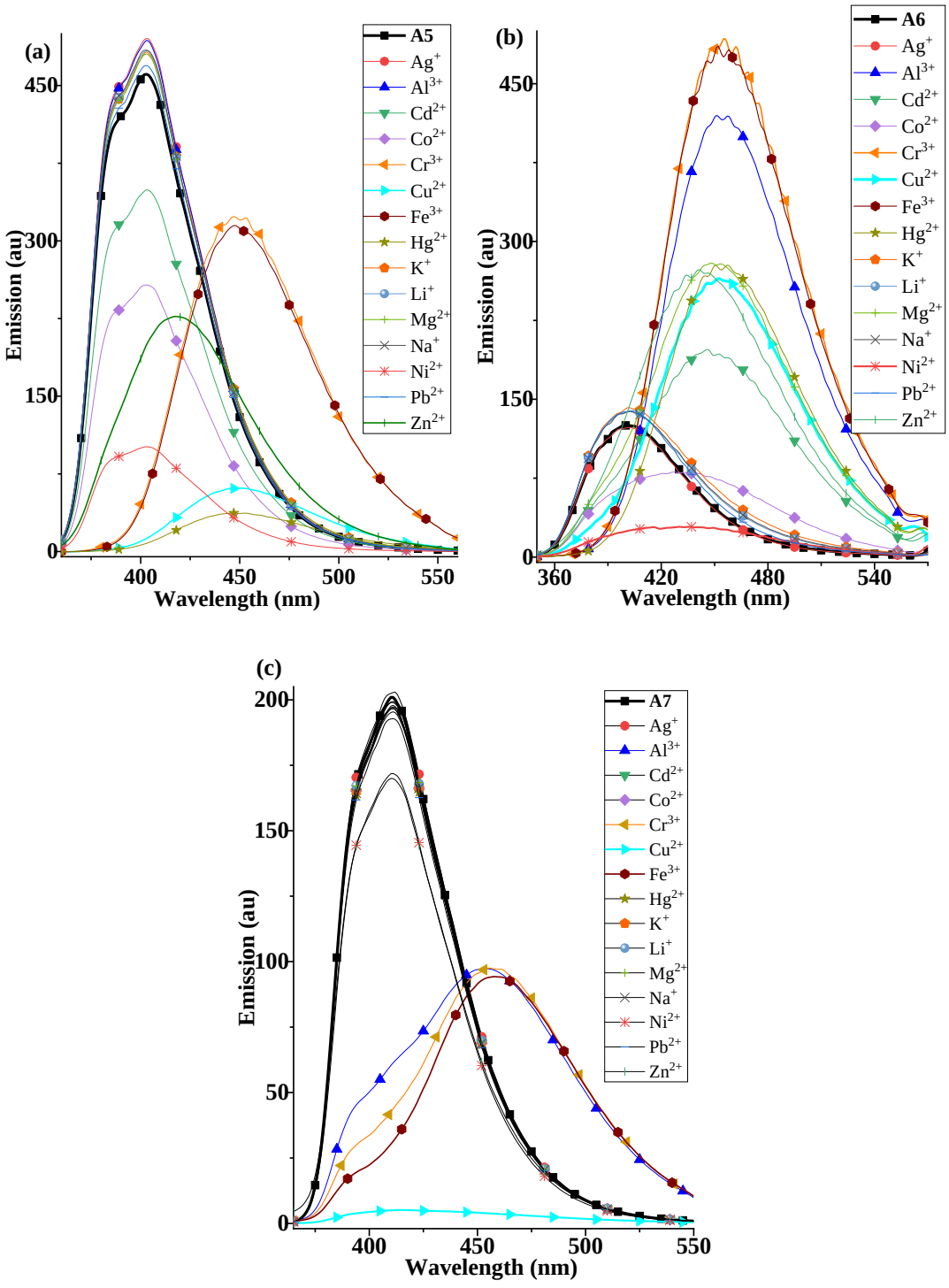

Figure 4.40: Emission spectra of (a) **A5** (b) **A6** and (c) **A7** in the presence of tested cations.

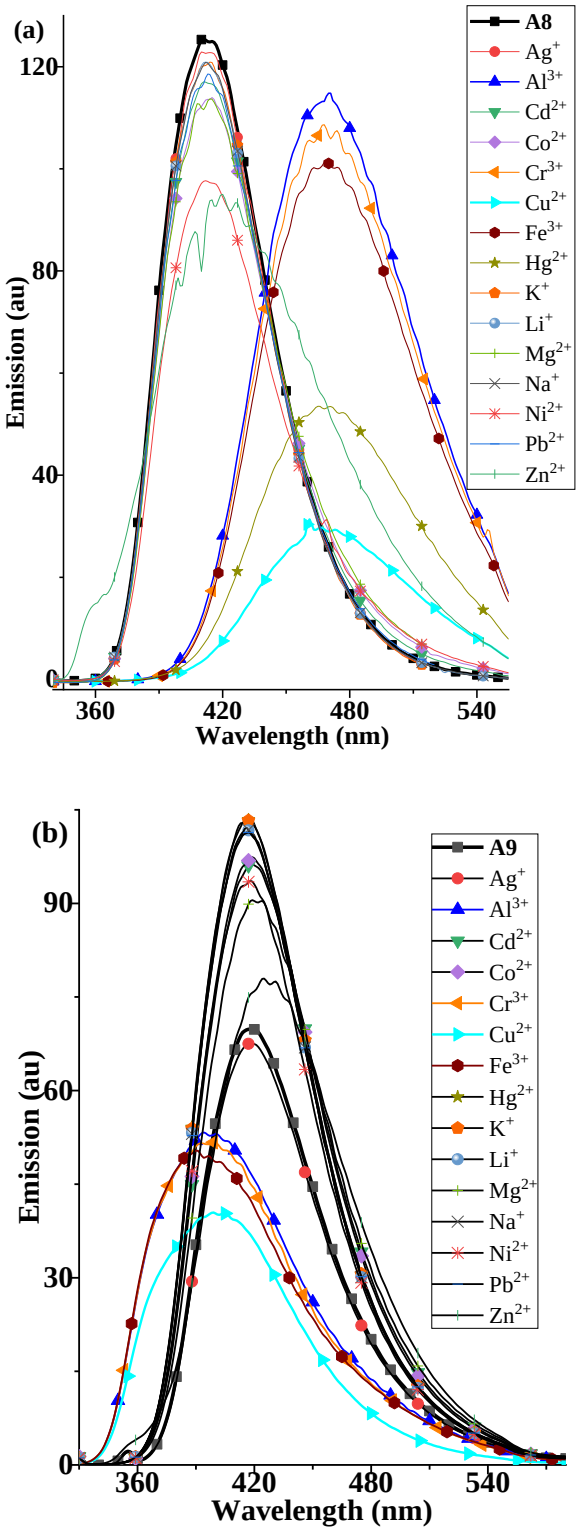

Figure 4.41: Emission spectra of (a) **A8** and (b) **A9** in the presence of tested cations.

4.8.3 Sensing properties of the NNO imines (I_1 – I_9) and NNN imines (I_{N2} – I_{N4})

The interaction of the NNO receptors with metal ions {Ag^+, Al^{3+}, Cd^{2+}, Co^{2+}, Cr^{3+}, Cu^{2+}, Fe^{3+}, Hg^{2+}, K^+, Li^+, Mg^{2+}, Na^+, Ni^{2+}, Pb^{2+}, and Zn^{2+}} is presented in **Fig. 4.42** {**N-H** analogues}, **Fig. 4.43** {**N-Me** analogues} and **Fig. 4.44** {**N-Ph** analogues}. **I_2** {**Fig. 4.42**[**b**]} and **I_4** {**Fig. 4.42**[**d**]} showed similar tendency as the imidazole amines towards +3 ions. Only **I_6** {**Fig. 4.43**[**b**]} and **I_9** {**Fig. 4.44**[**b**]} showed remarkable sensitivity towards Zn^{2+} ion, and **I_9** gave the best selectivity and ≈ 4-fold increase in fluorescence intensity.

Upon interaction with Zn^{2+}, **I_9** showed a red shifted emission {a major emission band at 503 nm with a shoulder at 422 nm – possibly due to keto-enol tautomerism}. Fluorescence titration {**Fig. 4.45**[**a**]} revealed a decrease in intensity at 422 nm with an increase at 503 nm. The UV-Vis titration {**Fig. 4.45**[**b**]} showed a gradual decrease in the π-π* region and the appearance of a metal-to-ligand charge transfer {MLCT} band {which increased with volume of Zn^{2+}} at 410 nm. These observations suggested formation of **I_9**-Zn^{2+}. ESI-MS {**Fig. S86**} gave a peak at *m/z* 593.6 {[**I_9** + Zn^{2+} + MeCN]$^+$, Calc. 594.99} suggesting a 1:1 interaction between **I_9** and Zn^{2+}; this was also corroborated by Job's plot {**Fig. 4.45**[**c**]}. The association constant of **I_9**-Zn^{2+} was determined by fluorescence titration to be 2.9 x 10^4 M^{-1} and the limit of detection {*LOD*} was 4.45 nM {R^2 = 0.989} (**Fig. 4.46**{**a**}). The addition of equivalent amount of solution of other metal ions tested to a solution of **I_9**-Zn^{2+} revealed a significant change in the emission associated with the enol form {lower wavelength} than the keto form {higher wavelength} (**Fig. 4.46**{**b**}) – the band at 422 nm was not seen upon addition of Cr^{3+}, Cu^{2+} and Fe^{3+} ions. Cu^{2+} ion showed the strongest inhibition of the Zn^{2+} turn-on {**Fig. 4.46**[**c**]}, while Cd^{2+} ion did not interfere. The weak effect of Cd^{2+} ion could be attributed to weak binding to the phenol group {phenolic -OH not removed} – while the presence of Zn^{2+} ion {**Fig. 4.47**} produced a change in the absorption spectrum of the ligands, Cd^{2+} did not. Since this change was observed for turn-on {**Fig. 4.47**[**a**] and [**b**]} and turn-off {**Fig. 4.47**[**c**]} systems, the increase in fluorescence intensities could be as a result of excited state phenomena (Wang *et al*., 2014; Saluja *et al*., 2014). The deprotonation of the phenolic -OH, in the presence of Zn^{2+} ions, could be seen in the crystal structures of **I_3**, **I_8** and **I_9** {**Fig. 4.4**}.

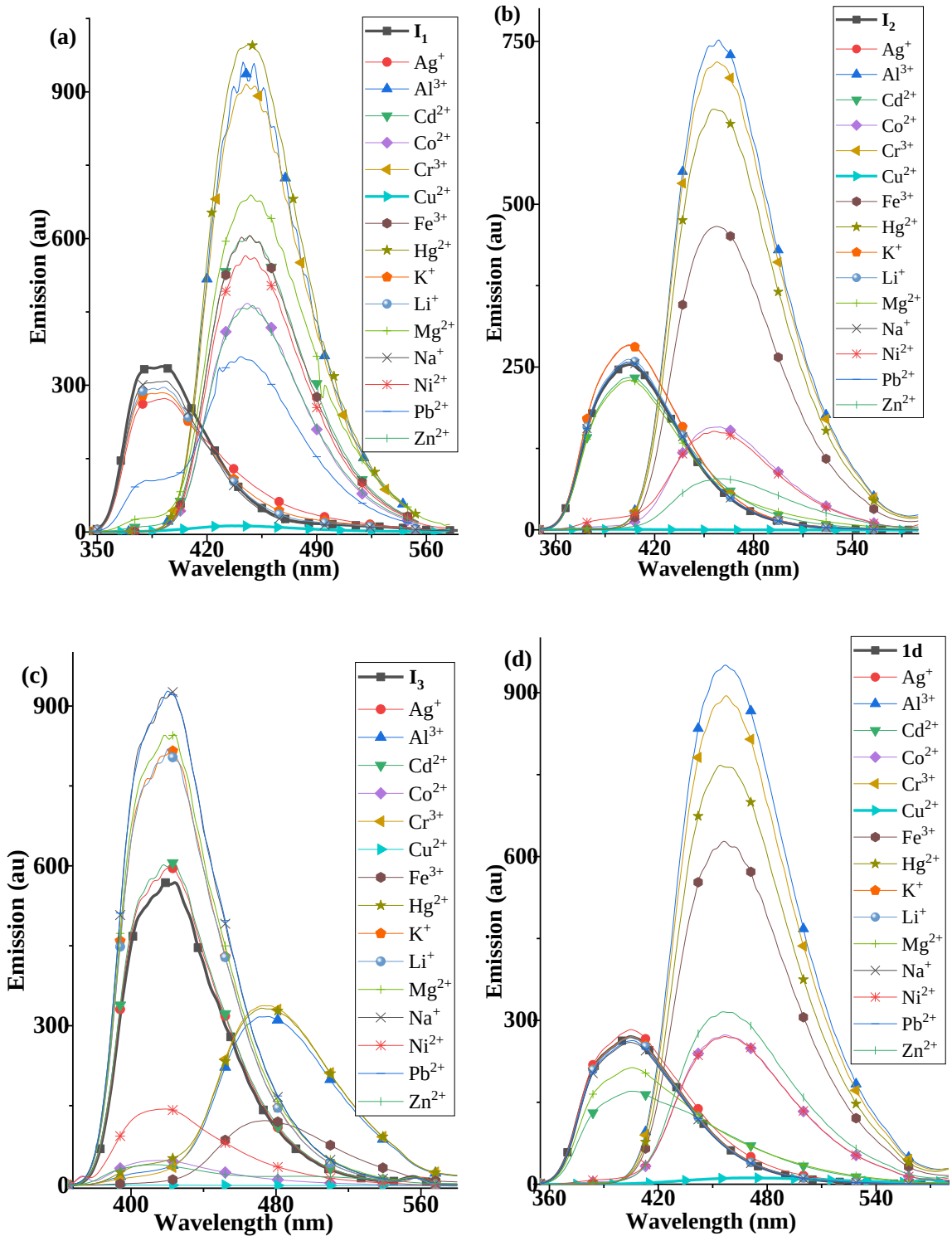

Figure 4.42: Emission spectra of (a) **I₁** (b) **I₂** (c) **I₃** and (d) **I₄** in the presence of tested cations.

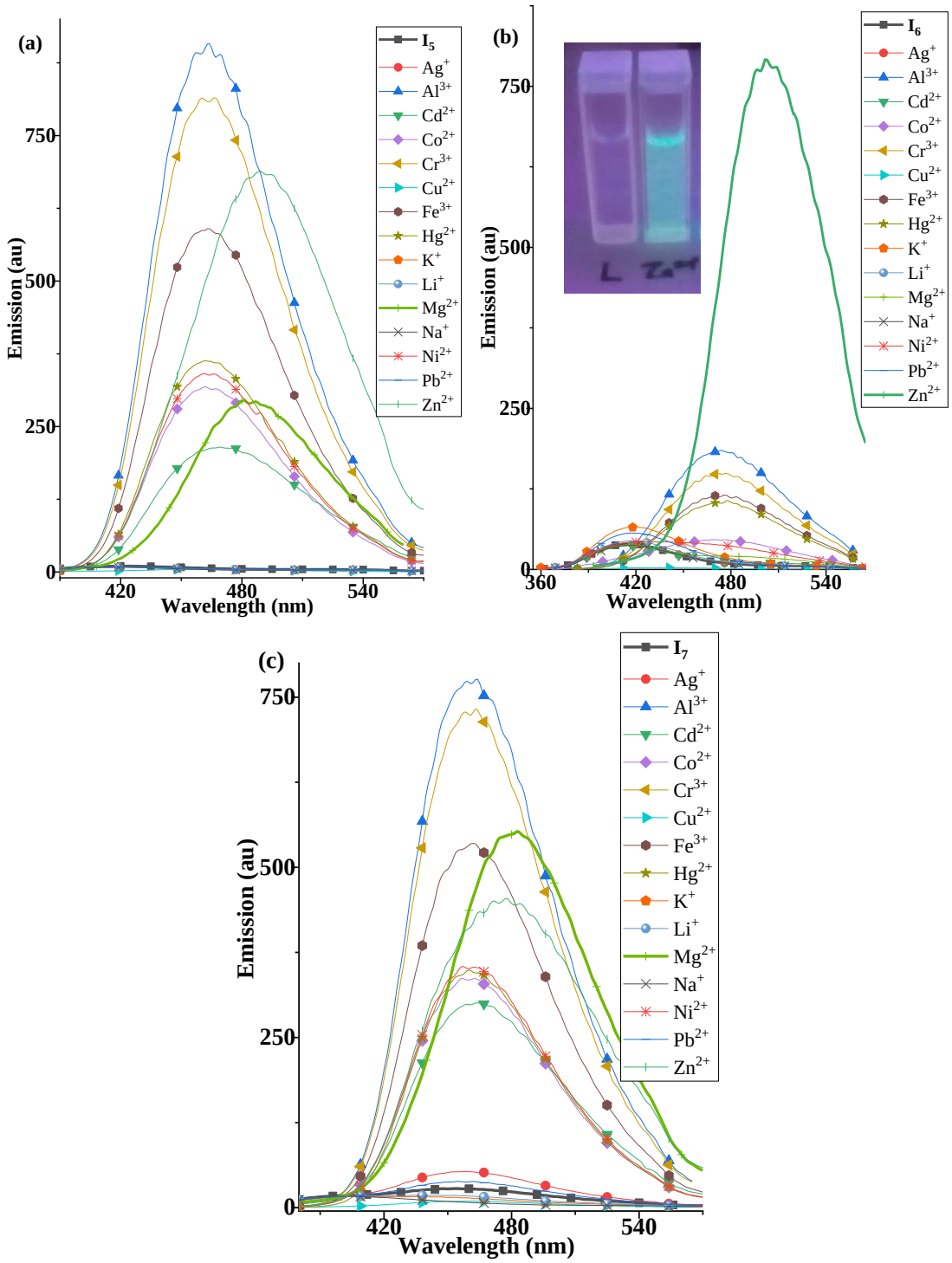

Figure 4.43: Emission spectra of (a) **I5** (b) **I6** and (c) **I7** in the presence of tested cations.

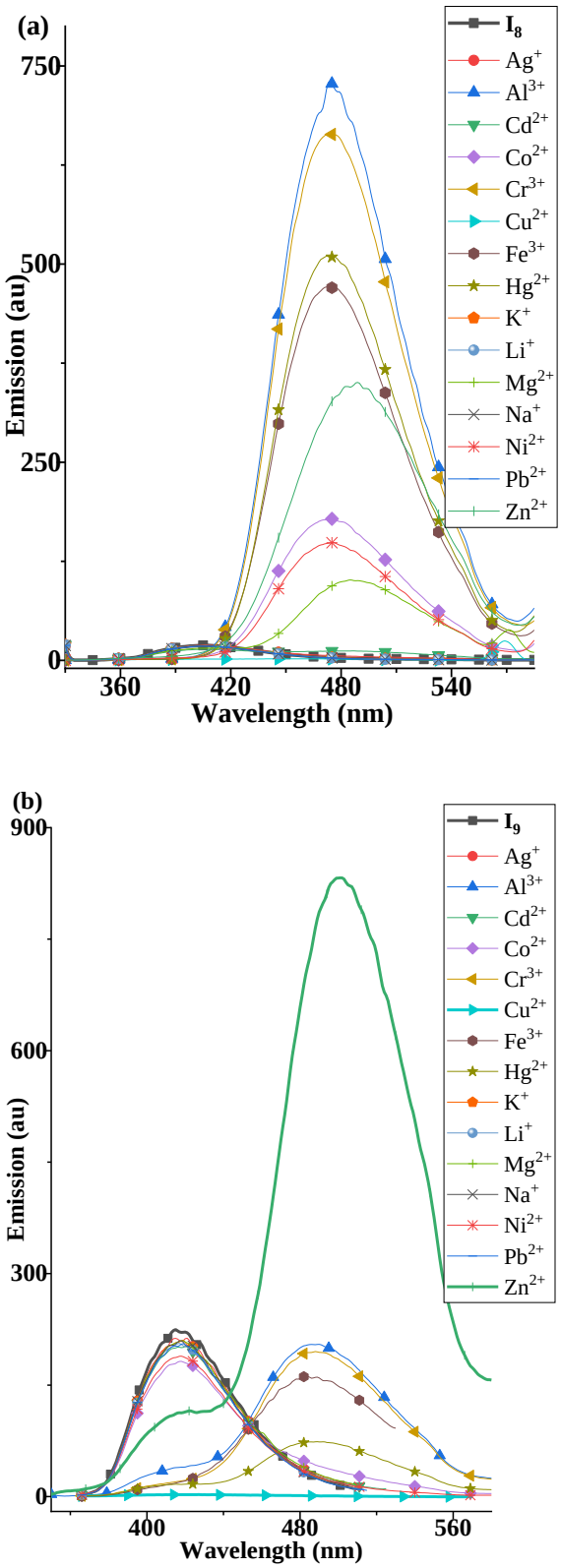

Figure 4.44: Emission spectra of (a) **I8** and (b) **I9** in the presence of tested cations.

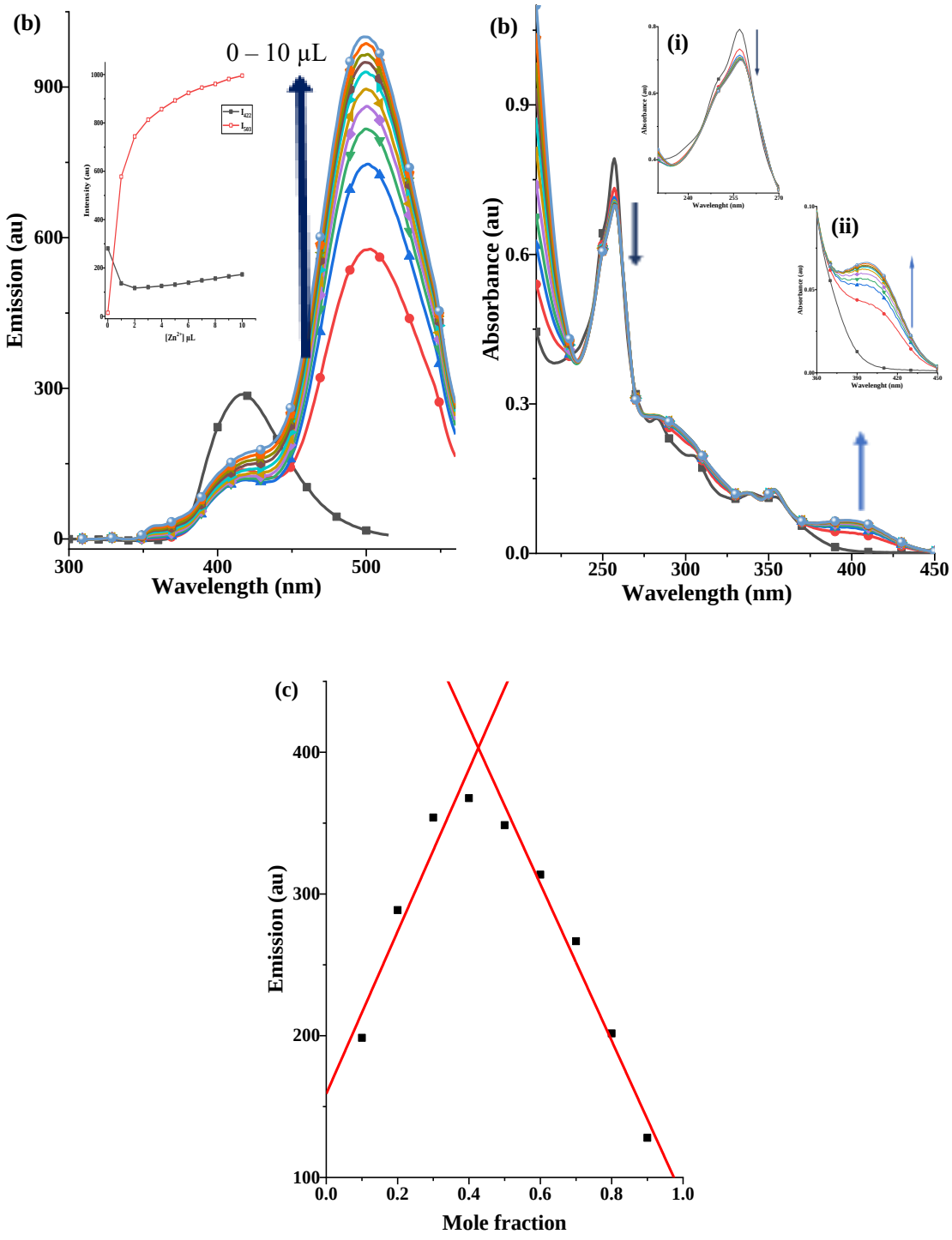

Figure 4.45: (a) Fluorescence titration (inset: intensity at 422 nm {black} and at 503 nm {red}) (b) UV-Vis titration of I_9 in presence of Zn^{2+} and (c) Job's plot for **I_9**-Zn^{2+}.

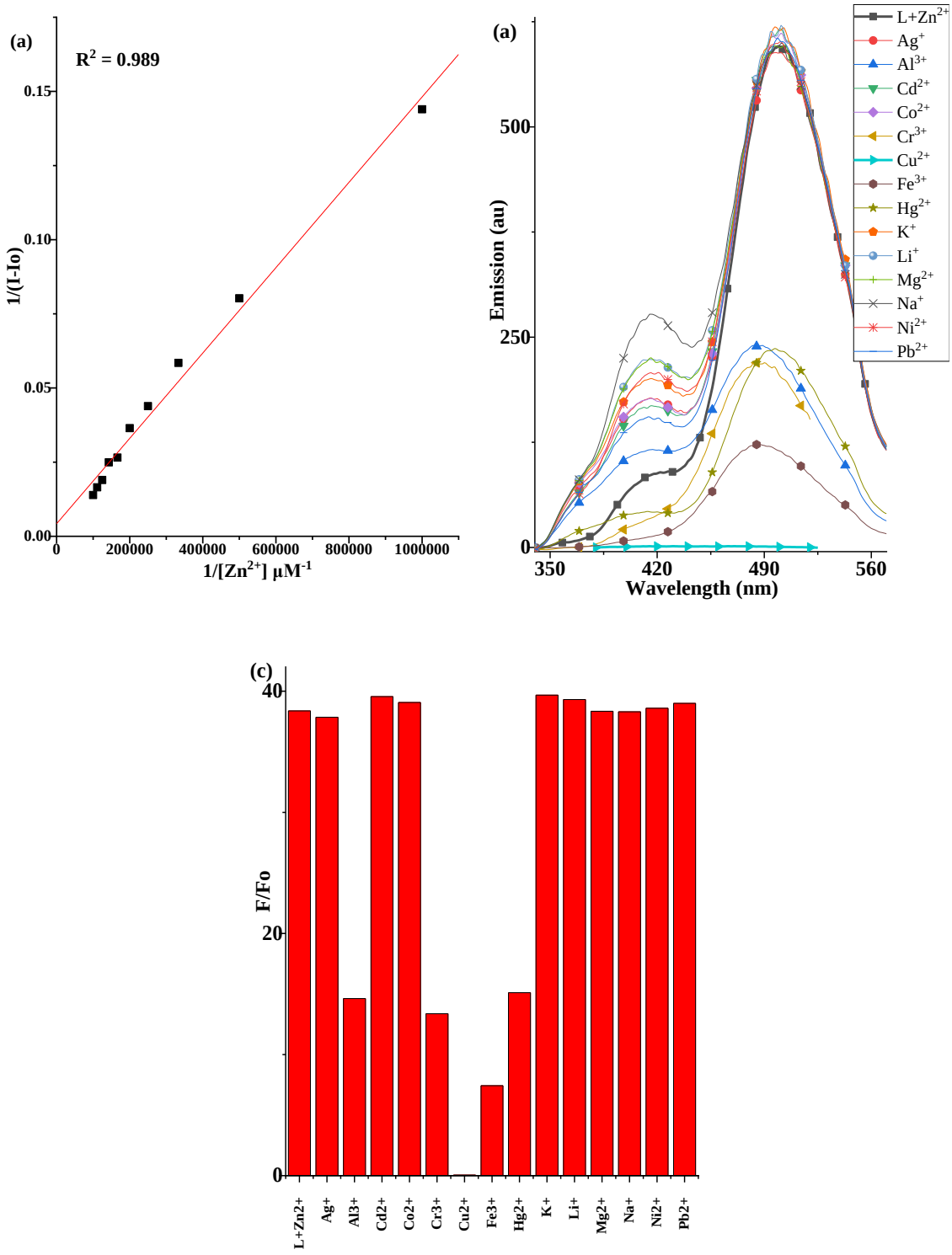

Figure 4.46: (a) *LOD* determination and competition experiment (b) and (c) of **I9**.

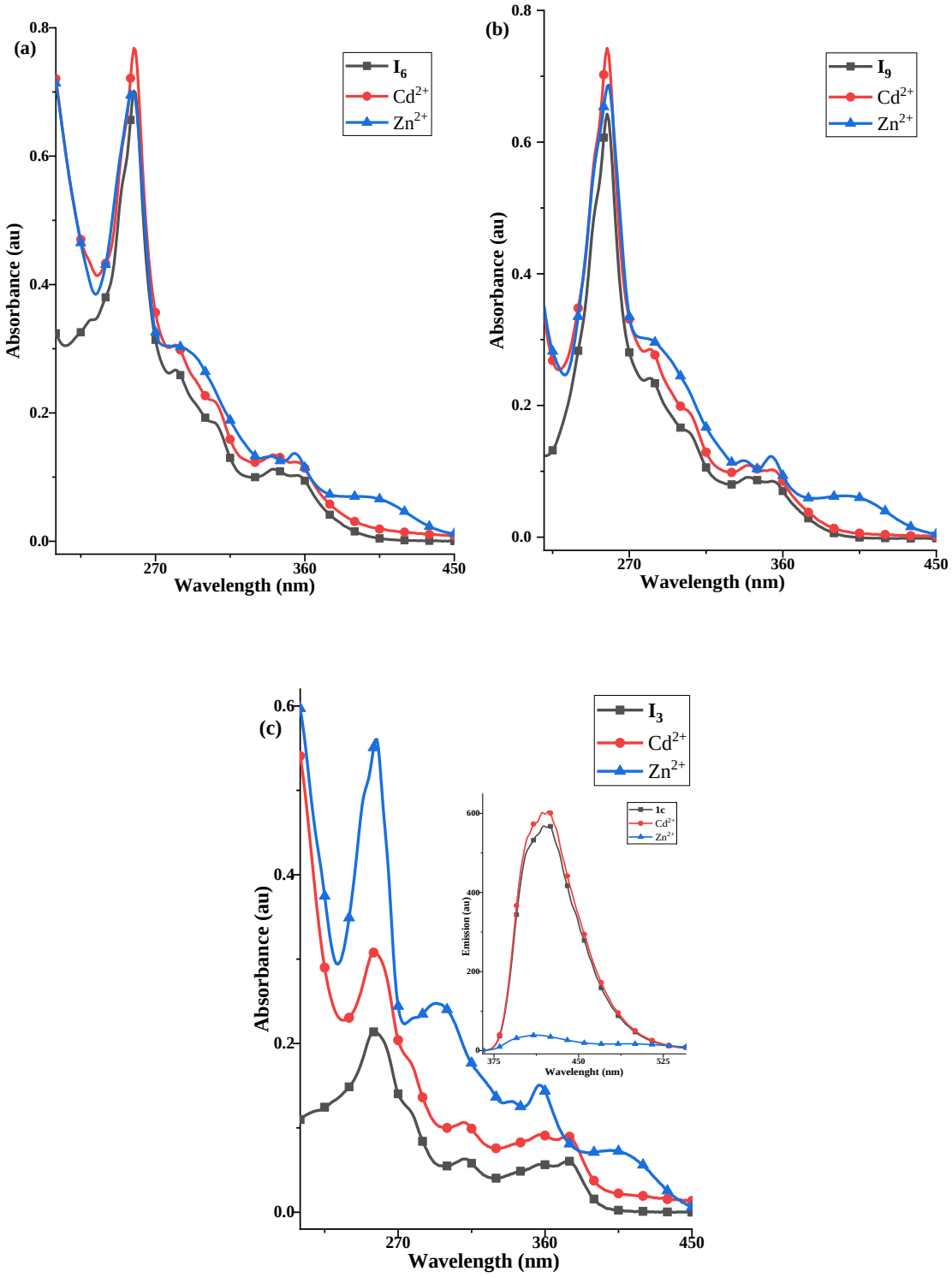

Figure 4.47: Absorption spectra of (a) **I6** (b) **I9** and (c) **I3** {inset: emission spectra} in the presence of equivalent amount of Cd^{2+} and Zn^{2+} ions.

Substitution of the phenol group (in **I_2**, **I_3** and **I_4**) with pyridine (in **I_{N2}**, **I_{N3}** and **I_{N4}**) favoured +3 {Al, Cr and Fe} ions detection, with **I_{N3}** showing the best selectivity {**Fig. 4.48**} – in comparison to the NNO analogues, the intensity of Zn^{2+} ion was almost completely diminished in the NNN analogues {**Fig. 4.49**}. In the presence of the trivalent ions, **I_{N2}** and **I_{N4}** gave almost 40-fold increase in fluorescence intensities {in comparison to **I_{N2}** and **I_{N4}** alone}, while **I_{N3}** gave the least {≈ 1-fold}, however, **I_{N3}** efficiently discriminates the M^{3+} ions from the M^{2+} and M^{+} ions. The receptors (**I_{N2}**, **I_{N3}** and **I_{N4}**) showed ratiometric behaviour {**Fig. 4.50**} and **I_{N3}** (**Fig. 4.50**{**b**}) exhibited the best performance.

Upon interaction with the metal ions, a red-shifted absorption {**Fig. 4.51**} was observed only in the presence of the +3 ions {Al, Cr, Fe}. Titration experiments {**Fig. 4.52**} indicated that this red-shift was more pronounced in **I_{N2}** and **I_{N4}** {in comparison to **I_{N3}**}. Job's plot {**Fig. 4.53**} suggested a 1:1 stoichiometric ratio, for all three {3} ions upon interaction with the receptors. Interference experiments {**Fig. 4.54**} showed that Co^{2+}, Cu^{2+}, Hg^{2+} and Zn^{2+} affected the detection of the +3 ions {Cu^{2+} ions showed the most effect, for all three [3] receptors}. In the case of **I_{N2}**, the effect of Hg^{2+} was more pronounced against Fe^{3+} {**Fig. 4.54**[**c**]}; and the effect of Zn^{2+} was more pronounced against Al^{3+} {**Fig. 4.54**[**a**]} – this effect of Zn^{2+} {against Al^{3+}} was seen also in **I_{N3}** {**Fig. 4.54**[**d**]}.

Although Cd^{2+} and Zn^{2+} ions do not show a turn-on with the receptors, they bring about a cyclisation of the receptors resulting in structures shown in **Fig. 4.6**.

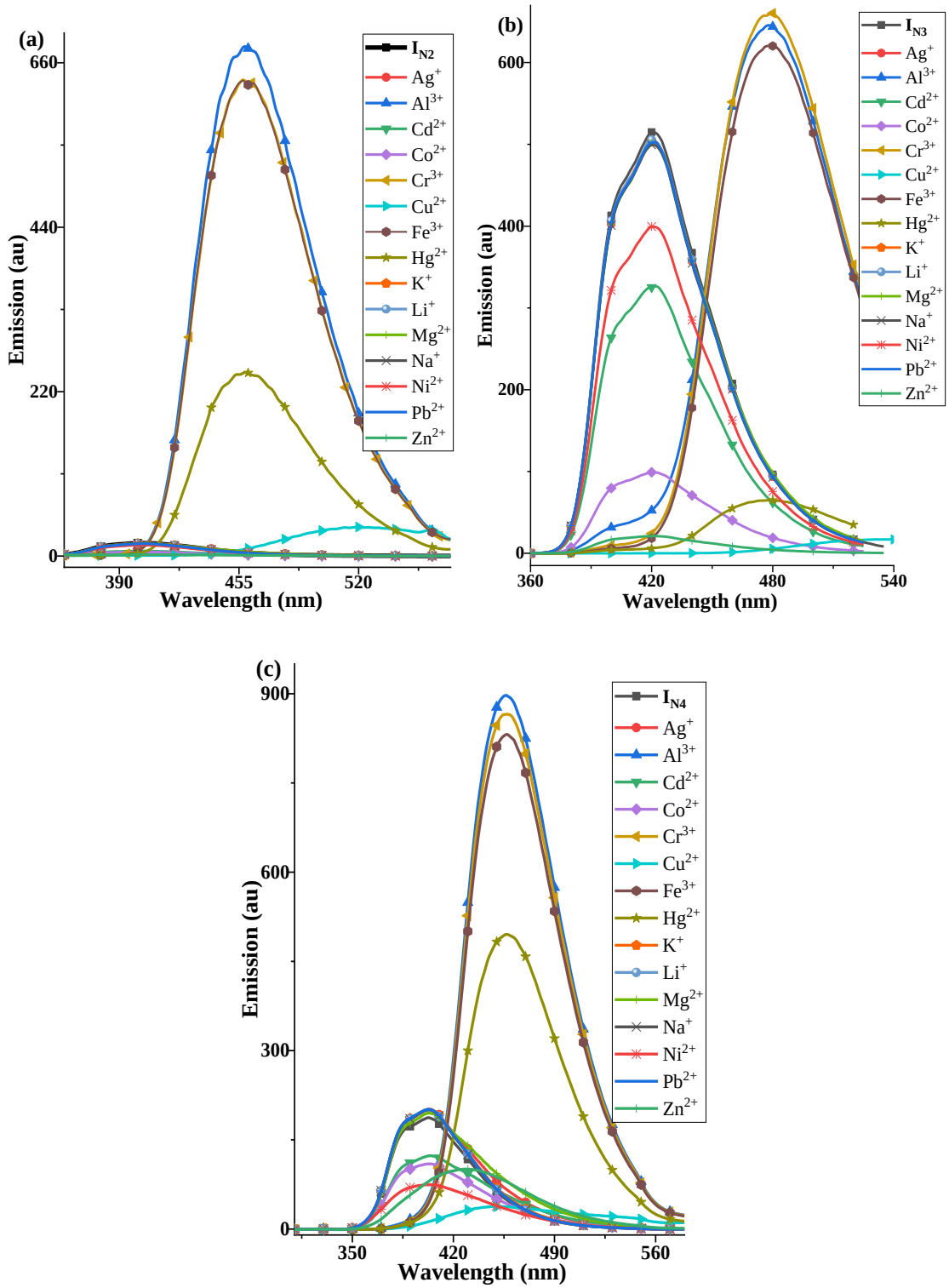

Figure 4.48: Emission spectra of (a) **I_{N2}** (b) **I_{N3}** and (c) **I_{N4}** in the presence of tested cations.

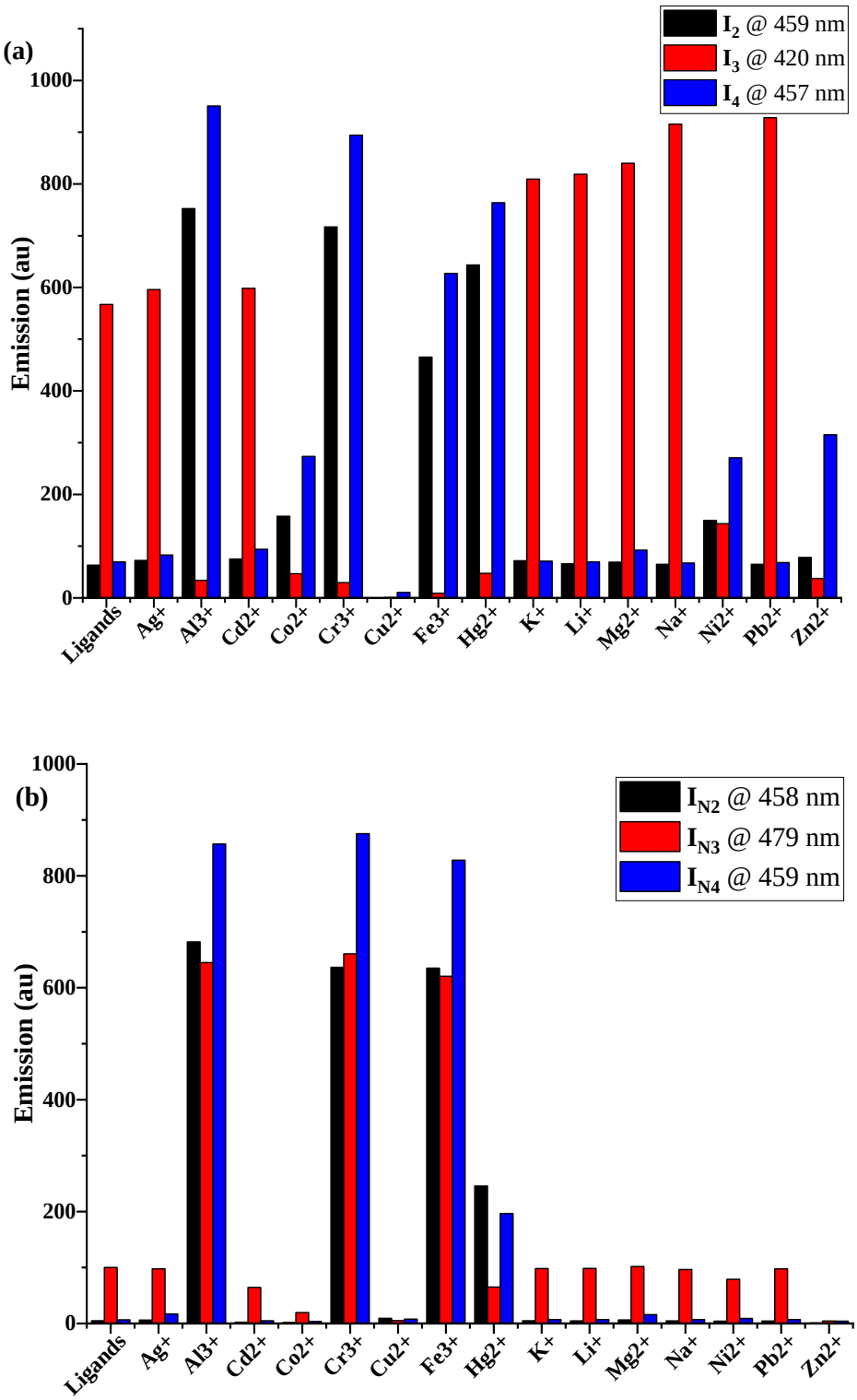

Figure 4.49: Emission intensities of (a) NNO and (b) NNN ligands and tested metal ions (upon interaction with respective ligands)

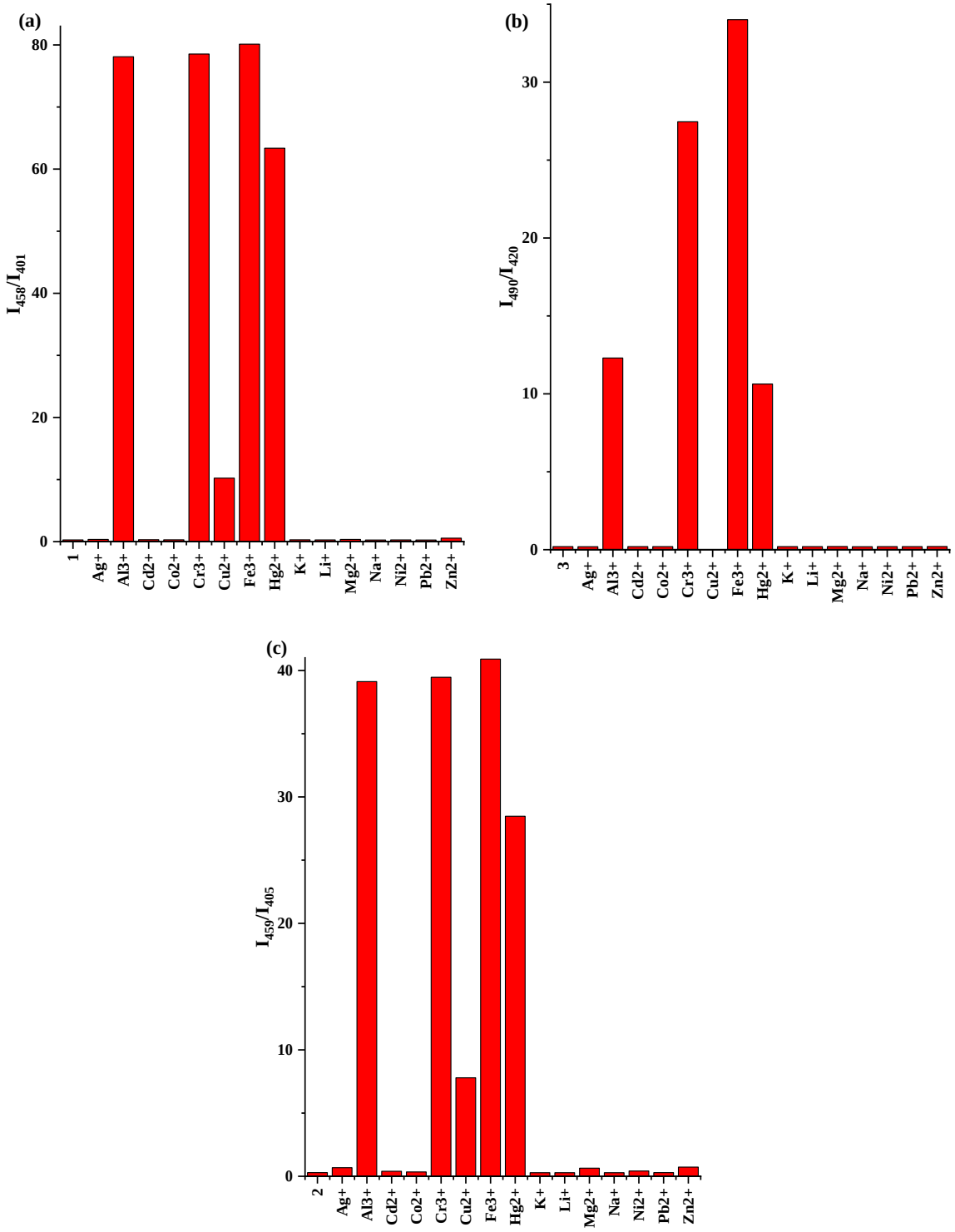

Figure 4.50: Bar chart showing fluorescence ratio of (a) $\mathbf{I_{N2}}$ (b) $\mathbf{I_{N3}}$ and (c) $\mathbf{I_{N4}}$ in the presence tested ions.

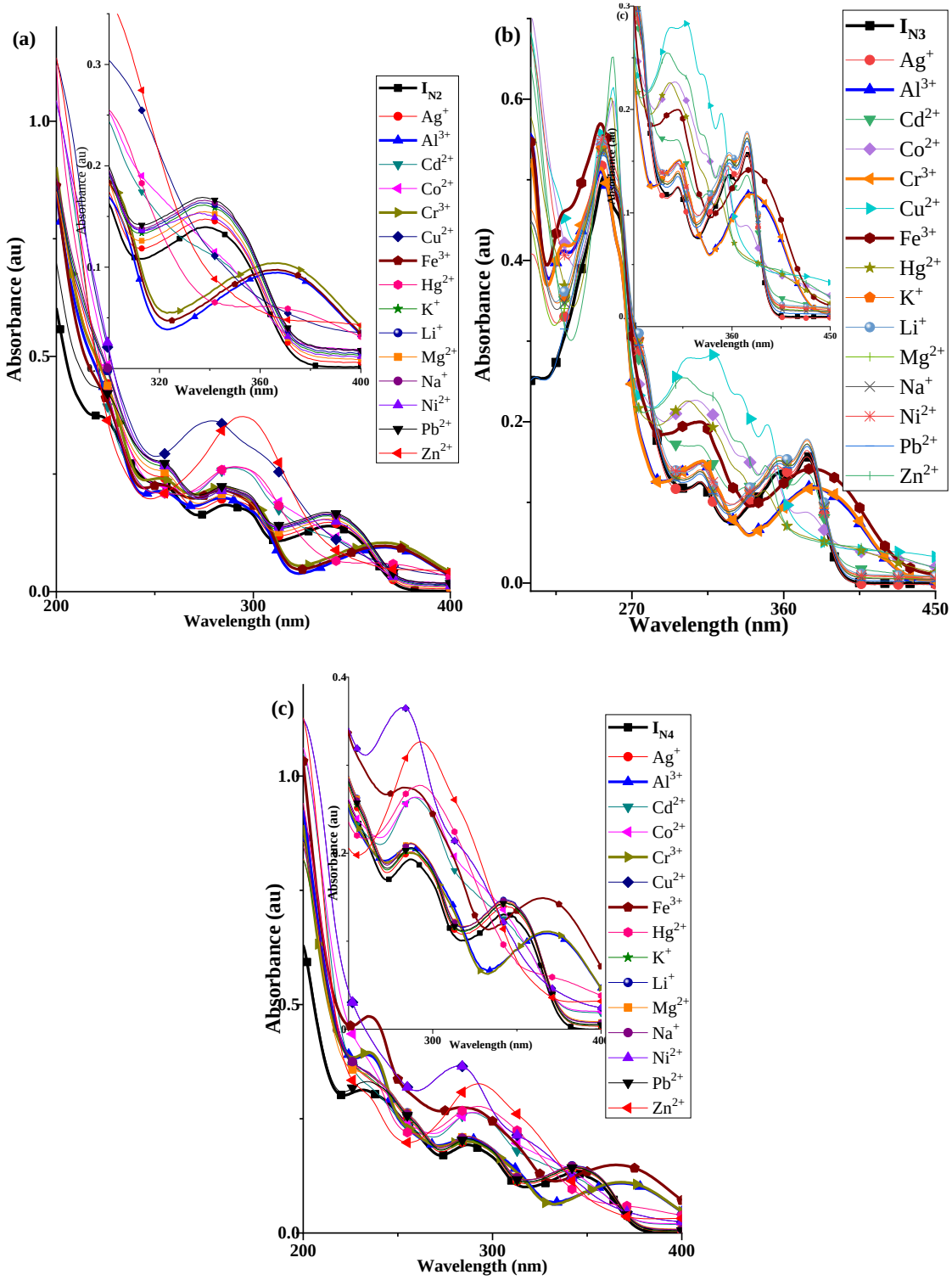

Figure 4.51: Absorption spectra of (a) $\mathbf{I_{N2}}$ (b) $\mathbf{I_{N3}}$ and (c) $\mathbf{I_{N4}}$ in the presence of tested cations

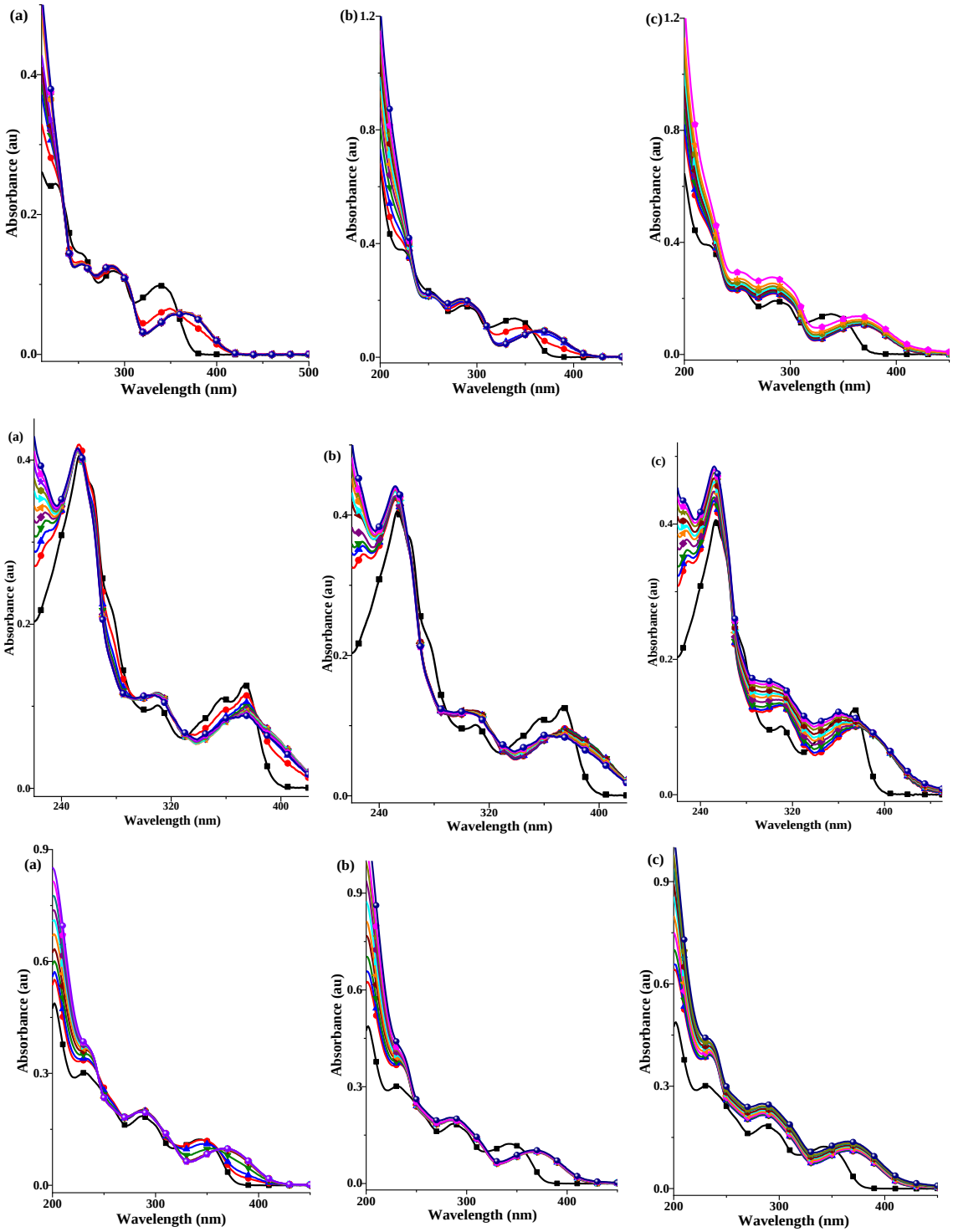

Figure 4.52: UV-Vis titration of (a) – (c) $\mathbf{I_{N2}}$, (d) – (f) $\mathbf{I_{N3}}$ and (g) – (i) $\mathbf{I_{N4}}$ with Al^{3+}, Cr^{3+} and Fe^{3+}, respectively.

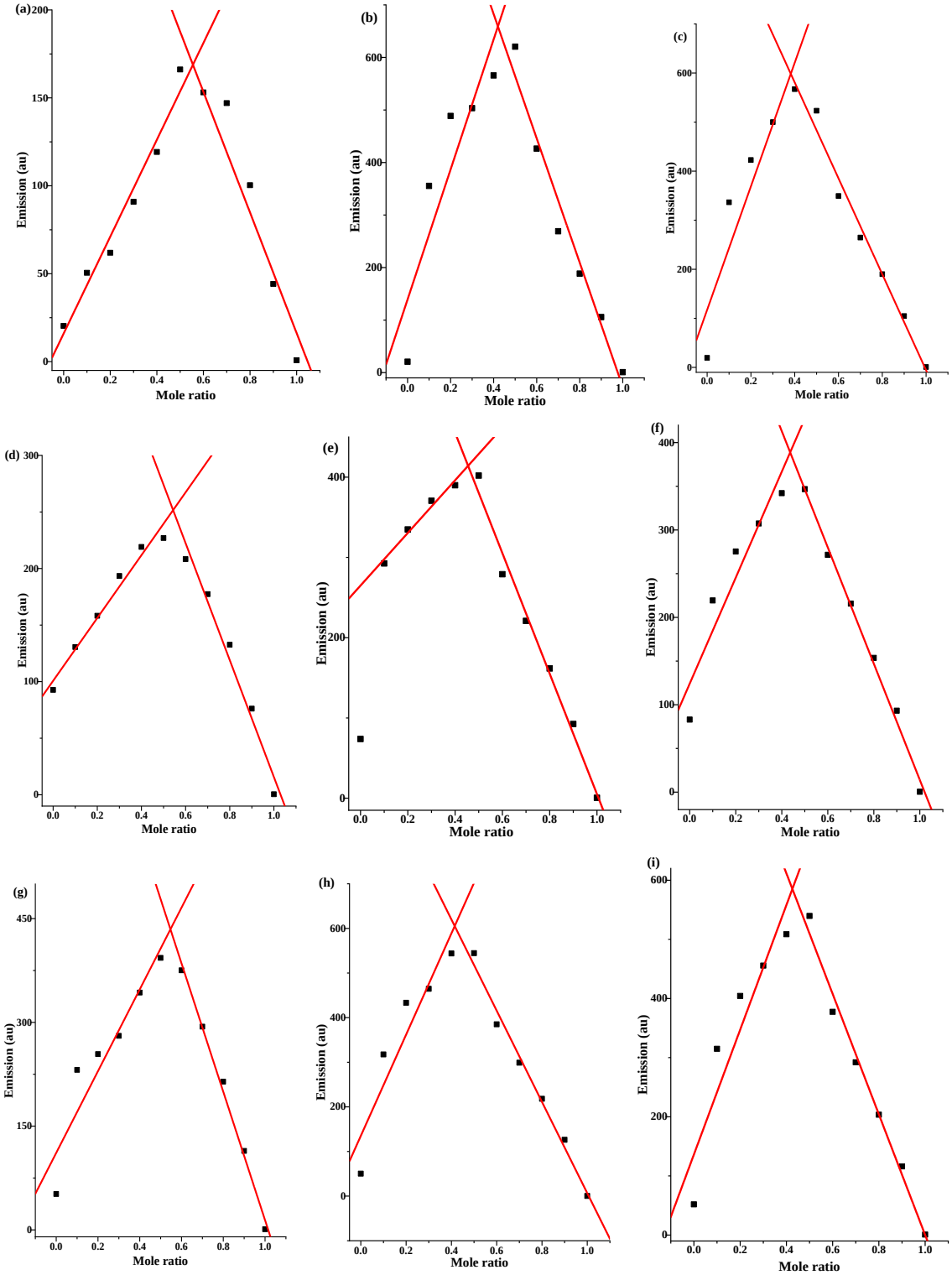

Figure 4.53: Job's plot of (a) – (c) **I_{N2},** (d) – (f) **I_{N3}** and (g) – (i) **I_{N4}** with Al^{3+}, Cr^{3+} and Fe^{3+}, respectively.

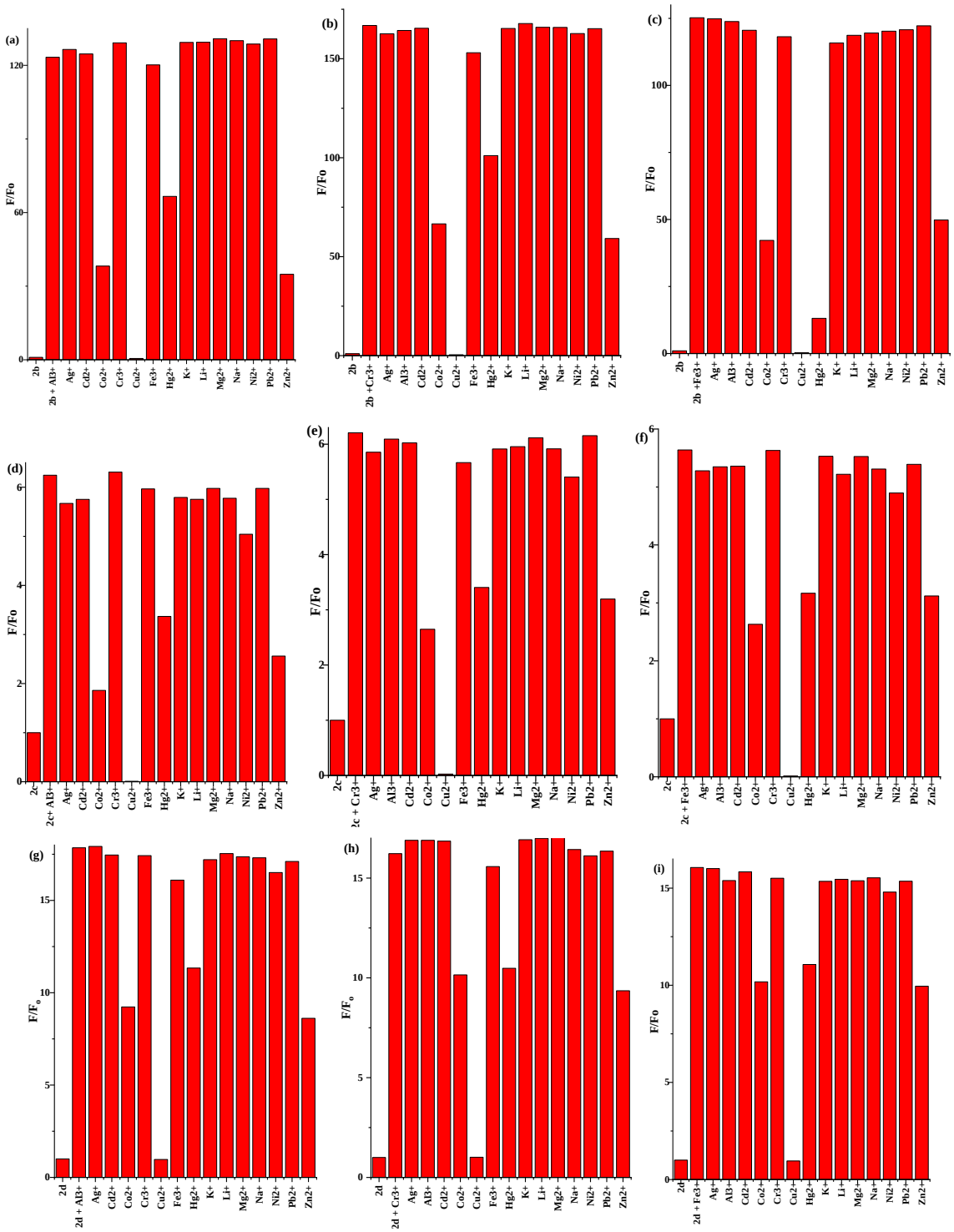

Figure 4.54: Interference experiment of (a) – (c) **IN2,** (d) – (f) **IN3** and (g) – (i) **IN4** with Al^{3+}, Cr^{3+} and Fe^{3+}, respectively, in the presence of other cations tested.

4.8.4 Sensing properties of the ONSNO/ONONO imines {H_2S1 – H_2O1}

The interaction of the pentadentate {ONSNO/ONONO} receptors with metal ions {Ag^+, Al^{3+}, Cd^{2+}, Co^{2+}, Cr^{3+}, Cu^{2+}, Fe^{3+}, Ga^{3+}, Hg^{2+}, In^{3+}, K^+, Li^+, Mg^{2+}, Na^+, Ni^{2+}, Pb^{2+}, Tl^{3+} and Zn^{2+}} is presented in **Fig. 4.55** and **Fig. 4.56**. Although the receptors bear similar heteroatoms to the NNO imines, their metal ions sensing patterns differ – they however showed tendency towards +3 ions {like the NNN imines}, especially group 13 ions.

H_2S1, **H_2S2** and **H_2S3** showed dual emissions in the presence of Al^{3+} ions {**Fig 4.55**}; with **H_2S1** and **H_2S3** exhibiting red-shifted emissions in the presence of Ga^{3+} and In^{3+} ions. These ligands in the presence of Al^{3+} ions, had the primary emissions at 302 nm, 354 nm and 312 nm, respectively; while the secondary emissions were observed at 473 nm, 494 nm and 485 nm, respectively. A 16 – 25-fold increase in fluorescence quantum yield was also observed. The red-shifted emissions {Ga^{3+} and In^{3+}} occurred at 497 nm and 509 nm, respectively {**H_2S1**}; as well as 530 nm and 537 nm {**H_2S3**} – with a 3 – 6-fold increase in fluorescence quantum yield. As in the case of the NNO imines, the dual emission was probably due to keto-enol tautomerism.

The introduction of electron-withdrawing groups {Br, NO_2} appeared to inhibit sensitivity towards group 13 ions (**Fig. 4.56**{**a**} – {**c**}); although **H_2S4** showed sensitivity towards the group 13 ions, a slight turn-on in the presence of Cd^{2+} ion was also observed (**Fig. 4.56**{**a**}).

Although dual emission had been reported to be more advantageous, in comparison to single emission (Upadhyay and Kumar 2010; Jung *et al*., 2009), **H_2O1** {with a single emission} showed a more appreciable and distinctive response in the presence of Al^{3+} ion {**Fig. 4.56**[**d**]} – with a colour change observable to the eye. Al^{3+} emits maximally at 482 nm {with ≈38-fold increase in fluorescence quantum yield}; while maximum emission in the presence of Ga^{3+} was at 487 nm {with ≈2-fold increase in fluorescence quantum yield} and In^{3+} at 501 nm {with ≈4-fold increase in fluorescence quantum yield}. Fluorescence titration of **H_2O1** with Al^{3+}, Ga^{3+} and In^{3+} {**Fig. 4.57**} showed, generally, a non-linear curve fitting. The UV-Vis titration {**Fig. 4.58**} showed a gradual decrease in the n-π^* transition at 341 nm with increase in volume of Al^{3+} {**Fig. 4.58**[**a**]}. ESI-MS {**Fig. S87**} showed a peak at *m/z* 492.2 {[**H_2O1** + Al^{3+} + NO_3] Calc. 495.42} which suggested a 1:1 interaction

between **H_2O1** and Al^{3+}, which was corroborated by Job's plot {**Fig. 4.59**[**a**]}. The association constant, determined by fluorescence titration, of **H_2O1**-Al^{3+} was 1.6 x 10^4 M^{-1} while the *LOD* was 5.48 nM {R^2 = 0.989} (**Fig. 4.59**{**b**}).

A comparison of the NMR spectrum of **H_2O1** and **H_2O1**-Al^{3+} {**Fig. S88**}, showed a loss of the phenolic proton {at ≈13 ppm}, change of the imine proton {at 9.00 ppm} from a singlet to a doublet and the appearance a new peak {around 10.25 ppm}, attributable to the formation of an iminium {=NH^+-} group. These observation, suggested a migration of the -OH proton to the imine N. Attempts to show this interaction by crystal growth did not yield any crystal, however, this migration was observed in the crystal structure of Zn^{2+} ion {**Fig. 4.11**[**b**]}. Thus, while donor-acceptor N···H–O functionality resulted in a turn-off effect in **H_2O1**, this same functionality gives rise to an ESIPT-inspired turn-on effect in the presence of Al^{3+} {**Scheme 4.16**}. Interference study {**Fig. 4.59**[**c**]} of **H_2O1**-Al^{3+} {upon addition of equivalent amounts of solutions of other metal ions tested} revealed **H_2O1** to be a good sensor for Al^{3+}. An investigation of the effect of water on Al^{3+} sensing by **H_2O1** is presented in {**Fig. 4.59**[**d**]}. Our result revealed that, contrary to the observation made by Li *et al.* (2017), the introduction of water does not affect Al^{3+} sensing by **H_2O1**. Attempts to use more than 10% water was not successful, as we could not achieve complete dissolution of the receptor at > 10% water.

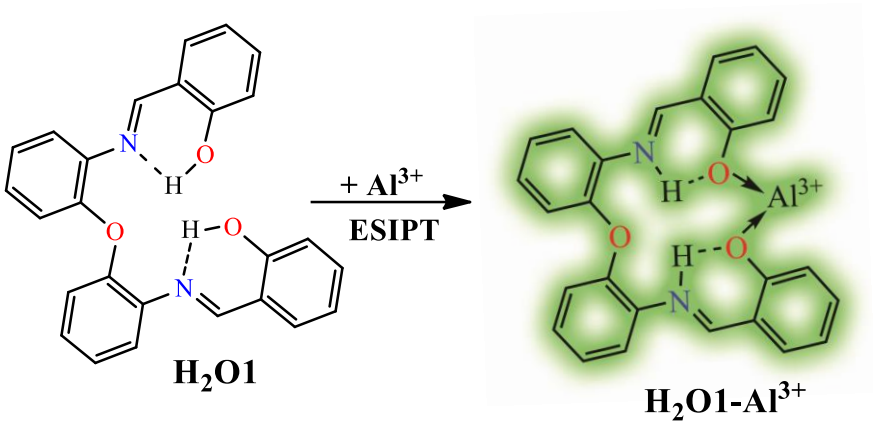

Scheme 4.16: Donor-acceptor N···H–O effect on fluorescent "turn-off/on" of **H_2O1** and **H_2O1**-Al^{3+}.

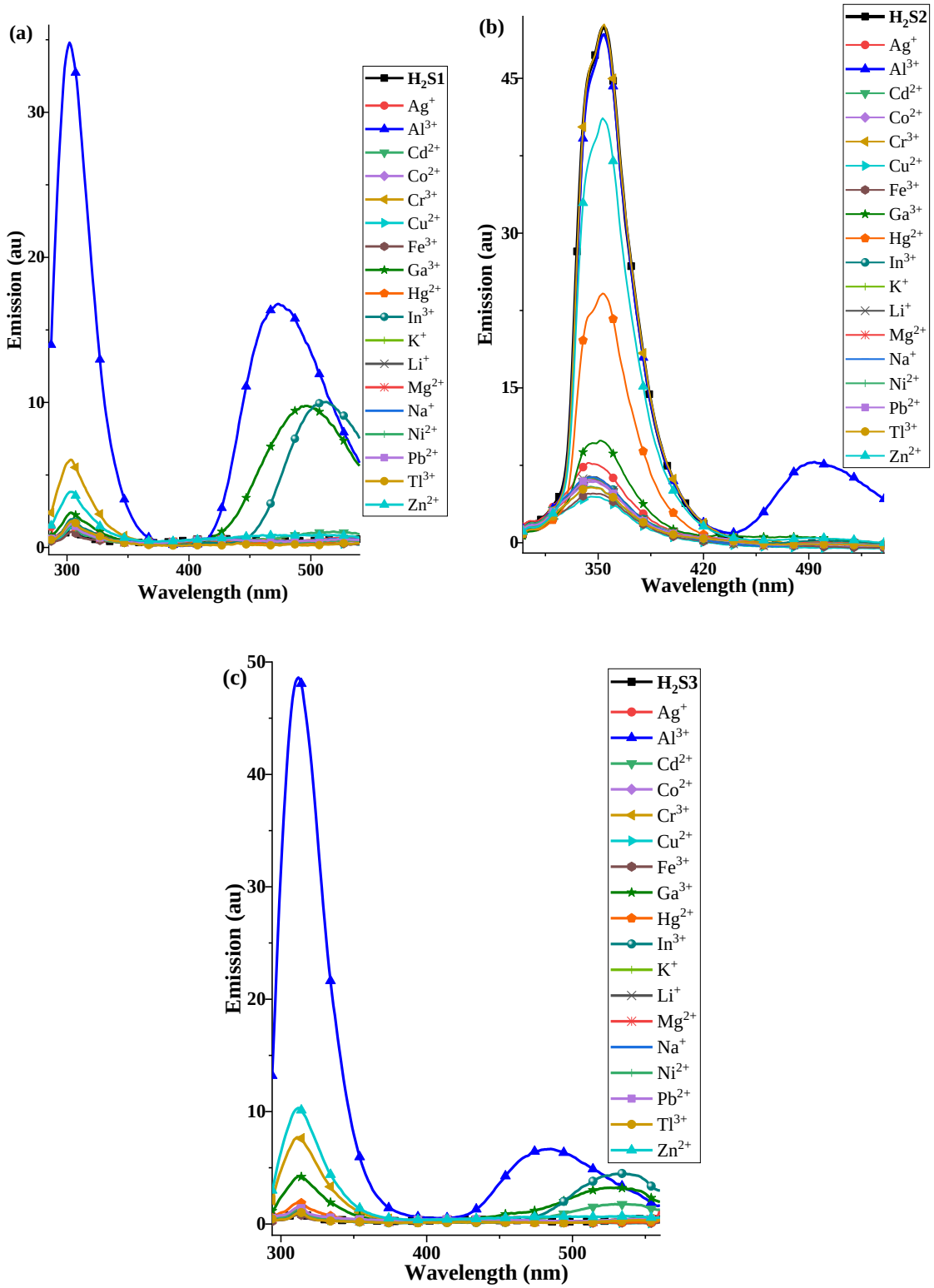

Figure 4.55: Emission spectra of (a) **H_2S1** (b) **H_2S2** and (c) **H_2S3** in the presence of tested cations.

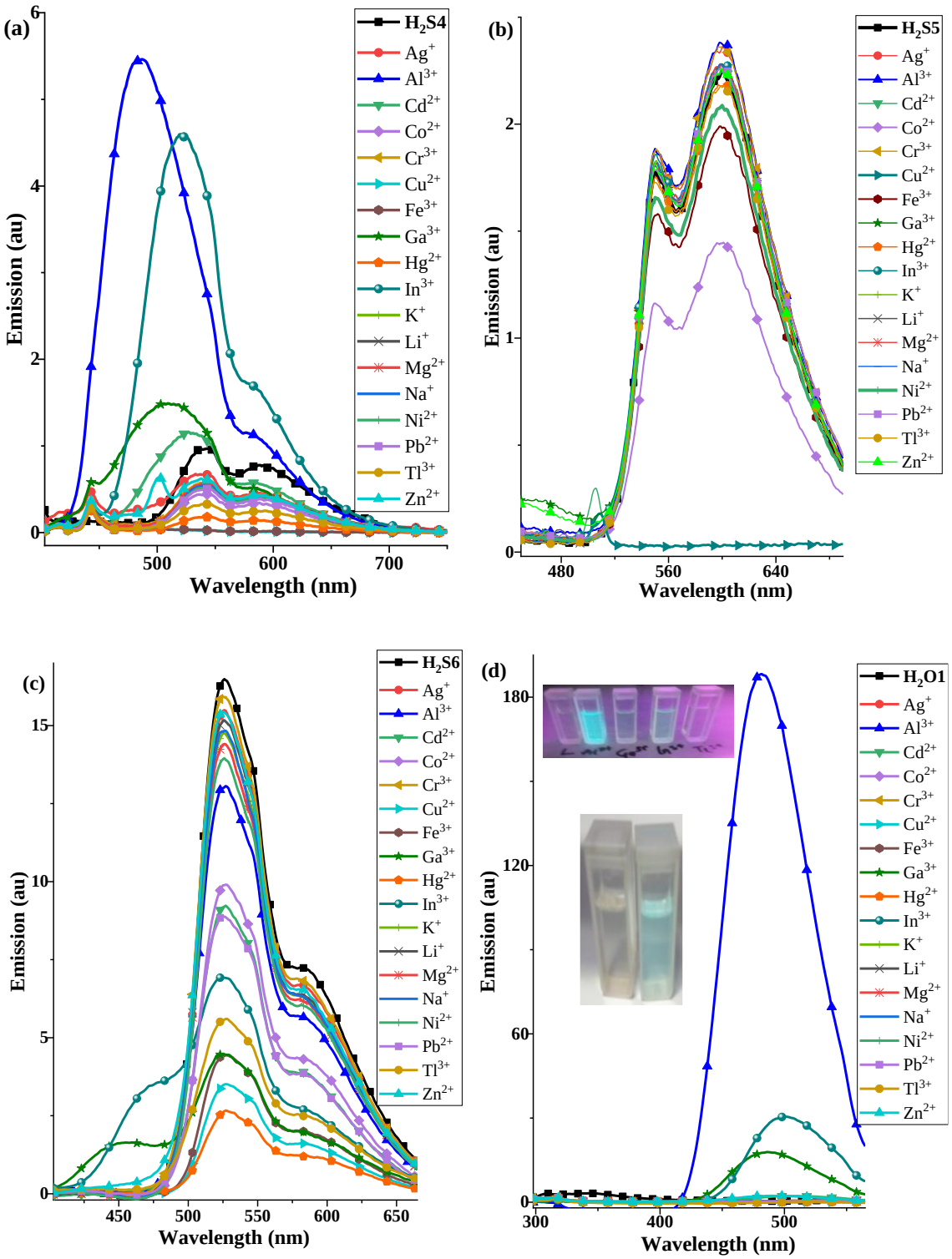

Figure 4.56: Emission spectra of (a) **H2S4** (b) **H2S5** (c) **H2S6** and (d) **H2O1** {Inset: colour change in the presence of Al^{3+}} in the presence of tested cations.

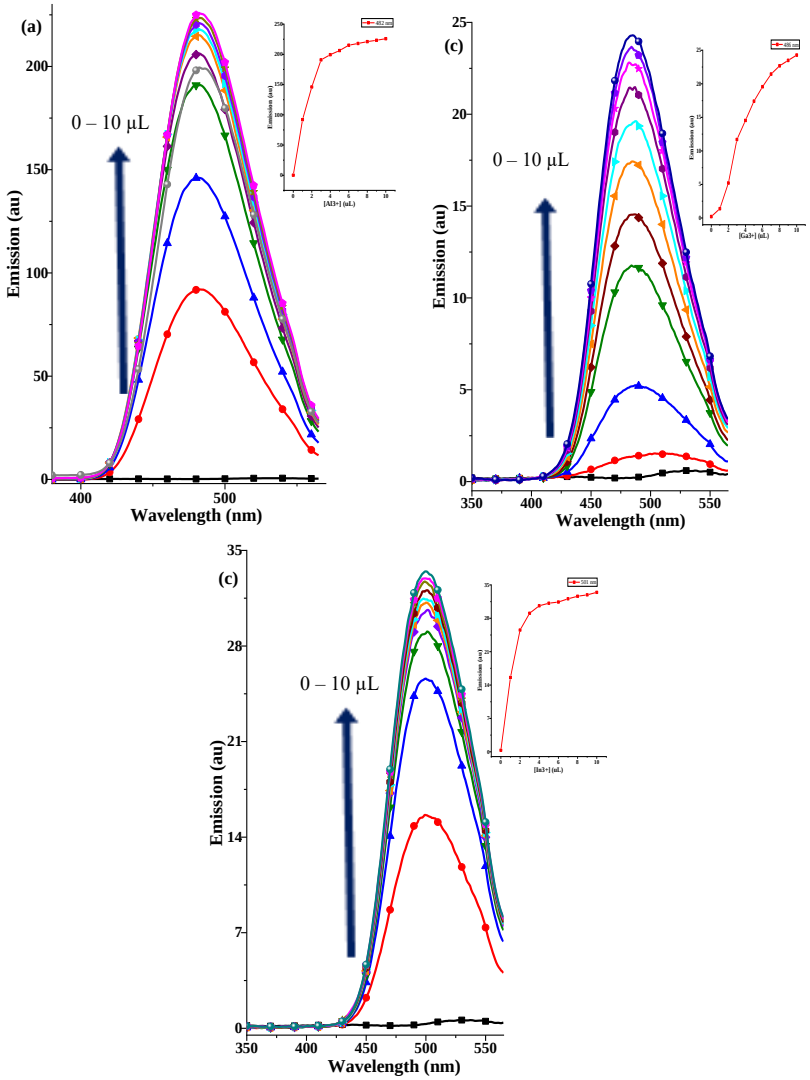

Figure 4.57: Fluorescence titration of **H_2O1** with (a) Al^{3+} (b) Ga^{3+} and (c) In^{3+} (Inset: Change in emission intensity at 482 nm, 487 nm and 501 nm, respectively)

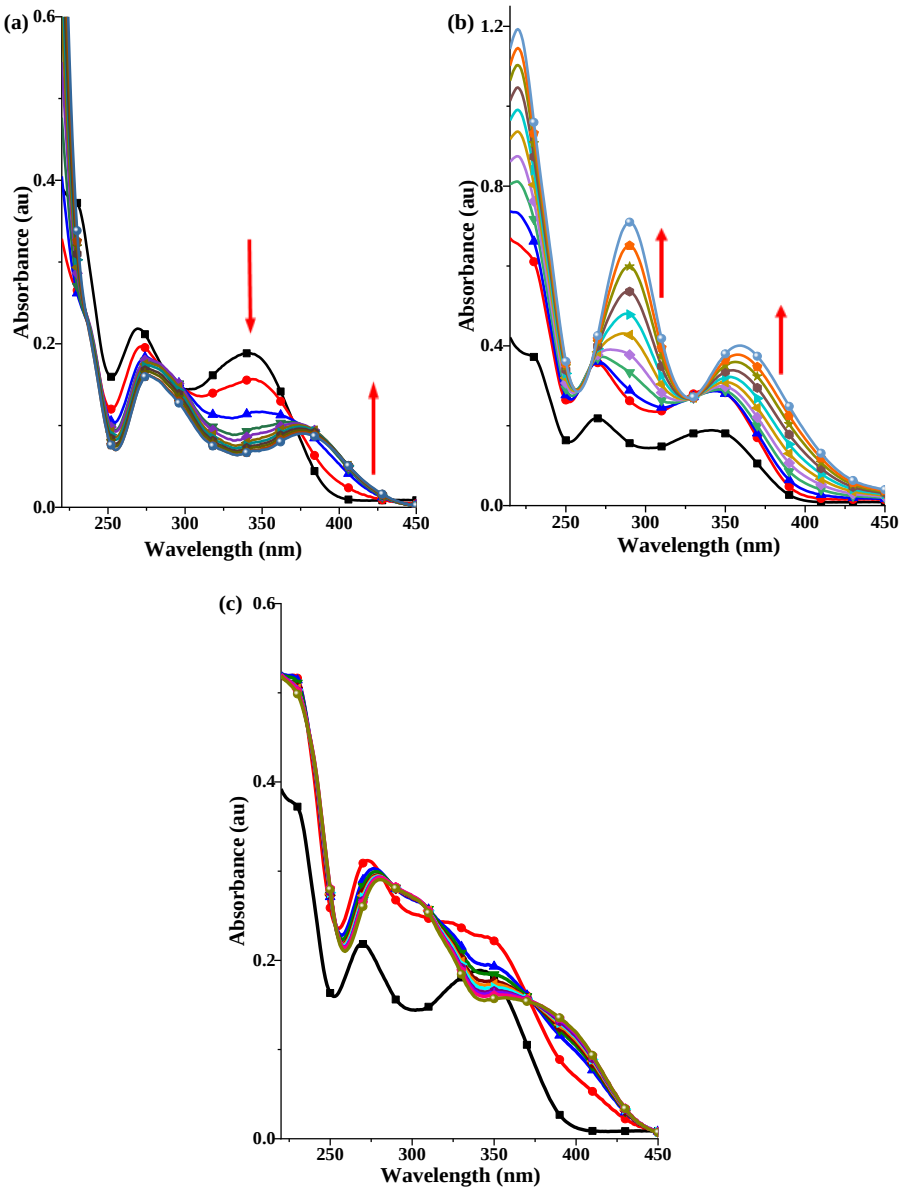

Figure 4.58: UV-Vis titration of **H_2O1** with (a) Al^{3+} (b) Ga^{3+} and (c) In^{3+} ions

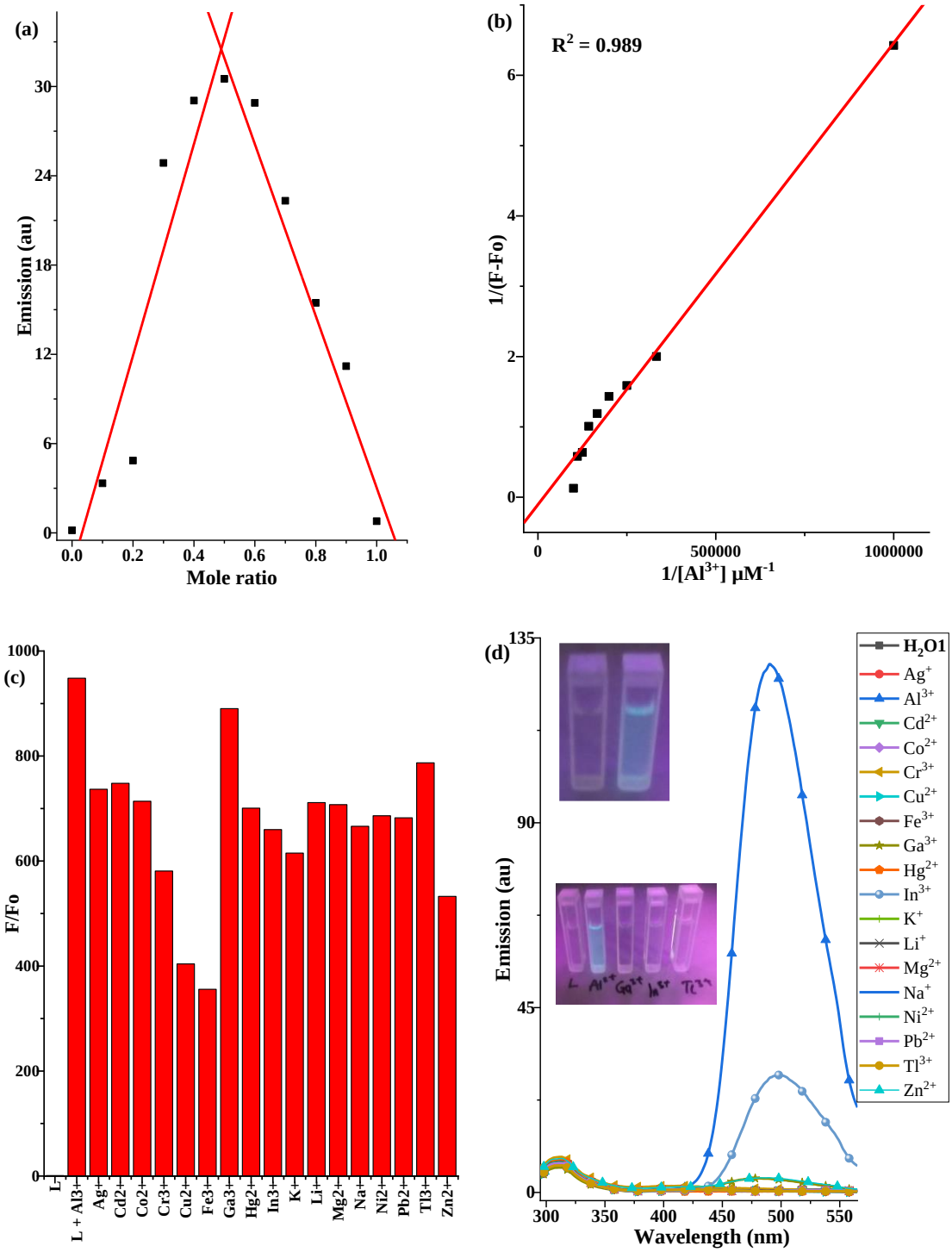

Figure 4.59: (a) Job's plot of **H₂O1** with Al^{3+} (b) Determination of *LOD* of Al^{3+} by **H₂O1** (c) Interference study of **H₂O1**-Al^{3+} by other ions and (d) Emission spectra of **H₂O1** using 9:1 MeOH/H_2O (inset colour change under UV-lamp) in the presence of tested cations.

4.8.5 Sensing properties of the azo-imines (**H_2AI_1** – **H_2AI_3**)

The interaction of the pentadentate *azo-imine* receptors with metal ions {Ag^+, Al^{3+}, Cd^{2+}, Co^{2+}, Cr^{3+}, Cu^{2+}, Fe^{3+}, Hg^{2+}, K^+, Li^+, Mg^{2+}, Na^+, Ni^{2+}, Pb^{2+} and Zn^{2+}} is presented in **Fig. 4.60** and **Fig. 4.61**. Substitution of the S/O groups in the pentadentate {ONSNO/ONONO} imines with the azo function {N=N} did not appear to affect Al^{3+} ion sensitivity. In addition to Al^{3+}, however, Cr^{3+} ion showed a turn-on effect. More so, the dual emission seen in analogous ONSNO receptors {**H_2S1** – **H_2S3**} was not observed for the *azo-imines*.

Methyl substitution gave similar sensing pattern {**Fig. 4.60**[**c**]} as the unsubstituted receptor {**Fig. 4.60**[**a**]}; while phenyl substitution produced a somewhat similar pattern {**Fig. 4.60**[**b**]}, Hg^{2+} ion also showed a turn-on effect {not seen in **H_2AI_1** and **H_2AI_3**}. Al^{3+} sensing in **H_2AI_1** and **H_2AI_3** exhibited a shoulder at 375 nm and 402 nm, respectively; while the major peaks were observed at 452 nm and 466 nm, respectively. In both cases, a change in colour was observed under UV light {**Fig. 4.60**{**a**}[**i**]} and {**Fig. 4.60**{**c**}[**i**]}; while Cr^{3+} showed a faint colour change in **H_2AI_1** a more intense colour is observed in **H_2AI_3**. Although Cu^{2+} ion showed low intensities, even in comparison to the receptors {**Fig. 4.61**}, a colourimetric effect was seen upon interaction of Cu^{2+} ion with **H_2AI_1** {**Fig. 4.60**{**a**}[**ii**]} and **H_2AI_3** {**Fig. 4.60**{**c**}[**ii**]}.

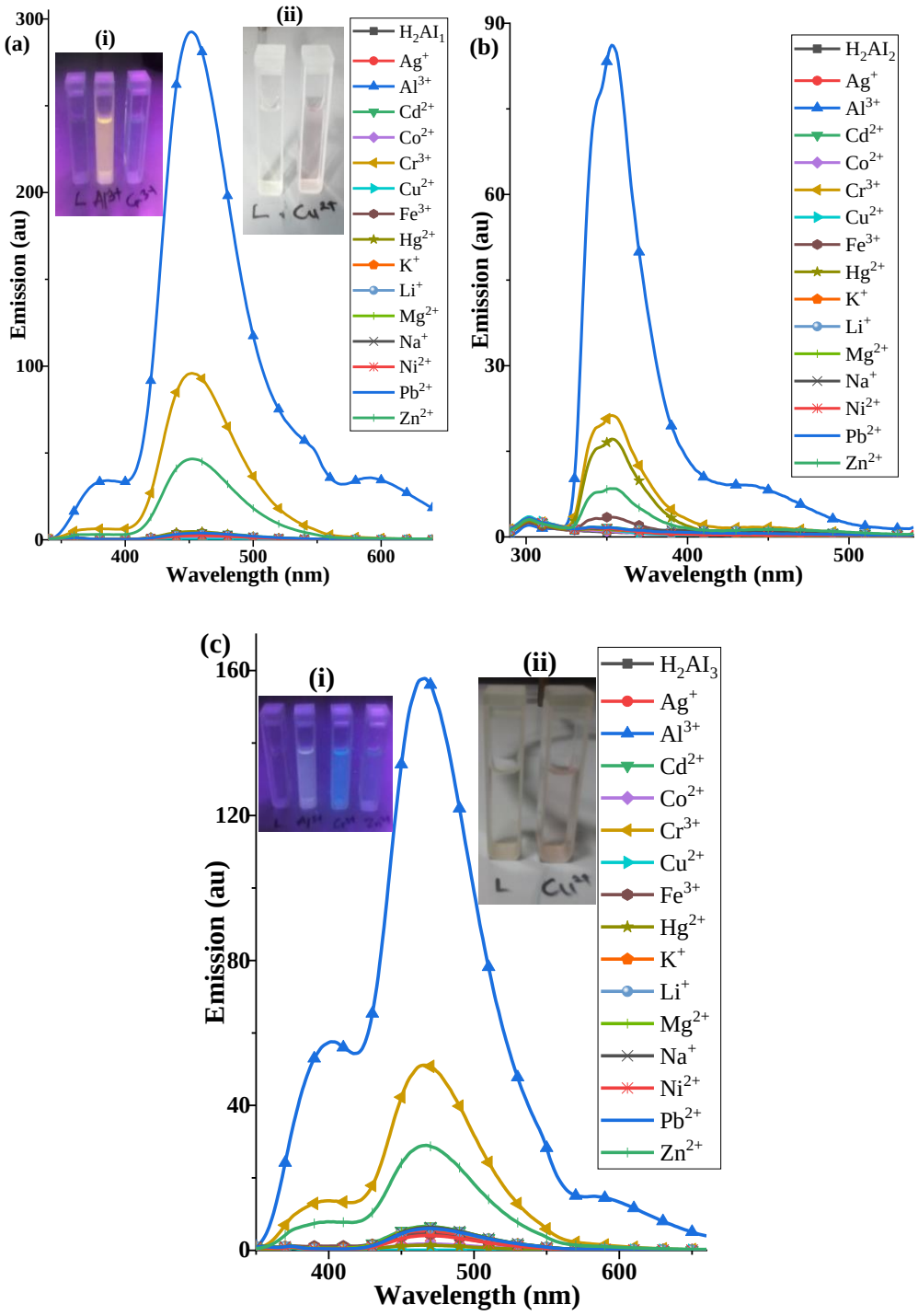

Figure 4.60: Emission spectra of (a) **H_2AI_1,** (b) **H_2AI_2** and (c) **H_2AI_3** in the presence of tested cations {Inset: (i) colour change in the presence of Al^{3+} under UV lamp and (ii) colourimetric detection of Cu^{2+}}.

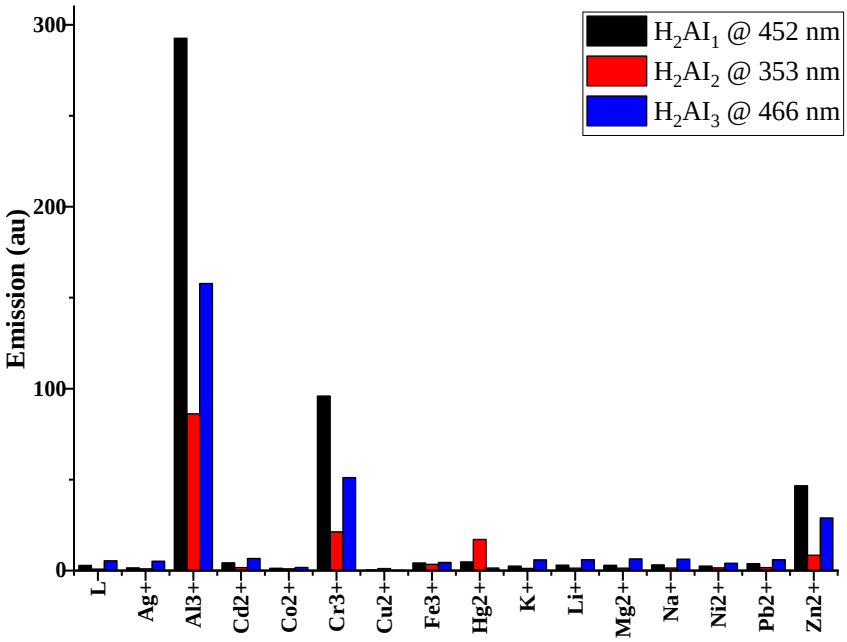

Figure 4.61: Emission intensities of the *azo-imines* and tested cations (upon interaction with respective receptors).

CHAPTER FIVE

SUMMARY, CONCLUSION AND RECOMMENDATIONS

5.1 Summary

This study reports the preparation of four {4} 1,3-bis-imidazoles {**BI_1** – **BI_4**}, three {3} 1,4-bis-imidazoles {**BI_5** – **BI_7**}, nine {9} nitro-imidazoles {**N1** – **N9**}, nine {9} imidazole amines {**A1** – **A9**}, nine {9} NNO imidazole-imines {**I_1** – **I_9**}, three {3} NNN imidazole-imines {**I_{N2}** – **I_{N4}**}, three {3} cyclisation products {imidazo quinazoline/quinazolin-1-ium}, eight {8} S-/O-bridged pentadentate imines {**H_2S1** – **H_2O1**}, and three {3} azo-bridged imines {**H_2AI_1** – **H_2AI_3**}. Forty-three {43} metal complexes were also prepared. NMR, MS, IR, UV-Vis, thermal and micro (elemental) analyses gave good agreement with expected outcomes, while X-ray crystallography confirmed the structures {and geometry} of some of the compounds.

The 1,2-bis-imidazole proved difficult to obtain {only 2,4,5-triphenyl-1*H*-imidazole was observed (**Fig. S8**)}; the preparation of the 1,4-bis-imidazoles was also challenging {with **BI_7** and **BI_6** obtained in 6 % and 38 % yields, respectively}, although **BI_5** was obtained in 88 % yield. The nitro-imidazole, imidazole amines as well as the tridentate NNO and NNN imines were obtained in good to excellent yield; the pentadentate {S-bridged, O-bridged and diazo-bridged} imines generally were obtained in excellent yield.

The S-/O-bridged bis-imines showed low quantum yields {desired for turn-on sensing} and although they fail to show ESIPT in the absence of analyte, this feature {ESIPT} proved useful upon analyte binding {especially in **H_2S1**, **H_2S2**, **H_2S3** and **H_2O1**}. Analogues possessing EDG or with no ring substituent showed sensitivity towards Al^{3+}, with the "hard" O-bridged **H_2O1** having the best selectivity. The Al^{3+} detection limit of **H_2O1** {5.48 nM} as well as its high fluorescence turn-on ratio {528-fold} and naked-eye visibility make it very attractive for Al^{3+} monitoring and detection.

The Kramer's d^3 Cr^{III} ion {in **$[CrO1(ONO_2)]0.5H_2O.0.2MeCN$**} did not show orbital contribution, while the Kramer's d^7 Co^{II} ions {in **$[Co_2S1_2]3H_2O$** – **$[Co_2O1_2]0.5H_2O$**} showed significant contribution to orbital angular momentum – the A_{2g}

{in Cr^{III}} and T_{1g} {in Co^{II}} ground terms were partially responsible for this observation. The magnetic behaviours of the Ni^{II} complexes {**[Ni_2S2_2]4H_2O** and **[NiS5(H_2O)]**} as well as the Cu^{II} complexes {**[Cu_3S1_2(OAc)$_2$]2.75H_2O**, **[Cu_3S2_2(OAc)$_2$]5.5H_2O**, **[Cu_2S2_2]2THF** and **[Cu_2O1_2]1.5H_2O**} showed correlation with structural features like nuclearity {which affected the direction of *D* in the Ni^{II} complexes}, Cu···Cu, Cu-O-Cu bond angles etc. Elongation along the *z*-axis {with $d_{x^2-y^2}$ ground state} of the six-coordinate Cu^{II} complexes was supported by esr.

5.2 Conclusion

Synthetic manipulations arising from systematic substituent variation showed benefit in the isolation and tuning of materials, based on imidazole and bis-phenol imine cores, with application in host-guest chemistry and magnetochemistry.

5.3 Recommendations

1. Imidazoles and Schiff bases (as well as their metal complexes) are known to exhibit biological potency – this property should be investigated
2. The copper complexes of the imidazoles should be prepared and their activity in phenoxazinone synthase investigated
3. Further attempts, possibly involving other methods of crystal growth, should be explored to establish the binding mode of **H_2O1** with Al^{3+}.
4. The interesting proton movement observed for the Zn(II) complex in **Fig. 4.11**{**b**} should be investigated in other families of the series.

5.4 Contribution to knowledge

A series of bis-imidazoles, imidazole amines/imines and bis-phenol imine ligands have been added to library of materials with potential for analyte recognition. The use of multi-donor ligand architecture was shown to be beneficial in the detection of M^{III} ions {with Al^{3+} successfully discriminated from other competing M^{III} ions}. The low detection limit exhibited by **I_9** {for Zn^{2+}} and **H_2O1** {for Al^{3+}} makes these compounds useful candidate molecular recognition. More so, relationship between structure and magnetic behaviour was established.

REFERENCES

Acharya, J., Sarkar, A., Kumar, P., Kumar, V., Gonzalez, J. F., Cador, O., Pointillart, F., Rajaraman, G. and Chandrasekhar, V. 2020. Influence of ligand field on magnetic anisotropy in a family of pentacoordinate Co^{II} complexes. *Dalton Transactions* 49.15: 4785 – 47964

Addison, A. W., Hendriks, H. M. J., Reedijk, J. and Thompson, L. K. 1981. Copper Complexes of the "Tripod" Ligand Tris(2-benzimidazolylmethyl)amine: Five- and Six-Coordinate Copper(II) Derivatives and Some Copper(I) Derivatives. *Inorganic Chemistry* 20.1: 103 – 110

Agarwal, S. 2011. The Effect of N-methylation on Photophysical Properties of 3-Aminoquinoline. *Journal of Fluorescence* 21: 1959 – 1967

Ahmadi, R. A. and Amani, S. 2012. Synthesis, Spectroscopy, Thermal Analysis, Magnetic Properties and Biological Activity Studies of Cu(II) and Co(II) Complexes with Schiff Base Dye Ligands. *Molecules* 17.6: 6434 – 6448

Akbolat, N., Yildiz, A., Temel, H., Gul, K. 2012. Antifungal studies of some complexes with Schiff base ligands. *Dicle University Journal of the Institute of Natural and Applied Science* 1.1: 15 – 22. https://dergipark.org.tr/en/pub/dufed/issue/54985/754391

Akintola, O., Buchholz, A., Görls, H. and Plass, W. 2021. Modulator Induced Formation of a Neutral Framework Based on Trinuclear Cobalt(II) Clusters and Nitrilotribenzoic Acid: Synthesis, Magnetism, and Sorption Properties. *European Journal of Inorganic Chemistry* 2021.23: 2266 – 2273

Alabdali, A. J., Ibrahim, F. M. 2014. Synthesis and Thermal Study of Co(II), Ni(II), Cu(II) Mixed Ligand Complexes Using Histidine as Tridentate Ligand. *IOSR Journal of Applied Chemistry* 6.6: 60 – 63

Alam, R., Bhowmick, R., Islam, A. S. M., katarkar, A., Chaudhuri, K. and Ali, M. 2017. A rhodamine based fluorescent trivalent sensor (Fe^{3+}, Al^{3+}, Cr^{3+}) with potential applications for live cell imaging and combinational logic circuits and memory devices. *New Journal of Chemistry* 41.16: 8359 – 8369

_____, Pal, K., Shaw, B. K., Dolai, M., Pal, N., Saha, S. K., Ali, M. 2016. Synthesis, structure, catalytic and magnetic properties of a pyrazole based five coordinated di-nuclear cobalt(II) complex. *Polyhedron* 106: 84 – 91

Alberga, D., Ciofini, I., Mangiatordi, G. F., Pedone, A., Roncali, G. L. J. and Adamo, C. 2017. Effects of Substituents on Transport Properties of Molecular Materials for Organic Solar Cells: a Theoretical Investigation. *Chemistry of Materials* 29.2: 673 – 681

Alenezy, E. K., Sabri, Y. M., Kandjani, A. E., Korcoban, D., Rashid, S. S. A. A. H., Ippolito, S. J. and Bhargava, S. K. 2020. Low-Temperature Hydrogen Sensor: Enhanced Performance Enabled through Photoactive Pd-Decorated TiO_2 Colloidal Crystals. *ACS Sensors* 12.5: 3902 – 3914

Alfonso, M., Ferao, A. E., Tárraga, A., and Molina, P. 2015. Electrochemical and Fluorescent Ferrocene-Imidazole-Based Dyads as Ion-Pair Receptors for Divalent Metal Cations and Oxoanions. *Inorganic Chemistry* 54.15: 7461 – 7473

Alhadi, A, A., Shaker, S. A., Nura, S. G, Yehye, W. A., Ali, H. M. 2012. Preparation, Spectroscopic Characterization of a new Cd(II) complex containing tridentate NNO Schiff Base derived and X-ray crystallographic structural study of 3,4,5-Trihydroxybenzoic acid[1-(pyridyl)-ethylidene]hydrazone. *Journal of the Chilean Chemical Society* 57.3: 1283 – 1286

Alonso, P. J., Arauzo, A. B., García-Monforte, M. A., García-Rubio, I., Martín, A., Menjón, B. and Rillo, C. 2011. Synthesis, characterisation and magnetic properties of octahedral chromium(III) compounds with six *C*-donor ligands. *Dalton. Transactions* 40.4: 853 – 861

Alreja, P. and Kaur, N. 2015. A New multifunctional 1, 10–Phenanthroline based fluorophore for anion and cation sensing. *Journal of Luminescence* 168: 186 – 191

Al-Adilee, K. J. 2015. Preparation and Characterization of Some Transition Metal Complexes with NovelAzo-Schiff base Ligand Derived from 2-(*E*)-(1*H*-benzo[*d*] imidazole-2-yly diazenyl)-5-((*E*)-benzylideneimino)phenol (BIADPI). *Research Journal of Pharmaceutical, Biological and Chemical Sciences* 6.5: 1297 – 1308

_____, Abedalrazaq, K. A. and Al-Hamdiny, Z. M. 2013. Synthesis and Spectroscopic Properties of Some Transition Metal Complexes with New Azo-Dyes Derived from Thiazole and Imidazole. *Asian Journal of Chemistry* 25.18: 10475 – 10481

Al-Rawi, M. S., Tomma, J. H., Mukhlus, A. A., Al-Dujaili, A. H. 2013. Synthesis and Characterization of New Schiff Bases Heterocyclic Compounds and Their N-Acyl, Thiourea and Imidazole Derived from D-Erythroascorbic Acid. *American Journal of Organic Chemistry* 3.1: 1 – 8

Al-Sha'alan, N. H. 2007. Antimicrobial Activity and Spectral, Magnetic and Thermal Studies of Some Transition Metal Complexes of a Schiff Base Hydrazone Containing a Quinoline Moiety. *Molecules* 12.5: 1080 – 1091

Ammeter, J. H., Bürgi, B., Gamp, E., Meyer-Sandrin, V. and Jensen, W. P. 1979. Static and Dynamic Jahn-Teller Distortions in CuN_6 Complexes. Crystal Structures and EPR Spectra of Complexes between Copper(II) and Rigid, Tridentate *cis,cis*-1,3,5-Triaminocyclohexane (tach): $Cu(tach)_2(ClO_4)_2$, $Cu(tach)_2(NO_3)_2$. Crystal Structure of $Ni(tach)_2(NO_3)_2$. *Inorganic Chemistry* 18.3: 733 – 750

Anacona, J. R., Calvo, J and Almanza, O. A. 2013. Synthesis, Spectroscopic, and Magnetic Studies of Mono- and Polynuclear Schiff Base Metal Complexes Containing Salicylidene-Cefotaxime Ligand. *International Journal of Inorganic Chemistry* 2013.108740: 7 pages
https://doi.org/10.1155/2013/108740

Anamika, Yadav, D. K., Manar, K. K., Yadav, C. L., Kumar, K., Ganesan, V., Drew, M. G. B. and Singh, N. 2020. New heteroleptic [Ni(II)1,1-dithiolate-phosphine] complexes: synthesis, characterization and electrocatalytic oxygen evolution studies. *Dalton Transactions* 49.11: 3592 – 3605

Anbu, S., Shanmugaraju, S., Ravishankaran, R., Karande, A. A., Mukherjee, P. S. 2012. A phenanthrene based highly selective fluorogenic and visual sensor for Cu^{2+} ion with nanomolar detection limit and its application in live cell imaging. *Inorganic Chemistry Communications* 25: 26 – 29

Anderson, E. B., Long, T. E. 2010. Imidazole- and imidazolium-containing polymers for biology and material science applications. *Polymer* 51.12: 2447 – 2454

Andruh, M. 2011. Compartmental Schiff-base ligands – a rich library of tectons in designing magnetic and luminescent materials. *Chemical Communications* 47.11: 3025 – 3042

Antal, P., Drahos, B., Herchel, R. and Trávníček, Z. 2016. Late First-Row Transition-Metal Complexes Containing a 2-Pyridylmethyl Pendant-Armed 15-Membered Macrocyclic Ligand. Field-Induced Slow Magnetic Relaxation in a Seven Coordinate Cobalt(II) Compound. *Inorganic Chemistry* 55.12: 5957 – 5972

Aranha, P. E., dos Santos, M. P., Romera, S., Dockal, E. R. 2007. Synthesis, characterization, and spectroscopic studies of tetradentate Schiff base chromium(III) complexes. *Polyhedron* 26.7: 1373 – 1382

Arauzo, A., Lazarescu, A., Shova, S., E. Bartolomé, E., Cases, R., Luzón, J., Bartolomé, J. and Turta, C. 2014. Structural and magnetic properties of some lanthanide (Ln = Eu(III), Gd(III) and Nd(III)) cyanoacetate polymers: field-induced slow magnetic relaxation in the Gd and Nd substitutions. *Dalton Transactions* 43.32: 12342 – 12356

Arora, H., Barman, S. K., Lloret, F. and Mukherjee, R. 2012. Isostructural Dinuclear Phenoxo-/Acetato-Bridged Manganese(II), Cobalt(II), and Zinc(II) Complexes with Labile Sites: Kinetics of Transesterification of 2-Hydroxypropyl-*p*-nitrophenylphosphate. *Inorganic Chemistry* 51.10: 5539 – 5553

Ashish, B. and Pandeya, S. N. 2011. Various Approaches for Synthesis of Imidazole Derivatives. *International Journal of Research in Ayurveda and Pharmacy* 2.4: 1124 – 1129

Ashiq, M., Danish, M., Mohsin, M. A, Bari, S., Mukhtar, F. 2013. Chemistry of Platinum and Palladium Metal Complexes in Homogeneous and Heterogeneous Catalysis: A Mini Review. *International Journal of Science: Basic and Applied Research* 7.1: 50 – 61

Ashokan, R., Akila, E. and Rajavel, R. 2014. Structural Elucidation of newly synthesized Potentially active Mononuclear Schiff Base Cu(II) & Ni(II) Complexes using Physicochemical methods derived from *o*-phenylenediammine. *Chemical Science Review and Letters* 3.12: 1142 – 1147

Aydin, D., Dinckan, S., Elmas, S. N. K., Savran, T., Arslan, F. N., Yilmaz, I. 2021. A novel phenolphthalein-based fluorescent sensor for Al^{3+} sensing in drinking water and herbal tea samples. *Food Chemistry* 337: 127659. https://doi.org/10.1016/j.foodchem.2020.127659

Babahan, I., Coban, E. P and Biyik, H. 2013. Synthesis, characterisation and antimicrobial activities of vicdioxime derivatives containing heteroaromatic hydrazone groups and their metal complexes. *Maejo International Journal of Science and Technology* 7.01: 26 – 41

Bai, L., Li, G., Li, L., Gao, M., Li, H., Tao, F., Deng, A., Wang, S., Wang, L. 2019. Schiff base functionalized PEG as a high efficient fluorescent chemosensor for Al^{3+} detection in 100% aqueous solution. *Reactive and Functional Polymers* 139: 1 – 8

Ball, P. W. 1969. The magnetic properties of polynuclear transition metal complexes. *Coordination Chemistry Reviews* 4.3: 361 – 383

Bandyopadhyay, D., Mora, Y., Cantu, J. A. T., and Banik, B. K. 2011. An easy and straightforward route for the synthesis of disubstituted imidazoles. *Heteroletters* 1: 61 – 63

_____, Smith, L. C., Garcia, D. R., Yadav, R. N., and Banik, B. K. 2014. An expeditious green route toward 2-aryl-4-phenyl-1H-imidazoles. *Organic and Medicinal Chemistry Letters* 4.9: 1 – 3

Banfi, E., Scialino, G., Zampieri, D., Mamolo, M. G., Vio, L., Ferrone, M., Fermeglia, M., Paneni, M. S., and Pricl, S. 2006. Antifungal and antimycobacterial activity of new imidazole and triazole derivatives. A combined experimental and computational approach. *Journal of Antimicrobial Chemotherapy* 58.1: 76 – 84

Barbucci, R., Bencini, A. and Gatteschi, D. 1977. Electron Spin Resonance Spectra and Spin-Hamiltonian Parameters for Trigonal-Bipyramidal Nickel(I) and Copper(II) Complexes. *Inorganic Chemistry* 16.8: 2117 – 2120

Bartholomew, G. P., Bazan, G. C., Bu, X. and Lachicotte, R. J. 2000. Packing Modes of Distyrylbenzene Derivatives. *Chemistry of Materials* 12.5: 1422 – 1430

Barra, A. L., Caneschi, A., Cornia, A., Fabrizi de Biani, F., Gatteschi, D., Sangregorio, C., Sessoli, R. and Sorace, L. 1999. Single-Molecule Magnet Behavior of a Tetranuclear Iron(III) Complex. The Origin of Slow Magnetic Relaxation in Iron(III) Clusters. *Journal of the American Chemical Society* 121.22: 5302 – 5310

Basak, D., van Leusen, J., Gupta, T., Kögerler, P., Bertolasi, V. and Ray, D. 2020. Unusually Distorted Pseudo-Octahedral Coordination Environment Around Co^{II} from Thioether Schiff Base Ligands in Dinuclear [CoLn] (Ln = La, Gd, Tb, Dy, Ho) Complexes: Synthesis, Structure, and Understanding of Magnetic Behavior. *Inorganic Chemistry* 59.4: 2387 – 2405

Bazhenova, T. A., Kopotkov, V. A., Korchagin, D. V., Manakin, Y. V., Zorina, L. V., Simonov, S. V., Yakushev, I. A., Mironov, V. S., Vasiliev, A. N., Maximova, O. V. and Yagubskii, E. B. 2021. A Series of Novel Pentagonal-Bipyramidal Erbium(III) Complexes with Acyclic Chelating N_3O_2 Schiff-Base Ligands: Synthesis, Structure, and Magnetism. *Molecules* 26.22: 6908. https://doi.org/10.3390/molecules26226908

_____, Zorina, L. V., Simonov, S. V., Manakin, Yu. V., Kornev, A. B., Lyssenko, K. A., Mironov, V. S., Gilmutdinov, I. F., Yagubskii, E. B. 2021. A novel family of hepta-coordinated Cr(III) complexes with a planar pentadentate N_3O_2 Schiff base ligand: synthesis, structure and magnetism. *Inorganic Chimica Acta* 522: 120358. https://doi.org/10.1016/j.ica.2021.120358

Belford, R. L. and Duan, D. C. 1978. Determination of Nuclear Quadrupole Coupling by Simulation of EPR Spectra of Frozen Solutions. *Journal of Magnetic Resonance* 29.2: 293 – 307

Benavent, L., Boudreault, P-L. T., Esteruelas, M. A., Lopez, A. M., Oñate, E., and Tsai, J-Y. 2020. Phosphorescent Iridium(III) Complexes with a Dianionic C,C′,N,N′-Tetradentate Ligand" *Inorganic Chemistry* 59.17: 12286 – 12294

Bencini, A., Bertini, I., Gatteschi, D. and Scozzafava, A. 1978. Single-Crystal ESR Spectra of Copper(II) Complexes with Geometries Intermediate between a Square Pyramid and a Trigonal Bipyramid. *Inorganic Chemistry* 17.11: 3194 – 3197

Benesi, H. A. and Hildebrand, J. H. 1949. A Spectrophotometric Investigation of the Interaction of Iodine with Aromatic Hydrocarbons. *Journal of the American Chemical Society* 71.8: 2703 – 2707

Benitez-Martin, C., Guadix, J. A., Pearson, J. R., Najera, F., Perez-Pomares, J. M. and Perez-Inestrosa, E. 2020. Indolenine-Based Derivatives as Customizable Two-Photon Fluorescent Probes for pH Bioimaging in Living Cells. *ACS Sensors* 5.4: 1068 – 1074

Benmansour, S., Setifi, F., Gómez-García, C. J., Triki, S., Coronado, E., Salaün, J-Y. 2008. A novel polynitrile ligand with different coordination modes: Synthesis, structure and magnetic properties of the series $[M(tcnoprOH)_2(H_2O)_2]$ (M = Mn, Co and Cu) ($tcnoprOH^-$= $[(NC)_2CC(OCH_2CH_2CH_2OH)C(CN)_2]^-$). *Journal of Molecular Structure* 890.1-3: 255 – 262

Berrones-Reyes, J., Muñoz-Flores, B. M., Gómez-Treviño, A., Treto-Suárez, M. A., Páez-Hernández, D., Schott, E., Zarate, X., Jiménez-Pérez, V. M. 2019. Novel fluorescent Schiff bases as Al^{3+} sensors with high selectivity and sensitivity, and their bioimaging applications. *Materials Chemistry and Physics* 233: 89 – 101

Bertini, I., Gatteschi, D. and Scozzafava, A. 1979. Six coordinate copper complexes with $g_{\|} < g_{\perp}$ in the solid state. *Coordination Chemistry Reviews* 29.1: 67 – 84

Bertrand, J. A. and Kelley, J. A. 1970. Polynuclear Copper(II) Complexes with Oxygen Bridges: The Relationship between Magnetic Properties and Structure. *Inorganica Chimica Acta* 4.2: 203 – 209

Bhargavi, G., Rajasekharan, M. V., Costes, J-P., Tuchagues, J-P. 2009. Synthesis, crystal structure and magnetic properties of dimeric Mn^{III} Schiff base complexes including pseudohalide ligands: Ferromagnetic interactions through phenoxo bridges and single molecule magnetism. *Polyhedron* 28.7: 1253 – 1260

Bhattacharjee, S., Zhao, Y., Hill, J. M., Percy, M. E. and Lukiw, W. J. 2014. Aluminum and its potential contribution to Alzheimer's disease (AD). *Frontiers in Aging Neuroscience* 6.62 https://doi.org/10.3389/fnagi.2014.00062

Biswas, A., Das, L. K., Drew, M. G. B., Aromí, G., Gamez, P. and Ghosh, A. 2012. Synthesis, Crystal Structures, Magnetic Properties and Catecholase Activity of Double Phenoxido-Bridged Penta-Coordinated Dinuclear Nickel(II) Complexes Derived from Reduced Schiff-Base Ligands: Mechanistic Inference of Catecholase Activity. *Inorganic Chemistry* 51.15: 7993 – 8001

_____, Drew, M. G. B., Ribas, J., Diaz, C., Ghosh, A. 2011. Synthesis, crystal structures and magnetic properties of two bis(μ-phenoxido)dicopper(II) complexes derived from reduced Schiff base ligands. *Inorganica Chimica Acta* 379.1: 28 – 33

Bonnet, L. G., Douthwaite, R. E., Kariuki, B. M. 2003. Synthesis of New Chiral N-Heterocyclic Carbene-Imine Ligands and Their Application to an Asymmetric Allylic Alkylation Reaction. *Organometallics* 22.21: 4187 – 4189.

Bowmaker, G. A., Waters, T. N., and Wright, P. E. 1975. E.s.r. and Optical Spectral Properties of Copper(II) Complexes with Schiff Base Ligands Derived from *o*-Aminobenzaldehyde. *Journal of the Chemical Society, Dalton Transactions* 1975.10: 867 – 870

Brandenburg, K. and Putz, H. 2022. *DIAMOND.* Crystal Impact GbR, Bonn, Germany.

Brechin, E. K., Soler, M., Christou, G., Helliwell, M., Teat, S. J., and Wernsdorfer, W. 2003. Dodecanuclear and octanuclear manganese rods. *Chemical Communications* 2003.11: 1276 – 1277

Brockman, J. T., Huffman, J. C. and Christou, G. 2002. A High Nuclearity, Mixed-Valence Manganese(III,IV) Complex: $[Mn_{21}O_{24}(OMe)_8(O_2CCH_2tBu)_{16}(H_2O)_{10}]$. *Angewandte Chemie International Edition* 41.14: 2506 – 2508

Brodowska, K., Łodyga-Chruścińska, E. 2014. Schiff bases – interesting range of applications in various fields of science. *Chemik Science-Technique-Market* 68.2: 129 – 134

Bronson, R. T., Michaelis, D. J., Lamb, R. D., Husseini, G. A., Farnsworth, P. B., Linford, M. R., Izatt, R. M., Bradshaw, J. S. and Savage, P. B. 2005. Efficient Immobilization of a Cadmium Chemosensor in a Thin Film: Generation of a Cadmium Sensor Prototype. *Organic Letters* 7.6: 1105 – 1108

Brooks, P. and Davidson, N. 1960. Mercury(II) Complexes of Imidazole and Histidine. *Journal of the American Chemical Society* 82.9: 2118 – 2123

Brown, D. A., Errington, W., Glass, W. K., Haase, W., Kemp, T. J., Nimir, H., Ostrovsky, S. M. and Werner, R. 2001. Magnetic, Spectroscopic, and Structural Studies of Dicobalt Hydroxamates and Model Hydrolases. *Inorganic Chemistry* 40.23: 5962 – 5971

_____, Glass, W. K., Fitzpatrick, N. J., Kemp, T. J., Errington, W., Clarkson, G. J., Haase, W., Karsten, F., Mahdy, A. H. 2004. Structural variations in dinuclear model hydrolases and hydroxamate inhibitor models: synthetic, spectroscopic and structural studies. *Inorganica Chimica Acta* 357.5: 1411 – 1436

Buchholz, A., Eseola, A. O., Plass. W. 2012. Slow magnetic relaxation in mononuclear tetrahedral cobalt(II)complexes with 2-(1*H*-imidazol-2-yl)phenol based ligands. *Comptes Rendus Chimie* 15.10: 929 – 936

Burrows, L. C., Jesikiewicz, L. T., Liu, P. and Brummond, K. M. 2021. Mechanism and Origins of Enantioselectivity in the Rh(I)-Catalyzed Pauson-Khand Reaction: Comparison of Bidentate and Monodentate Chiral Ligands. *ACS Catalysis* 11.1: 323 – 336

Buvaylo, E. A., Kokozay, V. N., Vassilyeva, O. Y., Skelton, B. W., Ozarowski, A., Titiš, J., Vranovičová, B. and Boča, R. 2017. Field-Assisted Slow Magnetic Relaxation in a Six-Coordinate Co(II)−Co(III) Complex with Large Negative Anisotropy. *Inorganic Chemistry* 56.12: 6999 – 7009

Cabrellon, G., Tampieri, F., Rossa, A., Barbon, A., Marotta, E. and Paradisi, C. 2020. Application of fluorescence based probes for the determination of superoxide in water treated with air non-thermal plasma. *ACS Sensors* 5.9: 2866 – 2875

Carabineiro, S. A., Bellabarba, R. M., Gomes, P. T., Pascu, S, I., Veiros, L. F., Freire, C., Pereira, L. C. J., Henriques, R. T., Oliveira, M. C. and Warren, J. E. 2008. Synthesis, Structure and Magnetic Behavior of Five-Coordinate Bis(iminopyrrolyl) Complexes of Cobalt(II) containing PMe_3 and THF Ligands. *Inorganic Chemistry* 47.19: 8896 – 8911

Castro, A. B., Jung, J., Golhen, S., Le Guennic, B., Ouahab, L., Cador, O. and Pointillart, F. 2016. Slow Magnetic Relaxation in Unprecedented Mono-Dimensional Coordination Polymer of Ytterbium Involving Tetrathiafulvalene-Dicarboxylate Linker. *Magnetochemistry* 2.2: 26. https://dx.doi.org/10.3390/magnetochemistry2020026

Castro, I., Calatayud, M. L., Barros, W. P., Carranza, J., Julve, M., Lloret, F., Marino, N. and De Munno, G. 2014. Ligand Effects on the Structure and Magnetic Properties of Alternating Copper(II) Chains with 2,2′-Bipyrimidine- and Polymethyl-Substituted Pyrazolates as Bridging Ligands. *Inorganic Chemistry* 53.11: 5759 – 5771

Chakov, N. E., Lee, S-C., Harter, A. G., Kuhns, P. L., Reyes, A. P., Hill, S O., Dalal, N. S., Wernsdorfer, W., Abboud, K. A. and Christou, G. 2006. The Properties of the $[Mn_{12}O_{12}(O_2CR)_{16}(H_2O)_4]$ Single-Molecule Magnets in Truly Axial Symmetry: $[Mn_{12}O_{12}(O_2CCH_2Br)_{16}(H_2O)_4].4CH_2Cl_2$. *Journal of the American Chemical Society* 128.21: 6975 – 6989

_____, Zakharov, L. N., Rheingold, A. L., Abboud, K. A. and Christou, G. 2005. New Polynuclear Manganese Clusters from the Use of the Hydrophobic Carboxylate Ligand 2,2-Dimethylbutyrate. *Inorganic Chemistry* 44.13: 4555 – 4567

Chakraborty, J., Ray, A., Pilet, G., Chastanet, G., Luneau, D., Ziessel, R. F., Charbonnière, L. J., Carrella, L., Rentschler, E., El Fallah, M. S. and Mitra, S. 2009. Syntheses, characterisation, magnetism and photoluminescence of a homodinuclear Ln(III) Schiff base family. *Dalton Transactions* 2009.46: 10263 – 10272

Chakradhar, R. P. S., Ramesh, K. P., Rao, J. L. and Ramakrishna, J. 2003. Mixed alkali effect in borate glasses – electron paramagnetic resonance and optical absorption studies in Cu^{2+} doped $x Na_2O$-$(30 - x)K_2O$-$70B_2O_3$ glasses. *Journal of Physics: Condensed Matter* 15.9: 1469 – 1486

Chan, C-Y., Tanaka, M., Lee, Y-T., Wong, Y-W., Nakanotani, H., Hatakeyama, T. and Adachi, C. 2021. Stable pure-blue hyperfluorescence organic light-emitting diodes with high-efficiency and narrow emission. *Nature Photonics* 15: 203 – 207

Chandra, S. and Gupta, K. 2002. Chromium(III), manganese(II), iron(III), cobalt(II), nickel(II) and copper(II) complexes with a pentadentate, 15-membered new macrocyclic ligand. *Transition Metal Chemistry* 27: 196 – 199

Chang, J-H. 2020. Equibiaxially stretchable colorless and transparent polyimides for flexible display substrates. *Reviews on Advanced Materials Science* 59.1: 1 – 9

Chang, Y-X., Wang, W-M., Zhang, R-X., Shen, H-Y., Zhou, X-P., Wang, N-N., Cui, J-Z. and Gao, H-L. 2017. Dinuclear Ln(III) complexes constructed from an 8-hydroxyquinoline Schiff base derivative with different terminal groups show differing slow magnetic relaxation. *New Journal of Chemistry* 41.14: 6251 – 6261

Chao, X., Qi, Y. and Zhang, Y. 2021. Highly Photostable Fluorescent Tracker with pH-Insensitivity for Long-Term Imaging of Lysosomal Dynamics in Live Cells. *ACS Sensors* 6.3: 786 – 796

Chaudhary, N. K. and Mishra, P. 2013. Synthesis, characterization and molecular modeling of Ni(II) & Cu(II) complexes with schiff base derived from *1H*-benzo[*d*]imidazole-4-amine and 2-hydroxy benzaldehyde. *Archieve of Applied Science Research* 5.5: 191 – 197

Chérif, I., Abdelhak, J., Amami, M., Hlil, E. K., Zid, M. F., Driss, A. 2013. A new bis(oxalato)chromate(III) salt: synthesis, crystal structure, thermal behavior and magnetic properties of $(C_3H_5N_2)[Cr(C_2O_4)_2(H_2O)_2].2H_2O$. *QScience Connect* 2013.1: 46.
http://dx.doi.org/10.5339/connect.2013.46

Chemate, S., Sekar, N. 2015. A new rhodamine based OFF–ON fluorescent chemosensors for selective detection of Hg^{2+} and Al^{3+} in aqueous media. *Sensors and Actuators B: Chemical* 220: 1196 – 1204

Chen, B., Chen, W., Liu, W., Li, Y., Wang, X., and Wang, E. 2011. Two new methylimidazole modified Herve´-sandwich-type polytungstoantimonates. *Journal of Coordination Chemistry* 64.1: 71 – 81

Chen, H-H., Wu, D-F., Duan, Y-Y., Li, L., Wang, Y-J., Zhang, X-M., Cui, J-Z. and Gao, H-L. 2020. The near-infrared luminescence and magnetism of dinuclear complexes with different local symmetries constructed from a β-diketonate co-ligand and bis-Schiff base ligand. *New Journal of Chemistry* 44.6: 2561 – 2570

Chen, J., Feng, D., Wang, C., Xing, X., Du, L., Zhu, Z., Huang, X. and Dachi Yang, D. 2020. Gas Sensor Detecting 3-Hydroxy-2-butanone Biomarkers: Boosted Response via Decorating Pd Nanoparticles onto the {010} Facets of $BiVO_4$ Decahedrons. *ACS Sensors* 5.8: 2620 – 2627

_____, Huang, D., She, M., Wang, Z., Chen, X., Liu, P., Zhang, S. and Li, J. 2021. Recent Progress in Fluorescent Sensors for Drug-Induced Liver Injury Assessment. *ACS Sensors* 6.3: 628 – 640

Chen, L., Ye, J-W., Wang, H-P., Pan, M., Yin, S-Y., Wei, Z-W., Zhang, L-Y., Wu, K., Fan, Y-N. and Su, C-Y. 2017. Ultrafast water sensing and thermal imaging by a metal-organic framework with switchable luminescence. *Nature Communications* 8.15985.
https://dx.doi.org/10.1038/ncomms15985

_____, Zhou, J., Cui, H-H., Yuan, A-H., Wang, Z., Yi-Quan Zhang, Y-Q., Ouyang Z-W. and Song, Y. 2018. Slow magnetic relaxation influenced by symmetry change from ideal C_i to D_{3d} in cobalt(II)-based single-ion magnets. *Dalton Transactions* 47.8: 2506 – 2510

Chen, S-S. 2016. The role of imidazole ligands in coordination supramolecular systems. *Crystal Engineering Communications* 18.35: 6543 – 6565

_____, Chen, Z-H., Fan, J., Okamura, T-A., Bai, Z-S., Lv, M-F., and Sun, W-Y. 2012. Synthesis and Characterization of Metal Complexes with Mixed 4-Imidazole-Containing Tripodal Ligand and Varied Dicarboxylic Acid. *Crystal Growth & Design* 12.5: 2315 – 2326

Chetia, B., Iyer, P. K. 2014. Selective fluoride anion sensing by simple benzimidazolyl based ligand. *Sensors and Actuators B: Chemical* 201: 191 – 195

Chilton, N. F., Anderson, R. P., Turner, L. D., Soncini, A. and Murray, K. S. 2013. PHI: A Powerful New Program for the Analysis of Anisotropic Monomeric and Exchange-Coupled Polynuclear *d*- and *f*-Block Complexes. *Journal of Computational Chemistry* 34.13: 1164 – 1175

_____, Lei, H., Bryan, A. M., Grandjean, F., Long, G. J. and Power, P. P. 2015. Ligand field influence on the electronic and magnetic properties of quasi-linear two-coordinate iron(II) complexes. *Dalton Transactions* 44.24: 11202 – 11211

Chitra, S., Parameswari, K., Selvaraj, A. 2010. Dianiline Schiff Bases as Inhibitors of Mild Steel Corrosion in Acid Media. *International Journal of Electrochemical Science* 5.11: 1675 – 1697

Cho, Y. I., Ward, M. L. and Rose, M. J. 2016. Substituent effects of N4 Schiff base ligands on the formation of fluoride-bridged dicobalt(II) complexes via B–F abstraction: structures and magnetism. *Dalton Transactions* 45.34: 13466 – 13476

Choi, D-H., Gonzales, M., Kitchen, G.B., Phan, D-T. and Searson, P. C. 2020. A Capacitive Sweat Rate Sensor for Continuous and Real-Time Monitoring of Sweat Loss. *ACS Sensors* 5.12: 3821 – 3826

Cisterna, J., Artigas, V., Fuentealba, M., Hamon, P., Manzur, C., Hamon, J-R. and Carrillo, D. 2018. Pentacoordinated Chloro-Iron(III) Complexes with Unsymmetrically Substituted N_2O_2 Quadridentate Schiff-Base Ligands: Syntheses, Structures, Magnetic and Redox Properties. *Inorganics* 6.1: 5; https://doi.org/10.3390/inorganics6010005

Ciupa, A., Mahon, M. F., De Bank, P. A. and Caggiano, L. 2012. Simple pyrazoline and pyrazole "turn on" fluorescent sensors selective for Cd^{2+} and Zn^{2+} in MeCN. *Organic & Biomolecular Chemistry* 10.44: 8753 – 8757

Cornia, A., Fabretti, A. C., Gatteschi, D., Pályi, G., Rentschler, E., Shchegolikhina, O. I. and Zhdanov, A. A. 1995. Molecule-Based Magnets: Ferro- and Antiferromagnetic Interactions in Nickel(II) Cyclohexasiloxanolate Sandwich Complexes. *Inorganic Chemistry* 34.21: 5383 – 5387

_____, Rigamonti, L., Boccedi, S., Clérac, R., Rouzières M. and Sorace, L. 2014. Magnetic blocking in extended metal atom chains: a pentachromium(II) complex behaving as a single-molecule magnet. *Chemical Communications* 50.96: 15191 – 15194

Costero, A. M., Gil, S., Sanchis, J., Peransi, S., Sane, V. and Williams, J. A. G. 2004. Conformationally regulated fluorescent sensors. Study of the selectivity in Zn^{2+} versus Cd^{2+} sensing. *Tetrahedron* 60.30: 6327 – 6334

Costes, J-P., Dahan, F. and Dupuis, A. 2000. Influence of Anionic Ligands (X) on the Nature and Magnetic Properties of Dinuclear $LCuGdX_3.nH_2O$ Complexes (LH_2 Standing for Tetradentate Schiff Base Ligands Deriving from 2-Hydroxy-3-methoxybenzaldehyde and X Being Cl, N_3C_2, and CF_3COO). *Inorganic Chemistry* 39.2: 165 – 168

_____, Dahan, F. and García-Tojal, J. 2002. Dinuclear Co^{II}/Gd^{III} and Co^{III}/Gd^{III} Complexes Derived from Hexadentate Schiff Bases: Synthesis, Structure, and Magnetic Properties. *Chemistry - A European Journal* 8.23: 5430 – 5434

Craig, G. A. and Murrie, M. 2015. 3*d* single-ion magnets. *Chemical Society Reviews* 44.8: 2135 – 2147

Cuéllar, E., Pastor, L., García-Herbosa, G., Nganga, J., Angeles-Boza, A. M., Diez-Varga, A., Torroba, T., Martín-Alvarez, J. M., Miguel, D. and Villafañe, F. 2021. (1,2-Azole)bis(bipyridyl)ruthenium(II) Complexes: Electrochemistry, Luminescent Properties, And Electro- And Photocatalysts for CO_2 Reduction. *Inorganic Chemistry* 60.2: 692 – 704

Das, D., Alam, R., Katarkar, A. and Ali, M. 2019. A differentially selective probe for trivalent chemosensor upon single excitation with cell imaging application: potential applications in combinatorial logic circuit and memory devices. *Photochemical & Photobiological Sciences* 18.1: 242 – 252

Das, S., Mukherjee, U., Pal, S., Maitra, S. and Sahoo, P. 2019. Selective sensing of Al^{3+} ions by nitrophenyl induced coordination: imaging in zebrafish brain tissue. *Organic & Biomolecular Chemistry* 17.21: 5230 – 5233

Daumann, L. J., Comba, P., Larrabee, J. A., Schenk, G., Stranger, R., Cavigliasso, G. and Gahan, L. R. 2013. Synthesis, Magnetic Properties, and Phosphoesterase Activity of Dinuclear Cobalt(II) Complexes. *Inorganic Chemistry* 52.4: 2029 – 2043

de Azambuja, F., Lenie, J. and Parac-Vogt, T. N. 2021. Homogeneous Metal Catalysts with Inorganic Ligands: Probing Ligand Effects in Lewis Acid Catalyzed Direct Amide Bond Formation. *ACS Catalysis* 11.1: 271 – 277

de Silva, A. P. 2012. FLUORESCENT SENSORS: Bright ideas. *Nature Chemistry* 4.6: 440 – 441

_____, Moody, T. S. and Wright, G. T. 2009. Fluorescent PET (Photoinduced Electron Transfer) sensors as potent analytical tools. *Analyst* 134.12: 2385 – 2393

Dehghani-Firouzabadi, A. A., Sobhani, M., Notash, B. 2016. Synthesis and characterization of metal complexes with NOS unsymmetrical tridentate Schiff base ligand. X-ray crystal structures determination of nickel(II) and copper(II) complexes. *Polyhedron* 119: 49 – 54

Demir, S., Boshart, M. D., Corbey, J. F., Woen, D. H., Gonzalez, M. I., Ziller, J. W., Meihaus, K. R., Long, J. R. and William J. E. 2017. Slow Magnetic Relaxation in a Dysprosium Ammonia Metallocene Complex. *Inorganic Chemistry* 56.24: 15049 – 15056

Dessingou, J., Joseph, R. and Rao, C. P. 2005. A direct fluorescence-on chemo-sensor for selective recognition of Zn(II) by a lower rim 1,3-di-derivative of calix[4]arene possessing bis-{N-(2-hydroxynaphthyl-1-methylimine)} pendants. *Tetrahedron Letters* 46.46: 7967 – 7971

Dey, S., Sarkar, S., Maity, D., Roy, P. 2017. Rhodamine based chemosensor for trivalent cations: Synthesis, spectral properties, secondary complex as sensor for arsenate and molecular logic gates. *Sensors and Actuators B: Chemical* 246: 518 – 534

Dilek, O. and Bane, S. L. 2016. Turn on Fluorescent Probes for Selective Targeting of Aldehydes. *Chemosensors* 4.1: 5; https://doi.org/10.3390/chemosensors4010005

Dilmaghani, K. A., Pur, F. N., and Nezhad, M. H. 2015. Synthesis and Antibacterial Evaluation of New Thione Substituted 1,2,4-Triazole Schiff Bases as Novel Antimicrobial Agents. *Iranian Journal of Pharmaceutical Research* 14.3: 693 – 699

Ding, Y-S., Han, T., Hu, Y-Q., Xu, M., Yang, S. and Zheng, Y-Z. 2016. Syntheses, structures and magnetic properties of a series of mono- and di-nuclear dysprosium(III)-crown-ether complexes: effects of a weak ligand-field and flexible cyclic coordination modes. *Inorganic Chemistry Frontiers* 3.6: 798 – 807

Dori, Z. and Gray, H. B. 1968. High-Spin, Five-Coordinate Cobalt(II) Complexes. *Inorganic Chemistry* 7.5: 889 – 892

Dridi, R., Dhieb, C., Cherni, S. N., Boudjada, N. C., Zouaoui, N. S., Zid, M. F. 2018. A new supramolecular chromium(III) complex: Synthesis, structural determination, optical study, magnetic and antibacterial activity. *Journal of Molecular Structure* 1152: 294 – 302

Drosou, M., Mitsopoulou, C. A., Orio, M. and Pantazis, D. A. 2022. EPR Spectroscopy of Cu(II) Complexes: Prediction of *g*-Tensors Using Double-Hybrid Density Functional Theory. *Magnetochemistry* 8.4: 36. https://doi.org/10.3390/magnetochemistry8040036

Duan, L., D'hooge, D. R., Cardon, L. 2020. Recent progress on flexible and stretchable piezoresistive strain sensors: From design to application. *Progress in Materials Science* 114: 100617. https://doi.org/10.1016/j.pmatsci.2019.100617

Duggan, M., Ray, N., Hathaway, B., Tomlinson, G., Brint, P. and Pelin, K. 1980. Crystal Structure and Electronic Properties of Ammine[tris(2-aminoethyl)amine]copper(II) Diperchlorate and Potassium Penta-amminecopper(II) Tris(hexafluorophosphate). *Journal of the Chemical Society, Dalton Transactions* 1980.8: 1342 – 1348

Durai, W. A., Ramu, A., Dhakshinamoorthy, A. 2020. A chromogenic and fluorescence turn-on sensor for the selective and sensitive recognition of Al^{3+} ions – A new approach by Schiff base derivative as probe. *Inorganic Chemistry Communications* 121: 108191. https://doi.org/10.1016/j.inoche.2020.108191

Ebata, H., Izawa, T., Miyazaki, E., Takimiya, K., Ikeda, M., Kuwabara, H. and Yui, T. 2007. Highly Soluble [1]Benzothieno[3,2-*b*]benzothiophene (BTBT) Derivatives for High-Performance, Solution-Processed Organic Field-Effect Transistors. *Journal of the American Chemical Society* 129.51: 15732 – 15733

Elmali, A., Elerman, Y. 2005. Magnetic properties and structure of a $Cu^{II}Dy^{III}$ heterodinuclear Schiff base complex. *Journal of Molecular Structure* 737.1: 29 – 33

El-Samanody, E-S. A., Emam, S. M., Emara, E. M. 2017. Synthesis, characterization, molecular modeling and biological activity of metal complexes derived from (*E*)-*N*'-(furan-2-ylmethylene) morpholine-4-carbothiohydrazide. *Journal of Molecular Structure* 1146: 868 – 880

El-Tabl, A. S. 1998. An e.s.r. study of copper(II) complexes of *N*-hydroxyalkylsalicylideneimines. *Transition Metal Chemistry* 23: 63 – 65

Erdemir, S., Malkondu, S. 2021. Detection of water content in alcohol solvents over Al^{3+} induced colorimetric and NIR-fluorescent sensor based on isophorone-phenylamine. *Microchemical Journal* 160.PartB: 105677. https://doi.org/10.1016/j.microc.2020.105677

Escuer, A., Mautner, F. A., Sanz, N., Vicente, R. 2004. New examples of the unusual X-phenylcyanamido bridging ligands. Crystal structure and magnetic properties of Mn^{II} derivatives. *Polyhedron* 23.8: 1409 – 1417

Eseola, A. O., Görls, H., Bangesh, M. and Plass, W. 2018. ESIPT-capable 2,6-di(1*H*-imidazol-2-yl)phenols with very strong fluorescent sensing signals towards Cr(III), Zn(II), and Cd(II): molecular variation effects on turn-on efficiency. *New Journal of Chemistry* 42.10: 7884 – 7900

_____, Li, W., Gao, R., Zhang, M., Hao, X., Liang, T., Obi-Egbedi, N. O. and Sun, W-H. 2009. Syntheses, Structures and Fluorescent Properties of 2-(1*H*-Imidazol-2-yl)phenols and Their Nuetral Zn(II) Complexes. *Inorganic Chemistry* 48.19: 9133 – 9146

_____, Li, W., Sun, W-H., Zhang, M., Xiao, L., Woods, J. A. O. 2011. Luminescent properties of some imidazole and oxazole based heterocycles: Synthesis, structure and substituent effects. *Dyes and Pigments* 88.3: 263 – 272

ETHzürich Retrieved on June 14, 2022, from https://epr.ethz.ch/education/basic-concepts-of-epr/cu2--complexes.html

Fabelo, O., Cañadillas-Delgado, L., Pasán, J., Delgado, F. S., Lloret, F., Cano, J., Julve, M. and Ruiz-Pérez, C. 2009. Study of the Influence of the Bridge on the Magnetic Coupling in Cobalt(II) Complexes. *Inorganic Chemistry* 48.23: 11342 – 11351

_____, Pasán, J., Cañadillas-Delgado, L., Delgado, F. S., Labrador, A., Lloret, F., Julve, M. and Ruiz-Pérez, C. 2008. (4,4) Rectangular Lattices of Cobalt(II) with 1,2,4,5-Benzenetetracarboxylic Acid: Influence of the Packing in the Crystal Structure. *Crystal Growth & Design* 8.11: 3984 – 3992

_____, Paśan, J., Cañadillas-Delgado, L., Delgado, F. S., Yuste, C., Lloret, F., Julve, M. and Ruiz-Perez, C. 2009. Novel cobalt(II) coordination polymers based on 1,2,4,5-benzenetetracarboxylic acid and extended bis-monodentate ligands. *Crystal Engineering Communications* 11.10: 2169 – 2179

Fan, L., Qin, J-c., Li, T-r., Wang, B-d., Yang, Z-y. 2014. A novel rhodamine chromone-based "Off-On" chemosensor for the differential detection of Al(III) and Zn(II) in aqueous solutions. *Sensors and Actuators B: Chemical* 203: 550 – 556

_____, Qin, J-c., Li, C-r., Yang, Z-y. 2019. A Schiff-base receptor based chromone derivate: Highly selective fluorescent and colorimetric probe for Al(III). *Spectrochimica Acta Part A: Molecular and Biomolecular Spectroscopy* 218: 342 – 347

Fink, K., Wang, C. and Staemmler, V. 1999. Superexchange and Spin-Orbit Coupling in Chlorine-Bridged Binuclear Cobalt(II) Complexes. *Inorganic Chemistry* 38.17: 3847 – 3856

Fleming, J. S., Mann, K. L. V., Couchman, S. M., JeVery, J. C., McCleverty, J. A. and Ward, M. D. 1998. Double-helical dinuclear copper(I) and mononuclear copper(II) complexes of a compartmental tetradentate bridging ligand: crystal structures and spectroscopic properties. *Journal of the Chemical Society, Dalton Transactions* 1998.12: 2047 – 2052

Fondo, M., Corredoira-Vázquez, J., García-Deibe, A. M., Sanmartín-Matalobos, J., Herrera, J. M., and Colacio, E. 2017. Designing Ligands to Isolate ZnLn and Zn_2Ln Complexes: Field- Induced Single-Ion Magnet Behavior of the ZnDy, Zn_2Dy, and Zn_2Er Analogues. *Inorganic Chemistry* 56.10: 5646 – 5656

Frantz, D. E., Morency, L., Soheili, A., Murry, J. A., Grabowski, E. J. J. and Tillyer, R. D. 2004. Synthesis of Substituted Imidazoles via Organocatalysis. *Organic Letters* 6.5: 843 – 846

Freedman, D. E., Harman, W. H., Harris, T. D., Long, G. J., Chang, C. J. and Long, J. R. 2010. Slow Magnetic Relaxation in a High-Spin Iron(II) Complex. *Journal of the American Chemical Society* 132.4: 1224 – 1225

Fresta, E., Volpi, G., Milanesio, M., Garino, C., Barolo, C. and Costa, R. D. 2018. Novel Ligand and Device Designs for Stable Light-Emitting Electrochemical Cells Based on Heteroleptic Copper(I) Complexes. *Inorganic Chemistry* 57.16: 10469 – 10479

Frost, J. M., Harriman, K. L. M. and Murugesu, M. 2016. The rise of 3-d single-ion magnets in molecular magnetism: towards materials from molecules?. *Chemical Science* 7.4: 2470 – 2491

Frutos, R. P., Gallou, I., Reeves, D., Xu, Y., Krishnamurthy, D., and Senanayake, C. H. 2005. Expedient synthesis of substituted imidazoles from nitriles. *Tetrahedron Letters* 46.48: 8369 –8372

Gandhi, S. and Duraisamy, C. 2013. Rhodamine based sensor for naked-eye detection and live cell imaging of Fluoride ions. *Journal of Materials Chemistry B* 1.42: 5768 – 5772

Gao, F., Cui, L., Liu, W., Hu, L., Zhong, Y-W., Li, Y-Z. and Zuo, J-L. 2013. Seven-Coordinate Lanthanide Sandwich-Type Complexes with a Tetrathiafulvalene-Fused Schiff Base Ligand. *Inorganic Chemistry* 52.19: 11164 – 11172

_____, Yao, M-X., Li, Y-Y., Li, Y-Z., Song, Y. and Zuo, J-L. 2013. Syntheses, Structures, and Magnetic Properties of seven-coordinate Lanthanide Porphyrinate or Phthalocyaninate Complexes with Kläui's Tripodal Ligand. *Inorganic Chemistry* 52.11: 6407 – 6416

Garg, B. S., Kurup, M. R. P., Jain, S. K. and Bhoon, Y. K. 1988. Manganese(II) complexes of substituted thio- and selenosemicarbazones of 2-acetylpyridine: E.s.r., magnetic and electronic spectral studies. *Transition Metal Chemistry* 13: 92 – 95

Garnier, F., Yassar, A., Hajlaoui, R., Horowitz, G., Deloffre, F., Servet, B., Ries, S. and Alnot, P. 1993. Molecular Engineering of Organic Semiconductors: Design of Self-Assembly Properties in Conjugated Thiophene Oligomers. *Journal of the American Chemical Society* 115.19: 8716 – 8721

Garribba, E. and Micera, G. 2006. The Determination of the Geometry of Cu(II) Complexes: An EPR Spectroscopy Experiment. *Journal of Chemical Education* 83.8: 1229 – 1232

Garrido, E., Alfonso, M., de Greñu, B. D., Marcos, M. D., Costero, A. M., Gil, S., Sancenón, F. and Martínez-Mánez, R. 2020. A Sensitive Nanosensor for the *in situ* Detection of the Cannibal Drug. *ACS Sensors* 5.9: 2966 – 2972

Gebrezgiabher, M., Bayeh, Y., Gebretsadik, T., Gebreslassie, G., Elemo, F., Thomas, M. and Linert, W. 2020. Lanthanide-Based Single-Molecule Magnets Derived from Schiff Base Ligands of Salicylaldehyde Derivatives. *Inorganics*, 8.12: 66. https://doi.org/10.3390/inorganics8120066

Gelens, E., De Kanter, F. J. J., Schmitz, R. F., Sliedregt, L. A. J. M., Van Steen, B. J., Kruse, C. G., Leurs, R., Groen, M. B., & R.V.A. Orru, R. V. A. 2006. Efficient library synthesis of imidazoles using a multicomponent reaction and microwave irradiation. *Molecular Diversity* 10: 17 – 22

Georgopoulou, A. N., Pissas, M., Psycharis, V., Sanakis, Y. and Raptopoulou, C. P. 2020. Trinuclear Ni^{II}-Ln^{III}-Ni^{II} Complexes with Schiff Base Ligands: Synthesis, Structure, and Magnetic Properties. *Molecules* 25.10: 2280; https://doi.org/10.3390/molecules25102280

Geue, J. P., Head, N. J., Ward, A. D., Lincoln, S. F. 2003. Complexation of alkali metal and alkaline earth ions by anthracene based fluorophores with one and two appended monoaza coronand receptors. *Dalton Transactions* 2003.4: 521 – 526

Ghosh, S., Aromí, G., Gamez, P., and Ghosh, A. 2014. The Impact of Anion-Modulated Structural Variations on the Magnetic Coupling in Trinuclear Heterometallic Cu^{II}-Co^{II} Complexes Derived from a Salen-Type Schiff Base Ligand. *European Journal of Inorganic Chemistry* 2014.21: 3341 – 3349

Gildea, B., Harris, M. M., Gavin, L. C., Murray, C. A., Ortin, Y., Müller-Bunz, H., Harding, C. J., Lan, Y., Powell, A. K. and Morgan, G. G. 2014. Substituent Effects on Spin State in a Series of Mononuclear Manganese(III) Complexes with Hexadentate Schiff-Base Ligands. *Inorganic Chemistry* 53.12: 6022 – 6033

Giri, D. and Patra, S. K. 2015. Benzodithieno-imidazole based π-conjugated fluorescent polymer probe for selective sensing of Cu^{2+}. *RSC Advances* 5.96: 79011 – 79021

Goswami, S., Aich, K., Das, A. K., Manna, A. and Das, S. 2013. A naphthalimide–quinoline based probe for selective, fluorescence ratiometric sensing of trivalent ions. *RSC Advances* 3.7: 2412 – 2416

Goswami, T. and Misra, A. 2012. Ligand Effects toward the Modulation of Magnetic Anisotropy and Design of Magnetic Systems with Desired Anisotropy Characteristics. *Journal of Physical Chemistry A* 116.21: 5207 – 5215

Gowda, C. M., Vasconcelos, F., Schwartz, E., van Eck, E. R. H., Marsman, M., Cornelissen, J. J. L. M., Rowan, A. E., de Wijs, G. A. and Kentgens, A. P. M. 2011. Hydrogen bonding and chemical shift assignments in carbazole functionalized isocyanides from solid-state NMR and first-principles calculations. *Physical Chemistry Chemical Physics* 13.28: 13082 – 13095

Gradinaru, J., Forni, A., Druta, V., Tessore, F., Zecchin, S., Quici, S. and Garbalau, N. 2007. Structural, Spectral, Electric-Field-Induced Second Harmonic, and Theoretical Study of Ni(II), Cu(II), Zn(II), and VO(II) Complexes with [N_2O_2] Unsymmetrical Schiff Bases of *S*-Methylisothiosemicarbazide Derivatives. *Inorganic Chemistry* 46.3: 884 – 895

Grigg, R., Lansdell, M. I. and Thornton-Pett, M. 1999. Silver Acetate Catalysed Cycloadditions of lsocyanoacetates. *Tetrahedron* 55.7: 2025 – 2044

Gulcin, İ. and Alwasel, S. H. 2022. Metal Ions, Metal Chelators and Metal Chelating Assay as Antioxidant Method. *Processes*, 10.1: 132, https://doi.org/10.3390/pr10010132

Guo, S-R. and Yuan, Y-Q. 2008. Crystal structure of 2,2′-bis(salicylideneamino)diphenyl sulfide, $C_{26}H_{20}N_2O_2S$. *Zeitschrift für Kristallographie - New Crystal Structures* 223.3: 269 – 270
https://doi.org/10.1524/ncrs.2008.0114

Guo, Y., Lu, X., Li, G., Zhao, L., Wei, S., Guo, W. 2017. Theoretical design of push-pull porphyrin dyes with π-bridge modification for dye-sensitized solar cells. *Journal of Photochemistry and Photobiology A: Chemistry* 332: 232 – 240

Guo, Y-N., Ungur, L., Granroth, G. E., Powell, A. K., Wu, C., Nagler, S. E., Tang, J., Chibotaru, L. F. & Cui, D. 2014. An NCN-pincer ligand dysprosium single-ion magnet showing magnetic relaxation via the second excited state. *Scientific Reports* 4.5471.
https://doi.org/10.1038/srep05471

Gupta, A. S., Paul, K. and Luxami, V. 2018. A new '*Turn-on*' PET-CHEF based fluorescent sensor for Al^{3+} and CN^- ions: applications in real samples. *Analytical Methods* 10.9: 983 – 990

Gupta, V. K., Singh, A. K., Kumawat, L. K. 2014. Thiazole Schiff base turn-on fluorescent chemosensor for Al^{3+} ion. *Sensors and Actuators B: Chemical* 195: 98 – 108

Hathaway, B. J. and Billing, D. E. 1970. The electronic properties and stereochemistry of mono-nuclear complexes of the copper(II) ion. *Coordination Chemistry Reviews* 5.2: 143 – 207

_____, Billing, D. E., Dudley, R. J., Fereday, R. J. and Tomlinson, A. A. G. 1970. Electronic and Electron Spin Resonance Spectra of Diamminocopper(II) Trithiocyanatoargentate(I) and Iodobis-(2,2′-bipyridyl)copper(II) Iodide. *Journal of the Chemical Society A: Inorganic, Physical, Theoretical* 1970.0: 806 – 811

Hazra, S., Karmakar, A., da Silva, M. F. C. G., Dlháň, L., Boča, R., Pombeiro, A. J. L. 2014. Dinuclear based polymeric copper(II) complexes derived from a Schiff base ligand: effect of secondary bridging moieties on geometrical orientations and magnetic properties. *Inorganic Chemistry Communications* 46: 113 – 117

He, H., Liu, D., Feng, Z., Guo, A., Liu, L. and Chen, X. 2020. Antifade Carbon Dots on a Plasmonic Substrate for Enhanced Protein Detection in Immunotherapy. *ACS Sensors* 5.12: 4027 – 4034

He, W., Song, P., Yu, B., Fang, Z., Wang, H. 2020. Flame retardant polymeric nanocomposites through the combination of nanomaterials and conventional flame retardants. *Progress in Materials Science* 114: 100687. https://doi.org/10.1016/j.pmatsci.2020.100687

Herman, R. G. 1979. Electron Paramagnetic Resonance Investigation of Copper(II) Complexes with Reversed *g* Values in A and Y Zeolites. *Inorganic Chemistry* 18.4: 995 – 1000

Hendrickson, D. N., Christou, G., Ishimoto, H., Yoo, J., Brechin, E. K., Yamaguchi, A., Rumberger, E. M., Aubin, S. M. J., Sun, Z., Aromí, G. 2001. Magnetization tunneling in single-molecule magnets. *Polyhedron* 20.11-14: 1479 – 1488

Hewitt, I. J., Tang, J., Madhu, N. T., Anson, C. E., Lan, Y., Luzon, J., Etienne, M., Sessoli, R. and Powell, A. K. 2010. Coupling Dy_3 Triangles Enhances Their Slow Magnetic Relaxation. *Angewandte Chemie International Edition* 49.36: 6352 – 6356

Hibbert, D. B. and Thordarson, P. 2016. The death of the Job plot, transparency, open science and online tools, uncertainty estimation methods and other developments in supramolecular chemistry data analysis. *Chemical Communications* 52.87: 12792 – 12805

Hirase, R., Ishihara, M., Katagiri, T., Tanaka, Y., Yanagi, H., Hotta, S. 2014. Alkyl-monosubstituted thiophene/phenylene co-oligomers: Synthesis, thin film preparation, and transistor device characteristics. *Organic Electronics* 15.7: 1481 – 1492

Holm, R. H. and Cotton, F. A. 1959. Magnetic Investigations of Spin-Free Cobaltous Complexes. I. Tetrahalo Cobalt(II) Ions. *Journal of Chemical Physics* 31.3: 788 – 792

_____ and Cotton, F. A. 1960. Magnetic Investigations of Spin-Free Cobaltous Complexes. II. Tetrahedral Complexes. *Journal of Chemical Physics* 32.4: 1168 – 1172

Hooft, R. W. W. 1998. COLLECT: Data Collection Software. Nonius BV, Delft, The Netherlands.

Horn Jr., A., Englert, D., Roberts, A. E., Comba, P., Schenk, G., Krenske, E. H. and Gahan, L. R. 2018. Synthesis, Magnetic Properties, and Catalytic Properties of a Nickel(II)-Dependent Biomimetic of Metallohydrolases. *Frontiers in Chemistry* 6.441. https://doi.org/10.3389/fchem.2018.00441

Hossain, Md. J., Yamasaki, M., Mikuriya, M., Kuribayashi, A. and Sakiyama, H. 2002. Synthesis, Structure, and Magnetic Properties of Dinuclear Cobalt(II) Complexes with a New Phenol-Based Dinucleating Ligand with Four Hydroxyethyl Chelating Arms. *Inorganic Chemistry* 41.15: 4058 – 4062

Hrdlovic, P., Donovalova, J., Stankovicova, H. and Gaplovsky, A. 2010. Influence of Polarity of Solvents on the Spectral Properties of Bichromophoric Coumarins. *Molecules* 15.12: 8915 – 8932

Huang, M-X., Lai, J-P., Sun, H., Wu, W-Z. 2019. A simple, highly selective and ultra-sensitive "off-on-off" fluorescent chemosensor for successive detection of aluminum ion and phosphate in water samples. *Microchemical Journal* 151: 104195. https://doi.org/10.1016/j.microc.2019.104195

Huang, W., Zheng, Z., Wu, D. 2017. Synthesis, structure and single-molecule magnet characterization of Dy_2 dinuclear complexes with an 8–hydroxyquinoline carbohydrazone ligand. *Inorganic Chemistry Communications* 84: 40 – 44

Huang, X-C., Zhou, C., Shao, D. and Wang, X-Y. 2014. Field-Induced Slow Magnetic Relaxation in Cobalt(II) Compounds with Pentagonal Bipyramid Geometry. *Inorganic Chemistry* 53.24: 12671 – 12673

Humphrey, E. R., Mann, K. L. V., Reeves, Z. R., Behrendt, A., Jeffery, J. C., Maher, J. P., McCleverty, J. A. and Ward, M. D. 1999. Copper(II) complexes of new potentially hexadentate or N_3S_3- or N_6-donor podand ligands based on the tris(pyrazolyl)borate or tris(pyrazolyl)methane core. *New Journal of Chemistry* 23.4: 417 – 423

Hung, M. C. and Ferreira, A. M. D. C. 2010. Synthesis and Characterization of new Copper(II) Complexes with Oxime–Imine and Oxime-Thiosemicarbazone Ligands. *Revista Cubana de Química* 22.1: 73 – 82

Hussain, S. and Park, S-y. 2020. Sweat-Based Noninvasive Skin-Patchable Urea Biosensors with Photonic Interpenetrating Polymer Network Films Integrated into PDMS Chips. *ACS Sensors* 5.12: 3988 – 3998

Hussein, H. A., Kandeil, A., Gomaa, M., Nashar, R. M. E., El-Sherbiny, I. M. and Hassan, R Y. A. 2021. SARS-CoV-2-Impedimetric Biosensor: Virus-Imprinted Chips for Early and Rapid Diagnosis. *ACS Sensors* 6.11: 4098 – 4107

Inan-Eroglu E, Ayaz A. 2018. Is aluminum exposure a risk factor for neurological disorders?. *Journal of Research in Medical Sciences* 23.51: 1 – 8.

Jana, S., Shaw, B. K., Bhowmik, P., Harms, K., Drew, M. G. B., Chattopadhyay, S. and Saha, S. K. 2014. Field-Induced Ferromagnetism and Multiferroic Behavior in End-on Pseudohalide-Bridged Dinuclear Copper(II) Complexes with Tridentate Schiff Base Blocking Ligands. *Inorganic Chemistry* 53.16: 8723 – 8734

Janakipriya, S., Chereddy, N. R., Korrapati, P., Thennarasu, S., Mandal, A. B. 2017. Selective interactions of trivalent cations Fe^{3+}, Al^{3+} and Cr^{3+} turn on fluorescence in a naphthalimide based single molecular probe. *Spectrochimica Acta Part A: Molecular and Biomolecular Spectroscopy* 153: 465 – 470

Janiak, C. 2003. Engineering coordination polymers towards applications. *Dalton Transactions* 2003.14: 2781 – 2804

Jang, H. J., Kang, J. H., Yun, D. and Kim, C. 2018. A multifunctional selective "turn-on" fluorescent chemosensor for detection of Group IIIA ions Al^{3+}, Ga^{3+} and In^{3+}. *Photochemical & Photobiological Sciences* 17.9: 1247 – 1255

_____, Kang, J. H., Yun, D., Kim, C. 2018. A Multi-Responsive Naphthalimide-Based "Turn-on" Fluorescent Chemosensor for Sensitive Detection of Trivalent Cations Ga^{3+}, Al^{3+} and Cr^{3+}. *Journal of Fluorescence* 28: 785 – 794

Jiang, S-D., Wang, B-W., Sun, H-L., Wang, Z-M. and Gao, S. 2011. An Organometallic Single-Ion Magnet. *Journal of the American Chemical Society* 133.13: 4730 – 4733

Jiang, Y-B., Kou, H-Z., Wang, R-J., Cui, A-L. and Ribas, J. 2005. Synthesis, Crystal Structure, and Magnetic Properties of Oxime-Bridged Polynuclear Ni(II) and Cu(II) Complexes. *Inorganic Chemistry* 44.3: 709 – 715

Jiménez, J-R., Díaz-Ortega, I. F., Ruiz, E., Aravena, D., Pope, S. J. A., Colacio, E. and Herrera, J. M. 2016. Lanthanide Tetrazolate Complexes Combining Single-Molecule Magnet and Luminescence Properties: The Effect of the Replacement of Tetrazolate N_3 by *β*-Diketonate Ligands on the Anisotropy Energy Barrier. *Chemistry - A European Journal* 22.41: 14548 – 14559

Jiménez-Sánchez, A., Rodríguez, M., Métivier, R., Ramos-Ortíz, G., Maldonado, J. L., Réboles, N., Farfán, N., Nakatanic, K. and Santillan, R. 2014. Synthesis and crystal structures of a series of Schiff bases: a photo-, solvato- and acidochromic compound. *New Journal of Chemistry* 38.2: 730 – 738

Jo, T. G., Bok, K. H., Han, J., Lim, M. H., Kim, C. 2017. Colorimetric detection of Fe^{3+} and Fe^{2+} and sequential fluorescent detection of Al^{3+} and pyrophosphate by an imidazole-based chemosensor in a near-perfect aqueous solution. *Dyes and Pigments* 139: 136 – 147

Johansson, F. B., Bond, A. D., Nielsen, U. G., Moubaraki, B., Murray, K. S., Berry, K. J., Larrabee, J. A. and McKenzie, C. J. 2008. Dicobalt II-II, II-III, and III-III Complexes as Spectroscopic Models for Dicobalt Enzyme Active Sites. *Inorganic Chemistry* 47.12: 5079 – 5092

Jose, A., Vijaykumar, G., Vardhanapu, P. K., Mandal, S. K. 2018. Abnormal NHC supported palladacycles: Regioselective arylation of heteroarenes via decarboxylation. *Journal of Organometallic Chemistry* 865: 51 – 57

Joseph, S. M., Dhanaraj, C. J., Joseph, J. and Joseyphus, R. S. 2017. Synthesis, Spectral Characterization and Anticancer Studies of Some Metal(II) Complexes Derived from Imidazole- 2-carboxaldehyde with 2-Amino-3-carboxyethyl-4,5-dimethylthiophene. *Oriental Journal of Chemistry* 33.3: 1477 – 1482

Joseyphus, R. S. and Nair, M. S. 2009. Synthesis, characterization and antimicrobial activity of transition metal complexes with the Schiff base derived from imidazole-2-carboxaldehyde and glycylglycine. *Journal of Coordination Chemistry* 62.2: 319 – 327

_____, Shiju, C., Joseph, J., Dhanaraj, C. J., Arish, D. 2014. Synthesis and characterization of metal complexes of Schiff base ligand derived from imidazole-2-carboxaldehyde and 4-aminoantipyrine. *Spectrochimica Acta Part A: Molecular and Biomolecular Spectroscopy* 133: 149 – 155

_____, Shiju, C., Joseph, J., Dhanaraj, C. J., and Bright, K. C. 2015. Synthesis and characterization of Schiff base metal complexes derived from imidazole-2-carboxaldehyde with L-phenylalanine. *Der Pharma Chemica* 7.6: 265 – 270

Jung, H. J., Singh, N., Lee, D. Y., Jang, D. K. 2009. Benzimidazole-based ratiometric fluorescent receptor exhibiting molecular logic gate for Cu^{2+} and Fe^{3+}. *Tetrahedron Letters* 50.40: 5555 – 5558

Jung, M., Sharma, A., Hinderberger, D., Braun, S., Schatzschneider, U. and Rentschler, E. 2009. Nitronyl Nitroxide Radicals Linked to Exchange-Coupled Metal Dimers – Studies Using X-ray Crystallography, Magnetic Susceptibility Measurements, EPR Spectroscopy, and DFT Calculations. *European Journal of Inorganic Chemistry* 2009.11: 1495 – 1502

Kamijo, S. and Yamamoto, Y. 2007. Recent progress in the Catalytic Synthesis of Imidazoles. *Chemistry - An Asian Journal* 2.5: 568 – 578

Kanagaraj, K., Bavanidevi, K., Chow, T. J. and Pitchumani, K. 2014. Selective "turn-off" fluorescent sensing of mercury ions using aminocyclodextrin: 3-hydroxy-N-phenyl-2-naphthamide complex in aqueous solution. *RSC Advances* 4.23: 11714 – 11722

Kanamori, J. 1959. Superexchange Interaction and Symmetry Properties of Electron Orbitals. *Journal of Physics and Chemistry of Solids* 10.2-3: 87 – 98

Kang, J. H. and Kim, C. 2018. Colorimetric detection of iron and fluorescence detection of zinc and cadmium by a chemosensor containing a bio-friendly octopamine. *Photochemical & Photobiological Sciences* 17.4: 442 – 452

Kang, L., Liu, Y-T., Li, N-N., Dang, Q-X., Xing, Z-Y., Li, J-L., Zhang, Y. 2017. A schiff-base receptor based naphthalimide derivative: Highly selective and colorimetric fluorescent turn-on sensor for Al^{3+}. *Journal of Luminescence* 186: 48 – 52

Kanmazalp, S. D., Doĝan, O. E., Taşdemir, V., Dege, N., Aĝar, E. and Fritsky, I. O. 2019. Crystal structure and Hirshfeld surface analysis of a Schiff base: (*Z*)-6-[(5-chloro-2-methoxyanilino)-methylidene]-2-hydroxycyclohexa-2,4-dien-1-one. *Acta Crystallographica Section E Crystallographic Comminucations* E75.Part3: 362 – 366

Kannappan, R., Tanase, S., Mutikainen, I., Turpeinen, U., Reedijk, J. 2006. Low-spin iron(III) Schiff-base complexes with symmetric hexadentate ligands: Synthesis, crystal structure, spectroscopic and magnetic properties. *Polyhedron* 25.7: 1646 – 1654

Karunadasa, H. I., Arquero, K. D., Berben, L. A. and Long, J. R. 2010. Enhancing the Magnetic Anisotropy of Cyano-Ligated Chromium(II) and Chromium(III) Complexes via Heavy Halide Ligand Effects. *Inorganic Chemistry* 49.11: 4738 – 4740

Kaur, N and Alreja, P 2015. An Imidazole based probe for relay recognition of Cu^{2+} and OH^- ions leading to AND logic gate. *Journal of Chemical Sciences* 127.7: 1253 – 1259

Kazantsev, M. S., Beloborodova, A. A., Frantseva, E. S., Rybalova, T. V., Konstantinov, V. G., Shundrina, I. K., Paraschuk, D. Yu., and Mostovich, E. A. 2017. Methyl substituent effect on structure, luminescence and semiconducting properties of furan/phenylene co-oligomer single crystals. *Crystal Engineering Communications* 19.13: 1809 – 1815

Keller, S., Constable, E. C., Housecroft, C. E., Neuburger, M., Prescimone, A., Longo, G., Pertegás, A., Sessolo, M. and Bolink, H. J. 2014. $[Cu(bpy)(P\text{^}P)]^+$ containing light-emitting electrochemical cells: improving performance through simple substitution. *Dalton Transactions* 43.44: 16593 – 16596

_____, Pertegás, A., Longo, G., Martínez, L., Cerdá, J., Junquera-Hernández, J. M., Prescimone, A., Constable, E. C., Housecroft, C. E., Ortí, E. and Bolink, H. J. 2016. Shine bright or live long: substituent effects in $[Cu(N\hat{}N)(P\hat{}P)]^{+}$-based light-emitting electrochemical cells where N^N is a 6-substituted 2,2'-bipyridine. *Journal of Materials Chemistry C* 4.17: 3857 – 3871

Kenney, G. E. and Rosenzweig, A. C. 2012. Chemistry and Biology of the Copper Chelator Methanobactin. *ACS Chemical Biology* 7.2: 260 – 268

Khan, F., Khan, S., Athar, A., Ahmed, W., Zia-ul-Haq and Khan, Z. 2015. Synthesis, Spectral Characterization and Antibacterial Study of a Schiff Base Metal Complexes Derived from N-[(*E*)-(5-Chloro-2-Hydroxyphenyl) Methylidene]-4-Nitrobenzenesulfonamide. *American-Eurasian Journal of Agricultural & Environmental Sciences* 15.2: 216 – 219

Khan, S., Giri, P., Bauzá, A., Harms, K., Frontera, A., Chattopadhyay, S. 2019. Synthesis, characterization and DFT study on two copper(II) complexes with a naphthalene-based Schiff base: Examples of stronger chelate–chelate interactions than those reported for classical π-π complexes. *Polyhedron* 157: 487 – 494

Khandar, A. A., Kirschbaum, K., Abedi, M., Mock, K., Tracy, G., Spasojevic, V. and Hosseini-Yazdi, S. A. 2015. Synthesis, characterization and crystal structures of mono and dinuclear macrocyclic cobalt(II) complexes with a new tetraaza m-xylyl-based macrocyclic ligand. *New Journal of Chemistry* 39.4: 2822 – 2831

Khattak, Z. A. K., Younus, H. A., Ahmad, N., Ullah, H., Suleman, S., Hossain, Md. S., Elkadi, M. and Verpoort, F. 2019. Highly active dinuclear cobalt complexes for solvent-free cycloaddition of CO_2 to epoxides at ambient pressure. *Chemical Communications* 55.57: 8274 – 8277

Kilic, H., Bozkurt, E. 2018. A rhodamine-based novel turn on trivalent ions sensor. *Journal of Photochemistry and Photobiology A: Chemistry* 363: 23 – 30

Kim, J-H., Kim, S-Y., Cho, D. W., Son, H-J. and Kang, S. O. 2019. Influence of bulky substituents on the photophysical properties of homoleptic iridium(III) complexes. *Physical Chemistry Chemical Physics* 21.13: 6908 – 6916

_____, Kim, S-Y., Choi, S., Son, H-J. and Kang, S. O. 2021. Peripheral Ligand Effect on the Photophysical Property of Octahedral Iridium Complex: o-Aryl Substitution on the Phenyl Units of Homoleptic $Ir^{III}(C\hat{}C)_3$ Complexes (C^C = 1-Phenyl-3-methylimidazolin-2-ylidene-C,$C^{2\prime}$) for Deep Blue Phosphorescence. *Inorganic Chemistry* 60.1: 246 – 262

Kim, H., Kim, H., Choi, J., Inn, K-S. and Seong, J. 2020. Visualization of Autophagy Progression by a Red-Green-Blue Autophagy Sensor. *ACS Sensors* 5.12: 3850 – 3861

_____, Kim, K. B., Song, E. J., Hwang, I. H., Noh, J. Y., Kim, P-G., Jeong, K-D., Kim, C. 2013. Turn-on selective fluorescent probe for trivalent cations. *Inorganic Chemistry Communications* 36: 72 – 76

Kim, S., Park, S., Cho, Y. S., Kim, Y., Tae, J. H., No, T. I., Shim, J. S., Jeong, Y., Kang, S. H. and Lee, K. H. 2021. Electrical Cartridge Sensor Enables Reliable and Direct Identification of MicroRNAs in Urine of Patients. *ACS Sensors* 6.3: 833 – 841

Kim, S-G and Ahn, K. H. 2000. Novel Artificial Receptors for Alkylammonium Ions with Remarkable Selectivity and Affinity. *Chemistry - A European Journal* 6.18: 3399 – 3403

Kivelson, D. and Neiman, R. 1961. ESR Studies on the Bonding in Copper Complexes. *Journal of Chemical Physics* 35.1: 149 – 155

Kobayashi, H., Haseda, T. and Mori, M. 1964. Magnetic Properties of Bi- and Uni-Nuclear Chromium(III) Complex Compounds at Low Temperatures. *Bulletin of the Chemical Society of Japan* 38.9: 1455 – 1461

Komatsu, K., Kikuchi, K., Kojima, H., Urano, Y. and Nagano, T. 2005. Selective Zinc Sensor Molecules with Various Affinities for Zn^{2+}, Revealing Dynamics and Regional Distribution of Synaptically Released Zn^{2+} in Hippocampal Slices. *Journal of the American Chemical Society* 127.29: 10197 – 10204

Kowalczyk, T., Ziliang, L. and Troy, V. V. 2010. Fluorescence Quenching by Photoinduced Electron Transfer in the Zn^{2+} Sensor Zinpyr-1: A Computational Investigation. *Journal of Physical Chemistry A* 114.38: 10427 – 10434

Kumar, A., Wang, C., Meng, F-Y., Jiang, C-P., Yan, G-F., Zhao, M., Jing, C-Q. and Wang, L. 2020. Ultrafast Detection and Discrimination of Methanol Gas Using a Polyindole-Embedded Substrate Integrated Waveguide Microwave Sensor. *ACS Sensors* 5.12: 3939 – 3948

Kumar, A. M. M. S., Pandiyan, B. V., Roopan, S. M., Rajendran, S. P. 2017. Efficient synthesis, fluorescence and DFT studies of different substituted 2-chloroquinoline-4-amines and benzo[*g*][1,8]Naphthyridine Derivatives. *Journal of Photochemistry and Photobiology A: Chemistry* 332: 72 – 86

Kumar, P. S., Ciattini, S., Laura, C., Elango, K. P. 2020. Fluorescent detection of Al(III) and CN^- in solid and aqueous phases and their recognition in biological samples. *Journal of Molecualr Liquids* 317: 113970. https://doi.org/10.1016/j.molliq.2020.113970

Kumar, V., Singh, V., Gupta, A. N., Manar, K. K., Drew, M. G. B. and Singh, N. 2014. Influence of ligand environments on the structures and luminescence properties of homoleptic cadmium(II) pyridyl functionalized dithiocarbamates. *Crystal Enginering Communications* 16.29: 6765 – 6774

Kundu, B. K., Mandal, P., Mukhopadhyay, B. G., Tiwari, R., Nayak, D., Ganguly, R., Mukhopadhyay, S. 2019. Substituent dependent sensing behavior of Schiff base chemosensors in detecting Zn^{2+} and Al^{3+} ions: Drug sample analysis and living cell imaging. *Sensors and Actuators B: Chemical* 282: 347 – 358

Kushch, L. A., Sasnovskaya, V. D., Dmitriev, A. I., Yagubskii, E. B., Koplak, O. V., Zorina, L. V. and Boukhvalov, D. W. 2012. New single-molecule magnet based on Mn_{12} oxocarboxylate clusters with mixed carboxylate ligands, $[Mn_{12}O_{12}(CN\text{-}o\text{-}C_6H_4CO_2)_{12}(CH_3CO_2)_4(H_2O)_4]\cdot 8CH_2Cl_2$: Synthesis, crystal and electronic structure, magnetic properties. *Dalton Transactions* 41.44: 13747 – 13754

Kushvaha, S. K., Arumugam, S., Shankar, B., Sarkar, R. S., Ramkumar, V. and Mondal, K. C. 2019. Isolation and Characterization of Different Homometallic and Heterobimetallic Complexes of Nickel and Zinc Ions by Controlling Molar Ratios and Solvents. *European Journal of Inorganic Chemistry* 2019.4:2871 – 2882

Kuwabara, J., Oi, K., Watanabe, M. M., Fukuda, T. and Kanbara, T. 2020. Algae-Inspired, Sulfur-Based Polymer with Infrared Transmission and Elastic Function. *ACS Applied Polymer Materials* 2.11: 5173 – 5178

Krzystek, J., Ozarowski, A., Telser, J. 2006. Multi-frequency, high-field EPR as a powerful tool to accurately determine zero-field splitting in high-spin transition metal coordination complexes. *Coordination Chemistry Reviews* 250.17-18: 2308 – 2324

Łabanowska, M., Bidzińska, E., Para, A., Kurdziel, M. 2012. EPR investigation of Cu(II)-complexes with nitrogen derivatives of dialdehyde starch. *Carbohydrate Polymres* 87.4: 2605 – 2613

Langley, S. K., Chilton, N. F., Massi, M., Moubaraki, B., Berry, K. J. and Murray, K. S. 2010. Synthesis and characterization of homo- and heterovalent tetra- hexa-heptaand decanuclear manganese clusters using pyridyl functionalized *β*-diketone, carboxylate and triethanolamine ligands. *Dalton Transactions* 39.31: 7236 – 7249

Larin, G. M., Shul´gin, V. F., Gusev, A. N. and Chernega, A. N. 2004. Molecular structures and ESR spectra of copper(II) complexes with 2-hydroxypropiophenone acyldihydrazones. *Russian Chemical Bulletin* 53.4: 775 – 779

Lau, Y. H., Price, J. R., Todd, M. H. and Rutledge, P. J. 2011. A Click Fluorophore Sensor that Can Distinguish Cu^{II} and Hg^{II} via Selective Anion-Induced Demetallation. *Chemistry - A European Journal* 17.10: 2850 – 2858

Lee, J. A., Eom, G. H., Park, H. M., Lee, J. H., Song, H., Hong, C. S., Yoon, S., and Kim, C. 2012. Selective Fe^{2+} Ion Recognition Using a Fluorescent Pyridinyl-benzoimidazole-derived Ionophore. *Bulletin of the Korean Chemical Society* 33.11: 3625 – 3628

Lee, J. C., Laydon, J. T., McDonnell, P. C., Gallagher, T. F., Kumar, S., Green, D., McNulty, D., Blumenthal, M. J., Heys, J. R., Landvatter, S. W., Stricker, J. E., McLaughlin, M. M., Siemens, I. R., Fisher, S. M., Livi, G. P., White, J. R., Adams, J. L. and Young, P. R. 1994. A protein kinase involved in the regulation of inflammatory cytokine biosynthesis. *Nature* 372: 739 – 746

Lee, J-H., Parthiban, P., Jin, G-Z., Knowles, J. C., Kim, H-W. 2021. Materials roles for promoting angiogenesis in tissue regeneration. *Progress in Materials Science* 117: 100732 https://doi.org/10.1016/j.pmatsci.2020.100732

Lee, S. W., Lee, W., Kim, I., Lee, D., Park, D., Kim, W., Park, J., Lee, J. H., Lee, G. and Yoon, D. S. 2021. Bio-Inspired Electronic Textile Yarn-Based NO_2 Sensor Using Amyloid-Graphene Composite. *ACS Sensors* 6.3: 777 – 785

Leirer, M., Knör, G., Vogler, A. 1999. Electronic spectra of 1,2-diiminetricarbonylrhenium(I)chloride complexes with imidazole derivatives as ligands. *Inorganica Chimica Acta* 288.2: 150 – 153

Leo, P., Briones, D., García, J. A., Cepeda, J., Orcajo, G., Calleja, G., Rodríguez-Diéguez, A. and Martínez, F. 2020. Strontium-Based MOFs Showing Dual Emission: Luminescence Thermometers and Toluene Sensors. *Inorganic Chemistry* 59.24: 18432 – 18443

Li, C-L., Lu, P-H., Fu, S-F. and Wu, A-T. 2019. A Highly Selective and Sensitive Fluorescent Chemosensor for Detecting Al^{3+} Ion in Aqueous Solution and Plant Systems. *Sensors* 19: 623. https://dx.doi.org/10.3390/s19030623

Li, C-r., Qin, J-c., Wang, B-d., Bai, X., Yang, Z-y. 2017. Fluorescence chemosensor properties of two coumarin-based compounds for environmentally and biologically important Al^{3+} ion. *Journal of Photochemistry and Photobiology A: Chemistry* 332: 141 – 149

Li, D-P., Wang, T-W., Li, C-H., Liu, D-S., Li, Y-Z. and You, X-Z. 2010. Single-ion magnets based on mononuclear lanthanide complexes with chiral Schiff base ligands $[Ln(FTA)_3L]$ (Ln = Sm, Eu, Gd, Tb and Dy). *Chemical Communications* 46.17: 2929 – 2931

Li, G., Zheng, J., Zhao, X., Fleetham, T., Yang, Y-F., Wang, Q., Zhan, F., Zhang, W., Fang, K., Zhang, Q. and She, Y. 2020. Tuning the Excited State of Tetradentate Pd(II) Complexes for Highly Efficient Deep-Blue Phosphorescent Materials. *Inorganic Chemistry* 59.18: 13502 – 13516

Li, J-L., Jiang, L., Wang, B-W., Tian, J-L., Gu, W., Liu, X., Yan, S-P. 2015. Bio-relevant cobalt(II) complexes with compartmental polyquinoline ligand: Synthesis, crystal structures and biological activities. *Journal of Inorganic Biochemistry* 145: 19 – 29

Li, M., Ge, H., Arrowsmith, R. L., Mirabello, M., Botchway, S. W., Zhu, W., Pascu, S. I., and James, T. D. 2014. Ditopic boronic acid and imine-based naphthalimide fluorescence sensor for Copper(II). *Chemical Communications* 50.80: 11806 – 11809

Li, P., Zhang, W., Li, K., Liu, X., Xiao, H., Zhang, W. and Tang, B. 2013. Mitochondria-Targeted Reaction-Based Two-Photon Fluorescent Probe for Imaging of Superoxide Anion in Live Cells and in Vivo. *Analytical Chemistry* 85.20: 9877 – 9881

Li, Y., Tu, L., Ma, X., Chen, H., Fan, Y., Zhou, Q. and Sun, Y. 2021. Engineering a Smart Nanofluidic Sensor for High-Performance Peroxynitrite Sensing through a Spirocyclic Ring Open/Close Reaction Strategy. *ACS Sensors* 6.3: 808 – 814

Li, Y-W., Li, J., Wan, X-Y., Sheng, D-F., Yan, H., Zhang, S-S., Ma, H-Y., Wang, S-N., Li, D-C., Gao, Z-Y., Dou, J-M. and Sun, D. 2021. Nanocage-Based N-Rich Metal-Organic Framework for Luminescence Sensing toward Fe^{3+} and Cu^{2+} Ions. *Inorganic Chemistry* 60.2: 671 – 681

Liao, Z., Liu, Y., Han, S-F., Wang, D., Zheng, J-Q., Zheng, X-J., Jin, L-P. 2017. A novel acylhydrazone-based derivative as dual-mode chemosensor for Al^{3+}, Zn^{2+} and Fe^{3+} and its applications in cell imaging. *Sensors and Actuators B: Chemical* 244: 914 – 921

Lin, P-H., Korobkov, I., Burchell T. J. and Murugesu, M. 2012. Connecting single-ion magnets through ligand dimerization. *Dalton Transactions* 41.44: 13649 – 13655

Linfoot, C. L., Leitl, M. J., Richardson, P., Rausch, A. F., Chepelin, O., White, F. J., Yersin, H. and Robertson, N. 2014. Thermally Activated Delayed Fluorescence (TADF) and Enhancing Photoluminescence Quantum Yields of $[Cu^{I}(diimine)(diphosphine)]^{+}$ Complexes- Photophysical, Structural, and Computational Studies. *Inorganic Chemistry* 53.20: 10854 – 10861

Lisowski, C. E. and Hutchison, J. E. 2009. Malonamide-Functionalized Gold Nanoparticles for Selective, Colorimetric Sensing of Trivalent Lanthanide Ions. *Analytical Chemistry* 81.24: 10246 – 10253

Liu, B., Chai, J., Feng, S., Yang, B. 2015. Structure, photochemistry and magnetic properties of tetrahydrogenated Schiff base chromium(III) complexes. *Spectrochimica Acta Part A: Molecualr and Biomolecular Spectroscopy* 140: 437 – 443

_____, Gurr, P. A. and Qiao, G. G. 2020 “Irreversible Spoilage Sensors for Protein-Based Food” *ACS Sensors* 5.9: 2903 – 2908

Liu, C-M., Zhang, D-Q. and Zhu, D-B. 2013. Field-Induced Single-Ion Magnets Based on Enantiopure Chiral *β*-Diketonate Ligands. *Inorganic Chemistry* 52.15: 8933 – 8940

Liu, G., Han, F., Liu, C., Wu, H., Zeng, Y., Zhu, R., Yu, X., Rao, S., Huang, G., and Wang, J. 2019. A Highly Active Catalyst System for Suzuki-Miyaura Coupling of Aryl Chlorides. *Organometallics* 38.7: 1459 – 1467

Liu, K., Han, X., Zou, Y., Peng, Y., Li, G., Shi, Z., Feng, S. 2014. Solvothermal synthesis, structures, and gas adsorption properties of two cadmium-organic frameworks. *Inorganic Chemistry Communications* 39: 131 – 134

Liu, L., Wang, A., Wang, G., Li, J., Zhou, Y. 2015. A naphthopyran-rhodamine based fluorescent and colorimetric chemosensor for recognition of common trivalent metal ions and Cu^{2+} ions. *Sensors and Actuators B: Chemical* 215: 388 – 395

Liu, P-P., Sheng, L., Song, X-Q., Xu, W-Y., Liu, Y-A. 2015. Synthesis, structure and magnetic properties of a new one dimensional manganese coordination polymer constructed by a new asymmetrical ligand. *Inorganica Chimica Acta* 434: 252 – 257

Liu, T-T., Xu, J., Liu, C-g., Zeng, S., Xing, Z-Y., Sun, X-J., Li, J-L. 2020. A novel dual-function probe for recognition and differentiation of Zn^{2+} and Al^{3+} and its application. *Journal of Molecular Liquids* 300: 112250. https://doi.org/10.1016/j.molliq.2019.112250

Liu, W., Christian, J. H., Al-Oweini, R., Bassil, B. S., van Tol, J., Atanasov, M., Neese, F., Dalal, N. S. and Kortz, U. 2014. Synthesis, Detailed Characterization, and Theoretical Understanding of Mononuclear Chromium(III)-Containing Polyoxotungstates $[Cr^{III}(HX^{V}W_7O_{28})_2]^{13-}$ (X = P, As) with Exceptionally Large Magnetic Anisotropy. *Inorganic Chemistry* 53.17: 9274 – 9283

Liu, X. and Hamon, J-R. 2019. Recent developments in penta-, hexa- and heptadentate Schiff base ligands and their metal complexes. *Coordination Chemistry Reviews* 389: 94 – 118

_____, Zhang, N., Zhou, J., Chang, T., Fang, C. and Shangguan, D. 2013. A turn-on fluorescent sensor for zinc and cadmium ions based on perylene tetracarboxylic diimide. *Analyst* 138.3: 901 – 906

Liu, Y., Zhang, L., Chen, L., Liu, Z., Liu, C., Che, G. 2021. 2-Hydroxynaphthalene based acylhydrazone as a turn-on fluorescent chemosensor for Al^{3+} detection and its real sample applications. *Spectrochimica Acta Part A: Molecualr and Biomolecualr Spectroscopy* 248: 119269. https://doi.org/10.1016/j.saa.2020.119269

Liu, Z., Yang, W., Li, Y., Tian, F. and Zhu, W. 2015. A facile synthesis of a highly water-soluble and selective fluorescent sensor towards zinc ions derived from β-cyclodextrin based on an unexpected sensing process. *RSC Advances* 5.122: 100482 – 100487

Lloret, F., Julve, M., Cano, J., Ruiz-García, R., Pardo, E. 2008. Magnetic properties of six-coordinated high-spin cobalt(II) complexes: Theoretical background and its application. *Inorganica Chimica Acta* 361.12-13: 3432 – 3445

Long, Y., Bai, Y-j., Zhou, J., Yang, B-q. 2017. Selective and sensitive off-on probes specific for palladium detection and their application in biological environments. *Journal of Photochemistry and Photobiology A: Chemistry* 332: 422 – 431

Longo, J. M., Sanford, M. J. and Coates, G. W. 2016. Ring-Opening Copolymerization of Epoxides and Cyclic Anhydrides with Discrete Metal Complexes: Structure-Property Relationships. *Chemical Reviews* 116.24: 15167 – 15197

Louie, M-W., Liu, H-W., Lam, M. H-C., Lau, T-C. and Lo, K. K-W. 2009. Novel Luminescent Tricarbonylrhenium(I) Polypyridine TyramineDerived Dipicolylamine Complexes as Sensors for Zinc(II) and Cadmium(II) Ions. *Organometallics* 28.15: 4297 – 4307

Lu, C., Xu, Z., Cui, J., Zhang, R. and Qian, X. 2007. Ratiometric and Highly Selective Fluorescent Sensor for Cadmium under Physiological pH Range: A New Strategy to Discriminate Cadmium from Zinc. *Journal of Organic Chemistry* 72.9: 3554 – 3557

Lu, Z., Fan, T., Guo, W., Lu, J., Fan, C. 2013. Synthesis, structure and magnetism of three cubane Cu(II) and Ni(II) complexes based on flexible Schiff-base ligands. *Inorganica Chimica Acta* 400: 191 – 196

Luo, R., Chen, L., Li, Q., Zhou, J., Mei, L., Ning, Z., Zhao, Y., Liu, M., Lai, X., Bi, J., Yin, W. and Gao, D. 2020. Bi^{3+}-Doped $BaYF_5$:Yb,Er Upconversion Nanoparticles with Enhanced Luminescence and Application Case for X-ray Computed Tomography Imaging. *Inorganic Chemistry* 59.24: 17906 – 17915

Mahdi, R. T., Ali, A. A. M., and Huda A. Noaman, H. A. 2014. Preparation and Characterization of Some Metal Complexes with New Heterocyclic Schiff-Azo Ligand. *Journal of Al-Nahrain University* 17.4: 51 – 58

Malinowski, J., Zych, D., Jacewicz, D., Gawdzik, B. and Drzeżdżon, J. 2020. Application of Coordination Compounds with Transition Metal Ions in the Chemical Industry – A Review. *International Journal of Molecular Sciences*, 21.15: 5443, https://doi.org/10.3390/ijms21155443

Mamiya, M., Suwa, Y., Okamoto, H. and Yamaji, M. 2016. Preparation and photophysical properties of fluorescent difluoroboronated β-diketones having phenanthrene moieties studied by emission and transient absorption measurements. *Photochemical & Photobiological Sciences* 15.2: 278 – 286

Manjunath, R., Hrishikesan, E., Kannan, P. 2015. A selective colorimetric and fluorescent sensor for Al^{3+} ion and its application to cellular imaging. *Spectrochimica Acta Part A: Molecular and Biomolecular Spectroscopy* 140: 509 – 515

Mariappan, K., Alaparthi, M., Caple, G., Balasubramanian, V., Hoffman, M. M., Hudspeth, M., and Sykes, A. G. 2014. Selective Fluorescence Sensing of Copper(II) and Water via Competing Imine Hydrolysis and Alcohol Oxidation Pathways Sensitive to Water Content in Aqueous Acetonitrile Mixtures. *Inorganic Chemistry* 53.6: 2953 – 2962

Massoud, S. S., Broussard, K. T., Mautner, F. A., Vicente, R., Saha, M. K., Bernal, I. 2008. Five-coordinate cobalt(II) complexes of tris(2-pyridylmethyl)amine (TPA): Synthesis, structural and magnetic characterization of a terephthalato-bridged dinuclear cobalt(II) complex. *Inorganica Chimica Acta* 361.1: 123 – 131

Matsuoka, N., Tsuchimoto, M. and Yoshioka, N. 2011. Theoretical Study of Magnetic Properties of Oxovanadium(IV) Complex Self-Assemblies with Tetradentate Schiff Base Ligands. *Journal of Physical Chemistry B* 115.26: 8465 – 8473

Mati, S. S., Chall, S., Konar, S., Rakshit, S., Bhattacharya, S. C. 2014. Pyrimidine-Based Fluorescent Zinc Sensor: Photo-physical Characteristics, Quantum Chemical Interpretation and Application in Real Samples. *Sensors and Actuators B: Chemical* 201: 204 – 212

Mayall, R. M., Smith, C. A., Hyla, A. S., Lee, D. S., Crudden, C. M. and Birss, V. I. 2020. Ultra-sensitive and label-free detection of the measles virus using an N-heterocyclic carbene-based electrochemical biosensor. *ACS Sensors* 5.9: 2747 – 2752

Mazlan, N. A., Ravoof, T. B. S. A., Tiekink, E. R. T., Tahir, M. I. M., Veerakumarasivam, A., Crouse, K. A. 2014. Mixed-ligand metal complexes containing an ONS Schiff base and imidazole/benzimidazole ligands: synthesis, characterization, crystallography and biological activity. *Transition Metal Chemistry* 39: 633 – 639

McGinley, J., McCann, M., Ni, K., Tallon, T., Kavanagh, K., Devereux, M., Ma, X., McKee, V. 2013. Imidazole Schiff base ligands: Synthesis, coordination complexes and biological activities. *Polyhedron* 55: 169 – 178

McLay, J. R. W., Sutton, J. J., Shillito, G. E., Larsen, C. B., Huff, G. S., Lucas, N. T. and Gordon, K. C. 2021. Transitioning from Intraligand π,π* to Charge-Transfer Excited States Using Thiophene-Based Donor-Acceptor Systems. *Inorganic Chemistry* 60.1: 130 – 139

Meng, J., Xu, H., Li, Z., Xu, S., Yao, C. 2017. A turn-on spiropyran derivative based reversible photo-driven colorimetric and fluorescent chemosensor for trivalent metal ions. *Tetrahedron* 73.47: 6637 – 6643

Mishra, V., Lloret, F., Mukherjee, R. 2006. Coordination versatility of 1,3-bis[3-(2-pyridyl)pyrazol-1-yl]propane: Co(II) and Ni(II) complexes. *Inorganic Chimica Acta* 359.12: 4053 – 4062

Misra, B. N. and Kripal, R. 1981. Study of ESR absorption and bonding character of copper(II) complex with L-Hydroxyproline. *Revue de Physique Appliquée* 16.8: 411 – 417

Mo, J., Messinis, A. M., Oliveira, J. C. A., Demeshko, S., Meyer, F. and Ackermann, L. 2021. Iron-Catalyzed Triazole-Enabled C-H Activation with Bicyclopropylidenes. *ACS Catalysis* 11.3: 1053 – 1064

Molina, P., Tárraga, A., and Otón, F. 2012. Imidazole derivatives: A comprehensive survey of their recognition properties. *Organic & Biomolecualr Chemistry* 10.9: 1711 – 1724

Mondal, A. K., Mondal, A. and Konar, S. 2019. Field Induced Single Ion Magnetic Behaviour in Square-Pyramidal Cobalt(II) Complexes with Easy-Plane Magnetic Anisotropy. *Magnetochemistry* 5.1: 12. https://doi.org/10.3390/magnetochemistry5010012

Monfared, H. H., Pouralimardan, O. and Janiak, C. 2007. Synthesis and Spectral Characterization of Hydrazone Schiff Bases Derived from 2,4-Dinitrophenylhydrazine. Crystal Structure of Salicylaldehyde-2,4-Dinitrophenylhydrazone. *Zeitschrift für Naturforschung B* 62b.5: 717 – 720

Monge, D; Bermejo, A; Vázquez, J; Fernández, R and Lassaletta, J. M. 2013. Design and synthesis of new bis-hydrazones and pyridine bis-hydrazones: application in the asymmetric Diels-Alder reaction. *Archive for Organic Chemistry* 2013.2: 33 – 45. https://doi.org/10.3998/ark.5550190.0014.205

Morgan, Sh. M., Diab, M. A., El-Sonbati, A. Z. 2018. Supramolecular assembly of hydrogen bonding, ESR studies and theoretical calculations of Cu(II) complexes. *Applied Organometallic Chemistry* 32.10: e4504. https://doi.org/10.1002/aoc.4504

Muddassir, M., Alarifi, A., Afzal, M., Sepay, N. 2020. Newly designed Mn(III)–W(V) bimetallic assembly built by manganese(III) Schiff–base and octacyanotungstate(V) building blocks: Structural topologies, and magnetic features. *Applied Organometallic Chemistry* 34.11: e5914. https://doi.org/10.1002/aoc.5914

Mukherjee, P., Drew, M. G. B., Gómez-García, C. J. and Ghosh, A. 2009. The Crucial Role of Polyatomic Anions in Molecular Architecture: Structural And Magnetic Versatility of Five Nickel(II) Complexes Derived from A N,N,O-Donor Schiff Base Ligand. *Inorganic Chemistry* 48.13: 5848 – 5860

Mustafa, G., Komatsu, S. 2016. Toxicity of heavy metals and metal-containing nanoparticles on plants. *Biochimica et Biophysica Acta (BBA) – Proteins and Proteomics* 1864.8: 932 – 944

Naiya, S., Biswas, C., Drew, M. G. B., Gómez-García, C. J., Clemente-Juan, J. M. and Ghosh, A. 2010. A Unique Example of Structural and Magnetic Diversity in Four Interconvertible Copper(II)-Azide Complexes with the Same Schiff Base Ligand: A Monomer, a Dimer, a Chain, and a Layer. *Inorganic Chemistry* 49.14: 6616 – 6627

Nakamoto K. 1963. *Infrared Spectra of Inorganic and Coordination Compounds*. New York: John Wiley & Sons, Inc., 328 pp**.**

Narang, K, K., Rao, T. R., Shrestha, S. and Shrestha, S. 2000. Synthesis, Characterization, Thermal and Electrical Properties of Yttrium(III) and Lanthanide(III) Complexes of Salicylaldehyde Benzoyl Hydrazone. *Synthesis and Reactivity in Inorganic Metal-Organic Chemistry* 30.5: 931 – 954

Narayanan, J., Solano-Peralta, A., Ugalde-Saldivar, V. M., Escudero, R., Höpfl, H., Sosa-Torres, M. E. 2008. New dinuclear cobalt(II) octaaza macrocyclic complexes with high oxidation redox potentials: Their crystal structure and unusual magnetic properties. *Inorganica Chimica Acta* 361.9-10: 2747 – 2758

Naskar, B., Modak, R., Maiti, D. K., Drew, M. G. B., Bauzá, A., Frontera, A., Mukhopadhyay, C. D., Mishra, S., Sahae, K. D., and Goswami, S. 2017. A Schiff base platform: structures, sensing of Zn(II) and PPi in aqueous medium and anticancer activity. *Dalton Transactions* 46.29: 9498 – 9510

Neese, F. 2001. Theoretical Study of Ligand Superhyperfine Structure. Application to Cu(II) Complexes. *Journal of Physical Chemistry A* 105.17: 4290 – 4299

Nematirad, M., Gee, W. J., Langley, S. K., Chilton, N. F., Moubaraki, B., Murray, K. S. and Batten, S. R. 2012. Single molecule magnetism in a μ-phenolato dinuclear lanthanide motif ligated by heptadentate Schiff base ligands. *Dalton Transactions* 41.44: 13711 – 13715

Nemec, I., Herchel, R. and Trávníček, Z. 2015. Suppressing of slow magnetic relaxation in tetracoordinate Co(II) field-induced single-molecule magnet in hybrid material with ferromagnetic barium ferrite. *Scientific Reports* 5: 10761. https://doi.org/10.1038/srep10761

Niu, M., Li, Z., Li, H., Li, X., Dou, J. and Wang, S. 2015. DNA/protein interaction, cytotoxic activity and magnetic properties of amino-alcohol Schiff base derived Cu(II)/Ni(II) metal complexes: influence of the nuclearity and metal ions. *RSC Advances* 5.47: 37085 – 37095

Nolan, E. M., Burdette, S. C., Harvey, J. H., Hilderbrand, S. A. and Lippard, S. J. 2004. Synthesis and Characterization of Zinc Sensors Based on a Monosubstituted Fluorescein Platform. *Inorganic Chemistry* 43.8: 2624 – 2635

Novikov, V. V., Pavlov, A. A., Nelyubina, Y. V., Boulon, M-E., Varzatskii, O. A., Voloshin, Y. Z. and Winpenny, R. E. P. 2015. A Trigonal Prismatic Mononuclear Cobalt(II) Complex Showing Single-Molecule Magnet Behavior. *Journal of the American Chemical Society* 137.31: 9792 – 9795

Novitchi, G., Jiang, S., Shova, S., Rida, F., Hlavička, I., Orlita, M., Wernsdorfer, W., Hamze, R., Martins, C., Suaud, N., Guihéry, N., Barra, A-L and Train, C. 2017. From Positive to Negative Zero-Field Splitting in a Series of Strongly Magnetically Anisotropic Mononuclear Metal Complexes. *Inorganic Chemistry* 56.24: 14809 – 14822

Nguyen, T. N., Wernsdorfer, W., Shiddiq, M., Abboud, K. A., Hill, S. and Christou, G. 2016. Supramolecular aggregates of single-molecule magnets: exchange-biased quantum tunneling of magnetization in a rectangular $[Mn_3]_4$ tetramer. *Chemical Science* 7.2: 1156 – 1173

Otwinowski, Z. and Minor, W. 1997. Macromolecular Crystallography Part A: Processing of X-ray Diffraction Data Collected in Oscillation Mode. Ed. Carter, Jr., C. W. *Methods in Enzymology*, 276.Chapter 20: 307 – 326. New York, Academic Press.

Pal, A. K., Krotkus, S., Fontani, M., Mackenzie, C. F. R., Cordes, D. B., Slawin, A. M. Z., Samuel, I. D. W. and Zysman-Colman, E. 2018. High-Efficiency Deep-Blue-Emitting Organic Light-Emitting Diodes Based on Iridium(III) Carbene Complexes. *Advanced Materials* 30.50: 1804231. https://doi.org/10.1002/adma.201804231

Pal, R., Singh, N., and Singh, P. S. 2011. Study of Imidazole Derivatives to Identify them as *Mycobacterium Tuberculosis* 14_{DM} Inhibitors. *International Journal of Research in Pharmacy and Chemistry* 1.4: 914 – 921

Pandey, P., Verma, A., Bretosh, K., Sutter, J-P., Sunkari, S. S. 2019. Template directed synthesis of half condensed Schiff base complexes of Cu(II) and Co(III): Structural and magnetic studies. *Polyhedron* 160: 80 – 89

Pang, Y., Cui, S., Li, B., Zhang, J., Wang, Y. and Zhang, H. 2008. Metal-Dependent Assembly of a Helical-[Co_3L_3] Cluster versus a Meso-[Cu_2L_2] Cluster with O,N,N′,O′-Schiff Base Ligand: Structures and Magnetic Properties. *Inorganic Chemistry* 47.22: 10317 – 10324

Park, S., Kwon, J. E., Kim, S. H., Seo, J., Chung, K., Park, S-Y., Jang, D-J., Medina, B. M., Gierschner, J. and Park, S. Y. 2009. A White-Light-Emitting Molecule: Frustrated Energy Transfer between Constituent Emitting Centres. *Journal of the American Chemical Society* 131.39: 14043 – 14049

Park, W., Shin, H., Choi, B., Rhim, W-K., Na, K., Han, D. K. 2020. Advanced hybrid nanomaterials for biomedical applications. *Progress in Materials Science* 114: 100686
https://doi.org/10.1016/j.pmatsci.2020.100686

Pasán, J., Sanchiz, J., Ruiz-Pérez, C., Lloret, F. and Julve, M. 2005. Polymeric Networks of Copper(II) Phenylmalonate with Heteroaromatic N-donor Ligands: Synthesis, Crystal Structure, and Magnetic Properties. *Inorganic Chemistry* 44.22: 7794 – 7801

Patai, S. 1970. *The chemistry of Carbon Nitrogen double bond*. John Wiley and Sons Ltd., New York

Patel, K. C. and Goldberg, D. E. 1972. *N*-Aralkylpolyamine Complexes. II. Five- and Six-Coordinate Complexes of Copper(II) with *N*,*N*'-Dibenzylethylenediamine. *Inorganic Chemistry* 11.4: 759 – 764

Patra, C., Bhanja, A. K., Sen, C., Ojha, D., Chattopadhyay, D., Mahapatra, A. and Sinha, C. 2016. Imine-functionalized thioether Zn(II) turn-on fluorescent sensor and its selective sequential logic operations with $H_2PO_4^-$, DFT computation and live cell imaging. *RSC Advances* 6.58: 53378 – 53388

Pearl, A. J., Reji, T. F. A. F. 2014. Synthesis, characterization and Biological studies on some metal complexes incorporating Imidazole-2- carboxaldehyde, 4-aminoantipyrine and 2- aminophenol. *International Journal of Advances in Pharmacy, Biology and Chemistry* 3.2: 507 – 515

Pedersen, E. and Toftlund, H. 1974. Electron Spin Resonance Spectra of Tetragonal Chromium(III) Complexes. I. *trans*-[$Cr(NH_3)_4XY]^{n+}$ and *trans*-[$Cr(py)_4XY]^{n+}$ in Frozen Solutions and Powders. A Correlation between Zero-Field Splittings and Ligand Field Parameters *via* Complete d-Electron Calculations. *Inorganic Chemistry* 13.7: 1603 – 1612

Peng, H., Peng, X., Huang, J., Huang, A., Xu, S., Zhou, J., Huang, S., Cai, X. 2020. Synthesis and crystal structure of a novel pyridine acylhydrazone derivative as a "turn on" fluorescent probe for Al^{3+}. *Journal of Molecular Structure* 1212: 128138 https://doi.org/10.1016/j.molstruc.2020.128138

Pérez-Pérez, J., Alvarado-Rodríguez, J. G., Andrade-López, N., Borbolla, J. C., Martínez-Otero, D., Vásquez-Pérez, J. M. 2016. Schiff pentadentate ligands based on an $[ON_2O_2]$ core displaying structural isomerism and their coordination to dibutyltin moieties. *Inorganic Chemistry Communications* 70: 75 – 78

Plaul, D., Böhme, M., Ostrovsky, S., Tomkowicz, Z., Görls, H., Haase, W. and Plass, W. 2018. Modeling Spin Interactions in a Triangular Cobalt(II) Complex with Triaminoguanidine Ligand Framework: Synthesis, Structure, and Magnetic Properties. *Inorganic Chemistry* 57.1: 106 – 119

Pogány, L., Brachňaková, B., Masárová, P., Moncol, J., Pavlik, J., Gál, M., Mazúr, M., Herchel, R., Nemec, I. and Šalitroš, I. 2019. Impact of the Schiff base ligand substituents on the solid state and solution properties of eleven iron(III) complexes. *New Journal of Chemistry* 43.35: 13916 – 13928

_____, Brachňaková, B., Moncol, J., Pavlik, J., Nemec, I., Trávníček, Z., Mazúr, M., Bučinský, L., Suchánek, L. and Šalitroš, I. 2018. Impact of Substituent Variation on the Presence of Thermal Spin Crossover in a Series of Mononuclear Iron(III) Schiff Base Complexes with Terminal Pseudohalido Co-ligands. *Chemistry – A European Journal* 24.20: 5191 – 5203

Poschenrieder, C., Busoms, S. and Barceló, J. 2019. How Plants Handle Trivalent (+3) Elements. *International Journal of Molecular Sciences* 20.16: 3984, 25 pages. https://dx.doi.org/10.3390/ijms20163984

Prabhakaran, D., Yuehong, M., Nanjo, H. and Matsunaga, H. 2007. Naked-Eye Cadmium Sensor: Using Chromoionophore Arrays of Langmuir-Blodgett Molecular Assemblies. *Analytical Chemistry* 79.11: 4056 – 4065

Pradhan, A., Khan, N., Goyal, H. 2015. A Convenient Approach for the Synthesis of Ingenous Imidazole Derivatives Using Microwaves. *Chemical and Process Engineering Research* 35: 128 – 134

Pratibha, Singh, S., Sivakumar, S., and Verma, S. 2017. Purine-Based Fluorescent Sensors for Imaging Zinc Ions in HeLa Cells. *European Journal of Inorganic Chemistry* 2017.36: 4202 – 4209

Preti, C., Tosi, G. and Zannini, P. 1977. Five-Coordinate Low-Spin Cobalt(II) Complexes with Benzeneseleninato Ions and Ethylenediamine as Ligands. *Transition Metal Chemistry* 2: 232 – 236

Presti, M. L., Sayed, S. E., Martínez-Máñez, R., Costero, A. M., Gil, S., Parra, M. and Sancenón, F. 2016. Selective chromo-fluorogenic detection of trivalent cations in aqueous environments using a dehydration reaction. *New Journal of Chemistry* 40.11: 9042 – 9045

Qin, B., Zhang, X., Qiu, J., Gahungu, G., Yuan, H. and Zhang, J. 2021. Water-Robust Zinc-Organic Framework with Mixed Nodes and Its Handy Mixed-Matrix Membrane for Highly Effective Luminescent Detection of Fe^{3+}, CrO_4^{2-}, and $Cr_2O_7^{2-}$ in Aqueous Solution. *Inorganic Chemistry* 60.3: 1716 – 1725

Qin, J-C., Cheng, X-y., Fang, R., Wang, M-f., Yang, Z-y., Li, T-r., Li, Y. 2016. Two Schiff-base fluorescent sensors for selective sensing of aluminum(III): Experimental and computational studies. *Spectrochimica Acta Part A: Molecular and Biomolecular Spectroscopy* 152: 352 – 357

Radhakrishnan, K., Sivanesan, S., Panneerselvam, P. 2020. Turn-On fluorescence sensor based detection of heavy metal ion using carbon dots@graphitic-carbon nitride nanocomposite probe. *Journal of Photochemistry and Photobiology A: Chemistry* 389: 112204 https://doi.org/10.1016/j.jphotochem.2019.112204

Rahman, G. T.; Md. Kudrat-E-Zahan; Haque, M. M.; Md. Alam, Md. M.; Farooque, Md. A. 2015. Structural analysis of newly synthesized NO donor Schiff base complexes of Cu(II), Ni(II), Co(II) and Fe(II) metal ions by conventional method. *Science Journal of Chemistry* 3.6: 91 – 94

Rajakannu, P., Kim, H. S., Lee, W., Kumar, A., Lee, M. H. and Yoo, S. 2020. Naphthalene Benzimidazole Based Neutral Ir(III) Emitters for Deep Red Organic Light-Emitting Diodes. *Inorganic Chemistry* 59.17: 12461 – 12470

Ravikumar, I. and Ghosh, P. 2011. Zinc(II) and PPi Selective Fluorescence OFF–ON–OFF Functionality of a Chemosensor in Physiological Conditions. *Inorganic Chemistry* 50.10: 4229 – 4231

Realista, S., Fitzpatrick, A. J., Santos, G., Ferreira, L. P., Barroso, S., Pereira, L. C. J., Bandeira, N. A. G., Neugebauer, P., Hrubý, J., Morgan, G. G., van Slageren, J., Calhorda, M. J. and Martinho, P. N. 2016. A Mn(III) single ion magnet with tridentate Schiff-base ligands. *Dalton Transactions* 45.31: 12301 – 12307

Ren, T-B., Xu, W., Zhang, W., Zhang, X-X., Wang, Z-Y., Xiang, Z., Yuan, L. and Zhang, X-B. 2018. A General Method To Increase Stokes Shift by Introducing Alternating Vibronic Structures. *Journal of the American Chemical Society* 140.24: 7716 – 7722

Renak, M. L., Bartholomew, G. P., Wang, S., Ricatto, P. J., Lachicotte, R. J. and Bazan, G. C. 1999. Fluorinated Distyrylbenzene Chromophores: Effect of Fluorine Regiochemistry on Molecular Properties and Solid-State Organization. *Journal of the American Chemical Society* 121.34: 7787 – 7799

Rigamonti, L., Forni, A., Pievo, R., Reedijk, J. and Pasini, A. 2011. Synthesis, crystal structures and magnetic properties of dinuclear copper(II) compounds with NNO tridentate Schiff base ligands and bridging aliphatic diamine and aromatic diimine linkers. *Dalton Transactions* 40.13: 3381 – 3393

_____, Forni, A., Pievo, R., Reedijk, J., Pasini, A. 2012. Copper(II) compounds with NNO tridentate Schiff base ligands: Effect of subtle variations in ligands on complex formation, structures and magnetic properties. *Inorganic Chimica Acta* 387: 373 – 382

Rodriguez, A., Sakiyama, H., Masciocchi, N., Galli, S., Gálvez, N., Lloret, F. and Colacio, E. 2005. Hexacyanocobaltate(III) Anions as Precursors of Co(II)-Ni(II) Cyano-Bridged Multidimensional Assemblies: Hydrothermal Syntheses, Crystal and Powder X-ray Structures, and Magnetic Properties. *Inorganic Chemistry* 44.23: 8399 – 8406

Romero, D. H., Heredia, V. E. T., García-Barradas, O., López, M. E. M., and Pavón, E. S. 2014. Synthesis of Imidazole Derivatives and Their Biological Activities. *Journal of Chemistry and Biochemistry* 2.2: 45 – 83

Rondeau, V., Jacqmin-Gadda, H., Commenges, D., Helmer, C. and Dartigues, J-F. 2009. Aluminum and Silica in Drinking Water and the Risk of Alzheimer's Disease or Cognitive Decline: Findings From 15-Year Follow-up of the PAQUID Cohort. *American Journal of Epidemiology* 169.4: 489 – 496.

Rosu, T., Pahontu, E., Maxim, C., Georgescu, R., Stanica, N., Gulea, A. 2011. Some new Cu(II) complexes containing an ON donor Schiff base: Synthesis, characterization and antibacterial activity. *Polyhedron* 30.1: 154 – 162.

Roth, A., Becher, J., Herrmann, C., Görls, H., Vaughan, G., Reiher, M., Klemm, D. and Plass, W. 2006. Trinuclear Copper(II) Complexes Derived from Schiff-Base Ligands Based on a 6-Amino-6-deoxyglucopyranoside: Structural and Magnetic Characterization. *Inorganic Chemistry* 45.25: 10066 – 10076

Roy, S. B., Rajak, K. K. 2017. A quinoline appended naphthalene derivative based AIE active "turn–on" fluorescent probe for the selective recognition of Al^{3+} and colourimetric sensor for Cu^{2+}: Experimental and computational studies. *Journal of Photochemistry and Photobiology A: Chemistry* 332: 505 – 514

_____, Mondal, J., Khuda-Bukhsh, A. R. and Rajak, K. K. 2016. A novel fluorene based ''turn on'' fluorescent sensor for the determination of zinc and cadmium: experimental and theoretical studies along with live cell imaging. *New Journal of Chemistry* 40.11: 9593 – 9608

Ryan, L. S., Gerberich, J., Haris, U., Nguyen, D., Mason, R. P. and Lippert, A. R. 2020. Ratiometric pH Imaging Using a 1,2-Dioxetane Chemiluminescence Resonance Energy Transfer Sensor in Live Animals. *ACS Sensors* 5.9: 2925 – 2932

Saha, D., Das, S., Karmakar, S., Dutta S. and Baitalik, S. 2013. Synthesis, structural characterization and anion-, cation and solvent-induced tuning of photophysical properties of a bimetallic Ru(II) complex: combined experimental and DFT/TDDFT investigation. *RSC Advances* 3.38: 17314 – 17334

Sahoo, S. K. and Crisponi, G. 2019. Recent Advances on Iron(III) Selective Fluorescent Probes with Possible Applications in Bioimaging. *Molecules* 24.18: 3267 https://dx.doi.org/10.3390/molecules24183267

Sajoto, T., Djurovich, P. I., Tamayo, A., Yousufuddin, M., Bau, R., Thompson, M. E., Holmes, R. J. and Forrest, S. R. 2005. Blue and Near-UV Phosphorescence from Iridium Complexes with Cyclometalated Pyrazolyl or N-Heterocyclic Carbene Ligands. *Inorganic Chemistry* 44.22: 7992 – 8003

Saluja, P., Bhardwaj, V. K., Pandiyan, T., Kaur, S., Kaur, N., and Singh, N. 2014. Imine-linked chemosensors for the detection of Zn^{2+} in biological samples. *RSC Advances* 4.19: 9784 – 9790

Samanta, S., Goswami, S., Ramesh, A., Das, G. 2014. A new fluorogenic probe for solution and intra-cellular sensing of trivalent cations in model human cells. *Sensors and Actuators B: Chemical* 194: 120 – 126

_____, Ray, T., Haque, F., Das, G. 2016. A turn-on Rhodamine B-indole based fluorogenic probe for selective sensing of trivalent ions. *Journal of Luminescence* 71: 13 – 18

_____, Sarkar, S., Pal, R., and Mallik, A. K. 2013. An Efficient and Green Method for Synthesis of 2,4,5-Triarylimidazoles without Use of Any Solvent, Catalyst, or Solid Surface. *Organic Chemistry International* Volume 2013.Article ID 512074: 5 pages https://doi.org/10.1155/2013/512074

Sangireddy, S., Okekeogbu, I., Ye, Z., Zhou, S., Howe, K. J., Fish, T. and Thannhauser, T. W. 2017. Effects of Al^{3+} and La^{3+} Trivalent Metal Ions on Tomato Fruit Proteomes. *Proteomes* 5.1: 7. https://dx.doi.org/10.3390/proteomes5010007

Santos, F. da S., da Silveira, C. H., Nunes, F. S., Ferreira, D. C., Victória, H. F. V., Krambrock, K., Chaves, O. A., Rodembusch, F. S. and Iglesias, B. A. 2020. Photophysical, photodynamical, redox properties and BSA interactions of novel isomeric tetracationic peripheral palladium(II)-bipyridyl porphyrins. *Dalton Transactions* 49.45: 16278 – 16295

Sarala, L., Merlin, J. P., and Elanthamilan, E. 2016. Catalyst free synthesis of imidazoles: Characterization and its antimicrobial activity. *Journal of Chemical and Pharmaceutical Research* 8.8: 255 – 258

Sarper, O., Sarkar, B., Fiedler, J., Lissner, F., Kaim, W. 2010. Organoosmium complexes of imidazole-containing chelate acceptor ligands. *Inorganic Chimica Acta* 363.12: 3070 – 3077

Sawada, T., Fukumaru, K. Sakurai, H. 1996. Coordination-Dependent ESR Spectra of Copper(II) Complexes with a CuN_4 Type Coordination Mode: Relationship between ESR Parameters and Stability Constants or Redox Potentials of the Complexes. *Chemical and Pharmaceutical Bulletin* 44.5: 1009 – 1016

Schultz, B. E., Ye, B-H., Li, X-y., and Chan, S. I. 1997. Electronic Paramagnetic Resonance and Magnetic Properties of Model Complexes for Binuclear Active Sites in Hydrolase Enzymes. *Inorganic Chemistry* 36.12: 2617 – 2622

Schuman, A. J., Raghavan, A., Banziger, S. D., Song, Y., Hu, Z-B., Mash, B. L., Williams, A. L. and Ren, T. 2021. Macrocyclic Chromium(III) Catecholate Complexes. *Inorganic Chemistry* 60.7: 4447 – 4455

Semenaka, V. V., Nesterova, O. V., Kokozay, V. N., Dyakonenko, V. V., Zubatyuk, R. I., Shishkin, O. V., Boča, R., Jezierska, J. and Ozarowski, A. 2010. Cr^{III}-Cr^{III} Interactions in Two Alkoxo-Bridged Heterometallic Zn_2Cr_2 Complexes Self-Assembled from Zinc Oxide, Reinecke's Salt, and Diethanolamine. *Inorganic Chemistry* 49.12: 5460 – 5471

Sessoli, R., Tsai, H-L., Schake, A. R., Wang, S., Vincent, J. B., Foiling, K., Gatteschi, D., Christou, G. and Hendrickson, D. N. 1993. High-Spin Molecules: $[Mn_{12}O_{12}(O_2CR)_{16}(H_2O)_4]$. *Journal of the American Chemical Society* 115.5: 1804 – 1816

Shahid, M., Shamshad, S., Rafiq, M., Khalid, S., Bibi, I., Niazi, N. K., Dumat, C., Rashid, M. I. 2017. Chromium speciation, bioavailability, uptake, toxicity and detoxification in soil-plant system: A review. *Chemosphere* 178: 513 – 533

Sheldrick, G. M. 2002. SADABS, Bruker-AXS Inc., Madison, WI, U.S.A.

_____. 2008. A short history of SHELX. *Acta Crystallographica Part A: Foundations and Advances*, 64.1:112 – 122

Shen, L., Hu, P., Yang, X-J., Xu, H., Huang, Y-L., Redshaw, C., Zhang, Q-L. 2022. Structural and magnetic characterization of tetranuclear $[Ni(II)_2Ln(III)_2]$ complexes bearing tetra-branched Schiff base ligands. *Polyhedron* 212: 115584. https://doi.org/10.1016/j.poly.2021.115584

Sherstobitova, T., Maryunina, K., Tolstikov, S., Letyagin, G., Romanenko, G., Nishihara, S. and Inoue, K. 2019. Ligand Structure Effects on Molecular Assembly and Magnetic Properties of Copper(II) Complexes with 3-Pyridyl-Substituted Nitronyl Nitroxide Derivatives. *ACS Omega* 4.17: 17160 – 17170

Shi, C., Li, F., Li, Q., Zhao, W., Cao, Y., Zhao, Q. and Yuan, A. 2021. B- and N-Embedded π-Conjugation Units Tuning Intermolecular Interactions and Optical Properties of Platinum(II) Complexes. *Inorganic Chemistry* 60.2: 525 – 534

Shi, J-M., Sun, Y-M., Liu, Z., Liu, L-D., Shi, W. and Cheng, P. 2006. Synthesis, crystal structure, magnetic properties and theoretical studies on a one-dimensional polynuclear copper(II) complex $[Cu_2(\mu_{1,3}\text{-}SCN)_2(\mu'_{1,3}\text{-}SCN)_2(MPyO)_2]_n$. *Dalton Transactions* 2006.2: 376 – 380

Shigemoto, A. K., Killjoy, A. A., Dayton, J., Virca, C. N. and McCormick, T. M. 2020. Increased binding of thiophene-based ligands to mercury(II) with water solubilizing functional
groups. *Molecular Systems Design & Engineering* 5.6: 1024 – 1036

Shrestha, S. and Maharjan, S. 2012. Synthesis and Characterization of Copper Complexes of Salicylaldehyde Benzoyl Hydrazone. *Journal of Nepal Chemical Society* 29: 11 – 17

Si, Y., Xu, L., Deng, T., Zheng, J. and Li, J. 2020. Catalytic Hairpin Self-Assembly-Based SERS Sensor Array for the Simultaneous Measurement of Multiple Cancer-Associated miRNAs. *ACS Sensors* 5.12: 4009 – 4016

Siamaki, A. R. and Arndtsen, B. A. 2006. A Direct, One Step Synthesis of Imidazoles from Imines and Acid Chlorides: A Palladium Catalyzed Multicomponent Coupling Approach. *Journal of the American Chemical Society* 128.18: 6050 – 6051

Simon, T., Shellaiah, M., Srinivasadesikan, V., Lin, C-C., Ko, F-H., Sun, K. W., Lin, M-C. 2016. A simple pyrene based AIEE active schiff base probe for selective naked eye and fluoresence off–on detection of trivalent cations with live cell application. *Sensors and Actuators B: Chemical* 231: 18 – 29

Singh, A., Singh, J., Singh, N., Jang, D. O. 2015. A benzimidazolium-based mixed organic-inorganic polymer of Cu(II) ions for highly selective sensing of phosphates in water: applications for detection of harmful organophosphates. *Tetrahedron* 71.36: 6143 – 6147

_____, Singh, R., Shellaiah, M., Prakash, E. C., Chang, H-C., Raghunath, P., Lin, M-C., Lin, H-C. 2015. A new pyrene-based aggregation induced ratiometric emission probe for selective detections of trivalent metal ions and its living cell application. *Sensors and Actuators B: Chemical* 207.Part A: 338 – 345

Singh, A. K., Gupta, V. K., Gupta, B. 2007. Chromium(III) selective membrane sensors based on Schiff bases as chelating ionophores. *Analytical Chimica Acta* 585.1: 171 – 178

Singh, V. P. 2008. Synthesis, electronic and ESR spectral studies on copper(II) nitrate complexes with some acylhydrazines and hydrazones. *Spectrochimica Acta Part A: Molecular and Biomolecular Spectroscopy* 71.1: 17 – 22

_____, Singh, S., Singh, D. P., Tiwari, K., Mishra, M. 2014. Synthesis, spectroscopic (electronic, IR, NMR and ESR) and theoretical studies of transition metal complexes with some unsymmetrical Schiff bases. *Journal of Molecular Structure* 1058: 71 – 78

Sinha, S., Chowdhury, B., Ghorai, U. K. and Ghosh, P. 2019. Multitasking behaviour of a small organic compound: solid state bright white-light emission, mechanochromism and ratiometric sensing of Al(III) and pyrophosphate. *Chemical Communications* 55.35: 5127 – 5130

Sinha, W., Sommer, M. G., Deibel, N., Ehret, F., Bauer, M., Sarkar, B. and Kar, S. 2015. Experimental and Theoretical Investigations of the Existence of Cu^{II}, Cu^{III}, and Cu^{IV} in Copper Corrolato Complexes. *Angewandte Chemie International Edition* 54.46: 13769 – 13774

Sívek, R., Bureš, F., Pytela, O., and Kulhánek, J. 2008. Imidazole-based Potential Bi- and Tridentate Nitrogen Ligands: Synthesis, Characterization and Application in Asymmetric Catalysis. *Molecules* 13.9: 2326 – 2339

Smith, A. G., Shuford, K. L. 2017. Electronic effects on a D-π-A organic sensitizer upon heteroatom substitutions in the π-bridge. *Journal of Photochemistry and Photobiology A: Chemistry* 332: 580 – 585

Smolko, L., Černák, J., Kuchár, J., Rajnák, C., Titiš, J. and Boča, R. 2017. Field-Induced Slow Magnetic Relaxation in Mononuclear Tetracoordinate Co(II) Complexes Containing Neocuproine Ligand. *European Journal of Inorganic Chemistry* 2017.24: 3080 – 3086

Solomatina, A. I., Kuznetsov, K. M., Gurzhiy, V. V., Pavlovskiy, V. V., Porsev, V. V., Evarestov, R. A. and Tunik, S. P. 2020. Luminescent organic dyes containing a phenanthro[9,10-*D*]imidazole core and $[Ir(N\hat{}C)(N\hat{}N)]^+$ complexes based on the cyclometalating and diimine ligands of this type. *Dalton Transactions* 49.20: 6751 – 6763

Song, E. J., Kang, J., You, G. R., Park, G. J., Kim, Y., Kim, S-J., Kim, C. and Harrison, R. G. 2013. A single molecule that acts as a fluorescence sensor for zinc and cadmium and a colorimetric sensor for cobalt. *Dalton Transactions* 42.43: 15514 – 15520

_____, Kim, H., Hwang, I. H., Kim, K. B., Kim, A. R., Noh, I., Kim, C. 2014. A single fluorescent chemosensor for multiple target ions: Recognition of Zn^{2+} in 100% aqueous solution and F^- in organic solvent. *Sensors and Actuators B: Chemical* 195: 36 – 43

Spillecke, L., Tripathi, S., Koo, C., Bahr, A., Swain, A., Haldar, R., Ansari, M., Jasinski, J., Rajaraman, G., Shanmugam, M. and Klingeler, R. 2022. Role of Coordination Geometry on the Magnetic Relaxation Dynamics of Isomeric Five-Coordinate Low-Spin Co(II) Complexes. *Inorganic Chemistry* 61.1: 317 – 327

Sreenivasulu, B., Vetrichelvan, M., Zhao, F., Gao, S. and Vittal, J. J. 2005. Copper(II) Complexes of Schiff-Base and Reduced Schiff-Base Ligands: Influence of Weakly Coordinating Sulfonate Groups on the Structure and Oxidation of 3,5-DTBC. *European Journal of Inorganic Chemistry* 2005.22: 4635 – 4645

Su, J., Duan, L. and Zheng, W. 2016. Chromium(III) complexes with 1,2,4-diazaphospholide and 2,6-bis(N-1,2,4-diazaphosphol-1-yl)pyridine ligands: synthesis, X-ray structural characterization, EPR spectroscopy analysis, and magnetic susceptibility studies. *Zeitschrift für Naturforschung* 71.7b: 795 – 802

Su, Z., Wang, Z-B., and Sun, W-Y. 2011. Syntheses, structures, and properties of lead(II) and nickel(II) complexes with 3,5-di(1*H*-imidazol-1-yl)benzoate. *Journal of Coordination Chemistry* 64.1: 170 – 178

Suban, K. S., Rati, K. B., Bikram, K. K., Minati, B. 2009. Excited State Intramolecular Proton Transfer in Methyl and Methoxy Substituted Salicylic Acid. *Chinese Journal of Chemistry* 27.10: 1897 – 1902

Sukpattanacharoen, C., Kumar, P., Chi, Y., Kungwan, N. and Escudero, D. 2020. Formation of Excimers in Isoquinolinyl Pyrazolate Pt(II) Complexes: Role of Cooperativity Effects. *Inorganic Chemistry* 59.24: 18253 – 18263

Sun, J., Wang, K., Jing, P., Lu, J. and Li, L. 2019. 2p-3d-4f Heterotrispin Chains and Ring-Chains Bridged by a Nitronyl Nitroxide Ligand: Structure and Magnetic Properties. *Crystal Growth & Design* 19.6: 3576 – 3583

Sun, Y-Q., Gao, D-Z., Ma, Y., Yang, G-M., Liao, D-Z. and Yan, S-P. 2009. Structure and Magnetism of two Polynuclear Complexes Containing both Macrocyclic and Azido Ligands. *Zeitschrift für anorganische und allgemeine Chemie* 635.15: 2682 – 2687

Sunitha, M., Jogi, P., Ushaiah, B., and Kumari, C. G. 2012. Synthesis, Characterization and Antimicrobial Activity of Transition Metal Complexes of Schiff Base Ligand Derived from 3-Ethoxy Salicylaldehyde and 2-(2-Aminophenyl) 1-*H*-benzimidazole. *E-Journal of Chemistry* 9.4: 2516 – 2523

Sushila., Dhamija, S., Patra, M., Pécaut, J., Kataria, R., Goswami, S., Bhowmik, S., Patra, R. 2022. Probing the structural features and magnetic behaviors in dinuclear cobalt(II) and trinuclear iron(III) complexes. *Inorganic Chimica Acta* 535: 120852. https://doi.org/10.1016/j.ica.2022.120852

Sutradhar, M., Kirillova, M. V., da Silva, M. F. C. G., Liu, C-M. and Pombeiro, A. J. L. 2013. Tautomeric effect of hydrazone Schiff bases in tetranuclear Cu(II) complexes: magnetism and catalytic activity towards mild hydrocarboxylation of alkanes. *Dalton Transactions* 42.47: 16578 – 16587

Suzuki, N., Suda, K., Yokogawa, D., Kitoh-Nishioka, H., Irle, S., Ando, A., Abegão, L. M. G., Kamada, K., Fukazawa, A. and Yamaguchi, S. 2018. Near infrared two-photon-excited and -emissive dyes based on a strapped excited-state intramolecular proton-transfer (ESIPT) scaffold. *Chemical Sciences* 9.10: 2666 – 2673

Tada, M. and Shino, R. 1991. The Interaction Between Cobalt(II) Complexes and Sulphur Compounds Studied by ESR Spectroscopy. *Journal of Inorganic Biochemistry* 44.2: 89 – 95

Tajima, K., Tada, K., Jinno, J., Edo, T., Mano, H., Azuma, N., Makino, K. 1997. Mechanisms for the formation of six-coordinate Fe(III)TPP-peroxide complexes studied by simultaneous ESR and optical measurements. *Inorganic Chimica Acta* 254.1: 29 – 35

Tang, X., Han, J., Wang, Y., Ni, L., Bao, X., Wang, L., Zhang, W. 2017. A multifunctional Schiff base as a fluorescence sensor for Fe^{3+} and Zn^{2+} ions, and a colorimetric sensor for Cu^{2+} and applications. *Spectrochimica Acta Part A: Molecular and Biomolecular Spectroscopy* 173: 721 – 726

Thakurta, S., Roy, P., Butcher, R. J., El Fallah, M. S., Tercero, J., Garribba, E. and Mitra, S. 2009. Ferromagnetic Coupling in a New Copper(II) Schiff Base Complex with Cubane Core: Structure, Magnetic Properties, DFT Study and Catalytic Activity. *European Journal of Inorganic Chemistry* 2009.29-30: 4385 – 4395

Thanayupong, E., Suttisintong, K., Sukawattanasinitt, M., Niamnont, N. 2017. Turn-on Fluorescence Sensor for Detection of Cyanide based a novel dicyanovinyl phenylacetylene. *New Journal of Chemistry* 41.10: 4058 – 4064

Thapa, P., Byrnes, N. K., Denisenko, A. A., Mao, J. X., McDonald, A. D., Newhouse, C. A., Vuong, T. T., Woodruff, K., Nam, K., Nygren, D. R., Jones, B. J. P. and Foss, Jr., F. W. 2021. Demonstration of Selective Single-Barium Ion Detection with Dry Diazacrown Ether Naphthalimide Turn-on Chemosensors. *ACS Sensors* 6.1: 192 – 202

Thet, N. T., Mercer-Chalmers, J., Greenwood, R. J., Young, A. E. R., Coy, K., Booth, S., Sack, A. and Jenkins, A. T. A. 2020. *SPaCE Swab*: Point-of-Care Sensor for Simple and Rapid Detection of Acute Wound Infection. *ACS Sensors* 5.8: 2652 – 2657

Thompson, A. M. W. C., Gatteschi, D., McCleverty, J. A., Navas, J. A., Rentschler, E. and Ward, M. D. 1996. Effects of Systematic Variation in Bridging Ligand Structure on the Electrochemical and Magnetic Properties of a Series of Dinuclear Molybdenum Complexes. *Inorganic Chemistry* 35.9: 2701 – 2703

Thompson, L. K., Ramaswamy, B. S. and Seymor, E. A. 1977. Cobalt(II) and zinc(II) complexes of the 'tripod' ligand tris(2-benzimidazylmethy1)amine. Some five-coordinate derivatives and some with mixed stereochemistries. *Canadian Journal of Chemistry* 55: 878 – 888

Tian, L., Xue, J., Yang, Z-y. 2018. A simple quinoline derivative as fluorescent probe with high sensitivity and selectivity for Al^{3+} in aqueous solution. *Tetrahedron Letters* 59.46: 4110 – 4115

Timmer, B. J. J., Kravchenko, O., Zhang, B., Liu, T. and Sun, L. 2021. Electronic Influence of the 2,2′-Bipyridine-6,6′-dicarboxylate Ligand in Ru-Based Molecular Water Oxidation Catalysts. *Inorganic Chemistry* 60.2: 1202 – 1207

Tomkowicz, Z., Ostrovsky, S., Foro, S., Calvo-Perez, V. and Haase, W. 2012. Magnetooptical and Structural Investigations of Five Dimeric Cobalt(II) Complexes Mimicking Metalloenzyme Active Sites. *Inorganic Chemistry* 51.11: 6046 – 6055

Tora, G., Degnan, A. P., Conway, C. M., Kostich, W. A., Carl D. Davis, C. D., Pin, S. S., Schartman, R., Xu, C., Widmann, K. A., John E. Macor, J. E., Dubowchik, G. M. 2013. Preparation of imidazoles as potent calcitonin gene-related peptide (CGRP) antagonists. *Bioorganic & Medicinal Chemistry Letters* 23.20: 5684 – 5688

Török, I., Gajda, T., Gyurcsik, B., Tóth, G. K., and Péter, A. 1998. Metal complexes of imidazole ligands containing histamine-like donor sets: equilibrium, solution structure and hydrolytic activity. *Journal of the Chemical Society, Dalton Transactions* 1998.7: 1205 – 1212

Tortajada, A., Correia, J. T. M., Serrano, E., Monleón, A., Tampieri, A., Craig S. Day, C. S., Juliá-Hernández, F. and Martin, R. 2021. Ligand-Controlled Regiodivergent Catalytic Amidation of Unactivated Secondary Alkyl Bromides. *ACS Catalysis* 11.16: 10223 – 10227

Treto-Súarez, M. A., Hidalgo-Rosa, Y., Schott, E., Zarate, X. and Páez-Hernández, D. 2019. Understanding the Selective-Sensing Mechanism of Al^{3+} Cation by a Chemical Sensor Based on Schiff Base: A Theoretical Approach. *Journal of Physical Chemistry A* 123.32: 6970 – 6977

Tudor, V., Marin, G., Lloret, F., Kravtsov, V. Ch., Simonov, Y. A., Julve, M., Andruh, M. 2008. New alkoxo-bridged mixed-valence cobalt clusters: Synthesis, crystal structures and magnetic properties. *Inorganic Chimica Acta* 361.12-13: 3446 – 3452

Tuna, F., Patron, L., Journaux, Y., Andruh, M., Plass, W. and Trombe, J-C. 1999. Synthesis and magnetic properties of a series of bi- and tri-nuclear complexes of copper(II) with the unsymmetrical tetradentate Schiff-base ligand 3-[*N*-2-(pyridylethyl)formimidoyl]salicylic acid, H_2fsaaep, and crystal structures of [{Cu(Hfsaaep)Cl}$_2$] and [{Cu(fsaaep)(H_2O)}$_2$]. *Journal of the Chemical Society, Dalton Transactions* 1999.4: 539 – 545

_____, Patron, L., Rivière, E., Boillot, M-L. 2000. Magnetic and spectral properties of two five-coordinate Lewis-base adducts of cobalt(II) Schiff-base complexes with a N_3O_2 ligand environment. *Polyhedron*, 19.13: 1643 – 1648

Turner, R. J. 2017. Metal-based antimicrobial strategies. *Microbial Biotechnology*, 10.5: 1062 – 1065

Ubani, O. C., Oforka, N. C., Ngochindo, R. I. and Odokuma. L. O. 2015. Synthesis, Characterization and Antimicrobial Studies of Cinnamaldehydebenzylamine Schiff base Metal ion Complexes. *Research Journal of Chemical Sciences* 5.3: 14 – 22

Udhayakumari, D., Velmathi, S. 2013. Colorimetric and fluorescent sensor for selective sensing of Hg^{2+} ions in semi aqueous medium. *Journal of Luminescence* 136: 117 – 121

Ulatowski, F., Dąbrowa, K., Bałakier, T. and Jurczak, J. 2016. Recognizing the Limited Applicability of Job Plots in Studying Host-Guest Interactions in Supramolecular Chemistry. *Journal of Organic Chemistry* 81.5: 1746 – 1756

Upadhyay, K. K. and Kumar, A. 2010. Pyrimidine based highly sensitive fluorescent receptor for Al^{3+} showing dual signalling mechanism. *Organic & Biomolecular Chemistry* 8.21: 4892 – 4897

Urano, Y. 2008. Sensitive and Selective Tumor Imaging with Novel and Highly Activatable Fluorescence Probes. *Analytical Sciences* 24.1: 51 – 53

Valle, S. R., Carrasco, J., Pinochet, D., Calderini, D. F. 2009. Grain yield, above-ground and root biomass of Al-tolerant and Al-sensitive wheat cultivars under different soil aluminum concentrations at field conditions. *Plant and Soil* 318: 299 – 310

Vallejo, J., Pascual-Álvarez, A., Cano, J., Castro, I., Julve, M., Lloret, F., Krzystek, J., De Munno, G., Armentano, D., Wernsdorfer, W., Ruiz-García, R. and Pardo, E. 2013. Field-Induced Hysteresis and Quantum Tunneling of the Magnetization in a Mononuclear Manganese(III) Complex. *Angewandte Chemie International Edition* 52.52: 14075 –14079

Varghese, S., Park, S. K., Casado, S., Fischer, R. C., Resel, R., Milián-Medina, B., Wannemacher, R., Park, S. Y. and Gierschner, J. 2013. Stimulated Emission Properties of Sterically Modified Distyrylbenzene-Based H-Aggregate Single Crystals. *Journal of Physical Chemistry Letters* 4.10: 1597 – 1602

Venkateswarulu, M., Mukherjee, T., Mukherjee, S. and Koner, R. R. 2014. Turn-on trivalent cation selective chemodosimetric probe to image native cellular iron pools. *Dalton Transactions* 43.14: 5269 – 5273

Vignesh, K. R., Langley, S. K., Murray K. S. and Rajaraman, G. 2017. Quenching Quantum Tunneling of Magnetization in Heterometallic Octanuclear {$TM^{III}_4Dy^{III}_4$} (TM = Co and Cr) Single-Molecule Magnets by Modification of the Bridging Ligands and Enhacing the Magnetic Exchange Coupling. *Chemistry A European Journal* 23.7: 1654 – 1666

_____, Soncini, A., Langley, S. K., Wernsdorfer, W., Murray, K. S. and Rajaraman, G. 2017. Ferrotoroidic Ground State in a Heterometallic $Cr^{III}Dy^{III}6$ Complex Displaying Slow Magnetic Relaxation. *Nature Communications* 8, 1023 https://doi.org/10.1038/s41467-017-01102-5

Visscher, A., Bachmann, S., Schnegelsberg, C., Teuteberg, T., Matac, R. A. and Stalke, D. 2016. Highly selective and sensitive fluorescence detection of Zn^{2+} and Cd^{2+} ions by using an acridine sensor. *Dalton Transactions* 45.13: 5689 – 5699

Wang, C., Han, Q., Liu, P., Zhang, G., Song, L., Zou, X. and Fu, Y. 2021. A Superstable Luminescent Lanthanide Metal Organic Gel Utilized in an Electrochemiluminescence Sensor for Epinephrine Detection with a Narrow Potential Sweep Range. *ACS Sensors* 6.1: 252 – 258

Wang, H., Cao, W., Liu, T., Duan, C. and Jiang, J. 2013. Synthesis, Structure, and Single-Molecule Magnetic Properties of Rare-Earth Sandwich Complexes with Mixed Phthalocyanine and Schiff Base Ligands. *Chemistry A European Journal* 19.7: 2266 – 2270

_____, Liu, C., Liu, T., Zeng, S., Cao, W., Ma, Q., Duan, C., Dou, J. and Jiang, J. 2013. Mixed (phthalocyaninato)(Schiff-base) di-dysprosium sandwich complexes. Effect of magnetic coupling on the SMM behavior. *Dalton Transactions* 42.43: 15355 – 15360

Wang, H-L., Peng, J-M., Zhu, Z-H., Mo, K-Q., Ma, X-F., Li, B., Zou, H-H and Liang, F-P. 2019. Step-by-Step and Competitive Assembly of Two Dy(III) Single-Molecule Magnets with Their Performance Tuned by Schiff Base Ligands. *Crystal Growth & Design* 19.9: 5369 – 5375

Wang, J., Li, Y., Duah, E., Paruchuri, S., Zhouc, D. and Pang, Y. 2014. A selective NIR-emitting zinc sensor by using Schiff base binding to turn-on excited-state intramolecular proton transfer. *Journal of Materials Chemistry B* 2.14: 2008 – 2012

_____, Li, Y., Patel, N. G., Zhang, G., Zhou, D. and Pang, Y. 2014. A single molecular probe for multi-analyte (Cr^{3+}, Al^{3+} and Fe^{3+}) detection in aqueous medium and its biological application. *Chemical Communications* 50.82: 12258 – 12261

_____, Wang, H., Ma, Y., Tang, J., Li, L., Wang, Q., Zhao, B., Cheng, P. and Ma, J. 2019. Enhancing Magnetic Behaviors of Dysprosium Single-Molecule Magnets from Crystal Field Perturbation by Deprotonating Schiff-Base Ligand. *Crystal Growth & Design* 19.6: 3365 – 3371

Wang, J-H., Gao, D-R., Wang, X-Y., Lu, Y-M., Shen, W-X., Lv, Y-Y. 2019. Near-infrared fluorescent probe for ratiometric Al^{3+} signaling and imaging through combined PET and ICT mechanisms. *Sensors and Actuators B: Chemical* 294: 14 – 23

Wang, L., Li, H., Cao, D. 2013. A new photoresponsive coumarin-derived Schiff base: Chemosensor selectively for Al^{3+} and Fe^{3+} and fluorescence "turn-on" under room light. *Sensors and Actuators B: Chemical* 181: 749 – 755

Wang, M., Liu, Z., Zhou, X., Xiao, H., You, Y. and Huang, W. 2020. Anthracene-Based Lanthanide Coordination Polymer: Structure, Luminescence, and Detections of UO_2^{2+}, PO_4^{3-}, and 2-Thiazolidinethione-4-carboxylic Acid in Water. *Inorganic Chemistry* 59.24: 18027 – 18034

Wang, Q., Gao, H-M., Xue, W-J., Chen, K-Y., Zhang, Q., Huang, M., Wang, R-F., Fan, W-L., Hua, Y-P., Fang, M. 2022. Four Ln_2 compounds constructed by a polydentate Schiff base ligand: Gd_2 compound displaying large magnetocaloric effect and Dy_2 compound showing single-molecule magnet behavior. *Polyhedron*, 212, 115578. https://doi.org/10.1016/j.poly.2021.115578

_____, Sun, H., Jin, L., Wang, W., Zhang, Z., Chen, Y. 2018. A novel turn on and reversible sensor for Al^{3+} and its applications in bioimaging. *Journal of Luminescence* 203: 113 – 120

Wang, S-Y., Wang, W-M., Zhang, H-X., Shen, H-Y., Jiang, L., Cui, J-Z and Gao, H-L. 2016. Seven phenoxido-bridged complexes encapsulated by 8-hydroxyquinoline Schiff base derivatives and β-diketone ligands: single-molecule magnet, magnetic refrigeration and luminescence properties. *Dalton Transactions* 45.8: 3362 – 3371

Wang, W-M., Gao, Y., Yue, R-X., Qiao, N., Wang, D-T., Shi, Y., Zhang, H. and Cui, J-Z. 2020. Construction of a family of Ln_3 clusters using multidentate Schiff base and β-diketonate ligands: fluorescence properties, magnetocaloric effect and slow magnetic relaxation. *New Journal of Chemistry* 44.22: 9230 – 9237

_____, Liu, H-H., He, L-T., Han, X-R., Wu, Z-L., Ran, Y-G., Zou, J-Y., Fang, M. 2017. Structures, luminescence properties, magnetocaloric effect and slow magnetic relaxation of three Ln(III) complexes based on 8 hydroxyquinoline Schiff-base ligand. *Polyhedron*, 133: 119 – 124

Wang, Y., Wu, H., Wu, W-N., Mao, X-J., Zhao, X-L., Xu, Z-Q., Xu, Z-H., Fan, Y-C. 2019. Novel rhodamine-based colorimetric and fluorescent sensor for the dual-channel detection of Cu^{2+} and Co^{2+}/trivalent metal ions and its AIRE activities. *Spectrochimica Acta Part A: Molecular and Biomolecular Spectroscopy* 212: 1 – 9

_____, Xu, Z., Dai, X., Li, H., Yu, S., Meng, W. 2019. A New Spiropyran-Based Sensor for Colorimetric and Fluorescent Detection of Divalent Cu^{2+} and Hg^{2+} Ions and Trivalent Ce^{3+}, Cr^{3+} and Al^{3+} Ions. *Journal of Fluorescence* 29: 569 – 575

Wang, Y-W., Liu, S-B., Ling, W-J. and Peng, Y. 2016. A fluorescent probe for relay recognition of homocysteine and Group IIIA ions including Ga(III). *Chemical Communications* 52.4: 827 – 830

Wei, L-Q., Zhang, K., Feng, Y-C., Wang, Y-H., Zeng, M-H. and Kurmoo, M. 2011. Microwave versus Traditional Solvothermal Synthesis of Ni_7^{II} Discs: Effect of Ligand on Exchange Reaction in Solution Studied by Electrospray Ionization-Mass Spectroscopy and Magnetic Properties. *Inorganic Chemistry* 50.15: 7274 – 7283

Wei, N., Murthy, N. N. and Karlin, K. D. 1994. Chemistry of Pentacoordinate $[LCu^{II}–Cl]^+$ Complexes with Quinolyl Containing Tripodal Tetradentate Ligands L. *Inorganic Chemistry* 33.26: 6093 – 6100

Wilbraham, L., Savarese, M., Rega, N., Adamo, C. and Ciofini, I. 2015. Describing Excited State Intramolecular Proton Transfer in Dual Emissive Systems: A Density Functional Theory Based Analysis. *Journal of Physical Chemistry B* 119.6: 2459 – 2466

Wolkenberg, S. E., Wisnoski, D. D., Leister, W. H., Wang, Y., Zhao, Z. and Lindsley, C. W. 2004. Efficient Synthesis of Imidazoles from Aldehydes and 1,2-Diketones Using Microwave Irradiation. *Organic Letters* 6.9: 1453 – 1456.

Wong, J. K.-H., Todd, M. H., and Rutledge, P. J. 2017. Recent Advances in Macrocyclic Fluorescent Probes for Ion Sensing. *Molecules* 22.2: 200. https://doi.org/10.3390/molecules22020200

Wong, R., Liu, D., Xu, K., Li, J. 2009. Substituent and solvent effects on excited state intramolecular proton transfer in novel 2-(2'-hydroxyphenyl)benzothiazole derivatives. *Journal of Photochemistry and Photobioliology A: Chemistry* 205.1: 61 – 69

Worku, M., Tian, Y., Zhou, C., Lin, H., Chaaban, M., Xu, L-j., He, Q., Beery, D., Zhou, Y., Lin, X., Su, Y-f., Xin, Y., Ma, B. 2020. Hollow metal halide perovskite nanocrystals with efficient blue emissions. *Science Advances* 6.17: eaaz5961 https://dx.org.doi/10.1126/sciadv.aaz5961

Wu, L., Jing, X., Zhu, H., Liu, Y., Yan, C. 2012. One-pot Synthesis of Polysubstituted Imidazoles from Arylaldehydes in Water Catalyzed by NHC Using Microwave Irradiation. *Journal of the Chilean Chemical Society* 57.3: 1204 – 1207

Wu, S-Q., Miyazaki, Y., Nakano, M., Su, S-Q., Yao, Z-S., Kou, H-Z. and Sato, O. 2017. Slow Magnetic Relaxation in a Mononuclear Ruthenium(III) Complex. *Chemistry A European Journal* 23.42: 10028 – 10033

Wu, X-M., Zhang, J-H., Feng, Z-S., Chen, W-X., Zhang, F. and Li, Y. 2020. An ultra-sensitive "turn-off" fluorescent sensor for the trace detection of rifampicin based on glutathione-stabilized copper nanoclusters. *Analyst* 145: 1227 – 1235

Wurzenberger, M. H. H., Gruhne, M. S., Lommel, M., Braun, V., Szimhardt, N. And Stierstorfer, J. 2020. Taming the Dragon: Complexation of Silver Fulminate with Nitrogen-Rich Azole Ligands. *Inorganic Chemistry* 59.24: 17875 – 17879

Xiang, J., Liu, J-J., Chen, X-X., Jia, L-H., Yu, F., Wang, B-W., Gao, S. and Lau, T-C. 2017. Slow Magnetic Relaxation in a Mononuclear 8-Coordinate Fe(II) Complex. *Chemical Communications* 53.9: 1474 – 1477

Xu, J., Zhang, Z., Gan, S., Gao, H., Kong, H., Song, Z., Ge, X., Bao, Y. and Niu, L. 2020. Highly-stretchable fiber-based potentiometric ion sensors for multichannel real-time analysis of human sweat. *ACS Sensors* 5.9: 2834 – 2842

Xu, K-x., Xie, X-m., Kong, H-j., Li, P., Zhang, J-l., Pang, X-b. 2014. Selective fluorescent sensors for malate anion using the complex of phenanthroline-based Eu(III) in aqueous solution. *Sensors and Actuators B*: *Chemical* 201: 131 – 137. https://doi.org/10.1016/j.snb.2014.04.086

Xu, Y., Zhang, D., Li, B., Zhang, Y., Sun, S. and Pang, Y. 2014. A near infrared fluorescent dye for trivalent ions sensing and working as a molecular keypad lock. *RSC Advances* 4.23: 11634 – 11639

Xue, C-L., Jing, R-Y., Ma, X., Yang, L-N., Chen, Y-Q., Bai, Y., Li, M-X., Yang, Z-P., Wu, Z-L. 2021. Larger magnetocaloric effect and single molecule magnet behavior in dinuclear Ln(III)-based compounds constructed from Schiff base ligand. *Inorganic Chimic Acta* 528: 120631. https://doi.org/10.1016/j.ica.2021.120631

Yamaguchi, Y., Matsubara, Y., Ochi, T., Wakamiya, T. and Yoshida, Z-i. 2008. How the π Conjugation Length Affects the Fluorescence Emission Efficiency. *Journal of the American Chemical Society*, 130.42: 13867 – 13869

Yamamoto, T., Kato, S., Aoki, D. and Otsuka, H. 2021. A Diarylacetonitrile as a Molecular Probe for the Detection of Polymeric Mechanoradicals in the Bulk State through a Radical Chain-transfer Mechanism. *Angewandte Chemie International Edition* 60.5: 2680 – 2683

_____ and Takimiya, K. 2007. Facile Synthesis of Highly π-Extended Heteroarenes, Dinaphtho[2,3-*b*:2′,3′-*f*]chalcogenopheno[3,2-*b*]chalcogenophenes, and Their Application to Field-Effect Transistors. *Journal of the American Chemical Society* 129.8: 2224 – 2225

Yamanoi, Y., Nakashima, T., Shimad, M., Maeda, H. and Nishihara, H. 2016. Effects of substitution on solid-State fluorescence in 9-Aryl-9-methyl-9H-9-silafluorenes. *Molecules* 21.9: 1173. https://doi.org/10.3390/molecules21091173

Yamashita, H. and Abe, J. 2014. Pentaarylbiimidazole, PABI: an easily synthesized fast photochromic molecule with superior durability. *Chemical Communications* 50.62: 8468 – 8471

Yamazaki, Y., Tsukuda, T., Furukawa, S., Dairiki, A., Sawamura, S. and Tsubomura, T. 2020. A Series of Mixed-Ligand Cu(I) Complexes Comprising Diphosphine-Disulfide Ligands: Effects of Diphosphine Ligands on Luminescent Properties. *Inorganic Chemistry* 59.17: 12375 – 12384

Yang, H., Liu, S-S., Meng, Y-S., Zhang, Y-Q., Pu, L., Wang, X. and Lin, S. 2022. Four mononuclear dysprosium complexes with neutral Schiff-base ligands: syntheses, crystal structures and slow magnetic relaxation behaviour. *Dalton Transactions* 51.4: 1415 – 1422

Yang, Y., Zhao, J. and Li, Y. 2016. Theoretical Study of the ESIPT Process for a New Natural Product Quercetin. *Scientific Reports* 6: 32152. https://doi.org/10.1038/srep32152

Yannone, S. M., Hartung, S., Menon, A. L., Adams, M. W. W. and Tainer, J. A. 2012. Metals in biology: defining metalloproteomes. *Current Opinion in Biotechnology*, 23: 89 – 95.

Yao, W., Cao, Y., She, M., Yan, Y., Li, J., Leng, X., Liu, P., Zhang, S. and Li, J. 2021. Imaging and Monitoring the Hydrogen Peroxide Level in Heart Failure by a Fluorescent Probe with a Large Stokes Shift. *ACS Sensors* 6.1: 54 – 62

Yimer, A. M. 2015. Review on Preparation and Description of Some First Series Divalent Transition Metal Complexes with Novel Schiff's Base Ligands. *Review of Catalysts* 2.1: 14 – 25

Youngme, S., Cheansirisomboon, A., Danvirutai, C., Pakawatchai, C., Chaichit, N., Engkagul, C., van Albada, G. A., Costa, J. S., Reedijk, J. 2008. Three new polynuclear tetracarboxylato-bridged copper(II) complexes: Syntheses, X-ray structure and magnetic properties. *Polyhedron* 27.7: 1875 – 1882

Yu, S., Hu, Z., Chen, Z., Li, B., Zhang, Y-Q., Liang, Y., Liu, D., Yao, D. and Liang, F. 2019. Two Dy(III) Single-Molecule Magnets with Their Performance Tuned by Schiff Base Ligands. *Inorganic Chemistry* 58.2: 1191 – 1200

Yuan, M., Zhao, F., Zhang, W., Wang, Z-M and Gao, S. 2007. Azide-Bridged One-Dimensional Mn^{III} Polymers: Effects of Side Group of Schiff Base Ligands on Structure and Magnetism. *Inorganic Chemistry* 46.26: 11235 – 11242

Yue, X-l., Wang, Z-q., Li, C-r., Yang, Z-y. 2018. A highly selective and sensitive fluorescent chemosensor and its application for rapid on-site detection of Al^{3+}. *Spectrochimica Acta Part A: Molecular and Biomolecular Spectroscopy* 193: 415 – 421

Yue, Y-F., Gao, E-Q., Fang, C-J., Zheng, T., Liang, J. and Yan, C-H. 2008. Three Azido-Bridged Mn(II) Complexes Based on Open-Chain Diazine Schiff-base Ligands: Crystal Structures and Magnetic Properties. *Crystal Growth & Design* 8.9: 3295 – 3301

Yuste, C., Bentama, A., Stiriba, S-E., Armentano, D., De Munno, G., Lloret, F. and Julve, M. 2007. Ligand effects on the structures and magnetic properties of tricyanomethanide-containing copper(II) complexes. *Dalton Transactions* 2007.44: 5190 – 5200

Zadrozny, J. M., Xiao, D. J., Atanasov, M., Long, G. J., Grandjean, F., Neese, F. and Long, J. R. 2013. Magnetic blocking in a linear iron(I) complex. *Nature Chemistry* 5: 577 – 581

Zaman, S., Mitsuru, K. and Abell, A. D. 2005. Synthesis of Trisubstituted Imidazoles by Palladium-Catalyzed Cyclization of *O*-Pentafluorobenzoylamidoximes: Application to Amino Acid Mimetics with a C-Terminal Imidazole. *Organic Letters* 7.4: 609 – 611

Zeng, M-H., Gao, S., Chen, X-M. 2004. A novel 3D coordination polymer containing pentacoordinate cobalt(II) dimers with antiferromagnetic ordering. *Inorganic Chemistry Communications* 7.7: 864 – 867

Zeng, S., Li, S-J., Liu, T-T., Sun, X-J., Xing, Z-Y. 2019a. A significant fluorescent "turn-on" chemosensor for Al^{3+} detection and application in real sample, logic gate and bioimaging. *Inorganic Chimica Acta* 495: 118962. https://doi.org/10.1016/j.ica.2019.118962

_____, Li, S-J., Sun, X-J., Li, M-Q., Xing, Z-Y., Li, J-L. 2019b. A benzothiazole-based chemosensor for significant fluorescent turn-on and ratiometric detection of Al^{3+} and its application in cell imaging. *Inorganic Chimica Acta* 486: 654 – 662. https://doi.org/10.1016/j.ica.2018.11.042

Zhai, Y-Q., Ge, N., Li, Z-H., Chen, W-P., Han, T., Ouyang, Z-W., Wang, Z. and Zheng, Y-Z. 2021. Magnetic Anisotropy: Structural Correlation of a Series of Chromium(II)-Amidinate Complexes. *Inorganic Chemistry* 60.3: 1344 – 1351

Zhan, Z., Jia, Y., Li, D., Zhang, X. and Hu, M. 2019a. A water-stable terbium-MOF sensor for the selective, sensitive, and recyclable detection of Al^{3+} and CO_3^{2-} ions. *Dalton Transactions* 48.40: 15255 – 15262

_____, Liang, X., Zhang, X., Jia, Y. and Hu, M. 2019b. A water-stable europium-MOF as a multifunctional luminescent sensor for some trivalent metal ions (Fe^{3+}, Cr^{3+}, Al^{3+}), PO_4^{3-} ions, and nitroaromatic explosives. *Dalton Transactions* 48.5: 1786 – 1794

Zhang, C., Sun, L., Yan, Y., Li, J., Song, X., Liu, Y. and Liang, Z. 2015. A luminescent cadmium metal–organic framework for sensing of nitroaromatic explosives. *Dalton Transactions* 44.1: 230 – 236

Zhang, K., Li, H., Wang, W., Cao, J., Gan, N. and Han, H. 2020. Application of Multiplexed Aptasensors in Food Contaminants Detection. *ACS Sensors* 5.12: 3721 – 3738

Zhang, L. and Liu, F. 2017. Synthesis of Bisimidazole Derivatives for Selective Sensing of Fluoride Ion. *Molecules* 22.9: 1519; https://doi.org/10.3390/molecules22091519

_____, Peng, X-M., Damu, G. L. V., Geng, R-X and Zhou, C-Z. 2014. Comprehensive Review in Current Developments of Imidazole-Based Medicinal Chemistry. *Medicinal Research Reviews* 34.2: 340 – 437

Zhang, L-K., Wu, G-F., Zhang, Y., Tian, Y-C., Tong, Q-X and Li, D. 2013. A two-in-one fluorescent sensor with dual channels to detect Zn^{2+} and Cd^{2+}. *RSC Advances* 3.44: 21409 – 21412

Zhang, M., Zhou, Q., Du, C., Ding, Y. and Song, P. 2016. Detailed theoretical investigation on ESIPT process of pigment yellow 101. *RSC Advances* 6.64: 59389 – 59394

Zhang, Z., Tian, R., Zhang, P., Lu, C. and Duan, X. 2020. Three-Dimensional Visualization for Early-Stage Evolution of Polymer Aging. *ACS Central Science* 6.5: 771 – 778

Zhao, F-H., Li, H., Che, Y-X., Zheng, J-M., Vieru, V., Liviu F. Chibotaru, L. F., Grandjean, F. and Long, G. J. 2014. Synthesis, Structure, and Magnetic Properties of $Dy_2Co_2L_{10}(bipy)_2$ and $Ln_2Ni_2L_{10}(bipy)_2$, Ln = La, Gd, Tb, Dy, and Ho: Slow Magnetic Relaxation in $Dy_2Co_2L_{10}(bipy)_2$ and $Dy_2Ni_2L_{10}(bipy)_2$. *Inorganic Chemistry* 53.18: 9785 – 9799

Zheng, X., Zhao, Y., Jia, P., Wang, Q., Liu, Y., Bu, T., Zhang, M., Bai, F. and Wang, L. 2020. Dual-Emission Zr-MOF-Based Composite Material as a Fluorescence Turn-On Sensor for the Ultrasensitive Detection of Al^{3+}. *Inorganic Chemistry* 59.24: 18205 – 18213

Zhong, J., Zhuo, Y., Hariyani, S., Zhao, W., Zhuang, W. and Brgoch, J. 2020. Thermally Robust and Color-Tunable Blue-Green-Emitting $BaMgSi_4O_{10}:Eu^{2+},Mn^{2+}$ Phosphor for Warm-White LEDs. *Inorganic Chemistry* 59.18: 13427 – 13434

Zhou, Z., Yu, M., Yang, H., Huang, K., Li, F., Yi, T. and Huang, C. 2008. FRET-based sensor for imaging chromium(III) in living cells. *Chemical Communications* 2008.29: 3387 – 3389

Zhu, C., Huang, K., Yuan, F., Xie, C. 2014. 2-Methyl-2,4-pentanediol gas sensor properties of nano-SnO_2 flat-type coplanar gas sensing arrays at low detection limit. *Materials Science-Poland* 32.2: 181 – 187

Zhu, Y-Y., Yin, T-T., Liu, C-W., Gao, C., Wu, Z-Q., Zhang, Y-Q., Wang, B-W. and Gao, S. 2014. Field-induced slow magnetic relaxation in a hydrogen-bonding linked Co(II) 1D supramolecular coordination polymer. *Supramolecular Chemistry* 27.5-6: 1 – 7. https://dx.doi.org/10.1080/10610278.2014.975703

Ziegenbalg, S., Hornig, D., Görls, H. and Plass, W. 2016. Cobalt(II)-Based Single-Ion Magnets with Distorted Pseudotetrahedral $[N_2O_2]$ Coordination: Experimental and Theoretical Investigations. *Inorganic Chemistry* 55.8: 4047 – 4058

Zolotukhin, A. A., Korshunova, A. A., Bubnov, M. P., Bogomyakov, A. S., Baranov, E. V., Cherkasov, V. K. 2020. Nickel(II) and Cobalt(III) bis(dioxolene) complexes with di(2-pyridyl)imine ligands: Synthesis and magnetic properties. *Inorganica Chimica Acta* 512: 119869. https://dx.doi.org/10.1016/j.ica.2020.119869

Appendix

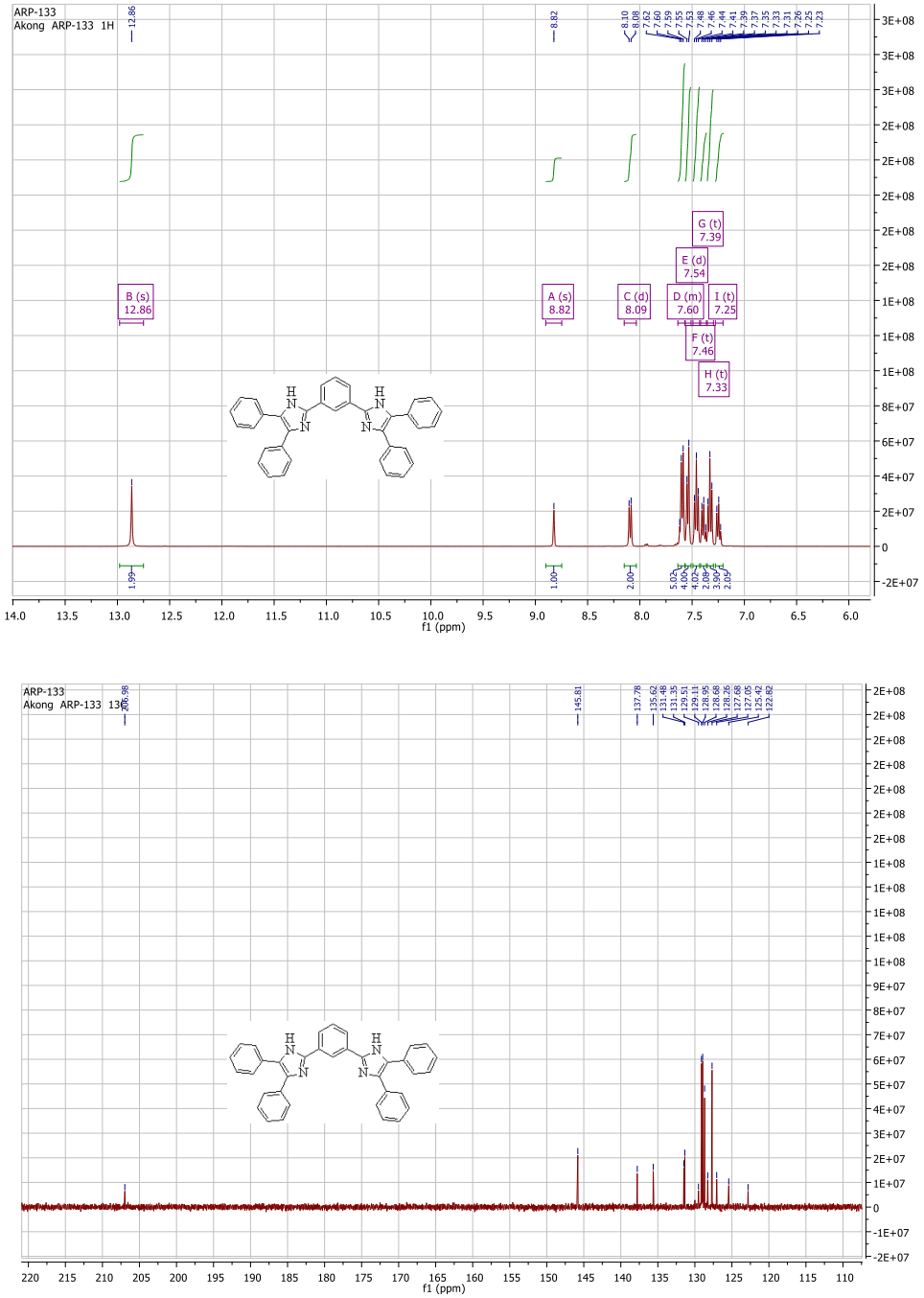

Figure S1: nmr of **BI$_1$**

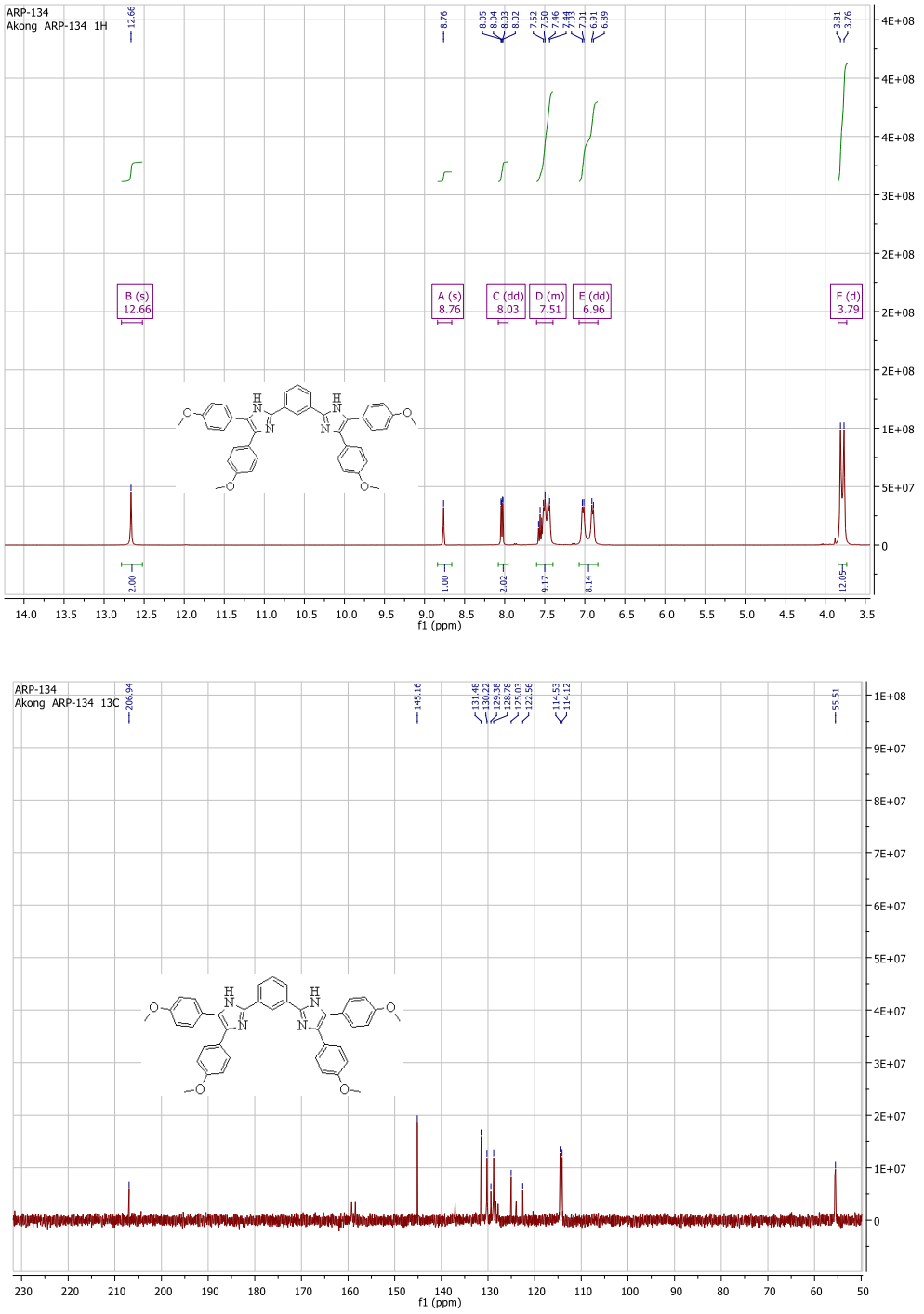

Figure S2: nmr of **BI**$_2$

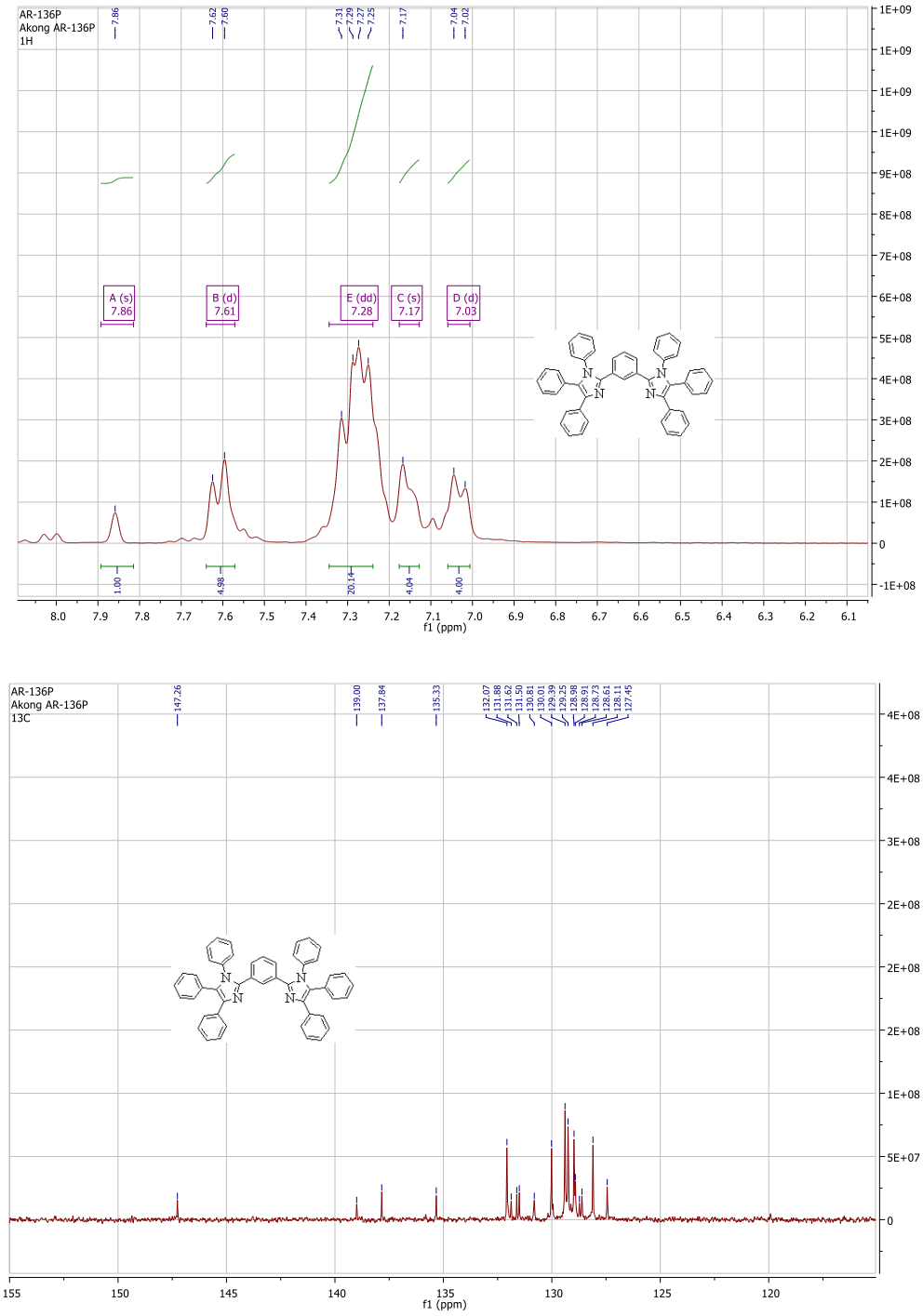

Figure S3: nmr of **BI$_3$**

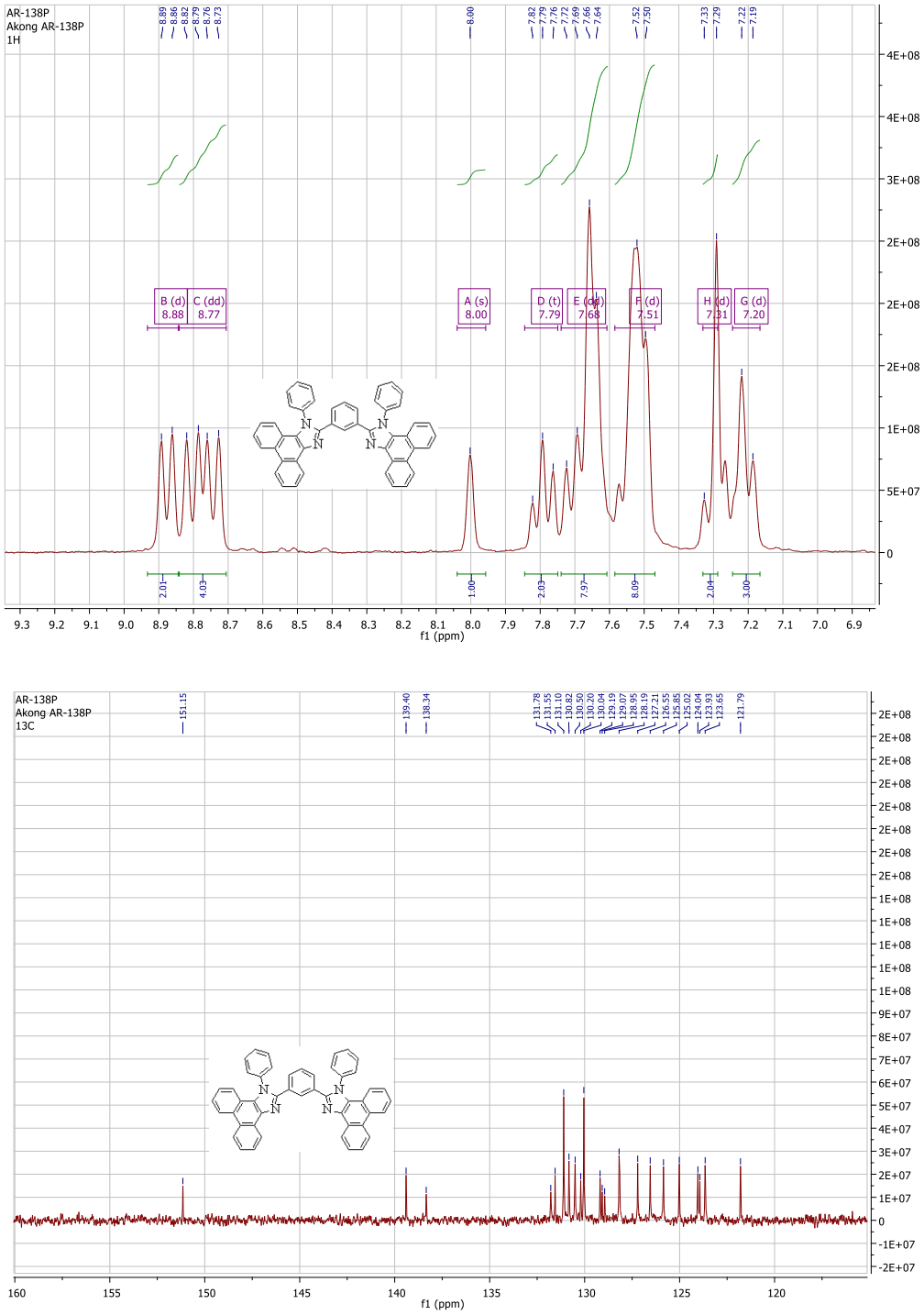

Figure S4: nmr of **BI$_4$**

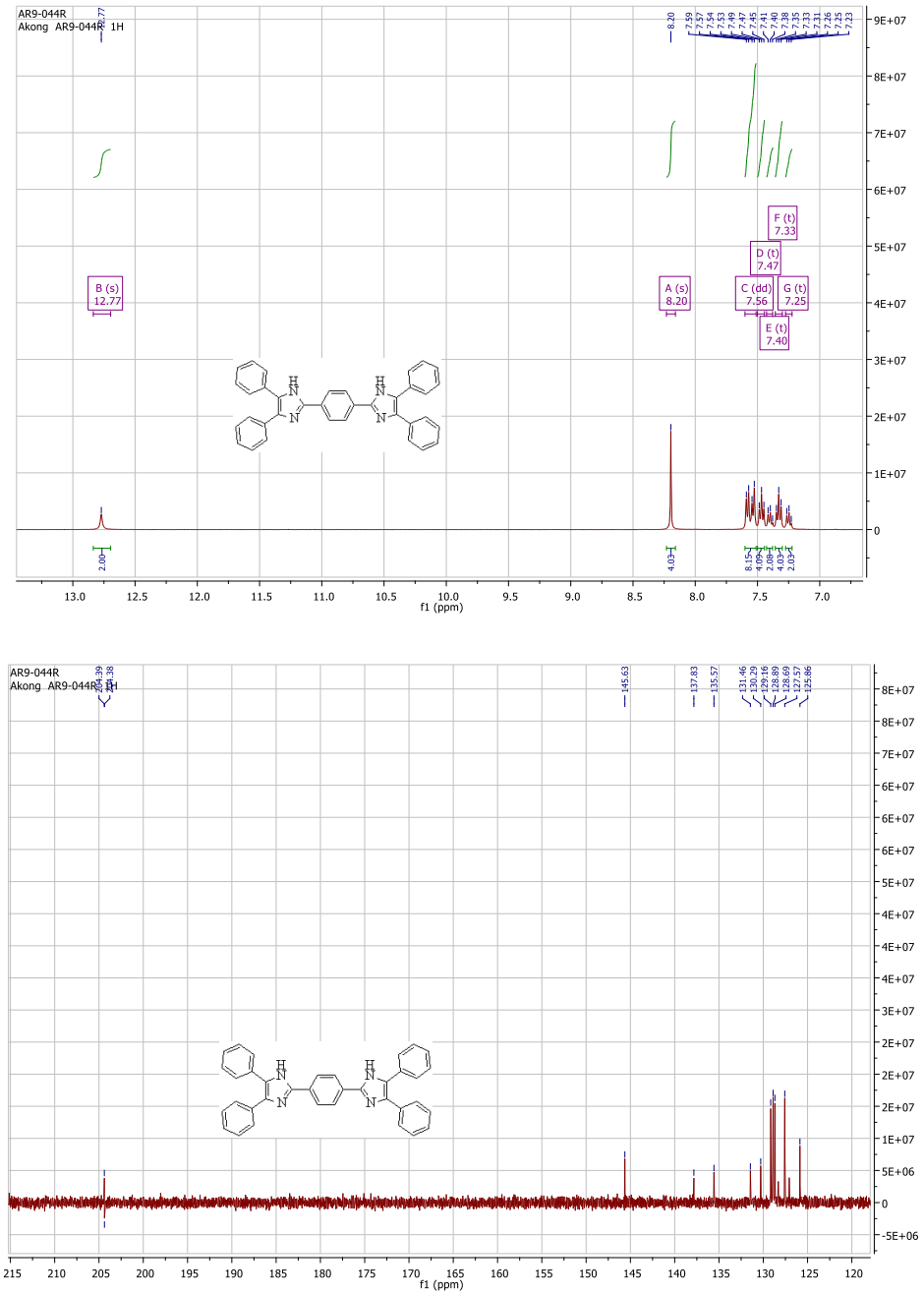

Figure S5: nmr of **BI$_5$**

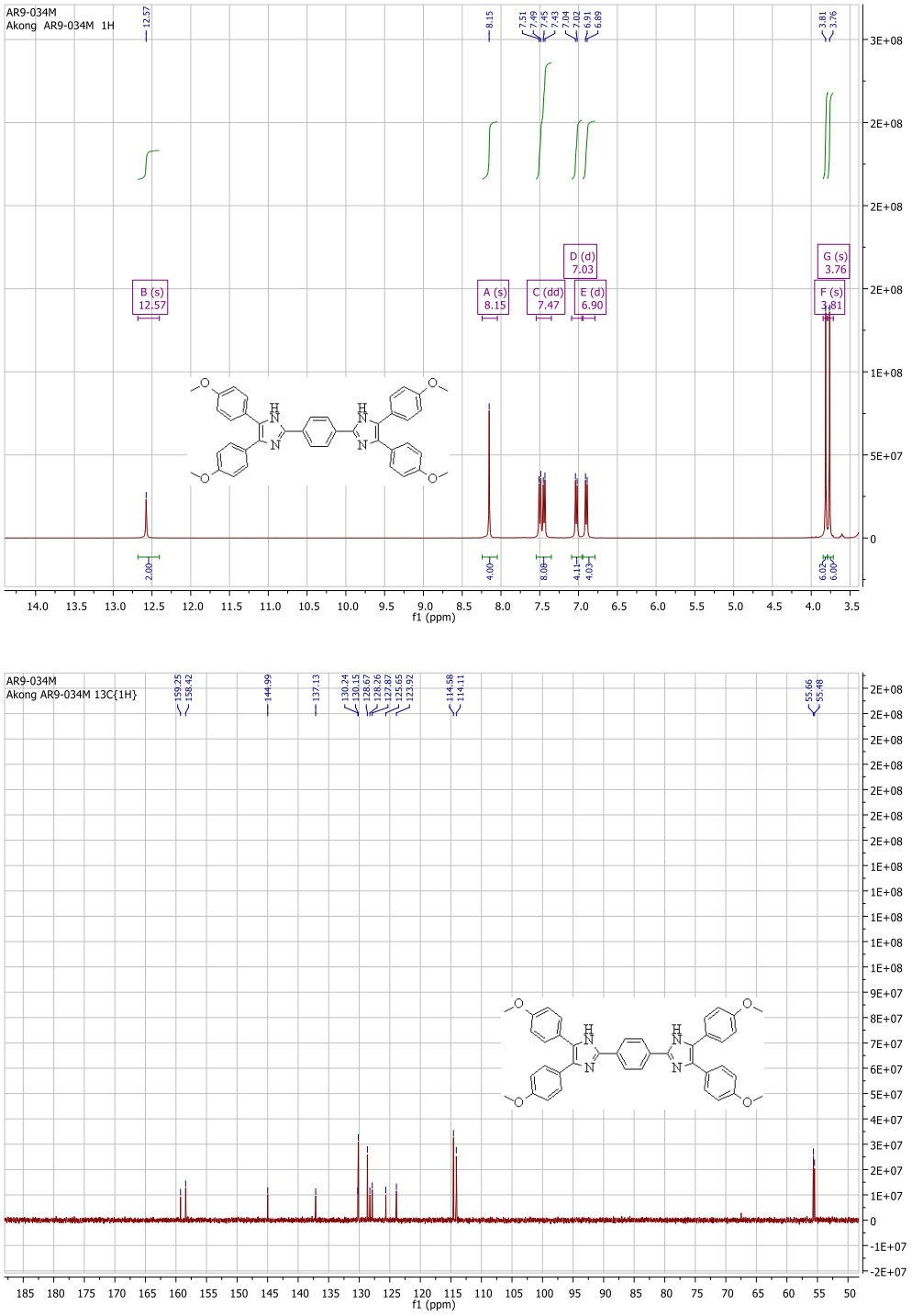

Figure S6: nmr of **BI$_6$**

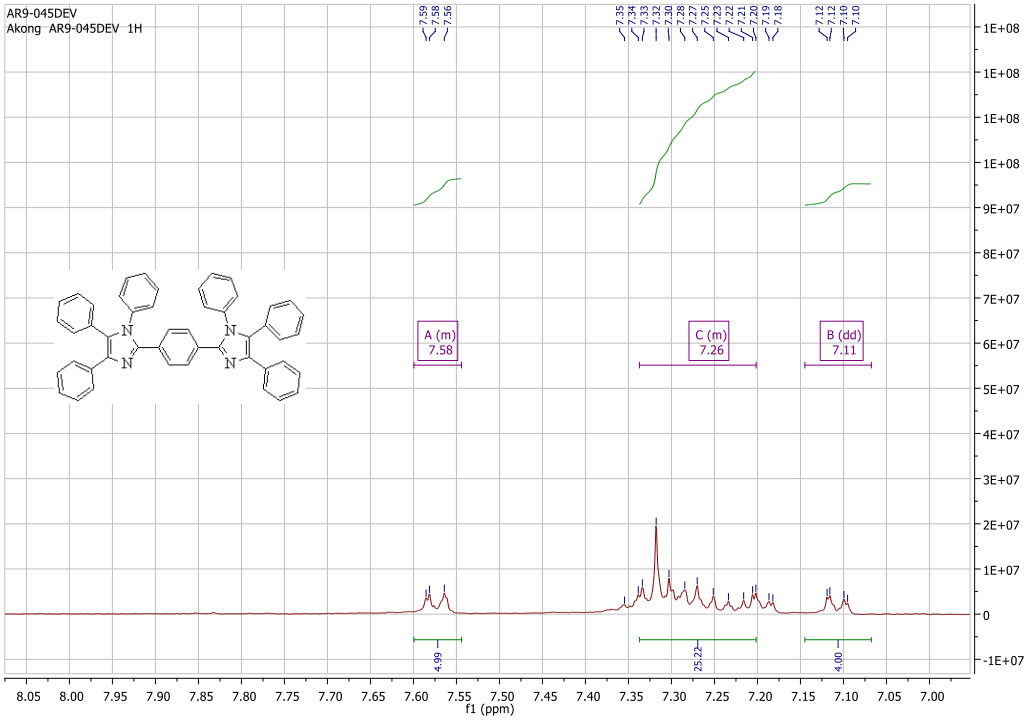

Figure S7: nmr of **BI**$_7$

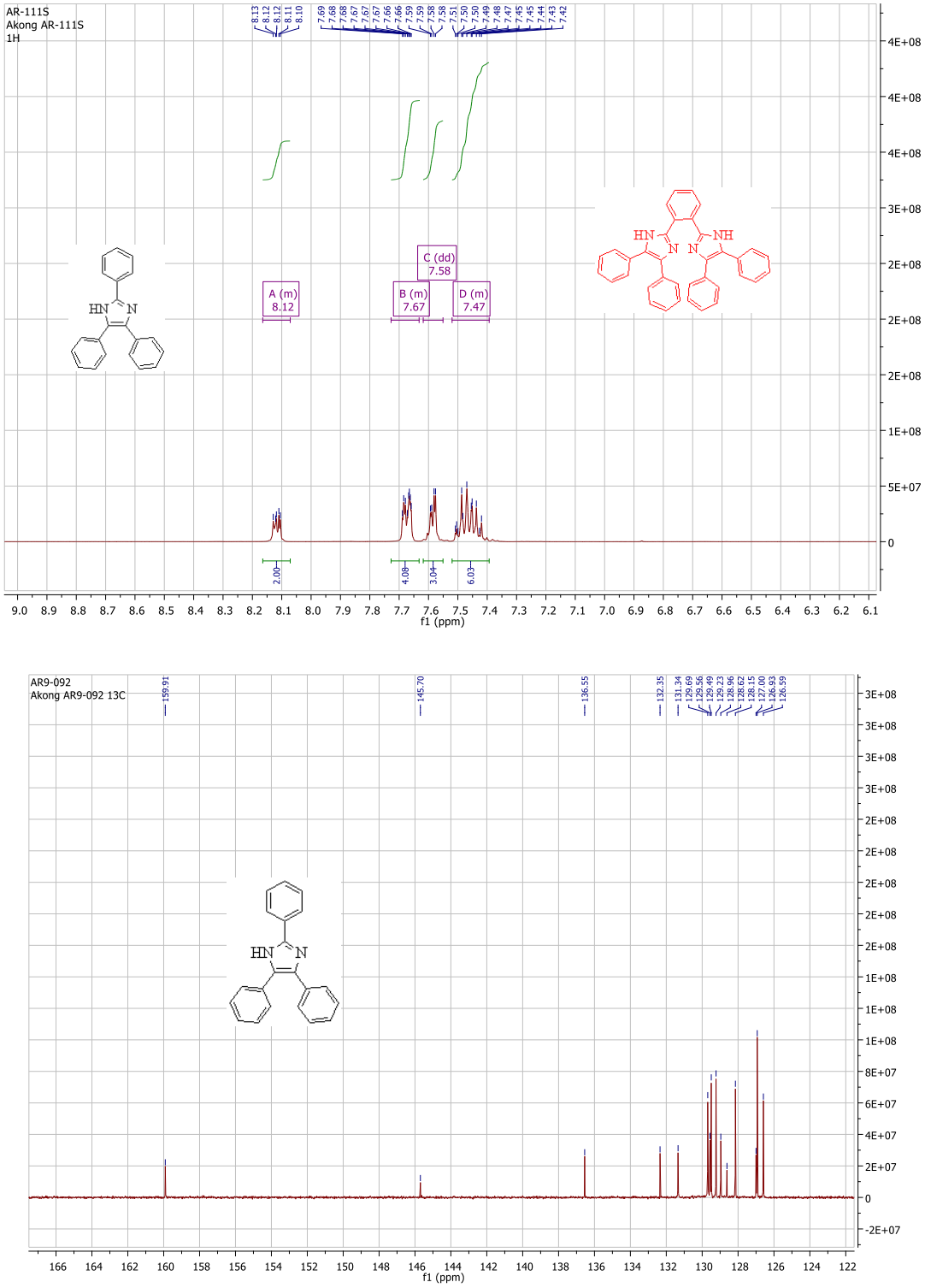

Figure S8: Failed attempt at the preparation of the 1,2-series

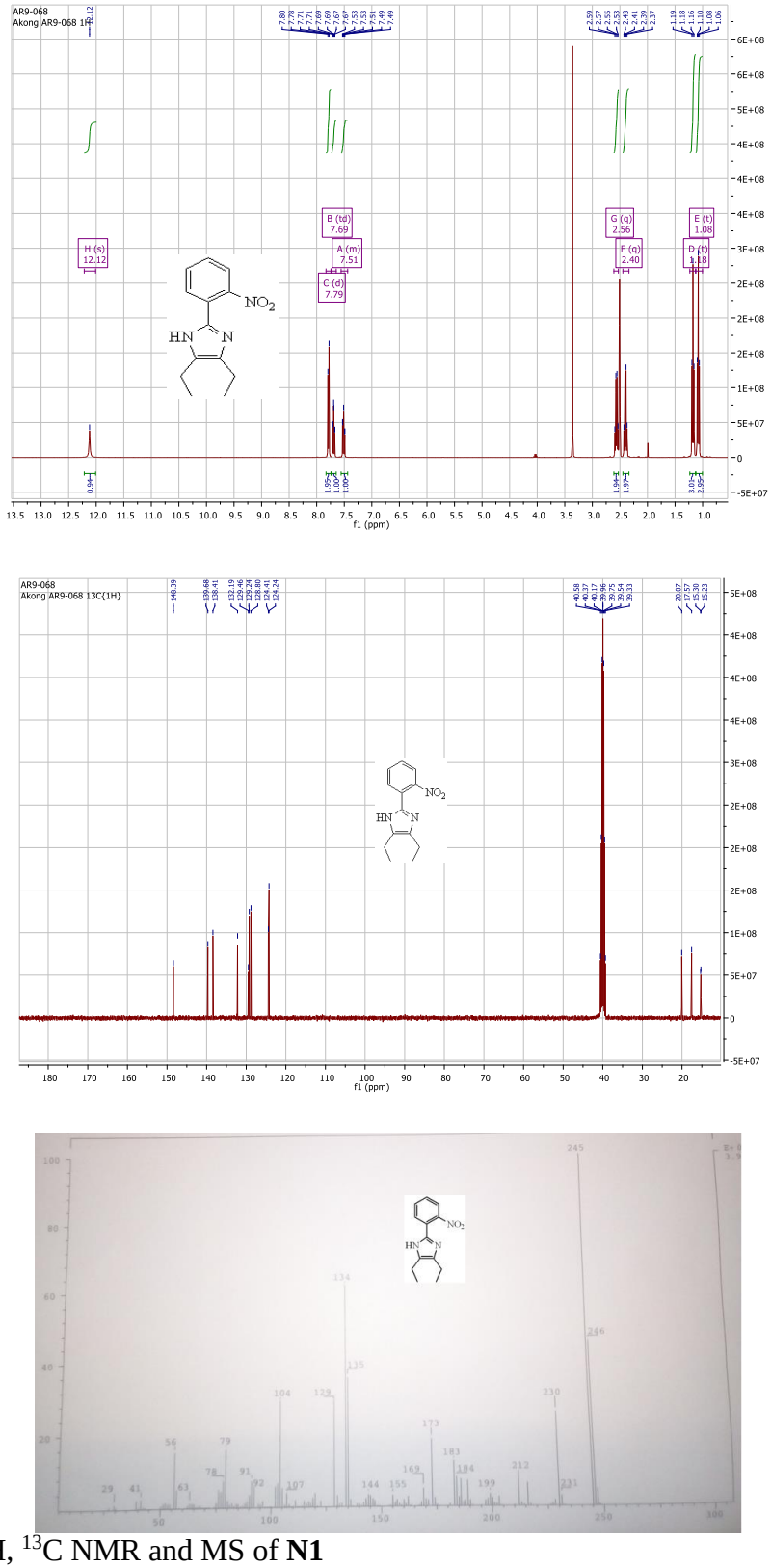

Figure S9: ^{1}H, ^{13}C NMR and MS of **N1**

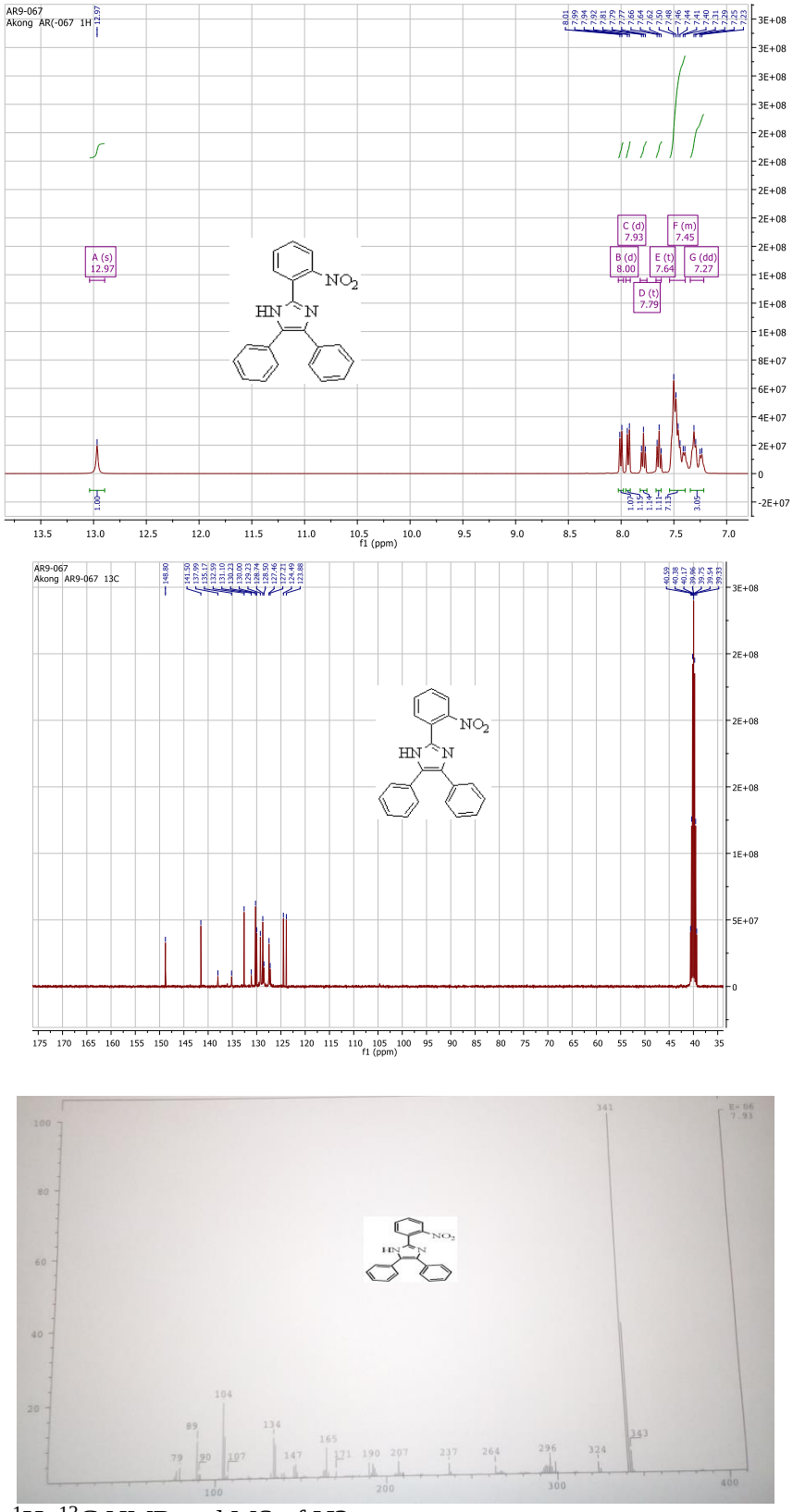

Figure S10: ^{1}H, ^{13}C NMR and MS of **N2**

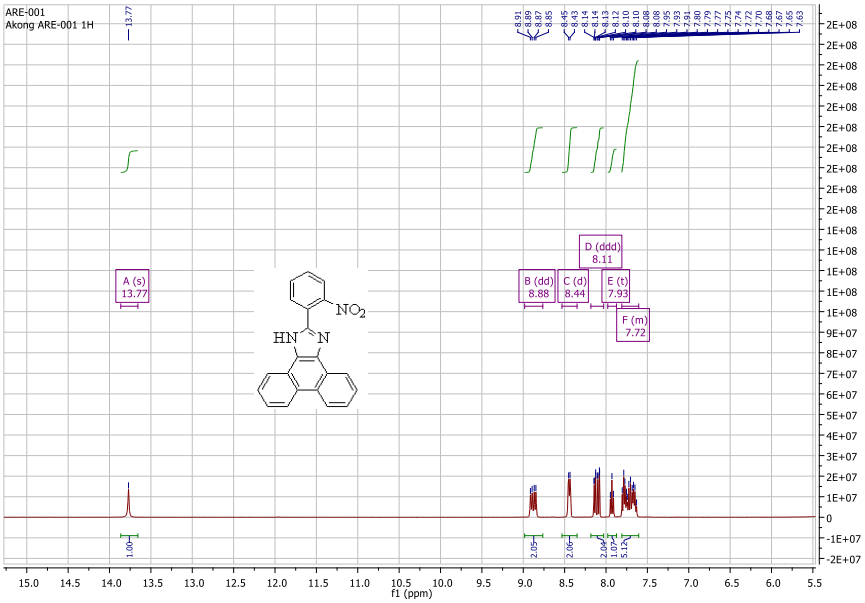

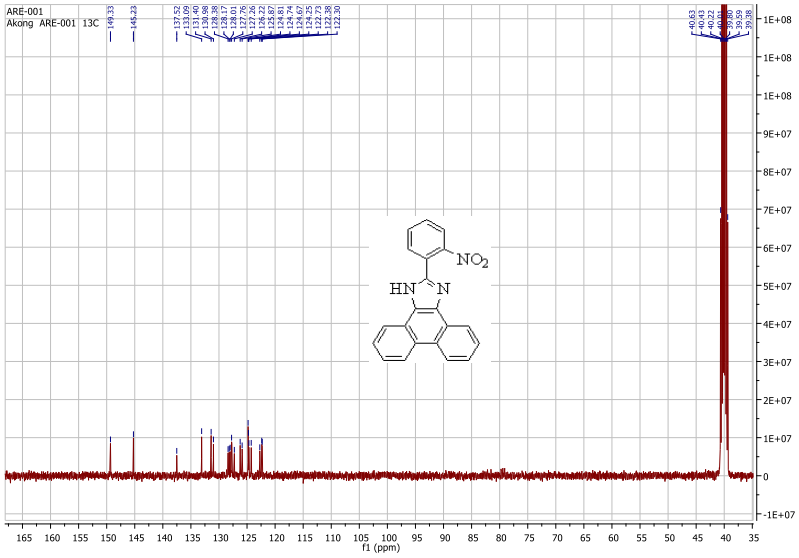

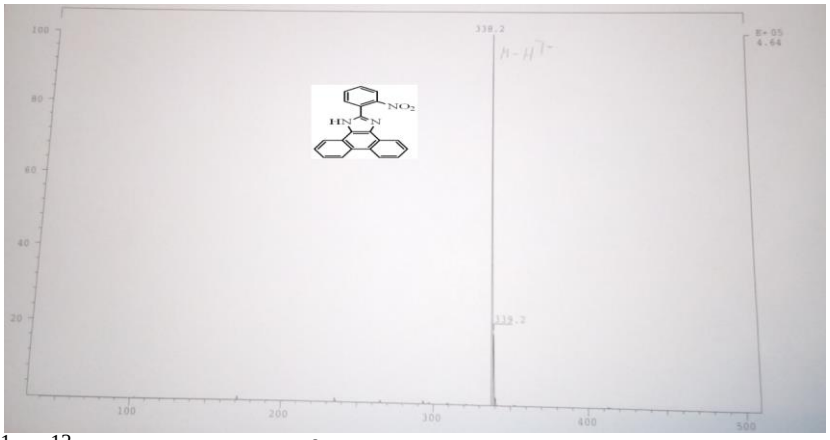

Figure S11: ^{1}H, ^{13}C NMR and MS of **N3**

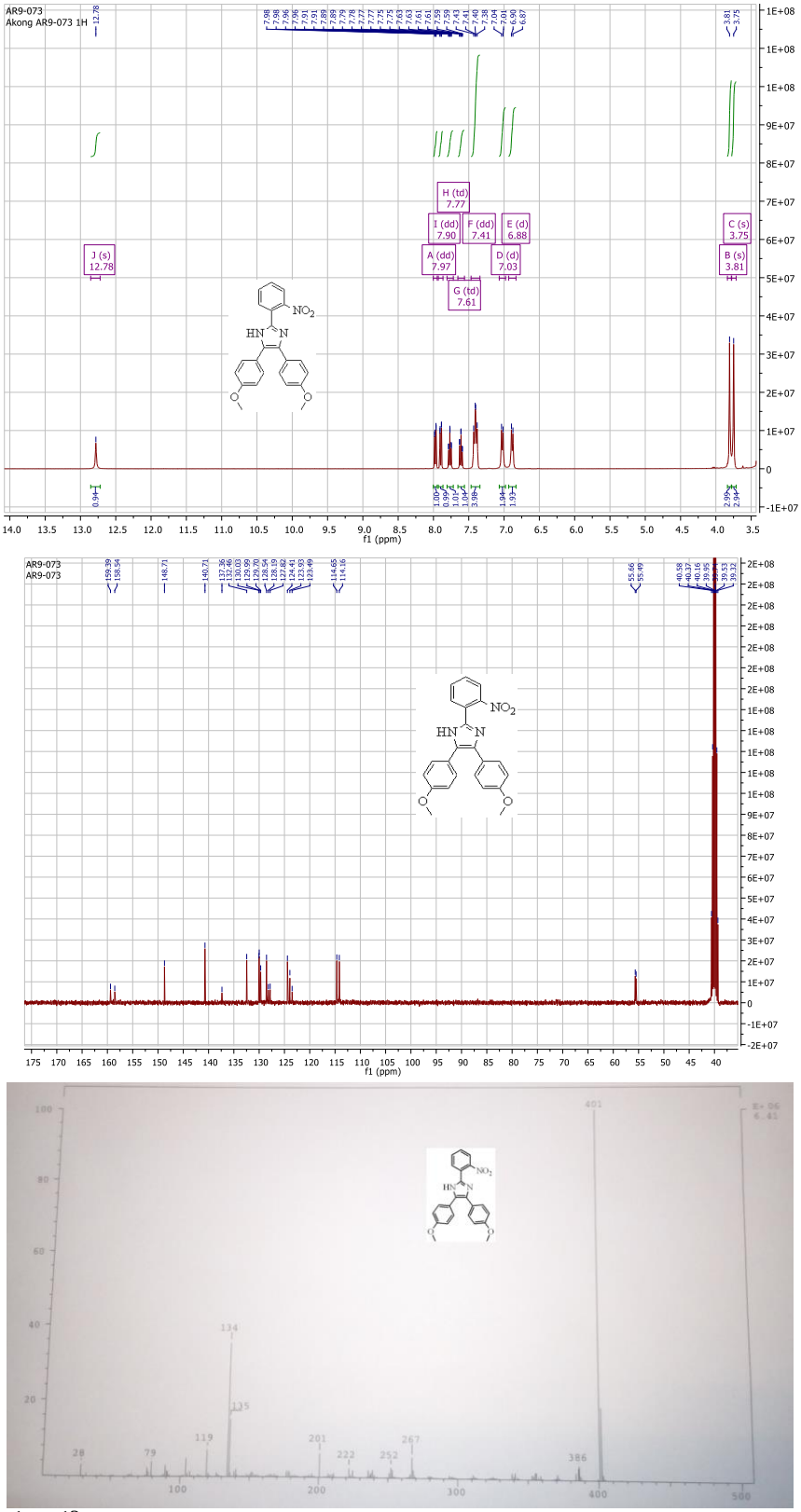

Figure S12: ^{1}H, ^{13}C NMR and MS of **N4**

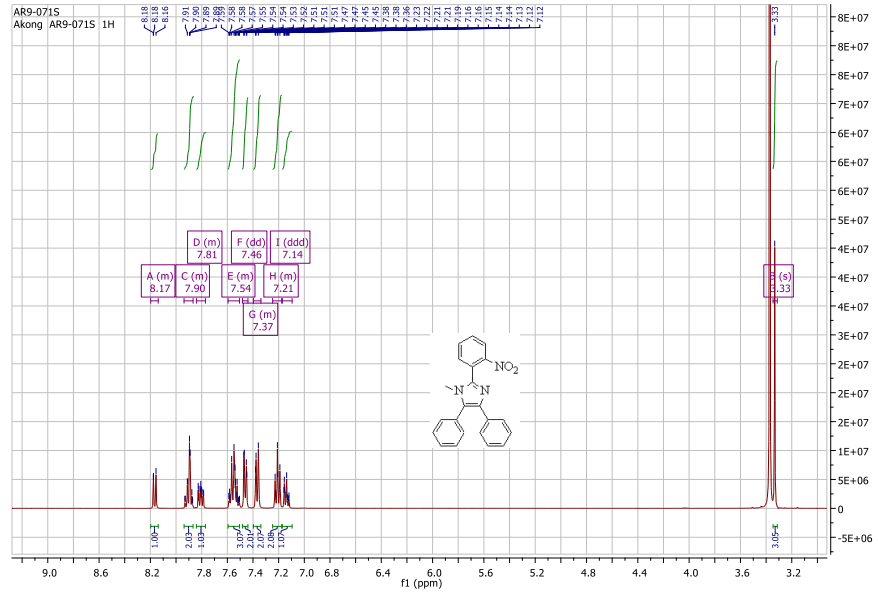

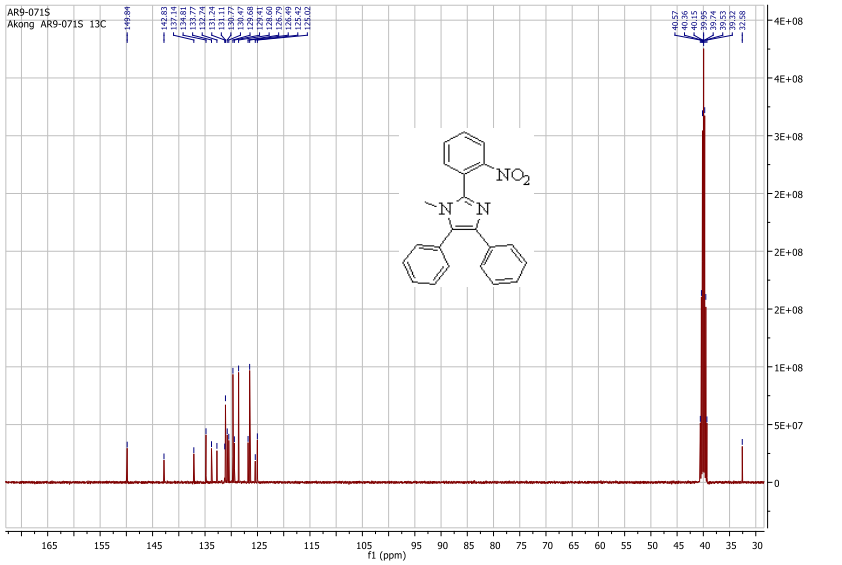

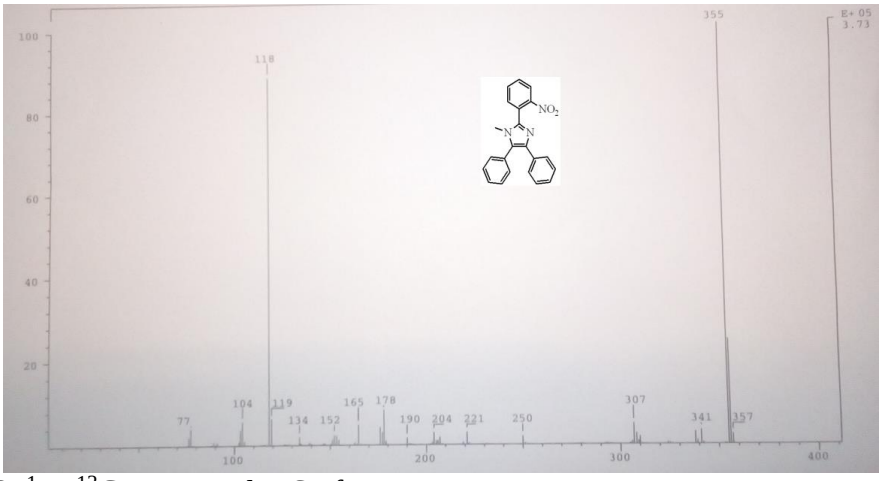

Figure S13: ^{1}H, ^{13}C NMR and MS of **N5**

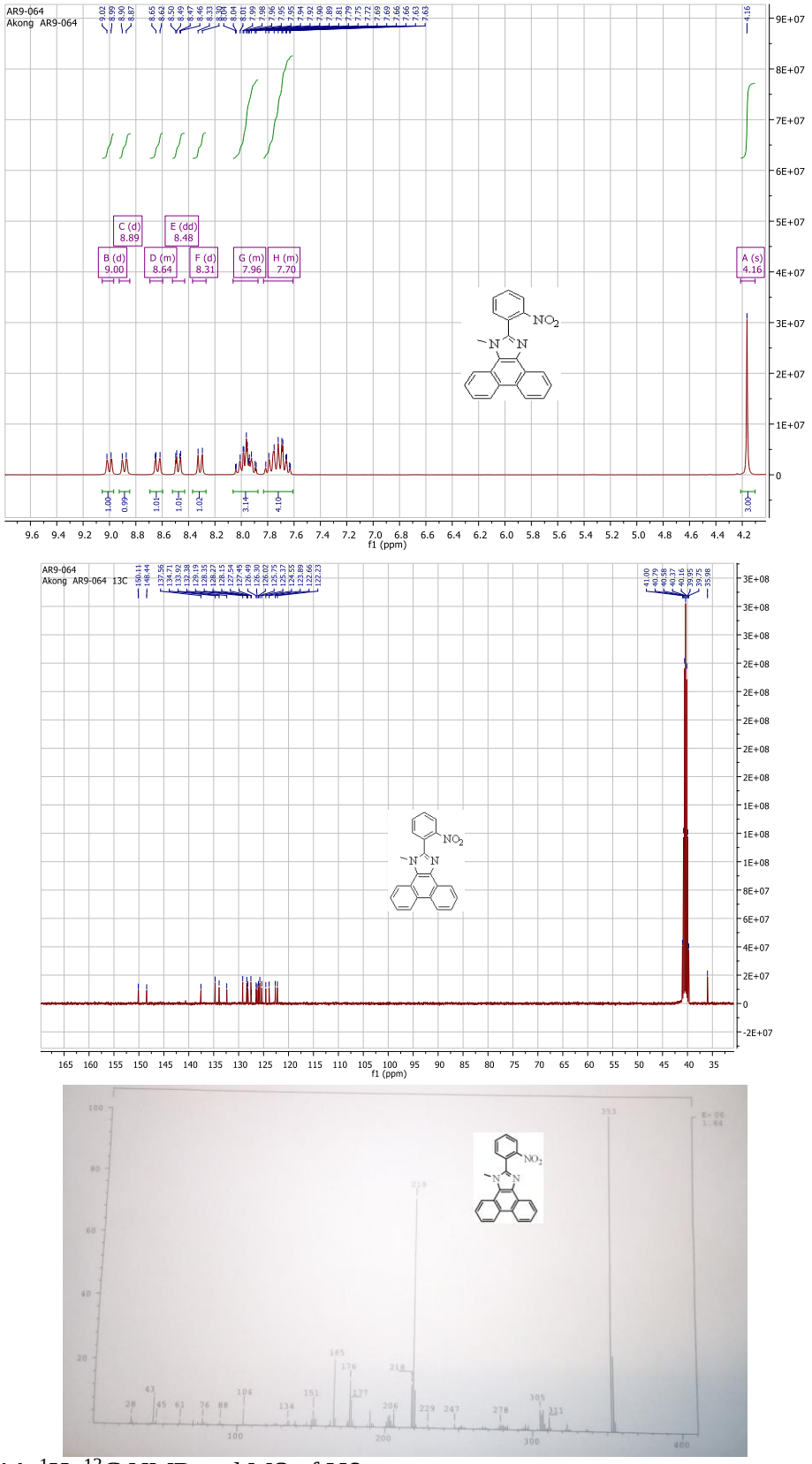

Figure S14: ^{1}H, ^{13}C NMR and MS of **N6**

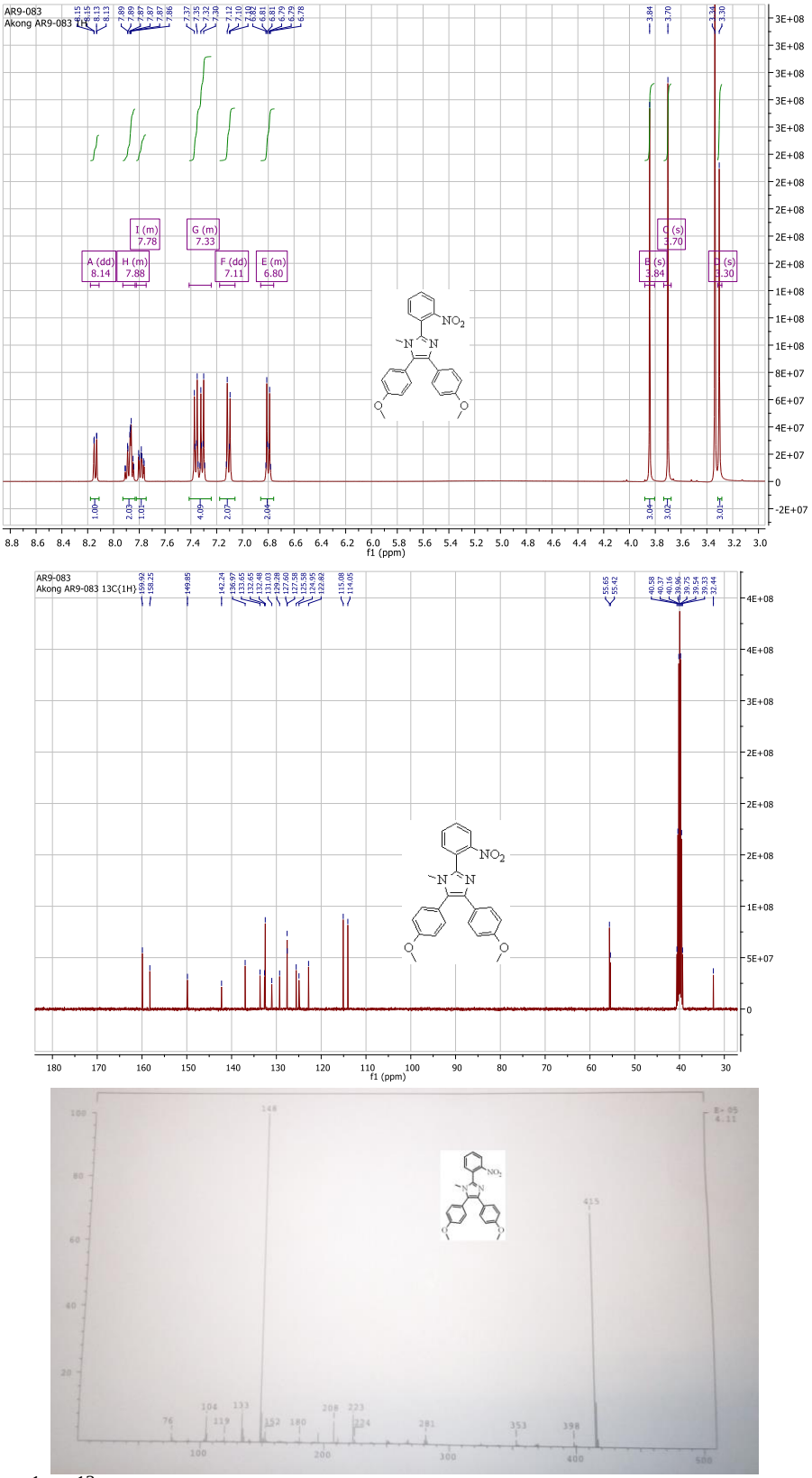

Figure S15: ^{1}H, ^{13}C NMR and MS of **N7**

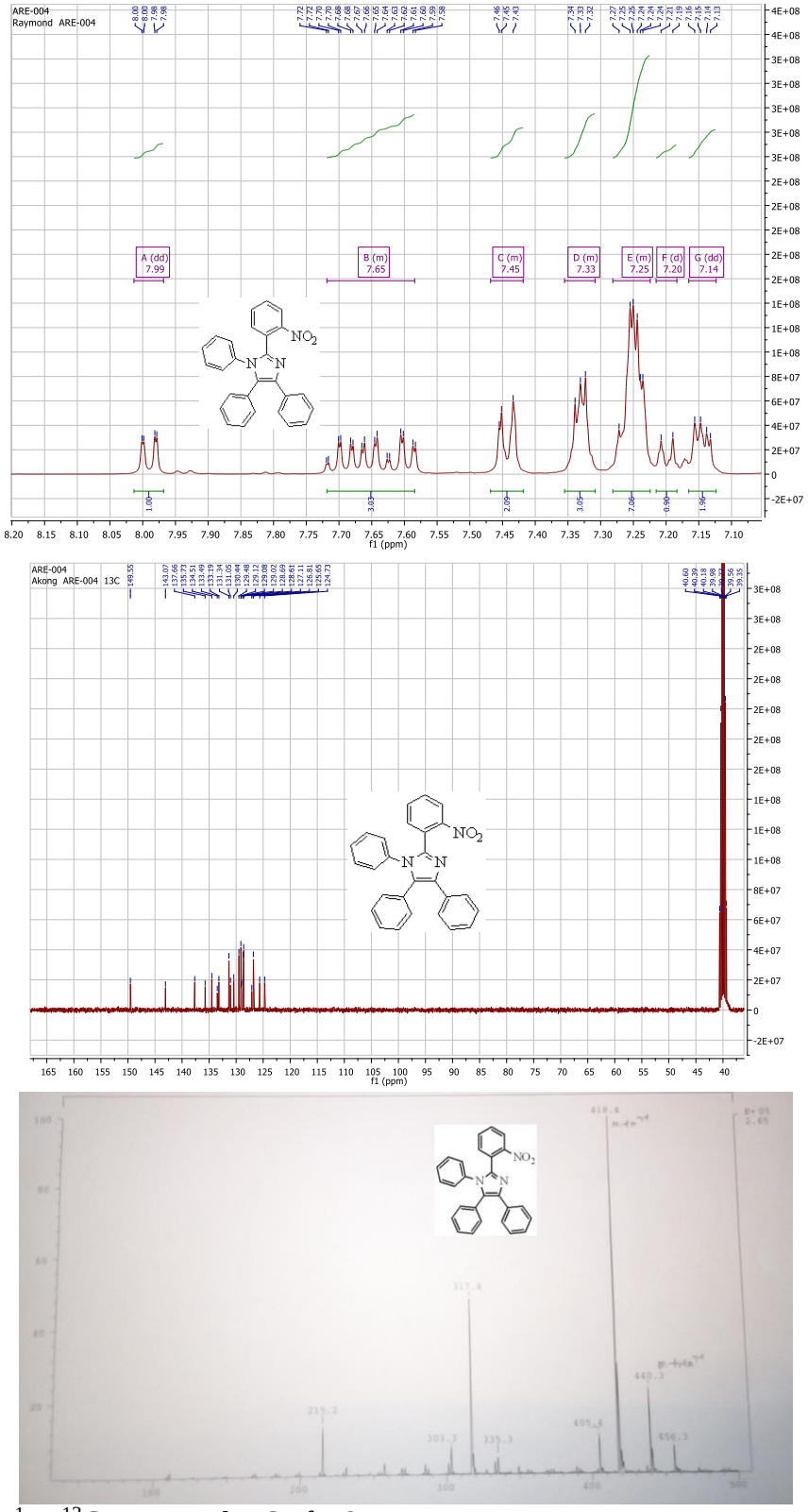

Figure S16: ^{1}H, ^{13}C NMR and MS of **N8**

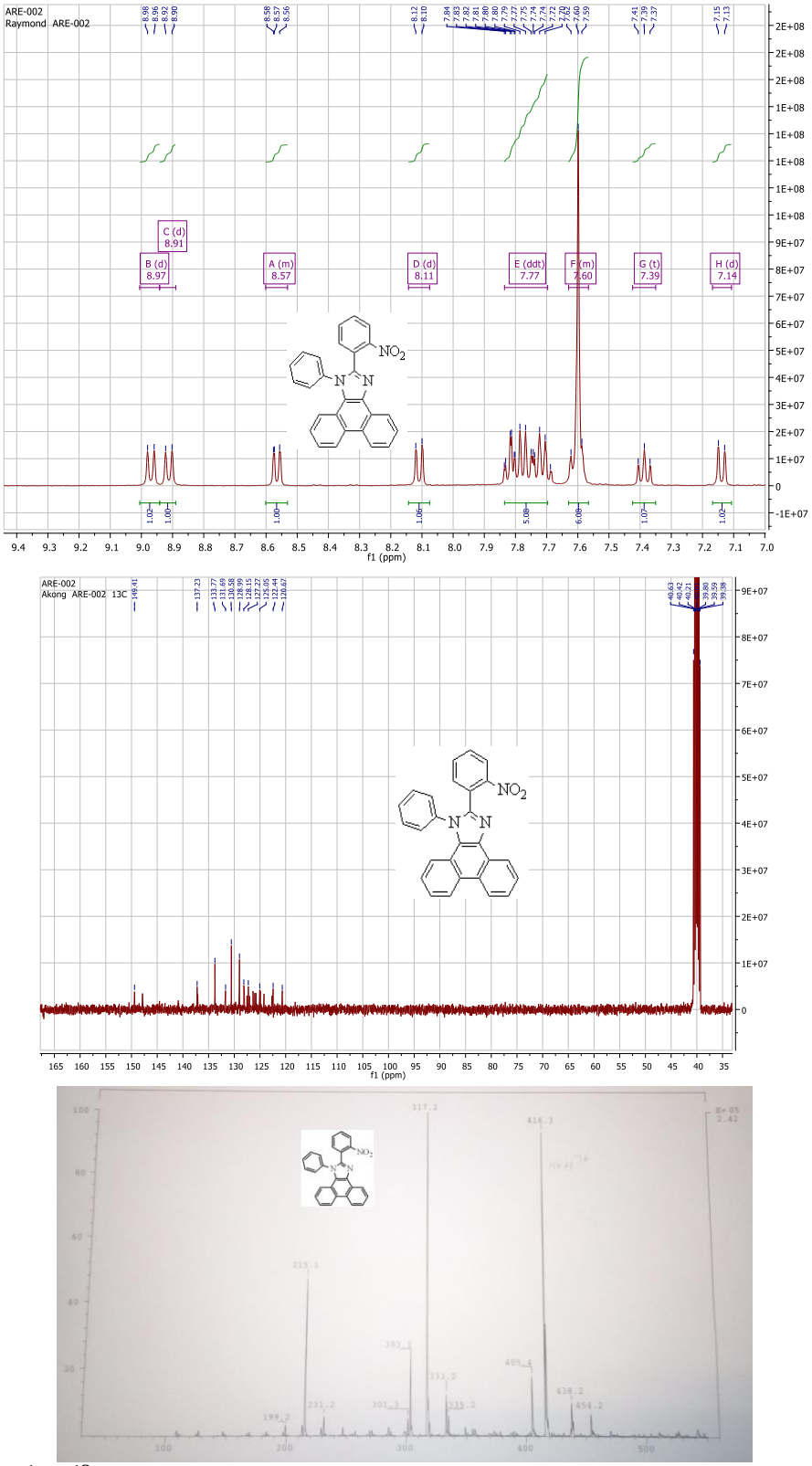

Figure S17: ^{1}H, ^{13}C NMR and MS of **N9**

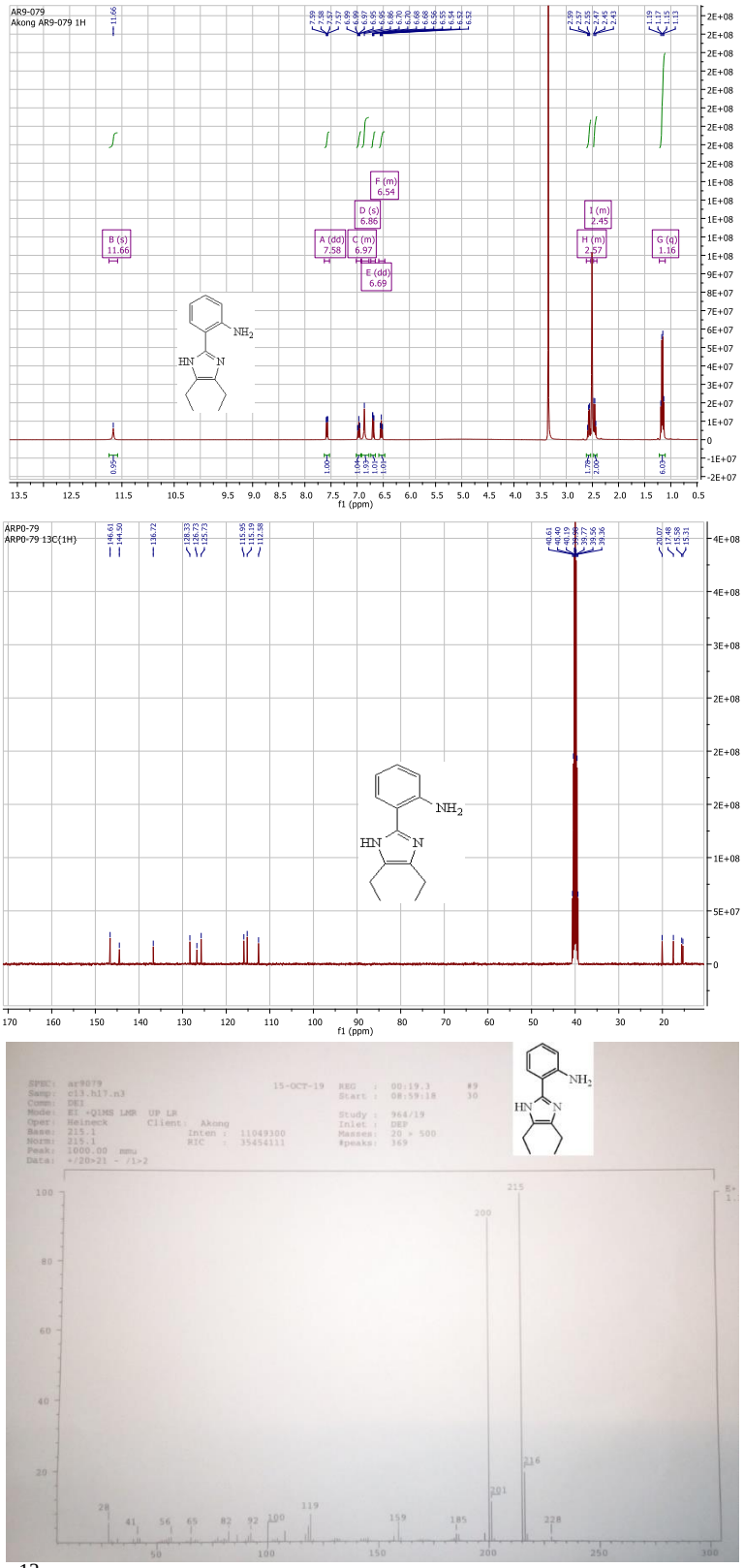

Figure S18: ^{1}H, ^{13}C NMR and MS of **A1**

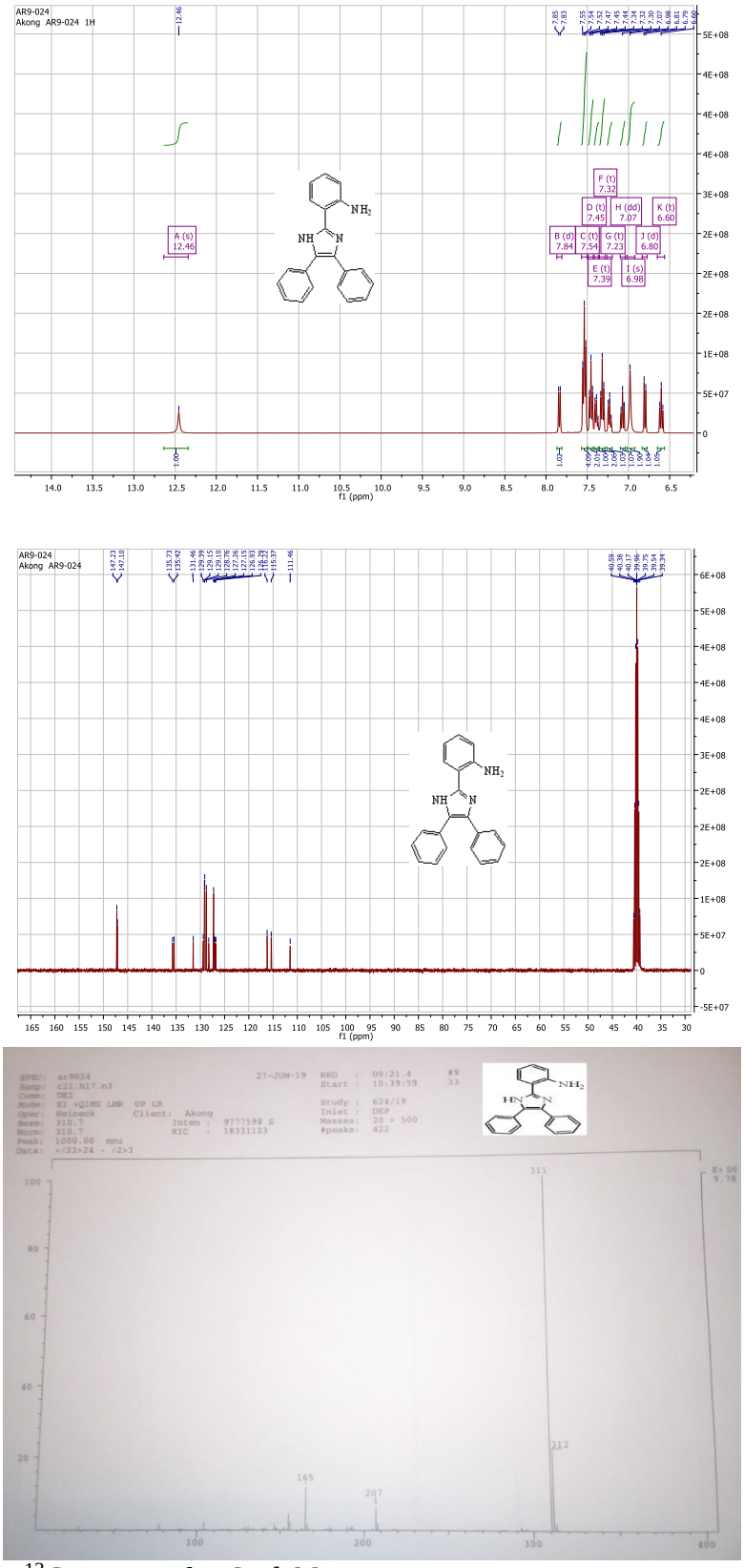

Figure S19: ^{1}H, ^{13}C NMR and MS of **A2**

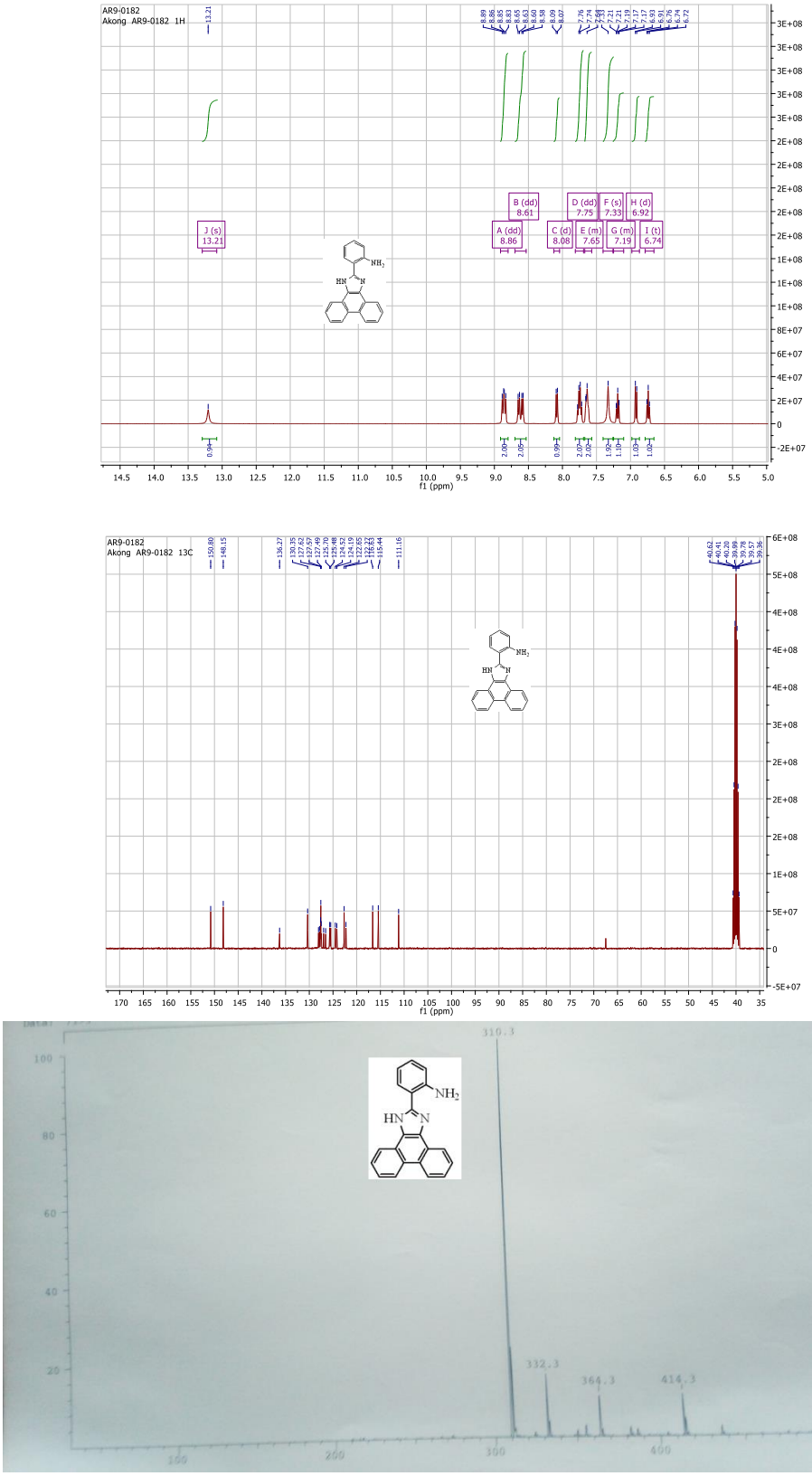

Figure S20: ^{1}H, ^{13}C NMR and MS of **A3**

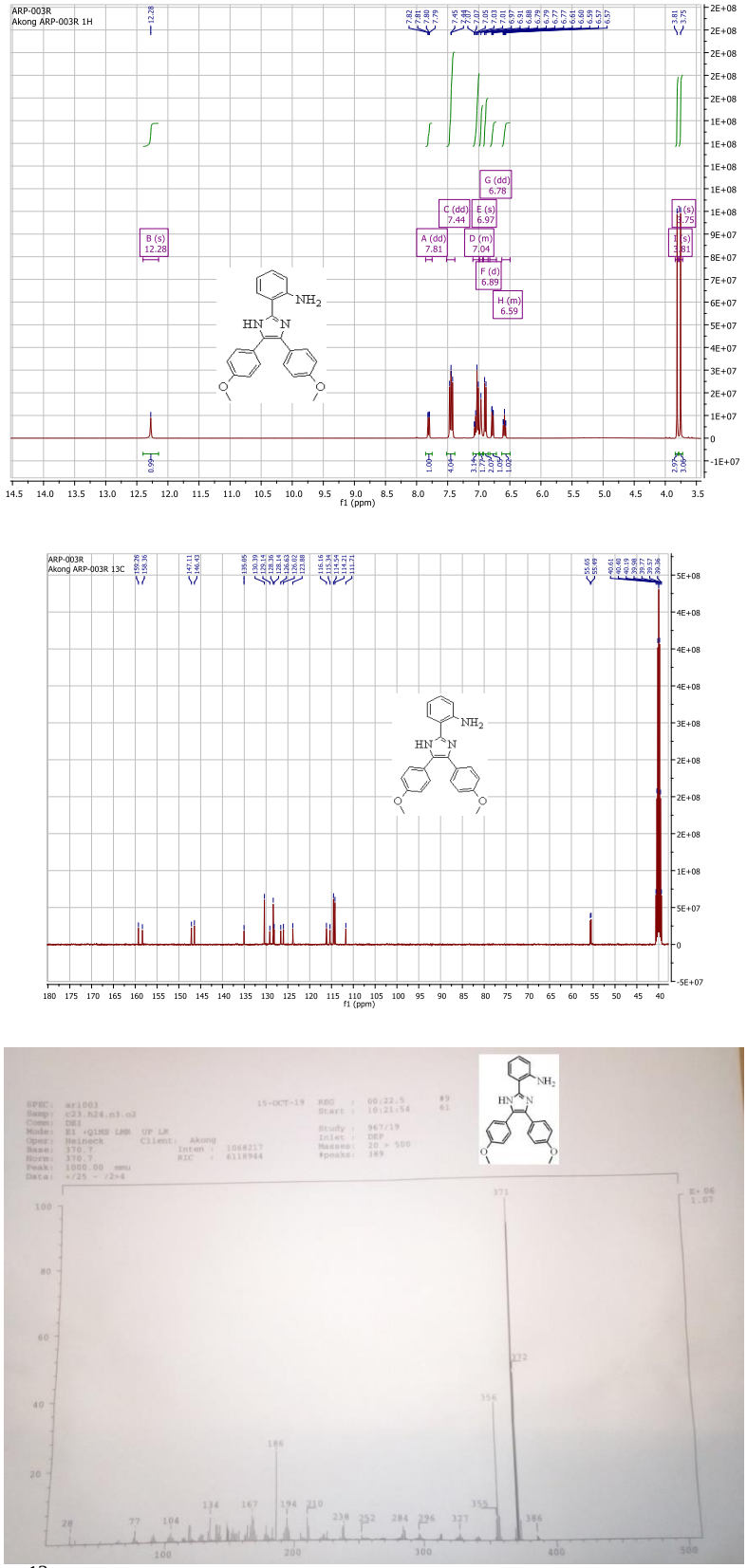

Figure S21: ^{1}H, ^{13}C NMR and MS of **A4**

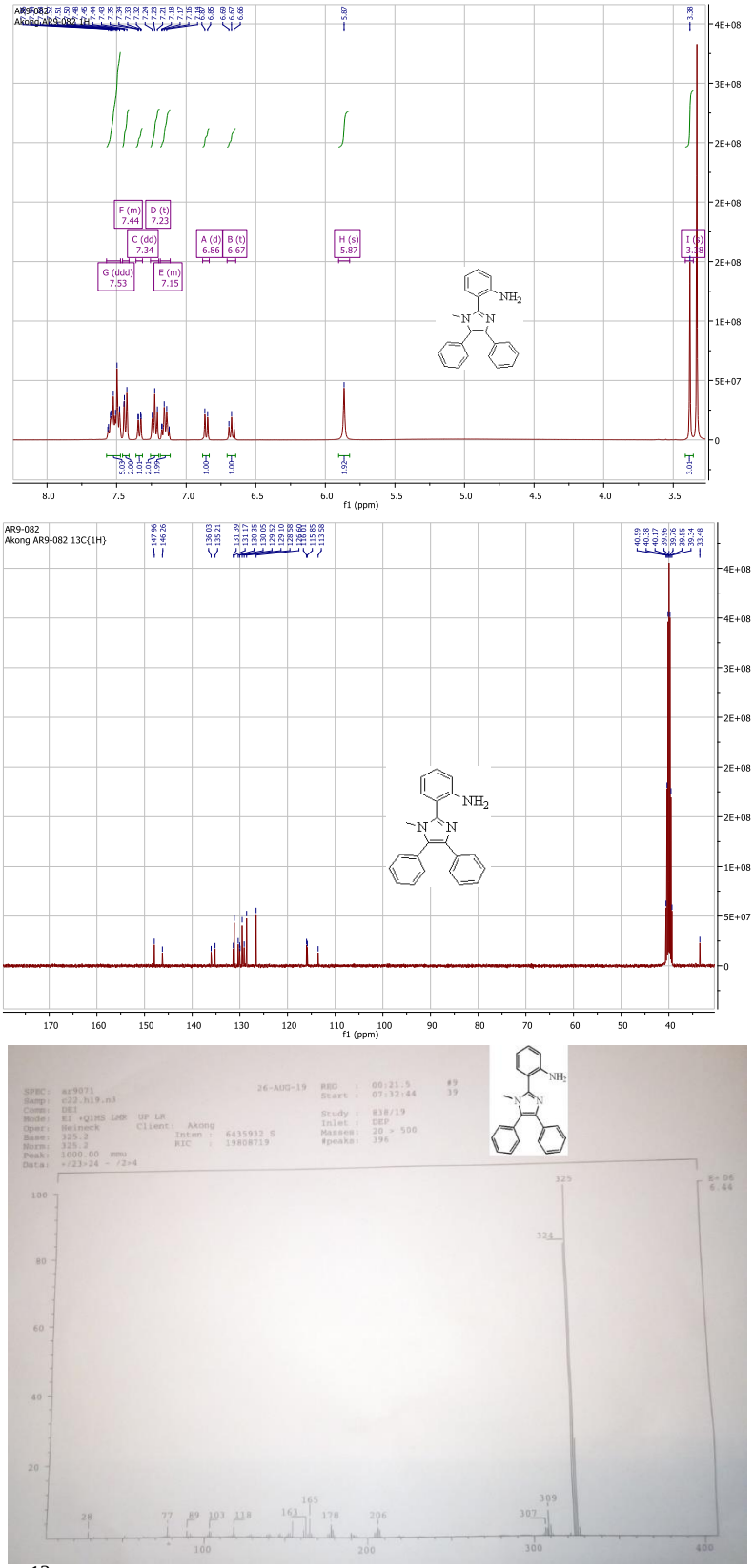

Figure S22: ^{1}H, ^{13}C NMR and MS of **A5**

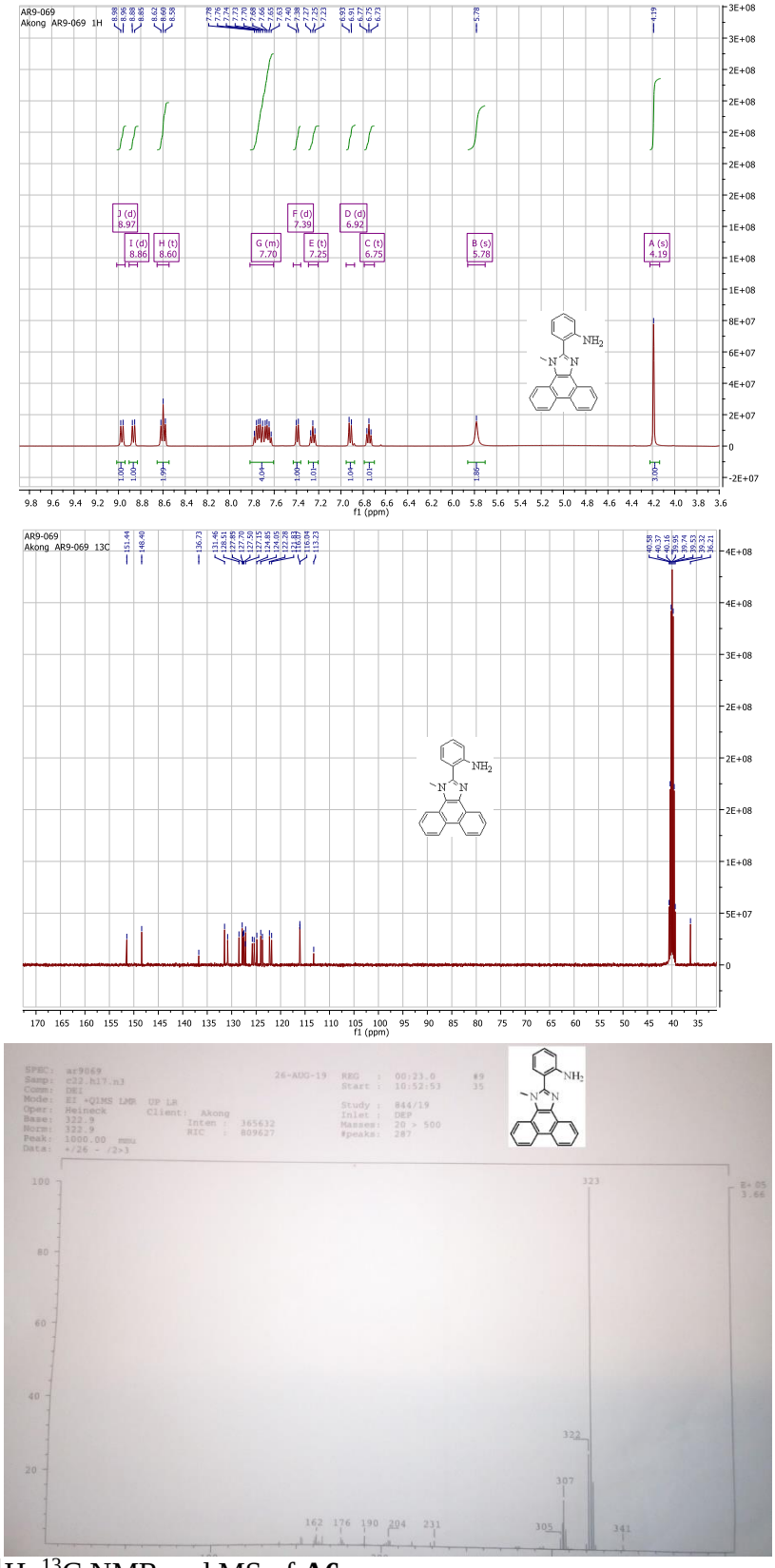

Figure S23: ^{1}H, ^{13}C NMR and MS of **A6**

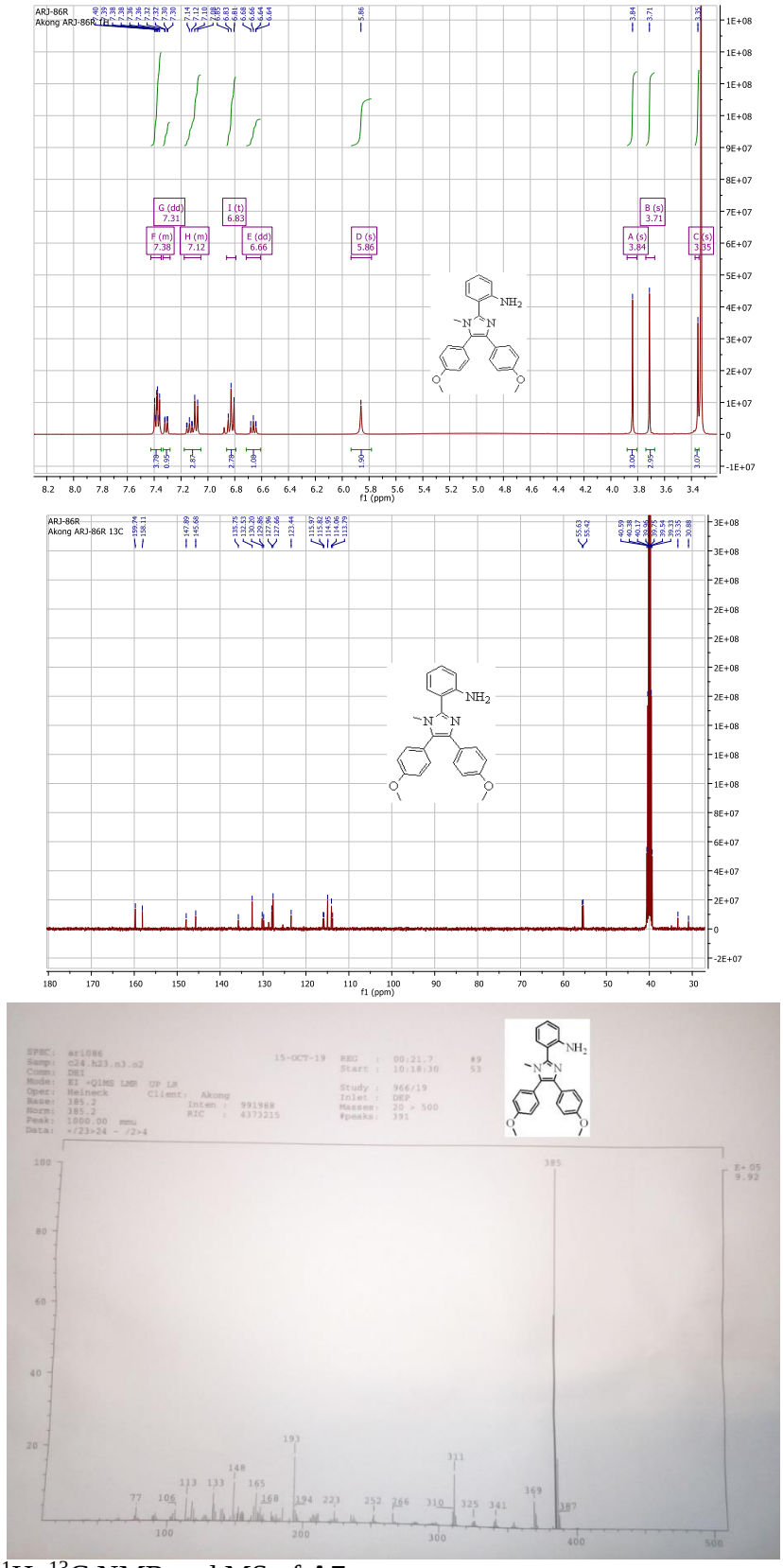

Figure S24: ^{1}H, ^{13}C NMR and MS of **A7**

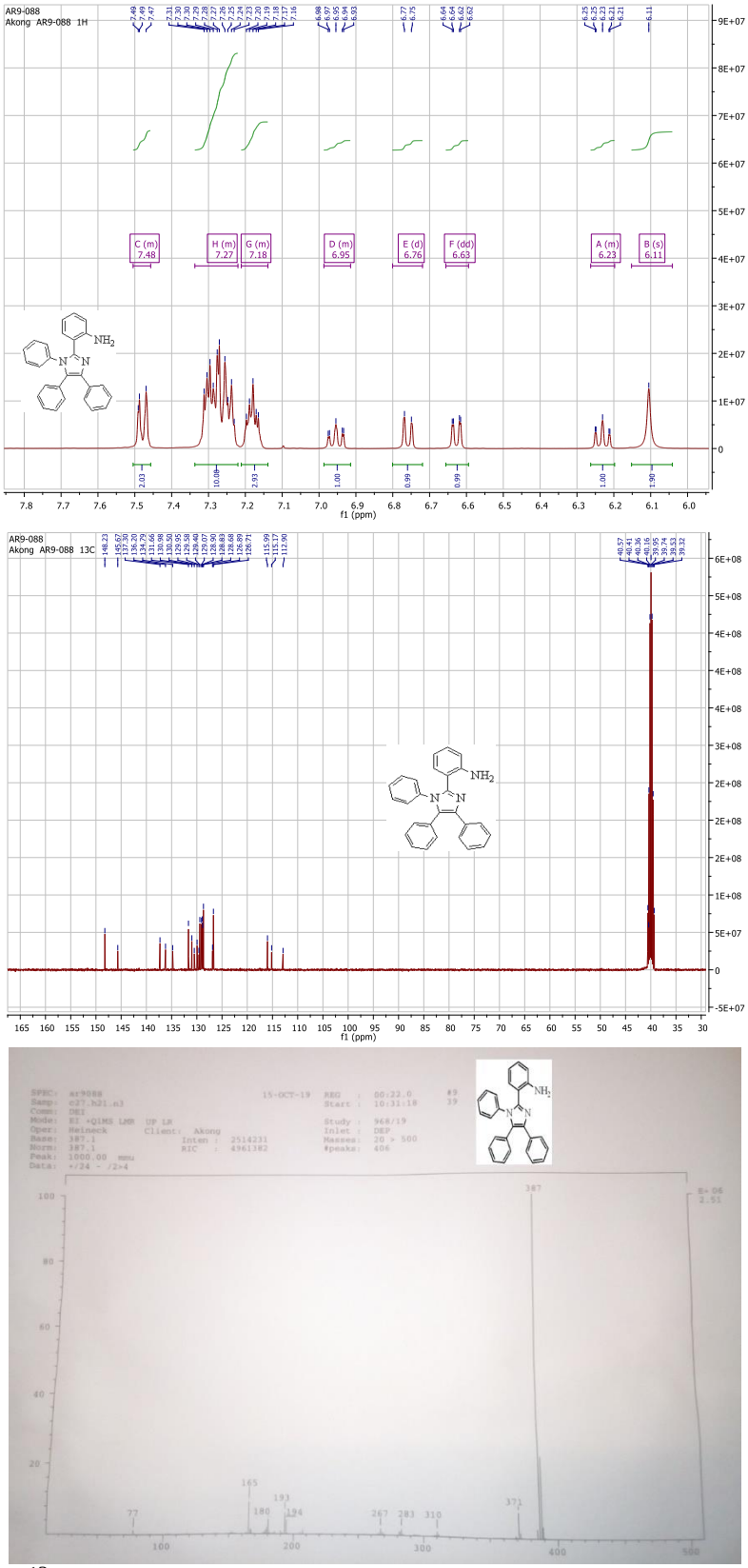

Figure S25: ^{1}H, ^{13}C NMR and MS of **A8**

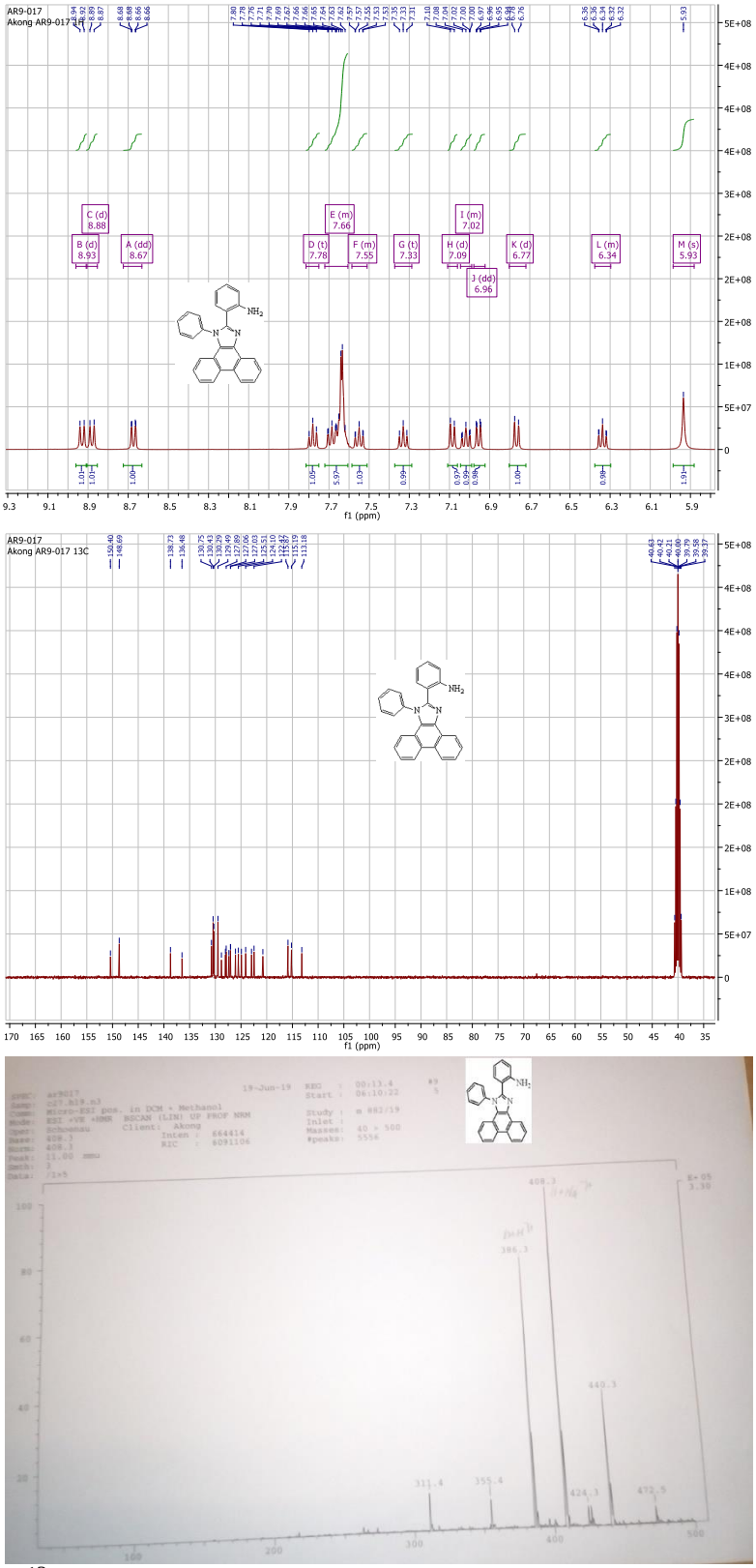

Figure S26: ^{1}H, ^{13}C NMR and MS of **A9**

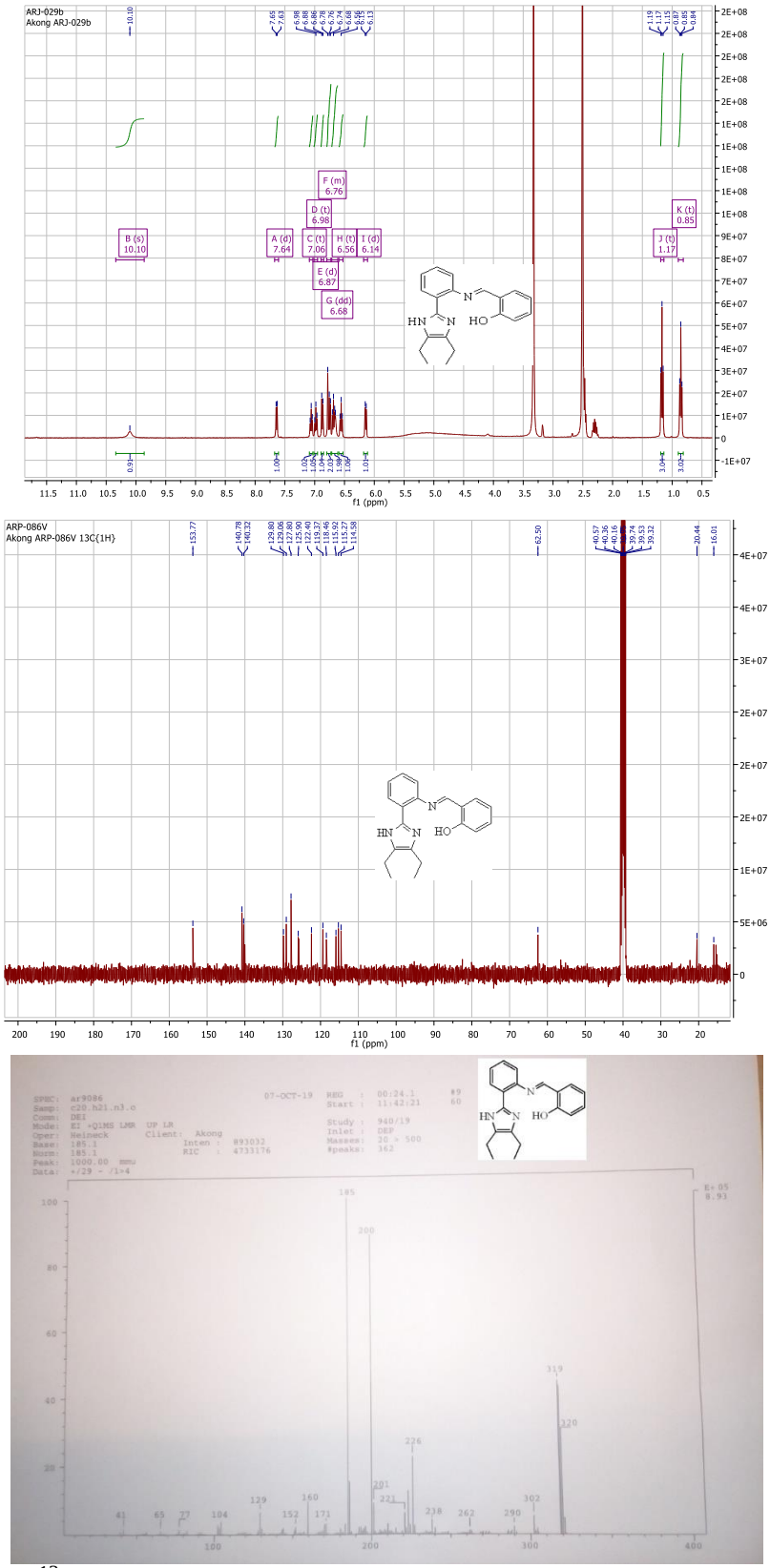

Figure S27: ^{1}H, ^{13}C NMR and MS of **I_1**

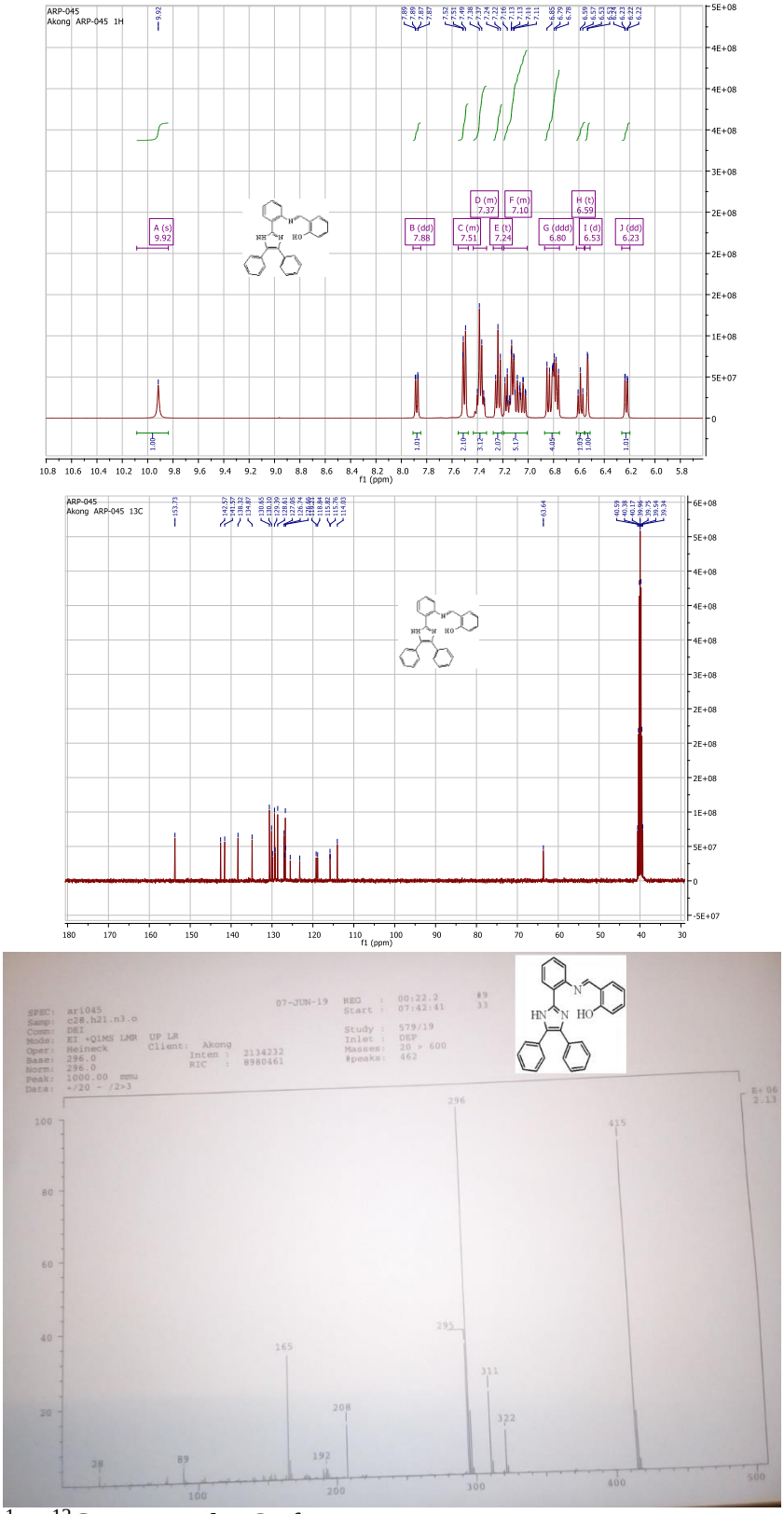

Figure S28: ^{1}H, ^{13}C NMR and MS of **I_2**

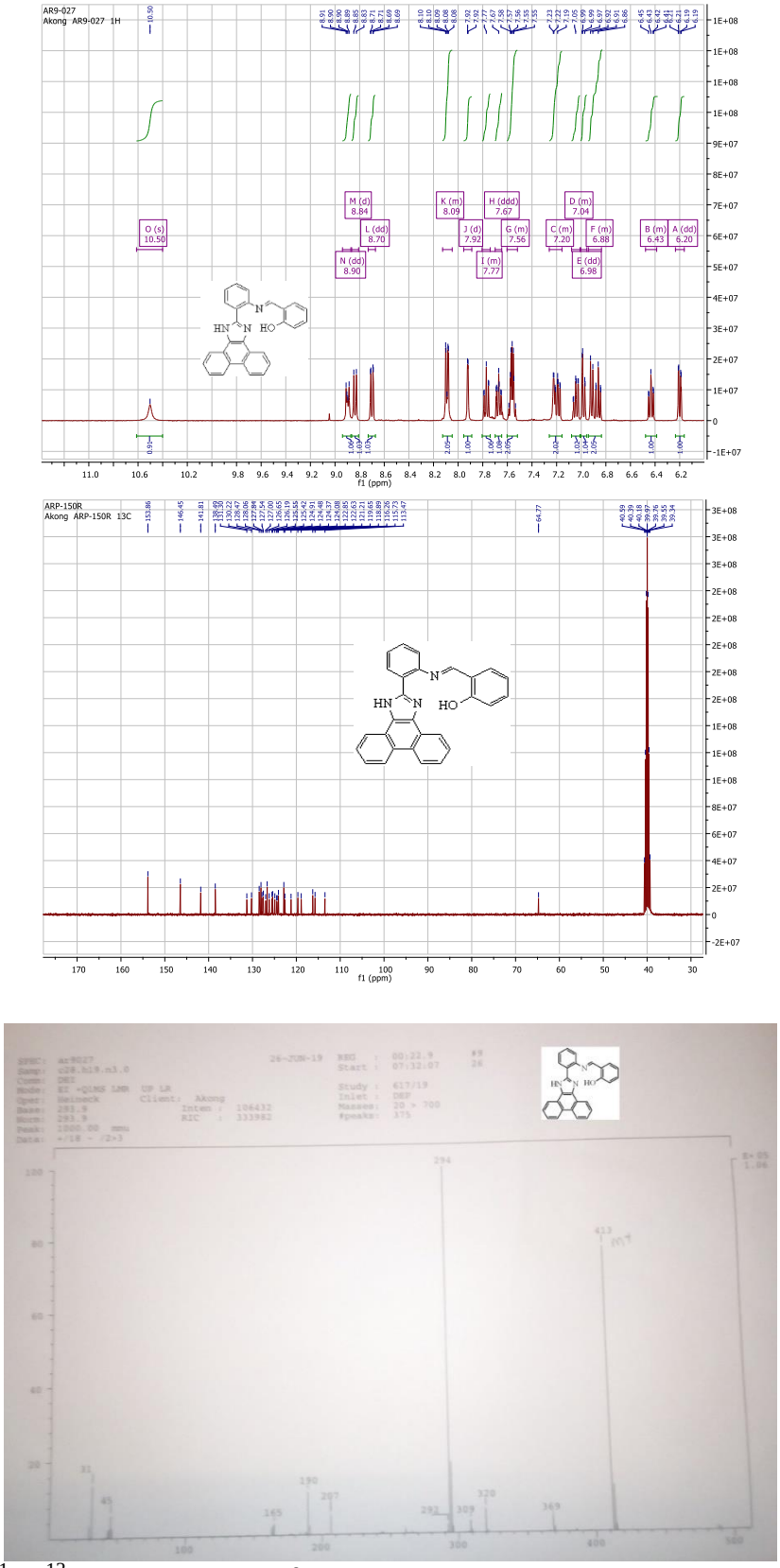

Figure S29: ^{1}H, ^{13}C NMR and MS of $\mathbf{I_3}$

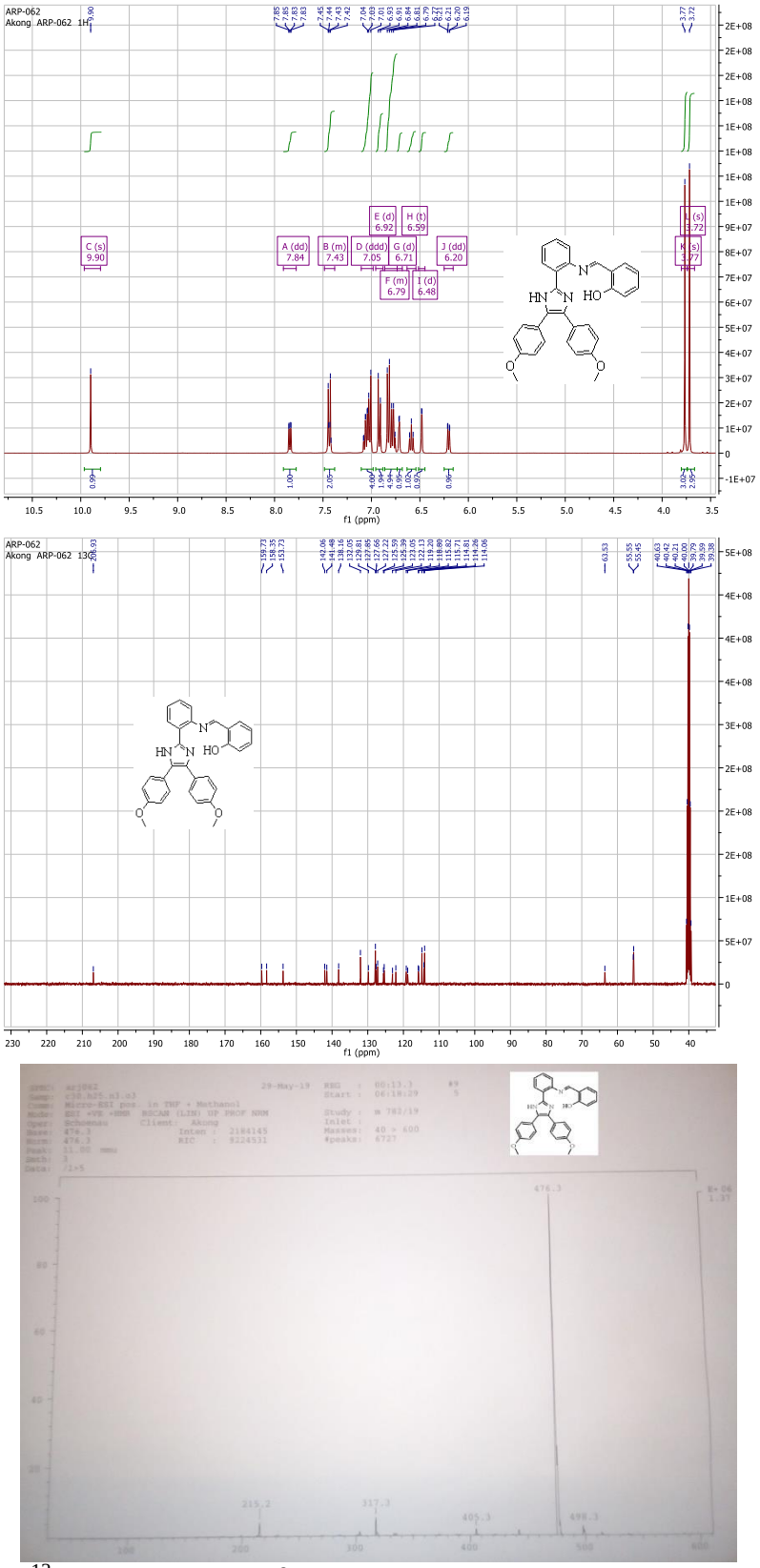

Figure S30: ^{1}H, ^{13}C NMR and MS of **I_4**

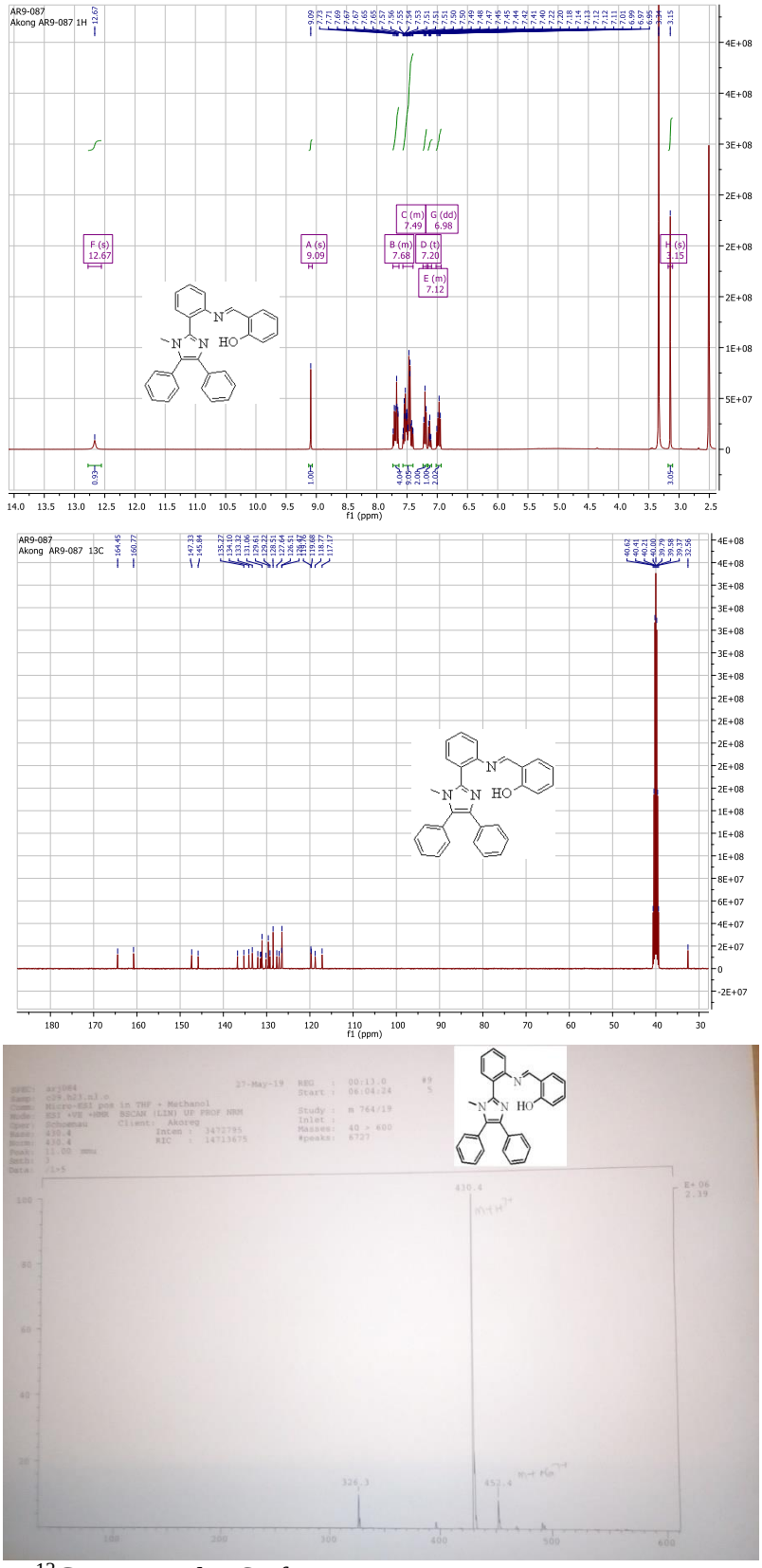

Figure S31: ^{1}H, ^{13}C NMR and MS of **I5**

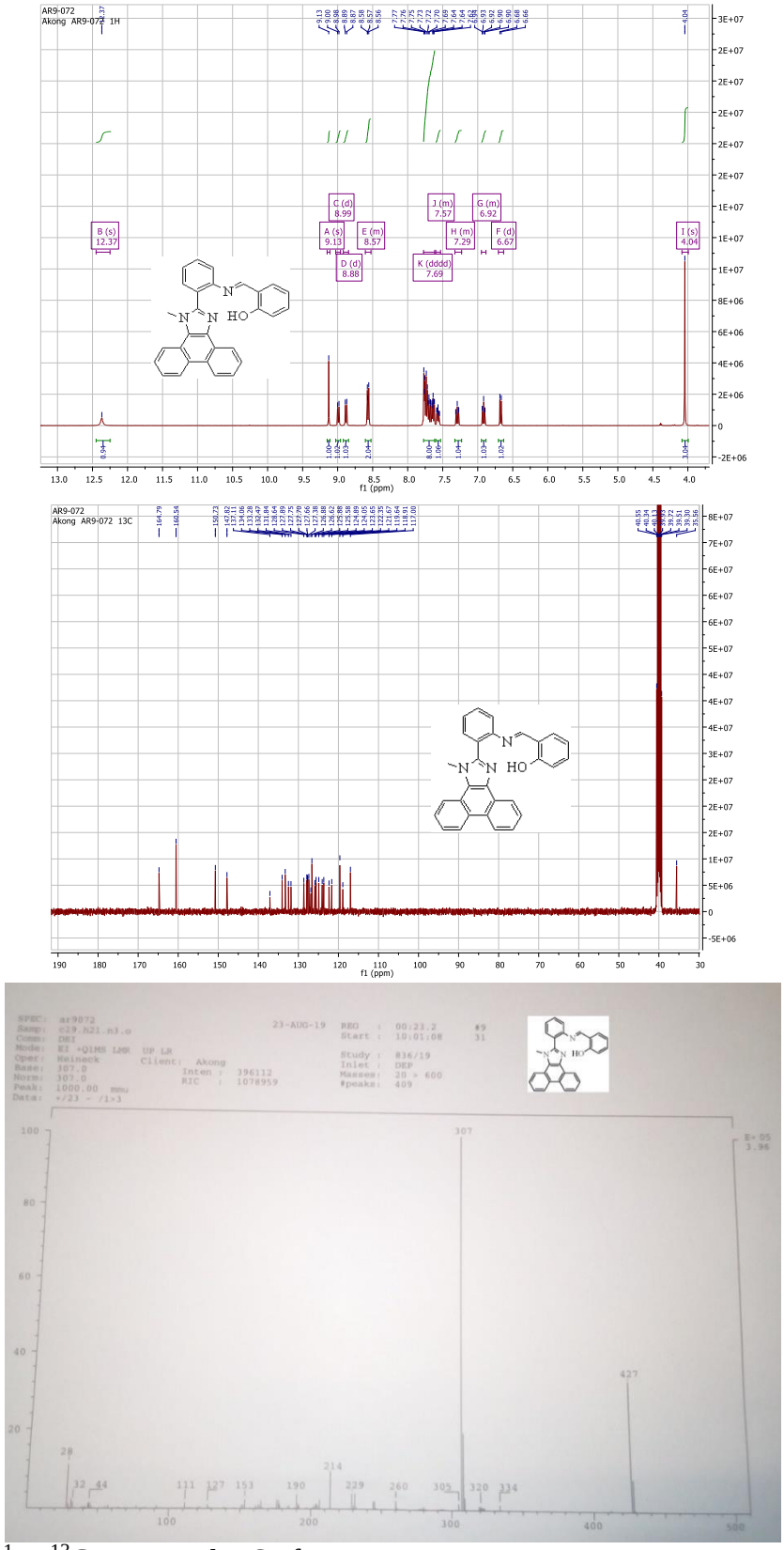

Figure S32: ^{1}H, ^{13}C NMR and MS of **I_6**

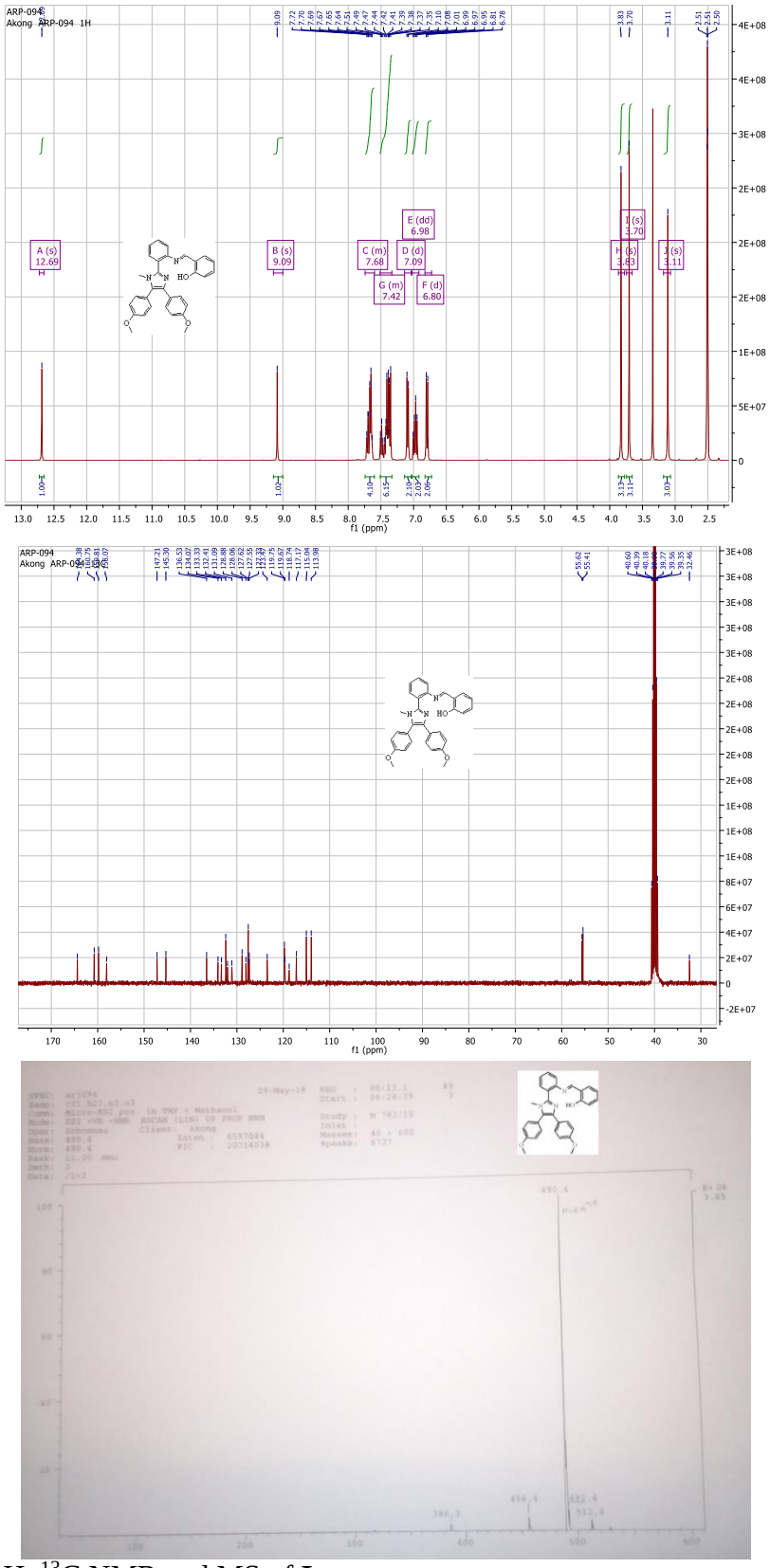

Figure S33: ^{1}H, ^{13}C NMR and MS of $\mathbf{I_7}$

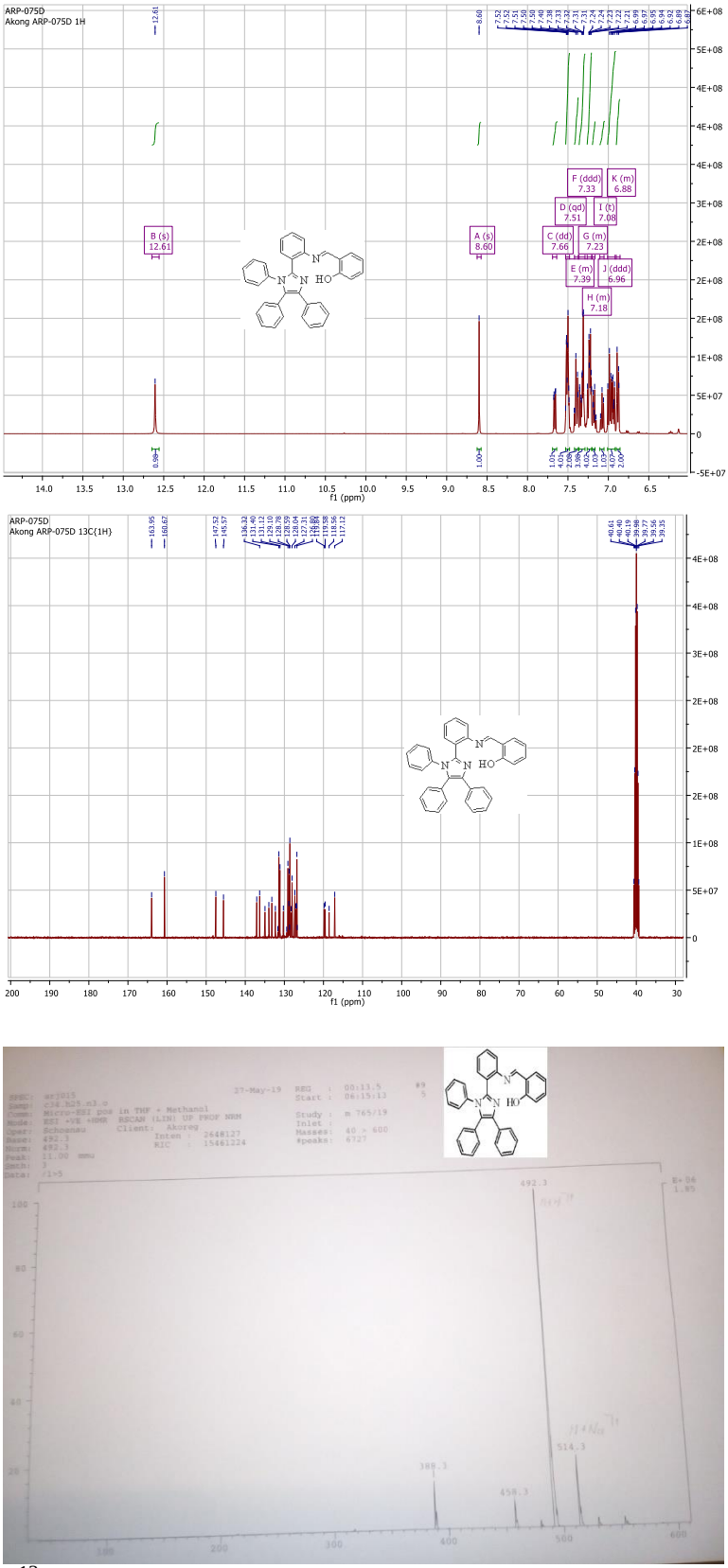

Figure S34: ^{1}H, ^{13}C NMR and MS of $\mathbf{I_8}$

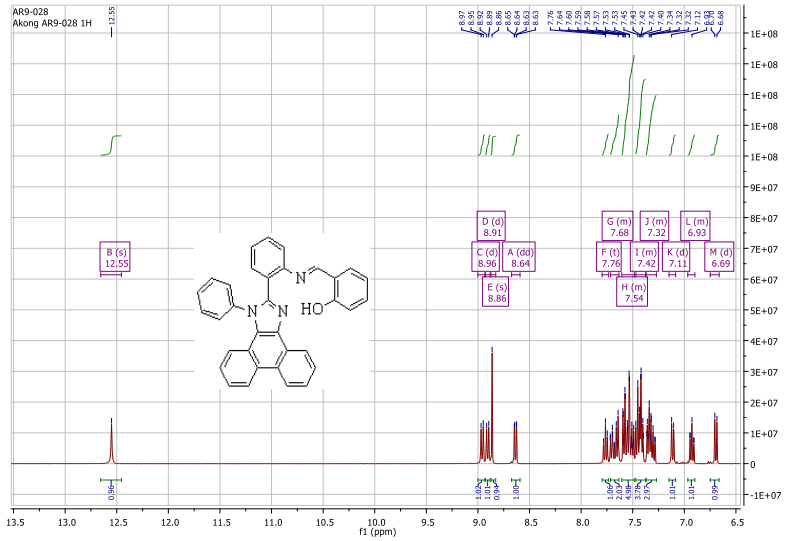

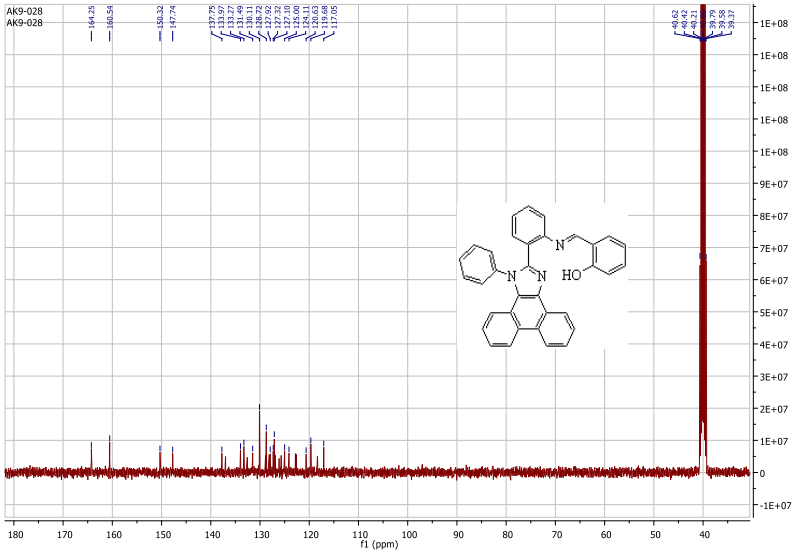

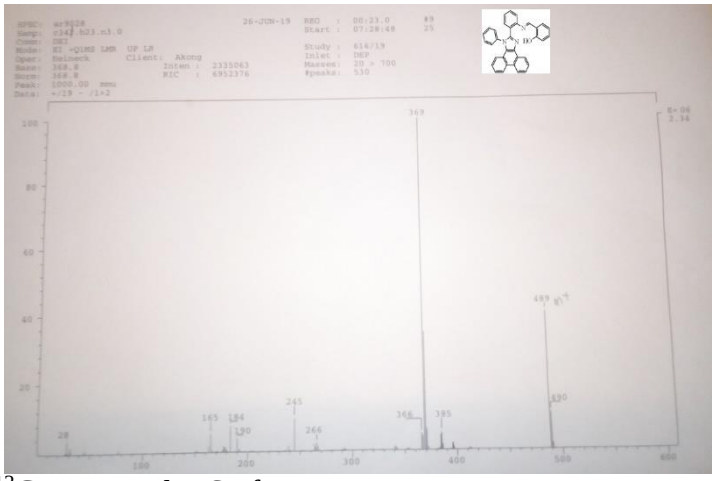

Figure S35: ^{1}H, ^{13}C NMR and MS of **I_9**

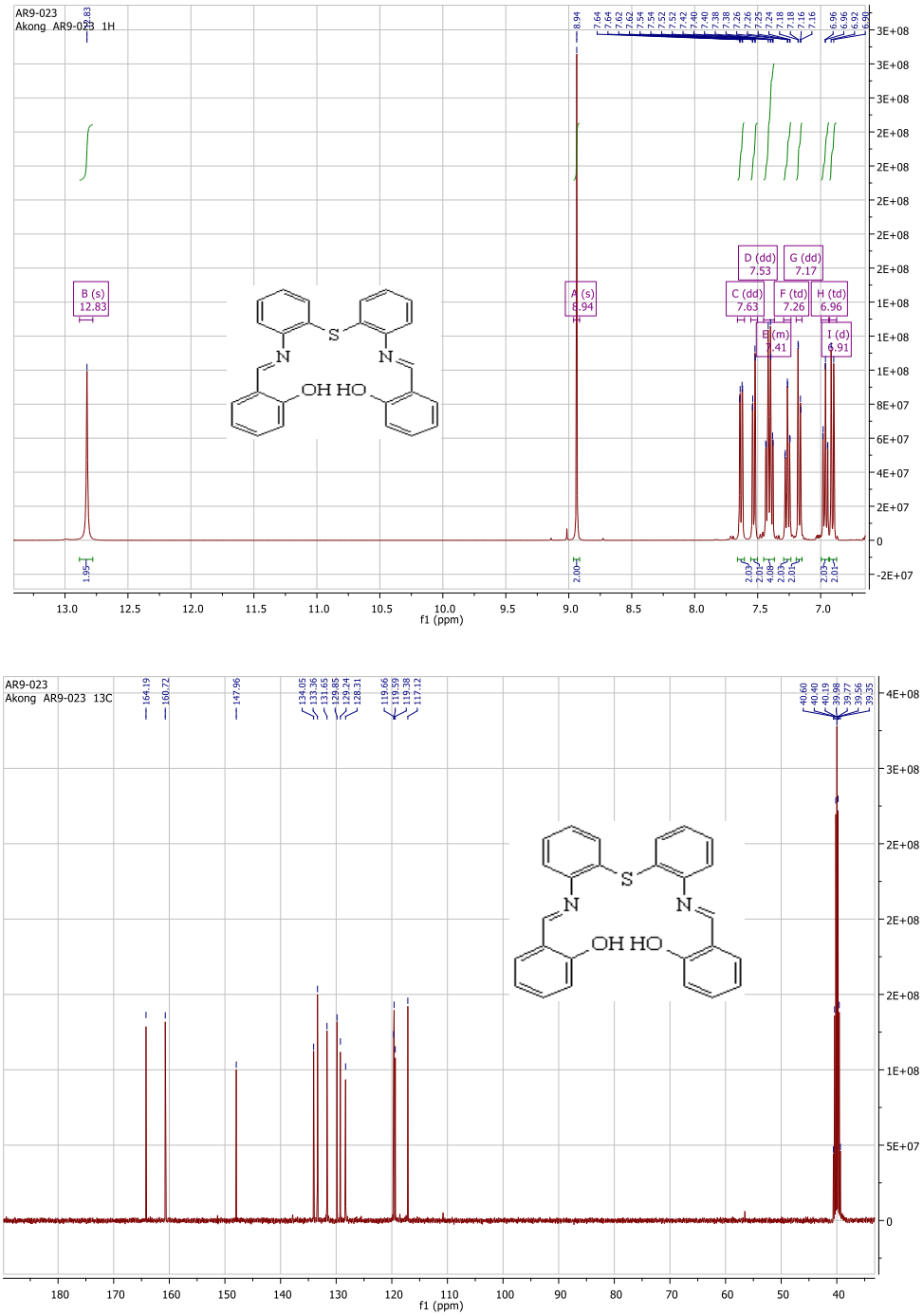

Figure S36: ^{1}H and ^{13}C NMR of **H_2S1**

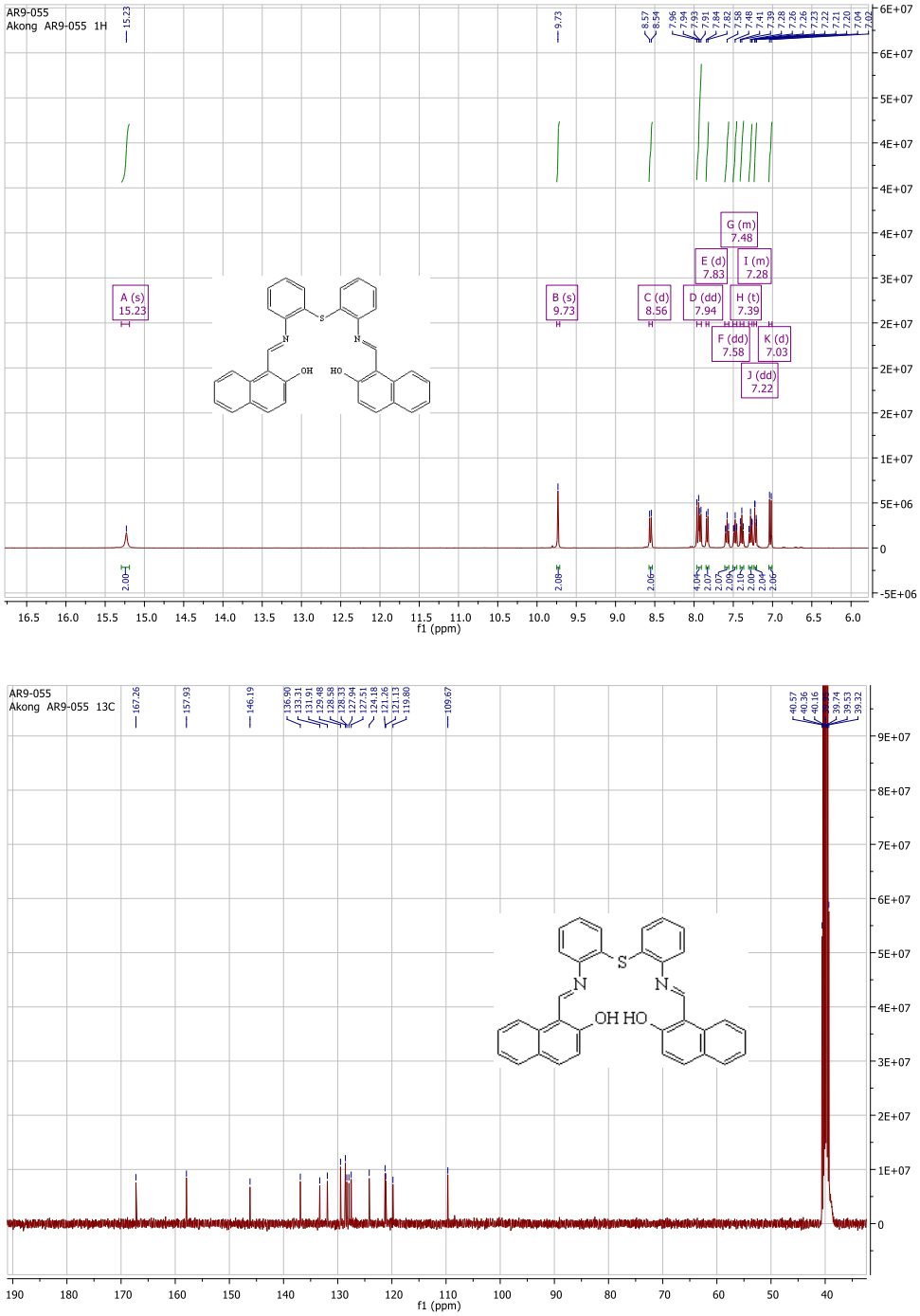

Figure S37: ^{1}H and ^{13}C NMR of **H_2S2**

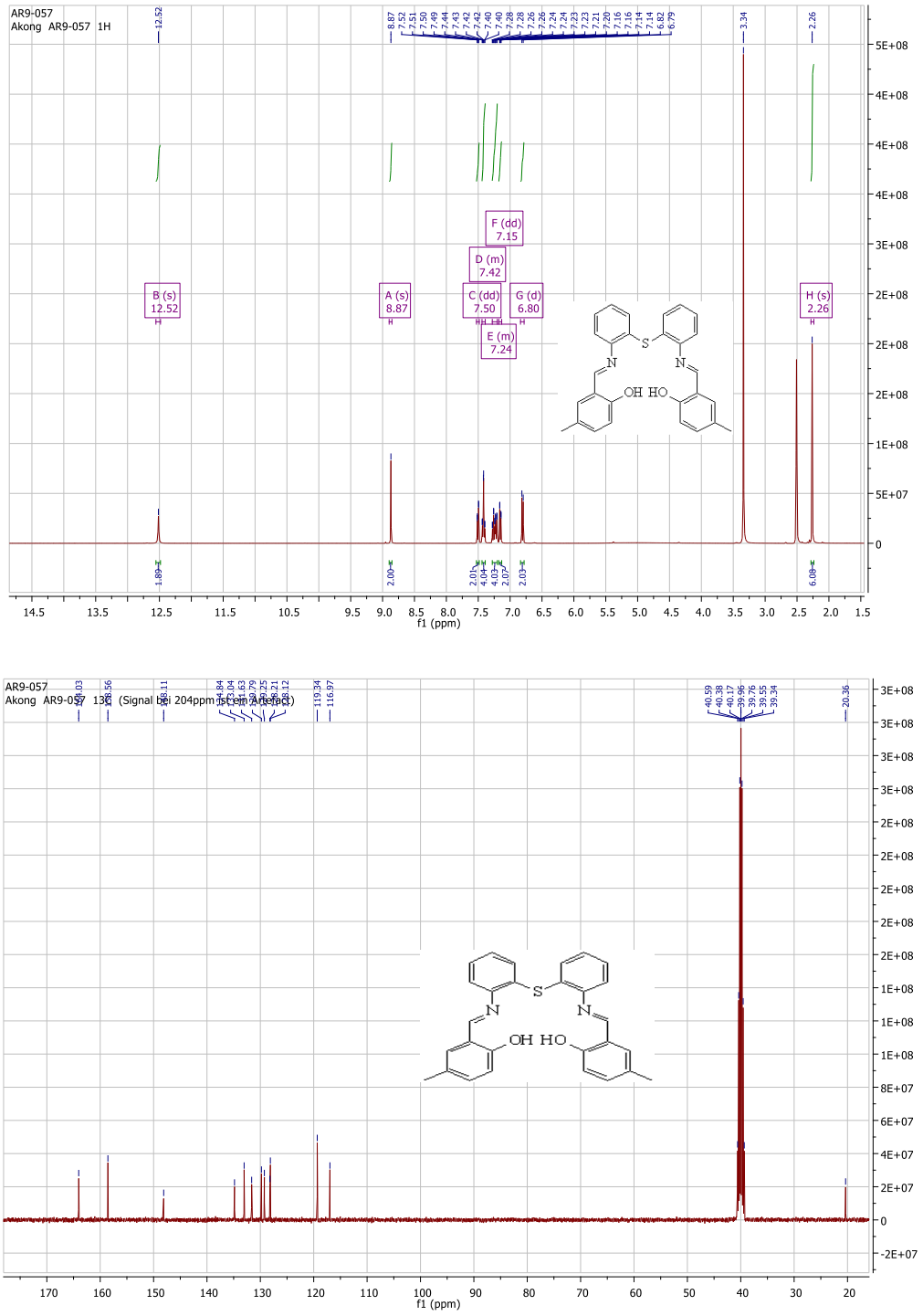

Figure S38: ^{1}H and ^{13}C NMR of **H_2S3**

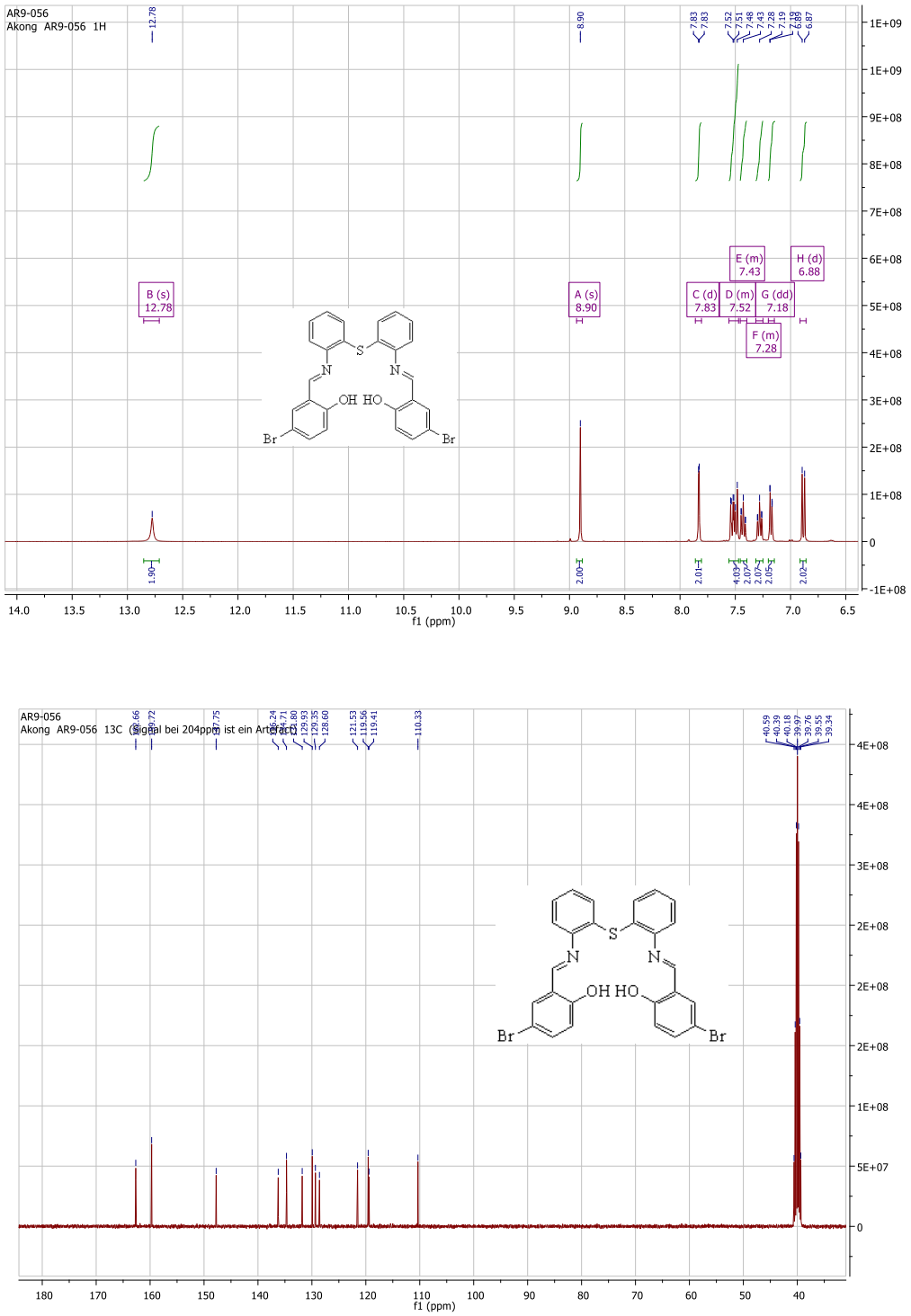

Figure S39: ^{1}H and ^{13}C NMR of **H_2S4**

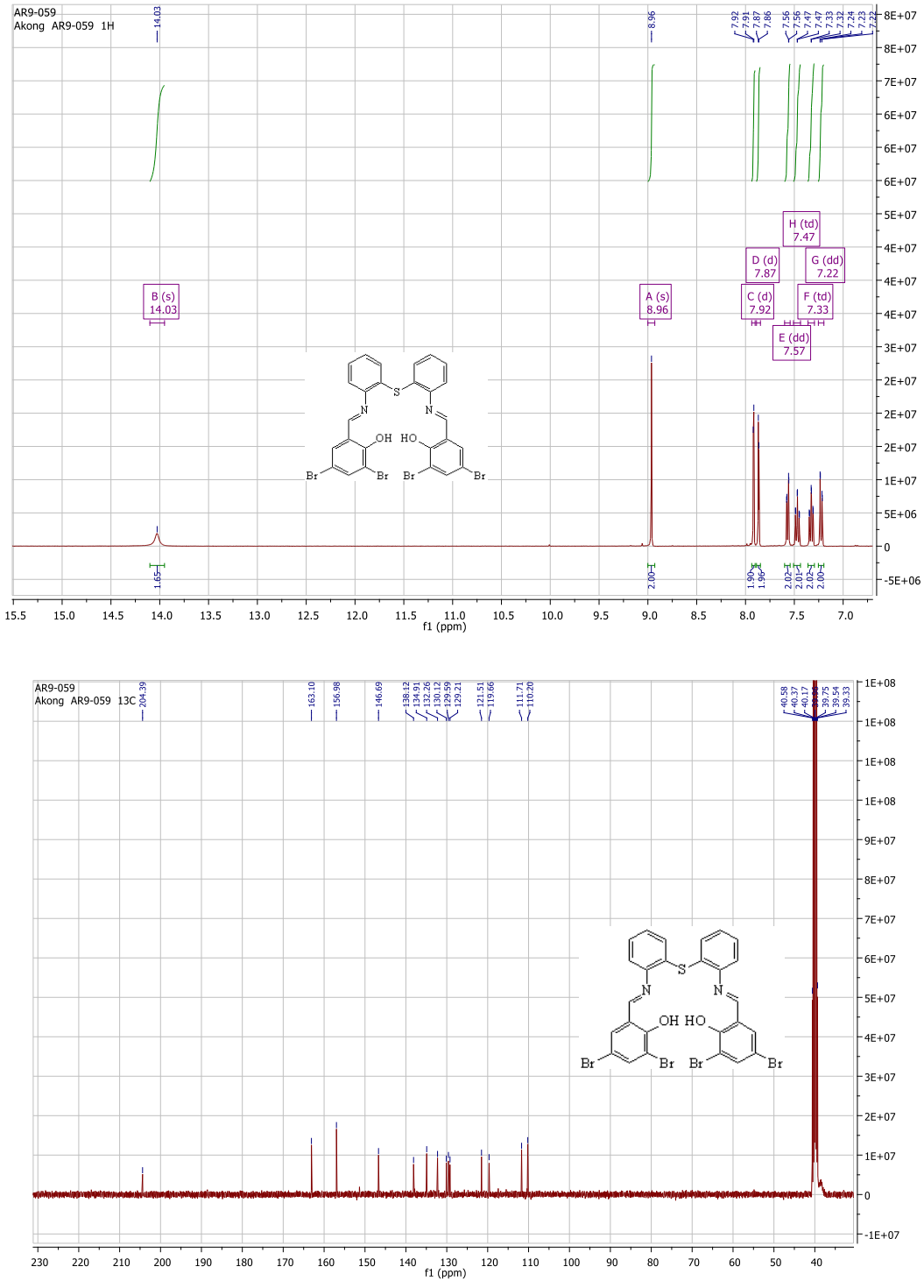

Figure S40: ^{1}H and ^{13}C NMR of **H_2S5**

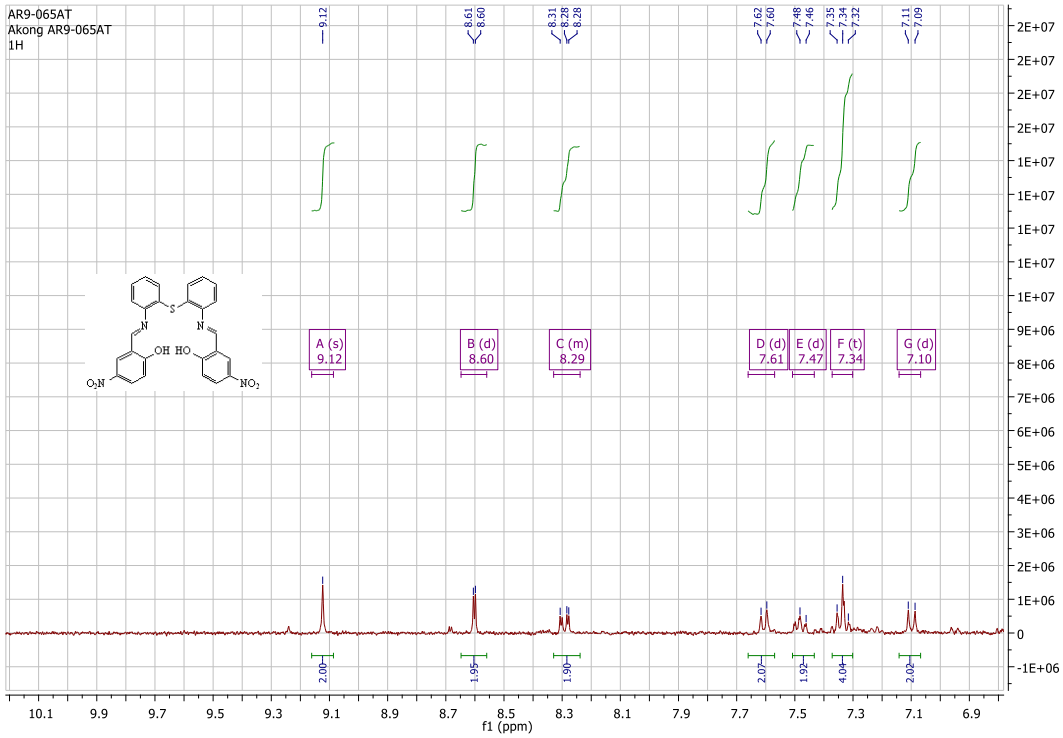

Figure S41: ^{1}H NMR of **H_2S6**

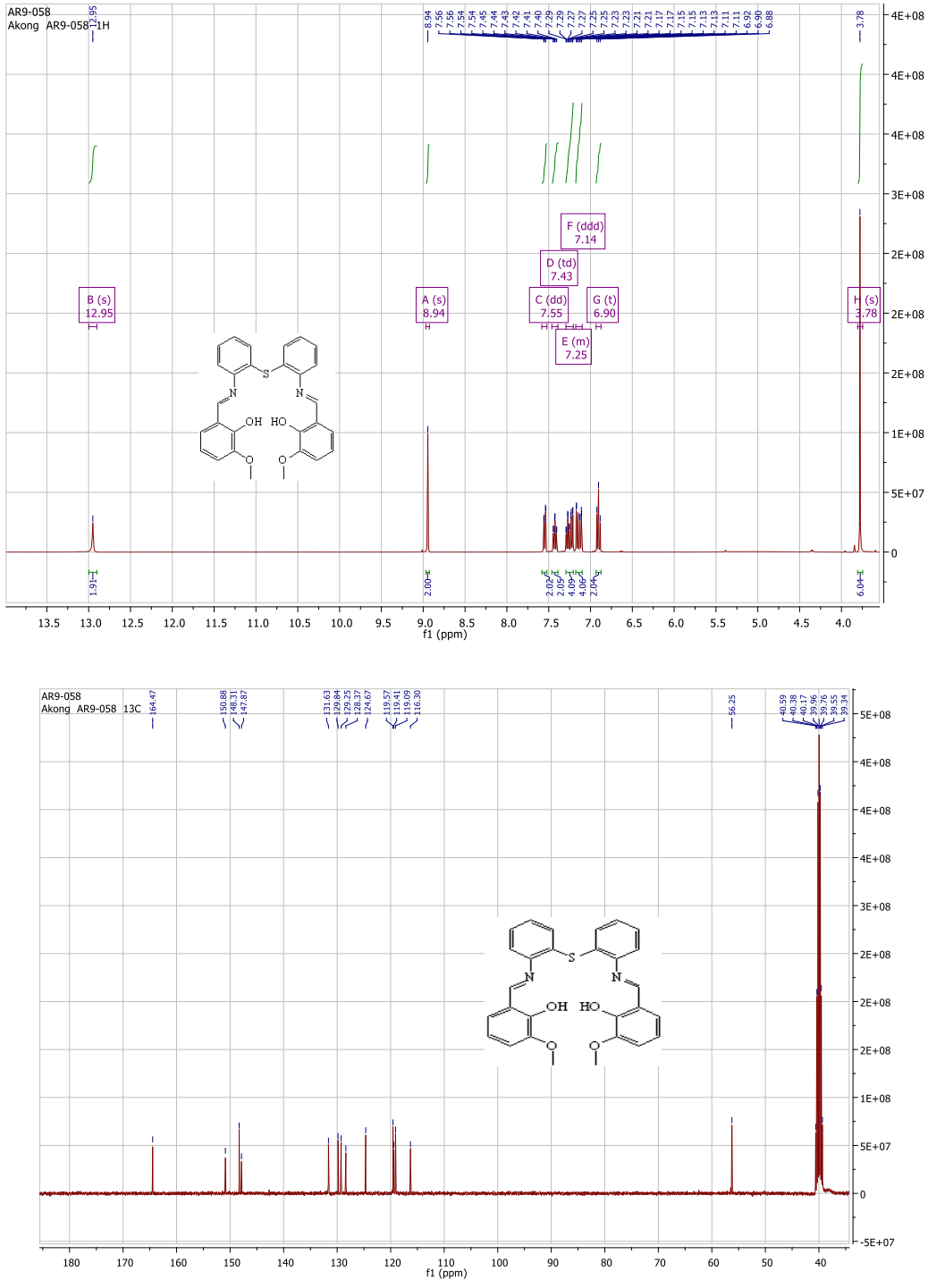

Figure S42: ^{1}H of **H_2S7**

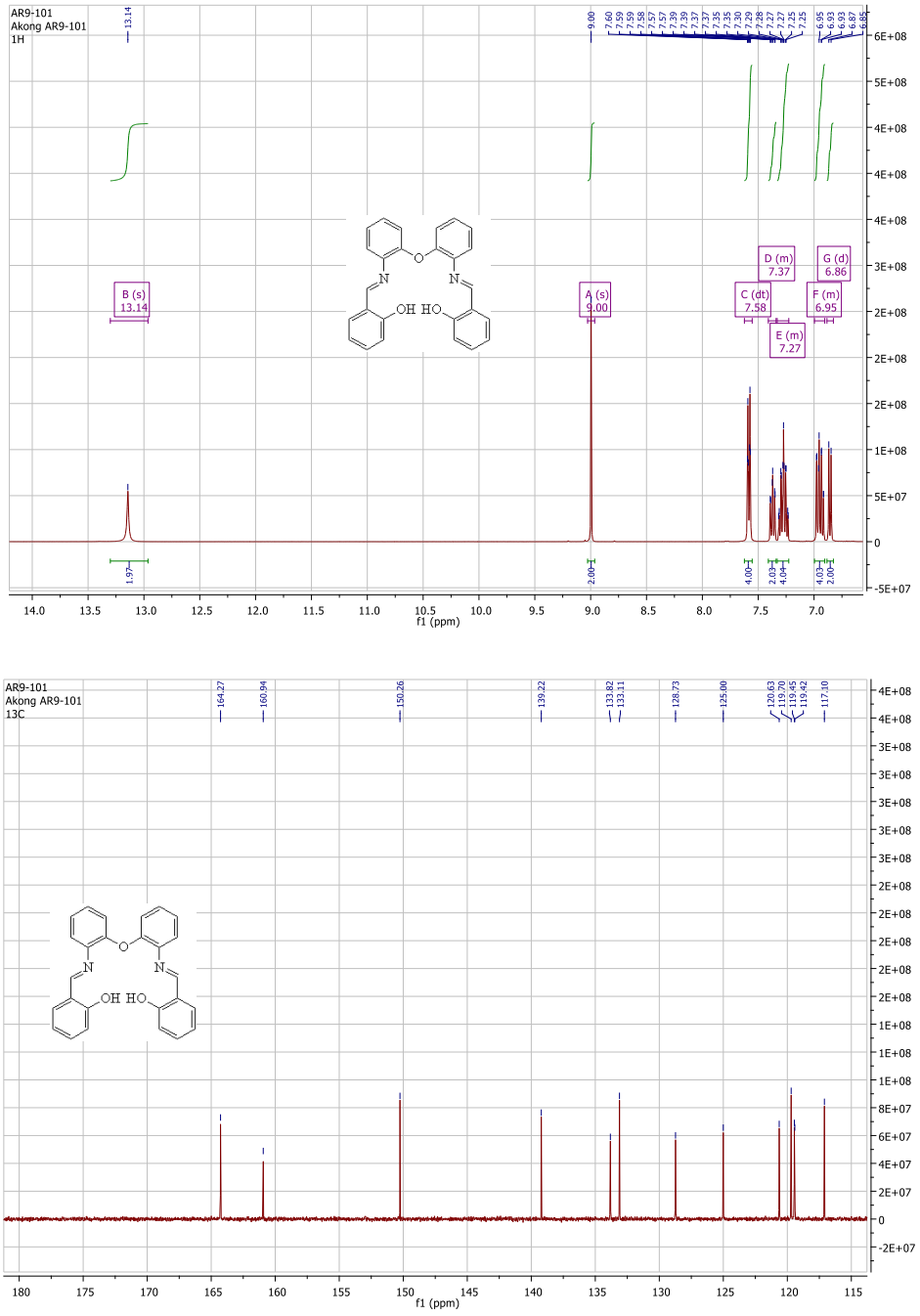

Figure S43: ^{1}H and ^{13}C NMR of **H_2O1**

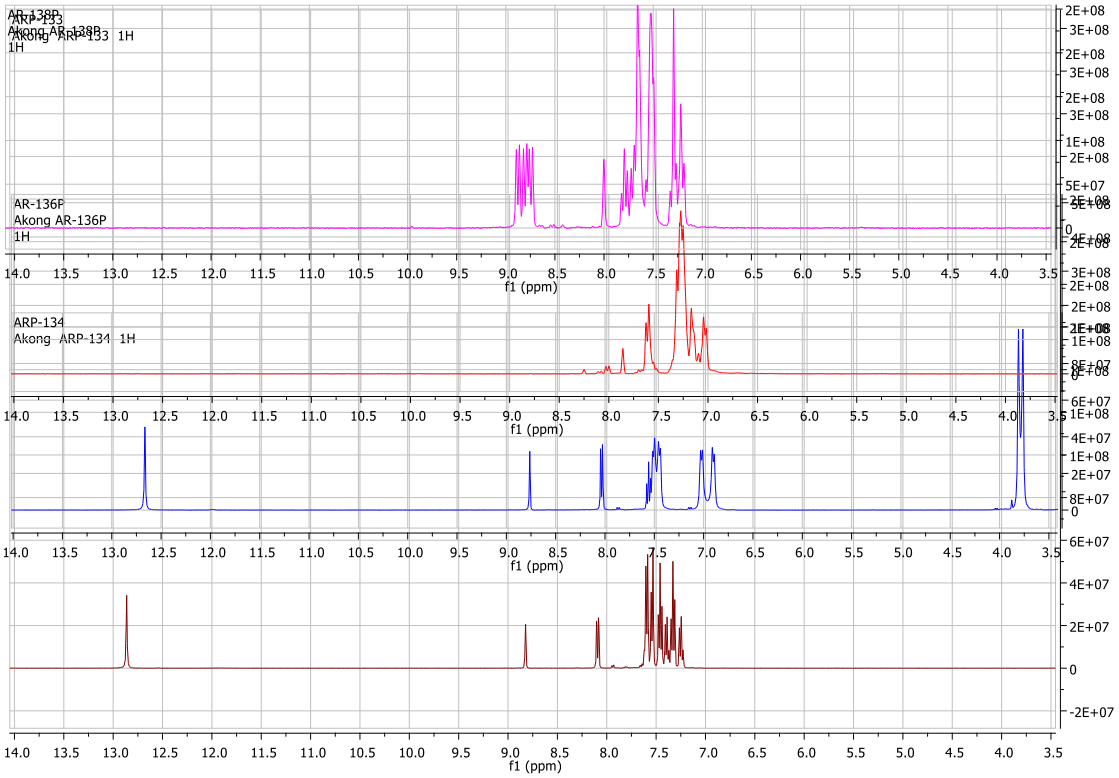

Figure S44: ^{1}H nmr of **BI$_1$** (dark red); **BI$_2$** (blue); **BI$_3$** (red) and **BI$_4$** (magenta)

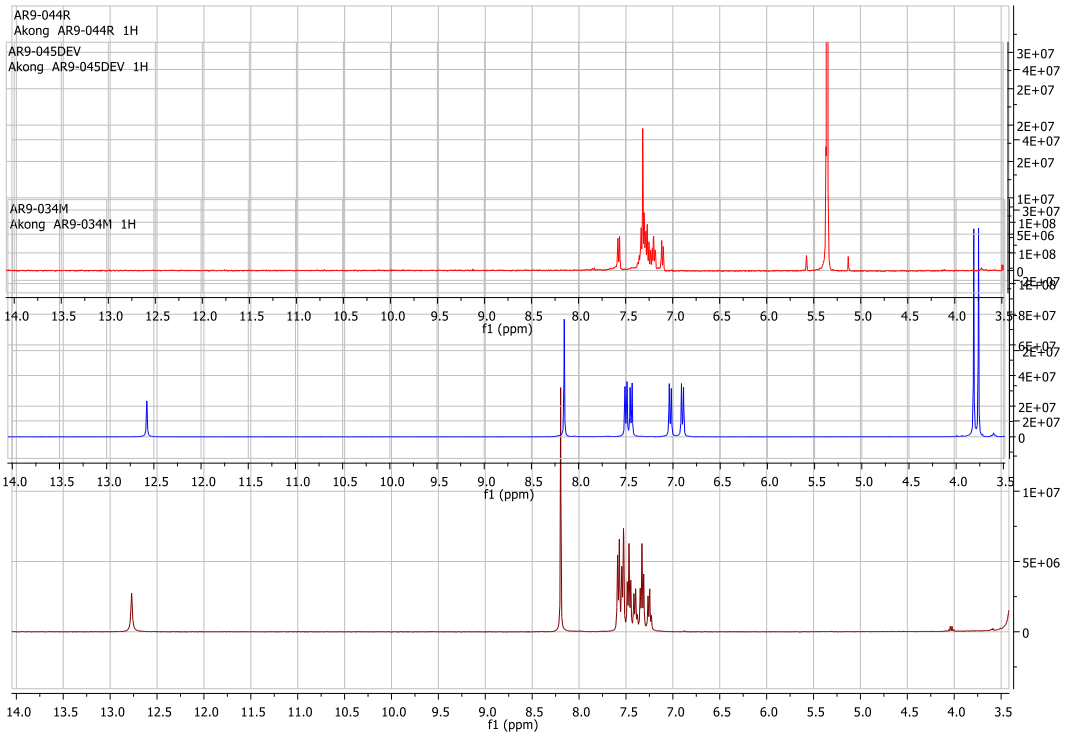

Figure S45: ^{1}H nmr of **BI$_5$** (dark red); **BI$_6$** (blue) and **BI$_7$** (red)

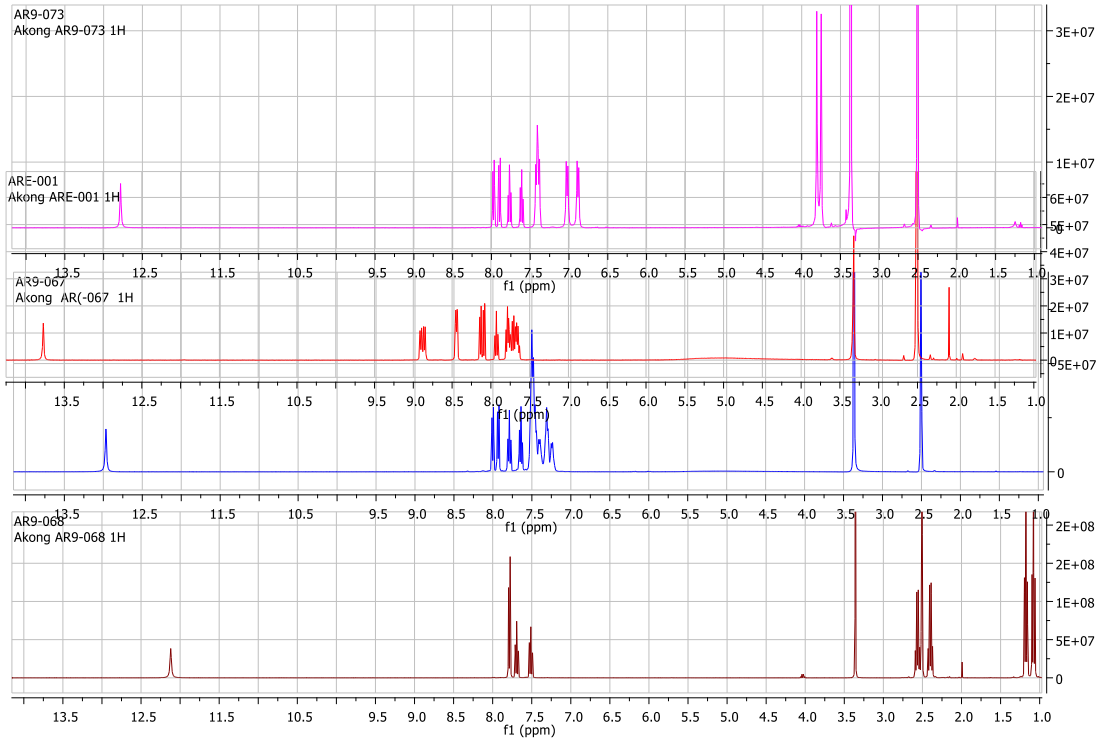

Figure S46: ^{1}H nmr of **N1** (dark red); **N2** (blue); **N3** (red) and **N4** (magenta)

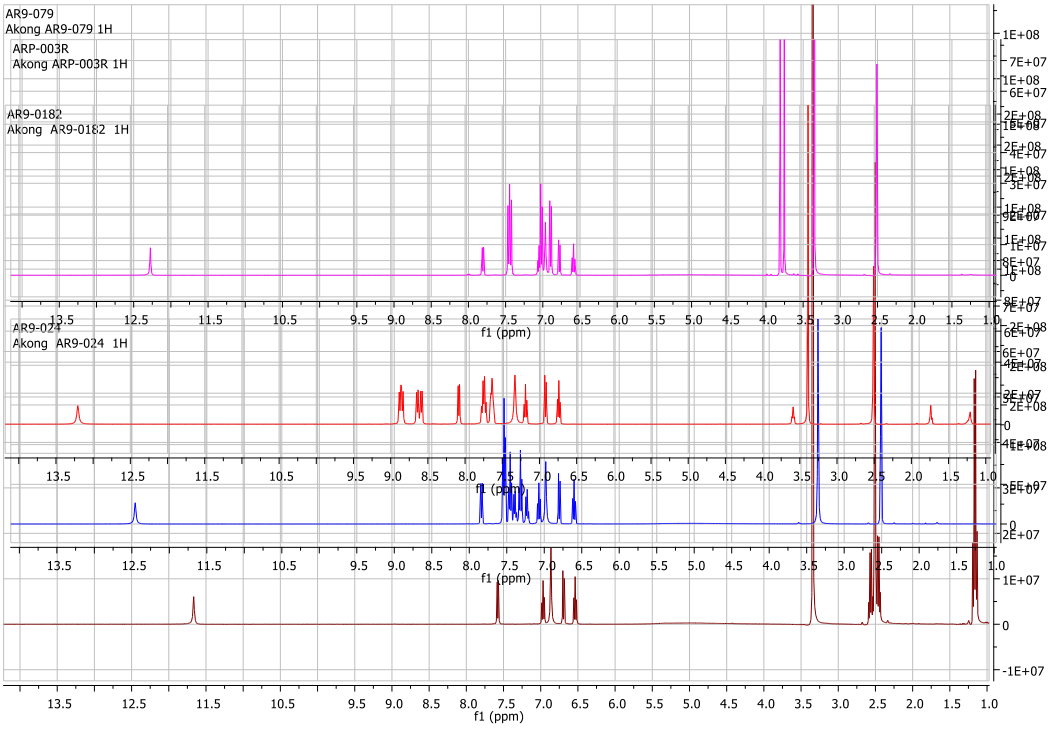

Figure S47: ^{1}H nmr of **A1** (dark red); **A2** (blue); **A3** (red) and **A4** (magenta)

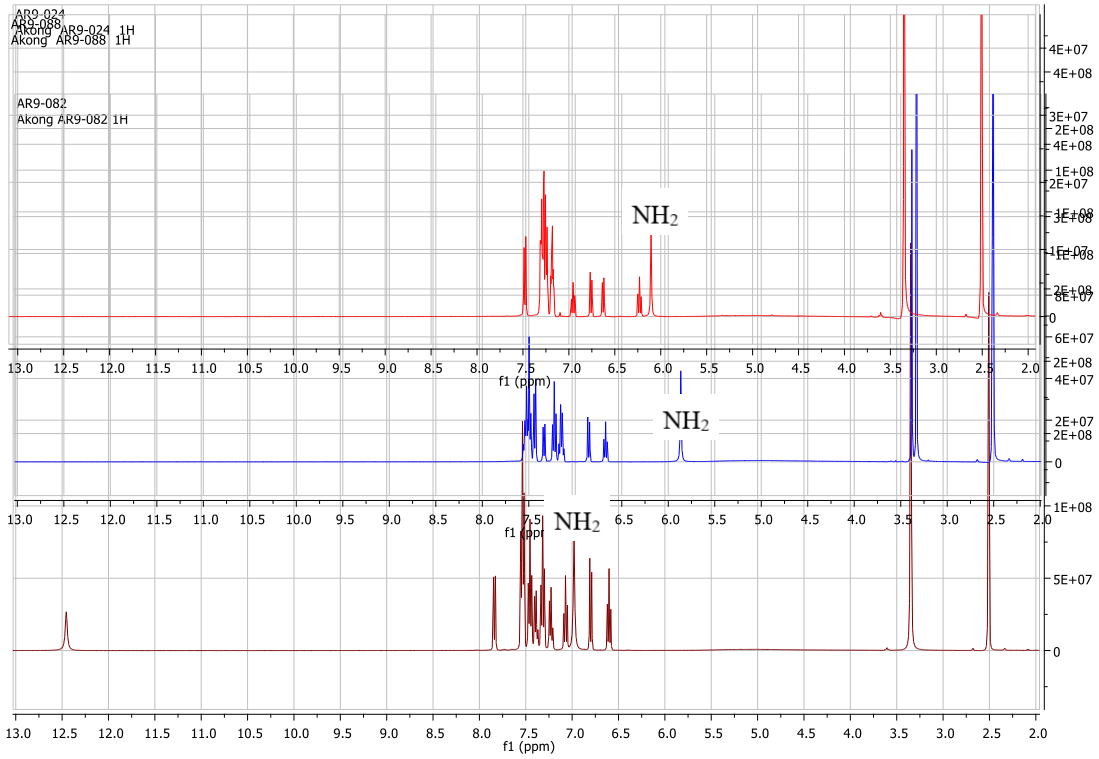

Figure S48: ^{1}H nmr of **A2** (dark red); **A5** (blue) and **A8** (red)

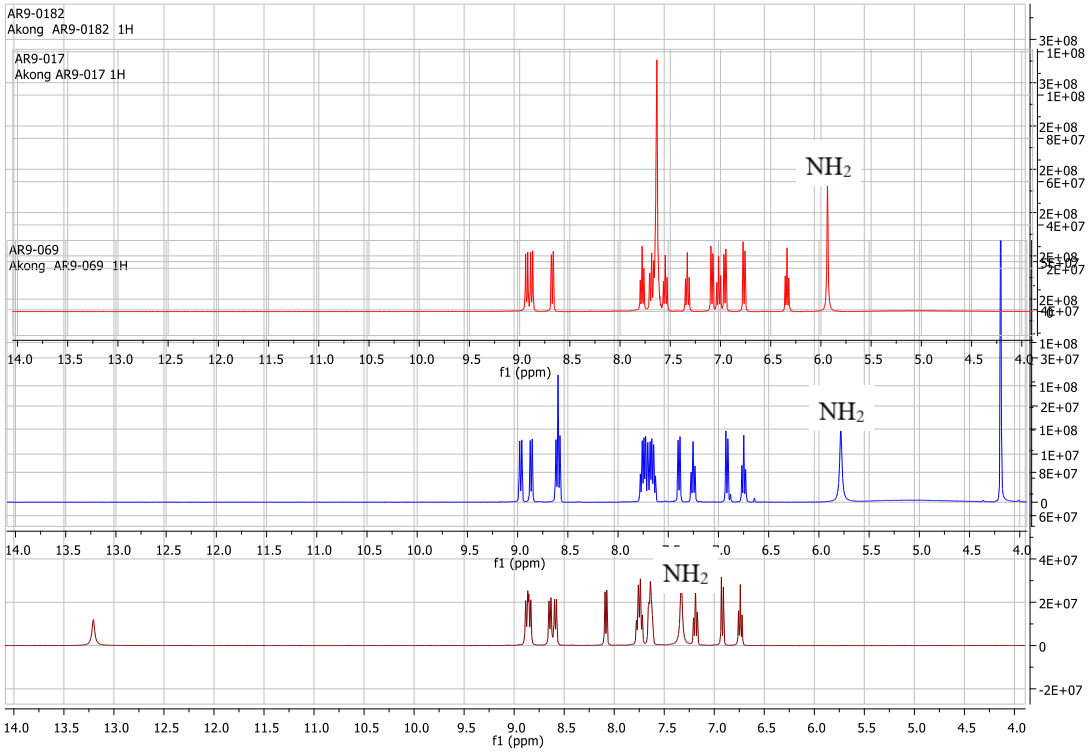

Figure S49: ^{1}H nmr of **A3** (dark red); **A6** (blue) and **A9** (red)

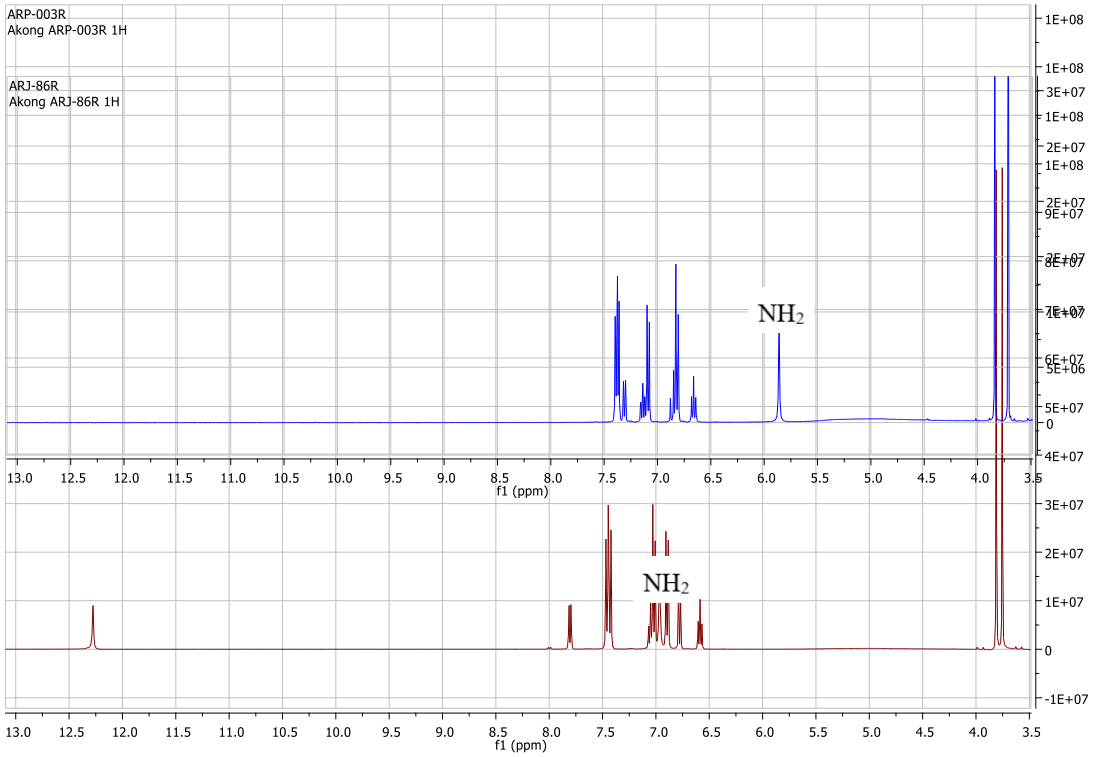

Figure S50: ^{1}H nmr of **A4** (dark red) and **A7** (blue)

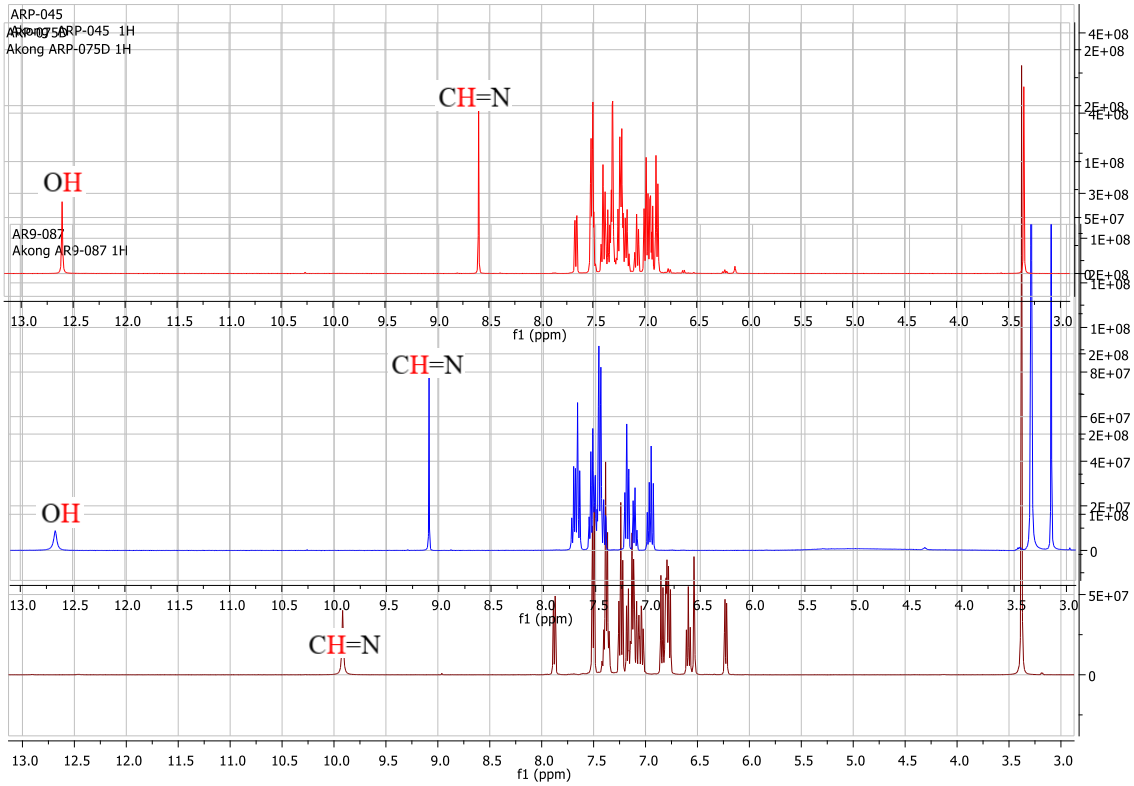

Figure S51: ^{1}H nmr of $\mathbf{I_2}$ (dark red); $\mathbf{I_5}$ (blue) and $\mathbf{I_8}$ (red)

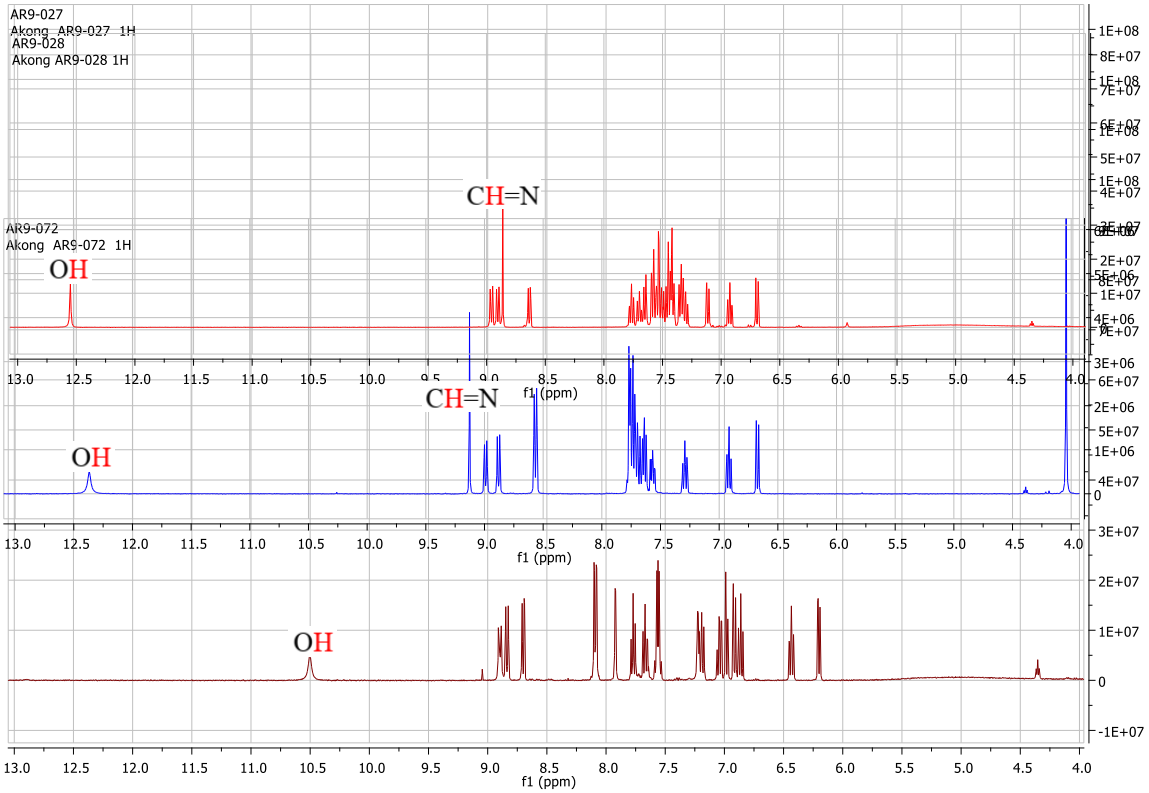

Figure S52: ^{1}H nmr of **I$_3$** (dark red); **I$_6$** (blue) and **I$_9$** (red)

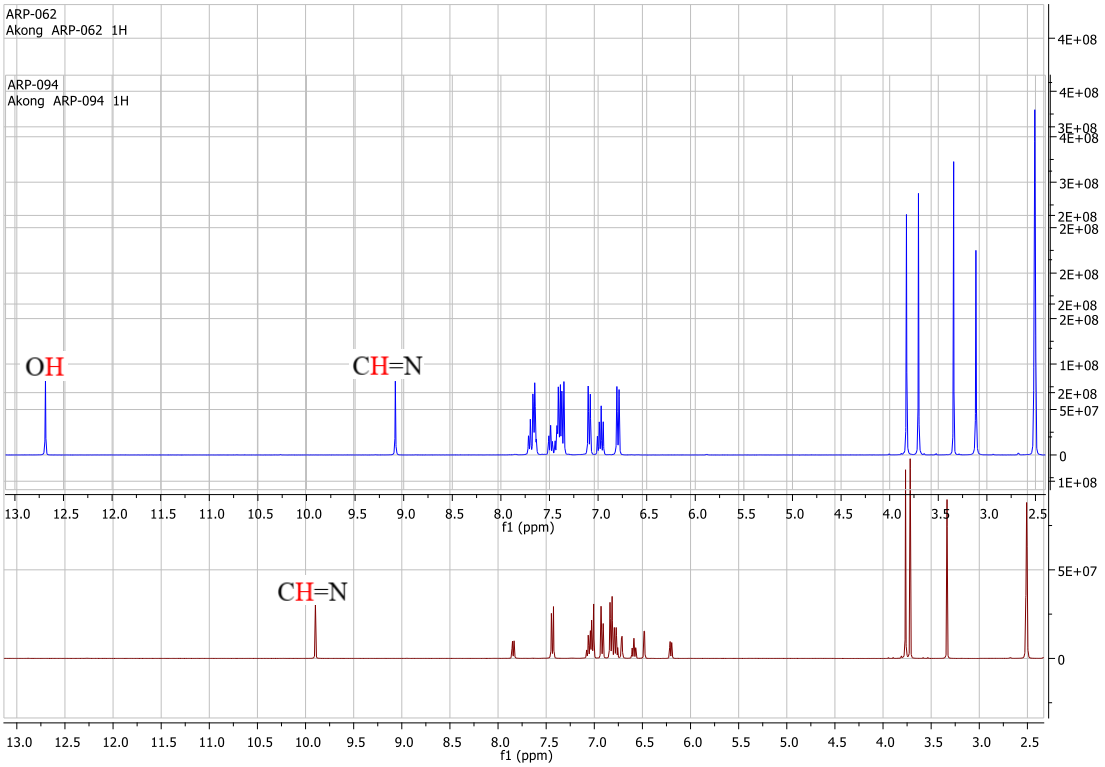

Figure S53: ^{1}H nmr of **I$_4$** (dark red) and **I$_7$** (blue)

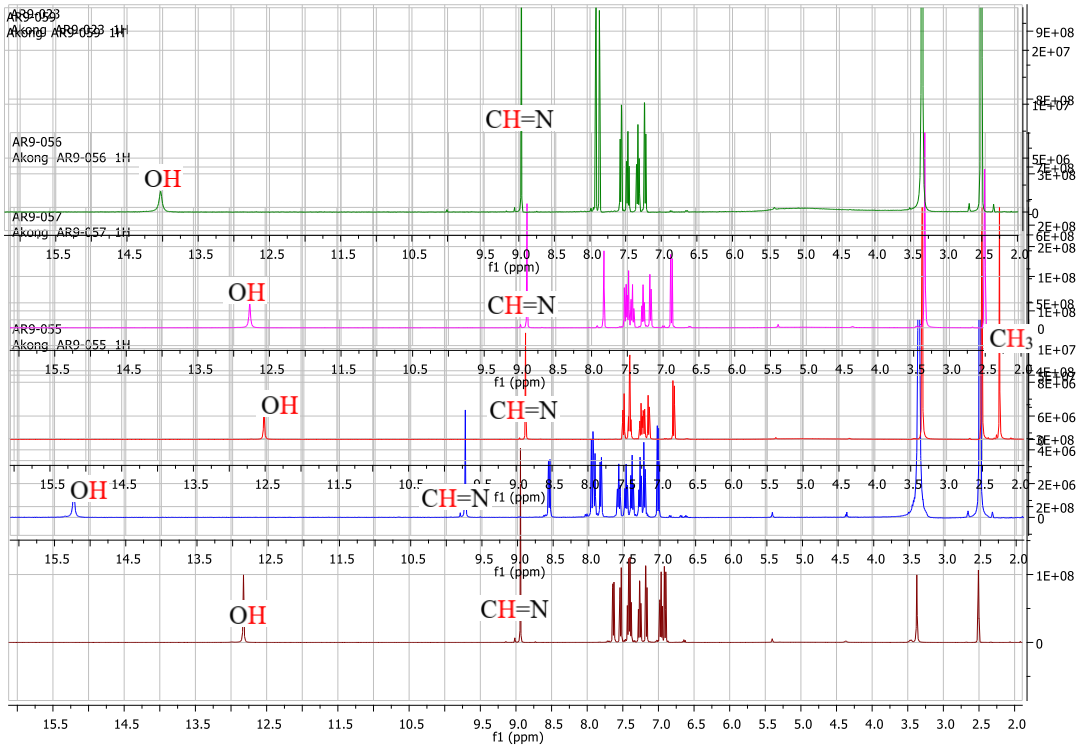

Figure S54: ^{1}H nmr of **H$_2$S1** (dark red), **H$_2$S2** (blue), **H$_2$S3** (red), **H$_2$S4** (magenta) and **H$_2$S5** (dark green)

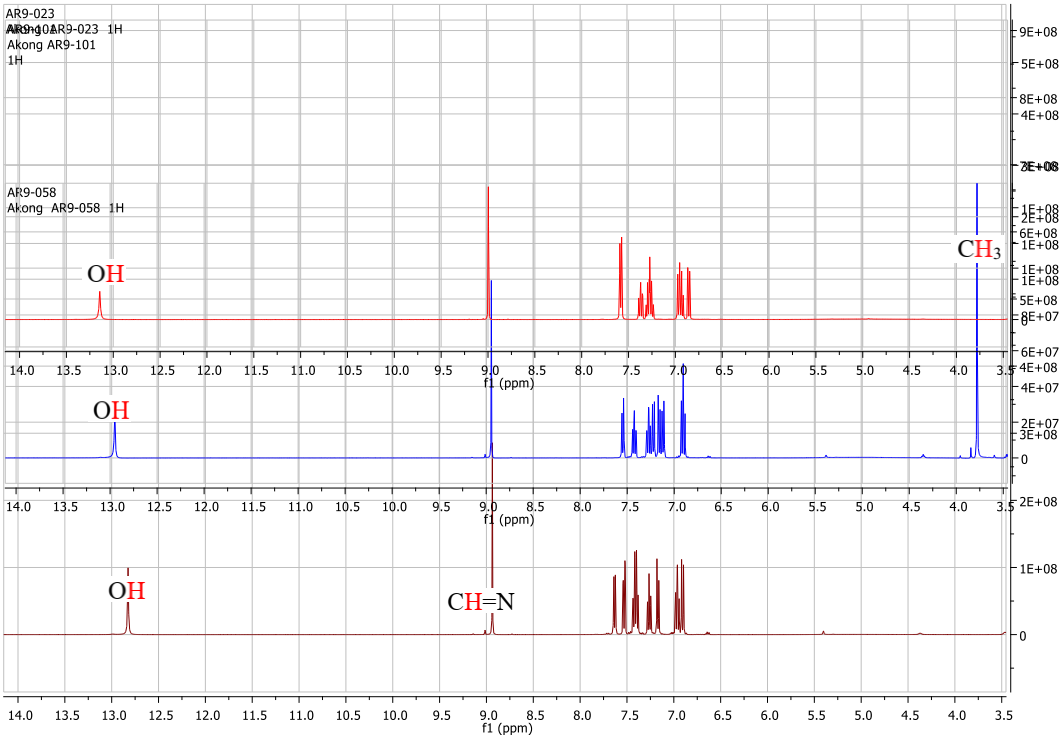

Figure S55: ^{1}H nmr of **H$_2$S1** (dark red), **H$_2$S7** (blue) and **H$_2$O1** (red)

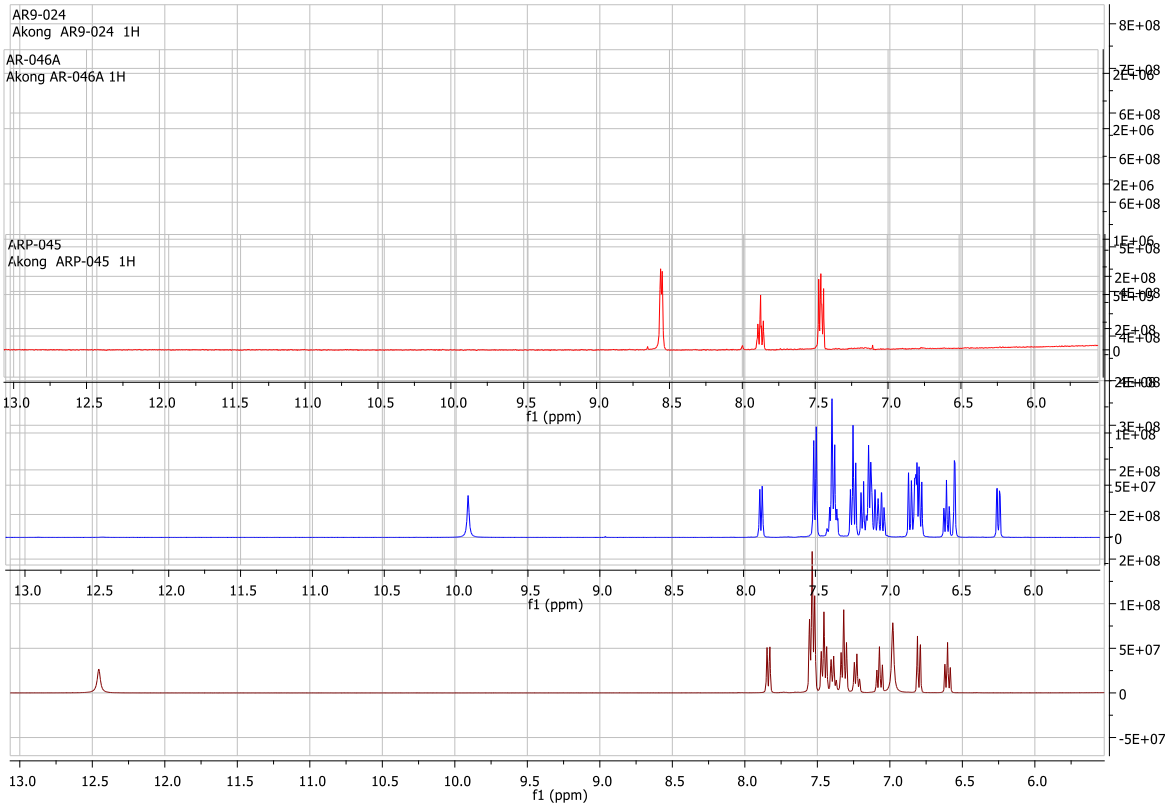

Figure S56: ^{1}H nmr of **A2** (dark red), **I$_2$** (blue) and **M2** (red)

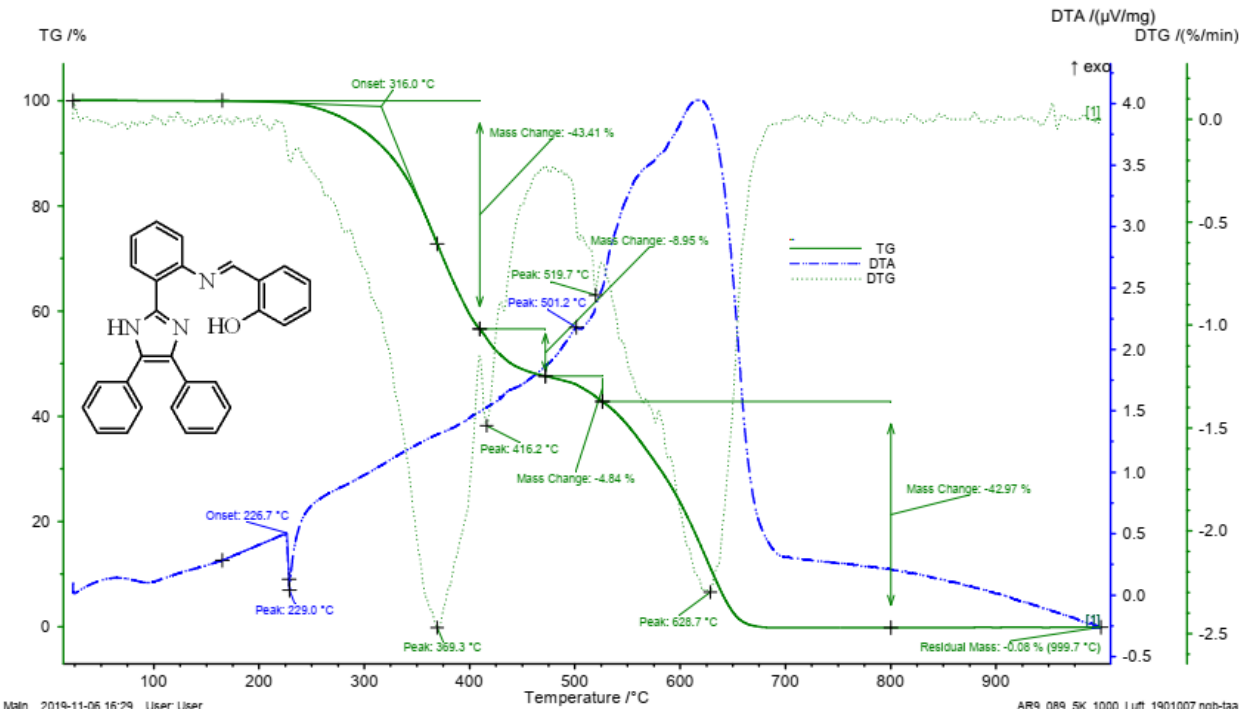

Figure S57: Thermal stability of **I$_2$**

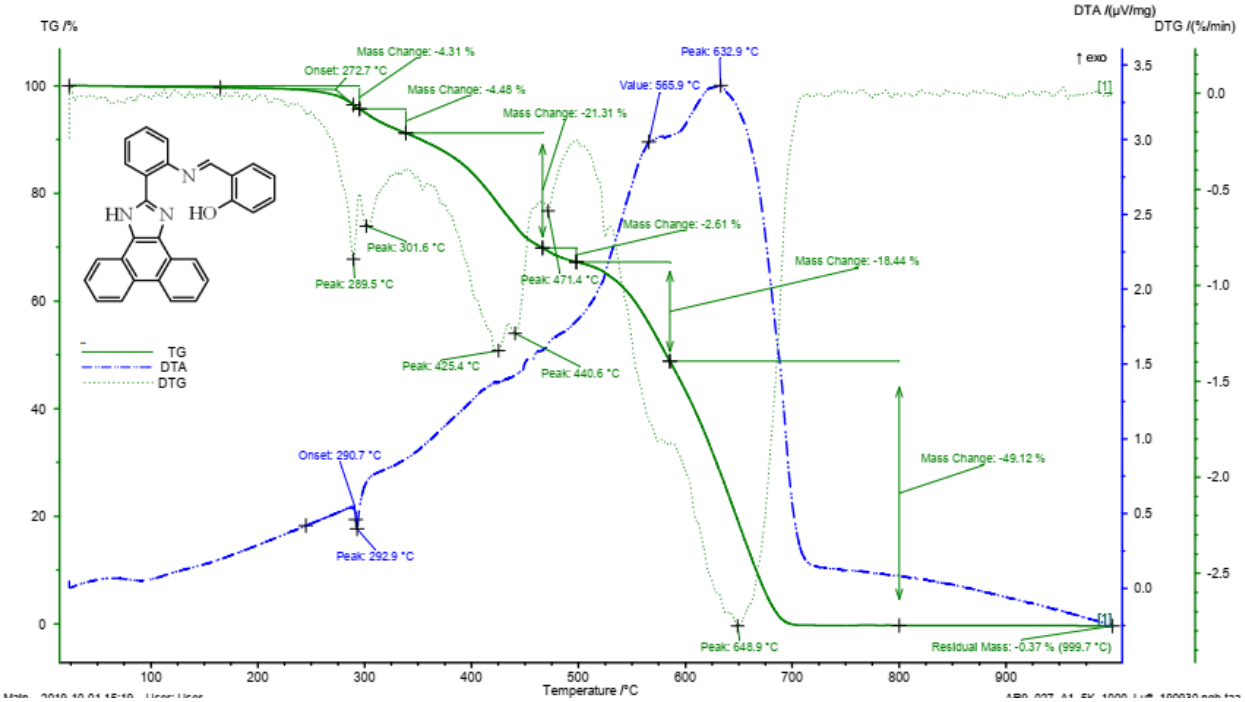

Figure S58: Thermal stability of **I₃**

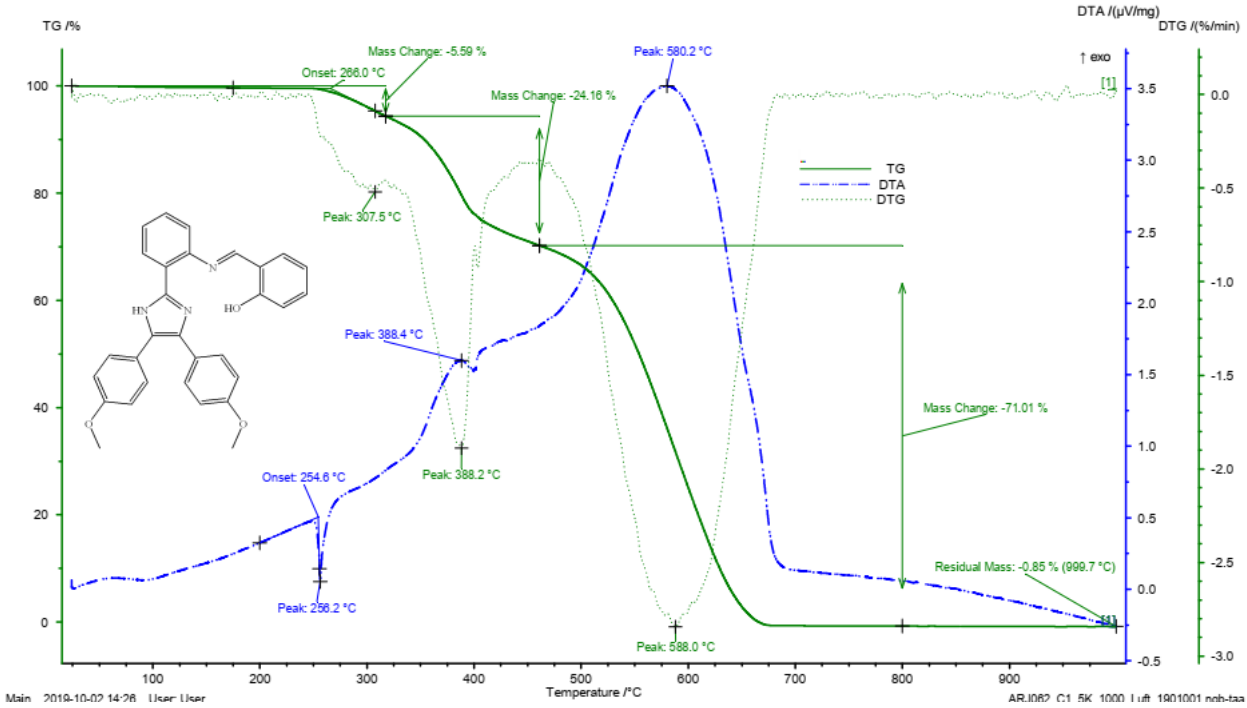

Figure S59: Thermal stability of **I₄**

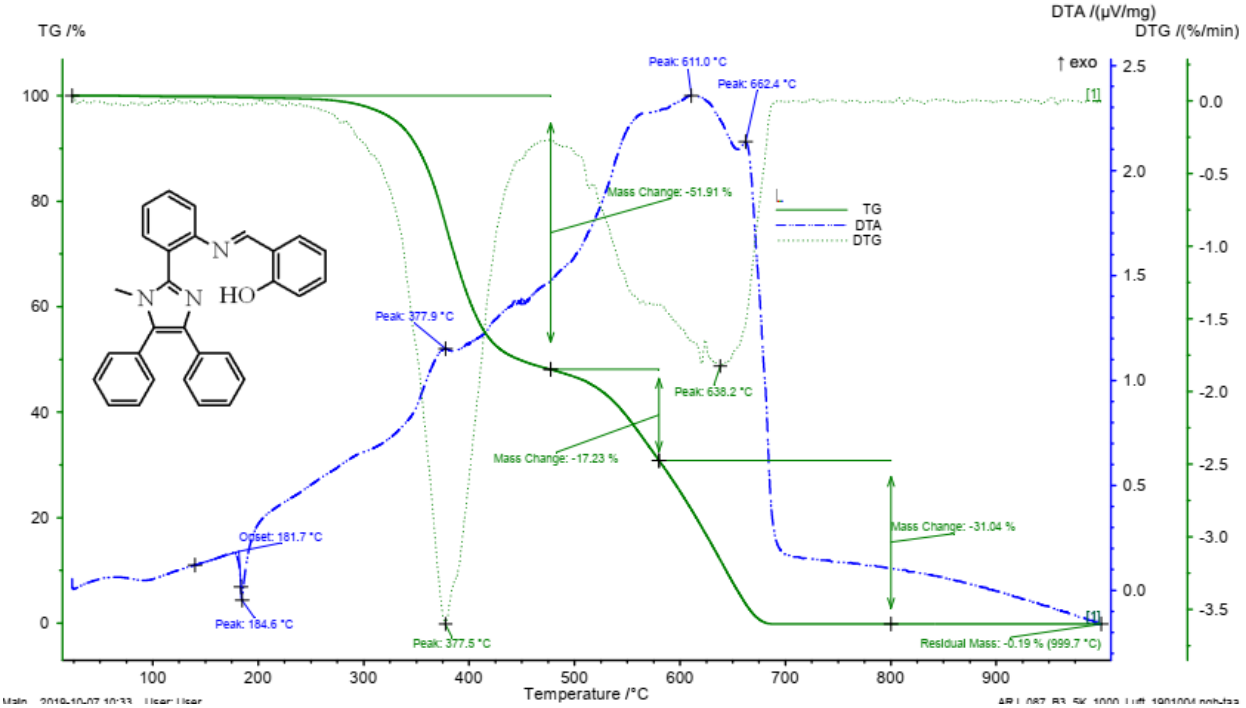

Figure S60: Thermal stability of **I**$_5$

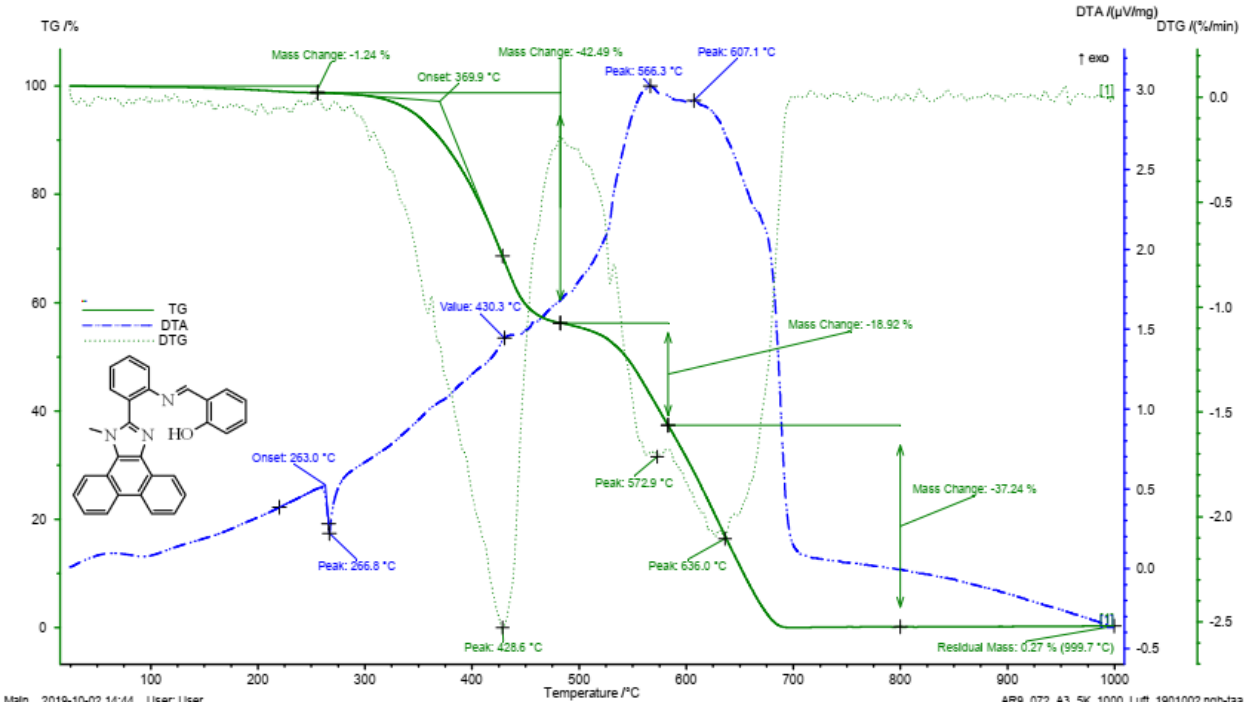

Figure S61: Thermal stability of **I**$_6$

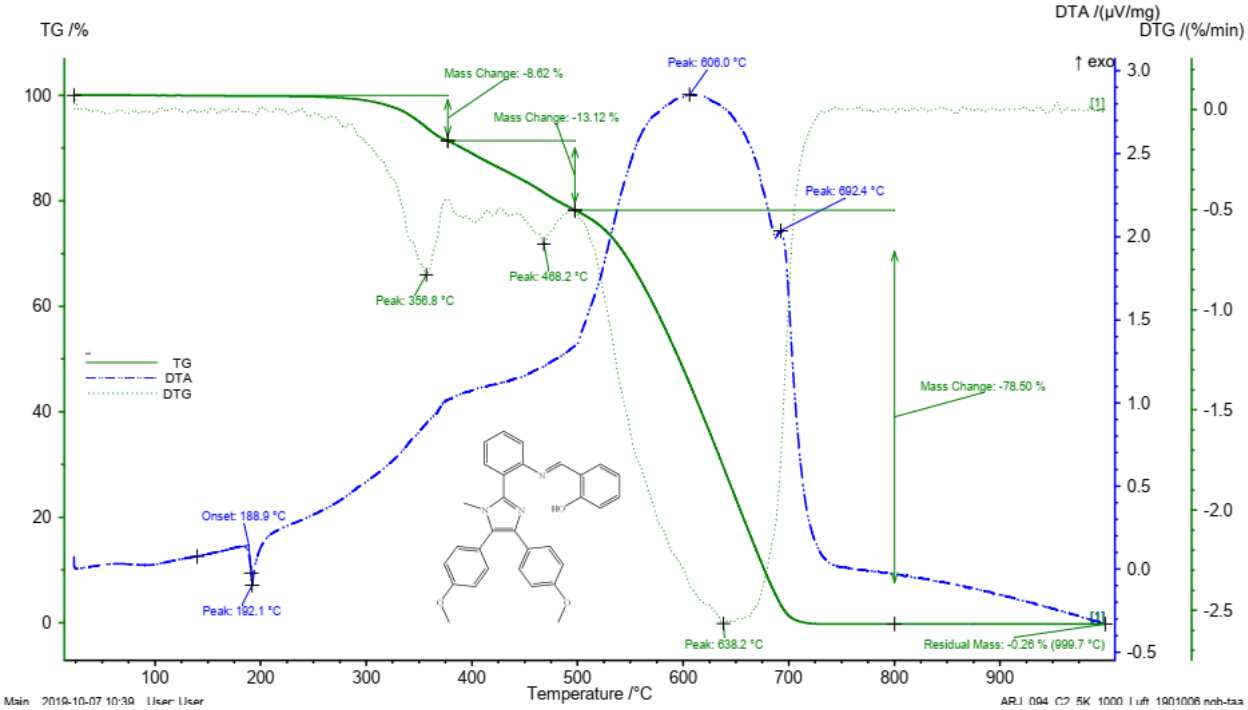

Figure S62: Thermal stability of **I**$_7$

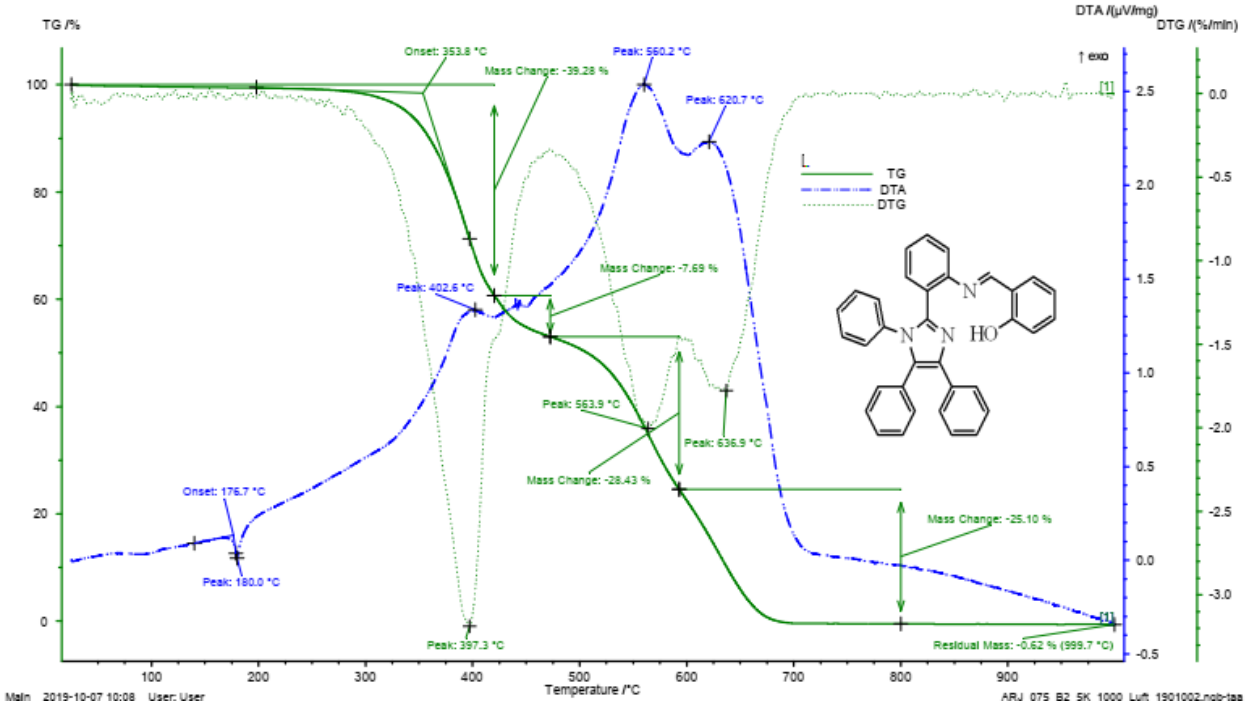

Figure S63: Thermal stability of **I**$_8$

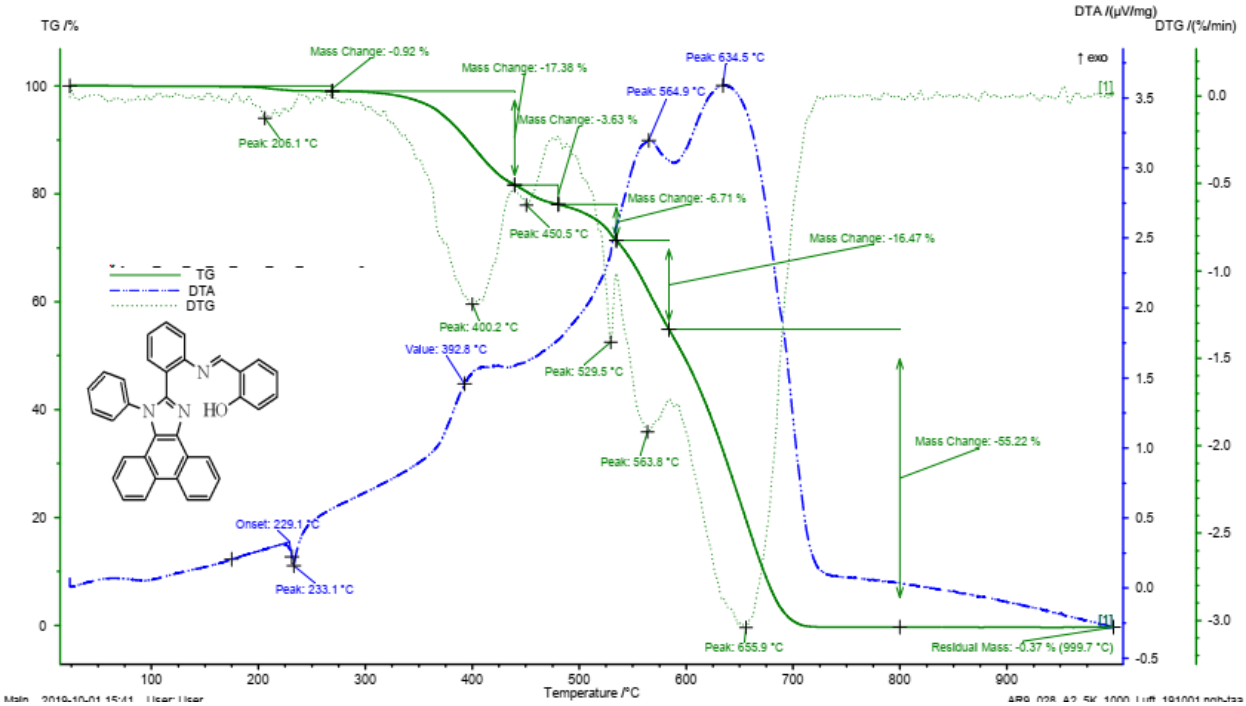

Figure S64: Thermal stability of **I9**

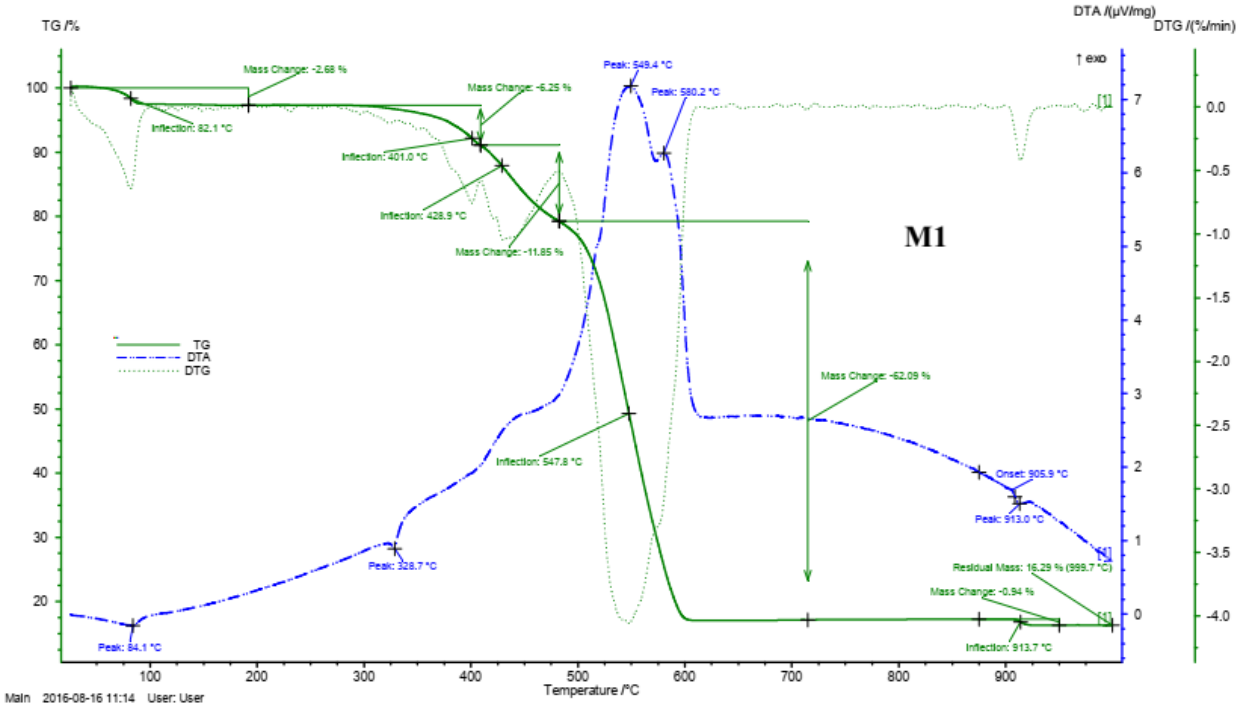

Figure S65: Thermal stability of **M1**

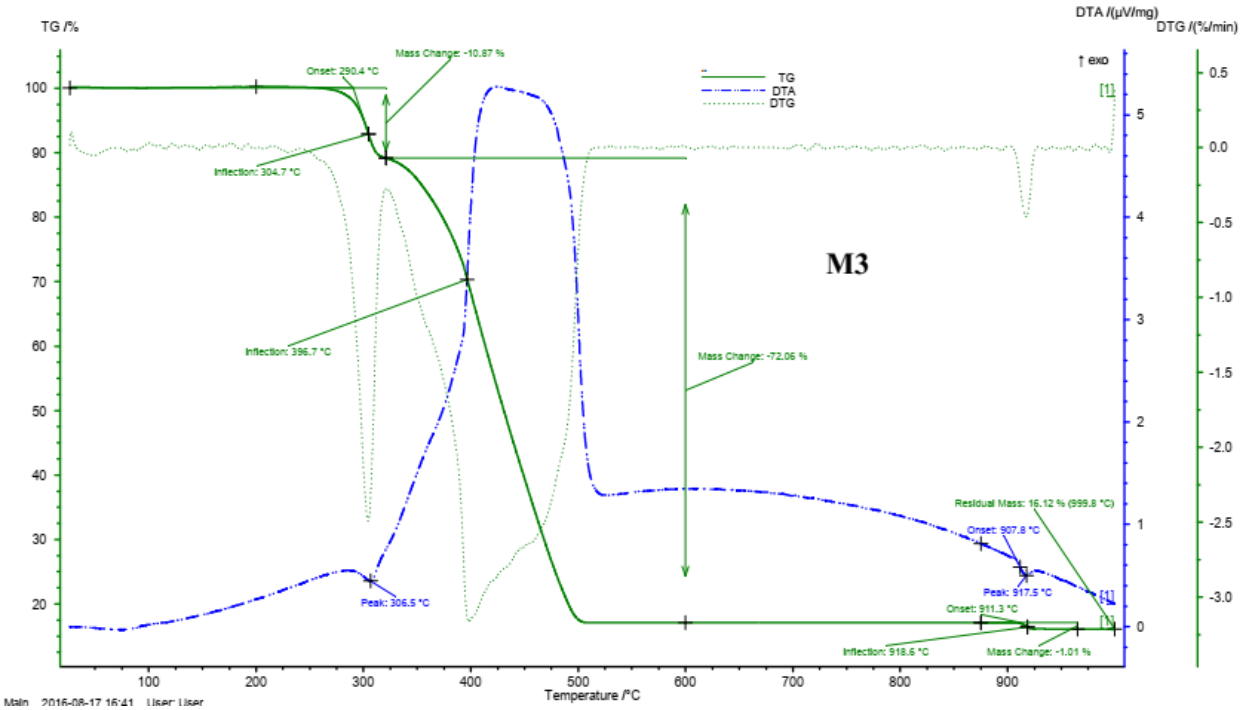

Figure S66: Thermal stability of **M3**

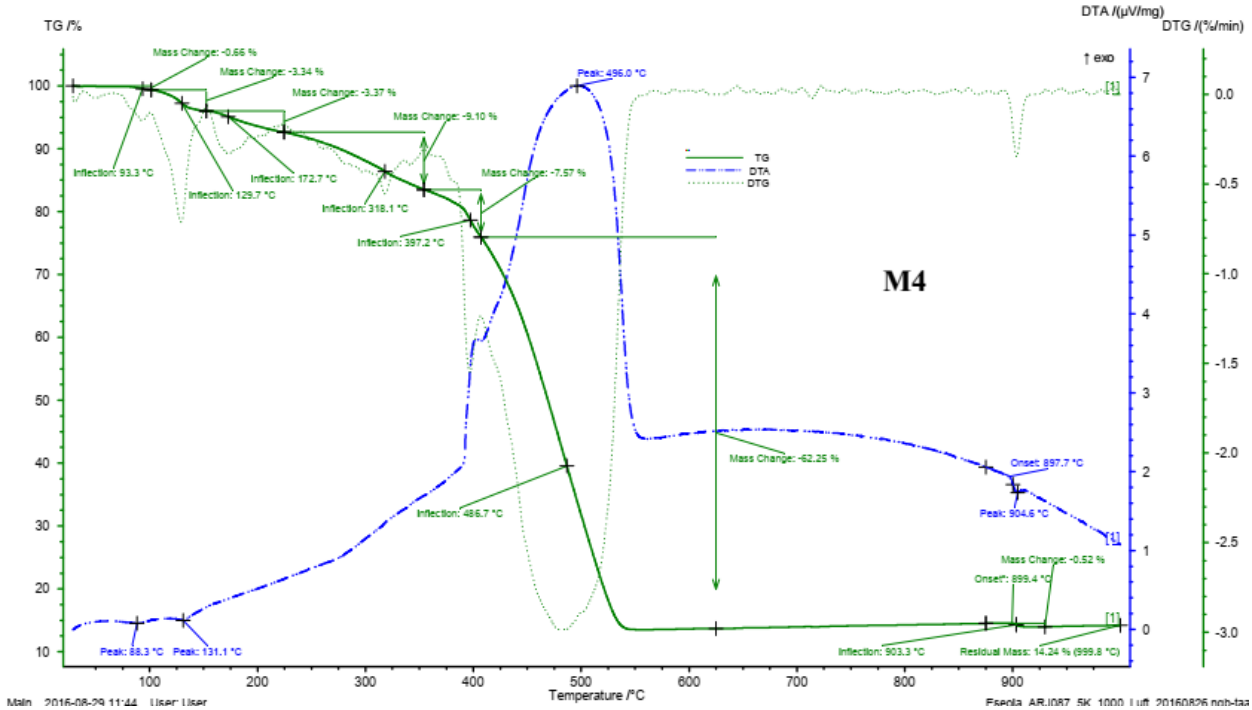

Figure S67: Thermal stability of **M4**

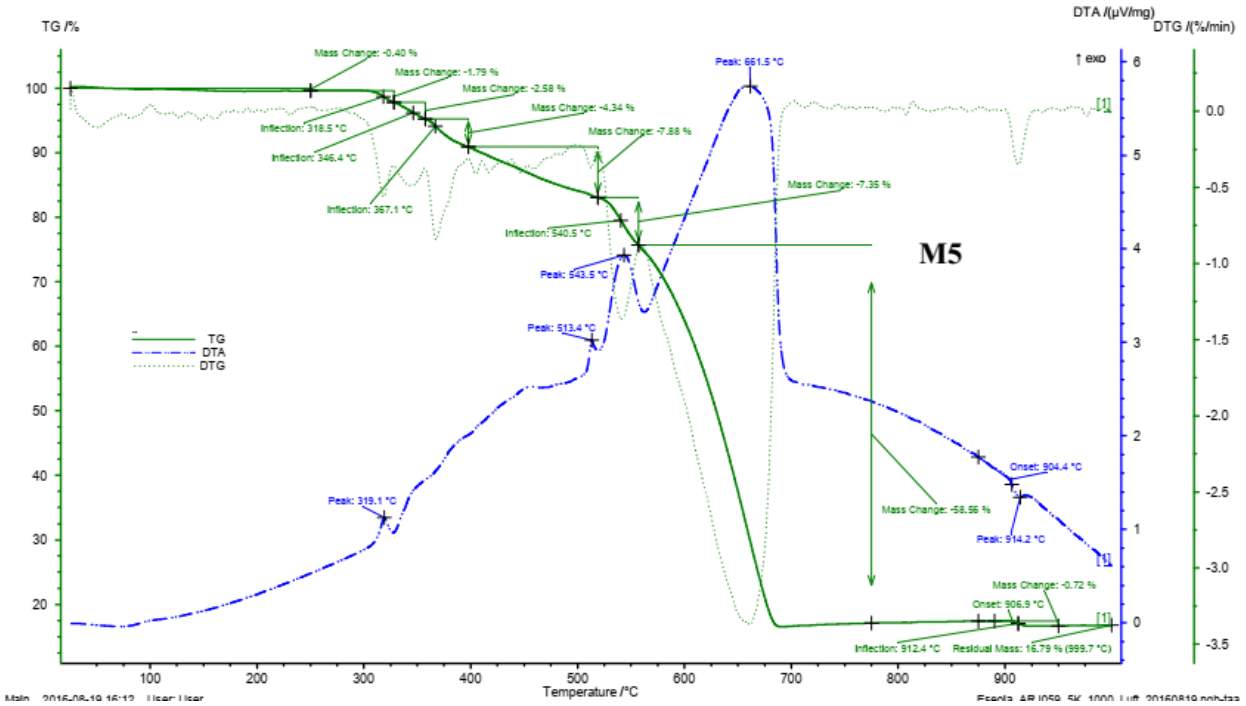

Figure S68: Thermal stability of **M5**

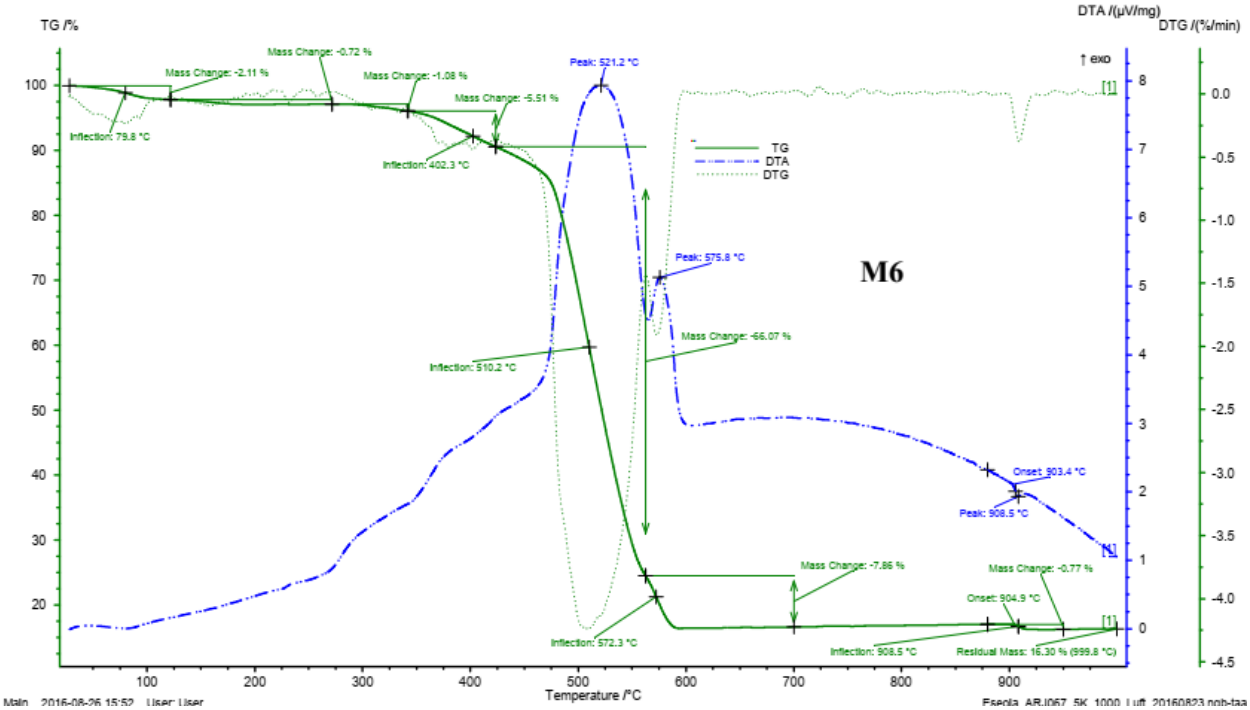

Figure S69: Thermal stability of **M6**

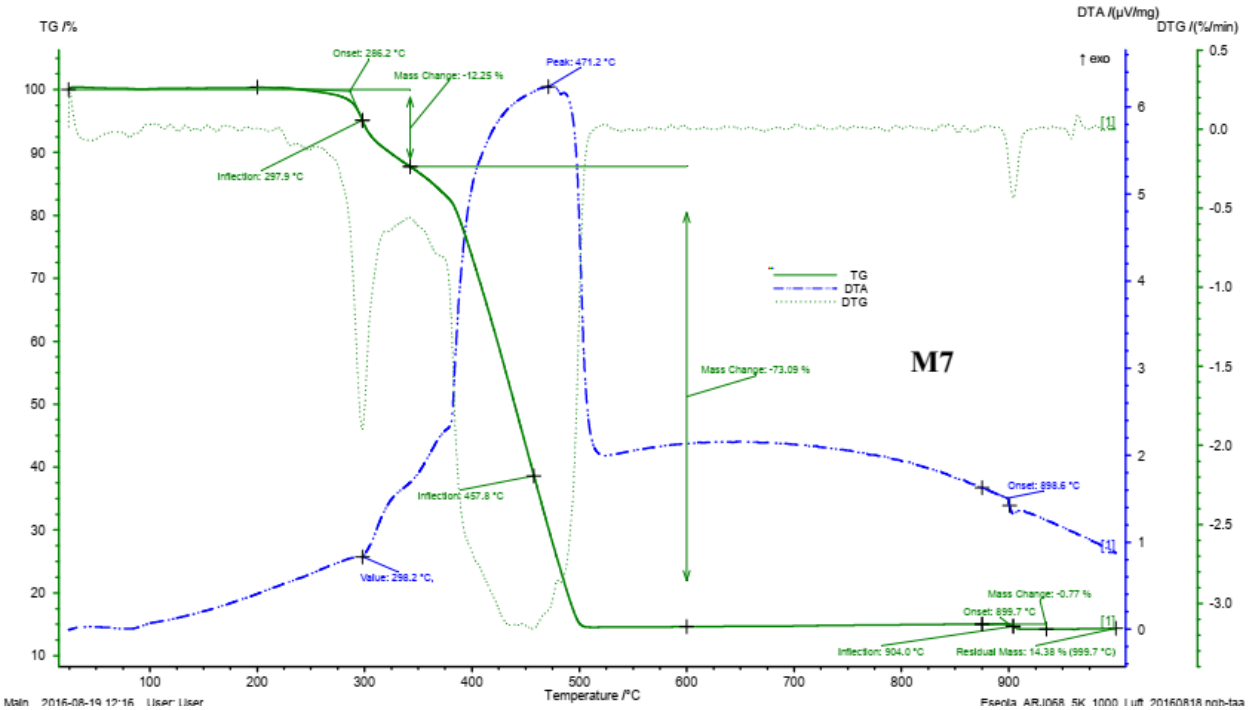

Figure S70: Thermal stability of **M7**

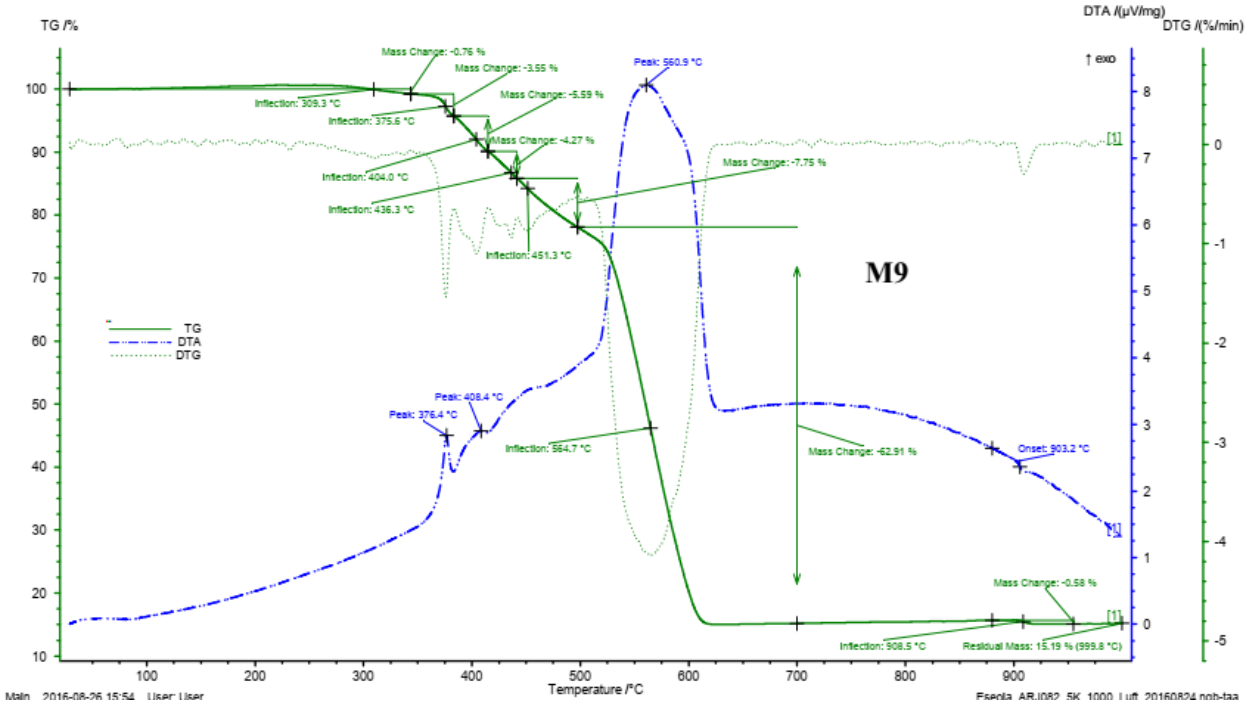

Figure S71: Thermal stability of **M9**

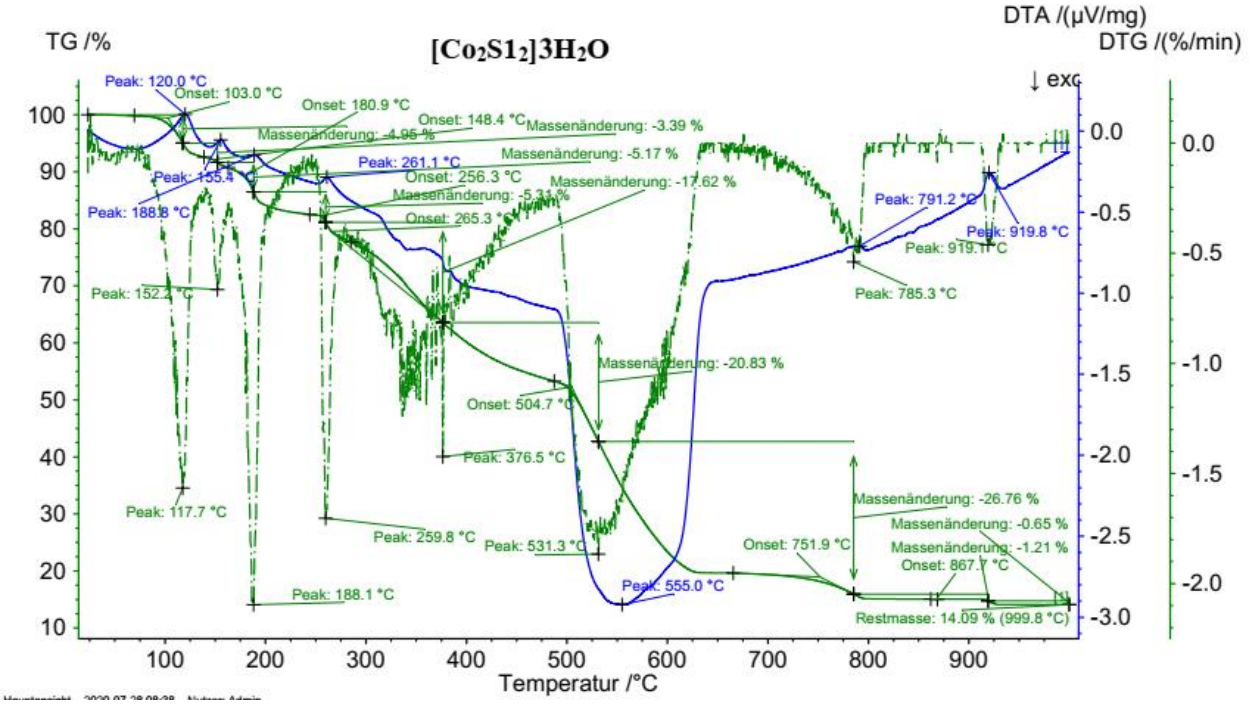

Figure S72: Thermal stability of **[Co2S12]3H2O**

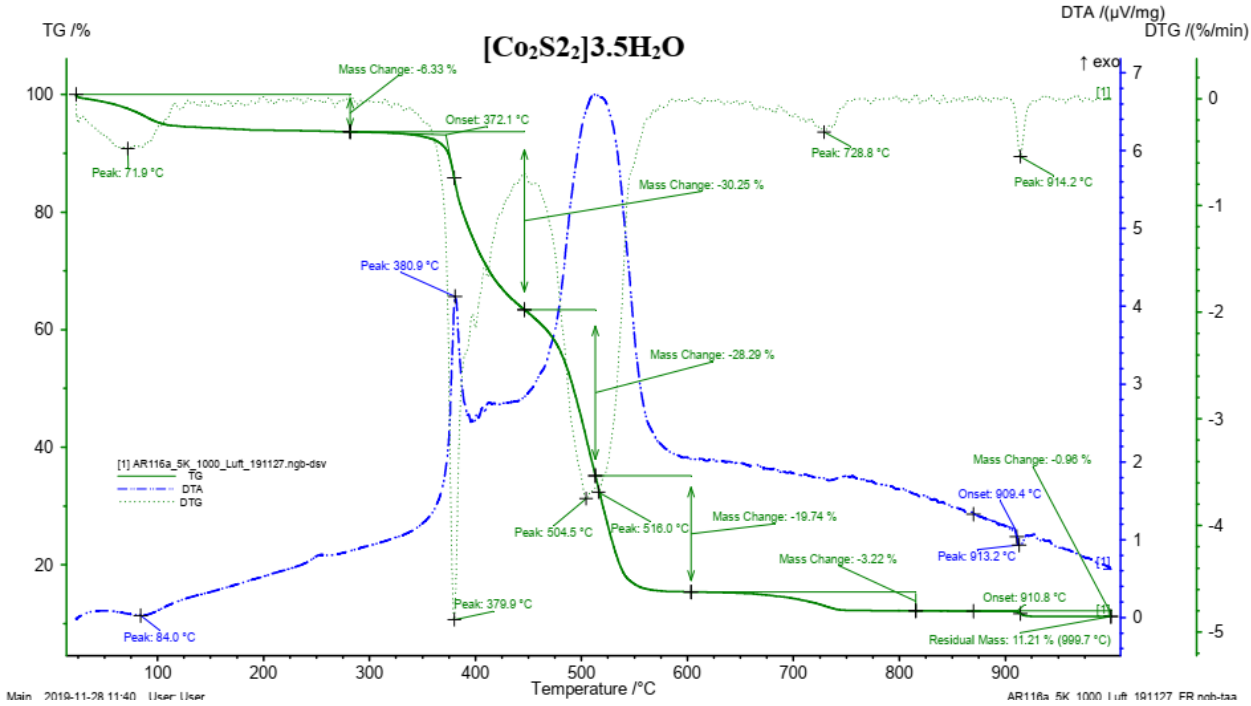

Figure S73: Thermal stability of **[Co2S2]3.5H2O**

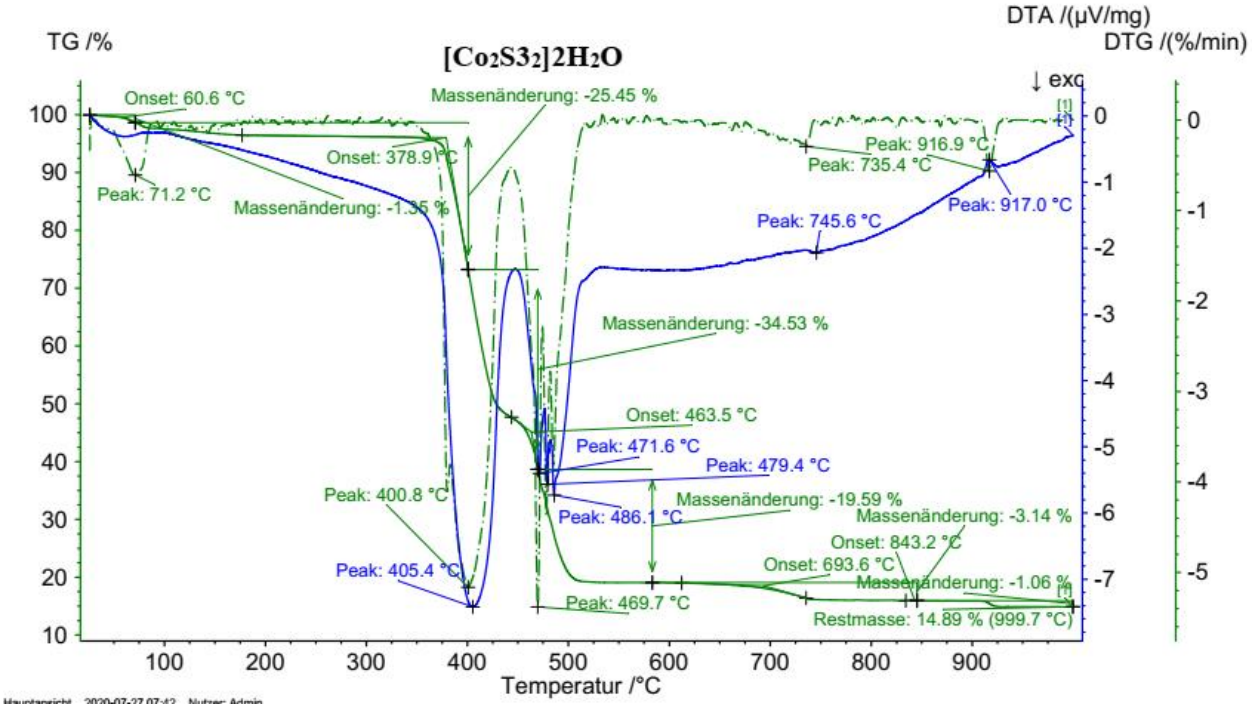

Figure S74: Thermal stability of **[Co2S3]2H2O**

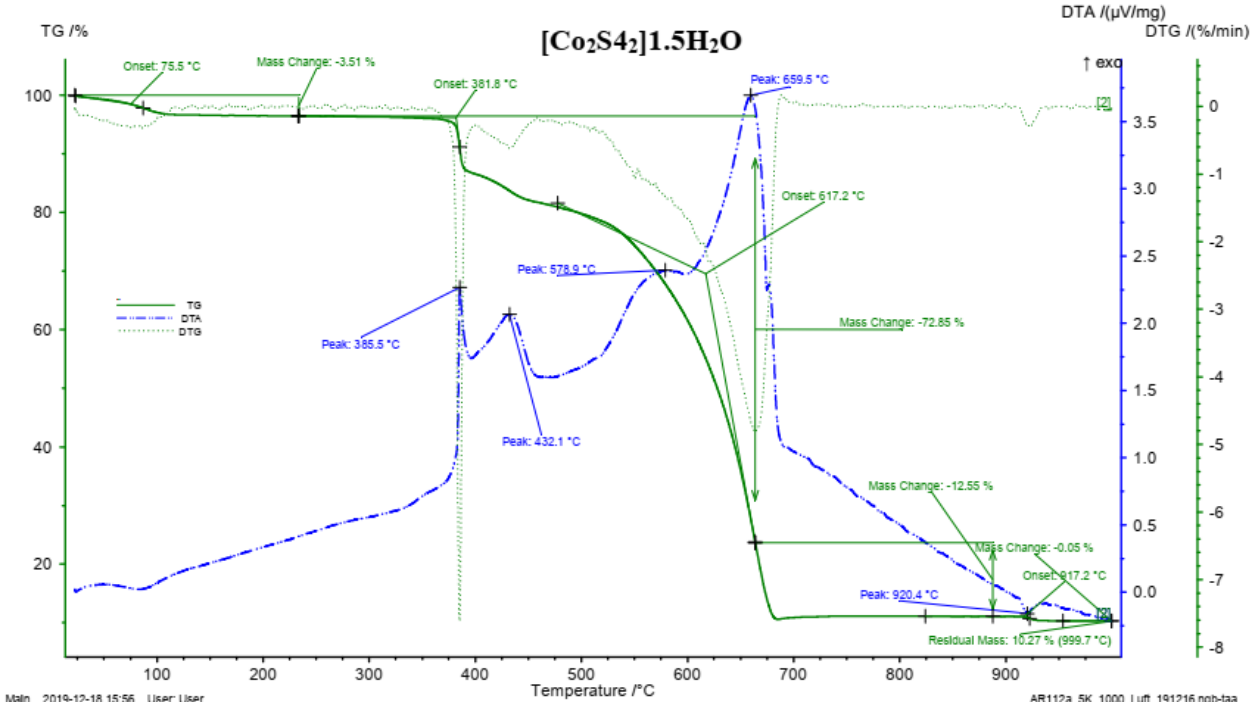

Figure S75: Thermal stability of **[Co2S4]1.5H2O**

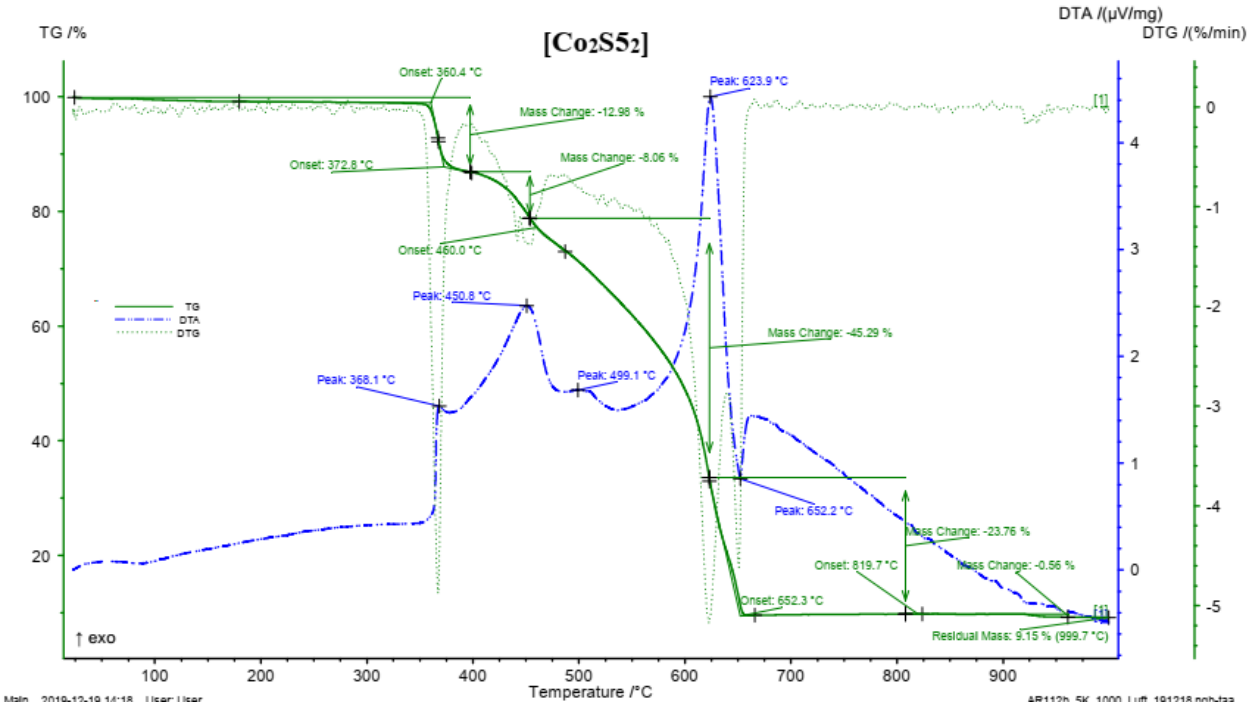

Figure S76: Thermal stability of **[Co2S52]**

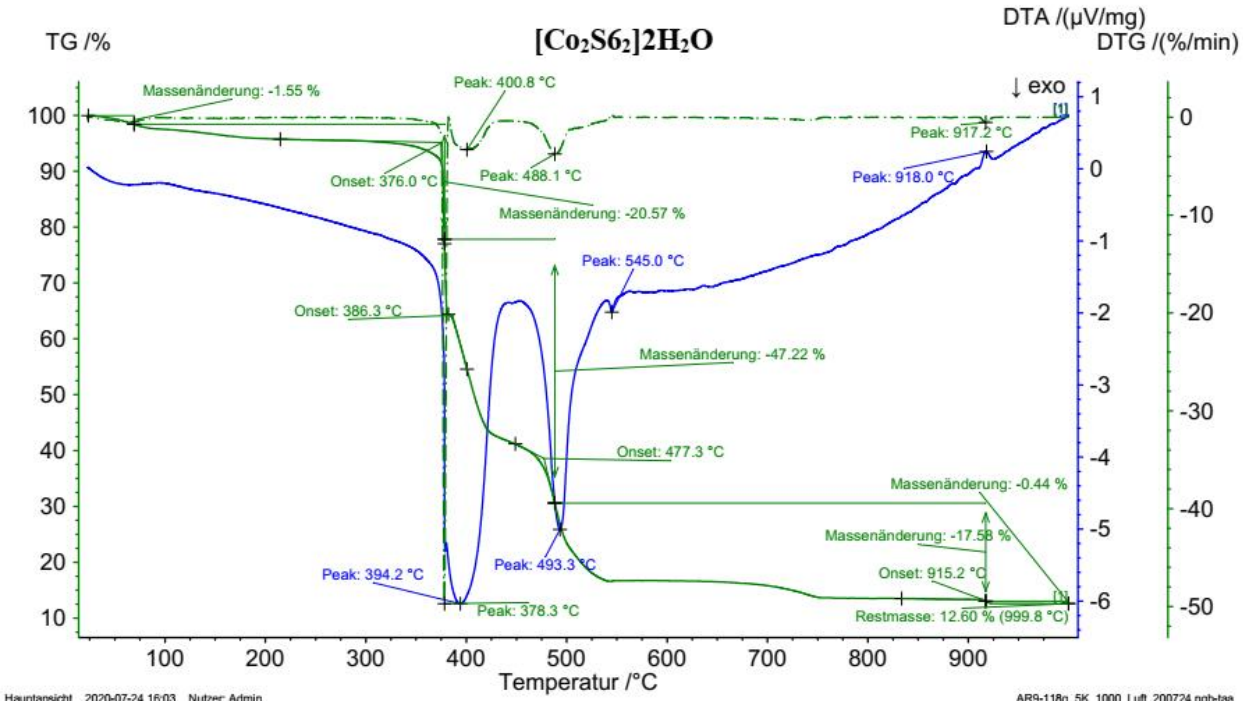

Figure S77: Thermal stability of **[Co2S62]2H2O**

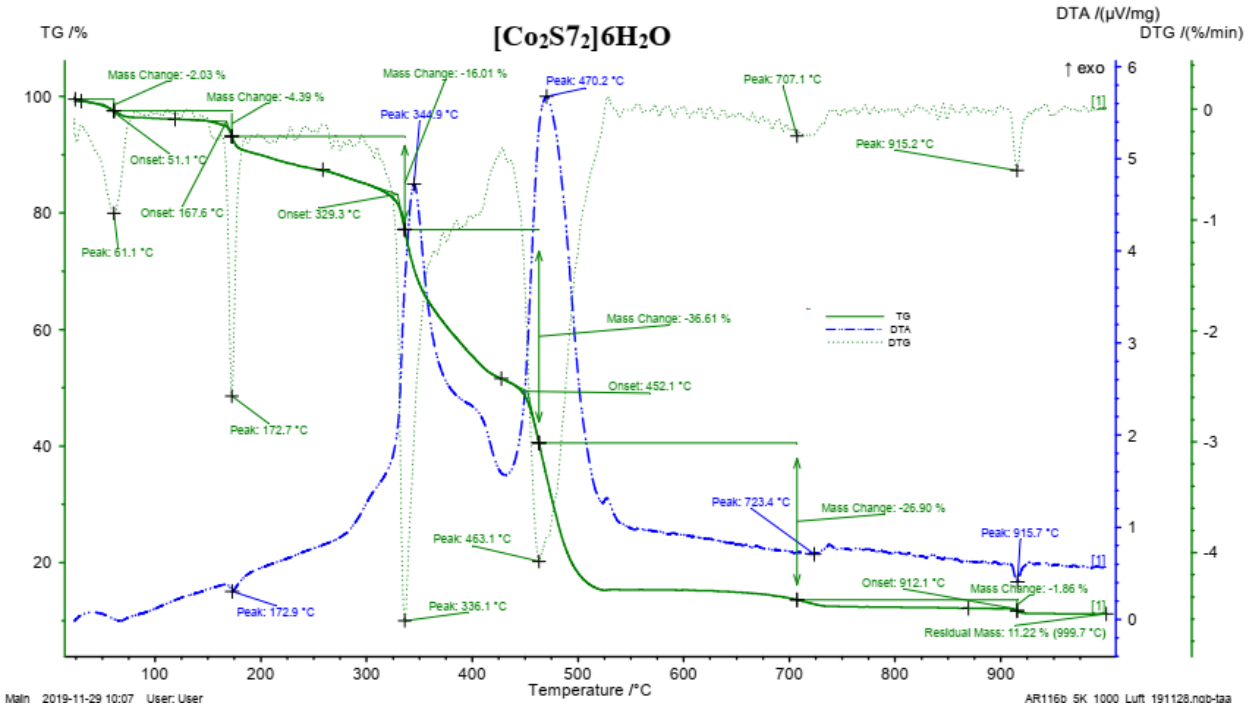

Figure S78: Thermal stability of **[Co2S72]6H2O**

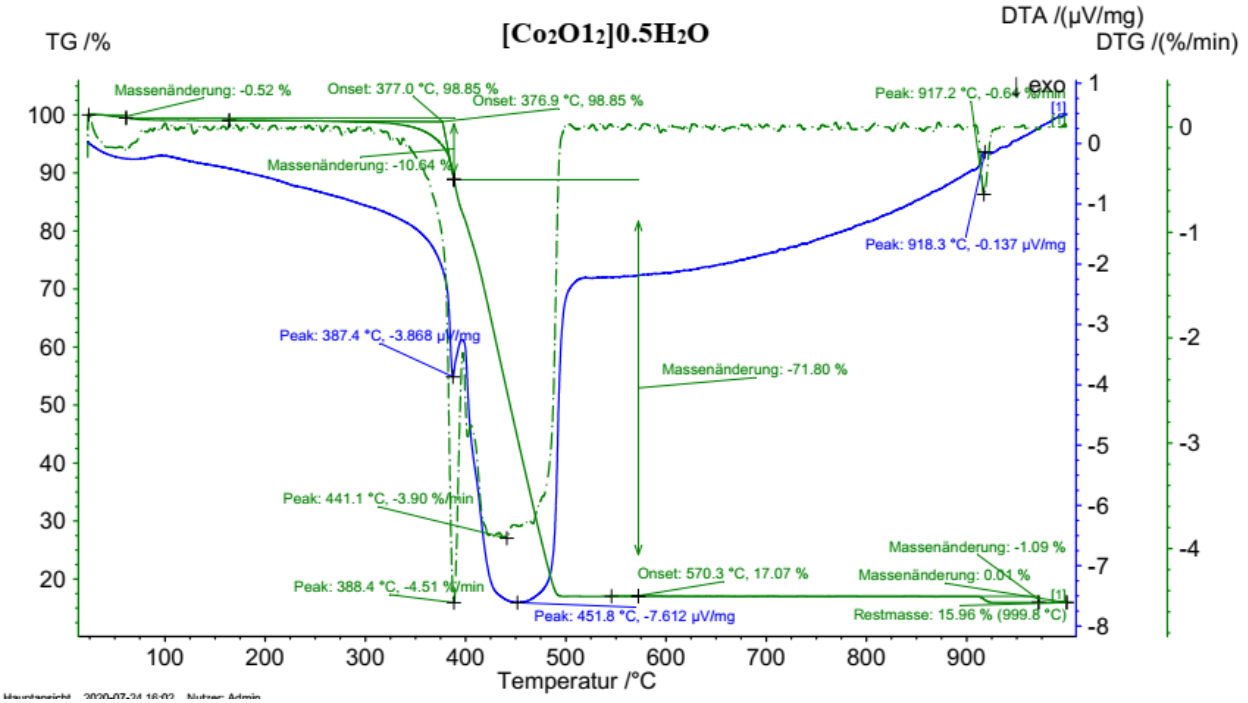

Figure S79: Thermal stability of **[Co2O12]0.5H2O**

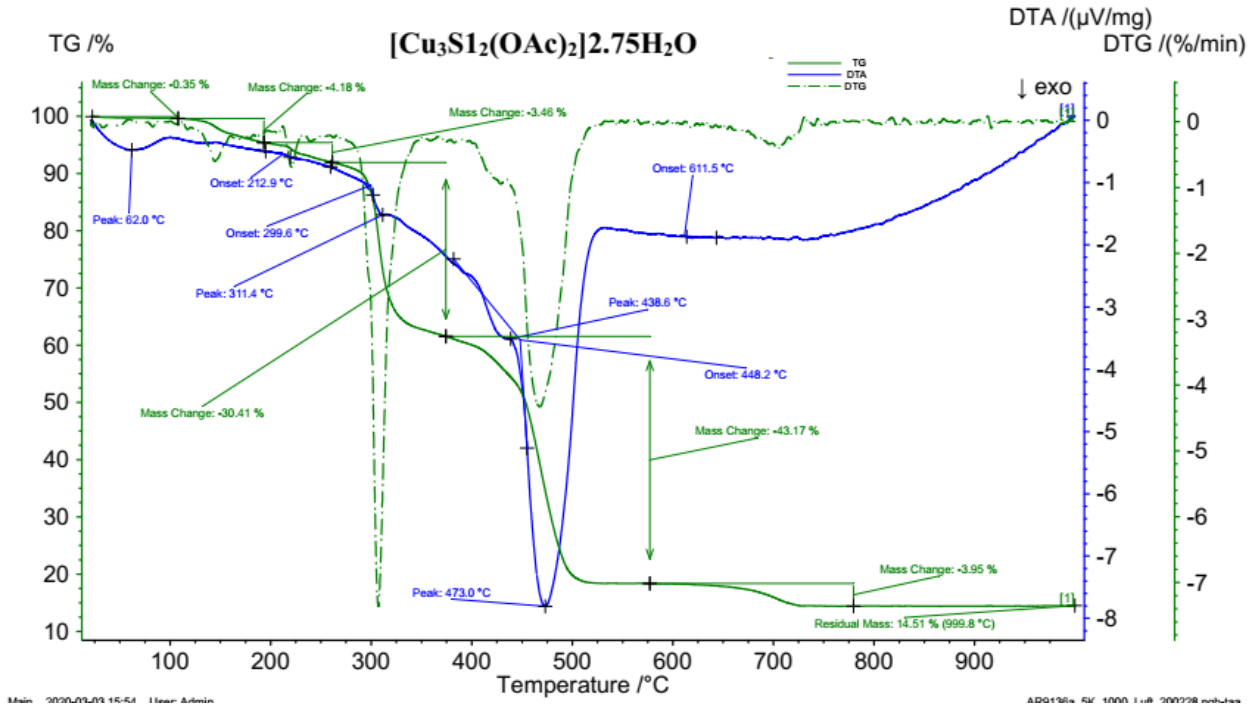

Figure S80: Thermal stability of **[Cu3S12(OAc)2]2.75H2O**

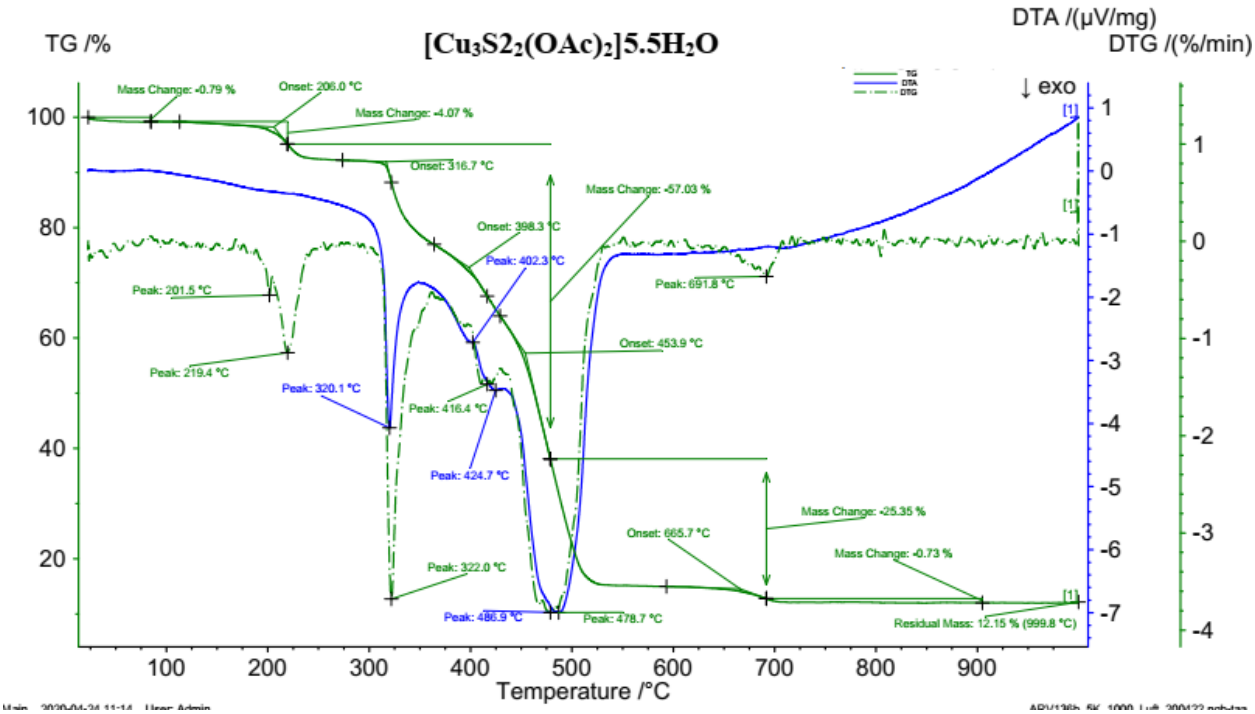

Figure S81: Thermal stability of **[Cu3S22(OAc)2]5.5H2O**

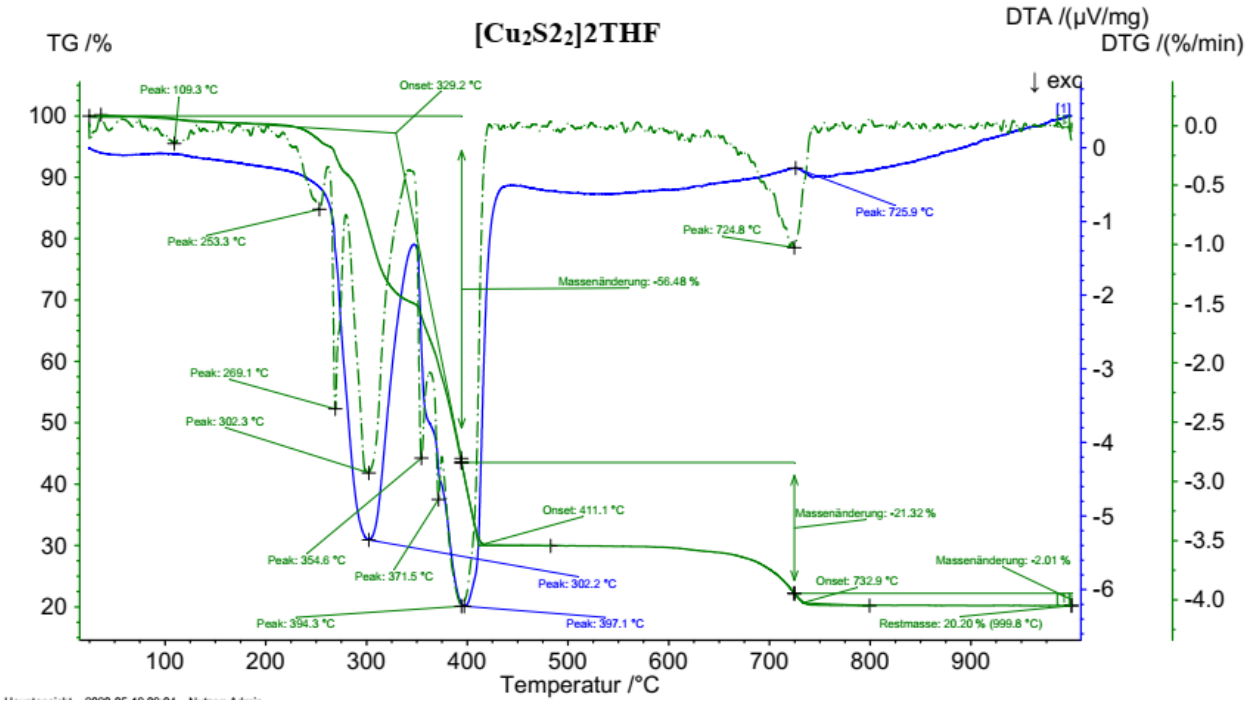

Figure S82: Thermal stability of **[Cu2S22]2THF**

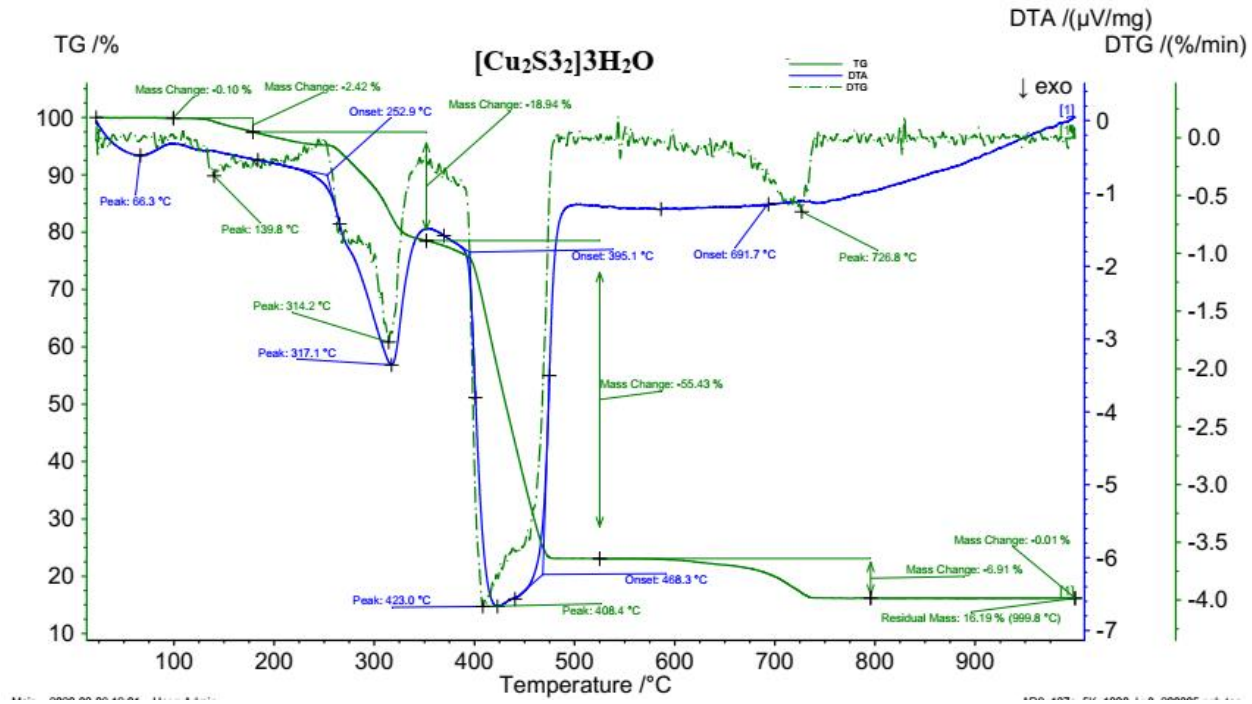

Figure S83: Thermal stability of **[Cu2S32]3H2O**

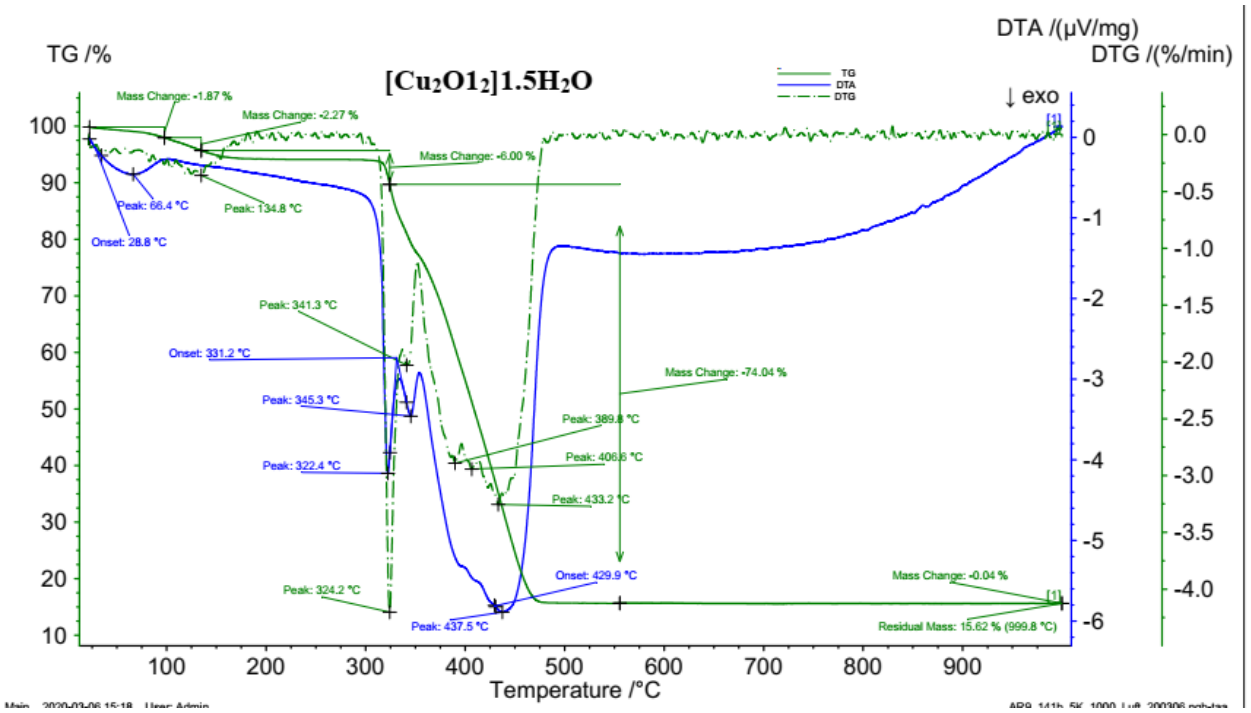

Figure S84: Thermal stability of **[Cu2O12]1.5H2O**

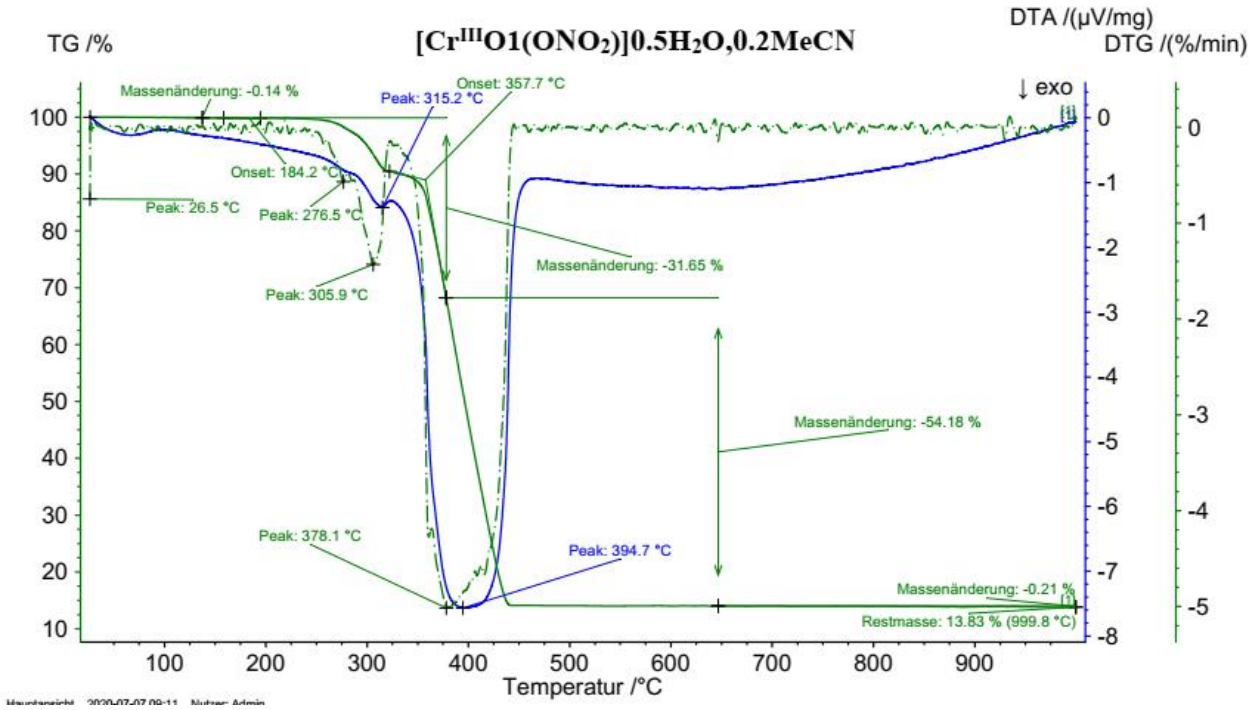

Figure S85: Thermal stability of **[Cr^{III}O1(ONO2)]0.5H2O,0.2MeCN**

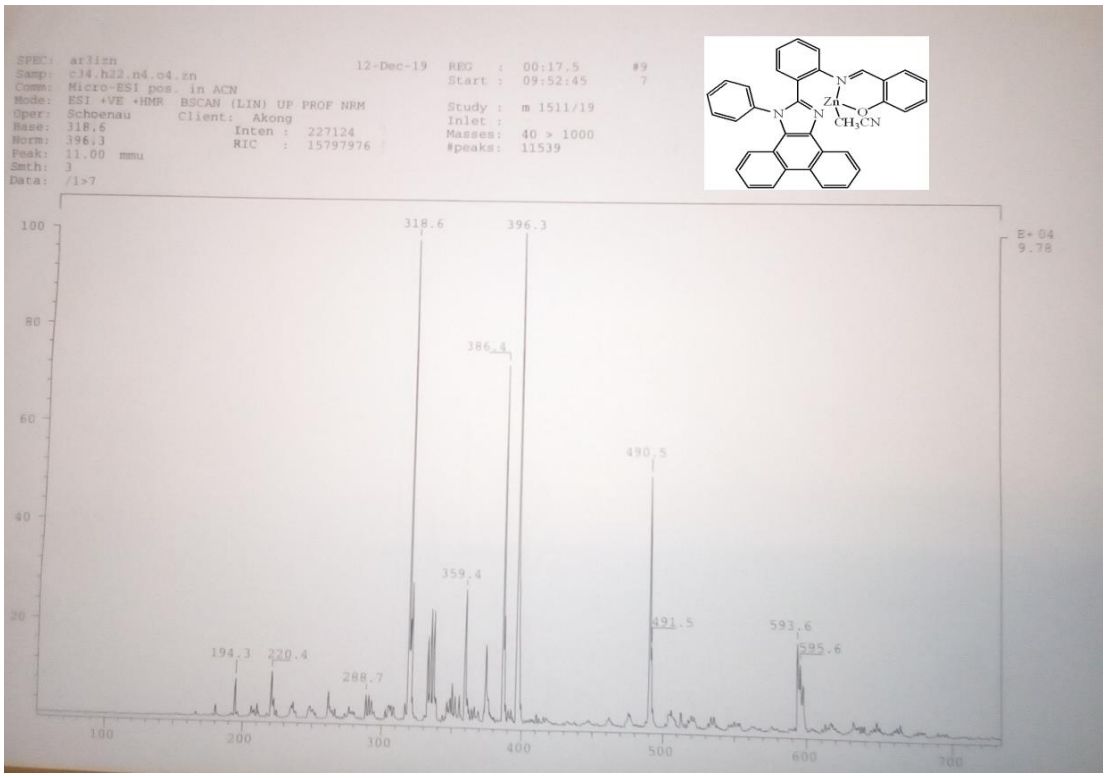

Figure S86: ESI-MS for **I$_9$**-Zn^{2+} in MeCN at 1 x 10^{-5} M

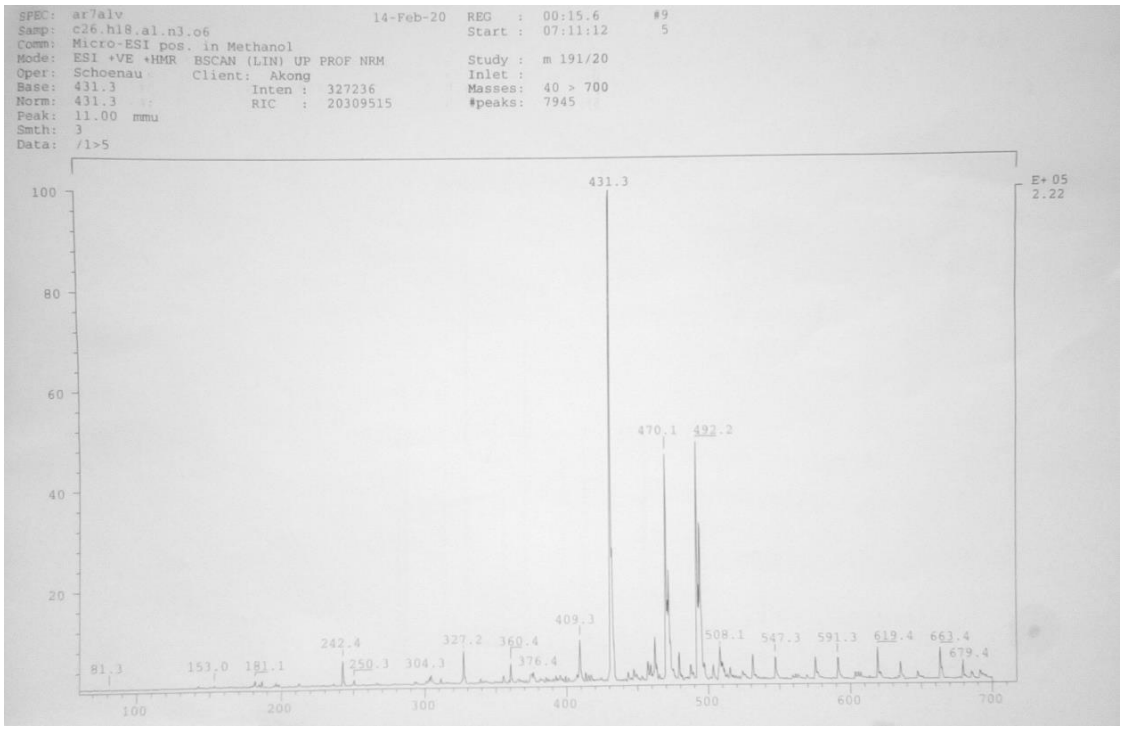

Figure S87: ESI-MS for **H$_2$O1**-Al^{3+} in MeOH at 1 x 10^{-5} M

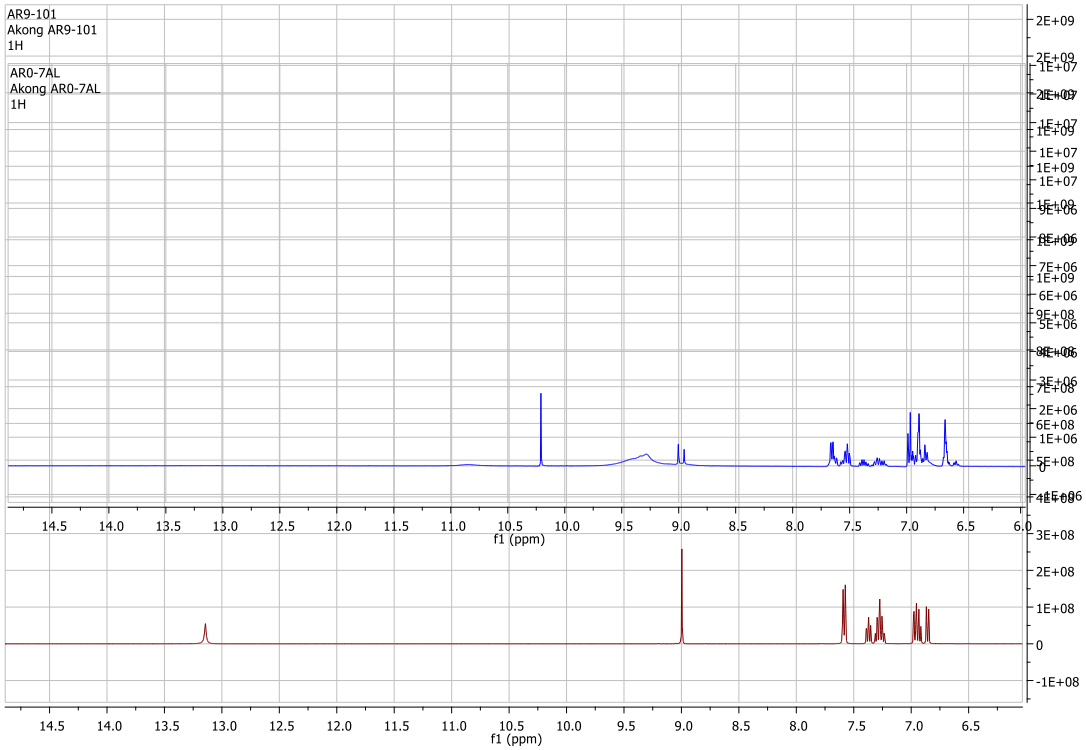

Figure S88: ^{1}H nmr spectra of **H$_2$O1** (dark red), **H$_2$O1**-Al^{3+} (blue) in DMSO.